

# Understanding complex polymer brush behaviour through improved reflectometry analysis methods

**Author:**

Gresham, Isaac

**Publication Date:**

2021

**DOI:**

<https://doi.org/10.26190/unsworks/4001>

**License:**

<https://creativecommons.org/licenses/by-nc-nd/3.0/au/>

Link to license to see what you are allowed to do with this resource.

Downloaded from <http://hdl.handle.net/1959.4/70954> in <https://unsworks.unsw.edu.au> on 2024-04-25



UNDERSTANDING COMPLEX POLYMER  
BRUSH BEHAVIOUR THROUGH IMPROVED  
REFLECTOMETRY ANALYSIS METHODS

**Isaac J. Gresham**

*A thesis submitted in fulfilment of the requirements for the  
degree of Doctor of Philosophy*

School of Chemical Engineering  
Faculty of Engineering

supervised by  
A/Prof. Stuart W. Prescott  
Dr. Andrew R.J. Nelson  
A/Prof. Patrick T. Spicer

12<sup>th</sup> March 2021

# Thesis submission for the degree of Doctor of Philosophy

Thesis Title and Abstract

Declarations

Inclusion of Publications  
Statement

Corrected Thesis and  
Responses

## Thesis Title

understanding complex polymer brush behaviour through improved reflectometry analysis methods

## Thesis Abstract

Polymer brushes are arrays of densely surface-tethered polymer chains, and are of interest for two reasons.

Firstly, they possess interfacial characteristics, such as antifouling and lubrication, that are desirable in many applications.

Secondly, they are model systems that can provide additional insight into polymer behaviour due to their unique geometry.

Observing the interfacial structure of these brush layers is critically important for understanding both their properties and the mechanisms driving the polymer behaviour.

To date, neutron reflectometry (NR) is the only technique that can demonstrably resolve the nanoscale structure of polymer brushes.

However, these diffuse interfaces produce subtle features in the reflectometry data that challenge interpretation, with typical analyses failing to quantify the derived structure's uncertainty.

Furthermore, the experimental potential of this technique for the study of brushes is only just being realised.

This Thesis advances NR as a tool for studying polymer brush systems by establishing a robust analysis methodology that overcomes previous hurdles and demonstrating novel experimental techniques.

In both cases, poly(*N*-isopropylacrylamide) (PNIPAM) brushes are used as model systems.

First, the polymer system is characterised through the novel observation of surface-initiated ARGET ATRP using time-resolved NR, and a study of the dry brush as a function of humidity and temperature.

Second, methodologies are developed that allow for robust determination of both solvated and confined brush structures.

Lastly, NR is used to elucidate the behaviour of PNIPAM brushes in complex environments.

A novel confinement apparatus is used to investigate the structure of a PNIPAM brush under mechanical confinement and contrast-variation provides unparalleled insight into PNIPAM–surfactant systems.

In each case, complementary techniques are essential in guiding reflectometry experiments and fully understanding the polymer system.

This work develops and demonstrates techniques that enhance the study of diffuse interfaces with the NR technique.

Moreover, the holistic structural examination of PNIPAM undertaken sheds new light on the phase behaviour of this ostensibly well-understood polymer and highlights its rich interaction with surfactants.



Thesis Title and Abstract	Declarations	Inclusion of Publications Statement	Corrected Thesis and Responses
---------------------------	--------------	-------------------------------------	--------------------------------

ORIGINALITY STATEMENT

☒ I hereby declare that this submission is my own work and to the best of my knowledge it contains no materials previously published or written by another person, or substantial proportions of material which have been accepted for the award of any other degree or diploma at UNSW or any other educational institution, except where due acknowledgement is made in the thesis. Any contribution made to the research by others, with whom I have worked at UNSW or elsewhere, is explicitly acknowledged in the thesis. I also declare that the intellectual content of this thesis is the product of my own work, except to the extent that assistance from others in the project's design and conception or in style, presentation and linguistic expression is acknowledged.

COPYRIGHT STATEMENT

☒ I hereby grant the University of New South Wales or its agents a non-exclusive licence to archive and to make available (including to members of the public) my thesis or dissertation in whole or part in the University libraries in all forms of media, now or here after known. I acknowledge that I retain all intellectual property rights which subsist in my thesis or dissertation, such as copyright and patent rights, subject to applicable law. I also retain the right to use all or part of my thesis or dissertation in future works (such as articles or books).

For any substantial portions of copyright material used in this thesis, written permission for use has been obtained, or the copyright material is removed from the final public version of the thesis.

AUTHENTICITY STATEMENT

☒ I certify that the Library deposit digital copy is a direct equivalent of the final officially approved version of my thesis.



# Thesis submission for the degree of Doctor of Philosophy

Thesis Title and Abstract	Declarations	Inclusion of Publications Statement	Corrected Thesis and Responses
---------------------------	--------------	-------------------------------------	--------------------------------

UNSW is supportive of candidates publishing their research results during their candidature as detailed in the UNSW Thesis Examination Procedure.

Publications can be used in the candidate's thesis in lieu of a Chapter provided:

- The candidate contributed **greater than 50%** of the content in the publication and are the "primary author", i.e. they were responsible primarily for the planning, execution and preparation of the work for publication.
- The candidate has obtained approval to include the publication in their thesis in lieu of a Chapter from their Supervisor and Postgraduate Coordinator.
- The publication is not subject to any obligations or contractual agreements with a third party that would constrain its inclusion in the thesis.

☒ The candidate has declared that **some of the work described in their thesis has been published and has been documented in the relevant Chapters with acknowledgement.**

A short statement on where this work appears in the thesis and how this work is acknowledged within chapter/s:

Chapters 3 and 4 are adapted from published works, the titles and DOIs of which are included at the start of the chapter. The names of the coauthors have been included at the beginning of the chapter, as well as in the section titled 'output of this PhD'. These details are also present in the frontmatter section titled 'Output of candidature'.

## Candidate's Declaration



I declare that I have complied with the Thesis Examination Procedure.

I hold two parties primarily responsible for this Thesis:

Heather and Simon Gresham, without whom it would never have been started, and  
Frederick Banting, without whom it would never have been finished.

Blame them.

# Abstract

Polymer brushes are arrays of densely surface-tethered polymer chains, and are of interest for two reasons. Firstly, they possess interfacial characteristics, such as antifouling and lubrication, that are desirable in many applications. Secondly, they are model systems that can provide additional insight into polymer behaviour due to their unique geometry. Observing the interfacial structure of these brush layers is critically important for understanding both their properties and the mechanisms driving the polymer behaviour.

To date, neutron reflectometry (NR) is the only technique that can demonstrably resolve the nanoscale structure of polymer brushes. However, these diffuse interfaces produce subtle features in the reflectometry data that challenge interpretation, with typical analyses failing to quantify the derived structure's uncertainty. Furthermore, the experimental potential of this technique for the study of brushes is only just being realised. This Thesis advances NR as a tool for studying polymer brush systems by establishing a robust analysis methodology that overcomes previous hurdles and demonstrating novel experimental techniques. In both cases, poly(*N*-isopropylacrylamide) (PNIPAM) brushes are used as model systems.

First, the polymer system is characterised through the novel observation of surface-initiated ARGET ATRP using time-resolved NR, and a study of the dry brush as a function of humidity and temperature. Second, methodologies are developed that allow for robust determination of both solvated and confined brush structures. Lastly, NR is used to elucidate the behaviour of PNIPAM brushes in complex environments. A novel confinement apparatus is used to investigate the structure of a PNIPAM brush under mechanical confinement and contrast-variation provides unparalleled insight into PNIPAM–surfactant systems. In each case, complementary techniques are essential in guiding reflectometry experiments and fully understanding the polymer system.

This work develops and demonstrates techniques that enhance the study of diffuse interfaces with the NR technique. Moreover, the holistic structural examination of PNIPAM undertaken sheds new light on the phase behaviour of this ostensibly well-understood polymer and highlights its rich interaction with surfactants.



# Contents

Acknowledgements . . . . .	vii
Output of candidature . . . . .	x
List of figures . . . . .	xiii
List of tables . . . . .	xx
<b>1 Introduction</b>	<b>1</b>
1.1 Polymer brushes . . . . .	3
1.1.1 Defining a polymer brush . . . . .	3
1.1.2 Why study brushes? . . . . .	4
1.1.3 Theoretical descriptions of neutral brush structure . . . . .	5
1.2 The phase behaviour of PNIPAM . . . . .	8
1.2.1 Free polymer . . . . .	10
1.2.2 Brush regime . . . . .	12
1.3 Materials . . . . .	13
1.4 Methods: PNIPAM synthesis via ARGET-ATRP . . . . .	14
1.4.1 Determination of molecular weight and grafting density . . . . .	16
1.5 Methods: experimental techniques . . . . .	18
1.5.1 Characterisation of polymer brushes . . . . .	18
1.5.2 Principles of reflectometry . . . . .	19
1.5.3 Neutron reflectometry . . . . .	20
1.5.4 X-ray reflectometry . . . . .	22
1.5.5 Ellipsometry . . . . .	22
1.5.6 Quartz crystal microbalance with dissipation monitoring . . . . .	23
1.6 Overall structure of this thesis . . . . .	26
<b>2 Grafting density control and <i>in situ</i> observation of surface-initiated ATRP</b>	<b>27</b>
2.1 Theoretical background . . . . .	29
2.1.1 Bimodality in surface-initiated ARGET ATRP . . . . .	29
2.1.2 Origin of the interior layer . . . . .	30
2.1.3 Initiation efficiency . . . . .	32

2.2	Materials and Methods . . . . .	34
2.2.1	Materials . . . . .	34
2.2.2	Synthetic details . . . . .	34
2.2.3	Bromination kinetics . . . . .	34
2.2.4	Preparation of molecular weight gradient brushes . . . . .	35
2.2.5	Variation of initiator density . . . . .	36
2.2.6	<i>In situ</i> NR synthesis . . . . .	38
2.2.7	Neutron reflectometry experiments . . . . .	39
2.2.8	Neutron reflectometry data analysis . . . . .	40
2.2.9	Interferometry . . . . .	41
2.3	Results . . . . .	42
2.3.1	Bromination kinetics . . . . .	42
2.3.2	Polymerisation kinetics . . . . .	42
2.3.3	Grafting density control . . . . .	44
2.3.4	<i>In situ</i> measurements . . . . .	45
2.3.5	Characterisation of resulting brush layers . . . . .	50
2.3.6	Origin of the interior layer . . . . .	51
2.4	Conclusion . . . . .	53
<b>3</b>	<b>Swelling of a thermosensitive polymer brush at different relative hu-</b>	
	<b>midities of water</b>	<b>55</b>
3.1	Theoretical background . . . . .	57
3.1.1	Relative Humidity . . . . .	57
3.1.2	Water content of polymer films at ambient conditions . . . . .	58
3.1.3	Swelling of polymer films at different solvent vapour pressures . . . . .	58
3.1.4	Determination of $\chi$ parameter from film swelling . . . . .	62
3.2	Method . . . . .	63
3.2.1	QCM-D . . . . .	63
3.2.2	Neutron reflectometry . . . . .	65
3.3	Results . . . . .	68
3.3.1	QCM-D . . . . .	68
3.3.2	Neutron reflectometry . . . . .	70
3.3.3	Calculation of $\chi$ parameter . . . . .	74
3.3.4	Implications for analysis of dry brushes . . . . .	75
3.4	Conclusion . . . . .	75

<b>4</b>	<b>Robust analysis of neutron reflectometry collected from polymer brushes</b>	<b>77</b>
4.1	Theoretical background . . . . .	79
4.1.1	Bayesian inference in neutron reflectometry modelling . . . . .	80
4.1.2	Parameterisation of reflectometry models . . . . .	83
4.1.3	Optimisation and uncertainty quantification . . . . .	84
4.2	Method . . . . .	86
4.2.1	Freeform volume fraction model . . . . .	86
4.2.2	Line simplification algorithm . . . . .	89
4.2.3	Simulating reflectometry from theoretical profiles . . . . .	90
4.2.4	Neutron reflectometry measurements . . . . .	91
4.2.5	Optimisation and sampling techniques . . . . .	92
4.2.6	Modelling of an exemplar PNIPAM system . . . . .	93
4.3	Results . . . . .	95
4.3.1	Model validation with synthesised dataset . . . . .	95
4.3.2	Determination of model complexity for a PNIPAM brush . . . . .	96
4.3.3	Modelling of the thermal collapse of PNIPAM . . . . .	98
4.3.4	Multimodality . . . . .	100
4.3.5	Effect of interfacial volume constraint . . . . .	101
4.3.6	Sensitivity to the diffuse tail . . . . .	102
4.3.7	Evolution of posterior probability during sampling . . . . .	103
4.3.8	Best practice . . . . .	106
4.4	Conclusion . . . . .	108
<b>5</b>	<b>Geometrical confinement modulates the thermoresponse of a PNIPAM brush</b>	<b>109</b>
5.1	Theoretical background . . . . .	111
5.2	Materials and Methods . . . . .	113
5.2.1	Materials . . . . .	113
5.2.2	Sample characterisation . . . . .	113
5.2.3	Neutron Reflectometry . . . . .	113
5.2.4	Confinement cell . . . . .	114
5.2.5	Neutron reflectometry data analysis . . . . .	115
5.2.6	Colloid probe modelling . . . . .	121
5.2.7	Self-consistent field theory . . . . .	125
5.3	Results . . . . .	127
5.3.1	Self-consistent field theory . . . . .	128
5.3.2	Stress-separation curves from colloid-probe AFM . . . . .	128



5.3.3	Reflectometry from a confined PNIPAM brush . . . . .	129
5.3.4	Behaviour of PNIPAM under confinement . . . . .	134
5.3.5	Brush recovery . . . . .	136
5.4	Conclusions . . . . .	138
<b>6</b>	<b>Investigation of the complex structures formed by mixtures of PNIPAM and surfactant</b>	<b>139</b>
6.1	Theoretical Background . . . . .	141
6.1.1	Surfactants: an overview . . . . .	141
6.1.2	Phenomenological studies of surfactant-polymer systems . . . . .	143
6.1.3	Structural studies of surfactant-polymer systems . . . . .	146
6.1.4	Chemical studies of surfactant-polymer systems . . . . .	146
6.1.5	Models for surfactant-PNIPAM interaction . . . . .	148
6.1.6	Effect of ionic strength on surfactant-polymer behaviour . . . . .	150
6.1.7	Implications of the brush geometry . . . . .	151
6.1.8	Open questions . . . . .	152
6.2	Materials and methods . . . . .	153
6.2.1	Materials . . . . .	153
6.2.2	Determination of optical parameters for surfactant solutions . . . . .	153
6.2.3	Fixed angle optical reflectometry . . . . .	153
6.2.4	Ellipsometry . . . . .	155
6.2.5	Quartz crystal microbalance with dissipation monitoring . . . . .	158
6.2.6	Neutron reflectometry . . . . .	158
6.2.7	Analysis of reflectometry data . . . . .	160
6.3	Results: Surfactant identity and concentration . . . . .	161
6.3.1	Ellipsometry . . . . .	161
6.3.2	Quartz crystal microbalance with dissipation monitoring . . . . .	164
6.3.3	Fixed-angle optical reflectometry . . . . .	166
6.3.4	Neutron Reflectometry . . . . .	169
6.3.5	Discussion . . . . .	177
6.4	Results: Effect of SDS on the confined behaviour of a PNIPAM brush . . .	181
6.4.1	Neutron Reflectometry . . . . .	181
6.4.2	Discussion . . . . .	184
6.5	Results: Effect of ionic strength . . . . .	187
6.5.1	Ellipsometry . . . . .	188
6.5.2	Quartz crystal microbalance with dissipation monitoring . . . . .	193
6.5.3	Neutron reflectometry . . . . .	196

6.5.4	Discussion . . . . .	200
6.6	Conclusion . . . . .	206
6.6.1	Understanding PNIPAM-surfactant systems . . . . .	206
6.6.2	Demonstration of improved NR analysis . . . . .	208
<b>7</b>	<b>Conclusions and future work</b>	<b>209</b>
7.1	Conclusions . . . . .	210
7.2	Future work . . . . .	212
	<b>Appendices</b>	<b>215</b>
A	Tabulated SLD values . . . . .	216
B	Definition of $\chi^2$ . . . . .	217
C	<i>In situ</i> polymerisation method development . . . . .	218
C1	Neutron Reflectometry . . . . .	218
C2	Solution exchange . . . . .	218
D	Determining $T_{\text{vap}}$ in chapter 3 . . . . .	220
E	Wafer characterisation . . . . .	222
F	<i>refellips</i> . . . . .	233
G	Implications of variable partial volumes (non-ideal mixing) . . . . .	235
H	QCM-D time-series . . . . .	240
H1	Surfactant identity . . . . .	240
H2	SDS temperature sweep . . . . .	244
H3	SDS-NaCl . . . . .	249
I	Recovery of brush after confinement in section 6.4 . . . . .	250
J	Python code required for replication of analysis . . . . .	251
J1	Freeform modelling where the adsorbed amount is not known from chapter 6 . . . . .	251
K	Parameter distributions for exemplar dataset in chapter 4 . . . . .	260
		<b>264</b>
	References . . . . .	264
	List of abbreviations . . . . .	294
	List of symbols . . . . .	298
	Glossary . . . . .	301

## Acknowledgements

---

*I lift up my eyes to the hills.  
From where does my help come?  
My help comes from the Lord,  
who made heaven and earth.*

---

At some point in late high school, I visited ANSTO on a field trip. I have a terrible memory, but I distinctly recall the feeling of awe I experienced upon entering the guide-hall observation deck, along with the accompanying feeling that I would never be brilliant enough to work in such a place or wear the white cotton mantle of ‘scientist’. I remembered that moment every time I walked west-to-east across the guide-hall floor, looking up at the observation deck; it served as a tangible reminder of how far I’d come. Of course, ‘how far I’d come’ often became ‘what’ve I done’ as the clock once again crept past midnight on the 4<sup>th</sup> day of a never-ending experiment. Regardless, I certainly wouldn’t have made it here (for better or for worse) without the guidance and support of a great many people.

To my wife, Sophie, who has supported me through stress and sickness and tolerated my frequent week-long trips to ANSTO, occasional melancholy, and sub-par income. I am certain that I’m not the easiest person to be married to at the best of times, and there have certainly been periods over the past four years that one would not describe as the best of times. Thank you for loving and supporting me through it all.

To my family — Mum, Dad, Rosie, Oscar and Sam (and Heinrich and Rosalie). Thanks for making me the person I am today. Thanks for always being steadfast in your support for me. Thanks for the rowdy dinners, lazy lunches and weekends away. I couldn’t ask for a better family.



To my primary supervisor, Stuart, who’s knowledge of everything-that’s-not-pop-culture never fails to amaze me. Thank you for making me feel like I was your only honours student in 4<sup>th</sup> year (I certainly wasn’t), and in doing so introducing me to the wide world of academia. Thank you for being patient with me when I’ve missed a key piece of literature, or misplaced (or just not placed) a comma, or not known the difference between a hyphen and an en dash. I’ve thoroughly enjoyed working together for the past few years, and I’m hopeful that we will have the chance to do so again in the future.

To my unofficial supervisor, Andy “danger close” Nelson, who taught me everything I know about neutron reflectometry and has instilled in me the belief that no experiment is more important than a timely lunch and a cup of tea. The excellent birthday-hat making skills of Elizabeth Nelson must also be acknowledged.

To my secondary supervisor, Patrick Spicer, thank you for your enthusiasm, humour and large collection of MacGyverable components (that I never once borrowed). I’m hoping that your ability to link fundamental science to everyday applications has rubbed off on me.

To my unofficial secondary supervisors — Erica Wanless and Grant Webber. Thank you for adopting me into the Newcastle brush group and for *trying* to get me to manage my projects better. I admire how fiercely you will fight against both grumpy reviewers and university bureaucracy on behalf of your students.

To the current and former members of the Newcastle brush group — Ed Johnson, Hayden Robertson, Kasimir Gregory, Josh Willott, Tim Murdoch and Ben Humphreys. Thanks for the manic nights in the Platypus cabin, the beers at the Lucas Heights motel, and for teaching me how to play *500*. All of you have contributed in massive ways to this thesis. Josh — thanks taking a chance on letting me visit you in Enschede, and for pushing me to actually write stuff instead of just cyclically analysing data forever. Tim — thanks for laying so much of the groundwork for chapter 4 of this thesis, and for showing me a good time in Pennsylvania (also thanks Eloise!). Ben — thanks for teaching me how to ATRP. Your ability to ‘measure’ the thickness of a polymer brush by watching it de-wet is the stuff of legend. Bring back the club and start the reactor. Ed — we may have started our PhDs at the same time, but you certainly did a better job of it (while simultaneously being in a band). Also, let the record show that it was your idea to combine both our PhDs (Brushes and salts and surfactants, oh my!) into what would become Section 6.5. A special thanks to both Ed and Hayden for introducing me to *Hamilton*, although I fear Sophie may never forgive you.

To the current and former members of the UNSW complex fluids group — Zengyi Wei, Maryam Hosseini, Xiaoyu Yang, Jie Song, Arslan Siddique, Firoozeh Babayekhorasani, Haiqiao Wang, Haoda Zhou, Zhiwei Li, Goldina Kwandou, Jonathan Mantzouridis, and Daniel Morris. Thanks for the group meetings, the exotic snacks and the birthday lunches. Zengyi — thanks for guiding my first steps in the world of neutron modelling, for introducing me to our lab, and for all your assistance on Platypus. Maryam — you are the mother of Jellyfish (I think that probably makes me the Jellyfish uncle?) and a delight to be around. Thank you for your enthusiasm and for all the work you did characterising our PNIPAM jellyfish. Remember me when you inevitably become a CEO. Xiaoyu — it’s a tragedy that COVID cut your lab-work short, because you were killing it. Thank you for all the work you did controlling the grafting density of SI-ATRP systems, much of which made it into chapter 2. Arslan — Thanks for your assistance during various beamtimes. I look forward to seeing you solve the mystery of epidemic thunderstorm asthma with the power of neutrons!

Thanks to the community at Grace City Church, who has been a constant source of support and encouragement. Special thanks to Jade and Maree for their help in putting this thesis together (motivation and proofreading, respectively). Thanks also to the post-grad and staff bible study group at UNSW, with whom I was blessed to spend lunch with once a week.

I would like to acknowledge the Gadigal people — who are the Traditional Custodians of the land on which the majority of this work was done — and pay my respects to their Elders past and present.

This PhD was made possible by a Research Training Program Scholarship awarded by the Australian Government. It was greatly supported by a PGRA scholarship generously awarded by AINSE Ltd. All neutron reflectometry experiments in this work were made possible by beamtime grants awarded by ANSTO.

## Output of candidature

### Publications included in this thesis

Geometrical confinement modulates the thermoresponse of a poly(*N*-isopropylacrylamide) brush

**Isaac J. Gresham**, Ben A. Humphreys, Joshua D. Willott, Edwin C. Johnson, Timothy J. Murdoch, Grant B. Webber, Erica J. Wanless, Andrew R.J. Nelson, Stuart W. Prescott

published: *Macromolecules*, 2021

DOI: [10.1021/acs.macromol.0c02775](https://doi.org/10.1021/acs.macromol.0c02775)

contributions: IJG performed the data analysis (including modelling of reflectometry and colloid probe data) and was the primary writer of the paper. BAH performed much of the preliminary data interpretation that informed the distribution model developed in this work. BAH, TJM, ECJ, GBW, SWP, ARJN performed the reflectometry experiment analysed in the paper. JDW performed the self-consistent field theory work included in this paper. TJM performed the colloid probe experiment analysed in this work and assisted significantly in the analysis of that data. SWP, GBW, EJW guided the project and assisted in assembling the manuscript. SWP developed the sample environment used in this work and was instrumental in assembling the manuscript. All authors assisted in proofreading the final paper.

Quantifying robustness of the neutron reflectometry technique for structural characterization of polymer brushes

**Isaac J. Gresham**, Timothy J. Murdoch, Edwin C. Johnson, Hayden Robertson, Grant B. Webber, Erica J. Wanless, Stuart W. Prescott, Andrew R.J. Nelson

published: *Journal of Applied Crystallography*, 2021

DOI: [10.1107/S160057672100251X](https://doi.org/10.1107/S160057672100251X)

contributions: IJG performed the characterisation, experimentation and analysis and was the primary writer of the paper. IJG and ARJN jointly developed the Freeform model. TJM is responsible for many of the ideas that underpin this work. ECJ and HR assisted in developing the analysis methodology through its use in their work. HR also conducted the experiments quantifying the hydration of the exemplar brush system. GBW, EJW guided the project and assisted in assembling and proofreading the manuscript. SWP and ARJN were instrumental in developing the methodology, refining the model implementation in Python, and assembling the manuscript. All authors assisted in proofreading the final paper.

## Additional publications

*The following papers are the result of work completed during the PhD candidature, but are not included in this Thesis.*

Temperature dependent specific ion effects in mixed salt environments on a thermoresponsive poly(oligoethylene glycol methacrylate) brush

Edwin C. Johnson, Timothy J. Murdoch, **Isaac J. Gresham**, Ben A. Humphreys, Stuart W. Prescott, Andrew R.J. Nelson, Erica J. Wanless, Grant B. Webber

published: *Physical Chemistry Chemical Physics*, 2019

DOI: [10.1039/C8CP06644B](https://doi.org/10.1039/C8CP06644B)

Structure and hydration of asymmetric polyelectrolyte multilayers as studied by neutron reflectometry: Connecting multilayer structure to superior membrane performance

**Isaac J. Gresham**, Dennis M. Reurink, Stuart W. Prescott, Andrew R.J. Nelson, Wiebe M. de Vos, Joshua D. Willott

published: *Macromolecules*, 2020

DOI: [10.1021/acs.macromol.0c01909](https://doi.org/10.1021/acs.macromol.0c01909)

Enrichment of charged monomers explains non-monotonic polymer volume fraction profiles of multi-stimulus responsive copolymer brushes

Edwin C. Johnson, Joshua D. Willott, **Isaac J. Gresham**, Timothy J. Murdoch, Ben A. Humphreys, Stuart W. Prescott, Andrew R.J. Nelson, Wiebe M. de Vos, Grant B. Webber, Erica J. Wanless

published: *Langmuir*, 2020

DOI: [10.1021/acs.langmuir.0c01502](https://doi.org/10.1021/acs.langmuir.0c01502)

Competitive specific ion effects in mixed salt solutions on a thermoresponsive polymer brush

Hayden Robertson, Edwin C. Johnson, **Isaac J. Gresham**, Stuart W. Prescott, Andrew R.J. Nelson, Erica J. Wanless, Grant B. Webber

published: *Journal of Colloid and Interface Science, 2020*

DOI: *10.1016/j.jcis.2020.10.092*

The direction of influence of specific ion effects on a pH and temperature responsive copolymer brush is dependent on polymer charge

Edwin C. Johnson, **Isaac J. Gresham**, Stuart W. Prescott, Andrew R.J. Nelson, Erica J. Wanless, Grant B. Webber

published: *Polymer, 2021*

DOI: *10.1016/j.polymer.2020.123287*

## List of figures

1.1	Tethered polymers in the mushroom regime and brush regime. . . . .	4
1.2	Theoretical polymer density profiles from AdG theory and strong stretching limit theory. . . . .	6
1.3	Theoretical polymer density profiles from nSCFT and classical strong-stretching limit theory, from the work of Milner. . . . .	7
1.4	Volume fraction profiles predicted by for polymer brush with increasing bidispersity and polydispersity, from the work of de Vos and Leermakers. .	8
1.5	Theoretical volume fraction profiles for brushes that exhibit a volume fraction dependent $\chi$ . . . . .	9
1.6	A summary of PNIPAM demixing curves from the work of Halperin, Kröger, and Winnik. . . . .	11
1.7	Summary of the ARGET ATRP reaction scheme used in this work. . . . .	14
1.8	Radius of gyration for PNIPAM at 20 °C along with corresponding reduced grafting density as a function of dry brush thickness. . . . .	16
1.9	native and deuterated structures of NIPAM. . . . .	21
1.10	Temperature calibration for QCM-D wafers used in this thesis. . . . .	24
2.1	GPC results from Martinez et al. . . . .	30
2.2	Experimental setups for section gradient molecular weight and gradient grafting density syntheses. . . . .	35
2.3	Chemical structures depicting the mechanism by which grafting density is varied. . . . .	36
2.4	Kinetics of the bromination reaction. . . . .	43
2.5	Polymer thickness as a function of reaction time. . . . .	44
2.6	Photos of select uniform wafers and the gradient wafer. . . . .	45
2.7	Relative polymer thickness as a function of the BiBB:BB ratio in the bromination step. . . . .	46
2.8	Characterisation of the silica and initiator layers . . . . .	47
2.9	Results for <i>in situ</i> experiment 1. . . . .	48
2.10	Results for <i>in situ</i> experiment 2. . . . .	49

2.11	Results for <i>in situ</i> experiment 3. . . . .	49
2.12	Ellipsometry thickness maps for <i>in situ</i> samples. . . . .	50
2.13	Volume fraction profiles as a function of temperature as measured by NR for brushes synthesised <i>in situ</i> . . . . .	51
3.1	Saturated vapour pressures of H <sub>2</sub> O and D <sub>2</sub> O from the work of Matsunaga and Nagashima. . . . .	58
3.2	Schematic of QCM-D experimental setup for humidity response experiment	63
3.3	Temperature and RH as a function of time for the QCM-D humidity re- sponse experiment. . . . .	64
3.4	Schematic of the sample environment used for the NR humidity response experiment. . . . .	66
3.5	Determination of the SLD of hydrogenated and deuterated PNIPAM. . . .	67
3.6	Normalised $\Delta f$ as a function of RH, measured by QCM-D. Calculated parameters (absorbed mass, volume and swelling ratio) are also included. .	69
3.7	NR data and corresponding model output for the humidity response ex- periment. . . . .	71
3.8	Experimental conditions and key model parameters from the NR humidity experiment as a function of time. . . . .	72
3.9	Thickness and corresponding SR as a function of RH. . . . .	73
3.10	$\chi$ as a function of RH and volume fraction solvent, from the QCM-D results in Figure 3.6. . . . .	74
3.11	SLD profiles from the PNIPAM brush in both ambient conditions and after evacuation, measured by NR. . . . .	75
4.1	An illustration of the application of Bayesian statistics to NR data analysis.	81
4.2	Description of a brush-coated interface in terms of the volume fraction profiles of the components present, using a smoothly varying spline function for the solvated polymer layer. . . . .	87
4.3	SLD profiles and corresponding reflectometry profiles as the volume fraction profile line simplification parameter is adjusted. . . . .	90
4.4	Round-trip comparison of the volume fraction profile used to create the syn- thetic reflectometry profile, along with corresponding reflectometry profiles.	95
4.5	Bayesian model evidence, $\text{prob}(D I)$ , as a function of the number of model knots. . . . .	96
4.6	Structural output from the nested sampling process used to estimate the model ratio evidence, corresponding to Figure 4.5. . . . .	97



4.7	Results from the analysis of a thermoresponsive PNIPAM brush with <i>FreeformVFP</i> with a PT-MCMC sampling approach. . . . .	98
4.8	Modelled reflectometry profiles and data corresponding to structures and conditions in Figure 4.7. . . . .	99
4.9	Demonstration of multimodal profiles produced by the PT-MCMC treatment in Figure 4.7. . . . .	100
4.10	Profiles of best fit taken from Figure 4.8, plotted on the same axes for direct comparison. . . . .	102
4.11	Profiles produced by PT-MCMC sampling for objectives with differing interfacial volume bounds. . . . .	103
4.12	Demonstration of the sensitivity of NR to the tail of the brush. . . . .	104
4.13	Log probability as a function of step number for the PNIPAM brush at different temperatures. . . . .	105
4.14	Log probability as a function of step number for broadening interfacial volume constraint. . . . .	105
5.1	Cross-section of the confinement cell used in this work. . . . .	115
5.2	Volume fraction profiles, SLD profiles, and corresponding reflectometry profiles that indicate that the confined NR experiments are sensitive to profile shape. . . . .	116
5.3	The construction of the separation distribution function used for the confined NR study. . . . .	117
5.4	Demonstration of the distribution model used in the confined NR study. . .	119
5.5	Demonstration of the flexibility of the thickness distribution used in confinement NR modelling. . . . .	121
5.6	Construction of the stress-separation curve used in the colloid-probe AFM. .	123
5.7	Schematic of the colloid-probe AFM system showing the curvature of the sphere resolved into a set of thin tiers. . . . .	124
5.8	Schematic of the colloid-probe AFM model at a single probe displacement, with area as a function of lateral position, as well as pressure and force profiles. . . . .	125
5.9	Brush volume fraction profiles calculated by nSCFT at increasing confining forces. . . . .	127
5.10	Re-analysis of the colloid-probe AFM data of Murdoch et al. . . . .	129
5.11	Separation distributions as determined by NR for the confined PNIPAM. .	130
5.12	Volume fraction profiles corresponding to the modal separation from Figure 5.11. . . . .	131

5.13	Fringe spacing analysis for the confined PNIPAM NR experiment. . . . .	132
5.14	The average value of the sub-critical edge data points for the confined PNIPAM NR experiment, showing the presence of H <sub>2</sub> O backed regions. . .	133
5.15	Volume fraction profiles depicting the thermoresponse of an unconfined PNIPAM brush before and after being subjected to 5 bar of mechanical confinement. . . . .	137
6.1	Chemical structures of the surfactants used in this chapter. . . . .	142
6.2	The critical micelle concentrations of different surfactants as a function of temperature. . . . .	144
6.3	Schematic of structures formed by PNIPAM-SDS complexes as a function of surfactant concentration and temperature. . . . .	148
6.4	Tail-mediated interaction model suggested by the NMR experiments of Chen et al. . . . .	149
6.5	CMC, micelle aggregation number and micelle hydrodynamic radius of SDS as a function of NaCl concentration. . . . .	150
6.6	Effect of different NaCl concentrations of the cloud point of PNIPAM as a function of SDS concentration, from the work of Patel et al. . . . .	151
6.7	Characterisation of the RI of surfactant solutions, for use in ellipsometry and optical reflectometry studies. . . . .	154
6.8	Thermoresponse of a 200 Å PNIPAM brush in solutions of different surfac- tants as measured by ellipsometry. . . . .	161
6.9	Thermoresponse of a 610 Å PNIPAM brush in solutions of different surfac- tants as measured by ellipsometry. . . . .	162
6.10	CST of PNIPAM in different surfactant solutions as measured by ellipsometry.	163
6.11	Change in frequency and dissipation for a 130 Å PNIPAM brush as a func- tion of surfactant concentration and identity at 20 °C. . . . .	165
6.12	Frequency and dissipation of a PNIPAM brush in SDS as a function of temperature. . . . .	166
6.13	Adsorption of different surfactants as measured by fixed-angle optical re- flectometry. . . . .	167
6.14	Amount of charge within the brush layer, calculated from FAOR results. .	168
6.15	Volume fraction profiles for a PNIPAM brush in solutions of SDS and C <sub>12</sub> E <sub>5</sub> derived using NR. . . . .	170
6.16	Volume fraction profiles for a PNIPAM brush in solutions of CTAB derived using NR. . . . .	171
6.17	SDS, C <sub>12</sub> E <sub>5</sub> and CTAB volume fraction profiles derived from NR experiments.	173

6.18	SLD profiles corresponding to volume fraction profiles in Figure 6.17. . . .	174
6.19	Distribution of surfactant volume fraction profiles attained by PT-MCMC for problem datasets from Figure 6.17. . . . .	176
6.20	Normalised separation as a function of surfactant concentration for the surface confined by 1 bar of stress at 35 °C and the surface confined by 5 bar of stress at 25 °C. . . . .	182
6.21	Fitted SLD and corresponding reflectivity profiles for the confined system at 35 °C and 1 bar with SDS and d-SDS. . . . .	182
6.22	Reflectivity profiles from Figure 6.21b plotted on alternative axes. Profiles are not offset to allow for direct comparison. . . . .	184
6.23	Ellipsometry-derived volume fraction profiles of a PNIPAM brush as a func- tion of SDS concentration, NaCl concentration and temperature. . . . .	191
6.24	Swelling ratios, extracted from the volume fraction profiles in Figure 6.23, plotted against NaCl concentration as a function of temperature and SDS concentration. . . . .	192
6.25	Data from Figure 6.24, plotted as $C_{\text{surf}}$ over $\text{CMC}^{\text{eff}}$ . . . . .	192
6.26	Frequency and dissipation for a 130 Å PNIPAM brush as a function of over- tone number, surfactant concentration and salt concentration, as measured by QCM-D. . . . .	194
6.27	Data from Figure 6.26, plotted as $C_{\text{surf}}$ over $\text{CMC}^{\text{eff}}$ . . . . .	195
6.28	Control (pure water) NR measurements for the NaCl-SDS-PNIPAM data presented in Figure 6.30. . . . .	196
6.29	Control (salt ramp) NR measurements for the NaCl-SDS-PNIPAM data presented in Figure 6.30. . . . .	197
6.30	Polymer and surfactant volume fraction profiles derived from Neutron Re- flectometry for PNIPAM brushes in mixtures of SDS and NaCl. . . . .	199
6.31	Schematic of the proposed structure for the NaCl-SDS-PNIPAM system. .	204
D1	Thickness and corresponding SR as a function of RH, where the relevant vapour temperature is taken as the sample temperature. . . . .	220
E1	Corner plot of important prior parameter distributions (related to the poly- mer layer) for the wafer used for the exemplar dataset in chapter 4 and in NR measurements in SDS and $\text{C}_{12}\text{E}_5$ solutions in section 6.3. . . . .	223
E2	Corner plot of important prior parameter distributions (related to the silica layer) for the wafer used for the exemplar dataset in chapter 4 and in NR measurements in SDS and $\text{C}_{12}\text{E}_5$ solutions in section 6.3. . . . .	224

E3	Example silica native-oxide layer volume fraction profile, derived from characterisation shown in Figure E2. . . . .	225
E4	Corner plot of important prior parameter distributions for the wafer used for NR measurements in CTAB solutions. . . . .	226
E5	Corner plot of important prior parameter distributions for the wafer used for the confined 35 °C 1 bar NR measurements in SDS in section 6.4. . . . .	227
E6	Corner plot of important prior parameter distributions for the wafer used for the confined 25 °C 5 bar NR measurements in SDS in section 6.4. . . . .	228
E7	Corner plot of important prior parameter distributions for the wafer used for SDS-NaCl NR measurements in section 6.5. . . . .	229
E8	Ellipsometry map of the wafer used for the exemplar characterisation in chapter 4 and for measurements in SDS and C <sub>12</sub> E <sub>5</sub> in section 6.3. . . . .	230
E9	Ellipsometry map of the wafer used for measurements in CTAB and DTAB in section 6.3. . . . .	230
E10	Ellipsometry map of the wafer used for confined PNIPAM-SDS (1 bar 35 °C) studied in section 6.4. . . . .	231
E11	Ellipsometry map of the wafer used for confined PNIPAM-SDS (5 bar 25 °C) studied in section 6.4. . . . .	231
E12	Ellipsometry map of the wafer used for PNIPAM-SDS-NaCl studies in section 6.5. . . . .	232
F1	Comparison of ellipsometry output for <i>refellips</i> and <i>wvase</i> . . . . .	233
G1	Schematic of the physical structure behind each of the examined treatments of the molar volume problem. . . . .	236
G2	SLD profile and (b) corresponding VF profiles based off varying polymer SLD as a fraction of the fitted SLD. . . . .	238
H1	Raw QCM-D data for SDS datapoints in Figure 6.11 . . . . .	241
H2	Raw QCM-D data for CTAB datapoints in Figure 6.11 . . . . .	242
H3	Raw QCM-D data for C <sub>12</sub> E <sub>6</sub> datapoints in Figure 6.11 . . . . .	243
H4	Raw QCM-D data from 0 mM SDS datapoints in Figure 6.12. . . . .	244
H5	Raw QCM-D data from 3 mM SDS datapoints in Figure 6.12. . . . .	245
H6	Raw QCM-D data from 5 mM SDS datapoints in Figure 6.12. . . . .	246
H7	Raw QCM-D data from 7 mM SDS datapoints in Figure 6.12. . . . .	247
H8	Raw QCM-D data from 14 mM SDS datapoints in Figure 6.12. . . . .	248
H9	Raw QCM-D data from the PNIPAM-SDS-NaCl study in Figure 6.26. . . . .	249
I1	Reflectometry profiles from the wafers used in the confinement study in section 6.4 showing that the brush recovers from repeated confinement. . . . .	250
K1	Parameter distributions corresponding to the 20 °C dataset in Fig. 4.7. . . . .	261

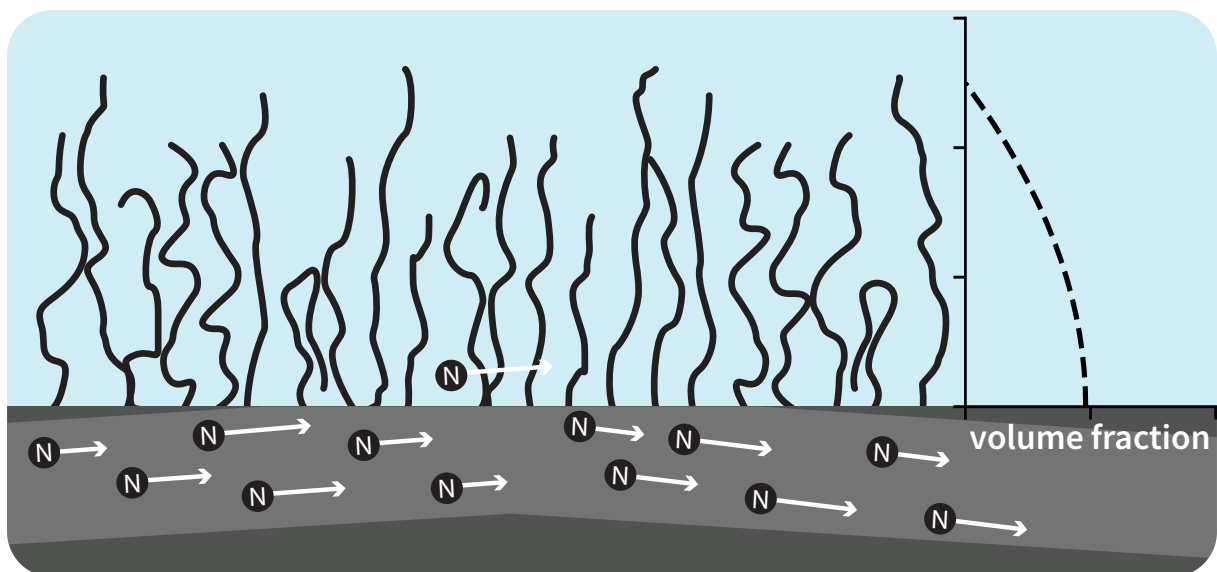
K2	Parameter distributions corresponding to the 25 °C dataset in Fig. 4.7. . .	261
K3	Parameter distributions corresponding to the 30 °C dataset in Fig. 4.7. . .	262
K4	Parameter distributions corresponding to the 32 °C dataset in Fig. 4.7. . .	262
K5	Parameter distributions corresponding to the 35 °C dataset in Fig. 4.7. . .	263
K6	Parameter distributions corresponding to the 40 °C dataset in Fig. 4.7. . .	263

## List of tables

1.1	Characterisation of grafted-from polymers via single-molecule force spectroscopy, from the work of Murdoch et al. . . . .	15
2.1	Experimental conditions for <i>in situ</i> synthesis. . . . .	38
4.1	Relation between the user-facing parameters and those used by the PCHIP splines in <i>FreeformVFP</i> . . . . .	88
4.2	Parameter bounds used for solvated sample analyses. . . . .	94
5.1	Dry thicknesses of the two samples used in the NR confinement study. . . .	113
6.1	References corresponding to marker symbols used in Figure 6.2. . . . .	145
6.2	Parameters used for determining sensitivity factor for FAOR. . . . .	156
A1	Tabulated SLDs of materials used in this thesis. . . . .	216

# Chapter 1:

## Introduction





In this chapter, the concepts, processes and techniques that underpin the entirety of this work will be discussed. First, an overview of polymer brushes will be given, with special focus on PNIPAM, in which the importance of these interfaces both as model systems and responsive coatings will be expounded. Then the synthesis techniques used to prepare the surfaces studied in this work will be detailed. Lastly, the techniques used in this work will be discussed, and the data analysis methods outlined where relevant. Chapter-specific background information will be provided at the beginning of the relevant chapter.

## 1.1 Polymer brushes

### 1.1.1 Defining a polymer brush

Polymer brushes are coatings consisting of surface-bound polymer chains, tethered at densities high enough to force lateral chain interaction and subsequent stretching away from the surface. Brushes are found in a range of natural [1] and synthetic [2] systems, where their nanoscale structure strongly influences interfacial properties. This structure is dictated by a balance of polymer solvation, molecular-level crowding, and entropic considerations [3–5], and as such is a function of both the system chemistry as well as the grafting density and molecular weight of the tethered polymers. All three factors are taken into account by the reduced grafting density [6],  $\Sigma$ , which can be written as:

$$\Sigma = \sigma \pi R_g^2 \quad (1.1)$$

where  $\sigma$  is the grafting density of the polymer in chains per unit area, and  $R_g$  is the radius of gyration of the respective polymer at the relevant solvent quality. In this work, we will use the Flory–Huggins interaction parameter [7–12],  $\chi$ , to describe the solvent quality. Low  $\chi$  corresponds to a high solvent-quality, while high  $\chi$  corresponds to a low solvent quality. For  $\Sigma < 1$  the grafted polymers exist in the so-called mushroom regime, where polymers are grafted so sparsely that they do not interact, forming spherical ‘mushrooms’ (Fig. 1.1a). For  $\Sigma > 5$  they are generally accepted to be in the brush regime [13]. An intermediate  $\Sigma$  value indicates that the layer is in the crossover regime [6]. It should be noted that as  $R_g$  depends on solvent quality, the same brush layer may exist in different regimes in different solvents (or, for a thermoresponsive brush, at different temperatures).

Polymer brushes can be created via two broad mechanisms: grafting-to and grafting-from. Grafted-to brushes are prepared via the attachment of pre-prepared polymers to a surface through either covalent bonding or physisorption. While the molecular weight distribution of brushes formed in this manner is typically well defined, the maximum  $\sigma$  of the polymer brushes formed is limited by the  $R_g$  of the polymer in solution. Conversely, grafted-from brushes are prepared by synthesising polymers from initiators that are already anchored to a surface. Grafting-from polymerisation can produce brushes with much higher grafting densities, but the molecular weight distribution of the grafted polymers is very difficult to quantify. In this thesis, we will work exclusively with grafted-from polymer brushes.

Brushes are typically only of interest in their solvated state, but useful information can be extracted from ‘dry’ brushes as well. In the dry state the total volume of the

polymer per unit area,  $\hat{V}_I$ , grafting density,  $\sigma$ , and number of repeat units in the polymer,  $N$ , are related by the density of the dry layer,  $\rho$ , and the monomer molecular weight,  $M_m$  [14]:

$$\rho = \frac{M_m N \sigma}{\hat{V}_I} \quad (1.2)$$

Practically, dry brushes will often contain moisture (which may be absorbed from the atmosphere or residue from the synthesis) or voids (which presumably form due to the glassy nature of many pure polymers). In this work, we use the *interfacial volume per unit area*,  $\hat{V}_I$ , to refer to the polymer's true dry thickness. In the ideal case where the dry layer is composed purely of polymer, the *dry thickness* will be equal to  $\hat{V}_I$ .

### 1.1.2 Why study brushes?

Generally, there are two reasons to study polymer brush systems.

The first of these is that polymer brushes have many desirable properties. Extended brush conformations possess low friction coefficients [15, 16] and antifouling properties [17, 18], whilst collapsed structures exhibit higher friction [16] and no fouling resistance [18]. Such surfaces already have many natural and commercial applications — lubricating kneecaps and stabilising active ingredients. However, to unlock their full potential, stimuli-responsive brushes must be considered. Coating interfaces with stimuli-responsive polymers allows for the creation of surfaces whose ‘brushy’ properties — such as hydropho-

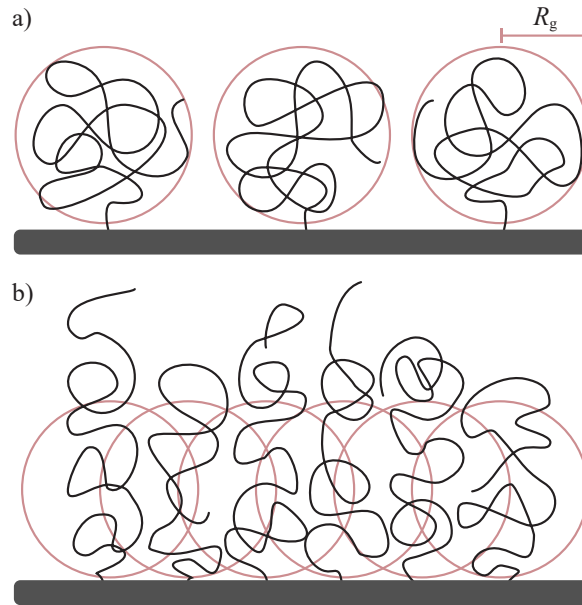


Figure 1.1: Tethered polymers in (a) the mushroom regime and (b) the brush regime.  $R_g$  is shown for context.

bicity and lubricity — can be modulated by small changes in environmental conditions such as temperature, [19, 20] pH [21, 22], and ionic strength and identity [23, 24]. These responsive polymer brushes enable reversible switching of interfacial properties, making them highly desirable in applications such as environmental remediation [25], biotechnology [26, 27], sensors [28], drug delivery [29], and membranes [30]. Thermoresponsive systems, such as brushes constructed out of poly(*N*-isopropylacrylamide) (PNIPAM), which we study in this thesis, are particularly attractive due to the ubiquity of temperature gradients in biological and industrial systems.

The second reason to study polymer brushes is to study complex polymer behaviour. Of course, the physical conformation of polymer in the brush regime is unique; this is part of what makes these systems so interesting from a polymer physics perspective. However, comparisons between free and brush-regime polymer can still be made that allow for general polymer behaviour to be better understood. . The brush geometry affords some advantages over conventional free-polymer techniques when it comes to unpicking the mechanisms that govern polymer behaviour, particularly for complex systems where additives are present. In the brush geometry we are able to access high polymer concentration regimes, which may be difficult to access through free-polymer techniques. Additionally, brush geometry polymers are held in place — they do not aggregate, settle, adsorb to vessel walls, self-assemble into macromolecular constructs, or any of the myriad of other behaviours that may impede observation of free-polymer<sup>i</sup> systems. Furthermore, when studying polymer-additive systems (i.e., salts, surfactants, co-solvents), the ratio of the additive to the polymer is effectively infinite, removing the potential for depletion of the additive. Lastly, the (planar) brush geometry allows the application of different experimental techniques to the study polymer behaviour. These techniques can provide insight into the structure and mechanical properties of polymers and measure the adsorption of additives into the layer.

For both of these motivations, understanding the structure of polymer brushes is essential. In the application and development of brush systems, structure is important because it dictates interfacial properties. For the understanding of polymer behaviour, brush structure gives invaluable insight into polymer conformation, polymer solvation, and interaction with additives.

### 1.1.3 Theoretical descriptions of neutral brush structure

A fundamental premise of the work conducted in this thesis is that polymer brush structure can be effectively reduced to a one-dimensional compositional profile. These profiles

---

<sup>i</sup>Here free polymer refers to a polymer in solution

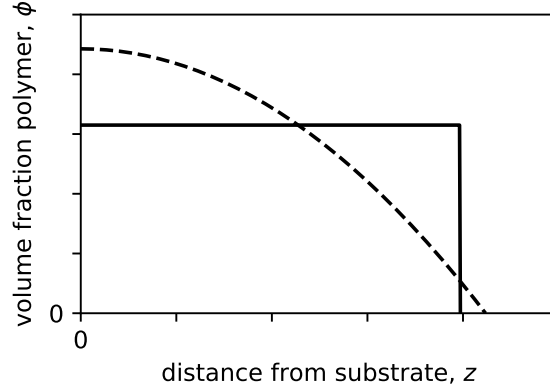


Figure 1.2: Theoretical polymer density profiles from (solid line) AdG theory and (dashed line) strong stretching limit theory, for equivalent  $N$  and  $\sigma$ .

are represented in a plot of system composition against the distance from the substrate,  $z$ , where  $z = 0$  at the base of the brush. In practice, this is often a volume fraction profile,  $\phi_{\text{poly}}(z)$ , whilst in theoretical approaches it is often termed a segment-density profile.

The first theoretical description of a polymer brush was put forward by Alexander [31] and de Gennes [32] (termed the AdG model) and describes the brush as a set of equally-stretched chains. The compositional profile produced by this model is a uniform slab with thickness  $d_{\text{AdG}}$  (Fig. 1.2), as chain ends are assumed to reside at the brush periphery, and all polymers are equally stretched. While simple, this model is powerful as it identifies the parameters with which brush thickness scales [14]:

$$d_{\text{AdG}} \approx N(w\sigma a^2)^{1/3} \quad (1.3)$$

where  $a$  is the Kuhn length (the displacement length of the polymer segment that can be considered a rigid-rod),  $N$  is the number of Kuhn segments in the polymer, and  $w$  is the excluded volume parameter. From Equation 1.3, it is clear that solvated brush thickness is proportional to  $N$ , and scales as  $\sigma^{1/3}$ .

The strong-stretching model relaxes the AdG assumption that all chain ends reside at the brush periphery and yields a more advanced parabolic description of brush structure [33]:

$$\phi(z) = \frac{\pi^2}{8wN^2}(d_{\text{parab}}^2 - z^2) \quad (1.4)$$

where  $w$  is the excluded volume parameter and  $d_{\text{parab}}$  is the maximum extent of the parabola (where  $\phi_{\text{poly}} = 0$ ), given by:

$$d_{\text{parab}} = N\left(\frac{12\sigma w}{\pi^2}\right)^{1/3} \quad (1.5)$$

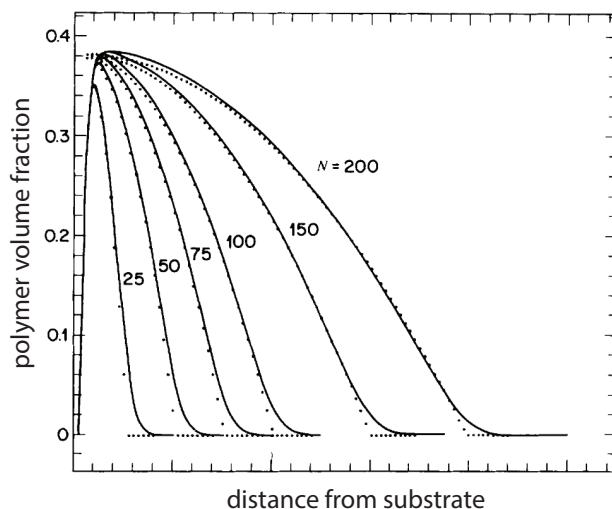


Figure 1.3: Theoretical polymer density profiles from (solid line) nSCFT and (dotted lines) classical strong-stretching limit theory. Reproduced from the work of Milner [34] with permission from the Royal Society of Chemistry.

The profile produced by equation 1.4 is shown in Figure 1.2. Importantly, the scaling relations of the AdG model are still true for these parabolic brushes.

In addition to the analytical techniques outlined above, computational approaches have been used to predict the structures formed by polymer brushes. Numerical self-consistent field theory (nSCFT) is the foremost amongst these techniques, as it is computationally inexpensive (compared to molecular dynamics methods, for instance) and can account for many of the nonidealities that real brush systems exhibit. For monodisperse brushes in the strong-stretching limit, nSCFT finds good agreement with the previously introduced parabolic model (Fig. 1.3). The one notable deviation between the structure predicted by nSCFT and classical strong-stretching limit theory is the behaviour as the polymer density approaches 0; the former predicts a gentle, near asymptotic approach, while the latter does not deviate from its parabolic path. The effects of polydispersity on brush structure have been investigated by de Vos and Leermakers [5] using nSCFT. Figure 1.4 shows selected results from their study, in which they found that a bi-disperse brush creates profiles that resemble the sum of two parabolas, while the brush structure transitioned from a parabolic to an exponential profile as polydispersity was increased.

While the theoretical descriptions of brush structure above are useful and form a comprehensive basis for understanding the behaviour of these structures, they make some assumptions regarding the polymer system. Perhaps most significantly (at least for the current work) the above theory assumes that the solvent quality,  $\chi$ , is not a function of polymer concentration. This assumption ignores the space required to form hydration

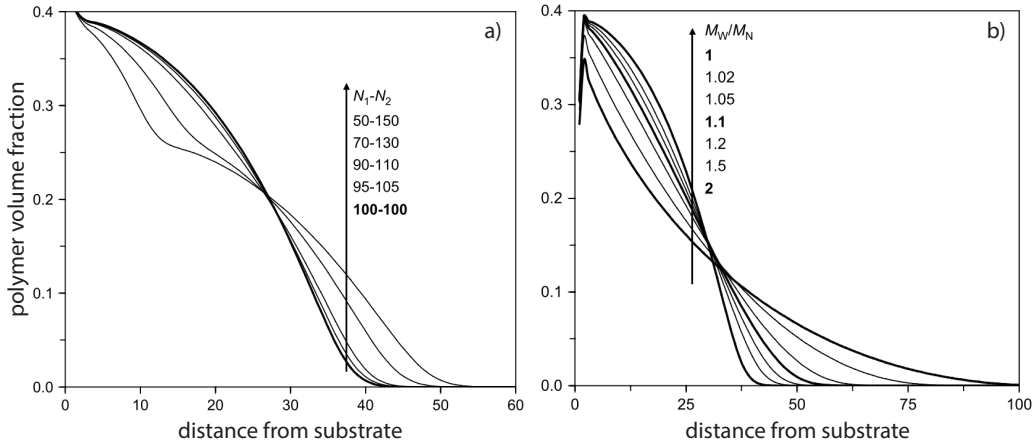


Figure 1.4: (a) Volume fraction profiles predicted by nSCFT for polymer brush with increasing (a) bidispersity (two populations of chains) and (b) polydispersity, taken from the work of de Vos and Leermakers [5]. Bidispersity creates profiles that resemble the sum of two parabolas, whilst polydispersity transforms the classic parabolic brush profile into an exponential decay. Figure reproduced with permission of Elsevier, from the work of de Vos and Leermakers [5]; permission conveyed through Copyright Clearance Center, Inc.

shells around individual monomers and the potential for monomers to arrange themselves in micelle-like clusters [35]. When theory incorporates a  $\chi$  that is dependent on  $\phi_{\text{poly}}$ ,  $\chi(\phi_{\text{poly}})$ , significant deviations from the parabolic and exponential profiles predicted above emerge. Baulin and Halperin [35] show that the  $\chi(\phi_{\text{poly}})$  derived for PNIPAM by Afroze, Nies, and Berghmans [36] results in a two-phase brush profile at some conditions (Fig. 1.5). This two phase structure will be discussed more in Section 1.2.

The profiles shown in Figures 1.4 and 1.5 show that a wide range of theoretically justifiable volume fraction profiles exist for uncharged homopolymers in pure solvents. This is important in justifying one of this thesis’s central efforts; the freeform modelling of polymer brush structure.

## 1.2 The phase behaviour of PNIPAM

This thesis uses PNIPAM brushes as a model system to explore brush behaviour and demonstrate how reflectometry techniques may be utilised to elucidate brush structure. As such, establishing a fundamental understanding of this polymer’s complex phase behaviour is necessary for successfully interpreting and contextualising our results. PNIPAM is perhaps the most well known thermoresponsive polymer, exhibiting a well-documented swollen to collapsed transition at its critical solution temperature (CST) of approximately 32 °C [37, 38], which has been studied in free polymer [36, 38–41], microgel [42–44] and



brush [20, 45–52] geometries. The CST-type behaviour of PNIPAM is sometimes incorrectly referred to as a hydrophilic to hydrophobic transition; PNIPAM as a bulk material can not be considered either [53]. Each PNIPAM monomer has hydrophilic and hydrophobic moieties [53], with the bulk polymer remaining reasonably hydrated (at least 20 % water) in the collapsed state [20, 44]; this is hardly the hallmark of a hydrophobic substance [53].

The macroscopic thermoresponse of PNIPAM should be understood as an entropically driven process, where the CST is the point at which the entropic penalty imposed by the ‘water cage’ required to hydrate the polymer backbone and propyl moiety outweighs the enthalpic benefit of the acrylamide’s hydration [54–57] (remember, the entropic contribution to Gibb’s free energy is temperature dependent). The process is complicated, and has been the subject of study since the thermoresponse of PNIPAM was first characterised by Heskins and Guillet [37] to the present day [57]. Briefly, the current understanding is that below the CST the amide and carbonyl groups form hydrogen bonds with the surrounding water molecules, while water-cages (themselves formed from complex hydrogen-bond networks) solvate the propyl group and polymer backbone [56, 57]. Above the CST the extended arrangement no longer represents the energy minimum due to the aforementioned entropic effects, rather the polymer is found in a collapsed globule configuration which minimises the exposure of the hydrophobic groups to water. Within this collapsed

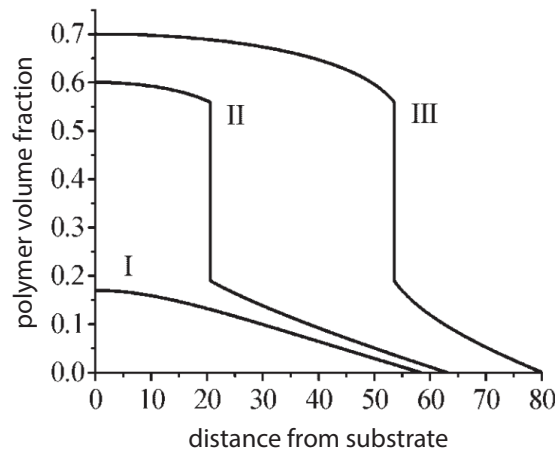


Figure 1.5: Theoretical volume fraction profiles for brushes that exhibit a volume fraction dependent  $\chi$ , using the mean-field theory developed by Baulin and Halperin [35] and the  $\chi(T, \phi_{\text{poly}})$  relationship derived from 28 °C PNIPAM data by Afroze, Nies, and Berghmans [36]. Profiles I through III correspond to increasing grafting densities, and exhibit the range of theoretically justifiable profiles possible in real brush systems. The distance from substrate is given as a multiple of the lattice spacing of the mean-field theory (conceptually equivalent to one Kuhn length). Figure reproduced with permission of John Wiley & Sons, from the work of Baulin and Halperin [35]; permission conveyed through Copyright Clearance Center, Inc.

globule PNIPAM forms hydrogen-bonds with both itself (inter and intra-chain) and water, which is thought to be responsible for the hysteresis observed in the thermoresponse [56, 57].

The precise transition temperature and breadth of the response appear to depend on many factors, including the molecular weight, end group identity, tacticity, volume fraction and geometry of the PNIPAM chains, as well as the solvent properties such as ionic strength, ion identity and presence of surfactants, discussed in more detail below.

### 1.2.1 Free polymer

The phase behaviour of free PNIPAM has recently been extensively reviewed by Halperin, Kröger, and Winnik [38]. In their review, they focus on the temperature of demixing (i.e., the cloud point), finding that while all reports show PNIPAM undergoing demixing, the temperature this occurs at is not consistent. Demixing temperatures have been reported to vary between 24 and 39 °C (Fig. 1.6). Halperin, Kröger, and Winnik [38] identify several reasons for this broad range of transition temperatures; most significantly the concentration of polymer in the system (Fig. 1.6). In Flory–Huggins terminology, the  $\chi$  of PNIPAM is not only dependent on  $T$  but also on  $\phi_{\text{poly}}$  (sometimes termed type II phase behaviour) [36, 38, 58]; the exact form of this function  $\chi(T, \phi_{\text{poly}})$  is still contested [38]. However,  $\phi_{\text{poly}}$  alone could not satisfactorily explain the range of reported demixing curves, even when attempts were made to account for experimental imperfections. Other notable factors appear to be the tacticity of the PNIPAM sample [59] (i.e., the stereochemistry of the side-group), the polymer end-groups (i.e., the polymerisation initiator group) and polymer molecular weight. Generally, atactic (randomly orientated) PNIPAM is more soluble than either syndiotactic (alternating) or isotactic (single-orientation) PNIPAM, presumably due to the increased crystallinity of the more-ordered PNIPAMs. As expected, hydrophilic end groups lower the CST and hydrophobic groups raise the CST. The end groups' effect is more significant on lower molecular weight polymers, and appears to disappear as  $N$  tends to infinity [60]. The degree of polymerisation has previously been found to increase the CST [61, 62], even when end-group effects are accounted for [60]. However, dependence of the CST on  $N$  is only valid for low molecular-weight PNIPAM — above 100 kDa the CST is independent of  $N$  [62].  $N$  dependence decreases as  $\phi_{\text{poly}}$  increases, indicating that the effect of molecular weight on the transition temperature has more to do with the local polymer concentration than it does the polymer molecular weight.

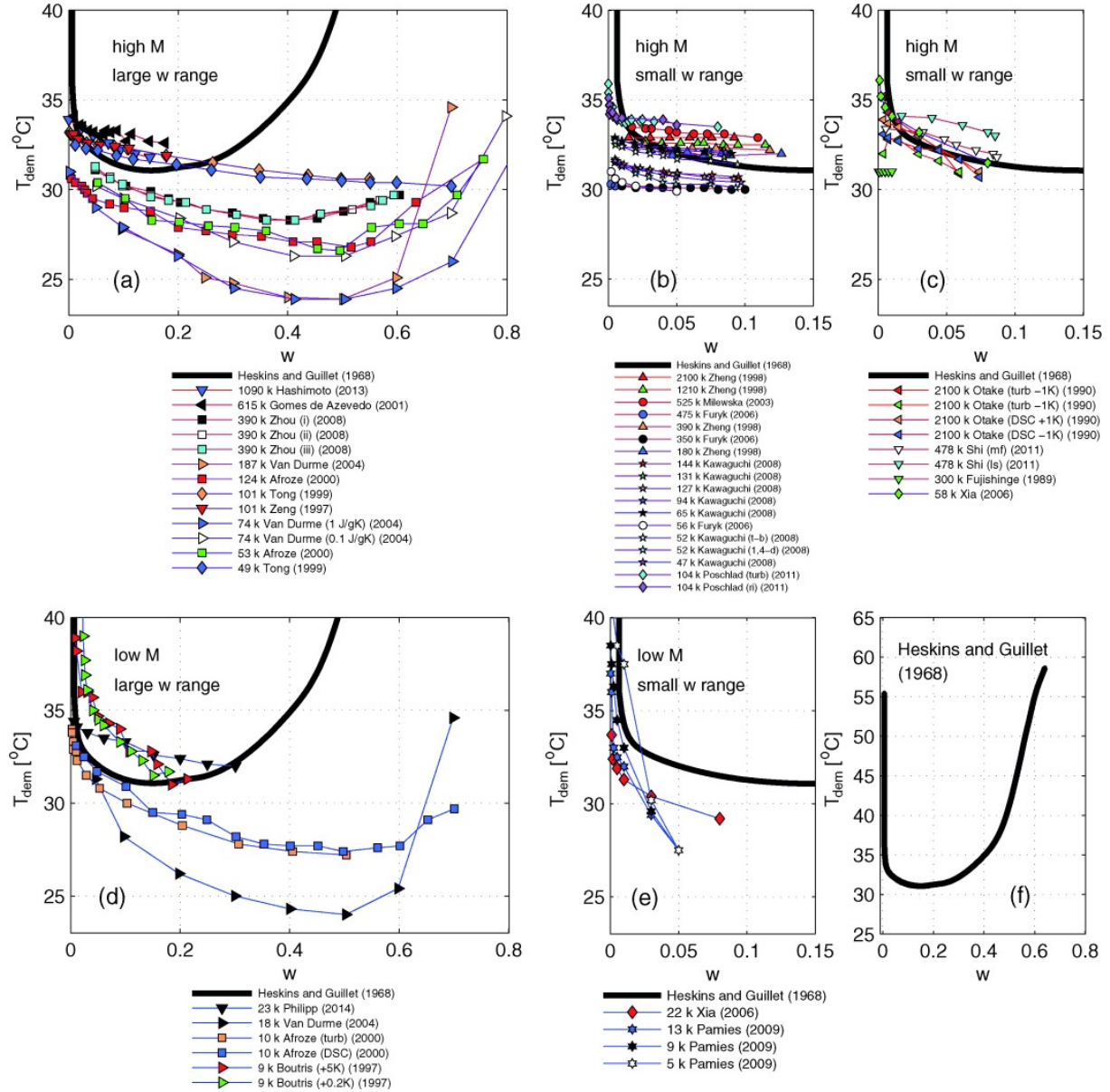


Figure 1.6: A summary of PNIPAM demixing curves from the work of Halperin, Kröger, and Winnik [38], showing the temperature of demixing as a function of PNIPAM weight fraction. The results are split into (a,b,c) high and (d,e) low molecular weight samples and experiments that probe (a, d) large and (b, c, e) small polymer weight fractions. (f) The original PNIPAM demixing curve, as measured by Heskins and Guillet [37]. Figure reproduced with permission of John Wiley & Sons, from the work of Halperin, Kröger, and Winnik [38]; permission conveyed through Copyright Clearance Center, Inc.

### 1.2.2 Brush regime

All of what is true for free polymer applies to chemically analogous brushes; however, the brush geometry does have additional implications for the phase behaviour of PNIPAM. The equivalent of the demixing temperature, as collated in Fig. 1.6, for brushes is the midpoint of the thermoresponse — often obtained by fitting a sigmoidal function to a plot of brush height versus temperature. The first implication is that (by definition) polymer chains in the brush geometry are forced to extend into solution further than they would be in free solution (i.e., the height of the brush is greater than  $R_g$ , Section 1.1). The stretched polymer state has lower entropy than the globule state, and as such the crowding adds yet another entropic contribution to the complex thermoresponse of PNIPAM. The second implication is that the local  $\phi_{\text{poly}}$  is reasonably high and very variable within the brush. In the review of Halperin, Kröger, and Winnik [38] (Fig. 1.6), demixing temperatures for PNIPAM solutions in the range of 0 to 80 wt% are reported; in a PNIPAM brush almost this entire range is accessible in a typical temperature cycle [20]; as the temperature increases the polymer collapses ( $\chi_{\text{eff}}$  increases), which changes the local  $\phi_{\text{poly}}$ , which in turn changes  $\chi_{\text{eff}}$ . Type II behaviour has interesting implications in the brush regime; namely vertical phase separation (Fig. 1.5) and could hypothetically indicate a reversal in the phase behaviour of PNIPAM at very high  $\phi_{\text{poly}}$  [36] (i.e., more hydrated at higher temperatures).

There is a wealth of experimental work examining PNIPAM brushes [19, 46, 48, 49, 52, 63–67]. As in the free polymer system, the behaviour of these systems depends on the molecular weight of the substituent polymers [52, 68]. However, it appears that the CST increases as  $N$  is increased for PNIPAM; this is the opposite of the trend observed in free solution. Furthermore, the system behaviour is only weakly dependent on the molecular weight; as long as  $N$  is sufficiently high the CST remains relatively constant. One reason why the CST may not increase for lower  $N$  PNIPAM brushes (as it does for free polymer) is that this effect is only present when the polymer is dilute, [38] which can never occur in brush systems. The swollen-to-collapsed transition is much broader for brushes than analogous free-polymer systems [20, 45, 48, 69], which has been attributed to the crowding induced by the geometry [48]. This broadened phase transition may also relate to the techniques available to measure brush height. Interestingly, it is consistently reported that the CST becomes better defined as  $N$  is increased [52, 68]. There has been some experimental evidence of type II phase behaviour in PNIPAM brushes, most notably the difference between CSTs measured using different techniques by Humphreys et al. [48] and the volume fraction profiles measured Murdoch et al. [20] using neutron reflectometry (NR).

### 1.3 Materials

Here we document the materials common to the chapters in this thesis; materials used in only one chapter are detailed therein. native oxide silicon wafers (100 mm diameter, 10 mm thick) were used as brush substrates for NR experiments, whilst appropriately sized wafers were cut from Native oxide silicon wafers (100 mm diameter, 1 mm thick) for ellipsometry experiments; all wafers were purchased from EL-CAT Inc. (USA). QSensor QSX 303 SiO<sub>2</sub> quartz crystal microbalance with dissipation monitoring (QCM-D) sensors (Biolin Scientific) were purchased from ATA scientific and cleaned before use by 30 seconds of plasma treatment followed by washing in 2 wt% sodium dodecyl sulphate (SDS), rinsing with MilliQ water, and drying under nitrogen.

*N*-isopropylacrylamide (NIPAM) ( $\geq 99\%$ ) was purchased from Sigma Aldrich, stored below 4 °C, and recrystallised from hexane before use. Solvents methanol ( $\geq 99.8\%$ ), ethanol (absolute), and tetrahydrofuran (THF) ( $>99\%$ ) were purchased from Sigma Aldrich, methanol and ethanol were used as received, THF was dried over 4 Å molecular sieves before use. Reagents (3-Aminopropyl)triethoxysilane (APTES) ( $\geq 99\%$ ),  $\alpha$ -bromoisobutyryl bromide (BiBB) ( $>98\%$ ), triethylamine (TEA) ( $>99\%$ ), Copper(II) bromide (CuBr) ( $>99\%$ ), L-Ascorbic Acid ( $>99\%$ ), and 1,1,4,7,10,10-hexamethyltriethylene-tetramine (HMTETA) ( $>97\%$ ) were purchased from Sigma Aldrich and used as received.

## 1.4 Methods: PNIPAM synthesis via ARGET-ATRP

The PNIPAM brushes studied in this thesis were synthesised following the method employed by Humphreys et al. [48], with solvent composition adjusted to control the reaction rate, as previously described by Murdoch et al. [20]. The reaction scheme is summarised in Figure 1.7. Reaction rate and reaction time were controlled to produce brushes with thicknesses suitable for the different techniques employed. The synthesis methodology can be divided into three steps. The first is the vapour-deposition of the APTES monolayer (the APTES deposition step), the second is the reaction of the anchored APTES with BiBB polymerisation initiator (the bromination step), which leaves the surface decorated with organobromine moieties, and the third is the polymerisation of PNIPAM from these initiators via activators regenerated by electron transfer (ARGET) atom transfer radical polymerisation (ATRP) (the polymerisation step). We detail this methodology below.

First, wafers were cleaned by rinsing with ethanol and MilliQ water, before being activated by either one minute of high intensity (30 W) air plasma (Harrick Plasma PDC-002) or fifteen minutes in a UV-Ozone cleaner (Bioforce,  $\approx 9 \text{ mW cm}^{-2}$  with  $\lambda = 254 \text{ nm}$ ), followed by rinsing with 10 wt% NaOH solution (as per the method of Humphreys et al. [48]) and copious amounts of MilliQ water. The wafers were then oven-dried, as the following steps are sensitive to moisture. A covalently attached APTES layer was formed on the samples via vapour deposition, carried out for thirty minutes at  $<5 \text{ mbar}$ . The deposited layer was then thermally annealed for thirty minutes at  $110^\circ\text{C}$ . This layer

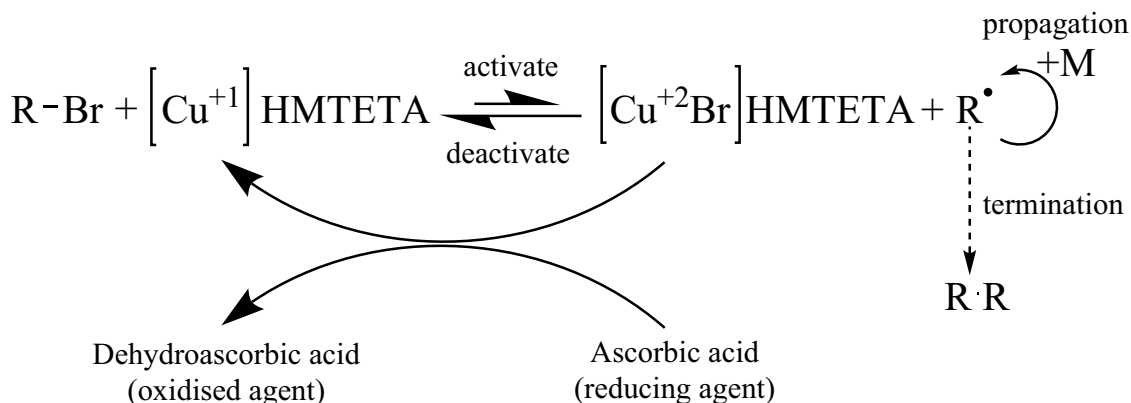


Figure 1.7: Summary of the ARGET ATRP reaction scheme used in this work, adapted from the work of Li et al. [70]. Briefly,  $\text{Cu}^{+1}$  complexes with HMTETA. The  $\text{Cu}^{+1}$  oxidises to  $\text{Cu}^{+2}$  through reacting with the bromine initiator group, temporarily removing it from the growing polymer chain and leaving a radical in its place. This radical allows for monomers to be added to the chain. After a short time period, the bromine and growing polymer chain recombine. The  $\text{Cu}^{+2}$  is then reduced back to  $\text{Cu}^{+1}$  by ascorbic acid, enabling the process to continue.

was functionalised with Br initiator moieties by immersion of the wafers in dry THF (stored over 4 Å molecular sieves) and the addition of 2.6 vol% BiBB and 3 vol% TEA. The functionalised wafers were washed with THF, ethanol, and copious amounts of MilliQ water before being dried under nitrogen.

To produce the surface grafted polymers an ARGET ATRP was carried out, using the bromine groups covalently bound to the surface as polymerisation initiators. The initiator-functionalised wafers were placed in clean, appropriately sized glass vessels, which were purged with nitrogen for at least fifteen minutes prior to the addition of a polymerisation solution. The polymerisation solution consists of a polymerisation solvent, monomer, copper catalyst and ligand. The polymerisation solvent was a mixture of methanol and water, the specific ratios of which were used to tune the reaction rate and hence the final thickness. For thickness targets less than 200 Å a 1:4 water:methanol volume ratio was used, whilst a 2:1 mixture was used for larger target thicknesses.<sup>ii</sup> NIPAM monomer was weighed out to 5 % of the total solvent mass and added to the solution. Copper bromide and HMTETA were added such that the molar ratio of NIPAM to HMTETA to CuBr<sub>2</sub> was 900:15:1.5, producing a pale blue solution. The solution was placed in a round-bottomed flask which was sealed and purged with nitrogen for fifteen minutes while stirring. After fifteen minutes of deoxygenation, ascorbic acid was weighed out and added such that the ratio of ascorbic acid to NIPAM was 900:10. Upon the addition of ascorbic acid, the solution became colourless with a faint yellow hue. The solution was deoxygenated for a further fifteen minutes before being added to the wafer vessels. Once the solution was added to the wafer vessels, they were kept under positive nitrogen pressure for the duration of the synthesis. Synthesis times varied between 30 min and 2 h, depending on the desired thickness. Further details regarding the synthetic method can be found in chapter 2.

Table 1.1: Characterisation of grafted-from polymers via single-molecule force spectroscopy, from the work of Murdoch et al. [20]

parameter	value
Interfacial volume, $\hat{V}_I$	$183 \pm 5 \text{ Å}$
Molecular weight	$201 \pm 48 \text{ kg mol}^{-1}$
Number of monomers, $N$	$1770 \pm 420$
Contour length	$4980 \pm 1180 \text{ Å}$
Grafting density, $\sigma$	$0.0007 \text{ Å}^{-2}$

<sup>ii</sup>We stress that these target thicknesses are the dry thickness of the polymer brush layer, not the length of the substituent polymers. The molecular weight and contour length of individual polymers are provided in Table 1.1.



### 1.4.1 Determination of molecular weight and grafting density

Single-molecule force spectroscopy (SMFS) has been used to characterise brushes prepared under identical conditions to those analysed in this thesis [20]; the results of this study are reproduced in Table 1.1 for convenience. Using Equation 1.1 and literature values for the radius of gyration for free PNIPAM in water, we can approximate  $\Sigma$  for the brushes used here. From the results of Kubota et al. [39] and the interpolation shown in Figure 1.8 we determine that the brush used in the SMFS study had a  $\Sigma$  of  $\approx 79$ , well above the  $\Sigma > 5$  threshold for the brush regime.

By making the workable assumption that grafting density is independent of molecular weight<sup>iii</sup> for grafted-from polymers, and by taking molecular weight as proportional to dry brush thickness (Eq. 1.2), we can extend this result to cover the range of brush thicknesses used in this work. This is summarised in Figure 1.8b, where the solid line indicates the  $R_g$  for PNIPAM at 20 °C (from the data in Fig. 1.8a), and the dashed line shows the  $R_g$  for a single collapsed PNIPAM chain.  $R_g$  is difficult to measure for collapsed PNIPAM

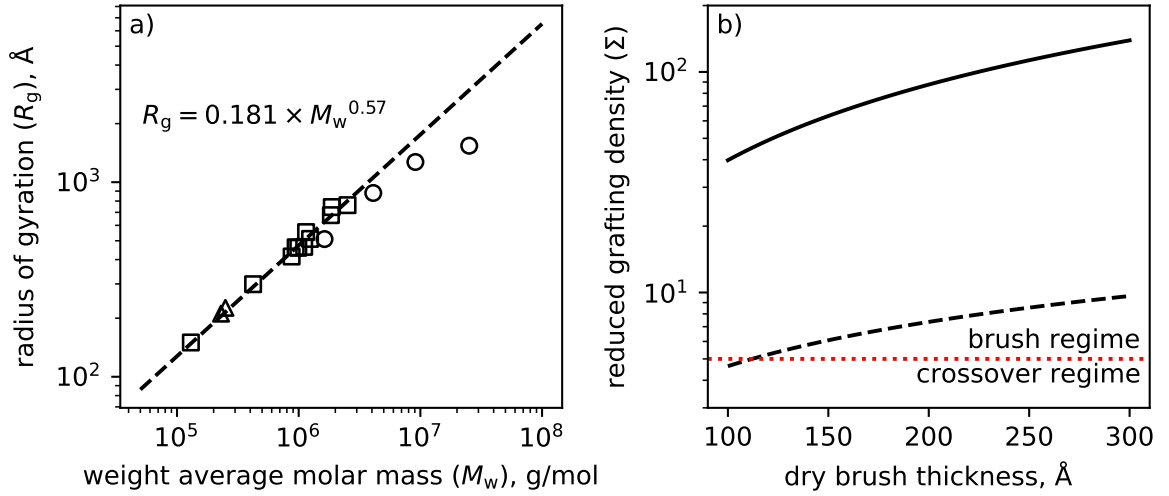


Figure 1.8: (a) Radius of gyration for PNIPAM at 20 °C from the light-scattering experiments of (□) Kubota et al. [39], (○) Kubota, Fujishige, and Ando [40] and (△) Kujawa et al. [41]. The dashed line is a power-law relation, fitted to the data of Kubota et al. [39]; the power law is a good description of the relationship between  $R_g$  and  $M_w$  for  $M_w < 10^7$ . (b) reduced grafting density as a function of dry brush thickness for the brushes studied in this thesis, based on the SMFS results of Murdoch et al. [20] (Table 1.1,  $\sigma = 0.0007 \text{ Å}^{-2}$ ). The solid curve is based off the relationship between  $R_g$  and  $M_w$  derived in (a), while the dashed line is the theoretical radius of gyration for a collapsed PNIPAM globule containing only 20 % solvent (roughly approximating PNIPAM at 40 °C). The dotted red line indicates the transition from the crossover regime to the brush regime.

<sup>iii</sup>This assumption is discussed and investigated in chapter 2

chains, as individual chains will aggregate with one another in free solution; instead, we approximate the  $R_g$  as the radius of a perfect sphere with a volume equal to 1.25 times the respective polymer volume. We stress that this approximation is only used for calculation of the reduced grafting density in Figure 1.8. This multiplier was chosen as it represents a globule that is 20% water by volume, which matches that determined for collapsed PNIPAM brushes in this work. Importantly, the conditions studied in this thesis are bounded by the swollen (solid) and collapsed (dashed) curves in Figure 1.8, and as such, all take place in the brush regime.

## 1.5 Methods: experimental techniques

### 1.5.1 Characterisation of polymer brushes

#### Volume fraction profile

One of the key aims of this work is to experimentally derive the volume fraction profile<sup>iv</sup> of polymer brushes. The volume fraction profile is the polymer volume fraction,  $\phi_{\text{poly}}$ , as a function of the distance from the substrate,  $z$ , and can be written as  $\phi_{\text{poly}}(z)$ . Solvated polymers are in constant thermal motion, with the conformation of any given chain changing rapidly; the volume fraction profile contains information about the average chain conformation in the brush. Neutron reflectometry is the only technique capable of resolving this volume fraction profile, although in chapter 4 we demonstrate that this is not a simple task. One important property of polymer brush volume fraction profiles is that their integral should remain constant, that is to say that  $\hat{V}_I$  is constant.

#### First moment

Often it is desirable to reduce  $\phi_{\text{poly}}(z)$  to a single thickness value (e.g., for ease of plotting or comparison to ellipsometry, which typically produces a layer thickness [71, 72]); this is achieved here by taking the equivalent thickness as twice the first moment of the profile [20, 49, 73, 74]

$$d_{1\text{st}} = 2 \frac{\int_0^\infty z \phi_{\text{poly}}(z) dz}{\hat{V}_I} \quad (1.6)$$

$d_{1\text{st}}$  is equivalent to the thickness of a uniform layer with the same first moment and  $\hat{V}_I$  as  $\phi_{\text{poly}}(z)$ .

#### Swelling ratio

The swelling ratio is a common way of normalising the behaviour of a layer in either the dry (i.e., humidity response) or solvated case. It is defined as the ratio of the swollen thickness to the interfacial volume [20, 75–78]

$$\text{swelling ratio} = \frac{d_{\text{swell}}}{\hat{V}_I} \quad (1.7)$$

---

<sup>iv</sup>In theoretical work this is often termed the segment density profile.

### 1.5.2 Principles of reflectometry

Reflectometry techniques measure the intensity of the specular reflection of radiation reflected from a planar surface,  $R$ , as a function of the scattering vector  $Q = \frac{4\pi}{\lambda}\sin(\theta)$ , where  $\lambda$  is the wavelength and  $\theta$  is the angle of incidence. In any reflectometry experiment, a range of  $Q$ -values can be accessed by changing either the angle of the reflection or the incident radiation's wavelength. The  $R$  vs  $Q$  profile produced by such an experiment is called a reflectometry profile (written as  $R(Q)$ ), and is sensitive to the surface-normal scattering length density (SLD) profile. SLD is an intrinsic property that describes the tendency of a material to scatter a given type of radiation, an SLD profile is the value of the SLD as a function of the distance from the reflecting interface,  $z$ . The SLD can be related to the system composition by

$$\rho(z) = \sum_{i=0}^n \rho_i \phi_i(z) \quad (1.8)$$

where  $\rho(z)$  is the SLD of the mixture at distance  $z$ ,  $\rho_i$  is the SLD of the pure component  $i$ , and  $\phi_i$  is the volume fraction of component  $i$  at distance  $z$ . Reflectometry is sensitive to  $\rho$  as a function of  $z$ , as such, the up to two terms from equation 1.8 can be found for a single reflectometry measurement (as  $\sum_{i=0}^n \phi_i = 1$ ). Resolving the compositional profile is contingent on there being a difference in the SLD of the interfacial components (i.e., sufficient contrast).

In this work, we study two-component systems, generally composed of a polymer and a solvent, and make the common space-filling assumption [20, 73, 79]:

$$\rho(z) = \phi_{\text{poly}}\rho_{\text{poly}} + (1 - \phi_{\text{poly}})\rho_{\text{water}} \quad (1.9)$$

which allows for transformation between the polymer volume fraction profile and SLD profiles provided the polymer and solvent SLDs are known. Unfortunately, there is no way to directly transform  $R(Q)$  into an SLD profile due to the loss of phase information in the experiment; thus, structural information needs to be extracted from collected reflectometry data through other means.

#### Fringe-spacing analysis

The simplest method of extracting structural information from reflectometry profiles is through a fringe-spacing analysis, which can determine the thickness of single well-defined

layers via

$$d = \frac{2\pi}{\Delta Q} \quad (1.10)$$

where  $\Delta Q$  is the averaged trough separation.

To unambiguously determine the fringe separation, we use a 1<sup>st</sup> derivative root-finding algorithm that locates peaks and troughs in collected reflectometry profiles. The algorithm uses a Savitzky–Golay filter (`scipy.signal.savgol_filter` [80]) to smooth  $R(Q)$  and calculates second-order accurate central differences to find the derivative of the smoothed profile.

### Plotting reflectometry data

There is not a standard format for plotting reflectometry data; plots of  $\log(R)$  against  $Q$ ,  $\log(RQ^4)$  against  $Q$ , and  $\log(R/R_F)^v$  against  $Q$  are common. The reflectometry profiles in this thesis are typically plotted as  $\log(RQ^4)$  against  $\log(Q)$ , as we believe that they best show the subtle features at low  $Q$  that contain important features regarding extended brush structure.

### 1.5.3 Neutron reflectometry

All NR measurements were carried out on the PLATYPUS time-of-flight neutron reflectometer at the the Australian Nuclear Science and Technology Organisations (ANSTOs) 20 MW Open-pool Australian Lightwater Reactor (OPAL) reactor source in Sydney, Australia [81]. All measurements were made at two angles, with the lower angle always capturing the critical edge (where present) to allow for data to be correctly scaled. Both air-solid and solid-liquid measurements were conducted in the upward reflecting geometry. The confined geometry experiments in chapters 5 and 6 were conducted in the downwards reflecting geometry. Choppers 1 and 4 were used for all experiments, and data reduction was performed using *refnx* and followed the standard procedure for Platypus [81] unless otherwise specified, producing a final resolution of  $\frac{\Delta Q}{Q} = 8.8\%$ .

PNIPAM brushes were first measured in air with NR determine  $\hat{V}_1$  prior to solvation. Their solvated structure was then measured in a standard solid-liquid cell, the temperature of which could be controlled. The volume of these cells is  $\approx 0.5$  mL; at least 5 mL was pumped through the cell to effect solvent exchange. Two solvent contrasts were used for solvated experiments, pure D<sub>2</sub>O and a 80.3:19.7 D<sub>2</sub>O:H<sub>2</sub>O mix by volume, designed to match the SLD of PNIPAM, hence referred to as  $\text{CM}_{\text{poly}}$ . The pure D<sub>2</sub>O measurements were sensitive to the structure of the polymer brush, whilst the  $\text{CM}_{\text{poly}}$  measurements

---

<sup>v</sup> $R_F$  is the Fresnel reflectivity; the signal from a bare fronting/backing interface.

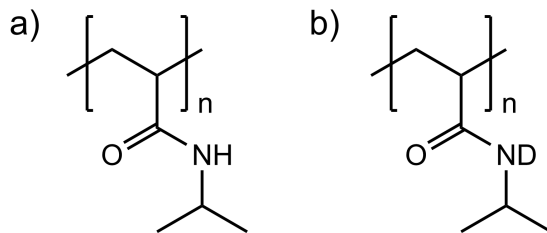


Figure 1.9: (a) native and (b) partially deuterated structures of NIPAM. The structure in (b) is the equilibrium monomer structure of PNIPAM in  $\text{D}_2\text{O}$ .

allowed for the determination of the structure of both the silica native-oxide layer and non-polymer chemical species within the brush. There may be small differences in structure between the two contrasts due to the isotope effect, however, NR is not able to determine the magnitude of the difference for this system, as we cannot resolve the structure of the brush in  $\text{H}_2\text{O}$  due to the poor contrast. We do, however, observe similar brush behaviour in both ellipsometry ( $\text{H}_2\text{O}$ ) and NR ( $\text{D}_2\text{O}$ ).

### Contrast variation

One advantage of NR is the ability to change the SLD of compounds through isotopic substitution. For example,  $\text{H}_2\text{O}$  has an SLD of  $-0.56 \times 10^{-6} \text{ \AA}^{-2}$ , while  $\text{D}_2\text{O}$  (D is deuterium or  $^2\text{H}$ ) has an SLD of  $6.34 \times 10^{-6} \text{ \AA}^{-2}$ . Isotopic substitution allows for the contrast between experimental components to be advantageously adjusted, either through ‘contrast matching’ specific components to make them invisible to neutrons or to highlight scattering from a component of interest. SLD values of compounds used in this thesis are given in appendix A.

### Hydrogen–deuterium exchange in PNIPAM

Widmann et al. [82] convincingly show that the amide in NIPAM can become deuterated (Fig. 1.9) by exposure to  $\text{D}_2\text{O}$  vapour. This H-D exchange appears to take place over approximately three days [82] at 90 % relative humidity and temperature of  $26.5^\circ\text{C}$ . It is expected that this H-D exchange would occur faster in a  $\text{D}_2\text{O}$  solution, rather than vapour, but this has not been confirmed. We investigate the SLD of both hydrogenous and deuterated PNIPAM in chapter 3.

### 1.5.4 X-ray reflectometry

X-ray reflectometry (XRR) was used as an additional method of characterising the dry brush thickness prior to the neutron reflectometry experiments. The specular reflectometry measurements were taken using a Panalytical X'Pert Pro X-Ray reflectometer with Cu K- $\alpha$  radiation ( $\lambda = 1.541 \text{ \AA}$ ). XRR data were modelled using a slab model, with a single slab for the silica layer (SLD of  $18$  to  $22 \times 10^{-6} \text{ \AA}^{-2}$ ) and a single slab for the polymer layer (SLD of  $8$  to  $12 \times 10^{-6} \text{ \AA}^{-2}$ ). The SLDs of air and silicon were taken as  $0$  and  $20.1 \times 10^{-6} \text{ \AA}^{-2}$  respectively.

### 1.5.5 Ellipsometry

Ellipsometry is a technique that measures the change in the polarisation of light upon reflection from an interface, generally as a function of wavelength, angle of incidence or a combination of the two. The incident monochromatic light beam is composed of  $S$  (surface-perpendicular) and  $P$  (surface-parallel) components. These components are not measured directly; instead, the relative amplitude ( $\Psi$ ) and phase difference ( $\Delta$ ) of the  $P$  and  $S$  components are the parameters of interest [71, 72]. In this thesis, we exclusively use nulling ellipsometry, which derives ellipsometric parameters from the angle of polarisers required to produce a zero-signal. Like the reflectometry techniques described above, ellipsometry is an indirect technique whereby the interfacial structure is obtained from a modelling process. Here, the optical refractive index (RI) and extinction coefficient are used instead of the SLD, but otherwise the process is similar, with ellipsometry being sensitive to the surface-normal interfacial structure with thicknesses between  $10$  to  $10\,000 \text{ \AA}$ . Ellipsometry can also be used to study solid-liquid interfaces, generally through the use of a ‘liquid cell’ with windows positioned at a suitable angle, in this configuration, the angle of incidence cannot be changed. The primary disadvantages of ellipsometry for studying polymer brushes are the lack of optical contrast between polymers and most solvents (including water) and the perception that ellipsometry is insensitive to structure.

Most ellipsometric studies of polymer brushes describe the polymer layer structure with a simple slab-like model and its RI with an effective medium approximation (EMA) [20, 48, 76, 83–86]. Generally, this EMA describes the RI of a mixed layer by linearly interpolating between the RI of two pure components based off a given composition (analogous to Equation 1.9), although non-linear interpolation options are available. These slab analyses produce a brush thickness, but offer no additional information regarding their structure. However, there are some studies that extract brush structure from ellipsometry, typically for brushes with  $\hat{V}_1$  of over  $1000 \text{ \AA}$  [64, 69, 87].

Two ellipsometers are used in this thesis, a Woollam M-2000 spectroscopic ellipsometer ( $\lambda$  range of 370 to 1000 nm) and an Accurion nanofilm EP4 spectroscopic imaging ellipsometer ( $\lambda$  range of 360 to 1000 nm). Two types of ellipsometry measurements were performed, each for distinct reasons: the first was mapping ellipsometry, whereby the macroscopic uniformity of dry samples intended for NR were characterised, the second is in-situ ellipsometry, where the thickness (or structure) of a solvated brush was measured as a function of solvent conditions. As the windows of the solid-liquid cells are constructed at a fixed angle, a spectroscopic instrument is essential for robust in-situ measurements. A spectroscopic instrument allows for measurements to be taken at multiple wavelengths, increasing the number of datapoints that the ellipsometry model is optimised against. Specific modelling techniques are discussed in the relevant chapters.

### 1.5.6 Quartz crystal microbalance with dissipation monitoring

QCM-D measures changes in the resonant frequency,  $\Delta f$ , and energy dissipation,  $\Delta D$ , of an electrically excited quartz crystal as a function of time and overtone number (overtones are harmonics of the fundamental frequency) [88, 89]. Originally, the QCM technique was used to measure gas-phase adsorption [90], but it has since been modified to work in a solid-liquid arrangement [91]. In either case, changes in  $\Delta f$  and  $\Delta D$  correspond to changes in adsorbed mass and the mechanical coupling of the surface and the fluid, respectively (all else being equal) [88].  $\Delta f$  and  $\Delta D$  are also sensitive to the sensor temperature and the fluid's density and viscosity [91]. The decay length (correlated to how far the QCM-D signal penetrates into the coated layer) shrinks with increasing overtone number; the 3<sup>rd</sup> overtone possesses a decay length of 2500 Å for brush systems with swollen thicknesses on the order of 1000 Å and is consequently sensitive to changes in mass throughout the entire brush [92]. Conversely the 13<sup>th</sup> overtone possesses a decay length of 700 Å, making it sensitive to changes nearer to the substrate [92]. Comparing  $\Delta f$  and  $\Delta D$  values from different overtones will then provide information regarding the distribution in adsorbed mass and viscoelasticity of the brush in the direction normal to the substrate. In this thesis, we tether polymer brushes to silica-coated QCM-D sensors using the method described in Section 1.4; when the brush swells,  $\Delta f$  decreases, as water molecules are sequestered by the brush, while  $\Delta D$  increases as the surface becomes more mechanically coupled to the solvent. All reported  $\Delta f$  values have already been divided by the overtone number; this is done automatically by the Qsense monitoring software.

Layer properties, such as adsorbed mass, viscosity, and thickness can often be calculated from changes in  $\Delta f$  and  $\Delta D$  [90, 93]. Modelling is typically carried out on systems where the layer of interest can be reasonably approximated as a single uniform layer.



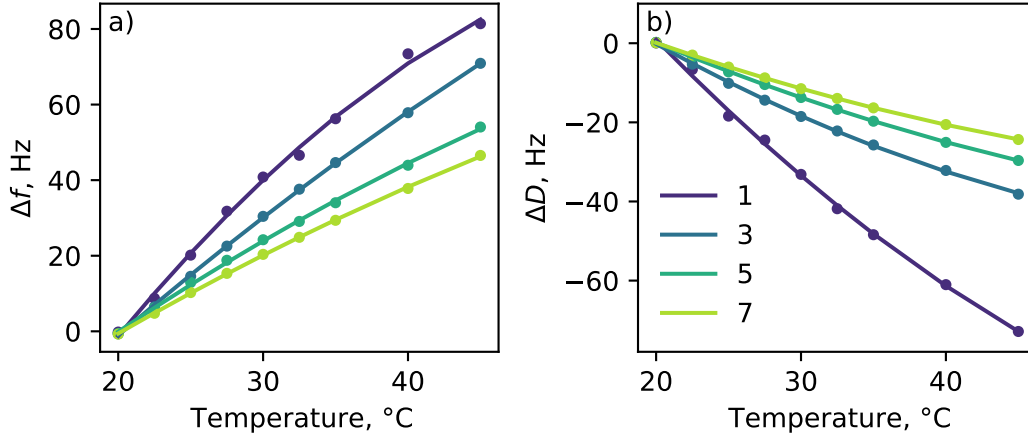


Figure 1.10: Temperature calibration of (a) frequency and (b) dissipation for QCM-D wafers used in this thesis at overtones 1 through 7. A second-order polynomial was fit to the collected data (solid lines), allowing the effect of temperature on the sensor to be accounted for later in the analysis.

For example, Sadman et al. [94] successfully model the swelling of a thermoresponsive hydrogel film using both Voigt and Power-law models. However, for brush systems this becomes more complex, as brushes cannot reasonably be described as a single uniform layer. Modelling is still possible in the case of very thin brush layers ( $\hat{V}_1 = 5$  nm), as in the work of Bittrich et al. [86], where the swollen layer thickness is below the Sauerbrey limit [94]. Recent work has shown that QCM-D is sensitive to the volume fraction profile of polymer brushes, but quantitative modelling of this volume fraction profile has not been undertaken [92]. Consequently, we will not attempt to model QCM-D data from swollen polymer brushes in this work, and will instead make inferences regarding the layer properties from temperature-corrected plots  $\Delta f$  and  $\Delta D$ .

QCM-D studies were performed using a QSense Analyzer (Biolin Scientific) using 5 MHz QSensor QSX 303 SiO<sub>2</sub> sensors. The system temperature was controlled using the inbuilt thermostat. As frequency and dissipation are very sensitive to the resonator's temperature, the effect of temperature on the response of the bare wafers in water was characterised prior to the polymerisation. The results of this characterisation for a single wafer are shown in Fig. 1.10, where a second-order polynomial was fit to both the frequency and dissipation curves. In all QCM-D experiments in this thesis, the change in signal is the measured change in signal less the change due to temperature.

## Characterisation of QCM-D wafers

Throughout this thesis, two brush-coated QCM-D wafers are used. During synthesis, QCM-D wafers were paired with silicon wafers ( $\approx 1.5 \times 3$  cm) as per the method of Humphreys et al. [48], resulting in similar brush coatings on the QCM-D and silicon wafers.<sup>vi</sup> The dry thickness of the brush on the silicon wafer was measured with variable-angle ellipsometry (Accurion nanofilm EP4,  $\lambda = 658$  nm, see section 1.5.5); the quartz–gold–silica layer structure of the QCM-D sensor prevented the dry thickness from being measured directly from the sensor surface. The thickness of the brushes on the paired wafers was  $145 \pm 8$  Å and  $200 \pm 10$  Å. Due to the adsorption of water within the PNIPAM film under ambient conditions, we assume the interfacial volume of the wafers to be 130 and 180 Å respectively (note that the interfacial volume is the volume of polymer per unit area, with units of length), 10 % thinner than under ambient conditions. This assumption is verified in section 3.3.4.

---

<sup>vi</sup>We have previously found that two silicon wafers prepared in the same reaction mixture possess similar ellipsometric thicknesses.

## 1.6 Overall structure of this thesis

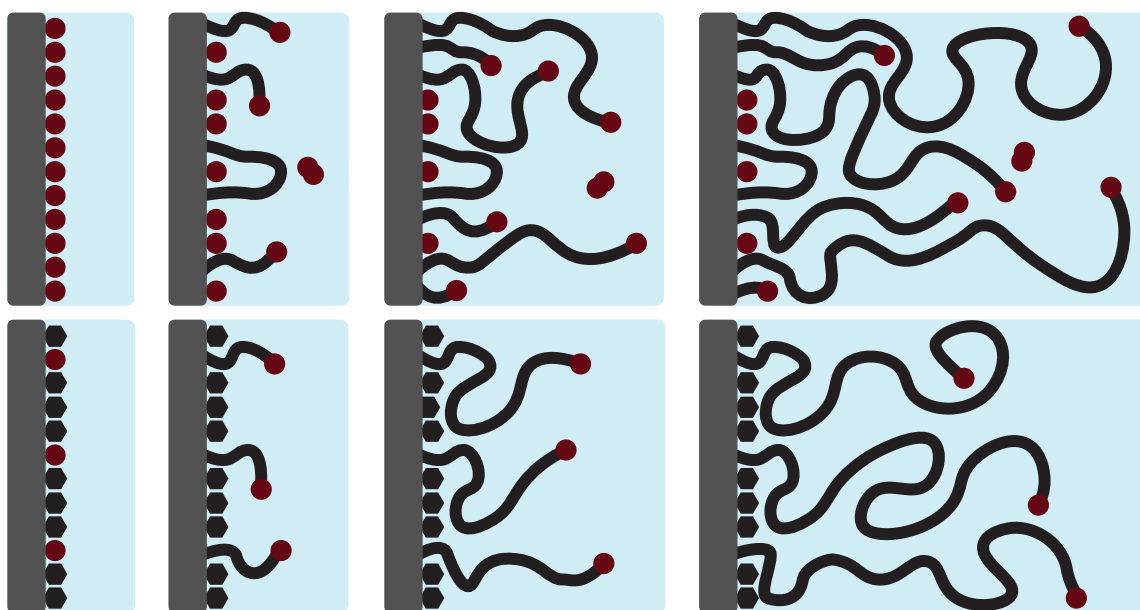
In this thesis we develop and demonstrate methods for the analysis of polymer brush systems with NR, using PNIPAM as a model system throughout. We start by characterising the synthesis and unsolvated behaviour of these layers. In chapter 2 time-resolved NR is used to observe the synthesis of a PNIPAM brush *in situ* for the first time. Syntheses from wafers with different initiator grafting densities are observed to determine the origin of the interior layer often observed by NR for these grafted-from systems. Chapter 3 is concerned with the behaviour of unsolvated PNIPAM films. The response to both relative humidity and temperature is investigated, and the SLD and solvent fraction of PNIPAM brushes in ambient conditions are determined.

We move on to detailing novel analysis methodologies in the following two chapters. Chapter 4 demonstrates and details a brush model that minimises assumptions regarding the structure of the brush, while allowing monotonicity and  $\hat{V}_1$  to be constrained. The validity of this approach is demonstrated before it is applied to model the thermoresponse of a PNIPAM layer. In Chapter 5, we develop a novel ‘distribution model’ that we use to analyse NR data from a unique sample environment that can subject a brush to molecular confinement.

In Chapter 6, the knowledge and NR analysis techniques developed in prior chapters are applied to answer open questions regarding polymer-surfactant phenomena, thereby demonstrating the use of the developed analysis methods in understanding the behaviour of complex brush systems.

## Chapter 2:

Grafting density control and *in situ* observation of surface-initiated ATRP



The molecular weight distribution of grafted-from polymers is known to differ from polymers produced by free initiators. Understanding the structures formed by grafting-from polymerisation is essential, as the system structure dictates the macroscopic properties of polymer brushes. This structure depends on many variables, including the polymer molecular weight distribution and grafting density. Neutron reflectometry can resolve the density profiles of polymer brushes, and as such is sensitive to the changes in VF profiles caused by bimodal or very broad molecular weight distributions. Previous neutron reflectometry studies of grafted-from brushes have observed a dense thin layer adjacent to the substrate (the ‘interior’ layer). The origin of this layer and how it relates to synthesis conditions are unknown.

In this chapter, we characterise the polymerisation methodology used in this thesis and develop a method for varying the initiator grafting density. We then investigate the origin of the interior layer using time-resolved neutron reflectometry, which can resolve the structure of the growing brush, from both high- and low-initiator density surfaces. To our knowledge, this is the first time that the structure of a polymer brush has been documented during its synthesis.

## 2.1 Theoretical background

Grafting-from polymerisation is often the only viable means by which polymer brush coatings can be prepared with the desired grafting density and molecular weight [95]. Surface-initiated atom transfer radical polymerisation (ATRP) is one of the most popular methods for performing grafting-from polymerisation [95, 96]. However, relatively little is known regarding the structures produced by planar surface-initiated ATRP, that is, the molecular weight distribution of the substituent polymers. This knowledge deficit arises because it is difficult to produce high enough polymer volumes on planar substrates to allow for cleavage and conventional analysis, for example, by gel permeation chromatography (GPC). The typical solution to this problem is to simultaneously synthesise from free initiators in the same reaction vessel and characterise them conventionally, assuming that the molecular weight distribution is independent of the polymer geometry [95]; however, it is well accepted that this assumption is flawed [95, 97–99].

Here, we investigate the growth of surface initiated polymers and demonstrate the use of time-resolved neutron reflectometry (NR) as a tool for studying surface-initiated polymerisation. We begin with a brief overview of the relevant literature, discussing evidence for poor control of surface-initiated ATRP and its mechanistic origins. We then extend the synthetic method described in section 1.4 by developing a method for modifying the initiator grafting density, supporting this method with studies of bromination and polymerisation kinetics. Finally, we employ time-resolved NR to study the structural evolution of the polymer layer during synthesis.

### 2.1.1 Bimodality in surface-initiated ARGET ATRP

Martinez et al. [97] study the molecular weight distribution of grafted-from poly(methyl methacrylate) (PMMA) chains by degrafting followed by GPC. To produce the volume of grafted-from polymer needed for study, they graft PMMA from a nylon membrane with a high specific surface area; while this is not directly comparable with polymers grafted-from planar surfaces, it illustrates the marked difference between free polymerisation and surface-initiated polymerisation. Martinez et al. show that while the molecular weight distribution of free-polymer is unimodal, grafted-from chains possess a bimodal molecular weight distribution, indicating the presence of a dense layer of short, surface-proximal polymer chains (Fig. 2.1). While the short polymer chains could not be completely characterised due to experimental limitations, they were approximated to have a molecular weight of  $\approx 2000$  Da, corresponding to approximately 20 MMA units. Significantly, reducing the initiator grafting density reduced the prevalence of these short chains (Fig. 2.1).

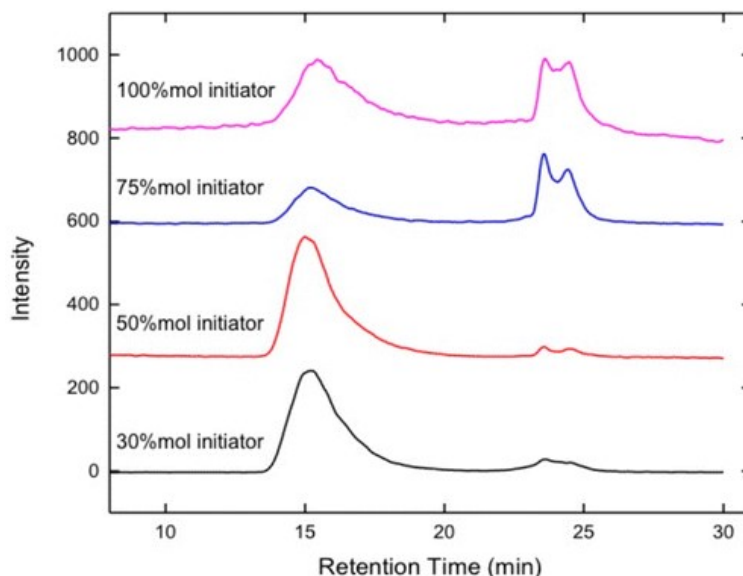


Figure 2.1: GPC results from Martinez et al. [97], showing that surface-initiated ATRP produces bimodal polymer distributions at high initiator densities. As GPC is sensitive to polymer mass, not the number of chains, the fraction of short chains is higher than it appears (calculated to be 0.98 for the 100 %  $\sigma$  sample and 0.93 for the 30 % sample, consistent with reports of ATRP initiation efficiency discussed in section 2.1.3). Reprinted with permission from Martinez et al. [97]. Copyright 2021 American Chemical Society.

Simulations offer several explanations for the bimodality observed by Martinez et al. [97]. The work of Keating IV, Lee, and Belfort [100] shows that the extremely low ratio of initiator to catalyst in planar polymer brush syntheses results in poor reaction control. They suggest adding free free initiator to the reaction solution, but Martinez et al. [97] report the the addition of free initiator does not reduce the reported bimodality. Martinez et al. [97] also perform molecular dynamics (MD) simulations of the surface initiated ATRP system, finding that chain-chain termination is the primary cause of this bimodality. Monomer shielding of shorter chains, where monomer diffusion to the active end of short chains is prevented by longer chains, is observed to be a secondary cause. The issue of bimodality is also linked the the concept of initiation efficiency, which is discussed in detail below. Understanding and controlling this bimodality is important as it can strongly influence the solvated brush’s structure (Fig. 1.4).

### 2.1.2 Origin of the interior layer

A phenomena adjacent to the bimodality observed by Martinez et al. [97] is the ‘interior layer’ observed by several previous NR studies of grafted-from brushes, which appears to be independent of the polymer composition [20, 22, 73, 85, 101–104]. In this chapter we seek to better understand the composition of this interior layer. Our motivation for doing

so is twofold: Firstly, understanding the structures formed by surface-initiated ATRP is key to improving the synthesis and properties of these interfaces. Secondly, knowing the origin (and subsequent properties) of this interior layer is helpful when designing models to describe solvated brush structure, which is a key element of this thesis.

Before continuing we address one obvious explanation for this interior layer: that it is simply made up of deposited polymerisation initiators. The thinnest interior layers reported for the surface preparation/polymerisation scheme used here are approximately 15 Å thick [20].<sup>i</sup> This thickness approaches that expected of a tightly-packed initiator monolayer; here our initiator layer is prepared in a two-step process, first (3-Aminopropyl)triethoxysilane (APTES) is vapour-deposited, then  $\alpha$ -bromoisobutyryl bromide (BiBB) is reacted with the APTES layer (section 1.4). Studies of vapour-deposited APTES layers on silica find that they have a thickness of between 3 and 9 Å [105–107]. However there is not yet a standard recipe for preparation of vapour-deposited APTES films. Zhang et al. [106] use a temperature of 150 °C, pressure of <4 mbar and reaction time of 5 min; Zhu, Lerum, and Chen [105] use a temperature of 70 °C, pressure of 1 atm and reaction time of 24 h; and Giraud et al. [107] use ambient temperature, pressure of <5 mbar and reaction time of 4 h. The method used here (and elsewhere [20, 21, 48, 73, 76, 83, 85, 101, 102, 108, 109]) is conducted at ambient temperature, a pressure of <5 mbar and for a reaction time of 30 min. From the ellipsometry study of Giraud et al. [107] we expect our APTES layers to have a hydrolysed thickness of  $\approx 3$  Å; this thickness is approximately half the ‘contour length’ of APTES ( $\approx 6$  Å [107]). It then follows that bromination increases the contour length of the tethered APTES by no more than 3 Å (the approximate length of BiBB), resulting in a final initiator interfacial volume of less than 4.5 Å. Here interfacial volume refers to the volume of a material per unit area, and has units of length. We do not expect this layer to hydrate due to its hydrophobic nature. Consequently, the initiator layer is not thick enough on its own to form the observed interior layer.

There are then two, non-mutually exclusive, explanations for the presence of this interior layer. It may be the result of early chain-termination through chain-chain termination or monomer shielding (as in the work of Martinez et al. [97]), or it could consist of polymer physisorbed to the substrate. The former explanation would result in the interior layer depending strongly on the initiator grafting density. Poly(*N*-isopropylacrylamide) (PNIPAM) is a good choice for investigating the formation of this interior layer, as its moderate hydrophilicity and lack of charge remove hydrophobic and charged-based arguments for the formation of the interior layer.

---

<sup>i</sup>Thicker layers appear elsewhere [103, 104], and may be explained by different phenomena.



### 2.1.3 Initiation efficiency

In this work, we control the grafting density by varying the initiator density. It is important to acknowledge that not all initiator sites result in a grafted polymer chain; the fraction that do (grafting density divided by initiator density) is termed the *initiation efficiency* [95]. The precise definition of the *initiation efficiency* is dependent on the definition of when an oligomer becomes a polymer chain and how it is measured (all measurement techniques are indirect) [95]. Here we define a successful initiation as an initiation that results in a polymer with a  $N$  greater than 5% of the modal polymer length. Our primary method of determining the grafting density is through the thickness of the subsequent polymer layer, which is insensitive to these short chains. Consequently, in the subsequent calculation of the lower bound for the *initiation efficiency* these short chains will be ignored and we will assume all long chains are of a similar molecular weight.

For the polymerisation scheme used in this work, a grafting density of  $0.0007 \text{ \AA}^{-2}$  has been reported (Table 1.1), based off the single-molecule force spectroscopy (SMFS) study of Murdoch et al. [20]. This value is lower than other values reported for initiator density as it is calculated via SMFS, which is a measure of the product of initiator grafting density and *initiation efficiency*. Furthermore, SMFS is sensitive only to the longest chains, so grafting density will be underestimated. Giraud et al. [107] approximate that a vapour-deposited APTES monolayer has a grafting density of  $0.1 \text{ \AA}^{-2}$ . They note that these APTES layers are not hydrolytically stable; similar studies have found that hydrolysis reduced the thickness of the vapour-deposited APTES monolayer by approximately half [105]. Consequently, we assume a hydrolysed initiator density of  $0.05 \text{ \AA}^{-2}$  and note that it is possible that the APTES density of our deposition method is lower than those reported elsewhere due to differences in temperature and exposure time [48, 105–107]. The difference between the density of polymer determined by SMFS and the initiator density calculated above can be explained by the *initiation efficiency*. With all caveats noted, and assuming a that the bromination reaction proceeds to completion, we can approximate a lower bound for our *initiation efficiency* of 1.4%. This value is of a similar order of magnitude to values reported in other surface-initiated ATRP studies [110].

There are a number of mechanisms through which low *initiation efficiencies* can be explained. These include chain-chain termination [97] and monomer shielding. Simulation has shown that the *initiation efficiency* is a strong function of the number of monomers added per activation cycle (rate of reaction), with more rapid reactions reducing the *initiation efficiency* [99]. This because chains that are initiated earlier will shield neighbouring initiators from monomer in solution; the efficacy of this shielding is dependent on the length of the polymer. Consequently, the effect of shielding early in the polymerisation

is strongly dependent on the number of monomers added per activation cycle [99]. It is generally accepted that initiation efficiency increases as initiator density decreases [95], as such, we expect the relationship between grafting density and initiator density to be non-linear.

## 2.2 Materials and Methods

### 2.2.1 Materials

Uniform brush samples for the bromination kinetics and grafting density studies were prepared on 1 mm thick silicon wafers cut to a size of approximately  $10 \times 20$  mm. Gradient brushes were prepared on 1 mm thick silicon wafers cut to dimensions of approximately  $10 \times 50$  mm, with the direction of the gradient along the long axis. All silicon wafers were purchased from EL-CAT Inc. (USA). Benzoyl bromide (BB) (97 %) and deuterated methanol (d-MeOD) were purchased from Sigma Aldrich and used as received. All other reagents are detailed in section 1.3.

### 2.2.2 Synthetic details

Here, we infer details regarding the polymers' grafting density and molecular weight from the thickness of the synthesised polymer layers. As in the rest of this thesis we use ARGET ATRP to prepare our brush layers, described in detail in section 1.4. To make measuring the thickness of these layers easier with ellipsometry and interferometry we desire thicker layers than are used elsewhere in this thesis. As such, we use a 2:1 water to methanol (MeOH) ratio in the experiments in this chapter. Increasing the solvent water fraction increases the reaction rate by increasing the solvent polarity (relative to the standard 1:4 ratio used elsewhere). Unless specified, reaction conditions are otherwise identical to those described in 1.4.

### 2.2.3 Bromination kinetics

Here, the bromination kinetics are of interest as they inform our grafting-density variation method. The kinetics of the bromination step were investigated by exposing APTES-coated wafers to the bromination solution (3.0 vol% triethylamine (TEA), 2.6 vol% BiBB in tetrahydrofuran (THF)) for varying amounts of time (between 5 and 3600 s). After the wafer had spent the allotted time in the BiBB solution it was removed and quickly washed with copious amounts of ethanol; remaining unanchored BiBB will react with the ethanol hydroxyl group and be quickly neutralised. The kinetics of the BiBB-APTES reaction was probed by polymerising from the wafers for a fixed period of time (150 min). The brush thickness was then measured with thin-film interferometry, with ten measurements taken randomly over each wafer.

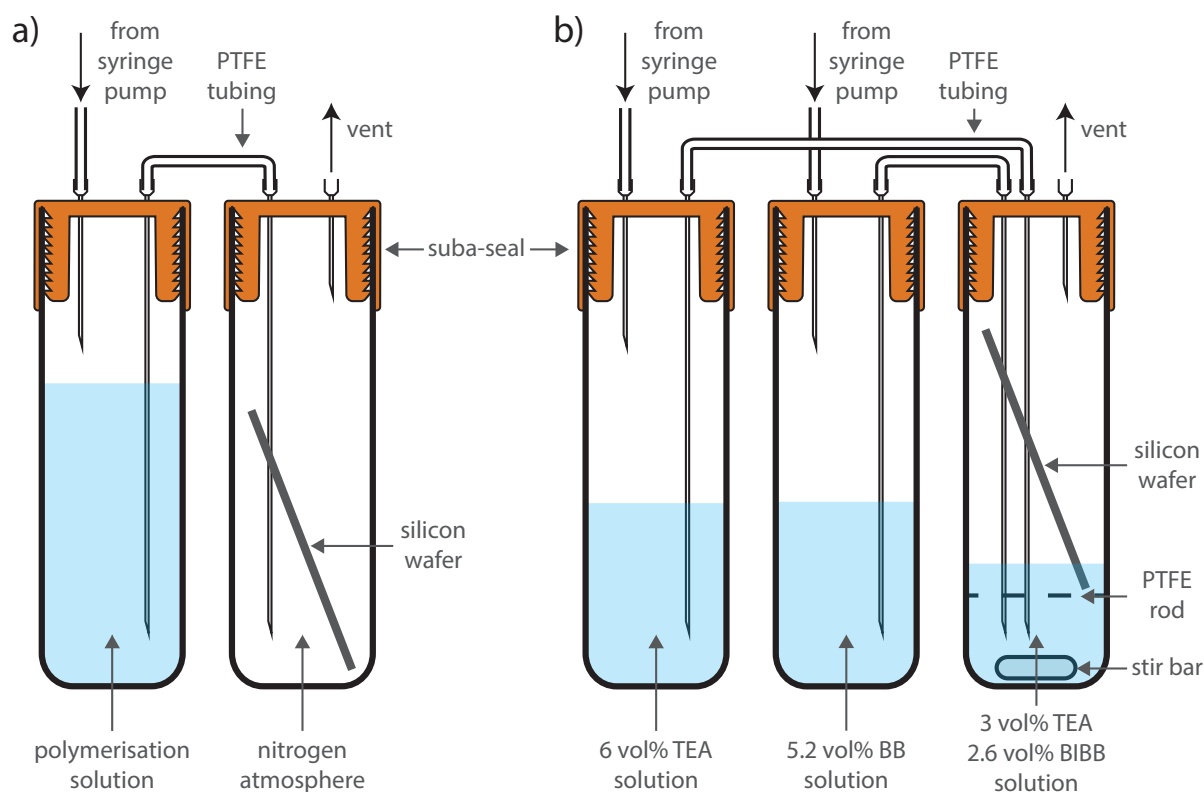


Figure 2.2: Experimental setups for (a) gradient molecular weight and (b) gradient grafting density syntheses. In both arrangements, the flowrate of reagent/s is controlled by pressurising feed solutions using a nitrogen-filled syringe pump running at a constant flowrate.

## 2.2.4 Preparation of molecular weight gradient brushes

Gradient molecular weight samples [111] were produced by gradually varying the time that different sections of a long silicon wafer (which had already been subject to APTES deposition and bromination steps) was exposed to the polymerisation solution. This was implemented by placing the wafer in a 50 mL glass vial (approximate radius and height 15 and 65 mm, respectively) which was then sealed with a Suba-seal and purged with nitrogen. The polymerisation solution was then transferred into the sample vial via the mechanism shown in Fig. 2.2a. A syringe pump (running at a fixed flowrate) was used to force liquid from the solution vial into the sample vial; the solution was not placed directly into a syringe to prevent contamination. The total polymerisation time (starting from when the solution made contact with the bottom of the wafer) was 160 min, the solution reached the top of the wafer at approximately 130 min. Thickness was determined via mapping ellipsometry, which measured the thickness of the polymer in the middle (widthways) of the wafer at 5 mm intervals along its length.

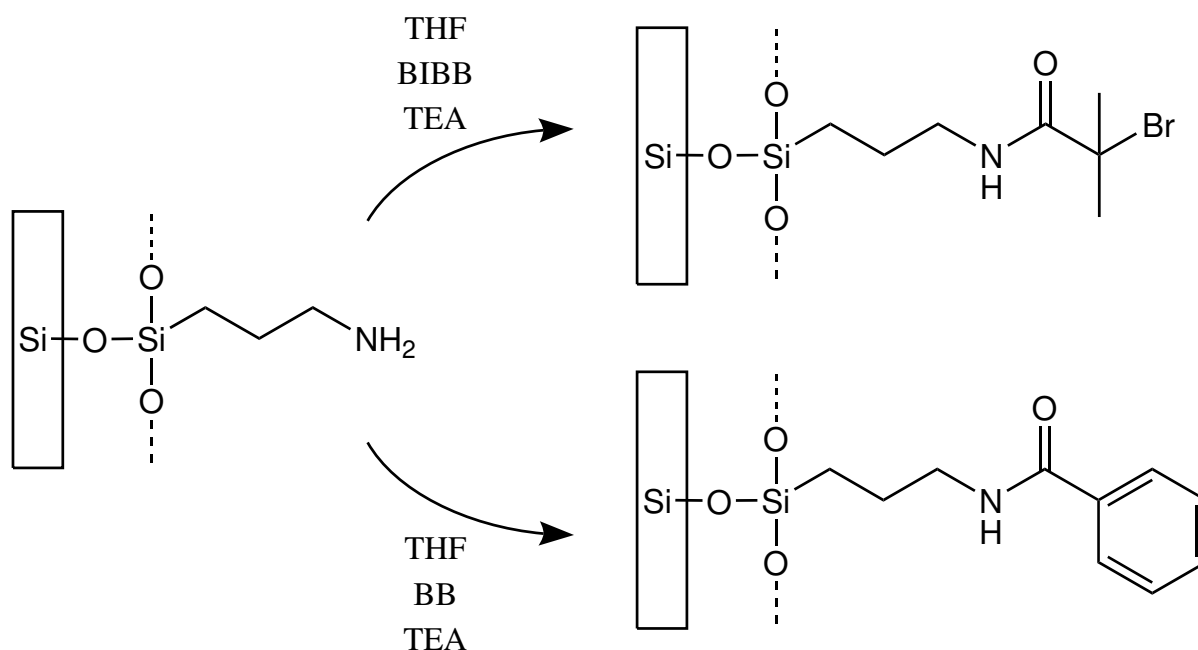


Figure 2.3: Mechanism by which grafting density is varied. The organobromine in the BiBB (top) is the polymerisation initiator, which is not present in BB. BiBB and BB react with the APTES layer via the same mechanism and have comparable molecular masses and volumes.

### 2.2.5 Variation of initiator density

We control the polymer grafting density by varying the density of bromine polymerisation initiators on the surface of a wafer; our method can be used to prepare both uniform and gradient wafers. We vary the initiator density at the bromination step, after the APTES monolayer has been deposited on the surface, through substituting the BiBB initiator with inert BB, as shown in Figure 2.3. Both BiBB and BB react with the APTES layer via the same mechanism, and have comparable molecular masses ( $229.9$  and  $185.0 \text{ g mol}^{-1}$ ) and volumes ( $123.6$  and  $117.8 \text{ cm}^3 \text{ mol}^{-1}$ ). However, only BiBB has the organobromine that acts as the ATRP polymerisation initiator.

It is worth noting that the grafting density of the polymer is not limited only by the grafting density of the initiator, but by the product of the initiator grafting density and the initiation efficiency, as discussed in section 2.1.3. If the initiation efficiency is inversely proportional to the initiator density, then the layer thickness will not scale linearly with initiator density. Future work should examine the initiator density with a spectroscopic technique (i.e., Raman spectroscopy), which would provide further insight into the polymer growth kinetics.

## Uniform wafers

The procedure for uniform grafting density variation is as follows. First, all glassware required was dried, as BiBB and BB form hydrobromic acid upon contact with water. 1 mL mixtures of pure BiBB and BB were then made up in 5 mL vials (sealed with a suba-seal to prevent contact with atmospheric water), to produce solutions with the desired molar ratio of BiBB to BB. These components must be mixed before they are added to the vessel containing the wafer, as the rapid initial reaction kinetics would result in the species added first saturating the surface (see section 2.3.1). After the initiator solution is mixed, reagents were syringed into a dry vial containing silica wafers to produce a 3.0 vol% TEA, 2.6 vol% initiator-mix solution in THF that covered the wafer. Generally, the total solution volume was 10 mL, but this volume was adjusted depending on wafer size. After all reagents had been added, the wafer is left in the solution for 60 min, before it is removed and rinsed in THF, ethanol and water. The resulting initiator grafting density of each sample was then probed by polymerising from the wafers (using the procedure outlined in section 2.2.2) for a fixed period of time (150 min), and measuring the resulting thickness with thin-film interferometry (section 2.2.9), with ten measurements taken randomly over each wafer.

## Gradient wafers

Gradient grafting density samples were produced by preparing the APTES layer according to the method in section 1.4. After this, the wafer was placed in a dry 50 mL glass vial (approximate radius and height 15 and 65 mm, respectively), along with a polytetrafluoroethylene (PTFE)-coated stir bar; the wafer was suspended above the base of the vial by a PTFE rod, which allowed the stir bar to spin freely (Fig. 2.2b). The vial was sealed with a Suba-seal, and 10 mL of THF, 0.26 mL of BiBB, and 0.3 mL of TEA was carefully syringed into the bottom of the vial. The wafer had been positioned such that the bottom 5 mm was submerged after addition of the BiBB solution. Solutions of BB and TEA (5.3 vol% and 6 vol%, respectively) in anhydrous THF were prepared, placed in glass vials, and connected to the sample tube as shown in Fig. 2.2b. Syringe pumps were used to slowly transfer the BB and TEA solutions to the sample vial at a constant flow rate (equal for both solutions) over the course of 120 min. The stirrer bar ensured that the solutions were well mixed upon introduction to the sample vial. BB and TEA solutions could not be mixed before injection into the sample vial as they form a white precipitate when mixed; the precipitation was expected in the bromination reaction, but the precipitate blocked tubing if the solutions were mixed pre-injection. After the gradient bromination had been completed, the wafers were cleaned with THF and ethanol, before

Table 2.1: Experimental conditions for *in situ* synthesis.

Synthesis Number	1	2	3
D <sub>2</sub> O : d-MeOD	2:3	1:2	1:2
BiBB : BB	1:0	1:0	1:3
NIPAM (mg mL <sup>-1</sup> )	24	50	50
HMTETA (mg mL <sup>-1</sup> )	0.86	1.70	1.70
CuBr <sub>2</sub> (mg mL <sup>-1</sup> )	0.16	0.16	0.16
Ascorbic acid (mg mL <sup>-1</sup> )	0.84	1.3	1.3
Temperature (°C)	5	5	5

being subject to polymerisation as described in section 1.4. Thickness was determined with mapping ellipsometry, which measured the thickness of the polymer in the middle (width-ways) of the wafer at 5 mm intervals along its length.

### 2.2.6 *In situ* NR synthesis

The structure of a PNIPAM brush was observed using time-resolved NR. For a detailed description of the NR technique, see section 1.5.3. Several adjustments to the synthetic recipe described in section 1.4 had to be made to enable the observation of the synthesis via time-resolved NR.

Firstly, a silicon block (section 1.3) was used instead of a silicon wafer. The NR experiment was sensitive to the structure of the brush within a 30 by 50 mm rectangle in the centre of the block. The synthesis was conducted in a solid-liquid cell designed for NR, with a solvent depth of  $\approx 0.1$  mm and a volume of  $\approx 0.5$  mL. It has been previously demonstrated that restricted geometries accelerate surface-initiated ATRP [112]. However, this effect appears to be insignificant at distances greater than 0.02 mm [112]; as such, we do not expect the solid-liquid cell used to affect the polymerisation kinetics.

The second modification that was made was the use of deuterated solvents (D<sub>2</sub>O and d-MeOD), which were required to enhance the contrast between the polymer and solvent. Deuteration is expected to increase the reaction rate, because more polar solvents increase the reaction rate of ATRP [113] and deuterium-oxygen moieties are more polar than their hydrogenous equivalents.

Thirdly, the solubility of the polymer in the reaction solution was decreased via the cononsolvency effect, whereby PNIPAM solubility decreases with MeOH mole fractions

between 0.2 and 0.5 [64, 67]. Reducing the polymer solubility in the reaction mixture allowed the polymer layer to be more clearly resolved. We targeted MeOH mole fractions of 0.4 and 0.47 (corresponding to a D<sub>2</sub>O to d-MeOD volume ratios of 1:2 and 2:3, respectively). These fractions balanced better temporal resolution (reduction of the reaction rate through higher d-MeOD concentrations) with better structural resolution (more collapsed layer due to cononsolvency). Reducing the polymer solubility via cononsolvency will likely increase the occurrence of monomer shielding in the growing chains, relative to the 1:4 H<sub>2</sub>O to MeOH ratio used elsewhere in this work. However, the ratios we use in our NR experiment have been reported elsewhere in the literature for the synthesis of PNIPAM brushes via ARGET ATRP [48], so the polymerisation behaviour at these conditions is still relevant.

Lastly, the method by which the polymerisation solution was prepared was modified to reduce the reaction volumes required. Below, we describe the method for *in situ* samples 2 and 3, the differences between these and sample 1 are summarised in Table 2.1 and discussed further in appendix C. Typically, polymerisation mixtures of 20 to 100 mL are produced using the method in section 1.4; however, reaction solutions of 3 mL were produced here to conserve deuterated solvent. Precursor solutions were prepared to enable accurate amounts of reagent to be added to the solution, both made up in D<sub>2</sub>O. The first solution contained 10.2 g L<sup>-1</sup> of 1,1,4,7,10,10-hexamethyltriethylenetetramine (HMTETA) and 0.99 g L<sup>-1</sup> of CuBr<sub>2</sub>, the second solution contained 7.81 g L<sup>-1</sup> of ascorbic acid. Both precursor solutions were deoxygenated and stored under a nitrogen atmosphere. 0.15 g of NIPAM and 0.5 mL of the first precursor solution were mixed with 2 mL of deuterated methanol (d-MeOD) and deoxygenated using dry nitrogen for 15 min. 0.5 mL of the second precursor solution was then added to the polymerisation mixture.

The last modification to the polymerisation method is the temperature. In an attempt to further slow the reaction kinetics, we used Julabo heater-chiller units to maintain the solid-liquid cell at 5 °C. The solid-liquid cell was placed in a box which was filled with dry N<sub>2</sub> to prevent condensation; the neutron beam accessed the cell through thin aluminium windows.

### 2.2.7 Neutron reflectometry experiments

Dry and standard (time-independent) solid-liquid experiments were carried out according to the method in section 1.5.3. Time-resolved NR experiments were conducted by continuously acquiring at an angle of 0.8°. Time-resolved reflectivity data were derived from the event-mode data acquisition post-experiment, with time slices adjusted to optimise temporal resolution and signal to noise ratio



The sample environment setup was as follows. A single solid–liquid cell containing a brominated wafer and filled with  $\text{D}_2\text{O}$  was placed in the centre of the sample stage and aligned. The pre-sample slits (slit 3 on *PLATYPUS*) were placed as close as possible to the sample<sup>ii</sup> to maximise the neutron flux and reduce the minimum time in which a usable reflectivity profile could be measured. A syringe pump was connected to the solid–liquid cell via a length of PTFE tubing; the syringe pump was placed on the sample stage to minimise the length of tubing required. Between the syringe pump and the solid–liquid cell was a three-way valve that allowed bubbles to be purged from the Luer-lock fitting upon connection of the syringe. The total volume of the valve and tubing are estimated to be less than 0.05 mL, with a corresponding residence time of approximately 1 s at the flowrates used; as such, the tubing is not expected to appreciably influence results. After alignment, but before polymerisation, the cell was filled with 2 mL of the same  $\text{D}_2\text{O}$ :d-MeOD mix that would be used in the polymerisation so that there would be no change in solvent composition during the injection. The polymerisation solution was drawn into a 5 mL syringe and placed into the syringe pump, which was programmed to wait for five minutes before beginning to pump at  $1.5 \text{ mL min}^{-1}$ . Once the syringe was in place, the timer was started and acquisition began on *PLATYPUS*. The programmed delay prior to the polymerisation solution being introduced allowed us to capture the reflectometry from the initiator-functionalised surface directly before polymerisation.

## 2.2.8 Neutron reflectometry data analysis

Data were reduced in the *refnx* reflectometry analysis package. Measurements that were not time-resolved were reduced with standard reduction procedures as outlined in section 1.5.3 and analysed using the freeform methodology developed in chapter 4. Time resolved reflectometry datasets were subdivided into 180 s intervals and reduced individually, with a final  $dQ/Q$  resolution of 8.8 %, identical to that obtained through standard reduction procedures elsewhere in this thesis.

The underlying silicon–silica interface was characterised by simultaneously modelling air,  $\text{H}_2\text{O}$ , and  $\text{D}_2\text{O}$  contrasts, which yielded the silica layer thickness, roughness and porosity with a high degree of certainty (Fig. 2.8); this process will be explained in more detail in chapter 4. Once the silica layer had been characterised, the time-resolved datasets were fit. Due to the low effective  $Q$ -range of the time-resolved datasets, a freeform approach (as detailed in chapter 4) could not be used. Instead, the data was either fit with a 1 or 2 slab model, one slab was used early in the polymerisation (less than  $\approx 360$  s), the 2 slab model was used for all other measurements. The first slab described the interior

---

<sup>ii</sup> “Danger close”

layer that has been observed by previous NR experiments (e.g., [20, 22, 73, 85, 103, 104]), while the second slab described the bulk of the growing brush. Large roughnesses were allowed to account for the diffuse brush interface, but these were manually constrained to be less than half of the adjacent layers' thickness. This constraint was enforced to prevent large roughnesses spilling across layers and creating artefacts in the scattering length density (SLD) profile. Each profile was optimised using a least-squares approach initiated from the parameter values of its neighbour (typically the longest-time sample was analysed first). For some datasets, select parameter values had to be manually set to ensure a consistent trend in the time series; for instance, once the interior layer had formed (600 s) its parameters were then fixed. However, important features such as the initial formation of the interior layer and the thickness of the 2<sup>nd</sup> slab were not constrained during fitting.

### 2.2.9 Interferometry

An Ocean Optics NanoCalc thin-film measurement system was used to measure the dry thicknesses of the uniform wafers. The technique measures the reflected intensity of white light incident upon the sample at an angle of 90° as a function of wavelength, extracting a thickness from this data via a modelling process. The instrument is rated to measure the thickness of thin films between 100 Å to 2500 Å. While the technique's output is similar to that of ellipsometry, interferometry must be measured relative to a reference sample, so absolute thicknesses from the technique are less reliable. Here an unmodified silicon wafer from the same batch as the brush-coated wafer was used as the reference sample. Modelling was performed in the nanocalc software, using a single layer model. The refractive index for PNIPAM in the model was set with Cauchy parameters from the work of Chen et al. [64]. Where thicknesses are reported, they represent the average value of ten measurements taken at random over the face of the wafer. Where errors are reported they represent the standard deviation of these ten measurements.

## 2.3 Results

First we report our findings on the rate of the bromination reaction, thus establishing the time frame required for gradient grafting density syntheses. We then report on the relationship between polymerisation time and average molecular weight, attained from a gradient polymerisation time synthesis. Control over polymer grafting density is then demonstrated, and implications of the non-linear relationship between  $d$  and  $\sigma$  are discussed. In this first part of the work, brush thickness is used to follow trends in grafting density, polymer molecular weight and initiation efficiency. We note that, for dry brushes,  $d$  is proportional to  $\sigma$  (unlike solvated brushes, section 1.1).

Finally, we present the *in situ* observation of the polymerisation using time-resolved NR and discuss volume fraction profiles corresponding to brushes with varying grafting density. We report details regarding the development of our method for the *in situ* observation in appendix C.

### 2.3.1 Bromination kinetics

The kinetics of the initiator layer formation were probed by examining the resulting dry polymer layer thickness. The bromination reaction was found to initially proceed rapidly, before slowly approaching equilibrium (Fig. 2.4). These kinetics are consistent with monolayer formation, where the reaction rate is proportional to the number of available reaction sites [114]. The implications of this experiment are twofold: firstly, when varying grafting density via substitution of BiBB with BB, the reagents should be mixed before being exposed to the APTES layer, since the binding of BIBB is sufficiently fast that sequential addition will not work. Secondly, the timescale of the gradient grafting density experiment should be on the order of one hour to allow for the reaction to go to completion. Figure 2.4 also demonstrates that bromination reaction time is a poor method to control initiator grafting density. It should be noted that the trend in Figure 2.4 is not due to the polymer molecular weight or initiation efficiency being strongly dependent on the grafting density. In section 2.3.3, we vary the initiator grafting density in a more controlled manner and do not see the rapid increase of polymer thickness with grafting density that is observed here.

### 2.3.2 Polymerisation kinetics

The kinetics of the polymerisation reaction were investigated by a gradient polymerisation time method, the results of which are shown in Figure 2.5. Over the polymerisation times

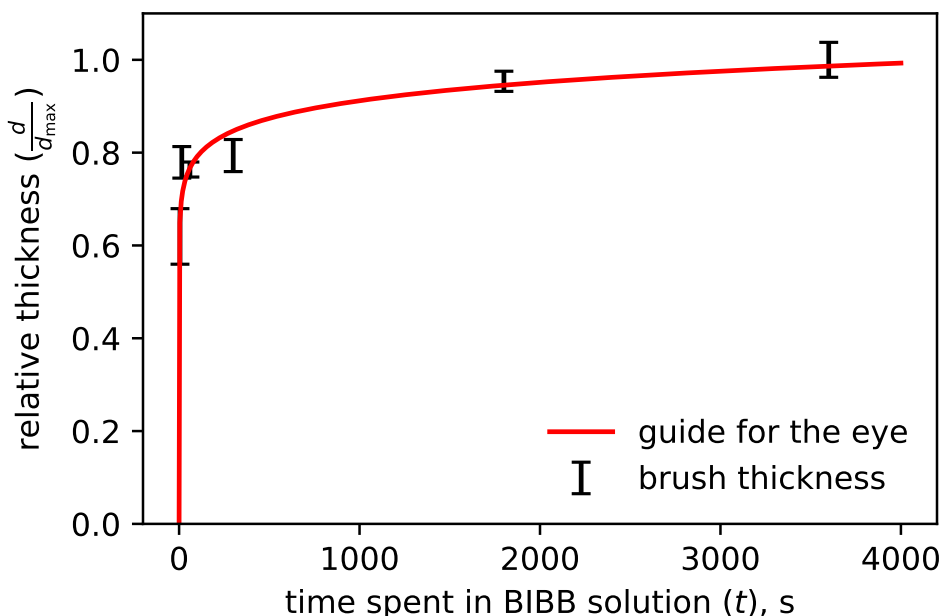


Figure 2.4: Thickness of the polymer layer grafted from silica wafers with varying bromination times (from 5 s to 60 min); the bromination and polymerisation procedures across wafers were identical in all other ways. Measurements were taken from ten locations on the sample surface; errorbars are plotted as one standard deviation from the mean. The red curve is included as a guide for the eye. After a 5 s reaction time the initiator grafting density is high enough to yield brushes, approximately 60 % of the maximum dry thickness; however, the rate of bromination reaction appears to dramatically decrease after approximately 1 min. A reaction time of approximately 30 min is required to reach 95 % of the final thickness.

investigated the growth appeared to be linear; however, linear extrapolation of the data does not pass through the origin, indicating the polymer growth is in-fact non-linear. The observed non-linear polymer growth was expected (the initiation efficiency was expected to be dependent on the initiator density), as similar growth kinetics have been reported for similar surface-initiated reaction schemes [97, 98, 115]. Literature explanations for this non-linearity include chain-chain termination due to the high initial initiator density, the monomer shielding of shorter chains, or the loss of living-ness of the ATRP through the diffusion of the bromide during the propagation step.

This confirmation of non-linearity has potential implications for the grafting-density and bromination kinetics studies, as both use equation 1.2 to relate  $\hat{V}_1$  to  $\sigma$ . If the non-linearity observed in 2.5 is dependent on the polymer grafting density, then this will affect grafting density values calculated through equation 1.2. However, given initiation efficiency has been shown to be a function of grafting density [95, 98, 115], the potential relationship between polymerisation linearity and initiator density will be a secondary effect. The cause of the non-linearity could be further explored by performing a gradient polymerisation (as in Fig. 2.5) with wafers of different initiator grafting densities.

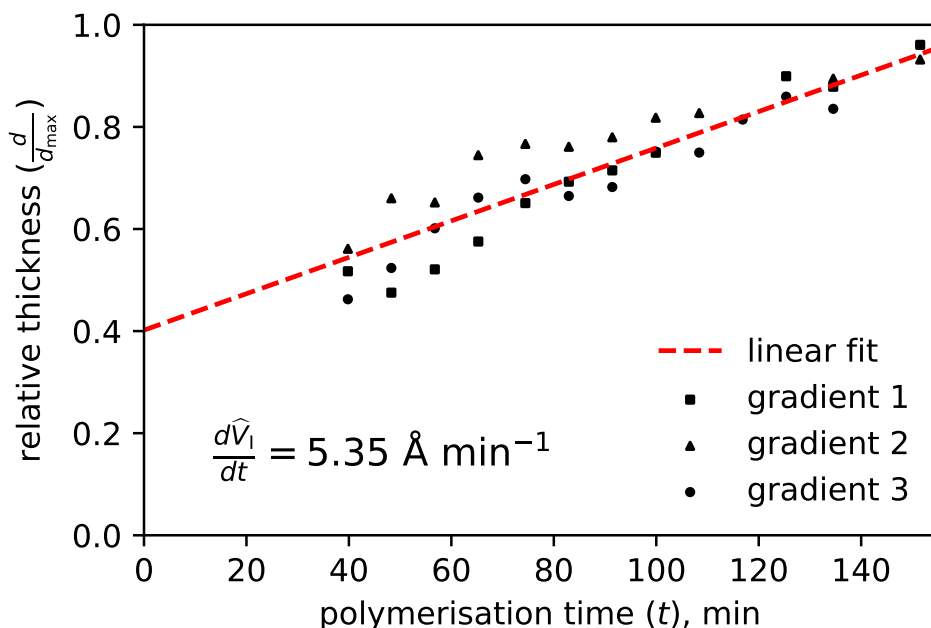


Figure 2.5: Thickness of the polymer layer grafted from a surface prepared as per section 1.4 as a function of polymerisation time. Sets of data points are from a single gradient wafer, section 2.2.4. Over the observed time period, the polymer growth appears to be linear, but does not pass through the origin when extrapolated (dashed red line). As such, it appears the polymer growth is non-linear. The interfacial volume gradient in the observed region is  $5.35 \text{ Å min}^{-1}$ .

### 2.3.3 Grafting density control

The effect of changing the initiator grafting density was investigated both on uniform wafers (Fig. 2.6 top) and in a gradient process (Fig. 2.6 bottom), with results from both studies plotted in Fig. 2.7. Polymer thickness is a strong function of the BiBB:BB ratio, demonstrating our method’s efficacy for varying grafting-density. Additionally, we find that the results from the gradient-grafting density wafer and the uniform wafers agree well, indicating that our method can be used to prepare polymer brush surfaces with grafting density gradients.

However, dry polymer thickness appears to scale as the square-root of the BiBB fraction across all sample groups. A similar relationship between the active initiator fraction and brush thickness was observed by Jones, Brown, and Huck [98]. Assuming BiBB and BB are equally mobile and reactive with the APTES, the initiator grafting density should scale linearly with the BiBB concentration. For the same polymer molecular weight distribution, the dry thickness should also scale linearly with grafting density, as per Equation 1.2. The experimentally observed non-linear relationship between dry thickness and grafting density can be explained by chain-chain termination or monomer shielding, indirectly supporting the findings of Martinez et al. [97] and explaining the non-linear

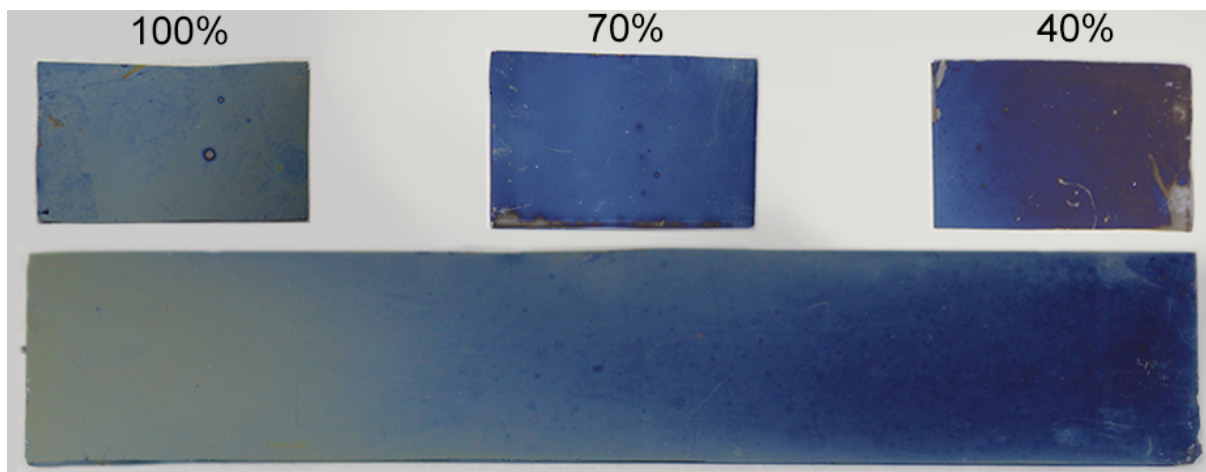


Figure 2.6: Photos of select uniform wafers (top) and the gradient wafer (bottom), with the approximate initiator grafting density shown above. The change in colour across the wafers is due to thin-film interference and can be directly correlated to the thickness of the PNIPAM brush (the same phenomena is used by interferometry).

growth in Figure 2.5. As these phenomena will be more prevalent at higher initiator densities, the average molecular weight of chains grown from higher-initiator density surfaces will be lower than those grown from lower-initiator density surfaces.

### 2.3.4 *In situ* measurements

We observe the temporal evolution of PNIPAM polymer brushes produced by surface-initiated activators regenerated by electron transfer (ARGET) ATRP at different reaction rates and from surfaces of varying initiator density. This marks the first time that the structure of a polymer brush has been observed during its synthesis. Due to the pioneering nature of the work, significant improvements were made to the methodology during the course of this study. Potential improvements to the method are discussed in appendix C.

The first significant finding from this experiment comes from the characterisation of the silica layer. The silicon blocks used for the *in situ* synthesis experiments had already undergone the APTES deposition and bromination steps of the synthesis procedure when they were measured by NR in air, H<sub>2</sub>O and D<sub>2</sub>O for the purpose of characterising the silicon oxide layer. When analysing this data, an additional slab was added to the model to account for the initiator layer; however, the dense layer observed in previous NR experiments was not required to match the collected data. This indicates that the previously observed interior layer does not consist of a dense initiator layer, as has been hypothesised. Instead, the interior layer was seen to form in the early stages of the polymerisation in

---

<sup>iii</sup>samples 2 (100 %) and 3 (25 %) from section 2.3.4, as well as a 75 % sample prepared using the same method that was not smooth enough for further analysis (see appendix C).

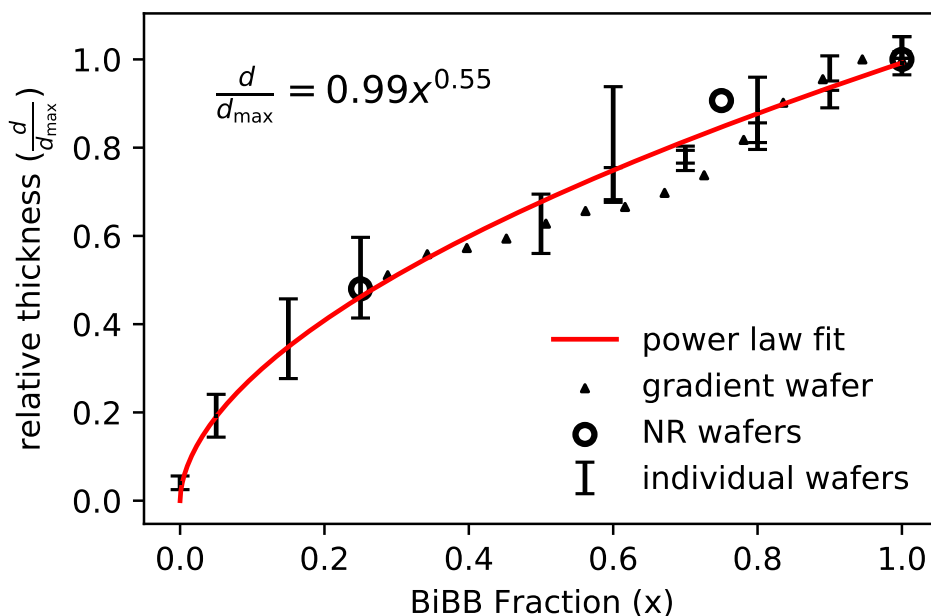


Figure 2.7: Normalised polymer thickness as a function of the BiBB:BB ratio in the bromination step. Results are from individual wafers (as per the method in section 2.2.5) measured by interferometry (error bars) and NR<sup>iii</sup> (circles), as well as a gradient wafer (Triangles, prepared as per section 2.2.5) measured by ellipsometry. Interferometry measurements were taken from ten locations on the sample surface; errorbars are plotted as one standard deviation from the mean. Errors from the NR modelling process were smaller than the marker size, and are not plotted. For an estimation of the thickness distribution across the NR wafers see Figure 2.12. For comparison, the thicknesses are normalised by dividing by the thickness at BiBB fraction of 1 ( $d_{\max}$ ). It must be noted that the thicknesses reported here are dry thicknesses, and as such are expected to scale linearly with  $\sigma$  (unlike solvated thickness, which scales as  $\sigma^{1/3}$ , section 1.1).

all samples (Fig 2.9, 2.11, 2.10), confirming that this layer consists primarily of NIPAM (in either polymer, oligomer or monomer form).

The progress of the polymerisation was observed under three distinct conditions (see Table 2.1). The first condition had an active initiator fraction of 100 % and a D<sub>2</sub>O:d-MeOD ratio of 2:3, which had two main consequences. The first is that the polymerisation progressed more rapidly than the other syntheses; Figure 2.9b shows that the growth rate is 4.7 Å min<sup>-1</sup>. The second is that the polymer was less soluble in the reaction mixture than in other syntheses (due to cononsolvency effects); Figure 2.9a shows that the polymer volume fraction in the bulk of the brush was around 0.3. The lower solubility resulted in obvious fringes appearing in the collected reflectometry profiles (Fig. 2.9c), promoting confidence in the modelled structure. However, as this polymerisation was performed as part of the commissioning of this *insitu* polymerisation technique, the polymerisation mixture for this experiment diverged significantly from those used elsewhere in this thesis. It is included here because the distinctive fringe structures produced demonstrate that

NR is sensitive to the structure of a polymer brush at the angle, resolution and time scale used here.

The second and third conditions are most informative when compared directly to one another, as both are carried out under identical reaction conditions with a  $D_2O$  to d-MeOD ratio of 1:2. The second and third conditions had an active initiator fraction of 100 and 25 %, respectively. The final dry thicknesses of the two wafers were 72 and 149 Å, which agree well with both the gradient and uniform grafting density experiments documented above (relative values plotted in Fig. 2.7), indicating that the initiator density modification was successful. The difference in grafting density is also manifest in the observed growth rate and volume fraction of the two datasets. The growth rate of the 100 % sample is  $2.07 \text{ Å min}^{-1}$ , while that of the 25 % sample is  $1.04 \text{ Å min}^{-1}$ ; reassuringly, the ratio of the growth rate is comparable to the dry thickness ratio. The volume fraction of the brush layer is lower at 25 % than it is at 100 % during the synthesis, conforming with common

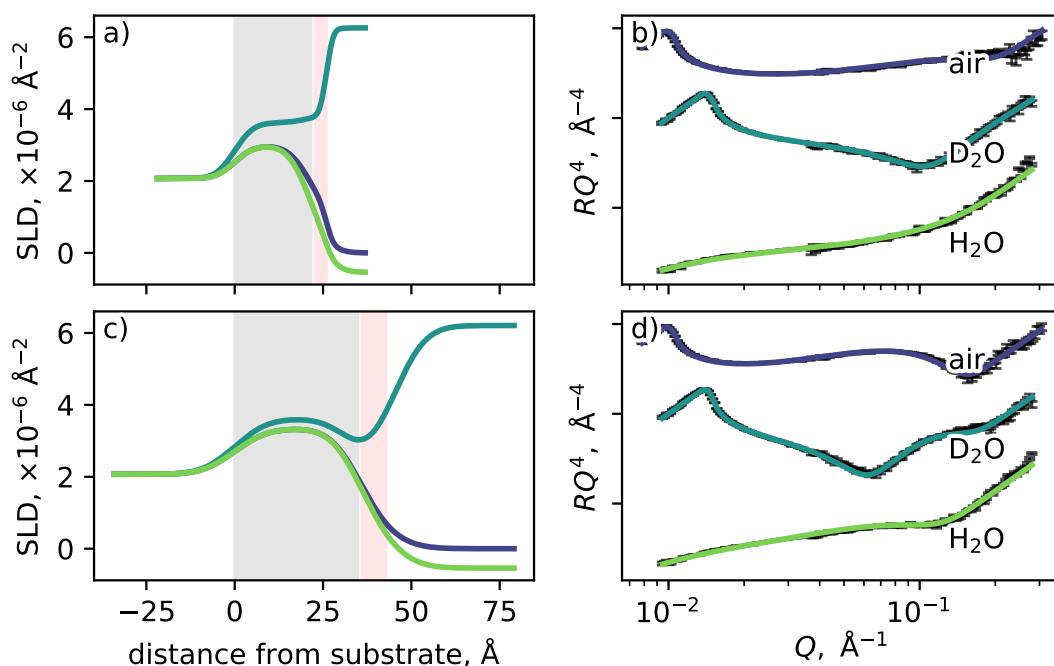


Figure 2.8: Characterisation of the silica and initiator layers for (a,b) synthesis 2 and (c,d) synthesis 3. The order of the slabs in the air contrast (backing layer silicon) has been reversed to allow for better comparison with the solvent contrasts (backing layer water). The silica (grey shaded region) and initiator layers (red shaded region) were fit with a slab each. The difference in the thickness and roughness of the silica layer between the (a) and (c) is due to the wafers' history and is not significant here. While a small initiator layer can be observed in the  $D_2O$  contrast, particularly in (c), the layer SLD is not as low as those observed in previous NR studies [20, 22, 73, 85, 101–104]. The 25 % sample (c) likely has a more observable initiator layer due to slight differences in the SLD and volume of BB relative to BiBB.



structural descriptions of brush structure, like those discussed in section 1.1. This is discussed further in section 2.3.5.

Most significantly, an interior layer is required to fit both the 25 % and 100 % data. In both cases, the interior layer is required to fit the data collected from early in the polymerisation. Another difference worth noting is that the initial (<500 s) polymer growth rate for both 100 % samples (experiments 1 and 2) is lower than the subsequent rate (Fig. 2.9b, 2.10b), this is not the case for the 25 % sample. At a growth rate of 2 to 4 Å min<sup>-1</sup>, these first few hundred seconds would be the time period wherein the 20-mers reported by Martinez et al. [97] would form. It is then possible that the early reduction in growth rate is due to chain-chain termination. It is also worth noting that, while there are indications of non-linear growth at around 3000 s, the polymer growth after 500 s is relatively linear for all syntheses observed. Figure 2.5 would indicate that the growth in this time regime should be non-linear. It is possible that the lower temperature of the *in situ* reactions resulted in fewer termination events, or that the flow of the solvent in the gradient polymerisation-time experiment resulted in a higher rate of chain-termination events. More experimentation is needed to determine the underlying cause of this discrepancy.

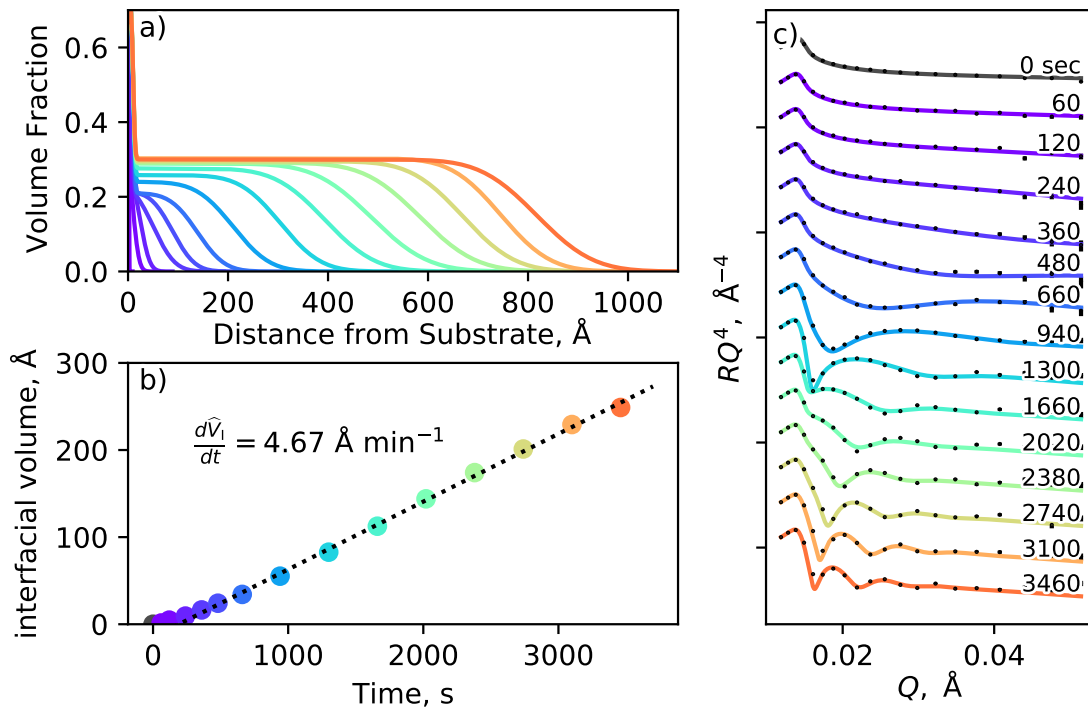


Figure 2.9: Results from *in situ* experiment 1 (100 % BiBB coverage, 2:3 D<sub>2</sub>O:d-MeOD), showing evolving (a) volume fraction profile and (b) interfacial volume of polymer, along with (c) corresponding reflectometry profiles. The polymer growth in the first five minutes is slower than in the remaining hour.

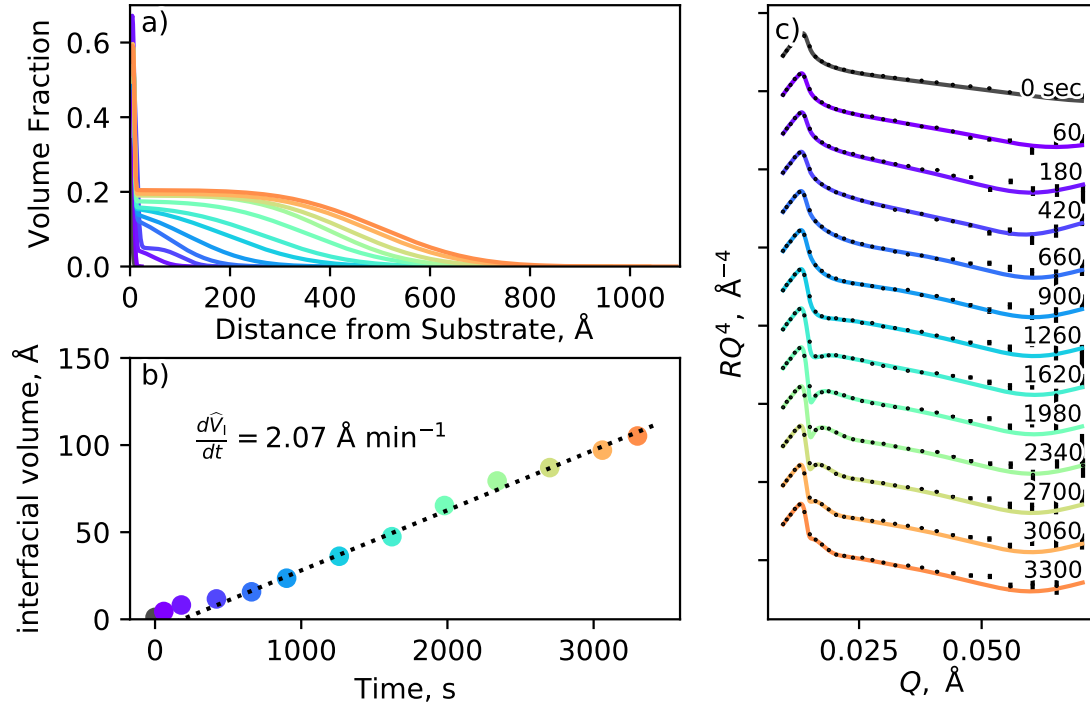


Figure 2.10: Results from *in situ* experiment 2 (100 % BiBB coverage, solvent 1:2  $\text{D}_2\text{O}$ :d-MeOD), showing evolving (a) volume fraction profile and (b) interfacial volume of polymer, along with (c) corresponding reflectometry profiles. The polymer growth in the first five minutes is slower than in the remaining hour, potentially due to chain-chain termination.

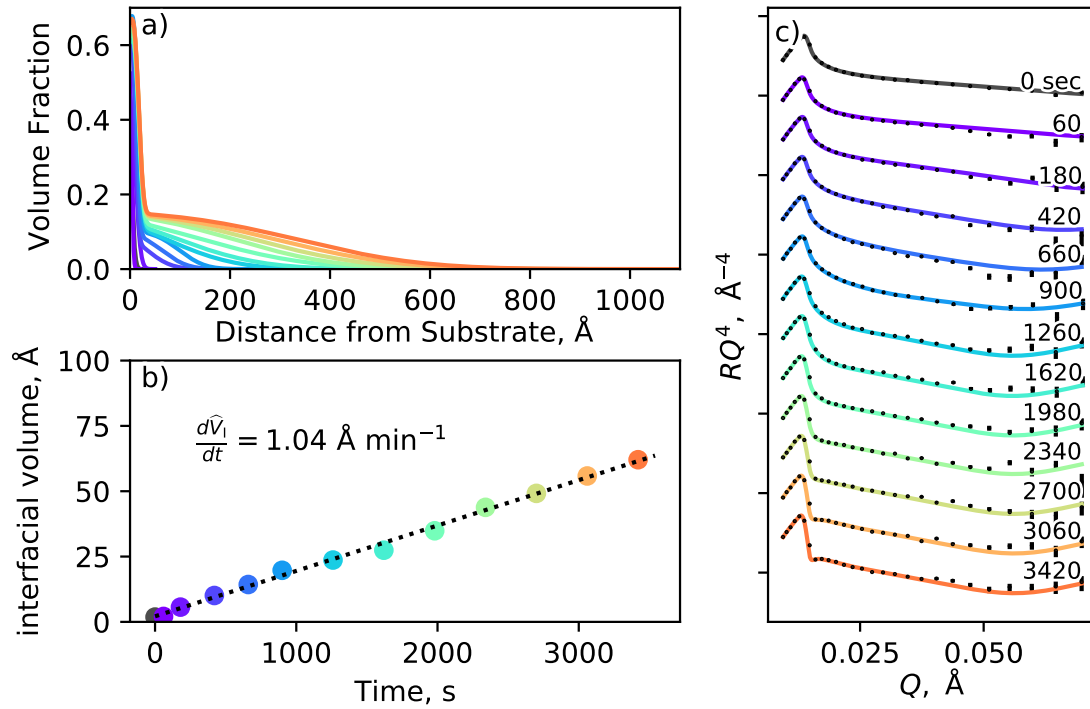


Figure 2.11: Results from *in situ* experiment 3 (25 % BiBB coverage, 1:2  $\text{D}_2\text{O}$ :d-MeOD), showing evolving (a) volume fraction profile and (b) interfacial volume of polymer, along with (c) corresponding reflectometry profiles. The polymer growth is linear throughout the experiment.

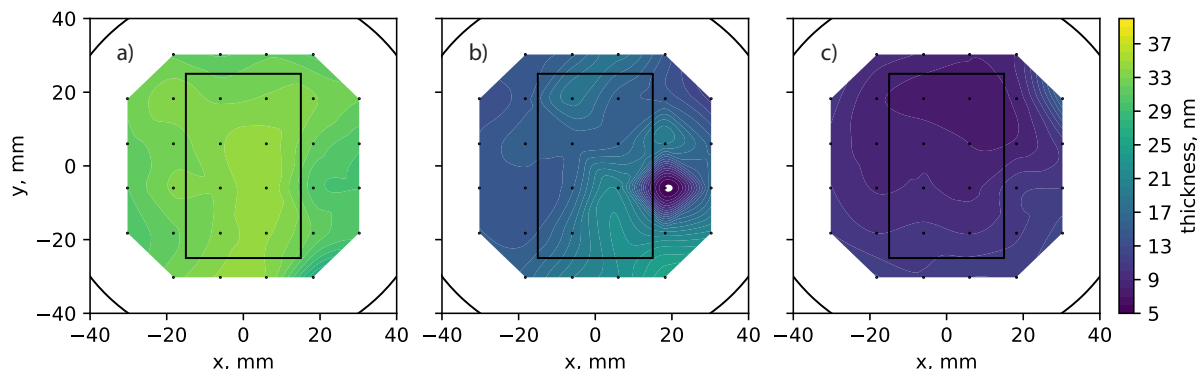


Figure 2.12: Thickness maps illustrating the macroscopic roughness of *in situ* polymerised wafers (a) 1, (b) 2, (c) 3 determined by mapping ellipsometry. The hydrophobic nature of the initiator layer resulted in bubbles forming in sample 2 (b). The primary reason for the change in relative roughness between samples 1 and samples 2 and 3 is that a larger reaction volume was pumped through the cell in sample 1 (5 mL vs 3 mL).

### 2.3.5 Characterisation of resulting brush layers

The thermoresponse of the PNIPAM layers produced during the *in situ* syntheses above were characterised in  $D_2O$  using NR and their smoothness was assessed using mapping ellipsometry (Fig. 2.12). It was verified that all three brushes were thermoresponsive, undergoing a collapse at around the reported critical solution temperature (CST) of  $32^\circ C$  (Fig. 2.13). No attempt was made to accurately determine the CST for each wafer using the limited NR time that was available. Once again, all substrates were found to exhibit an interior layer (Fig. 2.13); it should be emphasised that the fitting methodology did not assume the presence of this layer (more details of the analysis can be found in chapter 4). The volume fraction of the bulk of the brush appeared to be dependent on grafting density, with the 25 % sample exhibiting a more diffuse profile (Fig. 2.13c) than the equivalent 100 % sample (Fig. 2.13b). Classical strong-stretching limit theory (see section 1.1) states that the volume fraction in the bulk of the brush should scale with  $\sigma^{2/3}$ , and the thickness of the brush should scale with  $\sigma^{1/3}$ . Between samples 2 and 3 at  $15^\circ C$  we observe a reduction in the volume fraction of 50 %, and a reduction in the extent of  $\approx 20\%$ . This is indicative of a reduction in effective grafting density of between 35 and 50 %; consistent with the results from thickness measurements in Figure 2.7.

The difference between the profiles produced by *in situ* sample 1 (Fig. 2.13a) and 2 (Fig. 2.13b) is more significant than expected. While the solvent polarity and the concentration of reagents in the polymerisation solution were different for each sample, it was expected that both methods would produce similar brushes. Instead, the bulk of the brush in sample 1 is at much higher volume fraction than in sample 2. One explanation

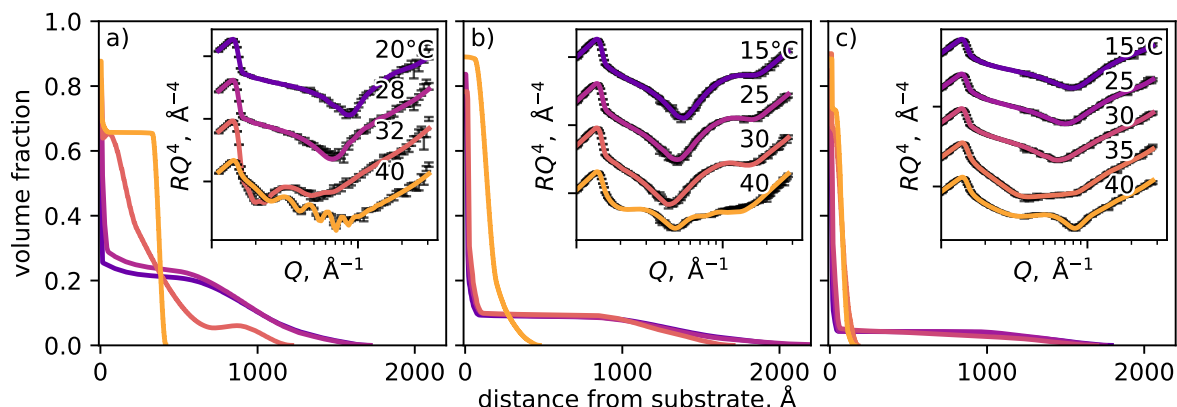


Figure 2.13: Volume fraction profiles as a function of temperature as measured by NR for brushes synthesised *in situ*, corresponding to *in situ* samples (a) 1, (b) 2 and (c) 3. Potential reasons for the difference in swelling ratio between (a) and (b, c) are discussed in the text.

is that the reaction conditions (higher local polymer concentration and faster reaction rate) lead to an increase in the number of chain-chain termination events, reducing the maximum length the chain can stretch. If the latter explanation is correct, then the solvent composition (or more broadly, the reaction rate) will have a dramatic effect on the structure of brushes produced by ARGET ATRP, resulting in brushes with markedly different swelling ratios.

The roughness of the wafers produced was characterised by mapping ellipsometry, the results are in Figure 2.12. Synthesis 1 produced a more even wafer relative to its thickness than either synthesis 2 or 3; this is thought to be due to both the filling method used and the volume of reaction solution injected into the cell. The differences between the methodologies are discussed further in appendix C. The difference between the final dry thickness reported in Figure 2.7 and the interfacial volume, as shown in panel (b) of Figures 2.9-2.11 can be attributed to shortcomings of the slab model used to describe the growing polymer brush.

### 2.3.6 Origin of the interior layer

From Figures 2.10, 2.11 and 2.13, it is clear that reducing the initiator grafting density does not result in the disappearance or reduction of the interior layer, indicating that the interior layer is not the result of termination in the very early stages of the reaction. This is not to say that there is no chain termination of monomer shielding; the non-linearity of  $\hat{V}_I$  both with respect to polymerisation time (Fig. 2.5) and initiator density (Fig. 2.7) indicate that both these events occur. However, they do not appear to be the cause of the interior layer. Our characterisation of the wafers prior to polymerisation shows that

the interior layer is not present before polymerisation, so the interior layer is not the initiator layer. The only remaining explanation of the interior layer is the adsorption of PNIPAM chains onto the wafer's surface. This interpretation explains why the 25 % initiator density sample possesses the most prevalent interior layer, as it would possess the most hydrophobic surface due to the attached BB. This hypothesis could be further tested by observing the structure of the brush in different solvents with NR, or through measuring the adsorption of free PNIPAM to a brominated silica surface using QCM-D.

## 2.4 Conclusion

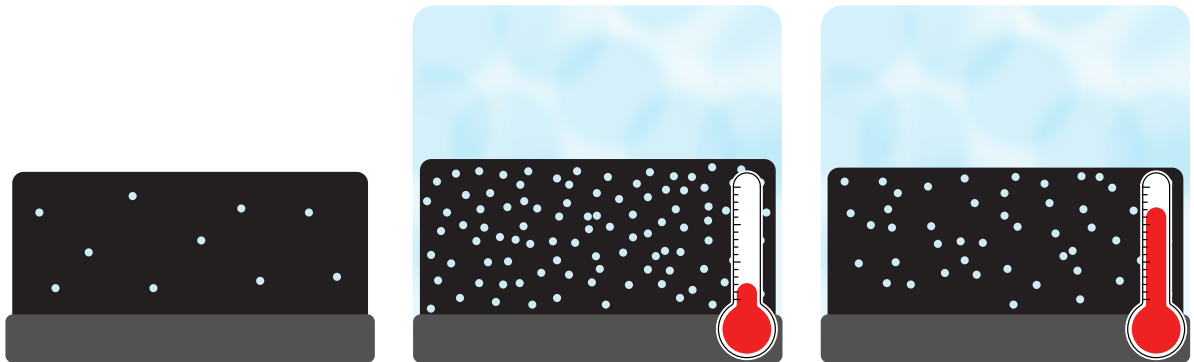
Here we have characterised the polymerisation methodology used in this thesis by studying the kinetics of the bromination and polymerisation reactions, as well as examining polymer growth as a function initiator grafting density. We find that the bromination reaction reaches 95 % completion in approximately 30 min and that the polymerisation rate slows as the polymerisation reaction progresses. We demonstrate that we are able to control the grafting density by substituting the active initiator,  $\alpha$ -bromoisobutyryl bromide, with the inert benzoyl bromide. The polymer grafting density is not a linear function of initiator density, indicating that the initiation efficiency is a function of initiator density; this suggests that monomer shielding or chain-chain termination occurs in the initial stages of the polymerisation for samples with dense initiator densities.

In order to determine the origin of the interior layer observed by previous neutron reflectometry studies, we have, for the first time, employed time-resolved neutron reflectometry to study the structural evolution of a polymer brush during its synthesis. Time-resolved neutron reflectometry shows that the interior layer is not due to a thick initiator layer, or the termination of chains early in the polymerisation, but rather adsorption of the PNIPAM brush onto the surface. Similar techniques could be used to study other time-dependent polymer behaviour, such as the top-down collapse reported in PNIPAM brush systems [64]. Future developments in reflectometer design (for instance, the proposed Freia reflectometer at the European Spallation Source) will further increase the power of time-resolved reflectometry techniques.



## Chapter 3:

Swelling of a thermosensitive polymer brush at different relative humidities of water





Characterising the structure and behaviour of polymer brushes in their dry state is required for subsequent study of their solvated structure. Furthermore, the study of dry polymer layers as a function of relative humidity contributes to our understanding of polymer-solvent interaction at low solvent-fractions, while thin, dry, polymer layers can be used as sensing surfaces and aid in gas-phase separation.

Here PNIPAM brushes are probed as a function of temperature and relative humidity by QCM-D and neutron reflectometry. Within the context of this work the current investigation serves to quantify the amount of water in the absorbed film, which we achieve by studying the thickness and hydration of the PNIPAM layer as a function of relative humidity and temperature. This knowledge enables a more accurate approximation of the interfacial volume of polymer and allows for the determination of the SLD of pure PNIPAM in both a native and deuterated state. These experiments allow us to determine whether the PNIPAM layer is thermoresponsive in the dry-state. More generally, these experiments provide insight into the behaviour of PNIPAM films at very low polymer-fractions, which is significant in understanding the phase behaviour of PNIPAM more broadly.

In this chapter, a brief review of the relevant literature is conducted before our experimental setups are detailed. The results from QCM-D and neutron reflectometry are compared and discussed, and the response of PNIPAM to humidity and temperature is explored. We then use our findings to calculate the Flory–Huggins parameter for PNIPAM as a function of temperature and solvent volume fraction. Finally, the results are used to inform our approximation of the interfacial volume and SLD.

### 3.1 Theoretical background

In this chapter, we are concerned with the behaviour of ‘dry’ poly(*N*-isopropylacrylamide) (PNIPAM) films as a function of relative humidity (RH) and temperature. In this thesis, in the context of brushes, the term ‘dry’ refers to systems that are not solvated by a bulk liquid. Under ambient conditions dry PNIPAM brushes contain some amount of solvent. However, what one might term the ‘true dry thickness’<sup>i</sup> of a brush layer is often an important parameter. In this thesis, the true dry thickness of a brush is referred to as the interfacial volume,  $\hat{V}_I$ .  $\hat{V}_I$  is required to accurately calculate the swelling ratio (SR) (see Section 1.5.1) of a film, which is one of the key metrics used to characterise the response of both dry [116] and solvated thin films. Furthermore, it is crucial to the structural characterisation of the solvated films, a point that will be demonstrated in chapter 4. However,  $\hat{V}_I$  is surprisingly difficult to measure, owing to the tendency of hydrophilic polymer films to absorb solvent from their environment [75, 77, 116–121]. Determining  $\hat{V}_I$  for PNIPAM films at ambient conditions will be an important outcome of this chapter.

Polymer films tend to absorb solvent from the vapour phase [75, 77, 116–121]. This absorption takes place even in vapour mixtures that are not close to saturation and has been observed to be a function of the relative humidity of the solvent [75, 77, 116–121]. Here we stress that this solvent absorption is very different to solvent condensation, which occurs due to the vapour being super-saturated at the surface temperature. These two phenomena occur for very different reasons. In this chapter, we have carefully controlled surface temperatures to eliminate the possibility of condensation.

#### 3.1.1 Relative Humidity

RH is the ratio of the partial pressure of a vapour-phase component ( $p_A$ ) to its saturation pressure ( $p_A^{\text{sat}}$ )

$$\text{RH} = 100 \frac{p_A}{p_A^{\text{sat}}(T)} \quad (3.1)$$

As the saturation pressure of a component is a function of temperature, RH is temperature-dependent. The saturation vapour pressure of H<sub>2</sub>O and D<sub>2</sub>O used here was determined from the work of Matsunaga and Nagashima [122], who use the functional form of Saul and Wagner [123]. The component of their work relevant to the current study is reproduced in Figure 3.1.

---

<sup>i</sup>the thickness of the layer if the polymer volume fraction were 100%.

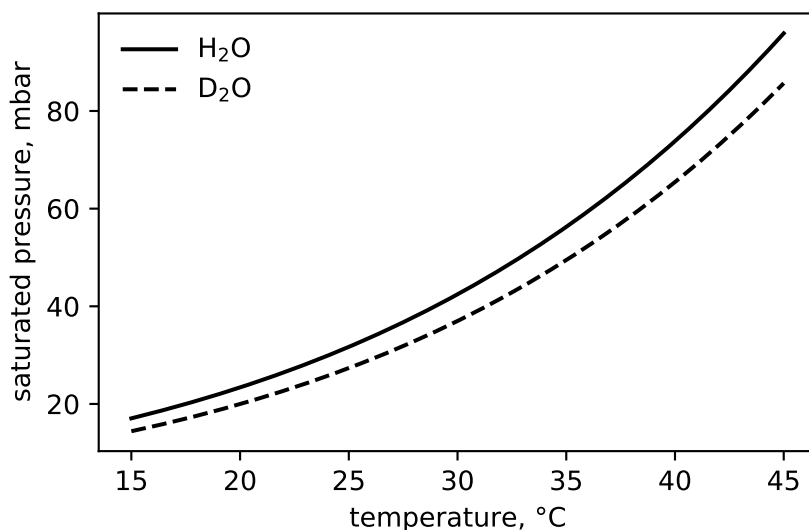


Figure 3.1:  $p_{\text{H}_2\text{O}}^{\text{sat}}$  and  $p_{\text{D}_2\text{O}}^{\text{sat}}$  from the work of Matsunaga and Nagashima [122].

### 3.1.2 Water content of polymer films at ambient conditions

Ko, Miles, and Genzer [117] document the difficulty of completely dehydrating polymer films, and hence quantify the consequences of taking thickness measurements at ambient conditions as  $\hat{V}_1$ . They studied spin-cast films of poly(methyl methacrylate) (PMMA), polyvinylpyrrolidone (PVP) and poly(methoxy diethylene glycol acrylate) (PMDEGA). The degree of quaternization of PMDEGA was also varied to study the effect of charge on the water content of a dry film; increasing charged moieties in the layer results in larger discrepancies between the calculated  $\hat{V}_1$  and the thickness at ambient conditions. Ko, Miles, and Genzer used a thermal method, wherein the thickness was measured over a range of temperatures, to determine  $\hat{V}_1$  for thin polymer layers. They assumed that at high temperatures ( $\approx 100^\circ\text{C}$ ) there was no water in the layer, and extrapolated the dry thickness from this high-temperature data, assuming a constant coefficient of thermal expansion. Significantly, they reported that this thermal method dries the thin film more completely than exposure to either exposure to a dry nitrogen stream or vacuum. Their results indicate that exposure to a 0% RH environment may not be enough to completely dry thin polymer layers.

### 3.1.3 Swelling of polymer films at different solvent vapour pressures

Below we discuss the existing literature regarding the swelling of thin polymer films as a function of humidity. Prior work is divided into categories to aid discussion.

### The effect of substrate and polymer geometry

Prior work suggests that substrate-solvent affinity plays a role in the swelling of thin films in humid vapours. Galvin and Genzer [78] studied poly(2-(dimethylamino)ethyl methacrylate) (PDMAEMA) spin-cast onto both untreated and hydrophobically modified (through deposition of an octyltrichlorosilane layer) silica wafers ( $\hat{V}_1 \approx 800 \text{ \AA}$ ). They found that the film with the hydrophobically modified substrate exhibited a significantly lower swelling ratio than the film on untreated silica (1.17 vs 1.25) at 92 % RH. Ederth and Ekblad [124] studied hydrogels composed of hydroxyethyl methacrylate and poly(ethylene glycol) methacrylate monomers (HEMA-co-PEG<sub>10</sub>MA) in humid environments on both gold and silicon substrates ( $\hat{V}_1 \approx 310 \text{ \AA}$ ). Hydrogels on silica exhibited an SR of 1.35, while identically prepared films on the more hydrophobic gold surface exhibited an SR of 1.23. Presumably the effect of the substrate hydrophobicity becomes less significant as film thickness increases.

It is also apparent from literature that the polymer geometry of the thin films influences their behaviour. Galvin and Genzer [77, 78] investigated the swelling of polyelectrolytes in humid environments. They compared the swelling of a PDMAEMA polymer brush with that of a spin-cast film of the same polymer, finding that the SR was significantly greater for the brush-geometry film [78]. They postulate that the orientation of the brush chains enables greater hydration of the film, although molecular weight and polydispersity effects could also have been responsible [78]. For tethered hydrogels, the SR has been found to be a strong function of the cross-linking density [116, 118]. This dependence on cross-link density suggests that one potential explanation for the results Galvin and Genzer [78] is that the spin-cast samples are more ‘tangled’ than the brush equivalent, i.e., the spin-cast films can be thought to have an effective cross-link density. This rationalisation views all thin films on a continuum from low to high cross-link density, where brushes have a cross-link density of zero.

Not all aspects of the polymer geometry appear to significantly affect their behaviour in humid vapours. Pandiyarajan, Prucker, and R  he [116] found that SR is independent of film thickness, reporting no significant difference in the SR of 500 and 7000  $\text{\AA}$  poly(*N*-dimethylacrylamide) (PDMAA) films. Similarly, Galvin and Genzer [78] found that the SR is not a strong function of brush grafting density.

### Adsorption kinetics

Pandiyarajan, Prucker, and R  he [116] studied the kinetics of hydration for a PDMAA film ( $\hat{V}_1 \approx 6000 \text{ \AA}$ ), finding that equilibrium was reached within ten minutes of a step-change in the RH; swelling kinetics appeared to be independent of the RH probed. Kreuzer

et al. [119] undertook kinetic experiments to observe the swelling of a poly(*N,N*-dimethyl-*N*-(3-methacrylamidopropyl)-ammonio)propane sulfonate) (PSPP)-poly(*N*-isopropylmethacrylamide) (PNIPMAM) diblock film ( $\hat{V}_1 \approx 600 \text{ \AA}$ ), finding that film swelling took approximately 20 min to reach an equilibrium value and concluding that diffusion into the polymer film was the rate limiting step in this process. Kreuzer et al. [120] studied swelling kinetics of both poly(sulfobetaine) (PSPE) and PNIPMAM films, finding that both reached equilibrium after approximately 20 min. Biesalski and R  he [75] also conducted kinetic studies of swelling upon a change in humidity; for RH less than 80 %, equilibrium was reached in under an hour, whilst greater RH took approximately three hours to reach equilibrium. However, as they achieved humidity control through saturated salt solutions, the rate-limiting step here was likely the evaporation of water.

It should be noted that a number of studies report extremely long equilibration times. Nieuwenhuis et al. [121] found that neither PNIPMAM or PMDEGA spin-cast films ( $\hat{V}_1 \approx 450 \text{ \AA}$ ) films reached equilibrium in a humid  $D_2O$  environment over a 3 h period. Widmann et al. [82] measured the kinetics of hydration of PNIPAM microgel films ( $\hat{V}_1 \approx 300 \text{ \AA}$ ), finding that equilibrium was reached for  $D_2O$  systems after 2 h (transitioning from 30 to 100 % RH. They did not observe the swelling ratio of the  $H_2O$  sample to stabilise after 6 h. Both Kreuzer et al. [120] and Nieuwenhuis et al. [121] reported swelling ratios much greater than comparable nonionic thin films in water vapour; it is possible that condensation phenomena could be occurring in these studies.

### Solvent affinity

The swelling of a thin film when exposed to a solvent vapour is predominantly dependent on the affinity between the solvent and the thin film. For humid (i.e., where the solvent vapour is water) environments, this results in polyelectrolyte films consistently swelling significantly more than neutral films. Galvin and Genzer [78] studied PDMAEMA films of varying thicknesses. In some samples the PDMAEMA was quaternized to examine the effect of charge density; films with higher charge densities absorbed more water. Biesalski and R  he [75] studied 7000  $\text{\AA}$  thick poly-4-vinyl(*N*-methyl pyridinium)iodide brushes, with a maximum SR of 1.55 reported. Kreuzer et al. [119] studied spin-cast films of zwitterionic PSPE and neutral PNIPMAM, reporting swelling ratios of 1.82 for PSPE ( $\hat{V}_1 \approx 340 \text{ \AA}$ ) and 1.07 for PNIPMAM ( $\hat{V}_1 \approx 280 \text{ \AA}$ ), both in water. Pandiyarajan, Prucker, and R  he [116] studied the swelling of a series of surface-tethered acrylamide hydrogels using optical waveguide spectroscopy as a function of RH and cross-link density. The SR of the acrylamide films varied between 1.05 and 1.45, with the SR increasing with the monomer's hydrophilicity. The SR of poly(*N*-propylacrylamide) films (chemically similar

to the PNIPAM used in this work) was 1.12. The tendency of polyelectrolyte layers to hydrate more than neutral polymer layers was borne out in a recent study by Brió Pérez, Cirelli, and de Beer [125], wherein the degrafting of silane-tethered polymer brushes in humid environments was examined; humid environments accelerate the degrafting of polyelectrolyte, but not of neutral polymers.

Regardless of the polymer chemistry, geometry, or the thickness of these thin polymer layers, good solvents are found to swell the layer. This is emphasised by the study of Elbs and Krausch [126], which examined the swelling of neutral polymer brushes in vapours of toluene, tetrahydrofuran and chloroform. These neutral brushes achieve swelling ratios as high as 4 in rich vapours of good solvents [126], greater than polyelectrolytes in water vapour [77, 78]. This indicates that it is the affinity of polyelectrolytes for the relevant solvent (in this case water) that cause the significant swelling reported [75, 77, 78], rather than an intrinsic property of their ionic nature.

There are some notable discrepancies in the SR values reported in literature. A number of studies report swelling ratios of  $\approx 1.1$  for PNIPAM-analogous polymers [116, 120], whereas others report values as high as 1.4 [82, 121]. All measurements are done in water vapour at ambient conditions. This difference is not due to a difference in polymer geometry (both low and high SR studies include work on microgels and spin-cast polymer). Likewise, the difference is not due to the substrate, as all studies use silicon substrates. We note that, at the high humidities probed by these experiments, small temperature gradients can cause condensation. If water condenses on the polymer surface it would induce significant layer swelling, explaining the extremely high SR observed. This interpretation is supported by the uncharacteristically sluggish kinetics (which sometimes do not reach equilibrium [82, 121]) reported in studies that observe high SR.

### Enrichment regions

Some studies report solvent enrichment regions at the peripheries of thin films in humid environments. Nieuwenhuis et al. [121] report these enrichment regions at the both the polymer-solvent and polymer-substrate interfaces for PMDEGA, but only at the polymer-substrate interface for PNIPMAM; both films are prepared by spin-coating the respective polymers. Galvin and Genzer [78] used neutron reflectometry (NR) to study the structure of PDMAEMA films as a function of RH, revealing that the silica-polymer and polymer-air interfaces are enriched with solvent relative to the bulk of the brush. These NR results agree well with reported X-ray reflectometry (XRR) and ellipsometry measurements, but uncertainty regarding the reported enrichment regions is not quantified. Kreuzer et al. [119] observed significant enrichment regions in their PSPP-PNIPMAM diblock films

( $\hat{V}_1 \approx 600 \text{ \AA}$ ) at both the silica substrate and air interfaces.

### Implications for the current study

From the above, four points are pertinent to the current study:

1. The SR for thin films is independent of thickness [116] and grafting density [78]
2. The expected SR of PNIPAM–analogous thin films at high relative humidities is  $\approx 1.1$  [116, 120]
3. The expected equilibration time for PNIPAM films upon a change of humidity is approximately one hour [75, 116, 119, 120].
4. The SR is dependent on the solvent-polymer affinity and RH, and hence can be used to calculate the solvent interaction parameter  $\chi$ .

While swelling of PNIPAM and PNIPAM–analogous thin films in response to RH have been studied, the behaviour of PNIPAM films as a function of both temperature and RH has not yet been investigated. It is also unknown whether PNIPAM exhibits a critical solution temperature (CST) in the dry state.

#### 3.1.4 Determination of $\chi$ parameter from film swelling

Using Flory–Huggins theory [127, 128] it is possible to derive a relationship between the solvent interaction parameter  $\chi$ , the solvent fraction ( $\phi_{\text{solv}}$ ) and RH (Eq. 3.1) [75, 77]

$$\ln\left(\frac{\text{RH}}{100}\right) = \ln(\phi_{\text{solv}}) + (1 - \phi_{\text{solv}}) + \chi(1 - \phi_{\text{solv}})^2 \quad (3.2)$$

This method is widely used to determine the  $\chi$  parameter of a polymer from both a calculation at a single point [77, 78, 118, 126] and through a curve-fitting procedure [75, 124]. Being able to calculate  $\chi$  in dry films is important as it yields insight into the solvent affinity of polymers at extremely low solvent fractions. Many polymers, including PNIPAM, have been shown to have volume fraction dependent solvent interaction parameters; calculating  $\chi$  allows for these to be experimentally quantified. Determining  $\chi$  is particularly important for brush systems, as their local polymer volume fraction varies as a function of their conformation.

## 3.2 Method

### 3.2.1 QCM-D

Quartz crystal microbalance with dissipation monitoring (QCM-D) experiments were performed using a Biolin Q-sense Analyzer connected to a vapour delivery system (VDS). The VDS mixed two nitrogen streams at 0 and 100 % RH, respectively, with a flowrate of  $200 \text{ mL min}^{-1}$ . The stream mix was set by controller with a target RH. Of course, RH is dependent on local temperature of the humidity probe, which was kept constant at  $40^\circ\text{C}$ . While the VDS was set to control RH and temperature, we kept the VDS feed stream at a constant temperature, and controlled the feed RH to provide the desired  $p_{\text{H}_2\text{O}}$ . The humid vapour was supplied to the QCM-D cells via a heated tube (at approx.  $50^\circ\text{C}$ ) with a total stream pressure of one atmosphere. Temperature control of the system was achieved using the thermostat in the Q-sense Analyzer. To ensure that the temperature of the incoming vapour and the sample were the same, the polytetrafluoroethylene (PTFE) tubing was coiled and attached to cell one with thermal tape (Fig. 3.2). The temperature of system components was monitored via thermocouples to ensure that no part of the system dropped below  $T_{\text{sample}}$ ; thermocouples were attached to cells one, three and four with thermal tape, and one was placed to measure the ambient temperature of the cell enclosure. The tubing used was translucent; at no point was any condensation observed.

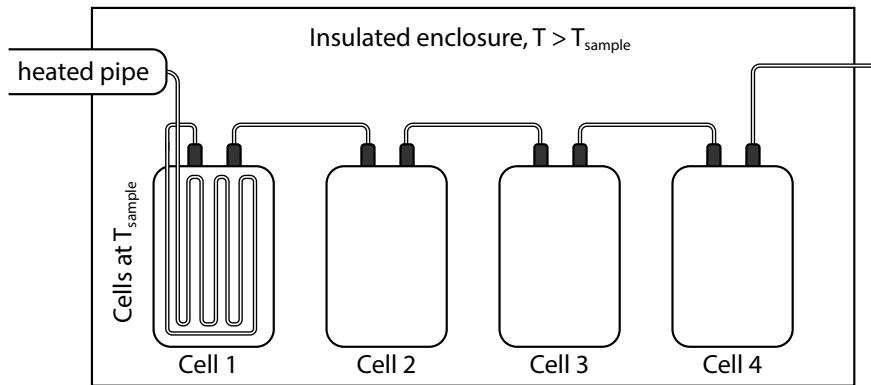


Figure 3.2: Schematic of QCM-D experimental setup; descriptions from left to right. A nitrogen stream with a set  $p_{\text{H}_2\text{O}}$  is supplied via a heated, insulated pipe at  $200 \text{ mL min}^{-1}$ . This vapour stream's temperature is greater than the cells' temperature, which is controlled via the built-in thermostat. This vapour stream passes through a coil, which was attached to the aluminium body of cell one via thermal tape, before travelling through cell one and two, both of which were fitted with blank wafers; air exiting cell two had reached  $T_{\text{sample}}$ . Cell three contained a blank  $\text{SiO}_2$  control wafer, while cell four contained a wafer coated with a  $200 \text{ \AA}$  PNIPAM brush. All four cells are enclosed in an insulated environment; the presence of the heated pipe in this enclosure ensured that its temperature remained above  $T_{\text{sample}}$  at all times.



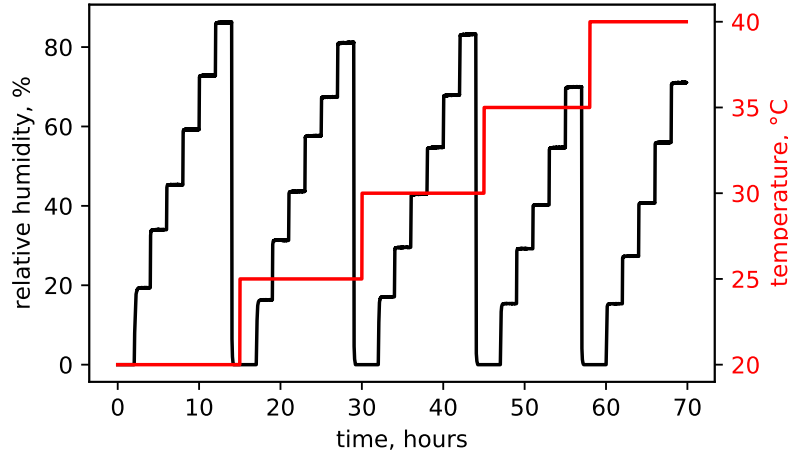


Figure 3.3: Temperature and RH as a function of time for the QCM-D experiment reported here. The equivalent diagram for the NR experiment is in Figure 3.8.

Experiments were carried out at a constant temperature ( $\pm 0.2^\circ\text{C}$ , as measured by the Q-sense Analyzer) and varying RH, as in Figure 3.3. Before the experiment began the environment was dried by exposing it to dry nitrogen for three hours (after this time the frequency and dissipation were observed to be constant). It is likely that this dry nitrogen state does not correspond to a completely dry brush layer, as the polymer films have been previously demonstrated to be difficult to completely dehydrate at temperatures accessible to the Q-sense Analyzer [117]. However, a small amount of residual water in our 0% RH condition will not affect the conclusions drawn from the QCM-D study. To avoid condensation the maximum RH targeted was 85%. At each condition, the system was given two hours to equilibrate; this was found to be sufficient time for the sensor frequency to plateau. The plateau value was taken as the frequency and dissipation for each condition. To account for baseline drift during the experiment, frequency and dissipation values are reported as the deviation from their 0% RH value at a given temperature (see Fig. 3.3). Subtracting the 0% RH value also removes the effect of temperature on crystal frequency, as temperature was kept constant while the RH sweep was conducted. The frequency of the  $\text{SiO}_2$  control wafer was found to be weakly dependent on RH ( $\approx 2\text{ Hz}$  between 0 and 85% RH); to remove the effect of vapour infiltrating the porous  $\text{SiO}_2$  layer the signal from the  $\text{SiO}_2$  control (in cell 3) was subtracted from the signal from the PNIPAM-coated crystal (in cell 4). The crystal was coated with a brush layer produced via the synthetic method in section 1.4, and its thickness determined by ellipsometry ( $\hat{V}_1 = 180\text{ \AA}$ , assuming that  $\hat{V}_1$  is 90% of the dry thickness as shown later in this chapter).

## Data analysis

For thin films in air, the change in absorbed mass can be determined from the change in crystal frequency through the Sauerbrey equation [90]

$$\frac{\Delta m}{A} = -\frac{\Delta f \sqrt{\rho_q \mu_q}}{2f_0^2} \quad (3.3)$$

where  $\Delta m$  is the change in absorbed mass,  $A$  is the active area of the sensor,  $\Delta f$  is the change in sensor frequency,  $\rho_q$  is the density of quartz ( $2.648 \text{ g cm}^{-3}$ ),  $\mu_q$  is the shear modulus of quartz ( $2.947 \times 10^{11} \text{ g cm}^{-1} \text{ s}^{-2}$ ) and  $f_0$  is the fundamental frequency ( $4.95 \times 10^6 \text{ Hz}$ ). The Sauerbrey equation treats the absorbed mass as an extension of the quartz itself, and as such is only valid for rigid films. These can be easily identified by QCM-D, as  $\Delta f$  is independent of overtone number for rigid films.

### 3.2.2 Neutron reflectometry

Specular reflectometry measurements were made at incident angles of  $0.65^\circ$  and  $3^\circ$ , yielding a useful  $Q$ -range of  $0.008\text{--}0.26 \text{ \AA}^{-1}$ ; for further details see section 1.5.3. The PNIPAM brush was prepared on a 100 mm wafer, which was placed inside a specialised sample environment consisting of a sealed chamber with quartz windows to allow the neutron beam to access the sample (Fig. 3.4). The sample stage within this chamber was connected to an external water bath for temperature control, and the exterior of the chamber was jacketed and heated above the dew point of the vapour mixture. The chamber was connected to a high-vacuum pump and a  $\text{D}_2\text{O}$  reservoir through a three-way valve, which was operated automatically by a pressure controller.

Initially, the sample environment was completely evacuated to remove any  $\text{H}_2\text{O}$  from the brush, before a temperature sweep was conducted at 0 mbar. The  $\text{D}_2\text{O}$  was then bled into the chamber until the vapour pressure of  $\text{D}_2\text{O}$  reached the desired level, at which point reflectometry profiles were measured at a number of different temperatures; this process was repeated until all temperature/humidity combinations of interest were covered (illustrated in Fig. 3.8a). To ensure that the system was in equilibrium, measurements were taken at a reflection angle of incidence of  $0.65^\circ$  at 20 min intervals before the final measurement; it was found that fringe spacing and depth reached constant values within 20 min of  $p_{\text{D}_2\text{O}}$  and  $T_{\text{samp}}$  reaching their target values, as expected from prior studies (section 3.1.3).

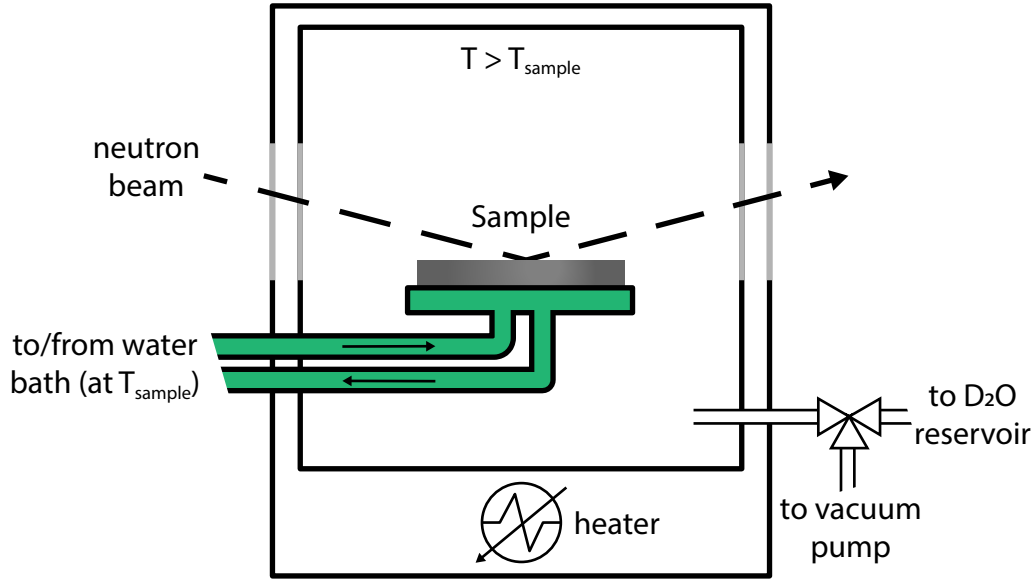


Figure 3.4: Schematic of the sample environment used for the NR experiments. A 100 mm silicon wafer is placed within a sealed chamber on a metal plate, the temperature of which ( $T_{\text{sample}}$ ) is controlled. The chamber is evacuated, and the  $p_{\text{D}_2\text{O}}$  is controlled by bleeding in  $\text{D}_2\text{O}$  from a reservoir. The chamber is jacketed and heated to prevent condensation. Aluminium windows on the chamber and the jacket allow the neutron beam to access the sample surface.

### Assumptions implicit in sample environment

In the selection of the sample environment and design of NR experiment it was assumed that the temperature of the relevant vapour (that is, the vapour in contact with the polymer layer),  $T_{\text{vap}}$ , would be identical to the sample temperature,  $T_{\text{samp}}$ . However, comparison of the NR and QCM-D results, discussed at length in appendix D, reveals that the assumption that  $T_{\text{vap}} = T_{\text{samp}}$  does not hold. Consequently, we analyse our data using a semi-empirical bulk vapour phase temperature

$$T_{\text{vap}} = 0.75 \times T_{\text{env}} + 0.25 \times T_{\text{samp}} \quad (3.4)$$

where  $T_{\text{env}}$  is the temperature of the sample environment, approximated from manual temperature readings taken throughout the experiment.

### Hydrogen–Deuterium exchange in PNIPAM

$\text{D}_2\text{O}$  was used as a water-proxy in this experiment to highlight the change in hydration of the polymer layer. Widmann et al. [82] show that the amide proton in PNIPAM can exchange for a deuterium (Fig. 1.9) when exposed to  $\text{D}_2\text{O}$  vapour. This H–D exchange appears to take place over approximately three days [82] at 90 % RH and temperature of

26.5 °C. The current experiment lasts for a similar time frame and subjects the polymer to a range of temperatures and D<sub>2</sub>O pressures; as such it is expected that H–D exchange will have to be accounted for in the data analysis. Furthermore, as we perform solvated brush NR measurements in D<sub>2</sub>O in this thesis, determining both the hydrogenated and deuterated scattering length density (SLD) of PNIPAM is important.

To explore the implications of the H–D exchange an additional experiment was undertaken, in which the SLD of two PNIPAM brushes ( $\hat{V}_1 = 235 \text{ \AA}^3$ ) were measured by NR before and after extended solvation in liquid H<sub>2</sub>O or D<sub>2</sub>O. After an initial measurement in atmospheric conditions (where both wafers are expected to be hydrogenous), the wafers were immersed in water for three days — one in H<sub>2</sub>O and one in D<sub>2</sub>O. The wafers were then removed from the water, quickly dried under nitrogen, and placed under vacuum on the *PLATYPUS* beamline. Reflectometry profiles were measured from the wafers at room temperature and 5 mbar of dry air pressure, before the temperature was increased to 50 °C then 100 °C, where additional profiles were acquired. The temperature was raised to ensure no water remained in the brush, as in the work of Ko, Miles, and Genzer [117]. The results of this experiment are presented in Figure 3.5.

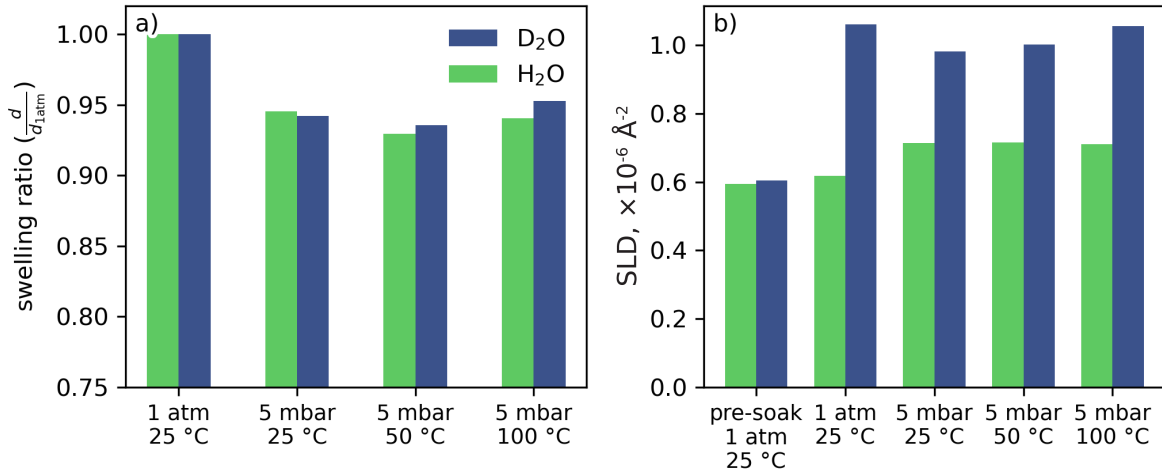


Figure 3.5: (a) Swelling ratio and (b) SLD of PNIPAM films in different conditions. The two films had been exposed to liquid H<sub>2</sub>O or D<sub>2</sub>O for three days before the experiment was conducted. The swelling behavior is similar for H<sub>2</sub>O and D<sub>2</sub>O, but the layer SLD for the D<sub>2</sub>O exposed wafer is significantly higher.

We conclude that the SLD of pure hydrogenated PNIPAM is  $0.72 \times 10^{-6} \text{ \AA}^{-2}$ , which corresponds to a theoretical density of  $0.973 \text{ g cm}^{-3}$ , or a monomer volume of  $193 \text{ \AA}^3$ . If the amide proton were to fully exchange the calculated SLD (assuming constant monomer volume) would be  $1.25 \times 10^{-6} \text{ \AA}^{-2}$ . This value is comparable to that observed experimentally in the vapour pressure experiment conducted in this chapter. The measured SLD of

the PNIPAM film soaked in  $D_2O$  was  $\approx 1.0 \times 10^{-6} \text{ \AA}^{-2}$ , which is higher than the hydrogenated SLD, but less than the value calculated for full exchange or attained in the NR modelling presented in Figures 3.7 and 3.8. We attribute this difference in calculated and measured deuterated SLD to slow exchange kinetics in the solvated sample.<sup>ii</sup> Accordingly, in the NR experiment, which took place over the course of the  $\approx 80$  h, the SLD of the film was allowed to vary between 0.72 and  $1.25 \times 10^{-6} \text{ \AA}^{-2}$ .

For the remainder of this thesis, the SLD of PNIPAM that has been exposed to  $D_2O$  is allowed to vary between  $0.72 \times 10^{-6}$  and  $1.25 \times 10^{-6} \text{ \AA}^{-2}$ . This (small) uncertainty in the SLD of the polymer has minor implications for the modelling process, discussed further in appendix G.

## Data analysis

The PNIPAM layer was modelled as a single uniform layer (‘slab’), the thickness and volume fraction of which were constrained such that the volume of polymer in the layer was constant, i.e.,

$$d_{\text{swell}} = \frac{\hat{V}_I}{\phi_{\text{poly}}} \quad (3.5)$$

The profiles were co-refined such that  $\hat{V}_I$ , the roughness of the polymer layer, and the thickness and roughness of the silica layer were kept constant across all datasets. Solvent volume fraction in the polymer layer was allowed to vary between 0 and 0.2 (which correspond to thicknesses of  $1 \times \hat{V}_I$  and  $1.25 \times \hat{V}_I$ ), while the SLD of PNIPAM was allowed to vary between  $0.72 \times 10^{-6}$  and  $1.25 \times 10^{-6} \text{ \AA}^{-2}$ . Optimisation was performed using the L-BFGS-B algorithm as implemented in *scipy* [129].

## 3.3 Results

### 3.3.1 QCM-D

The experimental setup for the QCM-D experiments afforded excellent control of both the temperature and  $p_{H_2O}$  in the system. No thermal gradients were measured in the cell in which the quartz crystal was placed, and as such, the RH in the cell can be determined with great confidence. The measured overtones were found to overlay, indicating that the dry brush is behaving as a rigid thin film, allowing the application of the Sauerbrey equation (Eq. 3.3). Overtones one to seven were averaged, with the result shown in Figure 3.6a;

---

<sup>ii</sup>The presence of  $D_2O$  could also have changed the structure of the dry layer, but we do not expect this to affect the layer SLD.

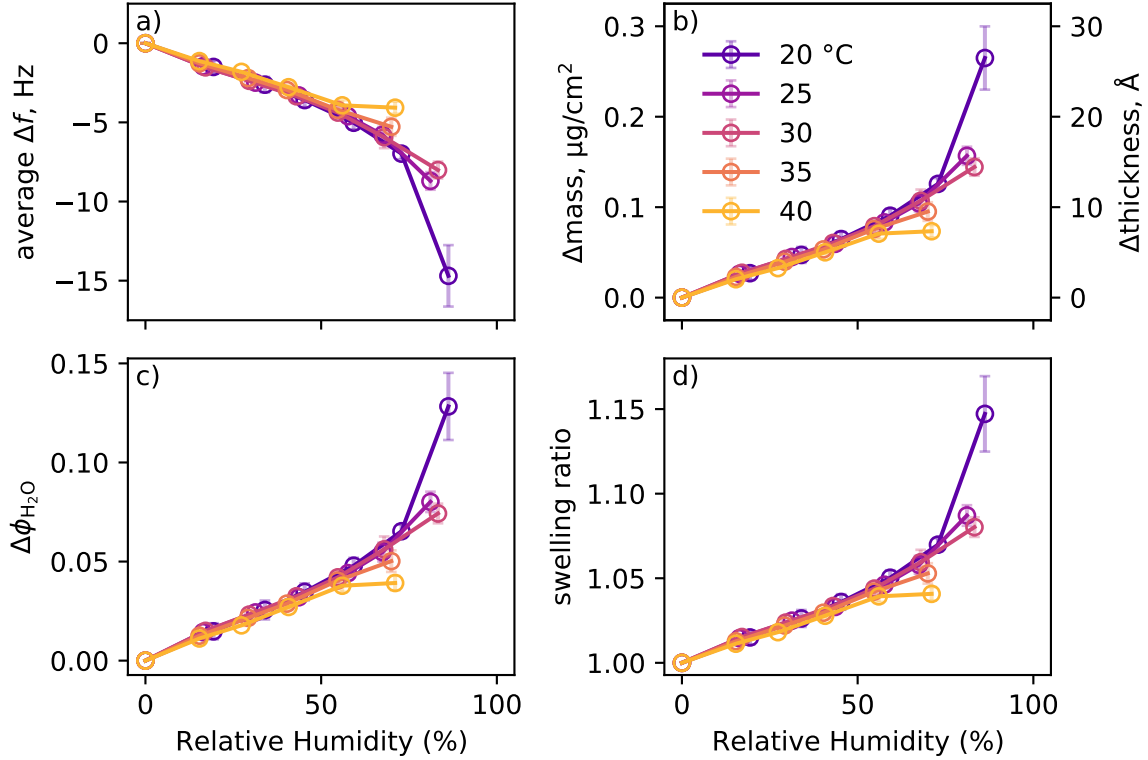


Figure 3.6: (a)  $\Delta f$ , averaged across overtones one through seven (error bars are the standard deviation), as a function of RH. (b) Calculated change in mass (*left axis*, Eq. 3.3) and thickness (*right axis*) corresponding to the data in (a). (c) Change in the volume fraction of solvent (Eq. 3.5). (d) SR of the film (Eq. 1.7). Calculations assume an interfacial volume of  $180 \text{ \AA}$  (Section 1.5.6).

the standard deviation of overtones are plotted as error bars. At a given temperature, the frequency decreases as RH is increased (Fig. 3.6a), corresponding to an increase in absorbed mass (Fig. 3.6b) as the film absorbs water. Below a RH of 50 %, temperature has little effect on the swelling of the brush, however, this effect grows as humidity is increased further. At a RH of 75 % there is a marked difference between temperatures, with PNIPAM absorbing significantly more water at lower temperatures. Unfortunately, experimental constraints prevented us from probing higher relative humidities. The key limitation was maintaining the QCM-D enclosure at a temperature greater than  $T_{\text{samp}}$ . In future experiments it might be possible to adapt a small cartridge heater to heat the space.

By assuming that the density of the absorbed water is  $1 \text{ g cm}^{-3}$ , the change in film thickness (Fig. 3.6b), and hence the change in volume fraction (Eq. 3.5, Fig. 3.6c) and SR (Fig. 3.6d) can be calculated. These calculations assume that no voids are present in the brush, i.e., that all space is occupied either by  $\text{H}_2\text{O}$  or polymer (Eq. 1.9), and do not account for the slight change in polymer and water density caused due to the changing

system temperature. However, we expect both the density of both water and polymer to change by less than 1 % over the temperature range investigated [130]. Figure 3.6 shows a maximum SR of 1.14, slightly greater than the result reported for PNIPAM hydrogels [116]; this is expected, as brushes have been shown to swell more than hydrogels [78].

### 3.3.2 Neutron reflectometry

NR is capable of resolving both the thickness and solvent fraction of the dry brush system. Here, we conduct reflectometry measurements at a number of  $p_{\text{D}_2\text{O}}$  and  $T_{\text{samp}}$  combinations. As discussed in 3.2.2, it was thought that  $T_{\text{vap}}$  would equal  $T_{\text{samp}}$  at positions close to the sample; hence controlling  $T_{\text{samp}}$  would allow for the control of RH in the immediate vicinity of the sample. However, the following results indicate that this was not the case (discussed at length in appendix D); as such, the results will first be discussed with respect to known parameters  $T_{\text{samp}}$  and  $p_{\text{D}_2\text{O}}$ . After this, the results will be recast in terms of RH using Equations 3.4 and 3.1, compared with the QCM-D findings. Finally, the SLD of PNIPAM and approximate water content of a dry PNIPAM film will be determined.

The collected reflectometry profiles are shown in Figure 3.7a. The thickness of the brush layer has been determined from the data in two ways, via a fringe-spacing analysis (Sec. 1.5.2, Fig. 3.7b) and a modelling process (Sec. 3.2.2, Fig. 3.7c). Here the fringe-spacing analysis confirms the veracity of our modelling analysis. Both methods yield identical trends, although the fringe-spacing analysis produces slightly higher thicknesses and swelling ratios. The difference is due to the effect of the silica native-oxide layer ( $\approx 20$  Å thick) on the fringe spacing. Swelling is observed to increase monotonically as the  $p_{\text{D}_2\text{O}}$  is increased, and is moderately dependent on the temperature at pressures under 20 mbar, where thicknesses appear to increase exponentially with pressure at all temperatures. Above 20 mbar, temperature becomes much more important, with higher temperatures deviating from the apparent exponential increase and plateauing, particularly in the modelled thicknesses (Fig. 3.4c).

Figure 3.8 shows key environment and fitting variables as a function of time, allowing the results to be more closely analysed. The NR experiments were carried out as temperature sweeps at constant  $p_{\text{D}_2\text{O}}$  (i.e., varying RH), so it can be soundly concluded that the layer was sensitive to temperature, as the solvent fraction decreases with increasing temperature. However, it is difficult to determine whether this behaviour is due to a change in RH or the thermoresponsive nature of PNIPAM. Partial pressure can be converted to RH if the saturated vapour pressure is known; in practice, this requires knowledge of the system temperature (Eq. 3.1, Fig. 3.1). Here we use Equation 3.4 to determine the relevant vapour temperature, producing the thickness vs RH plot in Figure 3.9. The trend in

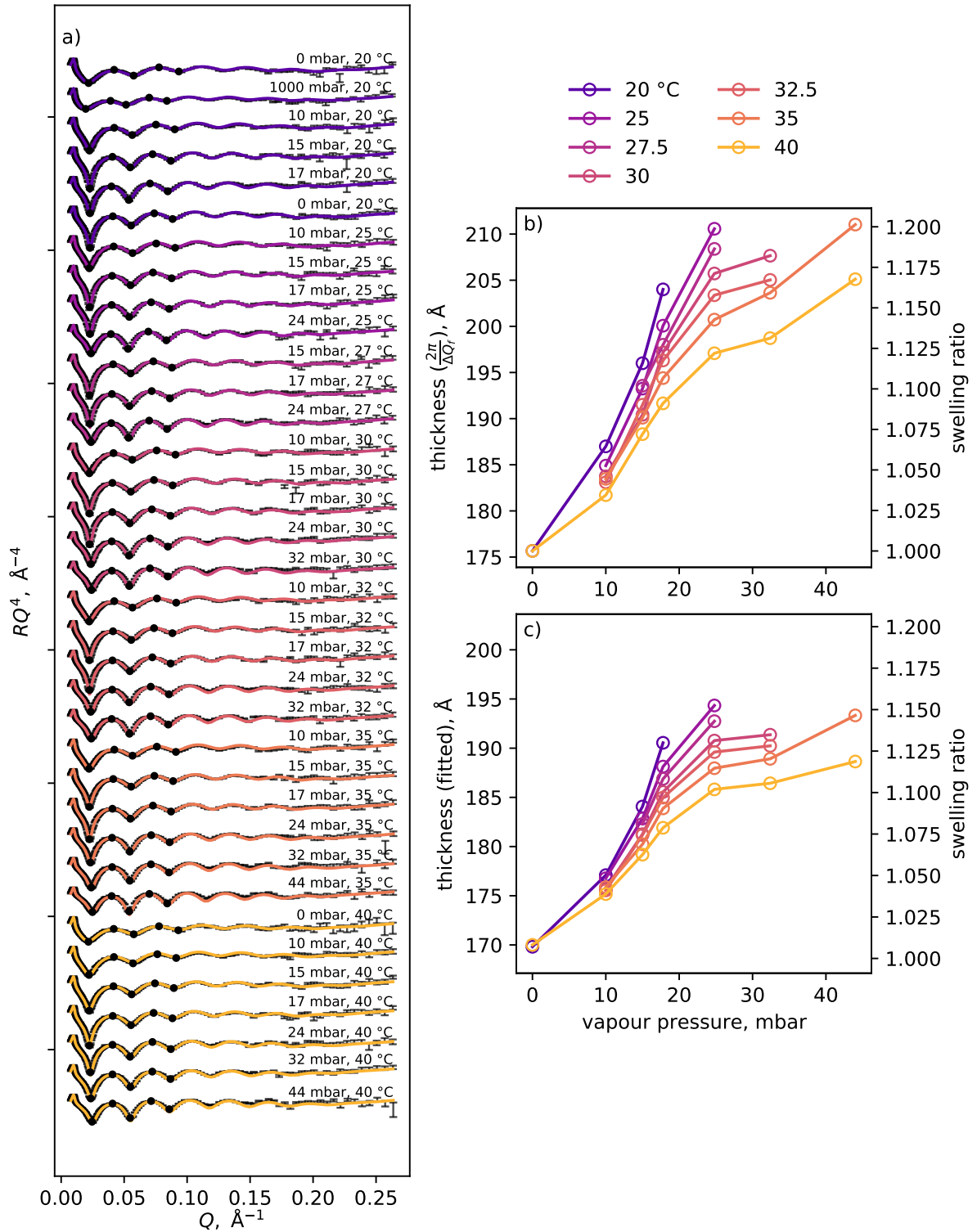


Figure 3.7: (a) Collected reflectometry profiles (*black error bars*) with corresponding fits (*coloured lines*) and fringe locations (*black dots*); modelled profiles satisfactorily match the collected data. (b) thickness (*left axis*) and corresponding SR (*right axis*) as calculated via analysis of the fringe spacing. (c) polymer thickness (*left axis*) and corresponding SR (*right axis*) from modelling of the reflectometry data. While the absolute values in (b) and (c) differ, they follow the same trend.



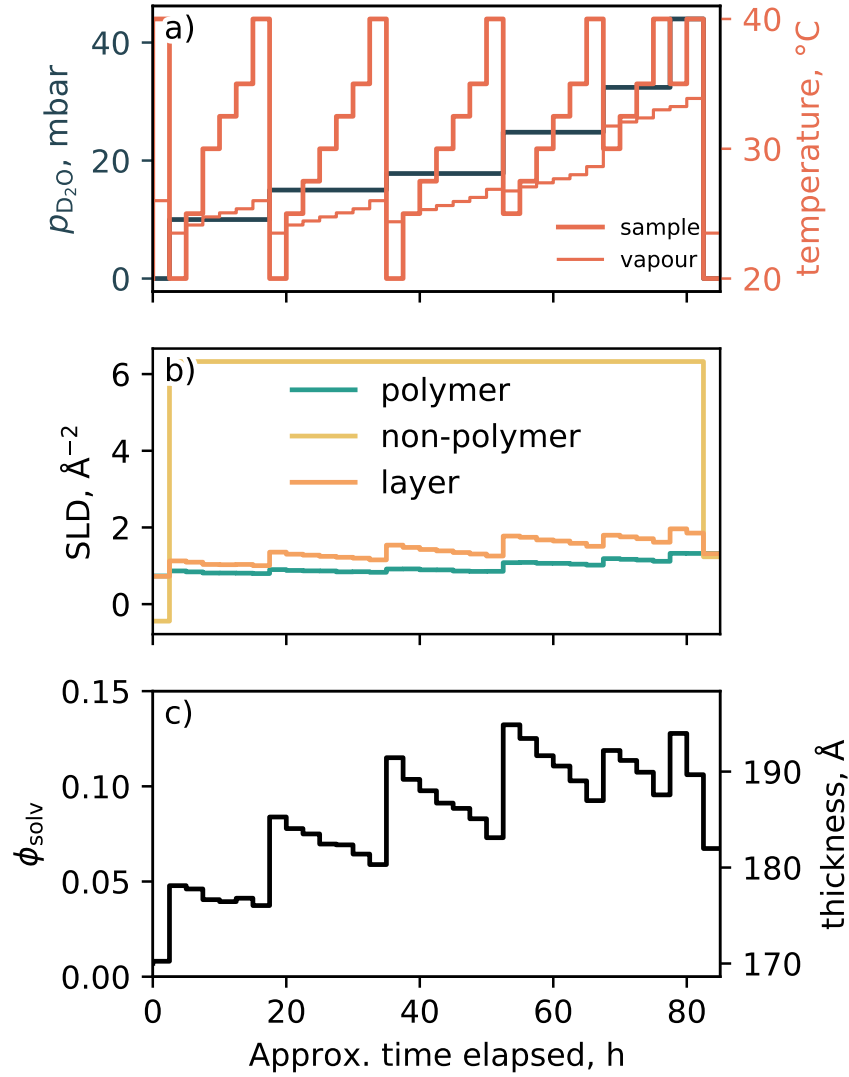


Figure 3.8: Experimental conditions and key model parameters from the NR experiment as a function of time. (a)  $p_{D_2O}$  (*left axis*) and temperature (*right axis*) of both the sample (measured) and vapour (approximated) in the NR sample environment. (b) the SLD of the polymer, the non-polymer component ( $H_2O/D_2O + \text{void}$ ) and the layer (via Eq. 1.9), extracted from the modelling process in Figure 3.7. (c) solvent fraction (*left axis*) and layer thickness (*right axis*), extracted from the modelling process documented in Figure 3.7.

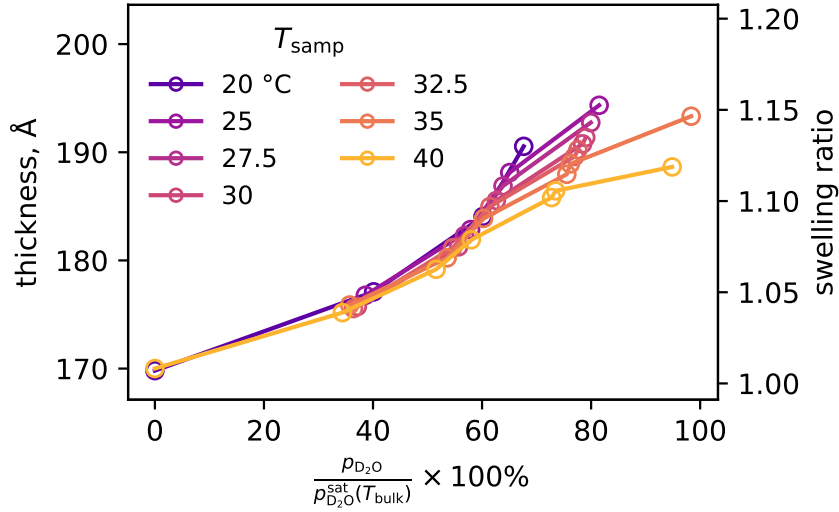


Figure 3.9: Thickness (*left axis*) and corresponding SR (*right axis*) as a function of RH assuming that the relative vapour temperature is a function of the bulk temperature.

Figure 3.9 matches that observed by QCM-D; however, the determination of the relevant vapour temperature is not trivial, as discussed in appendix D.

By constraining the interfacial volume of polymer between experiments, our analysis is able to determine the true polymer volume fraction of the layer at different conditions. Reassuringly, we find that initially the PNIPAM layer is almost completely dry, with a thickness approximately 92% of that in ambient conditions. This finding matched well with the experiment in which the SLD was determined, documented in Figure 3.5. We stress that the thickness of the dry layer (which may contain some voids) is not the same as the interfacial volume of that layer; this is discussed in-depth in section 3.3.4.

By the end of the experiment it appeared that the PNIPAM film had an SLD of  $1.25 \times 10^{-6} \text{ \AA}^{-2}$  (Fig. 3.8), indicating that almost all of the hydrogen in the amide had exchanged for deuterium. This supports our calculated SLD for deuterated PNIPAM ( $1.25 \times 10^{-6} \text{ \AA}^{-2}$ ). It is unknown why the exchange appeared to occur faster in  $D_2O$  vapour than it did in liquid  $D_2O$ . It is possible that the deuteration reaction is greatly accelerated by elevated temperatures, in which case the reaction of the block in vapour would proceed faster than in the block in liquid.

Another interesting feature evident in Figure 3.8 is that the solvent volume fraction does not return to zero at the end of the experiment. This irreversibility is evident in both the SLD and thickness of the fitted layer. The SLD of the non-polymer medium decreases to approximately  $1 \times 10^{-6} \text{ \AA}^{-2}$ , indicating that the layer is no longer swollen by  $D_2O$ . It appears that upon a sudden decrease in RH PNIPAM may vitrify before the layer can completely collapse, resulting in the presence of voids within the brush. The

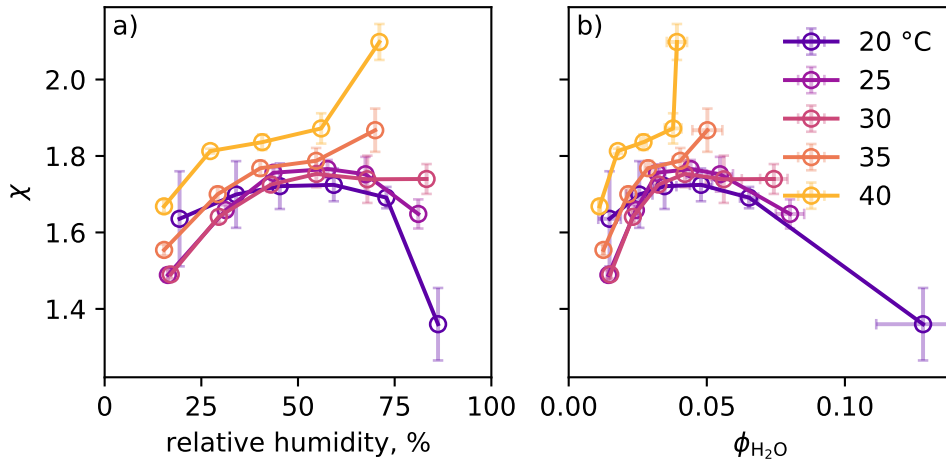


Figure 3.10:  $\chi$  as a function of both (a) RH and (b) volume fraction solvent, from the QCM-D results in Figure 3.6. There is a clear trend wherein solvent quality decreases (i.e., increasing  $\chi$ ) with increasing temperature. Furthermore,  $\chi$  also clearly depends on the solvent fraction.

vittrification is reversible, as we observed the reswelling of PNIPAM brushes after they had been aggressively dried (e.g., under vacuum, as in Figure 3.7, or even in a vacuum oven). This phenomena would be an interesting avenue for future investigations.

### 3.3.3 Calculation of $\chi$ parameter

From the QCM-D results presented in Figure 3.6d and Equation 3.2 the Flory-Huggins interaction parameter  $\chi$  can be calculated. QCM-D results are used here due to the better control of RH in these experiments; furthermore, other studies that have calculated the  $\chi$  from the swelling of polymer films in humid environments have done so at atmospheric pressure.  $\chi$  as a function of RH is shown in Figure 3.10. As indicated by Figure 3.6, the solvent affinity of PNIPAM is relatively independent of temperature at low relative humidities, but becomes more temperature-dependent as RH increases.

Plotting  $\chi$  as a function of solvent volume fraction provides insight into the apparent dependence of the thermoresponse on RH. Since NR finds that the film is almost completely dehydrated at 0% RH, we take  $\Delta\phi_{\text{solv}}$  from Figure 3.6c as  $\phi_{\text{solv}}$ . Figure 3.10b shows that the thermoresponse is dependent on the amount of solvent in the layer. It is well known that the thermoresponse of PNIPAM is not due to an intrinsic property of the polymer, but rather due to the entropic penalty imposed on solvating water molecules by the polymer [38]. It has also been noted that PNIPAM exhibits a volume fraction dependent thermoresponse [36, 131]. Hence the dependence of the thermoresponse on the water content of the film is expected. Interestingly, there still appears to be a critical

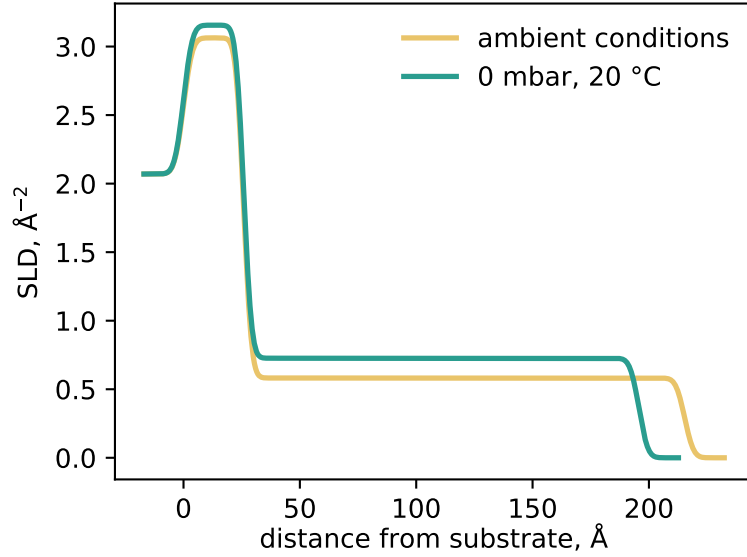


Figure 3.11: SLD profiles from the PNIPAM brush in both ambient conditions ( $\approx 21^\circ\text{C}$ ,  $\approx 52\%$  RH) and after evacuation ( $20^\circ\text{C}$ ,  $0\%$  RH). Upon evacuation the thickness decreases by  $\approx 10\%$ .

transition at around  $32^\circ\text{C}$ , as the  $\chi$  vs.  $\phi_{\text{solv}}$  curves overlay at  $20$  and  $25^\circ\text{C}$ , while the  $35$  and  $40^\circ\text{C}$  curves follow markedly different trends. The  $\chi$  parameter calculated here is higher than observed for PNIPAM-analogous polymers in solution [132], potentially another example of the dependence of  $\chi$  of  $\phi_{\text{poly}}$ .

### 3.3.4 Implications for analysis of dry brushes

In chapter 4, we will show that knowledge of the interfacial volume of polymer is crucial to the rigorous analysis of solvated brush datasets. This value is most easily attained through the measurement of the dry brush. However, in ambient conditions under which dry measurements are normally performed, the brush contains some moisture. This is evident in Figures 3.6 and 3.7, but is emphasised in Figure 3.11. Here, we find that a PNIPAM brush in ambient conditions ( $\approx 21^\circ\text{C}$ ,  $\approx 52\%$  RH) contains approximately  $10\%$  water by volume; in particularly humid laboratory conditions it may be as high as  $13\%$  (Fig. 3.7, 3.6). This water fraction must be taken into account when calculating the interfacial polymer volume from dry brush measurements.

## 3.4 Conclusion

In this chapter, we have investigated the properties of dry PNIPAM brush systems, revealing their behaviour as a function of both temperature and RH, and showing that these layers are not truly dry at ambient conditions. The water content of a PNIPAM

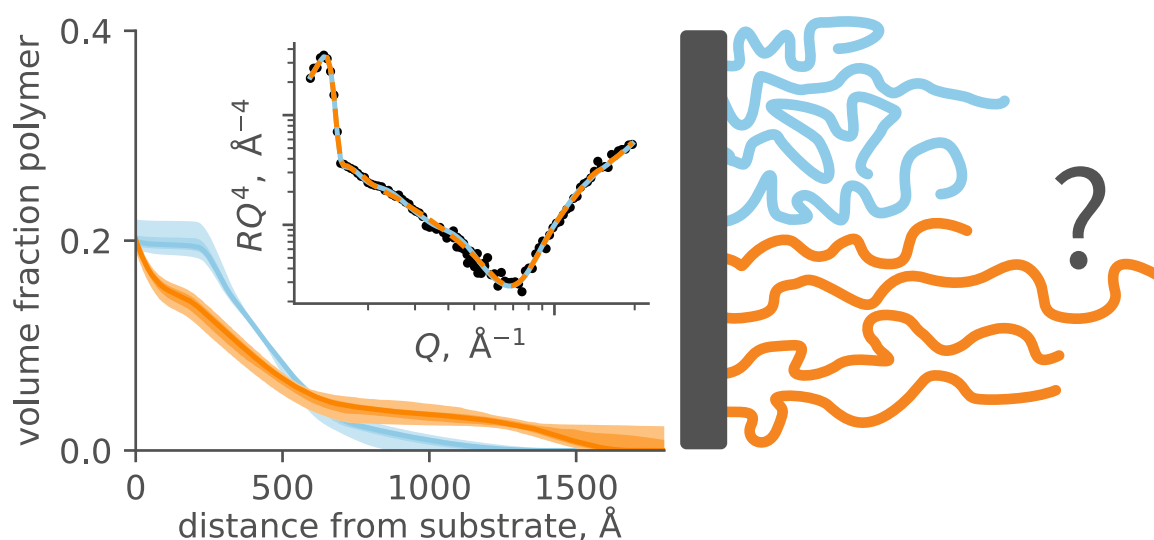
brush was found to depend both on temperature and RH, with temperature dependence becoming more evident as  $\phi_{\text{solv}}$  increases. Both QCM-D and NR studies suggest the  $\phi_{\text{solv}}$  of a dry PNIPAM film may be as high as 13 %, enabling much more accurate predictions of PNIPAM interfacial volume. While we identify potential systematic issues with the NR experiment, it is still useful in both confirming that the amide proton in PNIPAM is labile and determining the SLD of both native and deuterated PNIPAM.

The QCM-D experiments provide insight into the behaviour of PNIPAM at very high polymer fractions, allowing for the calculation the Flory–Huggins parameter for PNIPAM as a function of temperature and solvent volume fraction, within the  $\phi_{\text{poly}}$  range of 0.87 to 0.98.

# Chapter 4:

## Robust analysis of neutron reflectometry collected from polymer brushes

*Isaac J. Gresham, Timothy J. Murdoch, Edwin C. Johnson, Hayden Robertson, Grant B. Webber, Erica J. Wanless, Stuart W. Prescott, Andrew R.J. Nelson*



*Adapted from “Quantifying robustness of the neutron reflectometry technique for structural characterization of polymer brushes” by Gresham et al., published in the Journal of Applied Crystallography (2021)*

Neutron reflectometry is the foremost technique for the in-situ structural resolution of polymer brushes at solid-liquid interfaces, but is hindered by challenges that arise during data analysis regarding uncertainty in the fitted structure and the possible existence of other structures that match the collected data. These challenges relate both to the model and optimisation algorithm used in the analysis. Prior work has not established the extent of these problems in diffuse polymer brush systems or demonstrated a method for overcoming them.

In this chapter, a considered discussion of the challenges that arise from reflectometry studies of diffuse interfaces is offered. A carefully parameterised freeform model is presented that overcomes contemporary challenges by minimising assumptions regarding brush structure and applying careful constraints. This model is then coupled with a Markov chain Monte Carlo sampling approach, which allows for the characterisation of structural uncertainty and multimodality. The rigor of the approach is demonstrated via a round-trip analysis before it is applied to the well-characterised thermal collapse of a PNIPAM brush, where it is able to quantify profile uncertainty and identify multimodality.

This work highlights the importance of proper model selection and constraint in the analysis of neutron reflectometry data collected from polymer brush systems. The code used in our analysis is provided, enabling the reproduction of our results and the application of our method to similar problems.

## 4.1 Theoretical background

Neutron reflectometry (NR) [133] is particularly well suited to the study of soft-matter interfaces; studies have shown, for example, that it can resolve structures at the desired molecular length scale [1, 134], study buried interfaces [135], differentiate between light elements, and utilise the exchange of  $^2\text{H}$  for  $^1\text{H}$  (termed contrast variation) in order to highlight scattering from different components [136–138]. Since direct inversion of the scattering data is made difficult by the phase problem [139], NR data are typically analysed via a modelling process. A structural model is created that describes the neutron scattering length density (SLD) [140] profile perpendicular to the interface, which is used to calculate a reflectometry profile that can be compared to the collected data [133, 141–146]. The model is refined to maximise the agreement between the generated reflectometry profile and the data.

There are three well-documented [139, 147] challenges that occur in the analysis of NR data:

1. Inflexible models may preclude possible structural forms, while overly flexible models make optimisation challenging.
2. A combination of the phase problem, limited  $Q$ -resolution and experimental noise mean that there may be multiple structures that describe the data equally well (multimodality) [139, 147–150].
3. It is difficult to determine the distribution of acceptable profiles around each mode [149, 151–153].

Significant advances have been made in structural modelling, optimisation, and uncertainty quantification in NR analysis since its inception [141–143, 149, 153–155]. However, methods for estimating model uncertainty and multimodality have not yet been applied to brush systems, where these problems are exacerbated by the relatively featureless reflectometry patterns produced by slowly decaying real-space structures. Here we propose a methodology for the analysis of polymer brush NR data that answers all three challenges. The methodology utilises a carefully constrained freeform model to parameterise the interfacial structure, and a Bayesian parallel-tempered Markov chain Monte Carlo (PT-MCMC) based approach to quantify model uncertainty. The model takes advantage of the strongly-tethered nature of brushes by constraining the volume of polymer per unit area of surface (with units of length, referred to here as interfacial volume,  $\hat{V}_1$ ) of the polymer, while PT-MCMC explores large, multimodal, solution spaces.



The method is validated through the analysis of a synthesised reflectometry dataset and demonstrated through the modelling of a thermoresponsive poly(*N*-isopropylacrylamide) (PNIPAM) brush experimental dataset. PNIPAM brushes exhibit critical solution temperature (CST)-type behaviour, as detailed in section 1.2. The PNIPAM system was chosen as it is well-characterised and allows for a range of system conformations to be investigated for a single substrate and solvent combination.

Despite being developed for and applied to polymer brushes, the method could be applied to any diffuse interface where  $\hat{V}_I$  and SLD of the adsorbed material can be approximated. Our method is implemented in Python using the open-source *refnx* reflectometry analysis package (version 0.1.16) [141]. The software and files required to replicate our analyses are freely available (see Supporting Files), allowing our analysis to be reproduced and adapted.

#### 4.1.1 Bayesian inference in neutron reflectometry modelling

NR data is inherently  $Q$ -range limited and often noisy. Therefore, a method of statistical inference must be utilised to draw rigorous conclusions. Bayesian Inference is particularly appealing due to its inclusion of prior knowledge in the modelling process, compatibility with marginalisation, and its ability to rigorously determine model uncertainties [152, 153, 156]. We offer only a brief introduction to the use of Bayesian Inference for NR analysis, concentrating on the most important elements required for the problem at hand. For further information on the use of Bayesian Inference in reflectometry problems, the reader is referred to the work of Sivia and Webster [152] and Hogg, Bovy, and Lang [157].

With the Bayesian approach, the end goal is to find the posterior probability distribution for the model parameters. The posterior distribution,  $\text{prob}(\theta|D, I)$ , specifies the probability of the model parameters  $\theta$ , given a set of data  $D$ , and prior information  $I$  (Fig. 4.1). Bayes' theorem states that the posterior probability is proportional to the product of the prior and likelihood probabilities [141, 152]:

$$\text{prob}(\theta|D, I) = \frac{\text{prob}(\theta|I) \text{prob}(D|\theta, I)}{\text{prob}(D|I)} \quad (4.1)$$

The prior probability,  $\text{prob}(\theta|I)$ , brings information regarding the distribution of  $\theta$  which we possess through past experimentation, intuition or theory,  $I$ . The likelihood probability  $\text{prob}(D|\theta, I)$  captures how well the model and parameters describe the data. The denominator of equation (4.1),  $\text{prob}(D|I)$ , is called the evidence term and describes the probability of observing the data given a model.  $\text{prob}(D|I)$  is not required for the determination of the posterior distribution, but is useful for model selection [152]. Simply,

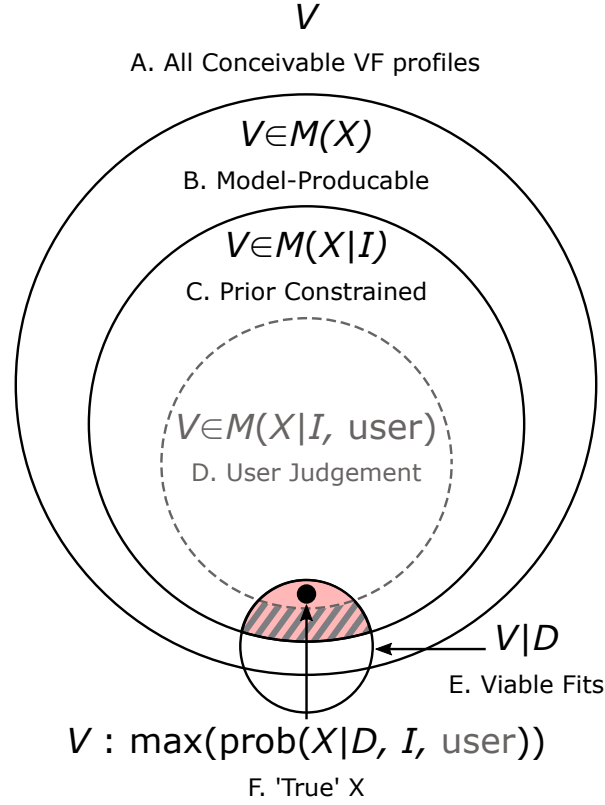


Figure 4.1: Volume fraction profiles,  $V$ , are in overlapping sets, illustrating the application of Bayesian statistics to NR data analysis. (A) Within the space of all possible volume fraction profiles, (B) only some are producible for a given model,  $M$ , for any parameter set,  $\theta$ . (C) Including additional prior information narrows the available  $V$  to  $M(\theta|I)$ , while (D) the user may (in practice) bring in un-encodable intuition to narrow the region further. (E) volume fraction profiles that produce acceptable reflectivity profiles may be unacceptable for any of the previous reasons, (F) ideally leaving only one family of volume fraction profiles that are representative of the ‘true’  $V$ . Problems arise when there are multiple acceptable families of profiles in the shaded regions (multimodality), although some modes may be discounted through user selection (hatched region).

$\text{prob}(D|I)$  is a measure of how much evidence there is to justify the use of a particular model. The evidence term accounts for both how well the model matches the data and the complexity of the model; both an overly complex model and a model that poorly describes the data will have low evidence terms [152].

Here we discuss the practical implications of the model and prior information (both qualitative and quantitative) on the Bayesian analysis of NR data, referring to Figure 4.1 as a guide. We start by acknowledging that a distribution of viable volume fraction profiles (i.e., profiles that are consistent with the data) exists within the space containing all conceivable profiles. This space is restricted by including additional information in the prior term (constraining maximum VF, monotonicity,  $\hat{V}_1$  etc.), as in Figure 4.1C; this

reasoning is conditional on the model being able to construct all volume fraction profiles allowable by the prior. If the model cannot reproduce the physical structure that produced the data, then any optimisation process will fail to converge on the correct solution. As such, one must ensure that the model has sufficient flexibility to cover all allowable profiles. Whilst this condition may be met by a well-developed theoretical model, it is guaranteed by a freeform model. A model does not need infinite freedom to be considered freeform; it only needs to be able to produce all observable, physically allowable profiles (Fig. 4.1C  $\subseteq$  Fig. 4.1B). In practice, the  $Q$ -range of the reflectometry measurement limits the observable spatial resolution, whilst the nature of the sample interface limits the physically allowable profiles. For instance, a freeform model intended to describe a diffuse layer does not need to produce an oscillating profile, but one describing a multi-layer system does. Of course, it is crucial that freeform profiles do not violate any well-established theory or produce physically impermissible profiles, but these criteria are not always trivial to enforce.

In practice, the prior-constrained space is further restricted by the judgement of the user [147]. In an ideal situation, all of the user's prior knowledge and intuition would be quantitatively included in the prior term. However, it is difficult to assign rigorous probabilities to intuition; for instance, if theory predicts a smoothly varying volume fraction profile but the model can produce sharp profiles as well, mathematical inclusion in the prior would require assigning an arbitrary probability penalty to undesirably sharp profiles. In these situations, it is better to exercise judgement on the output of the analysis rather than over-constrain a model [149].

User judgement is not mathematically rigorous, but it must not be discarded. Generally, reflectometry experiments are performed after extensive experimentation with more accessible techniques, and users will have well-developed hypotheses for the interfacial structure and its behaviour. If two comparably good fits to reflectometry data are found, one that matches the prior hypothesis and one that does not, it is clear the former will be preferred. The problem here is not the user applying judgement, but rather the lack of transparency and reproducibility in the process. From a Bayesian standpoint, this application of judgement can be thought of as updating the posterior probability derived from the modelling process with additional (qualitative) prior information. The implications of this are twofold. From a modelling perspective, every attempt should be made to maximise encodable information (such that Fig. 4.1C and Fig. 4.1D are equal). From an optimisation perspective, an ideal method will find all high probability regions of  $\text{prob}(\theta|D, I)$  (which may be included in the Supporting Information, for the sake of transparency), to which the user may then apply their judgement.

### 4.1.2 Parameterisation of reflectometry models

Reflectometry analysis is typically conducted via a modelling approach, whereby an interfacial structure is refined such that its corresponding reflectometry profile matches the collected data. The reflectivity calculation is typically performed using the Abeles matrix formalism [158], which requires that the interface be represented as a number of uniform-SLD layers (hence referred to as slabs). Parameterisation of the interfacial model can be achieved by direct specification of the slabs (the slab model), or indirectly through an intermediate compositional profile, which is then discretised to produce a set of slabs. In the slab model, each layer is defined by a thickness, a roughness, an SLD, and (optionally) a volume fraction value [49, 143]. The slab model is easy to implement and an effective method for describing films with reasonably sharp interfaces, such as collapsed polymer brushes [20, 138], oxide layers [48] and lipid leaflets, where the slab parameters can be ascribed a physical meaning. Slabs with large roughness [159–162] can be used to approximate diffuse interfaces; however, large roughness imposes a form on the transition between adjacent layers and may become less valid if the roughness is a significant fraction of the adjacent layer thicknesses.

Improved descriptions of interfacial structure can generate intermediate continuous SLD or volume fraction profiles. These continuous profiles are often created by a simple, functional relation, such as a parabola or an exponential decay [20, 104, 160, 163], allowing diffuse transitions while minimising the degrees of freedom. However, the use of specific geometric forms is difficult to justify without a detailed understanding of the system. Similarly, simulation or theory can generate continuous volume fraction profiles. Examples include models derived from: scaling theories [164, 165], directly from molecular structure [155, 166, 167], self-consistent field theory calculations [5, 168], or local cavity density functional theory calculations [169]. However, a theoretical model requires the development of a well-supported, system-specific theory that can account for the inherently non-ideal nature of the sample [155].

One potential solution to the problems with the above parameterisation methods is a freeform model, which minimise assumptions regarding the shape of the interfacial profile, allowing the profile to take many configurations. It is helpful here to partition freeform approaches into two categories: those that constrain a large set of slabs and those that describe continuous profiles by the use of a series of smooth functions. Previous constrained-slab approaches have used maximum entropy [149, 150], monotonicity constraints [170], or the groove tracking method [171–173], while continuous-profile approaches have used splines [152, 156, 174–176], and Chebyshev polynomials [177] to flexibly model interfacial regions. Freeform structures are a useful tool for modelling interfaces with no tested the-

oretical description of the interfacial structure. Previous freeform models have typically been unable to produce sharp features, as the spacing between spline knots or slabs is fixed [169, 175, 178], and have had to use penalty terms to suppress oscillations in the volume fraction profiles [149, 175]. Furthermore, they often require assumptions to be made regarding interfacial structure, often through a maximum allowable thickness [152, 179].

In addition to the shape of the SLD profile, the method used to define individual parameters is also important, as the parameterisation method dictates model stability and ease of constraint. We will go on to demonstrate the importance of proper constraint for a freeform approach, but here illustrate this concept through consideration of a simple slab model. Firstly, parameter definitions affect the model’s stability during optimisation; a slab model defined by (independent) thickness and roughness values may produce nonsense configurations where the roughness is larger than the thickness. If the roughness was instead defined as a fraction of the thickness, then nonsense configurations could be prevented. Secondly, parameter definitions determine the ease of model constraint; constraining *interfacial volume* (as needs to be done in polymer brushes) is more challenging when using a slab model defined by (independent) thickness and volume fraction values. However, if the thickness is scaled by  $\hat{V}_I$  divided by the integrated volume fraction profile,  $\hat{V}_I$  can be constrained, and nonsense solutions prevented. Both of the above concepts are employed in this work.

It is worth noting that in practice there are many factors to consider when converting between volume fraction and SLD profiles, particularly when conserving  $\hat{V}_I$ . These generally concern the dependence of molecular volume on polymer-solvent interactions. These are discussed further in appendix G.

### 4.1.3 Optimisation and uncertainty quantification

Regardless of the model used to define the interfacial structure, its parameters must be optimised to produce the structure whose corresponding reflectometry profile best matches the collected data. Conventional analyses minimise the sum of squared errors (i.e., the least-squares approach), using either ‘local’ gradient-based optimisers or ‘global’ stochastic optimisers. In both cases the assumption is made that this single best-fit solution is the *observed structure* (i.e., the global optimum). However, local optimisation approaches often find local optima close to the starting configuration of the model [151, 180], rather than the global optimum. Global optimisers are designed to find the optimum point in the entire parameter space but can not be guaranteed to do so. Foremost among these global methods in the reflectometry field are genetic methods [148, 181], in particular

differential evolution (DE) [151].

Well-defined features in an NR dataset, such as the Kiessig fringes created by a uniform film, typically lead to very small parameter uncertainties. Those well-defined features are typically missing when examining polymer brushes, as the real-space structure is diffuse, resulting in potentially larger parameter uncertainties. Large uncertainties could give rise to significantly different structural models, making uncertainty quantification vital. While conventional approaches allow the parameter covariance to be approximated at a given location [182], these do not deal adequately with non-normal parameter distributions, and the single solution they provide offers no assistance with multimodality. The model uncertainty is better quantified by the posterior probability density function (PDF) (Eq. 4.1) for the parameters, which describes the set of model parameters consistent with the data [152, 156, 183]. The likelihood,  $\text{prob}(D|\theta, I)$ , describes the probability of observing the data ( $D$ ) with a given set of parameters ( $\theta$ ):

$$\log[\text{prob}(D|\theta, I)] = -\frac{1}{2} \sum_n \left[ \left( \frac{y_n - y_{\text{model},n}}{\sigma_n} \right)^2 + \log(2\pi\sigma_n^2) \right] \quad (4.2)$$

where  $y_n$  and  $\sigma_n$  are the value and standard deviation of the  $n^{\text{th}}$  data point, respectively, and  $y_{\text{model},n}$  is the corresponding model value.

One method of approximating the posterior PDF for the parameter set is through Markov chain Monte Carlo (MCMC) methods [183–185], which are well suited to sampling from large parameter spaces. MCMC can estimate the posterior PDF, robustly deal with poorly constrained parameters, and allow for uninteresting but important ‘nuisance’ parameters to be integrated over when evaluating PDFs for parameters of interest (marginalisation) [152]. Furthermore, augmented MCMC approaches like the parallel tempering algorithm (PT-MCMC) [186] can be used to sample multimodal solution spaces [183, 186, 187]. Using PT-MCMC allows us to extend on the seminal work of Sivia and Webster [152] and consider multimodal posterior distributions. The ability to account for multimodality allows the relaxation of the single-optimum assumption; now, it is only required to assume that the observed structure will be *one of* the structures of best fit.

While MCMC techniques are well suited to evaluating the posterior PDF, they are not well suited for estimating the evidence term,  $\text{prob}(D|I)$ . While some MCMC techniques can approximate  $\text{prob}(D|I)$  (e.g. thermodynamic integration in PT-MCMC [186]), other methods, such as nested sampling, are better suited [188]. Nested sampling will be used to determine the required model complexity later in this work.

## 4.2 Method

### 4.2.1 Freeform volume fraction model

Here, we develop a new freeform model, *FreeformVFP*, that describes the volume fraction profile of a diffuse interface using polynomial spline interpolation, specifically a piecewise cubic Hermite interpolating polynomial (PCHIP) [80, 189] (Fig. 4.2). The PCHIP spline is defined by a set of control points, termed knots, and was chosen because it guarantees that the value of the spline is bounded by the positions of adjacent knots, allowing monotonicity to be enforced in the volume fraction profile if desired. The profile produced by the *FreeformVFP* component is extremely flexible, capable of producing both sharp interfaces (e.g., collapsed polymer brush) and diffuse profiles (e.g., swollen polymer brush). *FreeformVFP* uses  $\hat{V}_I$  as a model parameter, scaling the thickness of the interface to conform to  $\hat{V}_I$ ; we will show this is crucial in appropriately constraining the model profile.  $\hat{V}_I$  is a logical parameter to choose, as it can be measured directly for films that can be dehydrated, approximated through techniques such as the quartz crystal microbalance for other solid–liquid systems, and calculated from the surface pressure for air–liquid geometries. This model’s implementation is demonstrated in Figure 4.2a, where it describes a typical swollen  $\phi_{\text{poly}}$  profile of a polymer brush solvated by  $\text{D}_2\text{O}$ , tethered to a silica native oxide layer on a silicon substrate.

The interface is described by a thin, proximal, slab layer followed by the PCHIP spline. This proximal layer is required to describe the substrate roughness with a Gaussian error function, and is defined by a thickness  $d_{\text{initial}}$  and a VF,  $\phi_{\text{initial}}$ . The PCHIP spline interfaces smoothly with the proximal layer; that is, the profile derivative at the slab–spline intersection is 0. The spline then describes the decay of the volume fraction profile from  $\phi_{\text{initial}}$  to 0. In this method, the PCHIP spline is parameterised in such a way as to maximise performance and enable efficient constraints (e.g., monotonicity,  $\hat{V}_I$ ) to be enforced.

The PCHIP spline is constructed on a unit interval,  $\hat{z} \in [0, 1]$ , and is parameterised by a number of knots,  $k$ , each defined by a VF,  $\phi_i$ , and a location,  $\hat{z}_i$ . Two additional non-parameter knots are created on either side of the unit interval and fixed such that  $\phi_{-1} = \phi_0 = \phi_{\text{initial}}$  and  $\phi_{k+1} = \phi_{k+2} = 0$  to ensure value and gradient continuity; only the inner non-parameter knots,  $\phi_0$  and  $\phi_5$ , are shown alongside the parameter-knots in Figure 4.2. The intervening  $k$  user-defined knots are given VFs based off the fitted parameter  $f_i$ :

$$\phi_i = \phi_{i-1} f_i \quad (4.3)$$

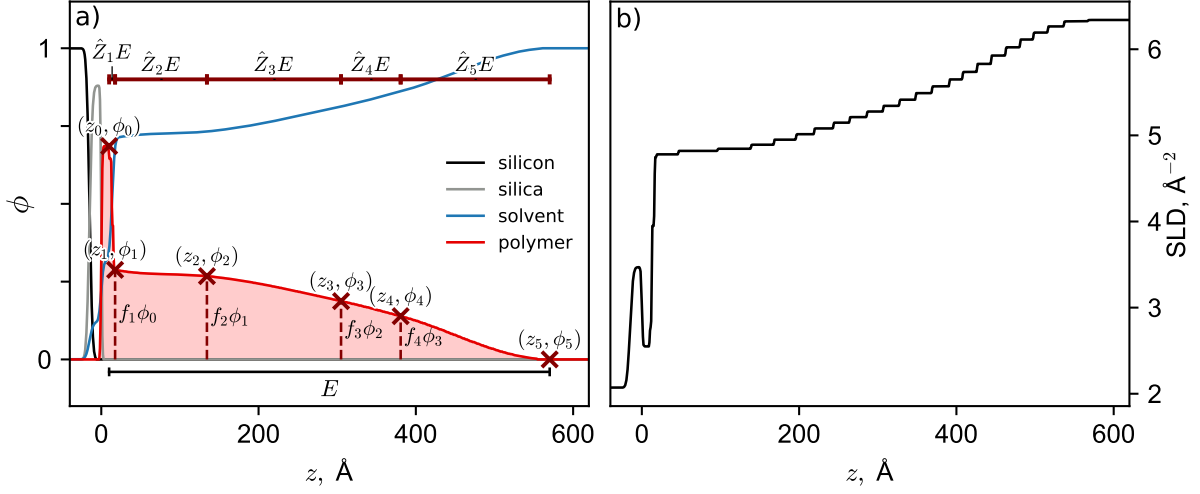


Figure 4.2: (a) Description of a brush-coated interface in terms of the volume fraction profiles of the components present, using a smoothly varying spline function for the solvated polymer layer. From left to right, the silicon and porous silicon oxide layers are topped by a proximal layer, followed by a polymer brush volume fraction profile that consists of a PCHIP spline parameterised by 4 spline knots with position  $(z_i, \phi_i)$ . (b) The discretised SLD profile corresponding to the volume fraction profile in (a) from which the reflectometry is calculated.

where  $f_i$  is greater than 0,  $i$  is an integer between 1 and  $k$  inclusive, and  $\phi_{i-1}$  is the volume fraction of the previous knot. Importantly, if the volume fraction profile is required to be monotonic then  $f_i$  can be constrained within the range 0 to 1, which ensures that a knot cannot have a volume fraction higher than its predecessor.

The locations of these  $k+1$  parameter-knots,  $\hat{z}_i$ , are controlled by the fitted parameters  $Z_j$ , which are the relative distances between knots. These relative distances are converted to absolute unit interval spacings via normalisation:

$$\hat{Z}_j = \frac{Z_j}{\sum_{l=1}^{k+1} Z_l} \quad (4.4)$$

The precise values of the  $Z_j$  are not important, only their values relative to the cumulative value of all the spacings;  $Z_j$  must also be greater than 0 to ensure knots are monotonically ordered. The location of the  $i^{\text{th}}$  knot,  $\hat{z}_i$ , is the sum of the  $\hat{Z}$  spacings up until that point:

$$\hat{z}_i = \sum_{j=1}^i \hat{Z}_j \quad (4.5)$$

The total extent of the spline region is calculated by dividing  $\hat{V}_1$  less the polymer contained



Table 4.1: Relation between the user-facing parameters and those used by the PCHIP splines in *FreeformVFP*.

spline	relationship	user
$\phi_{-1}, \phi_0$	$\phi_{-1}, \phi_0 = \phi_{\text{initial}}$	$\phi_{\text{initial}}$
$\phi_{k+1}, \phi_{k+2}$	$\phi_{k+1}, \phi_{k+2} = 0$	—
$\hat{z}_{-1}$	$\hat{z}_{-1} = -1.1$	—
$\hat{z}_0$	$\hat{z}_0 = 0$	—
$\hat{z}_{k+1}$	$\hat{z}_{k+1} = 1$	—
$\hat{z}_{k+2}$	$\hat{z}_{k+2} = 2.1$	—
$\phi_i$	$\phi_i = \phi_{i-1} f_i$	$f_i$
$E$	$E = \frac{\hat{V}_1 - \phi_{\text{initial}} d_{\text{initial}}}{\int_0^1 \phi d\hat{z}}$	$\hat{V}_1$
$\hat{z}_i$	$\hat{z}_i = \sum_{l=1}^i \frac{Z_l}{\sum_{j=1}^{k+1} Z_j}$	$Z_j$

in the proximal layer, by the area under the spline profile over the unit interval:

$$E = \frac{\hat{V}_1 - \phi_{\text{initial}} d_{\text{initial}}}{\int_0^1 \phi d\hat{z}} \quad (4.6)$$

The PCHIP interpolator is then scaled from the unit interval to cover this range ( $z = d_{\text{initial}} + \hat{z}E$ ). A summary of the spline parameterisation is given in Table 4.1. The programmatic implementation can be found in `FreeformVFP.py` (included in the supporting files and also in the `refnx-models` repository<sup>i</sup>) and is illustrated in Figure 4.2.

Defining the parameterisation of the spline in this way has two very important advantages: the variable knot spacing allows for sharp features to be produced independent of the number of knots, and it is computationally and conceptually easy to constrain physically relevant parameters. By referencing the spline back to  $\hat{V}_1$  in this manner, penalty terms (i.e., a Lagrange multiplier) are not required to enforce interfacial volume or monotonicity constraints [20, 22, 101, 159]. The low number of knots removes the need to penalise oscillating profiles, as they will not be produced by the model even when monotonicity is not enforced. The absence of penalty terms improves optimisation efficiency as penalties are applied only after choosing a set of parameters and calculating the residual;

<sup>i</sup>User-contributed reflectometry models, `refnx-models`: <https://github.com/refnx/refnx-models/>

in the current model, the optimiser will never be able to select an invalid set of parameters. Model stability is also improved in this manner, as any parameter combination will produce a physically sensible profile. Larger numbers of knots in the spline can be used to create increasingly detailed profiles at the expense of computational cost and the risk of over-fitting. There will be a lower bound to the number of knots, below which the model can no longer adequately reproduce the physical system. An approach for evaluating the required number of knots is presented later in this work.

For two component systems (i.e., a solvated polymer brush as shown in Fig. 4.2), the SLD profile for the layer was derived from the layer’s volume fraction profile using the space filling assumption [190]:

$$\rho(z) = \phi(z)\rho_{\text{polymer}} + [1 - \phi(z)]\rho_{\text{solvent}} \quad (4.7)$$

The resulting SLD profile was combined with other model components (e.g., the native oxide layer, solvent SLD etc.) to produce the interfacial SLD profile (Fig. 4.2b). To calculate the model interface’s reflectivity, the SLD profile was discretised into a number of microslices (Fig. 4.2b) and the reflection calculated using the Abeles matrix method [158]. To reduce computation time, a line simplification algorithm was used to ensure that each microslice was as thick as possible without compromising the structural resolution (steeper sections require finer slab slices than flat sections to accurately model the interface; see section 4.2.2). Instrument resolution smearing was accounted for in the reflectometry modelling using constant  $\Delta Q/Q$  from the data reduction process.

In this work, we assumed that the reflectometry data was free from systematic measurement errors (for implications of these see the work of Lu and Thomas [139] and Russell [145]), and do not pursue the option of direct-inversion [191, 192] due to associated practical limitations [147].

### 4.2.2 Line simplification algorithm

To express the freeform profile as a finite number of slabs a line simplification algorithm must be used. The algorithm employed by *refnx* (based on the algorithm used by Kienzle et al. [142] in the *Refl1d* package) increases the slab size within the constraint:

$$\text{structure.contract} > (\rho_{\text{max}} - \rho_{\text{min}}) \times (z_{\text{start}} - z_{\text{end}})$$

where **structure.contract** is a tuning parameter that sets a maximum for the product of the slab thickness and the change in SLD from the proceeding slab. For a general overview of simplification methods in reflectometry see the work of Russell [145]. In

Figure 4.3, `structure.contract` is increased from 0.5 to 20, resulting in more stepped SLD profiles where the freeform curve is discretised into fewer slabs. Figure 4.3 shows that values between 1 and 5 do not reduce the resulting reflectivity profile’s validity whilst making a small but significant difference in computation time. Computation time was approximated by measuring the time taken to calculate the reflection produced by the structure in Figure 4.3, averaged over 400 iterations. In the analysis of the PNIPAM thermocollapse (Fig. 4.8), `structure.contract` is set to 1 (corresponding to the dashed line in Fig. 4.3c), as validity was a higher priority than efficiency.

### 4.2.3 Simulating reflectometry from theoretical profiles

To validate both the efficacy of PT-MCMC sampling and the suitability of our model, we simulated a reflectivity dataset from the structure of polystyrene brushes in deuterated

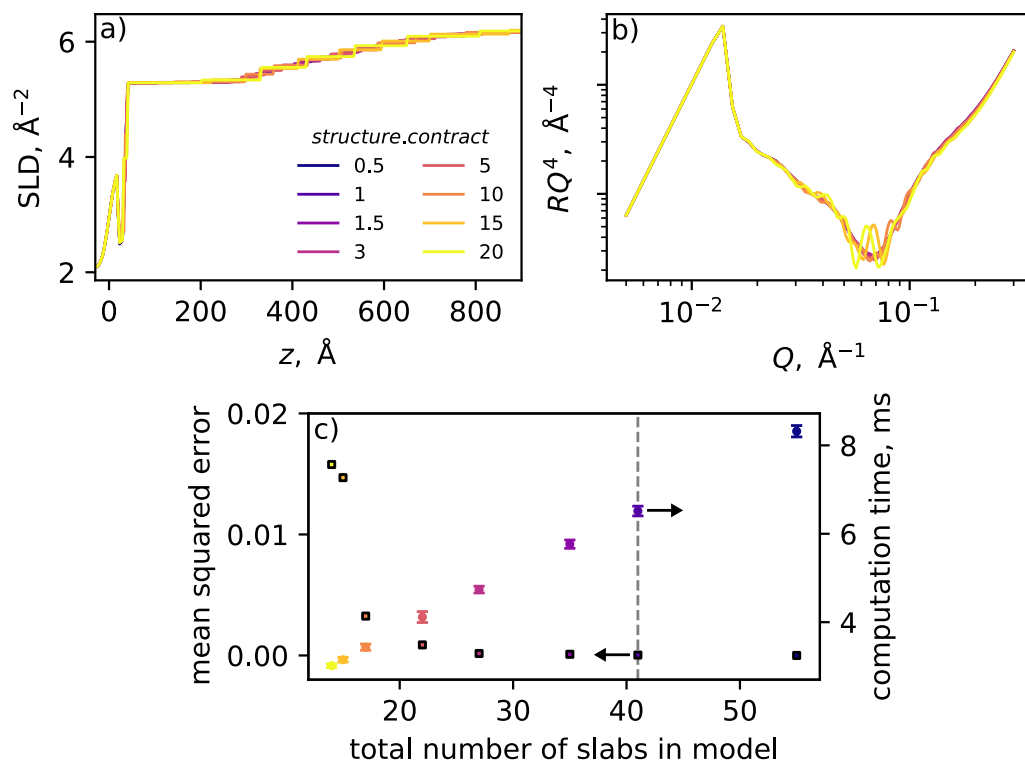


Figure 4.3: (a) SLD profiles and (b) corresponding reflectometry profiles as the `structure.contract` parameter is increased from 0.5 to 20. The (c, *squares*) resulting mean squared error (as compared to the `structure.contract` = 0.5 profile) and (c, *circles and error-bars*) computation time are also shown, plotted against the total number of slabs in the model (which decrease with increasing `structure.contract`). This profiling was performed using version 0.1.16 of *refnx*. The dashed line in (c) indicates the `structure.contract` value used in this work.

toluene (Fig. 2 of Karim et al. [193]), which possess a parabolic volume fraction profile. This simulated dataset allows the analysis of reflectometry data where the true structure is unambiguously known. Simulated datasets were created by randomly generating neutron events with a distribution consistent with the wavelength spectrum of the *PLATYPUS* neutron reflectometer at the OPAL research reactor [81]. The wavelength of each neutron event was jittered by the addition of uniformly distributed noise to account for the wavelength resolution components of a double chopper reflectometer. The angle of incidence was assigned using noise generated from a trapezoidal distribution, corresponding to the angular divergence of a beam collimated by a two-slit system. A neutron event was considered to have reflected if the reflectivity from the theoretical model (for the  $Q$  value corresponding to that event) was greater than uniformly distributed noise in the interval  $[0, 1)$ . By simulating many millions of events, a reflected beam spectrum (as a function of wavelength) can be constructed, which is then divided by a direct beam spectrum (from a different simulation) to give a reflectivity curve that has the same noise and instrument resolution that would be measured on a real time-of-flight instrument [194]. Error bars for each data point were calculated using Poisson counting statistics and error propagation.

#### 4.2.4 Neutron reflectometry measurements

The practical application of the model described above was demonstrated using reflectometry data collected from the thermal collapse of a PNIPAM brush. These brushes were grown from native-oxide silicon wafers (100 mm diameter, 10 mm thick) using the method outlined in section 1.4.

Specular reflectometry measurements were made at angles of  $0.6^\circ$  and  $3.6^\circ$  for dry and  $0.8^\circ$  and  $3.5^\circ$  for solvated measurements. The two angles were reduced using reduction protocols outlined in section 1.5.3, yielding useful data within  $Q$ -ranges of  $0.0073$  to  $0.31 \text{ \AA}^{-1}$  and  $0.0096$  to  $0.31 \text{ \AA}^{-1}$ , respectively. Ellipsometric mapping of the surface was used to check brush uniformity over the area illuminated by neutrons (Fig. E8). Solvated experiments were carried out in a standard silicon-backed solid-liquid cell, the temperature of which was controlled to within  $\pm 0.5^\circ\text{C}$ . Measurements were carried out at  $20$ ,  $25$ ,  $30$ ,  $32$ ,  $35$  and  $40^\circ\text{C}$ , in that order, covering the entire swollen-to-collapsed transition of PNIPAM. Measurements were performed in  $\text{D}_2\text{O}$  to maximise contrast between the polymer and the solvent, as well as water contrast-matched to the SLD of PNIPAM ( $80.3:19.7 \text{ H}_2\text{O}:\text{D}_2\text{O}$  mix by volume, henceforth referred to as  $\text{CM}_{\text{poly}}$ ) to facilitate characterisation of the native oxide layer.

### 4.2.5 Optimisation and sampling techniques

Nested sampling is a technique designed to compute the Bayesian model evidence for a given model and dataset. Briefly, it operates by generating ‘shells’ of constant likelihood via a stochastic sampling process. These shells can be integrated over, which allows for the proper normalisation of the likelihood — this is distinct to MCMC techniques, which only produce proportional likelihoods. The properly normalised likelihood allows for subsequent calculation of the model evidence via Equation 4.1. Nested sampling was undertaken using the *dynesty* Python package (version 1.0.1) [195], which implements the algorithm of Skilling [188]. Nested sampling was undertaken in static mode with 500 live points and multiple bounding ellipsoids to define the target distribution, with samples being drawn from a uniform prior distribution.

Differential evolution is a genetic optimisation technique, wherein a collection of randomly initiated parameter combinations are iteratively combined, with only successful (higher probability) combinations progressing further in the iteration process. DE is a widely used optimiser primarily because it does not require the optimised function to be continuously differential and is not as prone to becoming trapped in local optima as other gradient-based optimisers. However, the DE algorithm is not guaranteed to find the optimum solution. DE was performed using the SciPy Python module [80], which implements the algorithm of Storn and Price [196]. Where DE output is reported, it represents the highest posterior probability profile taken from twenty discrete DE optimisations.

Markov chain Monte Carlo is a stochastic sampling process that draws samples using a ‘Markov Chain’. In a typical Monte Carlo process, samples are drawn randomly from the prior probability; in MCMC samples are instead generated by taking a ‘step’ in a random direction from the current parameter combination. The probability of this step being accepted is proportional to the difference in likelihood relative to the previous position, such that the system obeys the detailed balance principle [184]. This algorithm results in parameter combinations (‘walkers’) progressing through the parameter space towards regions of higher probability. As time tends to infinity, the distribution of these walkers will approach the posterior probability distribution. Parallel-tempered Markov chain Monte Carlo is a modification of the typical MCMC algorithm that addresses the poor performance of MCMC when sampling from multimodal posterior distributions. In PT-MCMC walkers are created in different ‘temperature’ brackets, with higher temperature walkers being more likely to take steps that reduce the posterior probability than lower temperature walkers. These high-temperature walkers are then able to better explore the entire parameter space. Walkers can swap between temperature brackets via the same acceptance criterion as walkers taking a new step in conventional MCMC. This means

that walkers can start at a high temperature, locate a new optimum mode, then progress down to a low temperature where they fully explore this mode.

PT-MCMC was undertaken using the *ptemcee* Python package [184, 186], using the algorithm of Goodman and Weare [197]. This algorithm modifies the standard MCMC step selection function; instead of selecting the step direction randomly, it does so in a way that is informed by the shape of the parameter space, as derived from the current distribution of walkers. PT-MCMC sampling was initialised with 600 walkers and 10 temperature brackets, drawing initial parameter values from the prior distribution. Once initialised, PT-MCMC was allowed to proceed for 75 000 steps, with walker locations recorded every 500 steps. Final samples were taken from the walker locations at 75 000 steps; this does not represent the final equilibrium value for all objectives — where multiple modes with similar probabilities are present, convergence is expected to take an extremely long time. However, we have sampled for long enough to either identify multimodality (for objectives that exhibit such behaviour) or to determine spread, and in all cases PT-MCMC at 75 000 steps outperformed the conventional DE method. For more details, see Figure 4.13 and associated text. Refer to the work of Nelson and Prescott [141] for further information regarding the integration of MCMC techniques within *refnx*.

#### 4.2.6 Modelling of an exemplar PNIPAM system

Previous reflectometry experiments have shown that hydrated brushes prepared via this atom transfer radical polymerisation (ATRP) method consist of a thin, substrate-adjacent, high volume fraction interior layer made up of surface adsorbed polymer and initiator moieties (see Chapter 2), followed by a diffuse layer with unknown structural form [20]. Critically, the freeform model describes both the interior and diffuse PNIPAM layers, but does not enforce either the interior layers presence or the shape of the brush profile.

Before analysing the thermal collapse of a PNIPAM brush, parameter bounds were determined for the polymer SLD,  $\hat{V}_1$  of the polymer, and the native oxide structure, which are shown in Table 4.2. We bound the PNIPAM SLD value with the values determined for hydrogenous and deuterated PNIPAM in section 3.2.2. We use the hydrogenous SLD of PNIPAM to determine  $\hat{V}_1$  for the brush. In order to characterise prior PDFs, PT-MCMC was used to co-refine data from the PNIPAM brush in air at ambient conditions, D<sub>2</sub>O at 40 °C, and a PNIPAM contrast-matched H<sub>2</sub>O:D<sub>2</sub>O mix (CM) at 40 °C; details for this characterisation are included in the appendix E. The co-refining of these three datasets produced posterior parameter distributions (Fig. E1 and E2) for the silica layer parameters and  $\hat{V}_1$ .

Once the native oxide layer structure and interfacial volume had been characterised,

Table 4.2: Parameter bounds used for solvated sample analyses.

parameter	lower	upper
<i>model parameters</i>		
scale factor	0.95	1.05
background	$1 \times 10^{-8}$	$2 \times 10^{-6}$
<i>material parameters</i>		
$\rho_{\text{D}_2\text{O}}$	$6 \times 10^{-6} \text{ \AA}^{-2}$	$6.36 \times 10^{-6} \text{ \AA}^{-2}$
$\rho_{\text{polymer}}$	$0.72 \times 10^{-6} \text{ \AA}^{-2}$	$1.25 \times 10^{-6} \text{ \AA}^{-2}$
<i>silica layer parameters</i>		
thickness	†	†
roughness	†	†
$\phi_{\text{solv}}$	†	†
<i>polymer layer parameters</i>		
$d_{\text{initial}}$	5 Å	15 Å
$\phi_{\text{initial}}$	0.3	0.9
$\hat{V}_1$	†	†
$Z_1$	0.01	1
$f_1$	0.15	1
$Z_2$	0.01	1
$f_2$	0.15	1
$Z_3$	0.01	1
$f_3$	0.15	1
$Z_4$	0.01	1
$f_4$	0.15	1

†: parameter constraints are informed by the characterisation documented in section E and are implemented via a truncated normal distribution (see Fig. E2 and E1)

the temperature series was analysed with a four-knot freeform model. The SLD of silicon and D<sub>2</sub>O were taken to be  $2.07 \times 10^{-6} \text{ \AA}^{-2}$  and  $6.36 \times 10^{-6} \text{ \AA}^{-2}$  respectively; the SLD of D<sub>2</sub>O was allowed to vary to account for isotopic contamination with H<sub>2</sub>O. Prior terms for the silica layer parameters and  $\hat{V}_1$  were encoded as truncated normal distributions based off the previously determined parameter distributions (Fig. E2, E1). Further details regarding parameter bounds are included in Table 4.2. Once the prior distribution had been defined, PT-MCMC sampling was run for 75 000 steps for each temperature. All analyses were carried out in *Jupyter* notebooks, copies of which are provided in the Supporting Files.

## 4.3 Results

### 4.3.1 Model validation with synthesised dataset

Before analysing experimental datasets, we applied our freeform model to a synthetic dataset produced from a parabolic polymer volume fraction profile (Fig. 4.4a, black line) that corresponds to the structure of polystyrene brushes in deuterated toluene [193]. A four knot spline was used to remain consistent with the rest of the analyses presented here, however, similar results were observed using two and three knots. Prior-initialised PT-MCMC sampling produced a family of reflectometry profiles that find excellent agreement with the synthetic data (Fig. 4.4). The priors used for the freeform profile (i.e., the bounds on the knot locations) were the same as those used for the analysis of experimental data, and allowed for a wide range of profiles to be adopted.

The analysis of the synthetic dataset allows for the comparison of model output with the true ‘observed’ structure. We find good agreement between the true and modeled structures, with the freeform structure reproducing the parabolic form of the original structure (Fig. 4.4). We stress that no information regarding the shape of the original profile was encoded in the freeform profile. The success of this round-trip analysis validates the modelling and optimisation approach used.

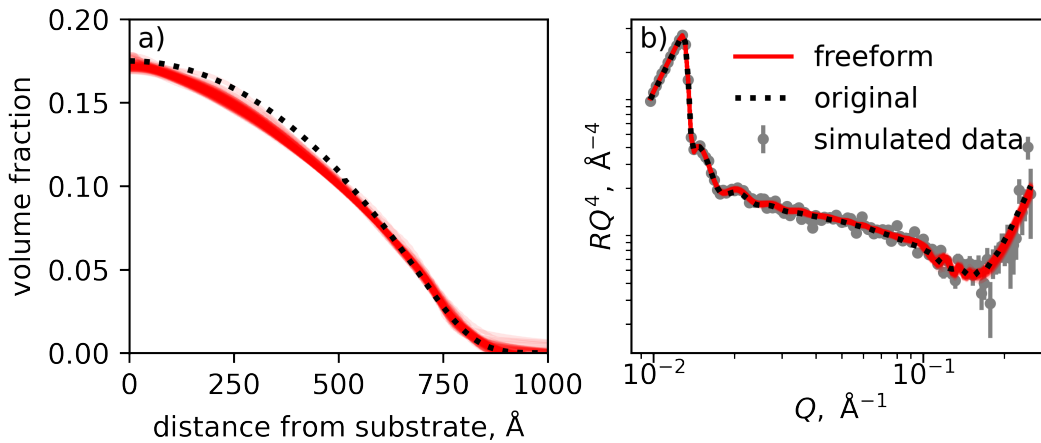


Figure 4.4: (a) Round-trip comparison of the volume fraction profile used to create the synthetic reflectometry profile, and the distribution of profiles produced by PT-MCMC when *FreeformVFP* was optimised against the synthetic dataset. (b) The synthetic reflectometry profile alongside those corresponding to freeform profiles and original profile in (a). The original volume fraction profile was based off the reported structure of end-grafted polystyrene in d-toluene at 21 °C on silicon [193].



### 4.3.2 Determination of model complexity for a PNIPAM brush

The number of knots required to describe a diffuse PNIPAM polymer brush satisfactorily was determined by calculating the evidence term,  $\text{prob}(D|I)$ , for a series of models with increasing numbers of knots using nested-sampling. Nested sampling is computationally demanding in a high dimensional problem space (especially if the likelihood is somewhat expensive to calculate). This demand can be reduced if the approximate location of the optimum is known. For this reason, we used a synthetic dataset, where the structure is known. The dataset was simulated from a structure that featured a dense interior layer (as expected for our experimental system) followed by a parabolic decay; the structure produced is similar to that attained by Murdoch et al. [20] for PNIPAM at 20°C and is included in Figure 4.6.  $\text{prob}(D|I)$  was determined for freeform models with a varying number of knots against that simulated dataset. Non-polymer parameters (e.g., SiO<sub>2</sub> layer) were set to known values, and freeform profile parameter bounds were tightened to restrict the size of parameter space during nested sampling.

Here  $\text{prob}(D|I)$  peaked at three knots, after which it slowly decayed. Additional knots resulted in an improved posterior probability but did not justify the additional model complexity. The optima at three knots indicates that a three-knot model is the best match for the synthesised dataset, although this may vary for different brush structures. However, estimating the log-evidence at each knot number for even a single experimental dataset is computationally comparable to PT-MCMC sampling until equilibration at each knot number, making model tuning computationally infeasible on a per-dataset basis (at

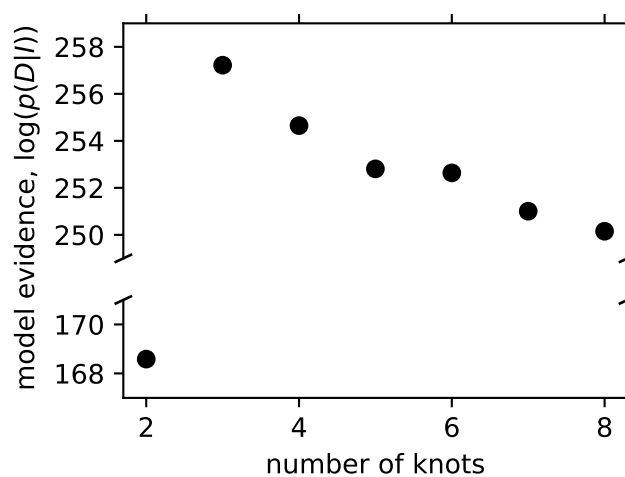


Figure 4.5: Bayesian model evidence,  $\text{prob}(D|I)$ , as a function of the number of model knots. A clear optimum appears at three knots, indicating that a three knot volume fraction profile is the best model for the simulated NIPAM dataset. The reflectometry dataset and original structure can be found in Figure 4.6.

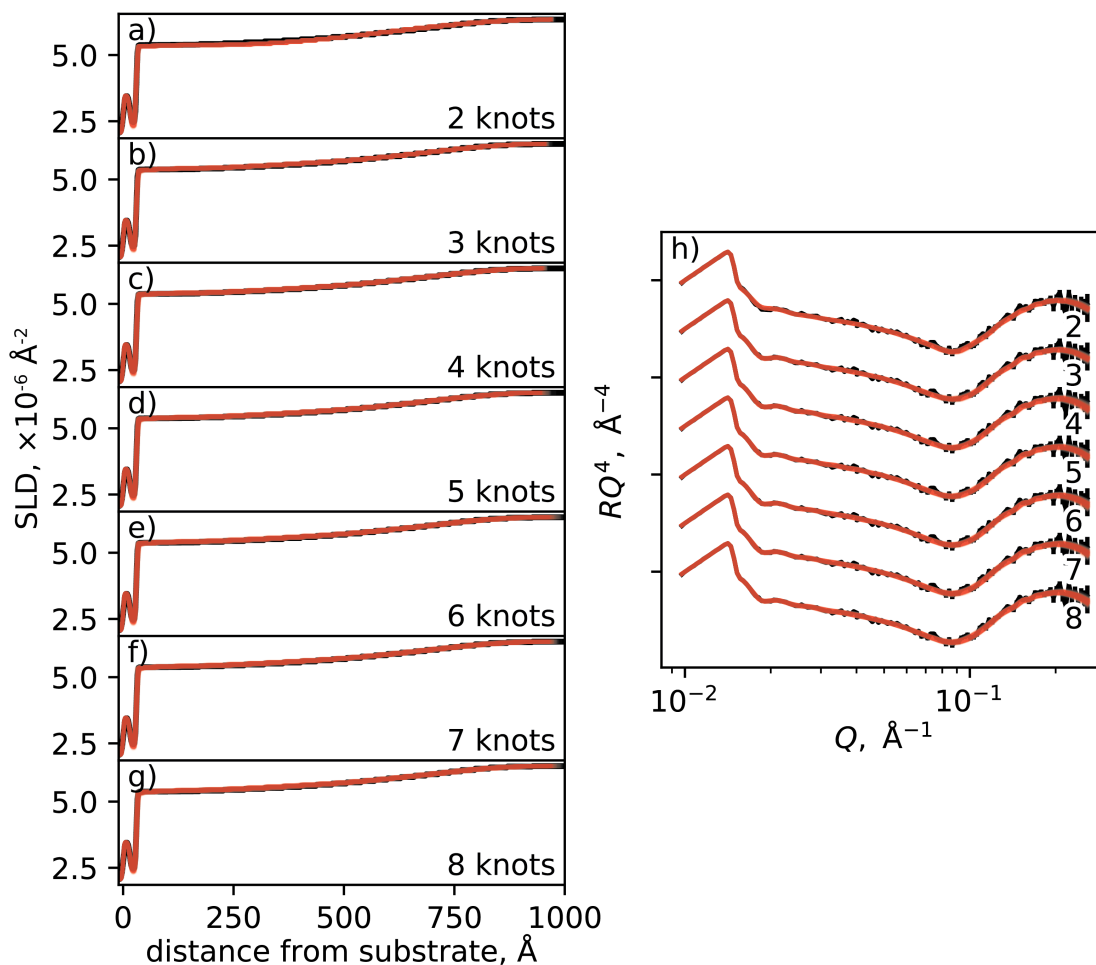


Figure 4.6: Structural output from the nested sampling process used to estimate the model ratio evidence, corresponding to Figure 4.5, processed to be analogous to the output of the MCMC processes used in this work.<sup>ii</sup> a-g) show that the nested sampler (red) converged on the true structure (black) for all numbers of knots used. (h) Corresponding reflectometry profiles are shown against the simulated data; fit quality is virtually identical for models with more than two knots.

present). Using the same number of knots for all datasets also removes user bias from the modelling process and enables batch-fitting of data. Consequently, we use four knots, one more than the minimum number required for the simulated dataset above, to model all datasets. We choose four knots as we anticipate the consequences of under-fitting to be more severe than over-fitting.

The SLD and reflectometry profiles corresponding to the model evidence given in Figure 4.5 are shown here in Figure 4.6. These profiles are generated by post-processing the nested-sampling output to produce samples with equal weight<sup>ii</sup>, corresponding to the

<sup>ii</sup>using `dynesty.utils.resample_equal`

output from a MCMC process. All SLD profiles match the structure used to generate the reflectometry data, while all models above two knots exhibit equally excellent fits to the reflectometry data.

### 4.3.3 Modelling of the thermal collapse of PNIPAM

The freeform analysis approach validated above was then applied to reflectometry data collected from a PNIPAM brush undergoing a swollen to collapsed thermotransition. In the following analysis both the model and the parameter bounds were identical for each temperature, reducing operator bias in the final structures. The output from both PT-MCMC sampling and conventional DE approaches is presented in Figure 4.7. As expected, both techniques produce similar profiles that transition from a swollen, diffuse structure at low temperatures to a collapsed structure at higher temperatures. The structures produced are broadly consistent with those found previously by Murdoch et al. [20], who use an approach where different models are used for different temperatures. The spread

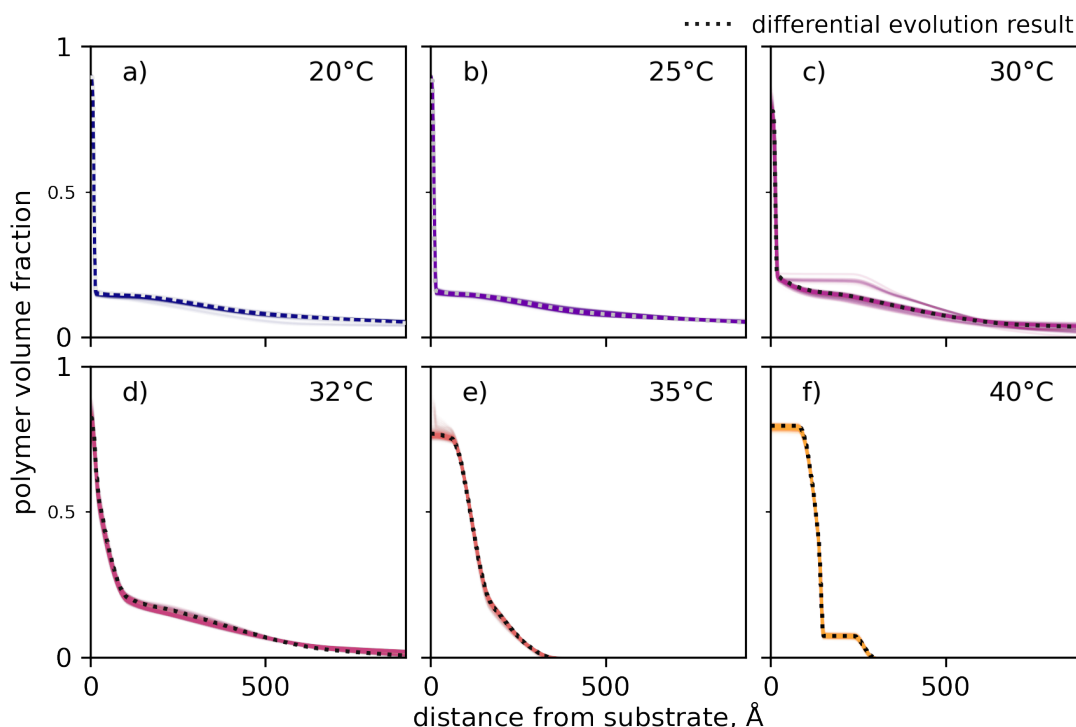


Figure 4.7: Results from the analysis of a thermoresponsive PNIPAM brush with *FreeformVFP*; all analyses use the same model and prior. (a-f) volume fraction profiles show the collapse of the layer as the temperature is increased from 20 to 40 °C, colored profiles correspond to PT-MCMC output, while the dotted lines indicate DE output. The structures produce excellent fits to the collected reflectometry data (see Fig. 4.8). Some profiles (c, 30 °C) exhibit multimodality, which is detailed in Figure 4.9. To allow for easy comparison, profiles are plotted on the same  $z$  axis in Figure 4.10.

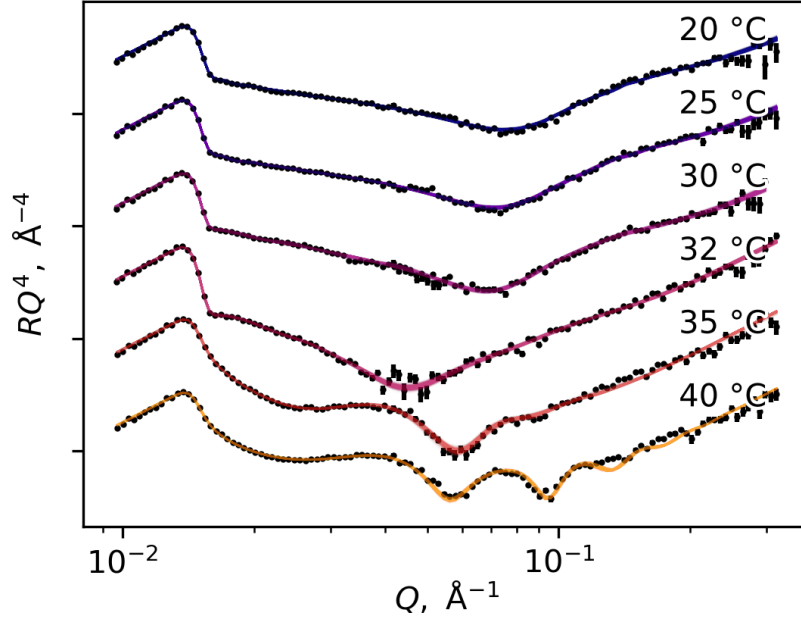


Figure 4.8: Modelled reflectometry profiles and data corresponding to structures and conditions in Figure 4.7. Error bars are included throughout but are smaller than the data marker in many cases.

of model structures displayed by the PT-MCMC samples is not large, indicating that for this system the volume fraction profile can be accurately determined. Our freeform analysis indicates that PNIPAM undergoes a vertical phase separation at intermediate temperatures ( $\approx 32^\circ\text{C}$ ), supporting the conclusions of prior studies [19, 20, 198]. While the final structures produced are very diffuse, they are physically reasonable; single-molecule force spectroscopy (SMFS) conducted on a PNIPAM brush with a dry thickness of  $180\text{ \AA}$  prepared via the same method yields a contour length of  $4980\text{ \AA}$  (Table 1.1). Adjusting for the difference in  $\hat{V}_1$  between the current ( $112\text{ \AA}$ ) and SMFS ( $\approx 181\text{ \AA}$ ) study places the contour length of the brushes studied here at approximately  $3600\text{ \AA}$ , much greater than the thickness of the freeform region in Figure 4.7.

In Figure 4.8, reflectometry data are plotted as  $RQ^4$  vs.  $\log(Q)$  to highlight any discrepancy between the collected data and the model. As is evidenced in Figure 4.8, the profiles produced by the freeform approach seen to exhibit excellent agreement with the collected data with a typical normalised  $\chi^2$  of less than two. The profiles found by PT-MCMC are either identical to (Fig. 4.7) or better than (in terms of  $\chi^2$ , see Figure 4.9) the profiles found by DE, demonstrating that PT-MCMC is capable of matching and even outperforming the conventional DE technique. We note that the  $40^\circ\text{C}$  data in Figure 4.8 exhibits a slightly poorer fit than the other datasets at  $Q > 0.1\text{ \AA}^{-1}$ . This reduction in fit

quality is expected as the reflection from the well-defined collapsed brush layer is more sensitive to layer imperfections (likely macroscopic lateral unevenness, see Fig. E8).

### 4.3.4 Multimodality

The ability of PT-MCMC to account for multimodality is demonstrated in several of the datasets analysed above, most notably in the 30 °C dataset, where two distinct families of fits are revealed (detailed in Fig. 4.9). The multimodal posterior probability distribution is consistent with the information we are able to mathematically encode in our model prior to analysis (chiefly the interfacial volume and profile monotonicity). However, additional qualitative prior information exists that is either impossible to encode, or would make analysis prohibitively complex. One such piece of information is the monotonic relationship between brush swelling and temperature. Prior work suggests that surface-tethered PNIPAM is less swollen at 30 than at 25 °C [48], which is only true for the more collapsed structure produced here (Fig. 4.9, orange); the more swollen structure (Fig. 4.9,

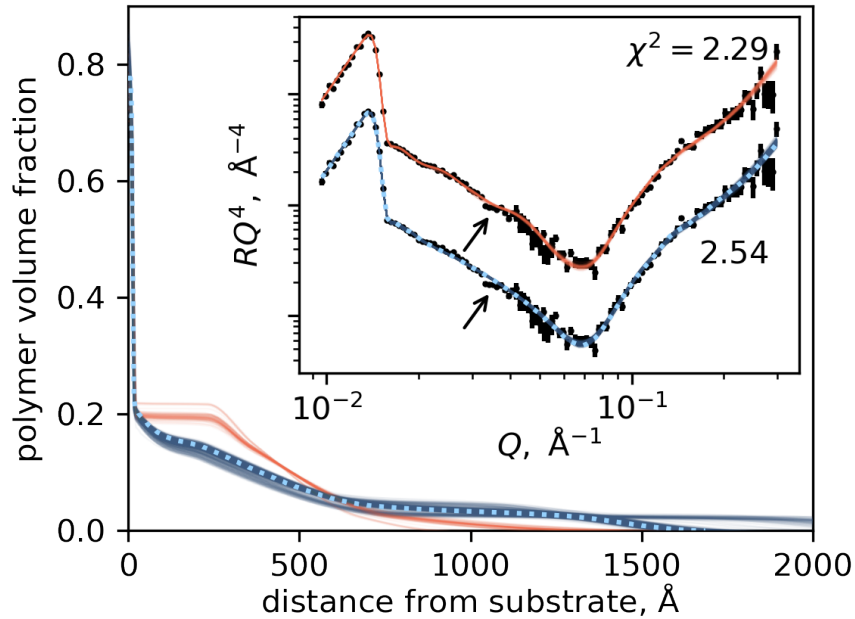


Figure 4.9: Profiles produced by the PT-MCMC treatment of the 30 °C dataset from Figure 4.7c. PT-MCMC reveals that this objective is multimodal; two distinct families of fits are found, separated post-analysis, and plotted in different colours. Both orange and blue profiles provide satisfactory fits to the collected data (inset). However, the more collapsed profile (orange) produces a slightly lower reduced  $\chi^2$  value due to its capture of a subtle feature at  $Q = 0.03 \text{ \AA}^{-1}$  (black arrows). Reduced  $\chi^2$  values are the median of those from each family. The DE fit (light blue, dashed) only captures one of these families; it converges on the family with the higher  $\chi^2$  (worse fit).

blue) is comparable to the profile at 25 °C. We then select the more collapsed structure as the optimal structure (from a posterior probability perspective) for subsequent plotting and discussion. From a Bayesian perspective we are qualitatively updating our posterior distribution based on additional evidence. While we cannot assign a rigorous numerical value to this updated probability, it would be wrong to disregard evidence simply because we do not know how to quantitatively encode it into our statistical framework. We suggest including plots of the (quantitative) posterior distribution in the Supporting Information, while presenting the (qualitative) optimal profile in the body of the work.

We note that the two families in Figure 4.9 provide approximately equal reduced  $\chi^2$  values and near-identical reflectometry profiles. Reassuringly, the more collapsed (orange) family that we selected as the (qualitatively) optimal profile above is also in better agreement with the data. Importantly, this is not the structure produced by a DE optimisation — DE has not found the optimum structure (from either a  $\chi^2$  or posterior probability perspective) due to its acceptance of a presumably more accessible mode. If PT-MCMC had not been used then the most plausible structure would not have been located. It should be noted that it is the combination of a freeform model with a sampling method that enables this rigorous analysis; if the model were more restrictive, only one of the two profiles would likely be detected.

The profiles with the highest posterior probability were taken from those shown in Figure 4.8 and plotted on the same axes in Figure 4.10 for direct comparison. The profiles follow a consistent trend from swollen at low temperatures to collapsed at high temperatures. The reader is referred to the work of Ballauff and Borisov [136] and Baulin and Halperin [35] for further discussion of the significance of these structures and their implications for the physical properties of the brush as it undergoes the thermotransition.

### 4.3.5 Effect of interfacial volume constraint

One of the reasons why global optimisation and multimodality are particularly challenging problems in freeform polymer brush modelling is the large parameter space needed to describe a potentially diffuse layer. Figure 4.7 serves as an illustration of the diverse range of structures that a freeform model must be capable of reproducing. Searching a large parameter space for optimum and near-optimum parameter combinations is fundamentally challenging due to the size of the space scaling to the power of the number of parameters. As such, any method of reducing the size of the parameter space while not restricting the model’s ability to produce sensible structures will both accelerate optimisation and reduce multimodality. In the model described above, the most significant way the parameter space is constrained is to apply bounds to  $\hat{V}_1$ . Figure 4.11 demonstrates

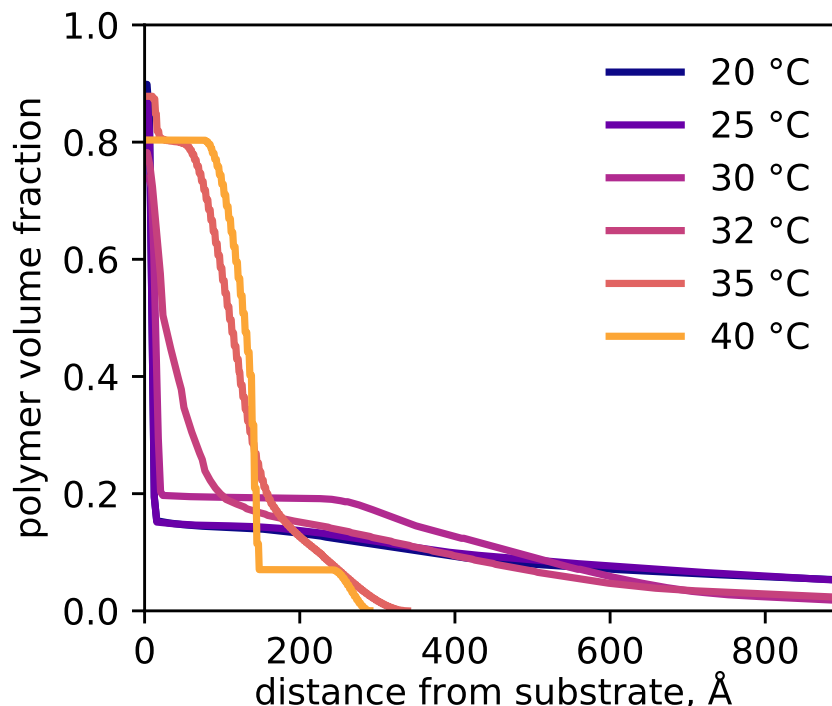


Figure 4.10: Profiles of best fit taken from Figure 4.8, plotted on the same axes for direct comparison.

the importance of implementing this volume constraint for the 32 °C dataset. Encoding a high degree of certainty in  $\hat{V}_I$  (the value and distribution of which can be derived from the dry measurement) in the modelling process was found to reduce the number of modal profiles consistent with the data (Fig. 4.11) at 75 000 steps, as well as accelerating the sampling process by orders of magnitude relative to the least constrained prior (Fig. 4.13). The structure presented in Figure 4.7d has tighter bounds on  $\hat{V}_I$  than Figure 4.11, and fittingly exhibits no multimodality. We conclude that relaxing the constraint on  $\hat{V}_I$  results in solution multiplicity. Consequently, if prior knowledge about  $\hat{V}_I$  is not included as a constraint during the analysis, physically unrealistic profiles will likely be produced, which may be erroneously accepted by typical least-squares analyses.

The interfacial volume constraint is particularly important for diffuse structures, as the reflectometry profile is less sensitive to the dilute brush tail (e.g., Fig. 4.7a at  $\approx 900$  Å); this is investigated briefly in section 4.3.6.

### 4.3.6 Sensitivity to the diffuse tail

Extended polymer brushes are extremely diffuse interfaces. The ‘tails’ of these brushes are dilute, with the SLD of the polymer layer differing only slightly from the bulk solvent,

making resolution of tail structure difficult (e.g., Fig. 4.9). The challenges associated with resolving these tail structures are qualitatively shown in Figure 4.12a, where structurally distinct profiles produce similar reflectometry profiles. Reflectometry is not totally insensitive to the shape of these tails (e.g., Fig. 4.12b); however we find that the reflectometry profile is most sensitive to the inner  $\approx 500$  Å of the swollen brush. If the inner structure is known and  $\hat{V}_1$  is conserved, then the possible structures the diffuse tail may take are tightly constrained and can therefore be deduced by reflectometry. We also find that profiles with similar shapes but different interfacial volumes produce similar reflectometry profiles (Fig. 4.12b), further enforcing the importance of the  $\hat{V}_1$  constraint.

### 4.3.7 Evolution of posterior probability during sampling

One method for inspecting the progress of an MCMC sampling process is to examine the posterior probability as a function of step number; this gives an indication of the number of modes, their relative probability, and how quickly walkers are migrating between modes. Figure 4.13 shows the posterior probability as a function of the step number for the PT-MCMC process that produced Figure 4.8 (best achievable fits to the temperature series). Some objectives converge on the optimum rapidly (within  $\approx 5000$  steps), whilst others have not fully converged by 75 000 steps. In the case of the 30 and 35 °C datasets, the optimum is not found until many thousands of steps, while for the 32 °C dataset the

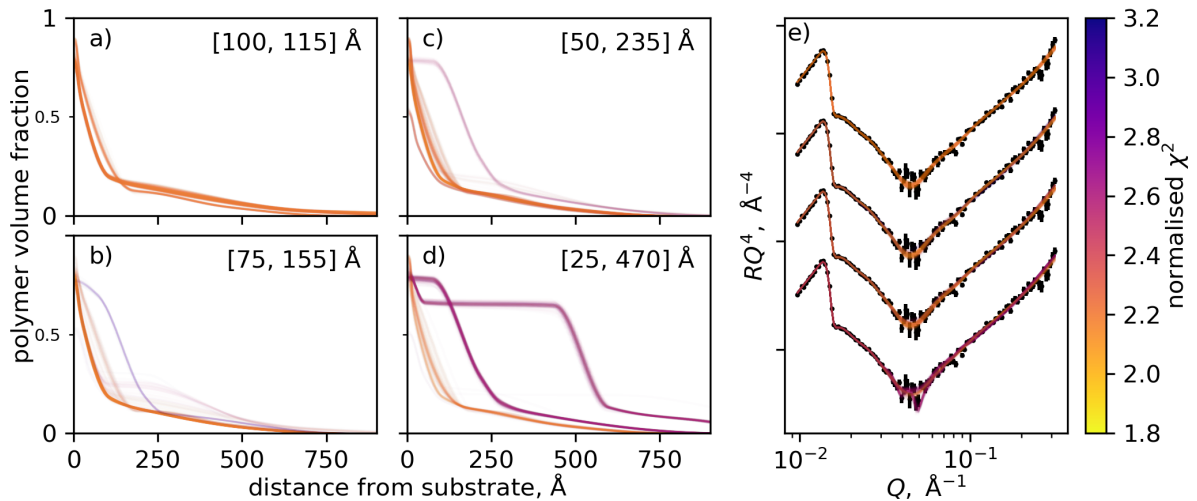


Figure 4.11: (a-d) The profiles produced by PT-MCMC sampling (75 000 steps) for differing interfacial volume bounds, as shown in each plot's top right corner, alongside (e) corresponding reflectometry profiles. The data shown here is for PNIPAM at 32 °C, and can be directly compared to Figure 4.7d, which has much tighter bounds on  $\hat{V}_1$  than (a) (110 to 113 Å, detailed in Fig. E1). The fit quality for all plots is color-coded, indicating that the profile that best adheres to the known adsorbed amount is still the best fit.



apparent optimum is located reasonably rapidly (10 000 steps) but convergence is slow (60 000 steps). From these cases we can conclude that convergence is slower when there are two structures with similar posterior probabilities. Figure 4.14 shows the posterior probability as a function of the step number for the PT-MCMC process that produced Figure 4.11 (exploration of the impact of constraining  $\hat{V}_I$ ). Convergence is clearly faster for the structures with tighter bounds — a direct result of the smaller parameter space.

The purpose of PT-MCMC sampling here is to give an indication of the families of profiles that match the collected reflectometry data. Specifically, we are interested in the number of profile modes that exist and the distribution of viable profiles around these modes. Given infinite time (that is, when the process is at equilibrium) the distribution of parameters produced by PT-MCMC will converge on the posterior distribution, allowing it to be precisely determined (as we show in Fig. E1 and E2), even for multimodal profiles. However, in most practical instances, a precise approximation of the posterior is not required; it is sufficient to know that (a) the experiment is sensitive to the structure of interest and (b) what the optimal set/s of parameters are. Figure 4.13 shows that some of the profiles in Figure 4.8 do not reach equilibrium after 75 000 steps. However, PT-MCMC serves the intended purpose of identifying multimodal solutions. If a detailed posterior probability distribution for the accepted mode is required then point-initiated

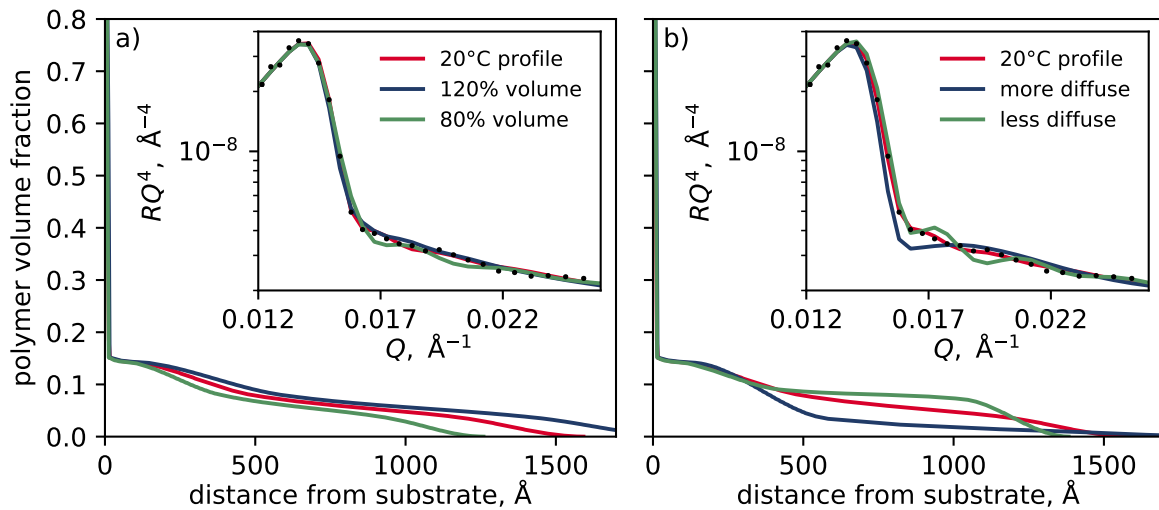


Figure 4.12: (a) profiles with the same shape as the 20 °C profile (Fig. 4.7a) but different interfacial volumes (produced by scaling  $\hat{V}_I$ ) and (b) profiles with the same inner structure but different diffuse decays. Corresponding reflectivity profiles are inset, with the 20 °C data for comparison; the differences between the reflectivity profiles is most distinct at the  $Q$ -range shown. While reflectivity is sensitive to the structure of the diffuse structure, the changes in the reflectometry profiles are slight; constraints are necessary to prevent multimodality. One implication of figure (a) in particular is that it is important that  $\hat{V}_I$  is correctly constrained.

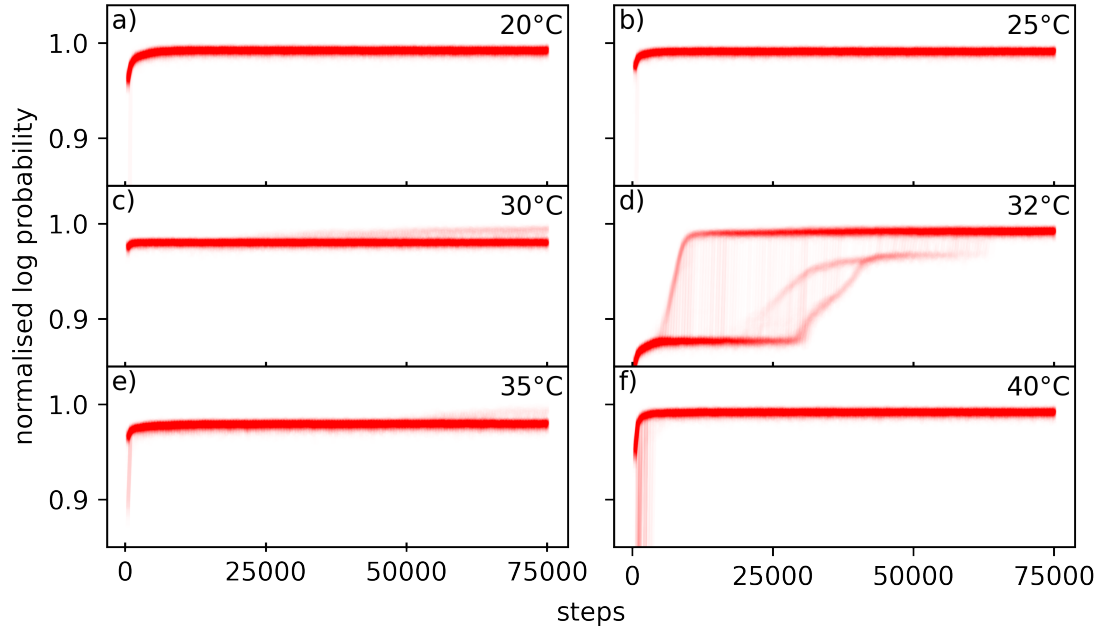


Figure 4.13: Log probability as a function of step number for the PNIPAM brush at different temperatures, with the position at step number 75 000 corresponding to volume fraction and reflectivity profiles in Figure 4.8. Some objectives (a,b) converge on the apparent global optimum rapidly, while others (c,e) exhibit some degree of multimodality, where two structures possess very similar posterior probabilities; the approach to equilibrium here is very slow. Other objectives (d) converge rapidly on a local optimum before locating a better solution.

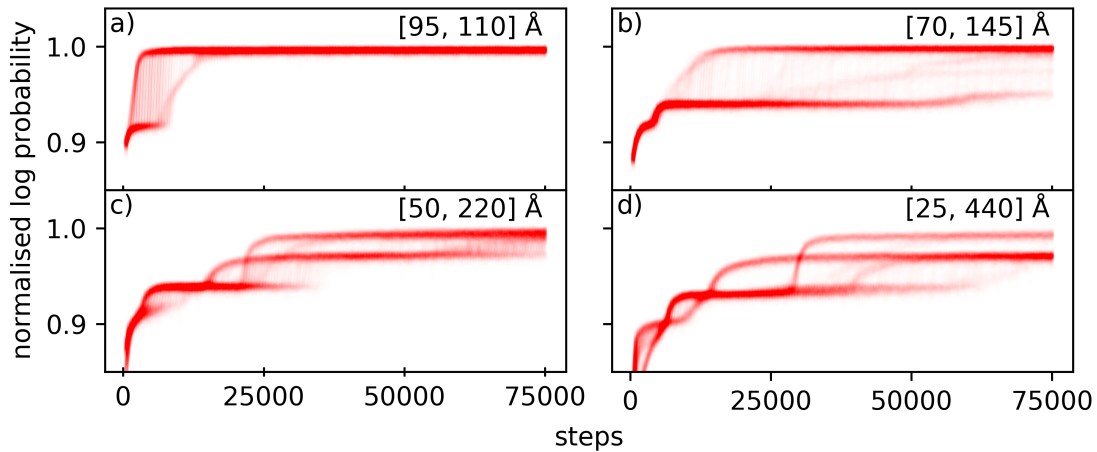


Figure 4.14: Log probability as a function of step number for broadening interfacial volume constraint, sampled from the 32°C data from Figure 4.8, with the position at step number 75 000 corresponding to volume fraction and reflectivity profiles in Fig. 4.11. Broader bounds appear to increase the number of local optima and increase convergence time. (a) cannot be directly compared to Figure 4.13d, as the prior distributions were different.

MCMC can be used to quickly determine the distribution around the mode.

It is worth explaining an apparent contradiction between Figure 4.13d and 4.14a: that the convergence appears faster in Figure 4.14a which has a broader interfacial volume prior distribution (a uniform distribution between 100 and 115 Å) than in Figure 4.13d (a truncated normal distribution between 110 and 113 Å). First we must recognise that Figure 4.14a is actually multimodal (see Figure 4.11a), with both modes having identical prior probabilities, while Figure 4.13d is not multimodal. Hence the contradiction can be explained due to the tighter prior distribution in Figure 4.13d reducing the posterior probability of one of the modes in Figure 4.14a.

### 4.3.8 Best practice

From the above work and prior experience in the field [20, 48, 73, 84, 85, 102, 175], we suggest the following guidelines for experimental best practice:

1. Where possible surface uniformity should be characterised via an ellipsometry or X-ray reflectometry map of the surface (Fig. E8) and encoded into the model (if required) [73].
2. The measured  $Q$ -range should extend until the incoherent background is reached.
3. Uninteresting structural layers (i.e. a native oxide layer) should be characterised independently [139] (Fig. E2) and their values encoded during the analysis of the layer of interest.

The methodology laid out in this chapter represents the current best practice for analysing neutron reflectometry data obtained from diffuse interfaces, particularly polymer brushes. The key recommendations of this work are:

1. The structural model must be able to replicate the physical phenomena that produced the data. Unless well suited theoretical descriptions exist, *FreeformVFP* (section 4.2.1) is suggested as a general candidate for modelling diffuse interfaces such as polymer brushes.
2. As far as is practical, the model should be constrained so that it only produces physically sensible profiles. Here, we emphasise two such constraints: the monotonicity of the profile and the total  $\hat{V}_I$ .
3. Spread around accepted structures (from a single-output optimiser) should be determined with a local sampling approach.

4. Multimodality should be checked using a suitable sampling approach, such as PT-MCMC.

It is recognised that current computing resources make the PT-MCMC sampling approach unfeasible on a large number of objectives; however, it can be applied to a selection of objectives that span the range of response probed by the experiment and to key datasets, to allow the uniqueness of the solution to be assessed, with DE being used otherwise. It is recommended that the DE optimisation be conducted several times and the fit with the highest probability/lowest error selected, as DE does not always find the global optimum (Fig. 4.7). If changes between reflectivity profiles and/or structures obtained from DE are qualitatively small, an optima-initialised MCMC sampling approach should be employed to guarantee the statistical significance of results.

## 4.4 Conclusion

We have developed a method for analysing neutron reflectometry data collected from polymer brushes and demonstrated that this method can reliably be used to determine the interfacial structure of such layers. Our approach minimises assumptions regarding the shape of the interfacial volume fraction profile through the use of a freeform model composed of a flexible PCHIP spline. The model can produce sharp features, is not prone to oscillations, allows monotonicity to be strictly enforced, does not require layer thickness to be estimated, and encodes  $\hat{V}_I$  as a model parameter to ensure only physically sensible profiles are produced. We couple this modelling with PT-MCMC sampling, which is well suited to ‘rough’ solution spaces and enables the uncertainties of the derived structural models to be quantified [186].

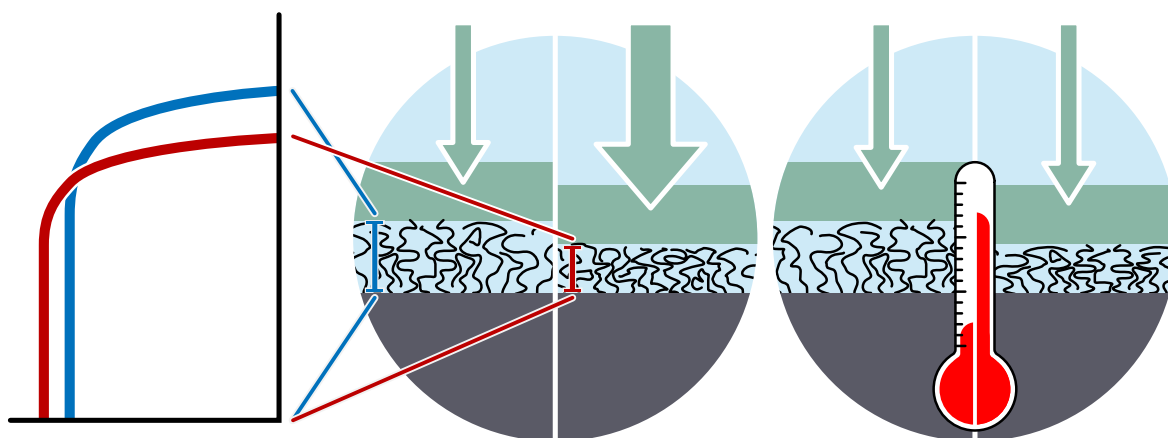
The method was validated through a round-trip analysis of simulated reflectometry data and applied to model real data collected from a thermoresponsive PNIPAM brush system. The volume fraction profiles produced were consistent with prior work, transitioning smoothly from swollen to collapsed as the temperature increases. Although the derived structural models for most datasets were unimodal and exhibited a small spread, our method identified datasets whose structures displayed multimodality. Constraining  $\hat{V}_I$  was vital for eliminating structural uncertainty and reducing multimodality.

We confirm that neutron reflectometry can resolve polymer brush structure with a high degree of certainty, provided care is taken to carefully constrain the model used. The software and model behind our approach are publicly accessible, and we have provided all material required to repeat our analysis methodology exactly or apply it to other systems.

## Chapter 5:

### Geometrical confinement modulates the thermoresponse of a PNIPAM brush

*Isaac J. Gresham, Ben A. Humphreys, Joshua D. Willott, Edwin C. Johnson, Timothy J. Murdoch, Grant B. Webber, Erica J. Wanless, Andrew R.J. Nelson, Stuart W. Prescott*



*Adapted from “Geometrical confinement modulates the thermoresponse of a poly(*N*-isopropylacrylamide) brush” by Gresham et al. 2021, published in *Macromolecules**

Polymer brushes are often touted as promising lubricating or antifouling surfaces. In both of these applications, a surface is in contact with the brush, subjecting it to mechanical confinement. Understanding the structure of responsive polymer brushes under confinement is essential, as brush applications are often accompanied by a surface-normal force, and brush properties are dependent on their structure. In this chapter we focus on examining the structure and behaviour of geometrically confined PNIPAM using neutron reflectometry, AFM and nSCFT.

For neutron reflectometry experiments, confinement is achieved using a custom-made sample environment, and corresponding reflectometry data is analysed using a novel ‘distribution model’. The neutron reflectometry and AFM experiments probe similar temperature-stress combinations and generally find qualitative agreement, with some variations highlighting path-dependent (isostress vs isothermal, respectively) behaviour. All techniques indicate that confinement removes the critical transition point in the thermoresponse of PNIPAM and results in the brush assuming a block-like volume fraction profile with uniform internal structure. The PNIPAM brushes recover from such treatment, regaining their thermoresponse upon re-solvation.

## 5.1 Theoretical background

The structure of poly(*N*-isopropylacrylamide) (PNIPAM) brushes as a function of temperature is reasonably well understood [38]. Unconfined PNIPAM brushes are known to undergo a gradual swollen to collapsed transition as the system temperature is raised above the critical solution temperature (CST) of 32 °C, described in detail in section 1.2. However, many potential applications of these surfaces, such as lubricating and stabilising coatings, are subject to macroscopic mechanical confinement where an opposing surface makes direct contact with the brush. For example, mammalian joint lubrication is partially due to polyelectrolyte brush-like lubricin structures [199, 200], which are effective at applied stresses of around 30 bar [201, 202]. Knowing how polymer brushes behave when they extend into solution is insufficient to design systems for such applications. To understand why biological systems function as they do, and to design systems that mimic them, observation of the structure of polymer brushes as a function of confining stress is required.

The influence of confining stress on the LCST type transition and internal structure of a PNIPAM brush is relatively unknown. Prior investigations of PNIPAM brushes with surface force apparatus (SFA) and atomic force microscopy (AFM) have probed these phenomena indirectly [20, 45, 47, 51, 52], typically measuring force as a function of displacement for either a symmetric (brush on brush) system [51] or an uncoated, confining body acting on a coated surface [20, 45, 47, 51, 52]. These SFA and AFM experiments have focused on indirectly elucidating the brush structure, rather than determining its confined behaviour. Colloid probe AFM experiments typically observe a jump to contact at large separations (on the order of the hydrated brush thickness), with repulsive forces quickly dominating as the probe compresses the brush. Similar SFA studies do not report this jump to contact [52]; the reason for this is unknown, but could be due to differences in polymer-surface affinity (mica vs silica), surface curvature, technique sensitivity to attractive forces, or experimental interest in the attractive regime. The maximum normalised force ( $\frac{F}{2\pi R_{\text{eff}}}$ ) required to collapse a swollen PNIPAM is a function of both molecular weight and grafting density [45, 52]; we expect the same to be true for the structures formed by brushes at a given confining stress. Importantly, AFM and SFA do not reveal the internal brush structure that gives rise to the measured intersurface forces. Previous investigations by de Vos and co-workers revealed the internal structure of thin polyelectrolyte multilayer films under confinement utilising neutron reflectometry (NR) and a unique type of surface force apparatus, which geometrically confines the surface of interest using a flexible, impermeable poly(ethylene terephthalate) (PET) membrane



[134].

In this work, we study the combined effects of confinement and temperature on the structure of a thermoresponsive PNIPAM brush. NR reveals the brush's thickness and structure as a function of increasing temperature at a fixed confining stress; this marks the first time that confined structure has been investigated for a temperature-responsive brush. Numerical self-consistent field theory (nSCFT) is used to predict how brush structure and thickness scale with confining stress, finding qualitative agreement between theoretical and experimental results. These theoretical structures also inform the model used to analyse the collected NR data. The colloid-probe AFM study conducted by Murdoch et al. [20] is analysed and compared to the theoretical and experimental results presented. The unconfined thermoresponse before and after confinement is also observed to determine whether confinement damages the coating.

## 5.2 Materials and Methods

### 5.2.1 Materials

A 50  $\mu\text{m}$  thick PET film (Melinex®, DuPont Teijin films Ltd.) was used as the flexible membrane for the NR confinement experiments. All other materials used are detailed in section 1.3. The brushes used in this study were synthesised on 100 mm silicon wafers appropriate for NR according to the method outlined in section 1.4.

### 5.2.2 Sample characterisation

The wafers' dry thickness was characterised using mapping ellipsometry, X-ray reflectometry (XRR), and NR before confinement. For details regarding each characterisation method see sections 1.5.5, 1.5.4, and 1.5.3, respectively. The result of these characterisations are presented in Table 5.1, further characterisation for brushes synthesised via this methodology are presented in section 1.4. NR was also used to characterise the pre-confinement thermoresponse for each wafer; data were analysed using the method outlined in chapter 4.

### 5.2.3 Neutron Reflectometry

Dry and solvated measurements were carried out according to the method outlined in section 1.5.3. Confined measurements were conducted in a downwards-reflecting geometry at angles of 0.35 and 1.5°, resulting in a useful  $Q$  range of 0.004 to 0.13  $\text{\AA}^{-1}$ . Data reduction followed the standard procedure for *PLATYPUS*, as outlined in section 1.5.3. Consistent with previous work [79, 134], an increase in off-specular signal is seen for confined measurements, owing to contributions from the PET film (and possibly dust).

Table 5.1: Dry thicknesses of the two samples used in the NR study, as measured by ellipsometry, XRR, and NR, all at ambient conditions ( $\approx 55\%$  relative humidity).

sample name	dry thickness, $\text{\AA}$		
	ellipsometry <sup>a</sup>	XRR <sup>b</sup>	NR <sup>b</sup>
1 bar	$224.4 \pm 3.3$	$224.5 \pm 0$	$234.3 \pm 1.1$
5 bar	$206.4 \pm 9.6$	$200.7 \pm 0$	$214.4 \pm 0.8$

<sup>a</sup> Average of nine discrete measurements equally spaced over the surface with one standard deviation reported as the uncertainty.

<sup>b</sup> Uncertainties are taken from the posterior probability distribution for the parameter derived from a Monte Carlo treatment of the collected data.

### 5.2.4 Confinement cell

The confinement experiments were performed in a custom-built sample environment (Fig. 5.1a), similar to that detailed in prior publications [79, 134]. Briefly, a 100 mm silicon wafer coated with an approximately 200 Å PNIPAM polymer brush (for dry thicknesses, see Table 5.1) was placed into the sample environment such that the path of the neutron beam to the sample was unimpeded (see Fig. 5.1a) and the brush-coated surface was parallel to, and 3 mm away from, a PET sheet. The pneumatic pressure on the sample-exterior side of the PET film was controlled via a digital pressure controller; as the pressure was increased the film was pressed against the surface of interest, subjecting it to molecular confinement with controllable surface-normal stress. The pressures are reported as applied pressures (the absolute pressure less 1 atm). Before confinement, the surface was wet with 1 mL of Milli-Q water and the pressure increased to 0.1 bar; this slightly deformed the PET sheet, dispersing the water across the entire sample surface. The system was left in this unconfined state to allow the brush to equilibrate with its solvent environment (over tens of minutes). After equilibration, the PET film was brought into molecular contact with the surface (Fig. 5.1c) by slowly increasing the pressure. When the pneumatic pressure was released at the end of the experiment, the water droplet reformed in the centre of the sample, indicating that the interface is always accessible to the solvent. Previous work has shown that this approach is capable of achieving molecular confinement [79, 134], forcing the water out from between the silica and PET at a minimum stress of 1 bar. Even at high stress, a solvent reservoir is maintained around the confined area (Fig. 5.1b). Molecular confinement was confirmed by a critical edge for confined measurements, which appeared at  $Q = 0.0054 \text{ \AA}^{-1}$ , the expected value for a silicon–PET interface.

Changes in the confining stress were effected by steadily raising the pneumatic pressure over 40 minutes; this minimises the potential for water pockets to become trapped between the layers, and allow the system to reach equilibrium.  $\text{H}_2\text{O}$  was used as the solvent as a  $\text{D}_2\text{O}$  contrast would result in the scattering length density (SLD) of the compressed PNIPAM layer matching that of the PET film. The experimental setup is sensitive primarily to the separation between the silica native oxide layer and the PET confining layer, apparent through the fringe spacing in the collected reflectometry profiles, discussed in section 1.5.2. However, it is also sensitive to the polymer’s surface-normal volume fraction profile in this confined environment, which we demonstrate in Figure 5.2.

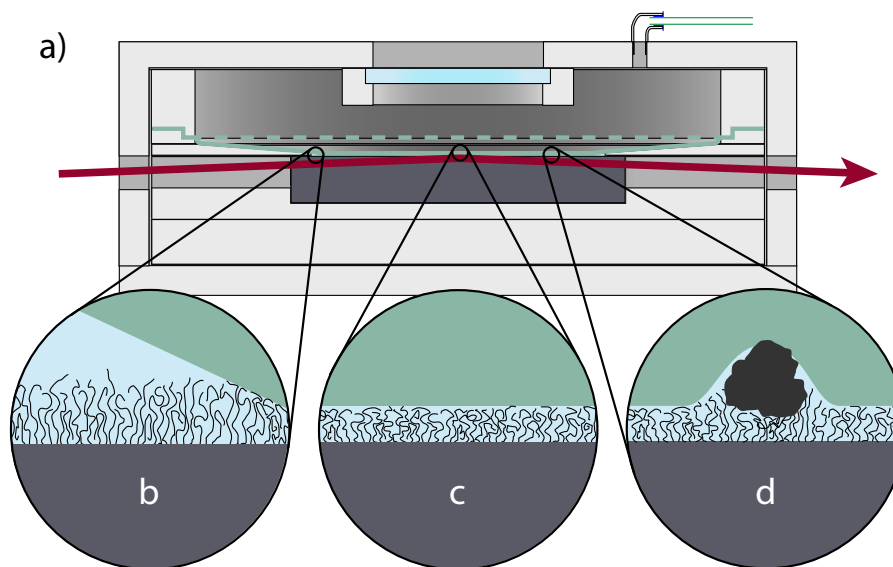


Figure 5.1: (a) Cross-section of the confinement cell used in this work. The apparatus is similar to that used by de Vos et al. [134]. (b) A solvent reservoir is maintained around the confined region, while the majority of the brush and all of the region being measured by NR is (c) evenly confined. de Vos et al. [134] identify (d) dust as a potential problem for this type of device, as it results in uneven confinement.

### Sensitivity of Neutron Reflectometry to the profile of the confined brush

Here we investigate the sensitivity of the reflectometry profile to the shape of the polymer volume fraction profile by examining simulated reflectometry profiles produced from different confined structures (Fig. 5.2). The exact polymer profile affects the relative fringe intensities (i.e., the first fringe depth relative to that of the second) of the corresponding reflectometry profile. The modelled profiles in Figure 5.11 capture the relative fringe intensity in the data. As the distribution model can change the fringe depth, but not the fringe intensity, we conclude that our analysis has the ability to confirm that the polymer volume fraction profile is slab-like. As such, our NR analysis supports the slab-like profiles predicted by the numerical nSCFT modelling.

#### 5.2.5 Neutron reflectometry data analysis

The dry brush was modelled as a single slab while unconfined solvated brushes were modelled using the freeform approach outlined in chapter 4. The confined data were analysed using a thickness distribution model with an interfacial volume constraint, implemented in Python through the *refnx* reflectometry analysis package [141]. This model was created to support the physical explanation proposed by de Vos et al. [134], who use a similar confinement apparatus. They posit that dust becomes trapped between the substrate and

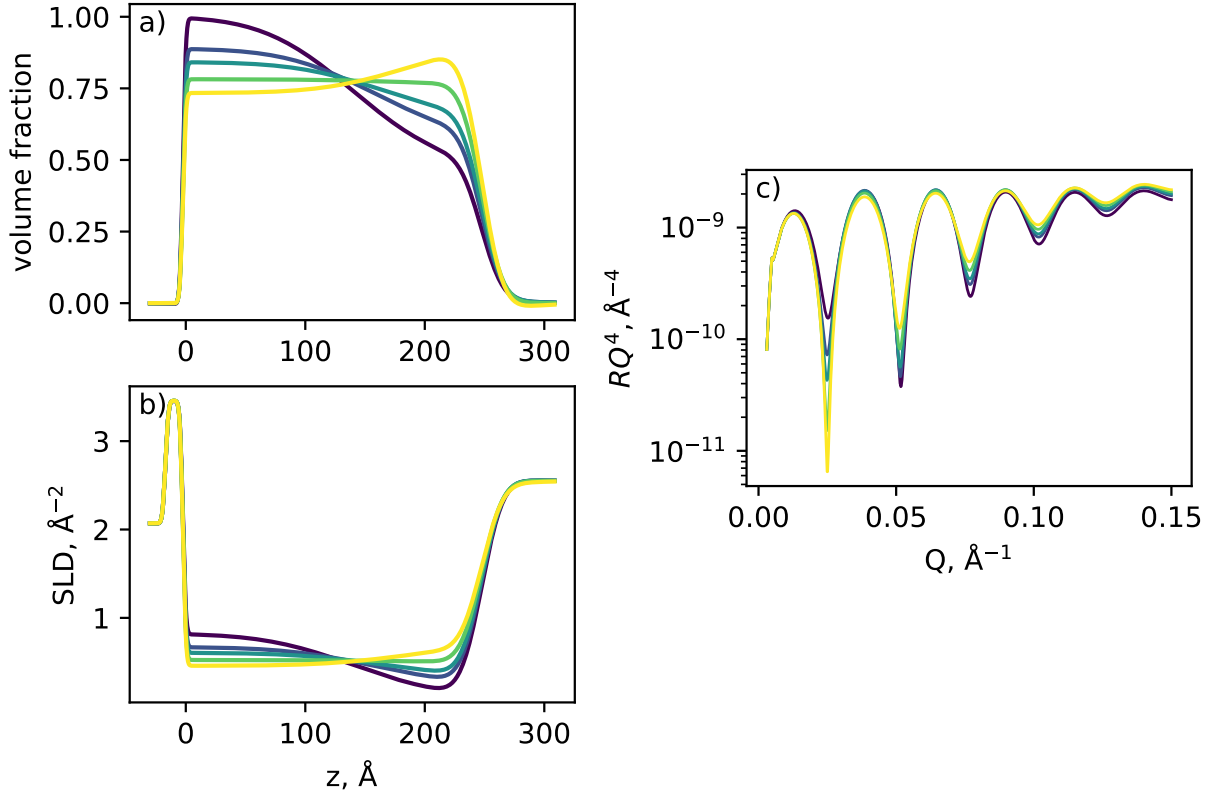


Figure 5.2: (a) Volume fraction profiles, (b) SLD profiles, and corresponding (c) reflectometry profiles for confined PNIPAM layers of constant thickness and interfacial volume with different profile shapes. The volume fraction profile’s shape does not change the fringe spacing but does change their relative intensity.

confining layer during confinement, resulting in unconfined areas local to the dust particles (Fig. 5.1d). Whereas de Vos et al. [134] account for this by incoherently averaging (see Fig. 6 of Majkrzak et al. [203]) the reflection from two distinct regions (confined and unconfined), we employ a ‘distribution model’ to more rigorously deal with both trapped dust and sample imperfections. From an implementation perspective, this approach is an extension of that used by Johnson et al. [73] and Murdoch et al. [175] to account for lateral variations in brush thickness; these approaches incoherently averaged reflections from two structures. A similar approach is used to model confined brushes by Hamilton et al. [204] to account for nanoscale roughnesses in their confining plates. Incoherent averaging of reflectometry profiles is appropriate when the different regions are separated by a lateral distance greater than the coherence length of a neutron (approximately 10 to 100  $\mu\text{m}$ ) [134, 203, 204]. The distribution model here calculates reflectometry profiles taken from a probability density function (PDF) of confinement thicknesses and incoherently averages them to produce a final profile, allowing for regions of no (i.e., an Si-H<sub>2</sub>O interface) and intermediate confinement that would surround dust particles (Fig. 5.1d) to be accounted

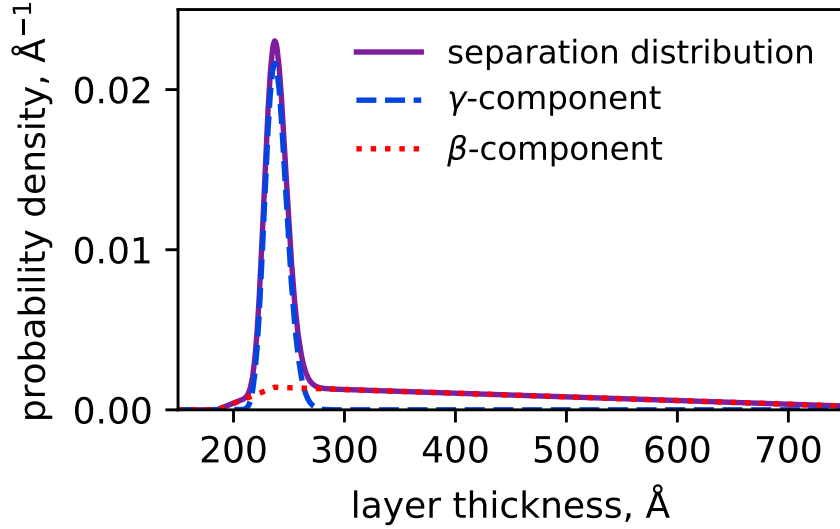


Figure 5.3: The construction of the separation distribution function from a gamma probability distribution ( $\gamma$ -component) and a simple linear tail ( $\beta$ -component). The composite functions are added and normalised to produce the final distribution.

for in the modelling.

We parameterise a flexible PDF that exhibits the features expected from the physical system (Fig. 5.5): a gamma probability distribution function ( $\gamma$ -component) to model the part of the brush that is strongly confined (the region of experimental interest), and a linear decay ( $\beta$ -component) to model the poorly confined region surrounding dust particles (Fig. 5.1d). The gamma probability distribution function was chosen purely for its flexibility (Fig. 5.5), and does not have any direct physical relevance; other similarly shaped distribution functions produce similar results. The width of the distribution accounts for the range of polymer thicknesses across the surface of the wafer, as well as small differences in the confining stress due to imperfections such as dust particles. The linearity of the  $\beta$ -component was chosen for mathematical simplicity as the fitting is not sensitive to the details of this component. As with previous confinement studies [134], the model also allows a water-backed region representing unconfined polymer (Fig. 5.3), which is required by the sloped critical edge and scale factor of less than 1. The scale factor for the measurements was determined from the intensity of the pre-critical edge reflection from unconfined measurements in  $D_2O$ . For a uniform Si-PET interface the critical edge would be flat and would have a scale factor of 1; for a uniform Si- $H_2O$  interface there would be no critical edge, instead in the corresponding region the slope would be proportional to  $Q^{-4}$  and the reflected intensity would be much less than one. What we observe is a mix between these two cases, and is detailed fully in section 5.3.3. Suffice

to say, by separating the  $\gamma$ -component of the distribution from the rest of the model, we isolate the region of experimental interest, that is, the confined PNIPAM brush.

The physical structure of the confined systems in the direction normal to the interface consists of a silicon fronting (SLD of  $2.07 \times 10^{-6} \text{ \AA}^{-2}$ ), a silica native oxide layer, a confined polymer layer and a PET backing (SLD of  $2.57 \times 10^{-6} \text{ \AA}^{-2}$ ). The SLDs of pure silica and pure PNIPAM were taken as  $3.47$  and  $0.8 \times 10^{-6} \text{ \AA}^{-2}$ , respectively, but were allowed to be solvated with  $\text{H}_2\text{O}$  (SLD of  $-0.54 \times 10^{-6} \text{ \AA}^{-2}$ ). The native oxide layer was modelled by a slab, with its thickness and porosity being determined before analysis of the confined samples via modelling of unconfined dry and solvated datasets. The confined polymer layer was modelled as a single slab, as per the work of de Vos et al. [134], with a distribution of thicknesses as described above. The solvent volume fraction of this slab was set to obey an adsorbed volume constraint, where the adsorbed volume was determined through dry measurements. The interior layer documented in Chapter 2 did not need to be included in the model, as the interior layer has a similar volume fraction to that of the collapsed polymer layer. The collapse to a slab structure is in agreement with theoretical results (Fig. 5.9).

A single reflectometry profile was produced from this distribution model through the following method. First, the PDF was discretised (Fig. 5.4a) into a series of SLD profiles, and a reflectometry profile for each discrete thickness was calculated (Fig. 5.4b). Then the reflectometry from the confined area,  $R_C$ , was calculated through the probability-weighted  $Q$ -wise sum of the discrete profiles (Fig. 5.4c). The reflectometry from the unconfined area of the surface,  $R_U$ , was modelled with an  $\text{H}_2\text{O}$  backed layer with a structure taken from unconfined  $\text{D}_2\text{O}$  measurements at the corresponding temperature (Fig. 5.15). The details of the model are given below.

## Model details

We start with the oft-utilised [20, 73, 79, 190] space-filling two-component assumption for the confined polymer film:

$$\phi_{\text{poly}} + \phi_{\text{water}} = 1 \quad (5.1)$$

$$\rho_{\text{layer}} = \phi_{\text{poly}}\rho(z) + (1 - \phi_{\text{poly}})\rho_{\text{water}} \quad (5.2)$$

where  $\phi_{\text{poly}}$  and  $\phi_{\text{water}}$  are the volume fractions of polymer and water in the layer, and  $\rho_{\text{layer}}$ ,  $\rho(z)$  and  $\rho_{\text{water}}$  are the SLDs of the confined layer, pure polymer and pure water respectively. As in previous work [20, 73, 79, 190] we make the further (implicit) assumption

that the molar volume of polymer is constant upon solvation:

$$\phi_{\text{poly}} = \frac{\hat{V}_{\text{I}}}{s_{\text{SM}}} \quad (5.3)$$

where  $s_{\text{SM}}$  is the separation between the silica substrate and the confining membrane.

Our physical understanding of the system indicates that a distribution of  $s_{\text{SM}}$  causes the smeared fringes at lower temperatures, because reflections from surface inhomogeneities larger than the coherence length of a neutron are incoherently averaged. We recreate the same phenomena in our model through the implementation of a distribution model.

We define a separation PDF,  $\mathcal{S}$ , made up of a gamma PDF,  $\gamma$ , and a linear background PDF,  $\beta$ ):

$$\mathcal{S}_{\text{SM}}(s_{\text{SM}}|L, k, \theta, b_{\text{mag}}, b_{\text{length}}) = \gamma(s_{\text{SM}}|L, k, \theta) + \beta(s_{\text{SM}}|L, k, \theta, b_{\text{mag}}, b_{\text{length}}) \quad (5.4)$$

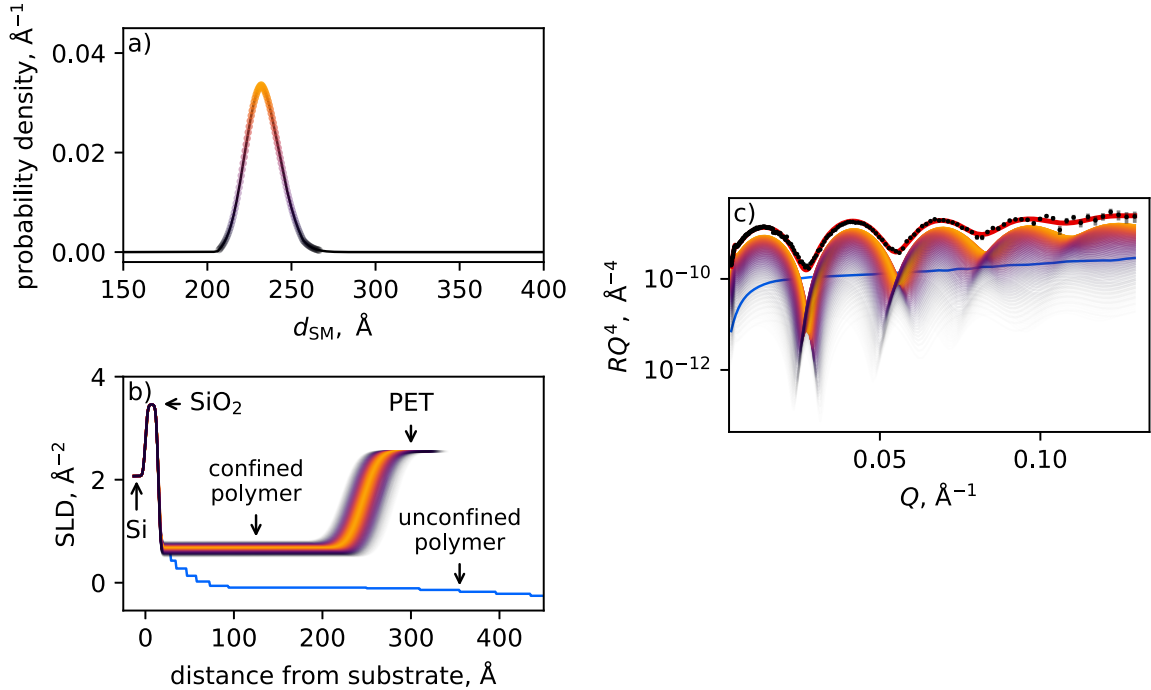


Figure 5.4: The distribution model used in this work transforms (a) a distribution of silica-PET thicknesses into (b) a set of SLD profiles, before (c) performing a probability-weighted summation of the corresponding reflectometry profiles (purple to orange lines) to produce an overall reflectivity profile (red line) that matches the experimental data (1 bar 27.5 °C is shown here). Note that the change in the SLD of the confined polymer layer in (b) is due to the volume fraction of polymer changing to obey the constrained total amount of polymer at the interface. A water backed region (b, c, blue line) can also be included in the model.



The gamma PDF uses the conventional definition:

$$\gamma(s_{\text{SM}}|L, k, \theta) = \frac{1}{(k-1)!\theta^k} (s_{\text{SM}} - L)^{k-1} \exp\left(-\frac{(s_{\text{SM}} - L)}{\theta}\right) \quad (5.5)$$

where  $L$  is the location offset parameter,  $k$  is the shape parameter, and  $\theta$  is the scale parameter. The background,  $\beta$ , is a function that increases linearly from the start of the  $\gamma$  distribution ( $t_{\text{start}}$ , defined as the point at which the cumulative distribution function of  $\gamma$  is 0.001), reaching its zenith at the mode of the  $\gamma$  distribution ( $b_{\text{peak}} = L + \theta(k-1)$ ), then linearly decaying over a distance  $b_{\text{length}}$ , reaching zero when  $s_{\text{SM}} = b_{\text{cut}} = b_{\text{peak}} + b_{\text{length}}$ . The magnitude of the background region is given by  $b_{\text{mag}}$ .

$$\beta(s_{\text{SM}}|L, k, \theta, b_{\text{mag}}, b_{\text{length}}) = \begin{cases} b_{\text{mag}} \times \frac{s_{\text{SM}} - b_{\text{start}}}{b_{\text{peak}} - b_{\text{start}}} & b_{\text{start}} < s_{\text{SM}} < b_{\text{peak}} \\ b_{\text{mag}} \times \frac{-s_{\text{SM}} + b_{\text{cut}}}{b_{\text{peak}} - b_{\text{start}}} & b_{\text{peak}} \leq s_{\text{SM}} < b_{\text{cut}} \\ 0 & \text{elsewhere} \end{cases} \quad (5.6)$$

The final distribution is then normalized:

$$\bar{\mathcal{S}}_{\text{SM}} = \frac{\mathcal{S}_{\text{SM}}}{\int_0^\infty \mathcal{S}_{\text{SM}} \, ds_{\text{SM}}} \quad (5.7)$$

The overall distribution is smooth and encompasses the confinement apparatus's underlying behaviour as observed in the system: most of the surface is at a modal distance with small variation ( $\gamma$ -component). At the same time, some larger separations are present due to dust ( $\beta$ -component). Examples of the various forms this distribution can take are given in Figure 5.5, and the Python implementation used in the current work is provided in section J.

The reflectometry profile from the confined section ( $R_C$ ) is calculated by taking the probability-weighted sum of the reflection  $R(Q, s_{\text{SM}})$ :

$$R_C(Q, \bar{\mathcal{S}}_{\text{SM}}) \approx \sum_{i=0}^n \bar{\mathcal{S}}_{\text{SM}}(s_{\text{SM},i}|L, k, \theta, b_{\text{mag}}, b_{\text{length}}) R(Q, s_{\text{SM},i}) \quad (5.8)$$

The range of  $s_{\text{SM}}$  over which this summation is performed is limited to where the separation probability is greater than 1 % of the maximum separation probability, so as to keep the calculation computationally reasonable:

$$s_{\text{SM},i} \in \mathbb{R} : \bar{\mathcal{S}}_{\text{SM}}(s_{\text{SM},i}|L, k, \theta, b_{\text{mag}}, b_{\text{length}}) > 0.01 \times \max(\bar{\mathcal{S}}_{\text{SM}}(s_{\text{SM},i}|L, k, \theta, b_{\text{mag}}, b_{\text{length}})) \quad (5.9)$$

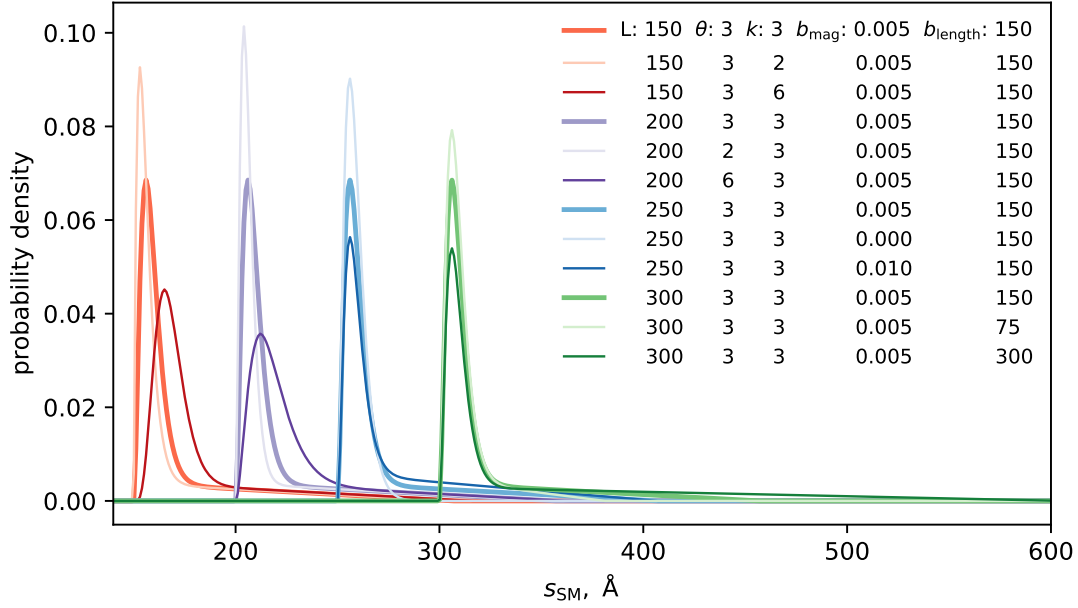


Figure 5.5: Effect of different parameters of the shape of the PDF, showing the effect of changing (red) gamma scale, (purple) gamma shape, (blue) tail intensity, and (green) tail length in isolation. The thick lines show the effect of changing the location parameter in isolation.

As a final step, we must include reflectivity from small regions of the sample where there is no confinement at all, owing to dust inclusions. The total reflectivity is obtained by incoherently averaging the confined contribution,  $R_C$ , with the reflectometry from the unconfined region,  $R_U$ , according to a fractional confined area,  $x_C$  [134]:

$$R(Q) = x_C R_C(Q, \bar{\mathcal{S}}_{SM}) + (1 - x_C) R_U(Q) \quad (5.10)$$

The above model was implemented in python; the location of the corresponding code can be found in section J.

### 5.2.6 Colloid probe modelling

Stress–separation curves were extracted from the experimental results of Murdoch et al. [20] through a Derjaguin-inspired analysis [205], in which the colloid-probe was modelled as an incompressible, tiered probe passing through a one-dimensional force field. Briefly, the approach parameterised a stress–separation curve, which was converted to a force–distance curve through discretising the probe as a tiered sphere. As in the Derjaguin approximation, interactions are only in one dimension (vertical) and the effects of surface roughness are not accounted for; unlike the Derjaguin approximation the force is evaluated

by numerical integration, so no assumptions regarding the size of the probe relative to the distance from the substrate needed to be made. We utilised a differential evolution [196] optimisation routine implemented in SciPy [80] to adjust the parameterised stress–separation curve so that the modelled force–distance curve matched the measured force–distance curves of Murdoch et al. [20]. Here, separation refers to the distance between a planar discretised tier of the modelled probe and the substrate, while distance refers to the minimum apparent separation between the colloid-probe and the substrate. These stress–separation curves were then recast as separation–temperature curves for chosen stresses, which can be directly compared to reflectometry experiments. Of course, in AFM experiments it is impossible to determine the true separation, as the zero-separation point is deduced from force–distance curves; this does not impact the validity of our results as we are mainly interested in scaling behaviour.

The algorithm can be summarised as:

1. Define a model stress–separation curve via Eq. 5.11, discussed below (Fig. 5.6).
2. Consider a discretised spherical probe (Fig. 5.8a) being incrementally moved toward a rigid planar substrate. For each step that this probe takes:
  - (a) Calculate the separation between each tier of the probe and the planar substrate (Fig. 5.8b).
  - (b) From the stress-separation curve, calculate the stress (pressure) experienced by each tier of the probe (Fig. 5.8c).
  - (c) Calculate the force acting on each tier of the probe (the product of tier area and stress) (Fig. 5.8c).
  - (d) Sum the forces acting on each tier of the probe to produce the force experienced by the entire probe.
3. The resulting force vs distance profile can be compared to collected colloid-probe AFM data. Parameters in Eq. 5.11 can now be optimised such that the modelled force vs distance profile fits the collected colloid-probe AFM data (Fig. 5.10a).

Detailed explanations of each step are given below.

### Definition of the stress–separation curve

The stress–separation curve is parameterized by the sum of a gamma PDF and two exponential functions. The gamma function describes the attraction observed at intermediate

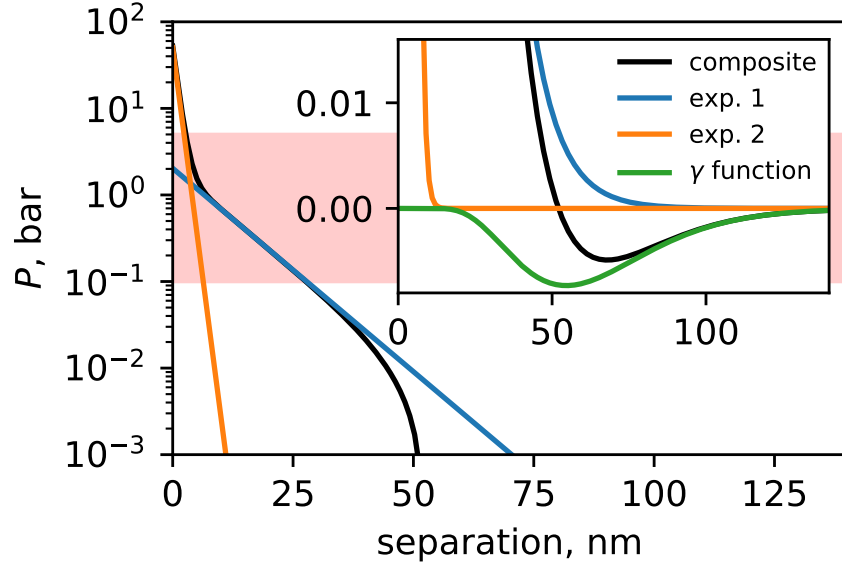


Figure 5.6: Composition of the stress–separation curve (black) from two exponential components (blue, orange) and a gamma function component (green). The red shaded area represents the region of experimental interest. The inset highlights the attractive region; the axes have the same units as the main plot.

distances, while the two exponentials describe the repulsion at close approach:

$$\sigma(s) = m_1 b_1^{-s} + m_2 b_2^{-s} + m_\Gamma \gamma(s, L_\Gamma, k_\Gamma, \theta_\Gamma) \quad (5.11)$$

where  $m_1$ ,  $m_2$  and  $m_\Gamma$  are the magnitudes of each component,  $b_1$  and  $b_2$  are the base terms for each exponential component,  $\Gamma$  is the gamma function (Eq. 5.5) with location  $L_\Gamma$ , shape  $k_\Gamma$  and scale  $\theta_\Gamma$ .<sup>i</sup>  $s$  is the separation between a point on the probe and the planar surface, defined for a spherical probe as

$$s(x) = D + R - \sqrt{R^2 - x^2} \quad (5.12)$$

where  $D$  is the minimum separation between the probe and the surface,  $R$  is the probe’s radius, and  $x$  is the lateral distance from the point of closest approach (Fig. 5.7). This model is not intended to replicate the physics of the compression of a polymer brush; instead it was designed to be flexible enough to capture the observed behaviour over a limited range of forces and separations.

<sup>i</sup>Here we used  $\Gamma$  to denote the gamma function, to differentiate it from the use of the gamma function in section 5.2.5.

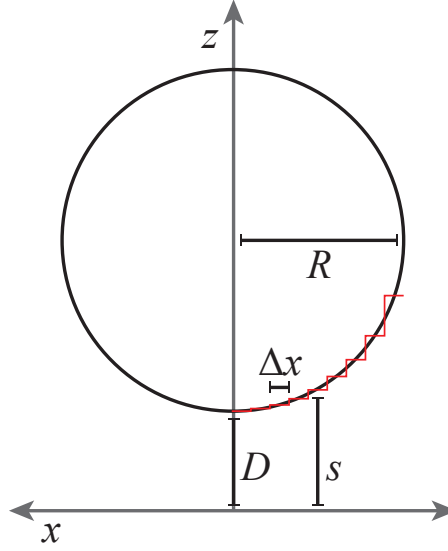


Figure 5.7: Schematic of the system showing the curvature of the sphere resolved into a set of thin tiers, each of width  $\Delta x$ .

### Calculation of force vs displacement

The parameterized stress–separation curve is transformed into a force vs displacement curve for a given size probe by considering a discretized hard-sphere contacting a perfectly flat, rigid surface (Fig. 5.7). Between these two surfaces is a deformable layer, the properties of which are defined by the aforementioned stress–separation curve (Eq. 5.11). The probe is discretized into many tiers; the area and distance between can be calculated for each tier (Fig. 5.8). The force acting on the tier can then be calculated using the stress–separation curve, tier–surface separation and tier area. Given definitions  $\sigma(s)$  and  $s(x)$  above, the force acting on any one tier of the probe can be written as:

$$F(x) = \sigma(s(x)) \times A(x) \quad (5.13)$$

where  $A(x)$  is the area of the tier,  $\pi(x^2 - (x - \Delta x)^2)$ ,  $\Delta x$  being the width of the tier. Integrating this force over the area of the probe will yield the force acting on the entire probe at a given  $D$ :

$$F(D) = \int \sigma(s) dA \quad (5.14)$$

We evaluate this integral numerically, via the summation:

$$F(D) = \sum_{x=0}^R \sigma(s(x)) \times A(x) \quad (5.15)$$

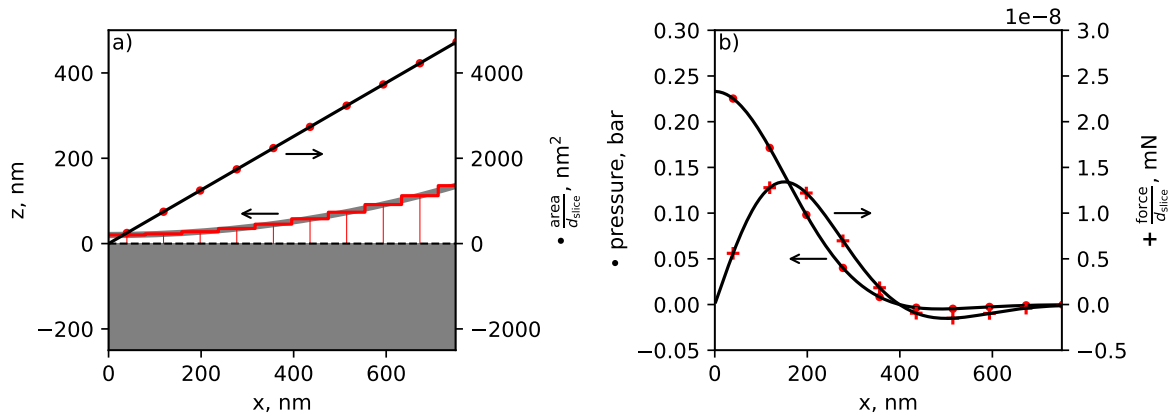


Figure 5.8: (a) Schematic of the model at a single probe displacement, with area as a function of lateral position. (b) Pressure (●) and force (+) profiles.

Evaluating force at a range of displacements yields a force–displacement curve, which can be directly compared to colloid-probe AFM data.

### Optimisation

The differential evolution method of Storn and Price [196] is used to optimize the model (Eq. 5.11) to match the experimental data. The outputs of this fitting process are the stress–separation curves in Figure 5.10, which exhibit excellent agreement with the experimental data in Figure 5.10a.

### 5.2.7 Self-consistent field theory

Self-consistent field theories are widely used to predict the conformation of polymer systems [5, 79, 206], generating a polymer structure in one or more dimensions that is consistent with the surrounding energy field. This energy field is derived from factors such as solvent quality ( $\chi$ ) and the charge and concentration of dissolved species and monomers. The nSCFT approach employed here follows the procedure of Abbott et al. [79], implementing the Scheutjens–Fleer lattice model [207]. This approach discretises the polymer–solvent system into many lattice sites, simplifying the problem and allowing it to be solved numerically. nSCFT has previously been found to successfully predict the behaviour of responsive polymer brush systems, including thermoresponsive polymers [84, 109, 132]. Prior work has used nSCFT to examine polymers in confinement [79], however, this has not yet been extended to responsive polymers. An impenetrable confining barrier was incrementally moved toward a substrate decorated by tethered polymer chains to simulate confinement. At each barrier position, the system structure and energetics

were calculated. The most relevant parameter derived from this process was the partial open free energy ( $U_f^{\text{po}}$ ) of the grafted polymer chains, which is equal to the system free energy minus the free energy of the solvent. The energy of interaction for the confining surface and the polymer layer ( $U_f^{\text{int}}$ ) is isolated by subtracting  $U_f^{\text{po}}$  at infinite separation from  $U_f^{\text{po}}$  at a given confinement distance

$$U_f^{\text{int}}(D) = U_f^{\text{po}}(D) - U_f^{\text{po}}(\infty) \quad (5.16)$$

where  $D$  is the distance of the confining layer from the substrate in units of lattice site spacing,  $L$ . This interaction energy represents the entropic and enthalpic penalty resulting from the polymer's spatial confinement. The force exerted by the confining surface on the brush,  $F$ , was calculated by considering the surface moving through an energy field.

$$F = -\frac{dU_f^{\text{int}}(D)}{dD} \quad (5.17)$$

Force is proportional to stress, so it allows for comparison of the theoretical and experimental scaling behaviour. We emphasise that we are only interested in the confined brush's scaling behaviour and do not make absolute comparisons. Typically the energy from such a simulation would be reported relative to  $k_B T$ , with the corresponding force relative to  $k_B T L^{-1}$  (here  $L$  is the lattice spacing). As the current work concerns a thermoresponsive system ( $\chi$  is a function of  $T$ ), we must take into account the temperature that corresponds to a given  $\chi$  value; our force values are reported relative to  $k_B$  and have units of  $\text{KL}^{-1}$ , where  $K$  is Kelvin. The model was made up of grafted chains, each consisting of 200 segments, with a grafting density of 0.025 chains per lattice site. This is roughly comparable to a polymer brush with a contour length of  $1000 \text{ \AA}$  and a grafting density of 0.1 chains per  $\text{nm}^2$  [79]. The  $\hat{V}_I$  of this simulation is  $5L$ . To simulate the thermoresponse of PNIPAM, the solvent–polymer Flory–Huggins interaction parameter,  $\chi$ , was varied (see section 1.1). Comparisons between physical temperatures and  $\chi$  values were made based on the work of Alves et al. [132], who derived a relationship between temperature and  $\chi$  for a poly(methyl methacrylate-*co*-*N*-isopropylacrylamide) from empirical data.

### 5.3 Results

First, we report predictions made by nSCFT and findings from an analysis of colloid-probe AFM data, thus establishing the expected behaviour of a confined PNIPAM system. Second, we present and discuss the NR data collected using our confinement apparatus, proposing a physical explanation for the features observed. We report separation as a function of stress and temperature for the surface and comment on the confined layer structure. Lastly, we examine the thermoresponse of a PNIPAM brush before and after confinement, showing that these layers completely recover from such treatment.

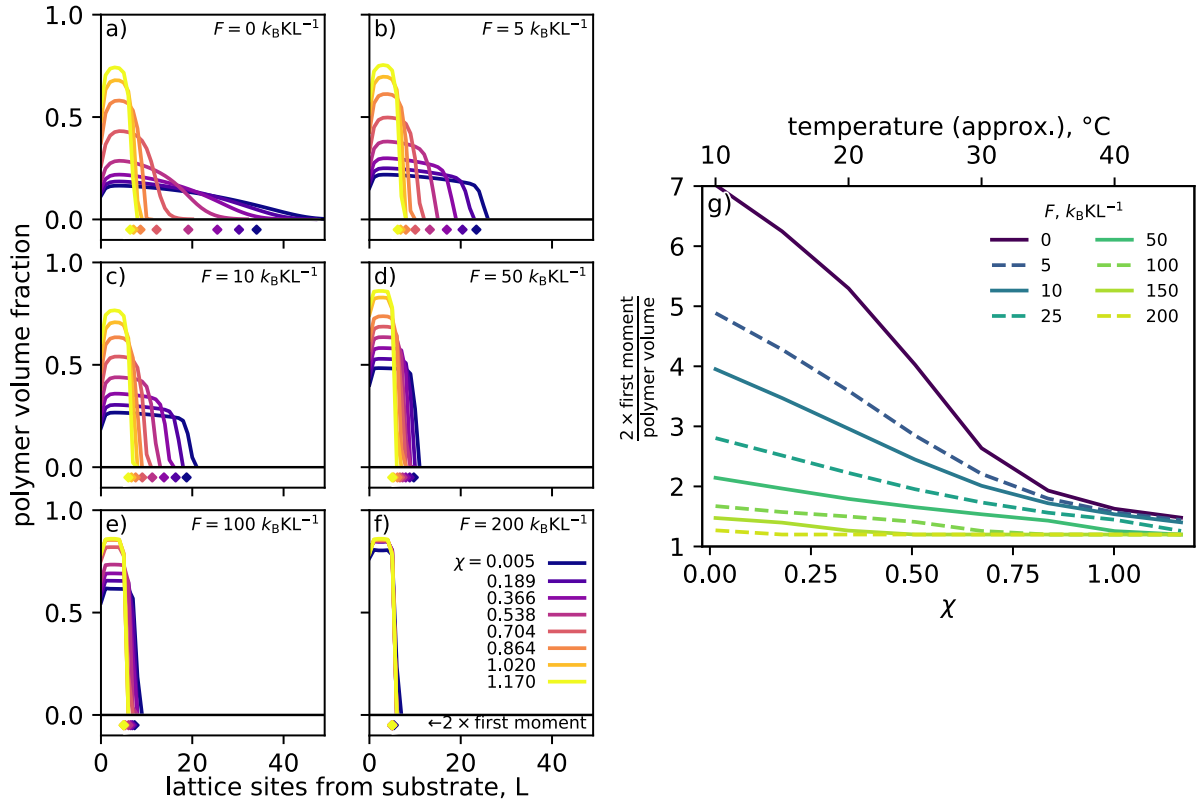


Figure 5.9: (a-f) Brush volume fraction profiles calculated by nSCFT at increasing confining forces (proportional to confining stress), with the profile's first moments below each plot for reference. When the brush interacts with the opposing confining surface, the (a) parabolic brush profiles transition to (b-e) slab-like profiles, where the polymer volume fraction is sensitive to  $\chi$  (analogous to temperature). At high enough forces (f) the profiles no longer exhibit a  $\chi$ -dependence over the probed  $\chi$ -range. Forces are reported relative to  $k_B$  and with units of kelvin per lattice spacing. (g) The results are summarised as twice the first moment of the polymer volume fraction profile (shown below each volume fraction profile) vs  $\chi$  at different forces, normalised by the total volume of polymer segments in the simulation. nSCFT predicts that applying a stress should change the temperature at which a PNIPAM brush is fully collapsed and remove its critical thermoresponsive behaviour.



### 5.3.1 Self-consistent field theory

nSCFT predicts that non-confined PNIPAM brushes (Fig. 5.9a) exhibit parabolic polymer volume fraction profiles at low temperatures, where water is a good solvent for PNIPAM. As the temperature increases (higher values of  $\chi$ ) the brush collapses, forming slab-like profiles. Once a confining force is applied (beginning in Fig. 5.9b), nSCFT predicts that the brush structure will transition to slab-like profiles at all temperatures. Under intermediate confining forces (starting from Fig. 5.9b), the brush remains thermoresponsive, although the applied force shifts the brush's temperature-induced collapse to lower temperatures (Fig. 5.9g). Some evidence of a critical thermoresponse is observed at low confining forces, with an inflection point visible in the plot of thickness against  $\chi$  (Fig. 5.9g) until approximately  $25 k_B \text{KL}^{-1}$  profile (Fig. 5.9b). Above this confining force, the critical transition that is seen for unconfined brushes disappears (Fig. 5.9a), with layer thickness changing approximately linearly until the brush is completely collapsed (i.e., the  $50 k_B \text{KL}^{-1}$  profile in Fig. 5.9d,g). The brush collapses completely at high applied confining stresses (i.e., Fig. 5.9f) for all  $\chi$  values (temperatures) examined.

### 5.3.2 Stress-separation curves from colloid-probe AFM

The further analysis of the colloid-probe AFM data of Murdoch et al. [20], as described above, allows for direct comparison with NR measurements presented here. Parameterised stress-separation plots are presented in Figure 5.10b, with corresponding force-separation plots that have been optimised against experimental data shown in Figure 5.10a. The stress-separation profiles in Figure 5.10b are recast as normalised separation vs temperature plots in Figure 5.10c, which will allow direct comparison to the NR experiments. As the true separation can never be determined by AFM, the data in Figure 5.10a is the apparent separation. The difference between the apparent separation and the true separation is expected to be constant for a given brush sample; so any error would result in the curves in Figure 5.10c being shifted vertically. The separation-temperature plots in Figure 5.10c show that a confining stress can remove the thermoresponse of PNIPAM altogether at the temperatures investigated, agreeing qualitatively with nSCFT. The present analysis indicates that the stress at which PNIPAM brushes become temperature-insensitive is approximately 1.5 bar, with the brush being substantially less temperature-sensitive and losing the criticality in the temperature transition by 1.0 bar. Moreover, Figure 5.10c indicates that a thermally collapsed brush (i.e., the brush at 40 °C) can be further compressed by stress. The system hydrodynamics does not influence the colloid-probe results, as a slow ramp rate of  $0.5 \mu\text{m s}^{-1}$  was used; previous work on a similar thermoresponsive

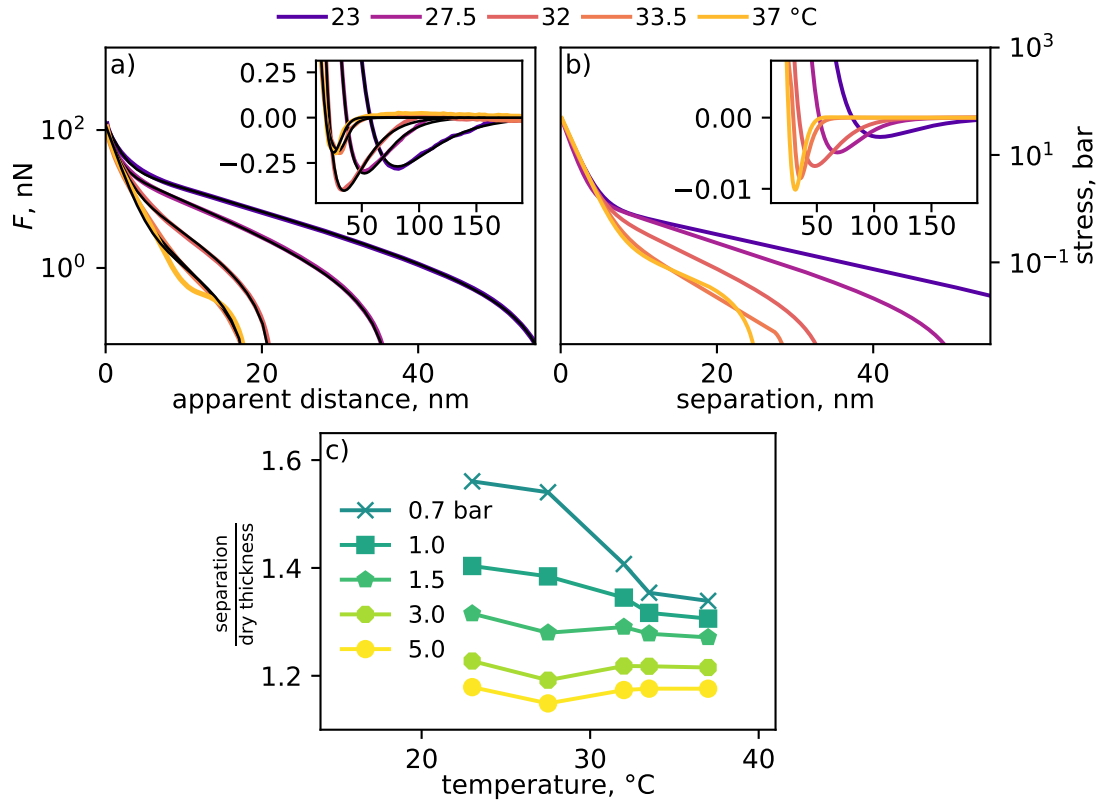


Figure 5.10: (a) Experimental force–distance data (coloured lines) from the colloid-probe AFM experiment of Murdoch et al. [20], overlaid with theoretical force–separation profiles (black lines) produced by considering a discretised hard-sphere passing through the stress-field described by particular (b) stress–separation curves. The stress–separation curves were optimised against the experimental data, exhibiting excellent agreement with the experimental data at both positive and negative loads. The stress–separation curves in (b) can be recast to (c) separation vs temperature plots, allowing the colloid-probe experiment to be compared to data from the neutron confinement cell.

system found that force profiles were relatively independent of probe velocity at speeds under  $3\mu\text{m s}^{-1}$  [175].

### 5.3.3 Reflectometry from a confined PNIPAM brush

#### Modelling

PNIPAM brushes were subjected to 1 and 5 bar of constant confining stress while the system temperature was varied; 1 bar is the lowest pressure accessible with the current instrumentation [134], while at 5 bar AFM analysis predicted the absence of a thermoresponse. Figure 5.11 shows the experimentally determined separation distribution profiles alongside corresponding reflectometry data. For both 1 and 5 bar samples, the profile exhibits

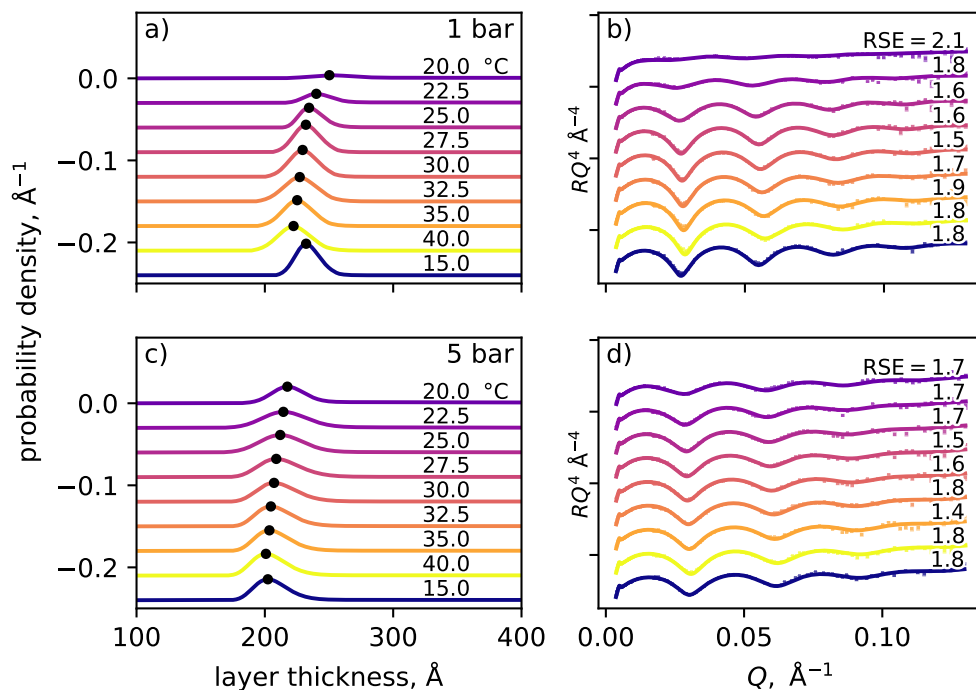


Figure 5.11: Experimentally determined separation distributions (in experimental order, top to bottom) with corresponding reflectometry profiles as a function of temperature for applied confining stresses of (a, b) 1 bar and (c, d) 5 bar. As the position of the fringes does not move appreciably with temperature, the modal thickness of the distribution (a,c, highlighted with a ●) moves only slightly, however, the width of the separation distribution (sharpness of fringes) is seen to be a strong function of temperature. Collapsed distribution breadths differ between pressures (a compared to c) due to a different substrate being used for each experiment. Some reswelling is observed upon a return to low temperatures for the (a) 1 bar data, but not (c) 5 bar. Reduced standard error (chi-squared statistic divided by the number of data points) values are included atop their respective reflectometry profiles, indicating that all fits are of comparable quality. Modal structures and modal thickness are shown in Figure 5.12.

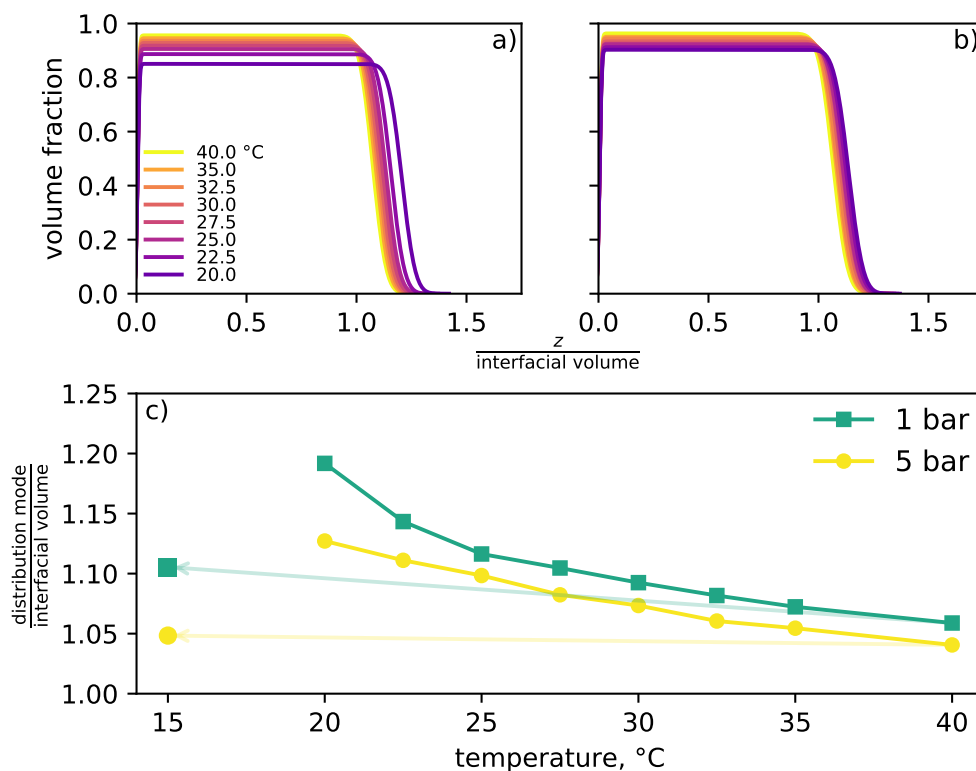


Figure 5.12: Volume fraction profiles corresponding to the modal separation for (a) 1 bar and (b) 5 bar data. (c) Normalised peak location as a function of temperature. The volume fraction profiles and thicknesses are normalised by  $\hat{V}_I$  to allow for comparison between data from different polymer brushes. The 5 bar layer is more dehydrated at any given temperature, with both layers still exhibiting a thermoresponse. The system displays significant hysteresis while the confining stress is maintained, as the layer does not recover when the temperature is reduced (indicated by arrow).

weak Kiessig fringes at the lowest temperature probed, which deepen as the temperature is increased (Fig. 5.11b, d). The fringe spacing does not appreciably change during this deepening (Fig. 5.13), ostensibly indicating that the interfacial thickness uniformity is increasing while its thickness remains relatively constant. Lateral inhomogeneities within the brush layer itself (i.e., macroscopic brush roughness) are not responsible for this behaviour, as ellipsometry mapping found the standard deviation of dry thicknesses to be small (Table 5.1); furthermore, such sample imperfections would not be temperature sensitive. Likewise, this fringe deepening is not due to an increase in contrast due to changes in the solvation state (and hence SLD) of the polymer. As there is a fixed amount of polymer in the system, any change in polymer solvation would result in a change in thickness and a subsequent change in fringe spacings. The modal separation profile for each temperature (Fig. 5.11a,c black dots) is presented in Figure 5.12, both as polymer

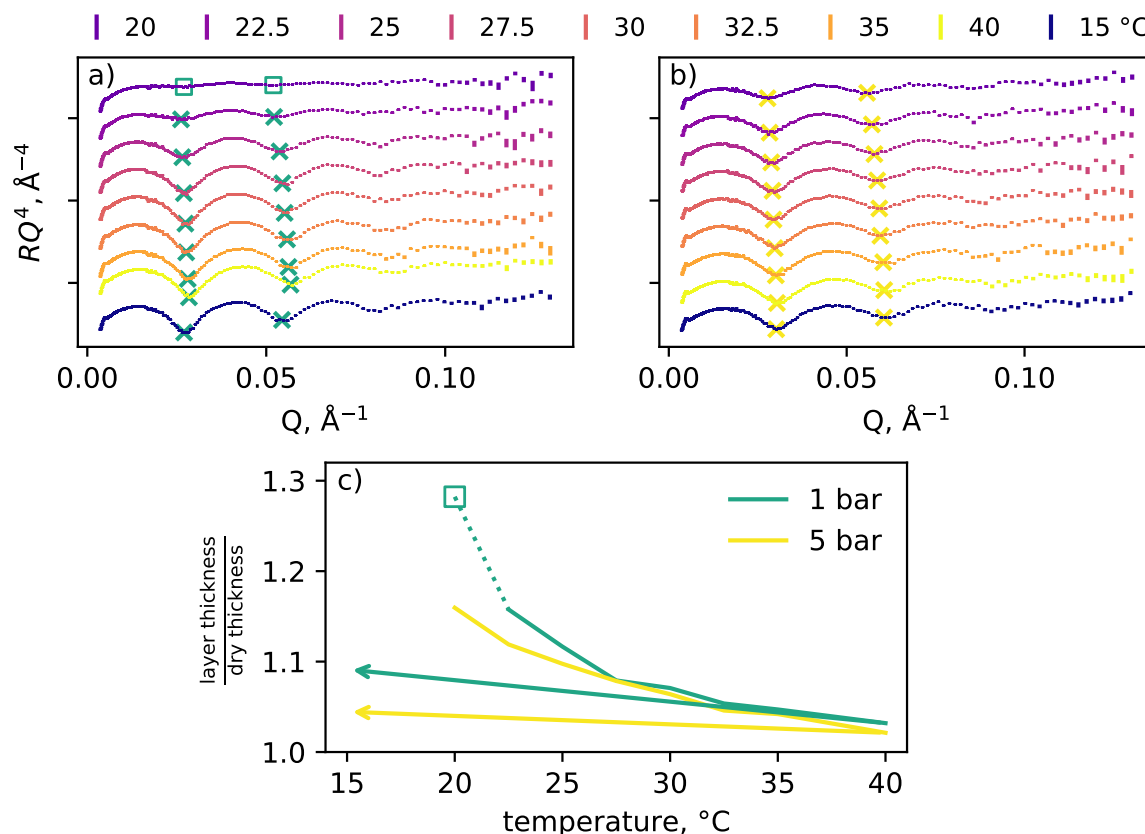


Figure 5.13: Reflectometry profiles for both (a) 1 bar and (b) 5 bar datasets with the fringe locations highlighted ( $\times$ ). (c) Thicknesses determined from the fringe spacings; fringe spacings were manually determined for 1 bar 20 °C.

volume fraction profiles (Fig. 5.12a,b) and as a plot of modal separation vs temperature for both pressures investigated (Fig. 5.12c). Figure 5.12c shows that PNIPAM exhibits a constant-stress-temperature response at both 1 and 5 bar, albeit without the criticality that is normally seen for this polymer.

### Fringe spacing analysis

Fringe spacing analysis was performed via the method outlined in section 1.5.2. The results produced (Fig. 5.13) are comparable to those from the full reflectometry modelling approach shown in Figure 5.11, verifying the output from the modelling and supporting our physical interpretation of the reflectometry data.

### Water-backed region

The distribution model allows for a water backed region to contribute to the overall reflectometry (Eq. 5.10), as in previous work [134]. Figure 5.14b (bold lines) shows that

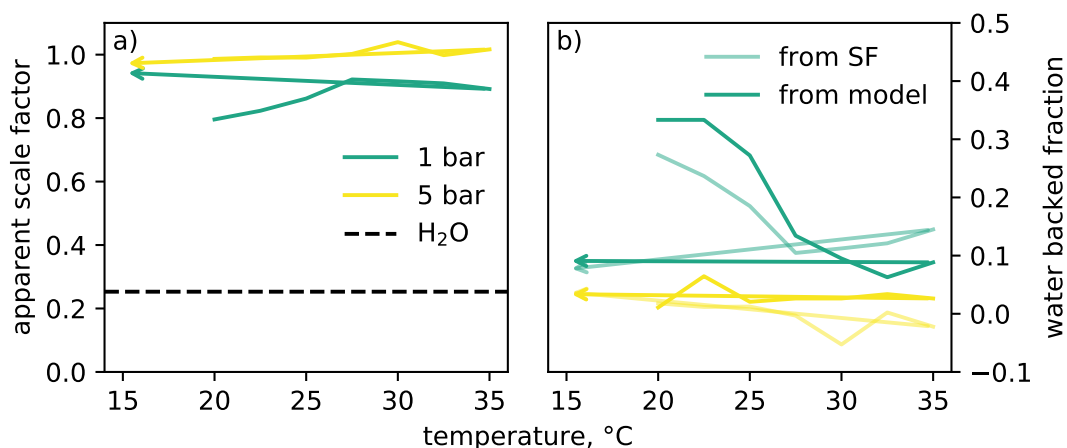


Figure 5.14: a) The average value of the sub-critical edge data points (i.e.  $<0.0045 \text{ \AA}^2$ ) as a function of temperature; one explanation for this deviating from unity is the presence of H<sub>2</sub>O backed regions, which would have an apparent scale factor of approximately 0.25 (dashed line). b) The water backed fraction required to fit collected data as a function of temperature, which finds reasonable agreement with the water backed fraction calculated from the scale factor.

the water backed region required by the model to match the collected data is sensitive to both temperature and pressure; this is not a fitting artefact, as modelled water backed regions agree with those calculated from the scale factor (Fig. 5.14b).

## Interpretation

The physical interpretation of the confined temperature series is as follows. At all temperatures and stresses studied, the majority of the polymer brush surface is in molecular contact with the confining PET film, as indicated by the presence of a critical edge in the reflectivity curves at all conditions (Fig. 5.11). The thickness of this collapsed film is dependent on grafting density and the average local molecular weight. As such, there is some variation across the surface (broadening the thickness distribution). Elsewhere in the confined layer, a small number of entrained dust particles cause areas of lower confining stress (so-called ‘tenting’), which is most prevalent at low temperatures, as the dust-proximal brush is resisting the reduced confining stress. This distribution of separations is enough to smear the reflection pattern from the confined section of the brush (e.g., 1 bar dataset at 20, 22.5 °C). However, as the temperature increases, so does the collapsed fraction of the surface, resulting in deeper fringes. While the laterally inhomogeneous collapse of the brush makes the data interpretation more challenging, these imperfections are accounted for in the model used. We did not observe any off-specular scattering from these dust particles, which is consistent with randomly distributed and sized particles.

As per the methodology described above, our model describes the collapsed section fraction of the brush using the  $\gamma$ -component, while reflections from the poorly-confined dust-proximal section are accounted for by the  $\beta$ -component. We isolate the behaviour of the evenly confined portion of the surface by taking the peak of the  $\gamma$ -component as the modal layer thickness, allowing observation of the effect of stress and temperature on the evenly confined portion of the layer. It is significant that a model consistent with this physical interpretation can recreate the collected reflectometry profiles. Additionally, the output from the model shown in Figure 5.12c agrees with a simple model-free fringe spacing analysis, indicating that our choice of model is correct. A replica of Figure 5.12c using the fringe spacing derived thicknesses, as well as details of the analysis, can be found in Figure 5.13 and associated text.

### 5.3.4 Behaviour of PNIPAM under confinement

The separation vs temperature curves (Fig. 5.12) extracted from the NR analysis allow comparison between NR, nSCFT, and colloid-probe AFM. When comparing these three techniques, it is important to consider the path these systems take to reach the state of interest. For the colloid-probe AFM, the system is equilibrated at the temperature of interest, then the probe is brought into contact with the layer. Conversely, in NR experiments, the confining layer is brought into contact with a swollen brush at 20 °C, before the temperature is incrementally raised to 40 °C. Lastly, nSCFT is path independent — it produces the system’s equilibrium structure. Additional points of difference are that the colloid-probe and reflectometry experiments probe different contact areas (1  $\mu\text{m}^2$  vs 50  $\text{cm}^2$ ) and time scales (1 s vs 1 h), albeit that no time-based effects have been reported in AFM measurements.

Firstly, we compare the structures produced by nSCFT with those obtained via NR. We can replicate the collected reflectometry profile using a constant volume fraction slab layer, noting that even small deviations from a slab-like profile would result in a change in relative fringe magnitude (i.e., the depth of the first fringe relative to the depth of the second fringe, Fig. 5.2), which is not observed here. The reproduction of the collected reflectometry profiles with uniform-volume fraction slabs affirms the slab-like profiles predicted by nSCFT.

As predicted by nSCFT, both NR and AFM show that the confined polymer does not exhibit critical thermoresponsive behaviour above a certain confining stress (determined to be around 1 bar); instead, the thickness decreases steadily with increasing temperature. Both colloid-probe (Fig. 5.10) and reflectometry experiments indicate that the thickness is sensitive to confining stress, although the colloid-probe technique observes a greater

change between 1 and 5 bar. Similarly, the thermoresponse observed at 1 bar is comparable between the two techniques, with a change in separation of approximately 10 % of the dry layer thickness between 20 and 40 °C. All techniques indicate that the thickness-response to temperature is reduced as confining stress increases, as one would naturally intuit. However, colloid-probe experiments observe no thermoresponse at 5 bar, while NR indicates that the thermoresponse at 5 bar is of a similar magnitude to the 1 bar.

The difference between the colloid-probe and NR experiments could be due to the increased lateral freedom of polymer chains in the colloid probe experiment compared to the NR experiment. The confined area in the AFM experiment (approximated as  $1.5 \mu\text{m}^2$ , by the method of Abbott et al. [79]) has a radius 1.4 times the contour length of the brush and contains approximately one hundred thousand polymer chains. However, due to the probe geometry, only a small fraction of this area is subjected to a confinement comparable to the NR study (approximate area  $0.06 \mu\text{m}^2$ , containing around 4000 polymer chains, with a radius of 0.3 contour lengths). Upon contact with the colloid probe chains in the most-confined area may laterally rearrange, reducing the effective resistance to the confining stress. As the repulsive force increases exponentially as confinement distance decreases, this effect would be most notable at high stresses. However, the work of Halperin and Zhulina [208] suggests that the local-compression assumption is valid for colloid probe tips. Another explanation is that different experimental techniques probe different dynamic behaviour. The AFM experiment is carried out at constant temperature, with stress varying. At the ramp rate employed in the AFM experiment ( $0.5 \mu\text{m s}^{-1}$ ), the probe will progress through the entire solvated brush in approximately 0.2 s. The hydrodynamic drainage of a brush confined by a colloid-probe over  $\approx 1.5 \mu\text{m}^2$  contact area at this time scale may result in a greater hydration of the layer, resulting in the sensitivity of thickness to pressure in the colloid-probe experiments.

In NR, the PNIPAM thermoresponse observed by NR was not fully reversible upon temperature reduction while the applied stress was maintained, while colloid-probe [20] and SFA [52] measurements are repeated many times against the same brush with no evidence of irreversibility. Colloid-probe and SFA experiments likely do not observe this irreversibility due to the small confined area, as discussed in the above paragraph. The thickness of the polymer layer in the NR experiment exhibited significant hysteresis when the temperature was reduced from 40 to 15 °C, not returning to its initial thickness (arrows on Fig. 5.12c). This hysteresis is not due to damage to the brush layer; we show in the following section that the brush recovers its response after confinement is released. Some reswelling upon a decrease in temperature was observed at 1 bar, indicating that there was solvent available to the brush in the sample environment; minimal reswelling was observed at 5 bar. It is unlikely that the hysteresis is caused by slow solvation dynamics



imposed by the large confined area; the slight re-swelling observed was not accompanied by a broadening of the separation distribution that would be expected if the brush were reswelling slowly from the edge inwards. The origin of the hysteresis observed in the reflectometry experiment is currently unclear and is indicative of a complex energy landscape and that illustrates the path-dependence of the structures that are formed in the confined brush.

One explanation for this behaviour lies in the complex phase behaviour of PNIPAM, which has previously been extensively reviewed [38]. Free PNIPAM in aqueous solution exhibits slow remixing upon being cooled from temperatures significantly above its LCST [38, 41, 209], attributed to ‘partial vitrification’ of the polymer. The temperature to which the sample was heated and the time that it remained at that temperature increased the stability of this collapsed PNIPAM phase. Hence, it is reasonable to link this slow remixing phenomenon with both the volume fraction (concentration) of PNIPAM in the collapsed state, and the time it spent collapsed. Here, parallels can be drawn with the NR experiment (where high PNIPAM volume fractions were maintained over long periods) to explain the hysteresis; the collapsed brush does not reswell over the time scales probed as it is in this partially vitrified state. This explanation is also consistent with the reversibility of the colloid-probe AFM measurements, as the timescale of the confinement is very small in these experiments.

It should be noted that different forms of hysteresis have been observed in heating/cooling curves for unconfined surface-tethered PNIPAM, where both the mechanical properties [46] and structure [210] differ between the heating and cooling of the layer. Varma, Bureau, and Débarre [210] characterise this hysteresis as a shift in the apparent transition temperature, which they report to be lower by 1 °C. In contrast to the partial vitrification phenomenon, there is no apparent stability of the collapsed state. An investigation into this hysteresis in brushes as a function of maximum temperature and time spent at maximum temperature is needed to assess whether partial vitrification plays a role in the unconfined thermoresponse of a PNIPAM brush.

### 5.3.5 Brush recovery

An important, but often overlooked aspect of applying responsive polymer brush systems to solve antifouling, steric stabilisation, and lubrication challenges is their stability under macroscopic contact. Their durability is particularly relevant for lubrication applications, where brush-coated surfaces are repeatedly required to resist normal and shear forces. Of course, the durability of brush systems is dependent on many factors [211]; however, recovery of the thermoresponse after direct compression is a minimum criterion for this

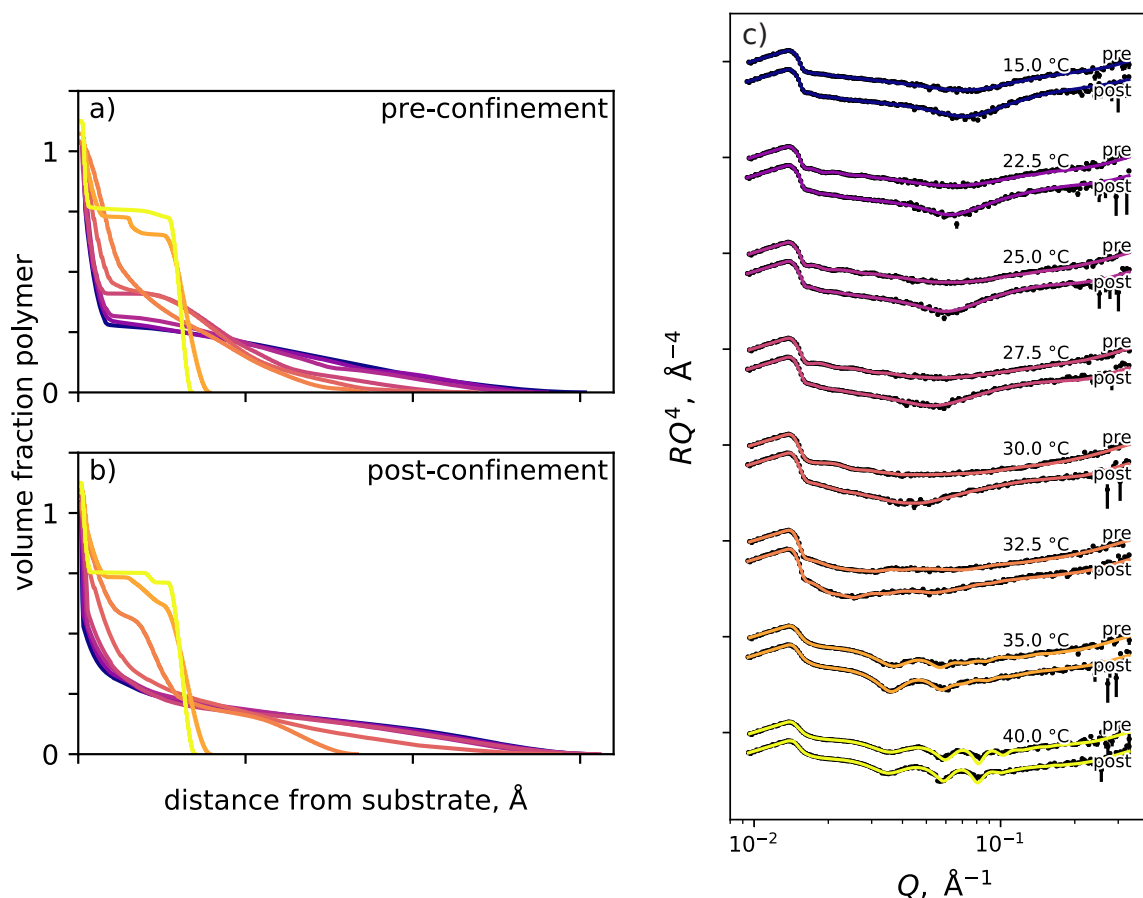


Figure 5.15: Volume fraction profiles depicting the thermoresponse of an unconfined PNIPAM brush (a) before and (b) after being subjected to 5 bar of mechanical confinement, demonstrating that the brush recovers from being confined. Corresponding reflectometry profiles are included in (c).

system. Fig. 5.15 shows that the grafted-from PNIPAM remains bound to the silicon block (i.e., no clear chain degrafting) and that the thermoresponse is largely unchanged even after being subjected to 5 bar of confining stress for 24 h, separated from the confining layer, and then rehydrated. Furthermore, this indicates that the PNIPAM brush has recovered from the hypothesised partially vitrified state. There are minor differences in the reflection profiles before and after confinement, most notably the fringe appearance at  $0.07 \text{\AA}^{-1}$  from 15 to 30 °C (Fig. 5.15). The modelling shows that the fringe is due to a change in the transition between the ‘interior’ polymer layer and the brush proper, perhaps due to the grafted polymer becoming untangled during the various hydration, collapse, and rinsing processes. The brush’s conformation at a given temperature is mostly unchanged, with the most significant discrepancy around the LCST, where the structure is most sensitive to temperature.

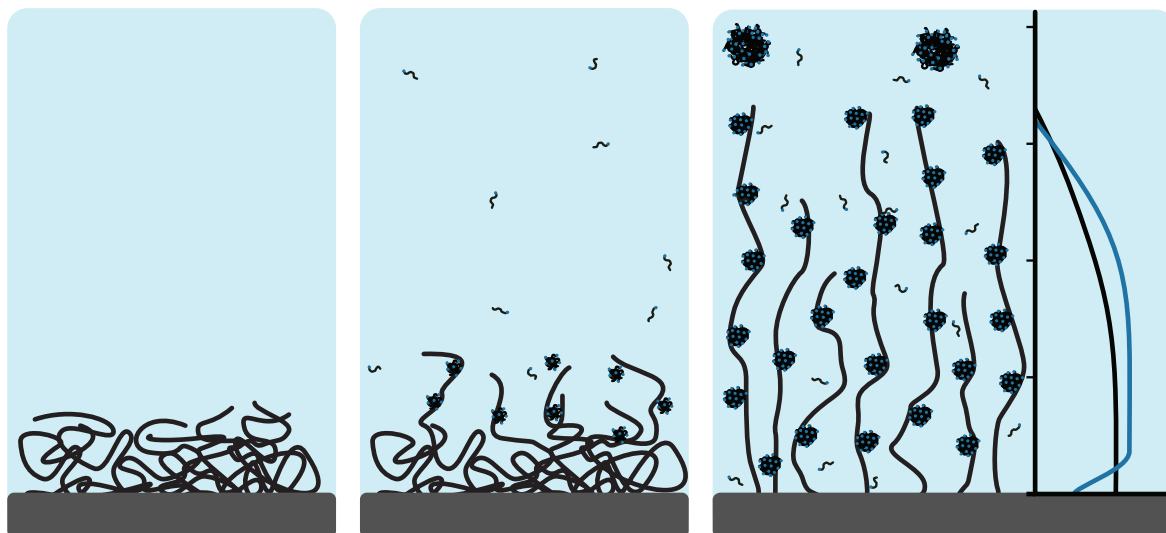
## 5.4 Conclusions

We have studied the conformation of a PNIPAM brush layer subjected to mechanical confinement by NR, modelling this complex system with a novel separation distribution model. We compared the model output with a model-free fringe-spacing analysis of the same data, nSCFT results, and stress-separation curves derived from AFM colloid-probe studies analysed using a Derjaguin-inspired modelling approach.

NR and nSCFT indicated that any confining stress results in the polymer brush density profile becoming slab-like, losing its characteristic parabolic profile. Even though the confined PNIPAM layer was more compressed than it would be under full thermal collapse, it still exhibits a temperature-dependent thickness. The confined layer exhibits hysteretic swelling behaviour; a PNIPAM brush at low temperature (swollen) that is then confined is substantially thicker than a confined brush at high temperature (collapsed) that is then cooled. This behaviour is without precedent in brush systems, as mainstream techniques (AFM and SFA) have not been used to probe constant-stress temperature ramps. Hysteretic behaviour may be due to the stability of the extremely collapsed PNIPAM layer, analogous to the partial vitrification phenomenon observed when PNIPAM is heated far above its CST. Further investigation of this hysteresis is required to confirm its mechanism. An important outcome of this work is that the macroscopic confinement does not permanently damage the response of a grafted-from PNIPAM brush layer.

## Chapter 6:

Investigation of the complex structures formed by mixtures of PNIPAM and surfactant



So far we have observed the structures formed by surface-initiated ATRP, determined the behaviour of PNIPAM brushes in their dry state, developed methods for modelling them in their solvated state, and observed how they behave under confinement. Now we will conclude by turning the knowledge gained and techniques developed toward a singular problem: The interaction between PNIPAM and surfactants. PNIPAM–surfactant systems are of interest for at least three reasons. Firstly, polymer-surfactant systems are ubiquitous in commercial and industrial products — better understanding their interaction will lead to improvements in lubricants, personal care products and separation processes. Secondly, the brush geometry simplifies control of experimental conditions — the polymer ‘concentration’ is fixed, and the solvent to polymer ratio is practically infinite, allowing for better control of variables and avoiding some of the problems encountered by previous phenomenological studies. Furthermore, brushes can be studied with techniques such as neutron reflectometry, QCM-D and ellipsometry, which allow for the direct study of polymer conformation. Thirdly, and more specifically, the potential to affect the conformation of a PNIPAM brush with a small amount of a specific molecule enhances their potential as a smart surface — surfactants, particularly SDS, are already known to modify the structure of PNIPAM.

## 6.1 Theoretical Background

### 6.1.1 Surfactants: an overview

The term surfactant (**surface active agent**) refers to a broad family of molecules that spontaneously assemble at interfaces, resulting in a reduction in interfacial energy. Surfactants typically possess an amphiphilic nature and vary in size, shape and efficacy, ranging from small molecules such as ethanol [212] to peptides [213] and even nanoparticles [214]. Surfactants find application in a host of industrial, commercial and medical products, and are ubiquitous in biological processes. Surfactants are the active ingredient in detergents and soaps, enable mineral extraction through froth flotation, and are the building block from which cell membranes are constructed. Surfactants are generally made up of a number of distinct solvophilic and solvophobic chemical groups, although this definition breaks down somewhat for proteins and particles.

Above a critical free-solution concentration, surfactants will spontaneously form supramolecular assemblies to maximise contact between the solvophilic components and the solvent, and solvophobic components and themselves. In the simplest case, these assemblies are spherical [215, 216] and are termed *micelles*, while the critical concentration at which they form is referred to as the *critical micelle concentration* (CMC) [217]. The relative geometry of the solvophilic and solvophobic sections of the surfactant dictates the structures that these assemblies take [217]; surfactants can be chosen to produce bilayer sheets [218] and liposomes (vesicles) [219], complex cubic-phase structures [220] and more.

The CMC of a surfactant is an important parameter in determining its behaviour and depends on a number of different factors, including temperature [217, 221–224] and (for ionic surfactants) ionic strength [216, 225, 226]. Not all surfactant–solvent pairings have an accessible CMC, but the behaviour of systems that do scales around this critical point. Above the CMC, discrete surfactant molecules are in a dynamic equilibrium with micelle-bound molecules such that the concentration of discrete molecules is fixed; increasing the concentration of surfactant increases the concentration of micelles, but not of discrete surfactant molecules. As such, system properties such as the interfacial tension reach a plateau above the system CMC, as added surfactant is incorporated into micelles instead of partitioning to an interface. Because surfactant behaviour depends on the surfactant concentration relative to the CMC, here we will refer to surfactant concentration as a multiple of their respective CMC. Absolute concentration will be given relative to the CMC in pure water at 25 °C, indicated by a  $^{\circ}$ , e.g.,  $0.5 \times \text{CMC}^{\circ}$ . The concentration of the surfactant relative to the actual CMC (modulated by ionic strength and temperature) will be given as a multiple of the effective CMC, i.e.,  $0.5 \times \text{CMC}^{\text{eff}}$ .

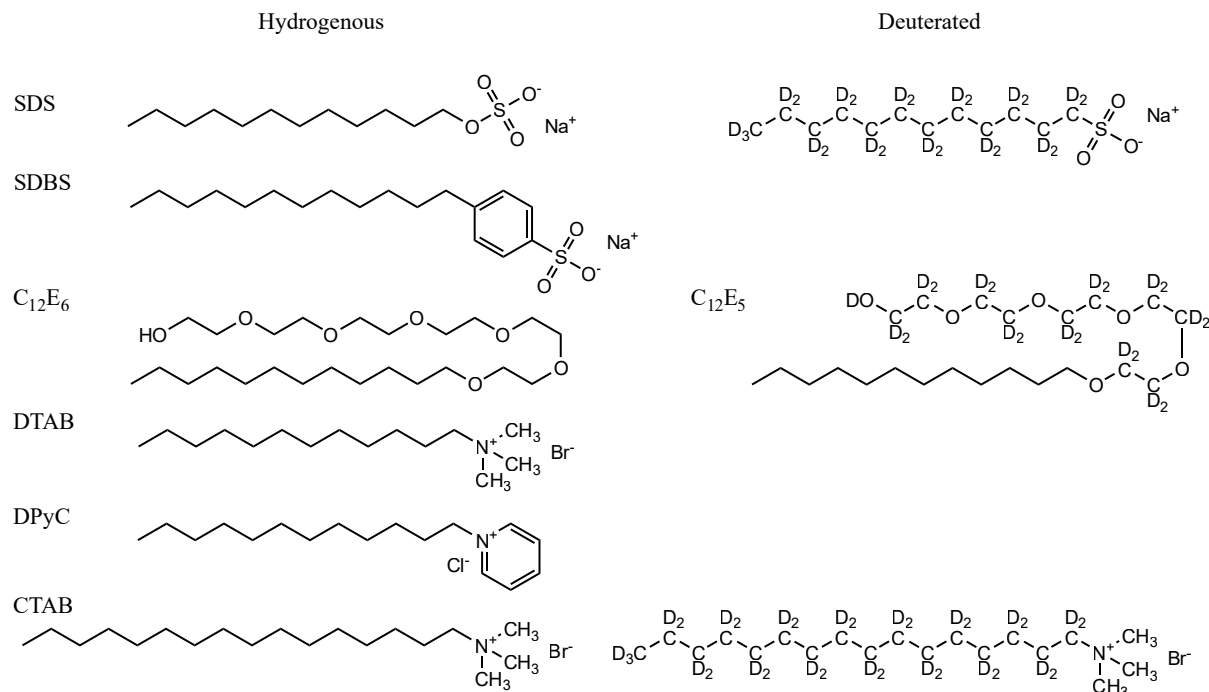


Figure 6.1: Chemical structures of the surfactants used in this work. Deuterated surfactants are used to provide additional contrast in neutron reflectometry (NR) studies.

In this chapter, we are interested in the interaction of these surfactants with poly(*N*-isopropylacrylamide) (PNIPAM) brushes; this requires surfactant behaviour to be understood. In this work, ‘surfactant’ exclusively refers to a small ( $<500 \text{ g mol}^{-1}$ ), amphiphilic molecule with one hydrophilic group and one hydrophobic group. We focus on surfactants with a single alkyl-chain tail between 12 and 16 carbons and either an anionic, neutral or cationic headgroup. Herein, in the context of surfactants, the term ‘head’ will refer to the surfactant’s polar/ionic section, while the term ‘tail’ will refer to the alkyl chain. The chemical structures of the surfactants used are shown in Figure 6.1, and their CMCs are shown in Figure 6.2.

As PNIPAM is a thermoresponsive polymer, the surfactant-polymer system’s behaviour as a function of temperature will be investigated. The effect of changes in temperature on the surfactant component of the system is characterised in Figure 6.2. The relationship between temperature and the CMC generally resembles a parabola; increasing temperature decreases the CMC at low temperatures and increases the CMC at high temperatures. The temperature range we are interested in here is 20 to 40 °C, as this is the range at which PNIPAM brushes typically respond to changes in temperature [20, 38, 68]; over this range changes in the CMC of  $\approx 15\%$  are typical. For this reason, we choose surfactant concentrations that are significantly lesser or greater than the surfactant CMC. The discrepancy in the sodium dodecylbenzene sulfonate (SDBS) results is

due to different isomers having different CMCs; here we use an isomeric mix with a CMC of approximately 3 mM.

There are a number of important parameters that govern surfactant behaviour in addition to the CMC. The Krafft point is the point at which a surfactant's solubility is equal to its CMC. At temperatures below (or concentrations above) the Krafft point the surfactant will precipitate out of solution, forming pearlescent crystal structures that are obvious to an observer. These hydrated crystal structures are in equilibrium with surfactant in the bulk phase [227]. All surfactant solutions are kept above their Krafft points during experiments, with the exception of cetyl trimethylammonium bromide (CTAB), as discussed below. The degree of micelle ionisation,  $\alpha$ , is the fraction of ionised surfactant headgroups in a micelle at a given condition; clearly, this parameter only applies to ionic surfactants. At 25 °C the  $\alpha$  of sodium dodecyl sulphate (SDS), CTAB and dodecyl trimethylammonium bromide (DTAB) is 0.26 [228, 229], 0.23 [228] and 0.21 [223], respectively. As these values are similar, we expect the surfactant micelles in this work to have similar specific charges. Lastly, we stress that surfactant behaviour scales around the concentration of free surfactant (i.e., not bound to an interface or polymer) relative to the CMC. There may be a significant difference between the gravimetric and free surfactant concentrations in the case where there is a considerable degree of surfactant adsorption (e.g., to polymer chains). In the brush geometry the concentration of polymer is vanishingly small, so the gravimetric and free surfactant concentrations are effectively identical.

### The Krafft point of CTAB

The Krafft point of CTAB is commonly reported to be between 20 and 40 °C [227]. In this work, we include studies of CTAB at temperatures within this range, and while no pearlescence or opacity was observed in CTAB solutions at any condition, many of the experiments on CTAB were likely carried out above the solubility limit of CTAB. As such, CTAB solutions may never truly reach their CMC. Consequently, the behaviour of CTAB is expected to scale around the solubility limit (lower than the CMC) instead, which result in the effect of CTAB on PNIPAM being underestimated. We expect the behaviour of CTAB solutions significantly below the CMC to be unchanged, as these will not encroach upon any solubility limits.

### 6.1.2 Phenomenological studies of surfactant-polymer systems

Molecular specificity in PNIPAM-surfactant systems has been reported for some time [239]. Anionic sulfate-headed surfactants ( $\text{XC}_n\text{S}$ ) interact strongly with PNIPAM for  $n$  between 7 and 14 [240] ( $n$  is the length of the tail), although it is primarily sodium do-



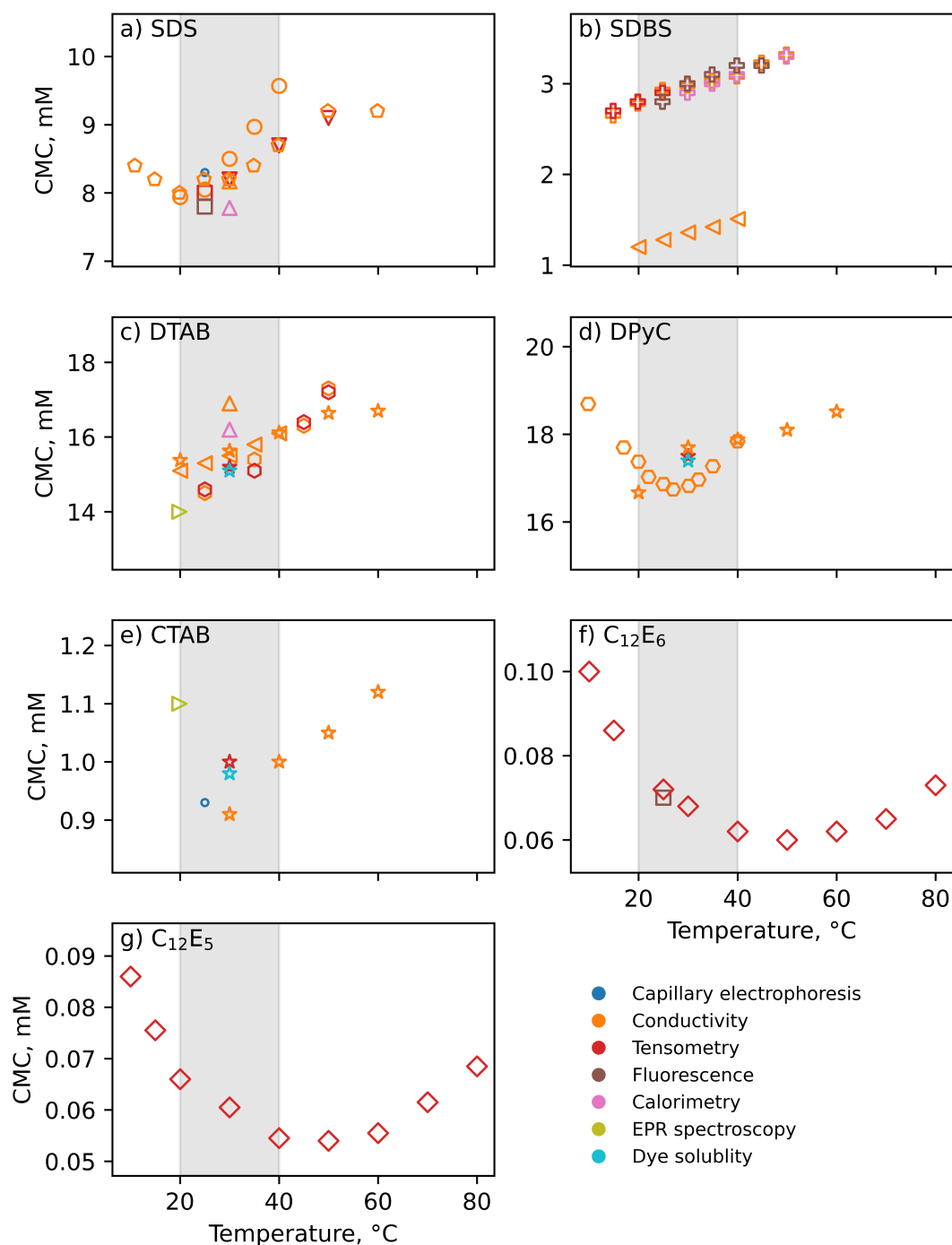


Figure 6.2: The CMC of different surfactants as a function of temperature, collected from a range of sources detailed in Table 6.1. Marker colour corresponds to the technique used, while the marker symbol corresponds to the source. The grey shaded region indicates the temperature range relevant to the present study. A large discrepancy is observed for different SDBS sources due to isomeric impurities.

decyl sulphate ( $\text{NaC}_{12}\text{S}$ , or SDS) that is studied. SDS raises the cloud point of PNIPAM [241, 242], cooperatively assembles with PNIPAM at the air–water interface [243], and is found to swell PNIPAM gels [239], microgels [244] and particle-grafted polymer brushes [74]. System behaviour for  $\text{XC}_n\text{S}$  appears to scale as a function of free surfactant concentration around the CMC of the surfactant. The interaction starts at a critical aggregation concentration (CAC) [217, 225, 245] and increases until a plateau value is reached at or just above the surfactant CMC [239–242]. In all cases, SDS is seen to both swell/stretch PNIPAM under isothermal conditions and increase its critical solution temperature (CST) dramatically, effectively removing its thermoresponsive properties at concentrations close to and above the CMC of SDS [74, 239, 241, 242].

The response of PNIPAM to similarly structured but cationic trimethyl ammonium surfactants ( $\text{C}_n\text{TAX}$ ) surfactants is very different. PNIPAM- $\text{C}_n\text{TAX}$  systems do not exhibit critical phenomena with free surfactant concentration; instead the CST varies linearly with surfactant concentration, only significantly affecting the behaviour of PNIPAM well above the surfactant CMC ( $5$  to  $10 \times \text{CMC}$ ), if at all [241, 242]. In studies using the bromide counterion ( $\text{C}_n\text{TAB}$ ), surfactants with hydrocarbon tails of  $n = 14$  or greater were observed to have a measurable effect on the cloud point of PNIPAM over the  $0$  to  $50$  mM concentration range investigated [241] (Note that the CMC of these surfactants is  $\approx 1$  mM). This tail-length threshold fits well with reports that dodecylpyridine bromide ( $\text{C}_{12}\text{PyBr}$ ) has no effect on PNIPAM microgels [244] and that  $\text{C}_{16}\text{TACl}$  does [242]. There is some evidence that the surfactant counterion influences the PNIPAM-surfactant inter-

Table 6.1: References corresponding to marker symbols used in Figure 6.2.

marker	source
◦	Cifuentes, Bernal, and Diez-Masa [230]
○	Shah, Jamroz, and Sharif [221]
▽	Markarian, Harutyunyan, and Harutyunyan [231]
□	Fegyver and Mészáros [232]
△	Naskar, Dey, and Moulik [233]
◡	Marcolongo and Mirenda [234]
◁	Chauhan and Sharma [235]
⊕	Hait et al. [222]
▷	Tedeschi et al. [236]
☆	Mata, Varade, and Bahadur [237]
◻	Shah, Chatterjee, and Bhattarai [223]
◻	Galán et al. [224]
◊	Chen et al. [238]

action, found in the discrepancy in the behaviour of  $C_{12}TACl$  [239] and  $C_{12}TABr$  (also called DTAB) [241] systems; explainable by the differing dissociation coefficients [237], the difference in experimental techniques (free polymer, turbidity vs gel, volume change) and the existence of specific ion effects (although Cl and Br are reasonably close on the Hofmeister series). Studies of PNIPAM and nonionic surfactants unanimously conclude that there is no appreciable modulation of the CST in free polymer [241, 243] or gel [239] architectures, or cooperative adsorption at air–water interfaces [242].

### 6.1.3 Structural studies of surfactant-polymer systems

Whilst the techniques used in the phenomenological studies provide insight into the surfactant-specific response of PNIPAM, they do not directly study the physical structure or chemistry of these systems. More powerful techniques have been applied to study the PNIPAM-surfactant system, but these have exclusively (to the authors' knowledge) been applied to the study of PNIPAM-SDS systems. One such technique is small-angle neutron scattering (SANS). Mears et al. [246] report the presence of small polymer-attached micelles forming below the CMC (and above the CAC) in PNIPAM microgels, reporting that the size of these micelles increases with surfactant concentration, with the maximum observed radius of (approximately 15 Å) fixed by the maximum pore size of the microgel. Lee and Cabane [247] perform a similar study on free PNIPAM, once more reporting that SDS adsorbs to the polymer as whole micelles, measuring a centre-to-centre inter-micellar distance of  $\approx 63$  Å at 40 °C which increases as the temperature is lowered, and reporting 15 Å as the size of the micelle. They observe that this inter-micellar distance is independent of concentration and that, at 40 °C, chains are either solubilised by SDS micelles (existing in a coiled state) or not (existing in a collapsed globule state) — no intermediate state was observed. This seems to imply that the number of micelles per chain is relatively constant and that more SDS either increases the number of solubilised PNIPAM chains or the micelles size.

### 6.1.4 Chemical studies of surfactant–polymer systems

Time-resolved fluorescence depolarisation and time-resolved fluorescence quenching have both been used to elucidate the chemical environment of the SDS micelle core in the presence of PNIPAM. Walter et al. [248] make bold claims using the depolarisation technique, claiming that PNIPAM acts distinctly to both polyethylene oxide (PEO) and polyvinylpyrrolidone (PVP) model systems, with PNIPAM being incorporated into the micelle core instead of adsorbing onto the micelle surface. They also suggest that there are

two modes through which SDS micelles interact with polymer between the CAC and the CMC; quasi-free micelles are loosely bound to the polymer (perhaps surface adsorbed), whilst polymer-bound micelles are anchored to the polymer chain (polymer incorporated in the micelle core). Mylonas, Staikos, and Lianos [249] used the quenching technique to observe how the PNIPAM-bound SDS micelles change with SDS concentration; unlike Walter et al. [248] they did not find evidence for two types of micelle association. Interestingly, they report that the number of micelles per chain increased with surfactant concentration until it reached a critical value (well below the CMC). At this point, it plateaued, with additional surfactant becoming incorporated into existing micelles. This resulted in the formation of small micelles, with aggregation number  $\approx 8$ , at low surfactant concentrations, which increased in size as the surfactant concentration approached the CMC, with a final aggregation number of  $\approx 22$ . These small micelles are presumably stabilised by the presence of the polymer. This fits with the scattering study of Lee and Cabane [247] (above), in that it is the size of the micelles, not their number or separation, that changes with surfactant concentration. Time-resolved fluorescence anisotropy has also been used to study the molecular environment of labelled PNIPAM molecules in the presence of SDS [250]. The results of such studies are similar to analogous scattering, viscometry and turbidity experiments.

More recently, Chen et al. [251] conducted a series of nuclear magnetic resonance (NMR) studies on PNIPAM-SDS systems, examining their behaviour as a function of temperature [251] and surfactant concentration [252]. They observed polymer-bound micelles at low temperatures, which appeared to detach as the temperature was increased above the CST. nuclear overhauser effect spectroscopy (NOSEY) revealed an association between the surfactant tail and the isopropyl groups on the PNIPAM, indicating that the interaction of the two species was at least in part due to the hydrophobic effect. Chen et al. [251] observed that the total concentration of free surfactant remained constant at 0.86 mM (the CAC) below the CMC and increased linearly above, indicating that no additional surfactant bound to the polymer above the CMC. They found that  $\approx 3200$  SDS molecules were bound to each PNIPAM chain at the CMC [252]. Given that the average number of monomers in a chain was approximately 1000 (they report a molecular weight of  $1.2 \times 10^5 \text{ g mol}^{-1}$ ), it can be reasoned that approximately 3.2 SDS molecules are bound per monomer unit, yielding a mass ratio of SDS to PNIPAM of approximately 8. Intuitively, this seems too high, and contradicts the binding curve of both Mylonas, Staikos, and Lianos [249] and Mears et al. [246], who give mass binding ratios (grams of SDS per gram of PNIPAM) of 0.6 and 0.5 at the CMC, respectively. The reason for this large discrepancy is unclear; we will compare our experimental findings to these figures in section 6.6.1.

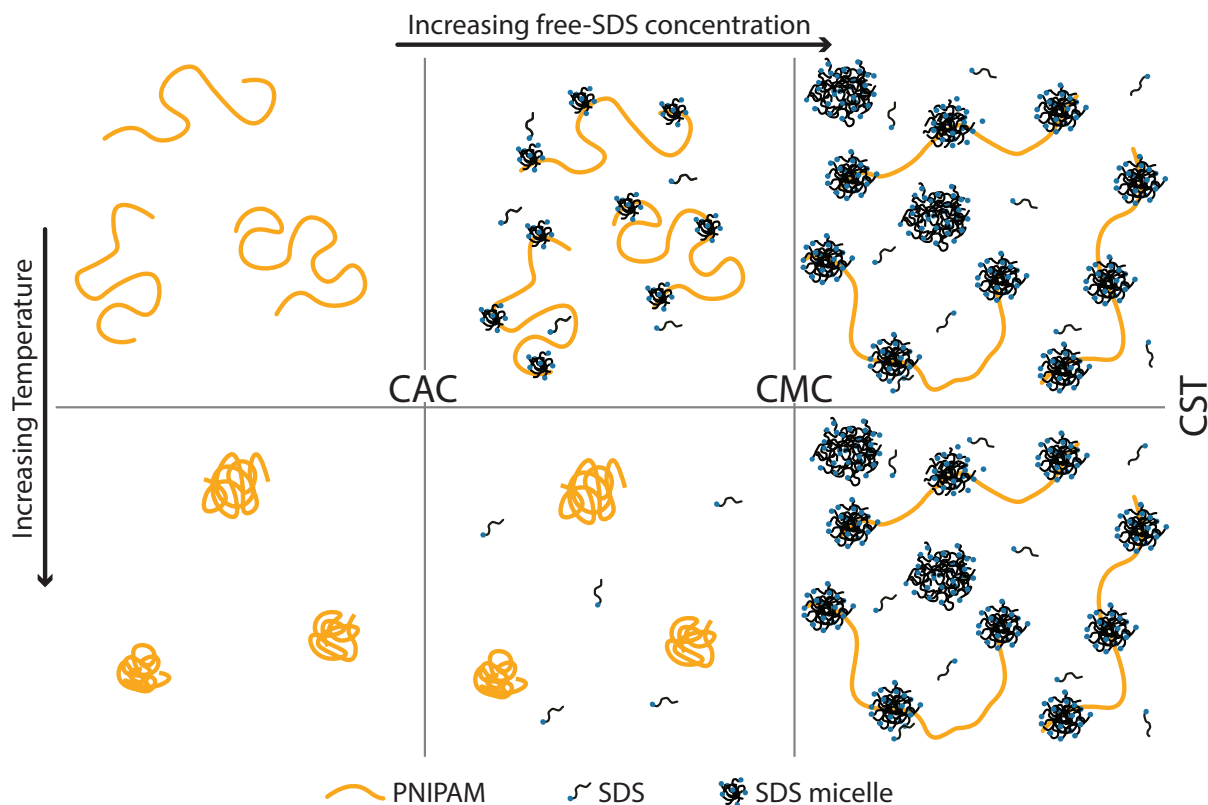


Figure 6.3: Schematic of structures formed by PNIPAM-SDS complexes as a function of surfactant concentration and temperature. In pure water (*left panels*) PNIPAM exhibits its classic thermoresponse, undergoing a swollen-to-collapsed transition at its CST of 32 °C [38]. At low SDS concentration, below the (free-solution) CMC of SDS (*middle panels*), surfactant adsorbs to the polymer in small micelles of 5-8 units [246, 247, 249]. Here an increase in temperature causes the PNIPAM to collapse and the expelled bound SDS [247, 251]. At SDS concentrations approaching and above the CMC (*right panels*), bound SDS micelles increase in size [246, 247, 249] and the thermoresponse of PNIPAM is suppressed [74, 239, 241, 242]. Note that the relevant surfactant concentration is the concentration of free surfactant (i.e., not bound to an interface or polymer).

### 6.1.5 Models for surfactant-PNIPAM interaction

From NMR, fluorescence techniques and SANS it is clear that SDS adsorbs to PNIPAM as complete micelles [246–249, 251, 252], as in the ‘pearl-necklace model’ first suggested by Shirahama, Tsujii, and Takagi [253]. These adsorbed micelles are smaller than equivalent free micelles [246, 247, 249], with their aggregation number depending strongly on free surfactant concentration [247, 249]. It also seems that when the polymer undergoes a thermal collapse, micelles are ejected from the system [247, 251]. These conclusions are graphically summarised in Figure 6.3. However, whilst the molecular structure of PNIPAM-SDS systems is well understood, the phenomenological studies of broader ranges of surfactants raise questions regarding the interaction mechanisms proposed. Many studies suggest

that the reason for the PNIPAM-surfactant interaction is hydrophobic interaction between the aliphatic surfactant tail and the PNIPAM backbone and isopropyl carbons, as in Figure 6.4 [246, 248, 252, 254]. If this were true, then anionic and cationic surfactants would behave similarly. However, it is almost universally reported that SDS has a large influence on both the conformation and CST of PNIPAM, whilst its cationic and nonionic counterparts have little or no measurable effect [239, 240, 242, 243]. Due to these differences, it appears that the mechanism through which anionic, nonionic and cationic (or at least sulphate, ethylene glycol and trimethyl ammonium headed) surfactants interact with PNIPAM differs, due both to the difference in the magnitude of the shift in CST and the concentration of surfactant required (relative to the CMC) for the shift to occur. This discrepancy leads to the reasonable conclusion that the headgroup plays an important role in binding the surfactant micelle. This does not mean that the tail is not also important; only that the presence of a hydrophobic tail alone is not sufficient to induce significant interaction with the PNIPAM.

There has been some debate about whether it is the size of the headgroup [246, 248, 252, 254, 255] or the sign of its charge that is responsible for this discrepancy. The molecular dynamics (MD) simulations of Shang, Wang, and Larson [256] provide some insight into the nature of neutral, water-soluble polymer surfactant interaction, although they use

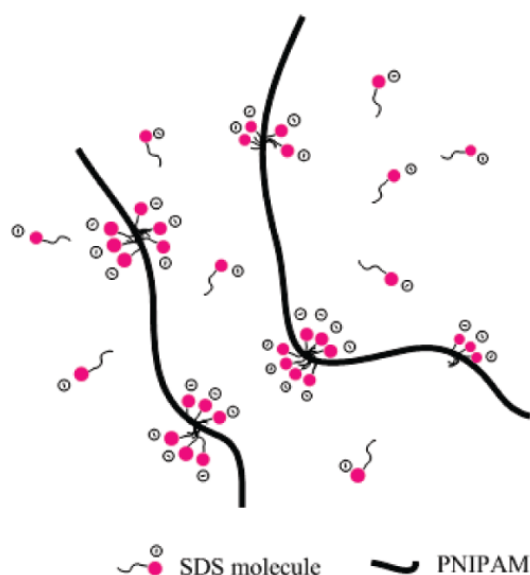


Figure 6.4: Tail-mediated interaction model suggested by the NMR experiments of Chen et al. [251]. Reprinted with permission from Chen et al. [251]. Copyright 2021 American Chemical Society.

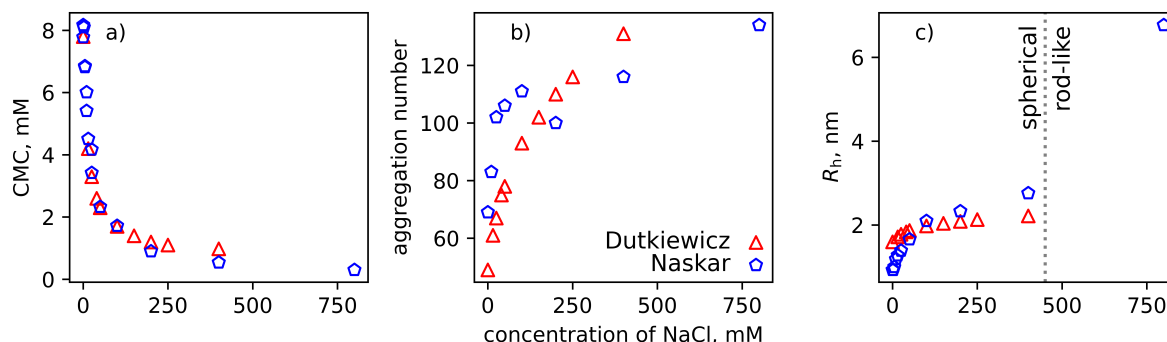


Figure 6.5: (a) CMC of SDS, (b) aggregation number of SDS micelles, and (c) hydrodynamic radius of SDS micelles as a function of NaCl concentration from the work of Dutkiewicz and Jakubowska [226] and Naskar, Dey, and Moulik [233]. The dashed line in (c) indicates the sphere-to-rod transition point reported by Hayashi and Ikeda [216].

PEO as their model polymer. They conclude that the polymer chain wraps around the micelles, shielding exposed hydrocarbon tails from the aqueous environment [256, 257]. By swapping the charges of the SDS and DTAB in the simulation they convincingly show that it is the headgroup charge, not size, that dictates the binding strength [256].

### 6.1.6 Effect of ionic strength on surfactant-polymer behaviour

The CMC of surfactants is sensitive to temperature and the ionic strength<sup>i</sup> of the solution. In this chapter we will look at the behaviour of ternary PNIPAM-SDS-NaCl systems, so it is important first to understand the implications of salinity on SDS. Figure 6.5 shows that increasing the concentration of NaCl reduces the CMC of SDS. This will prove significant, as polymer-surfactant behaviour is relative to the CMC. The effect of NaCl concentration on the shape of SDS micelles should also be noted. It is well accepted that SDS exists as spherical micelles in pure water [215, 216, 233] with an aggregation number around  $\approx 70$  (Fig. 6.5). However, as the NaCl concentration increases so to does the size of the micelles, with an aggregation number of 116 being reported for 400 mM salt solutions [233]. Above 450 mM NaCl the shape of SDS micelles has been reported to transition from spherical to worm-like [215, 216, 233]. At higher NaCl concentrations of  $\approx 1500$  mM, SDS will become less soluble in water, and crystalline precipitates will form [258]. None of our experiments approach this hypersaline regime.

To our knowledge, the only study of a PNIPAM-surfactant-salt system was carried out by Patel et al. [241], who examine ternary PNIPAM-SDS-NaCl systems. Their results are shown in Figure 6.6, and indicate that NaCl reduces the degree to which SDS suppresses

<sup>i</sup>as well as the identity of those ions, but that is beyond the scope of this work.

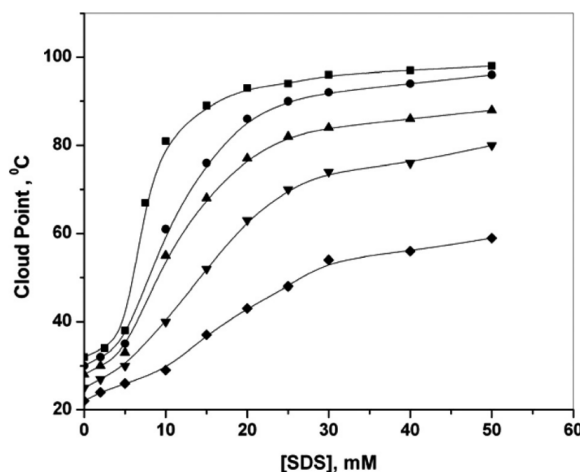


Figure 6.6: Effect of different NaCl concentrations of the cloud point of PNIPAM in SDS solutions of increasing concentration, from the work of Patel et al. [241]. The NaCl concentrations are denoted as follows: ■ pure water, ● 100 mM, ▲ 200 mM, ▼ 500 mM, ◆ 800 mM. Reprinted with permission from Patel et al. [241]. Copyright 2021 Taylor & Francis.

the CST of PNIPAM. These experiments were carried out in a 1 wt% solution of PNIPAM, and probe SDS solutions up to 1.4 wt%. The molar ratio of PNIPAM monomers to SDS molecules at the highest SDS concentration is approximately 1:0.6. As such, depending on the binding ratio of SDS to PNIPAM, and how it changes with NaCl concentration, it is possible that the free-SDS is being depleted in the system. We will compare this with our results in section 6.5.4.

### 6.1.7 Implications of the brush geometry

While studying polymer-surfactant interactions in the planar-brush has significant advantages (as outlined in the abstract), the brush geometry does in itself influence polymer behaviour. The implications of the brush regime on a pure neutral polymer system is discussed in detail in section 1.1. Upon the adsorption of surfactants onto the polymer backbone (as per the pearl-necklace model), the PNIPAM effectively becomes charged. The implications of this charge will depend greatly on the strength of the PNIPAM-micelle binding energy, but may result in the polymer acting as a pseudo-polyelectrolyte. Polyelectrolytes in the brush regime behave differently to neutral brushes, as there is an additional repulsive electrostatic interaction. These electrostatics encourage polymer self-avoidance and result in brush swelling. Furthermore, the charged moieties carry with them hydration shells, further swelling the brush.

The behaviour of polyelectrolyte brushes can be divided into two regions, depending on the solvating environment's ionic strength. At low salt concentrations, the brush is



in the osmotic regime. In short, the behaviour in the osmotic regime is dominated by the osmotic pressure of the high local salt concentration within the brush. The local salt concentration is higher within the brush as the charged monomers attract oppositely charged ions. At high salt concentrations, the brush is in the salted regime, where the concentration of ions in the brush is similar to that in the bulk solution and monomer charges are effectively screened. Here the chain extension is dictated by excluded-volume interactions between polymer chains, and the brush collapses. The behaviour of weak and strong polyelectrolytes is similar in the salted regime, but diverges significantly in the osmotic regime, in which weak polyelectrolytes require some salt to swell. This is because low salt concentrations enable dissociation of charged groups in the weak polyelectrolyte. For an in-depth review of the implications of salt on polyelectrolyte brush behaviour see the work of Willott et al. [108].

### 6.1.8 Open questions

In this chapter, we leverage several surface-sensitive techniques to unpick the behaviour of PNIPAM-surfactant systems. Our results will confirm that the surfactant head-group plays a significant role in the PNIPAM-surfactant interaction, supporting the phenomenological studies laid out in section 6.1.2. We will show that anionic surfactants exhibit a unique interaction with PNIPAM, imbuing it with polyelectrolyte-like properties. The behaviour of the PNIPAM brush–anionic surfactant systems will be shown to be dependent on the concentration of free surfactant relative to the CMC, agreeing with the prior work laid out in sections 6.1.2–6.1.4. We show that the surfactant’s presence changes the layer’s mechanical properties by examining its structure as a function of applied surface–normal force via the method developed in chapter 5. Finally, we explore the polyelectrolyte-like properties of these polymer-surfactant complexes by studying the effect of system salinity on their behaviour, finding that the ‘salting out’ effect common to polyelectrolytes are absent in these systems.

To improve clarity, the results in this chapter will be split across three sections. First, the effect of surfactant identity and concentration will be examined, then the mechanical properties of the PNIPAM-SDS layer will be explored. Lastly, we will investigate the effects of ionic strength on the system.

## 6.2 Materials and methods

### 6.2.1 Materials

The surfactants CTAB ( $\geq 99\%$ ), DTAB ( $\geq 98\%$ ), hexaethyleneglycol monododecyl ether ( $\text{C}_{12}\text{E}_6$ ) ( $\geq 98\%$ ), SDBS (technical grade), dodecylpyridinium chloride (DPyC) ( $\geq 98\%$ ) and SDS ( $\geq 98\%$ ) were purchased from Sigma Aldrich, SDS and SDBS were recrystallised in ethanol before use, remaining surfactants were used as received. The surfactants deuterated SDS (d-SDS) and deuterated CTAB (d-CTAB) were purchased from Cambridge isotope laboratories and used as received. deuterated  $\text{C}_{12}\text{E}_5$  (d- $\text{C}_{12}\text{E}_5$ ) was supplied by Dr. Peixun Li, Oxford Deuteration Facility (STFC). For materials relating to wafer preparation and polymer synthesis, see section 1.3. The brushes used in this study were synthesised according to the method outlined in section 1.4.

### 6.2.2 Determination of optical parameters for surfactant solutions

Ellipsometry and fixed-angle optical reflectometry (FAOR) are sensitive to the solution optical properties. Furthermore, to extract adsorbed amounts from FAOR the  $dn/dC$  of the adsorbent (in this case the surfactant) must be known. Here, the  $dn/dC$  is the change in the solution refractive index (RI) with the change in the surfactant concentration. The RI of surfactant solutions were determined as a function of surfactant identity, surfactant concentration and wavelength using a digital refractometer. A Cauchy model was fit to this data, which allows for interpolation of results and use with spectroscopic ellipsometry modelling software. The Cauchy model describes the RI as a function of wavelength via the relation

$$n(\lambda) = A + \frac{B}{\lambda^2} \quad (6.1)$$

where  $A$  and  $B$  are the Cauchy parameters.

An example of the data collected for a single surfactant (SDS) is shown in Figure 6.7a. A summary of the fitted Cauchy parameters is shown in Figure 6.7a and b.  $A$  is found to be a linear function of surfactant concentration, while  $B$  appears to be constant for the surfactant concentrations studied.

### 6.2.3 Fixed angle optical reflectometry

FAOR is a simple optical technique which studies adsorption at a solid-liquid interfaces by measuring the polarisation of reflected light. FAOR uses a single wavelength and is

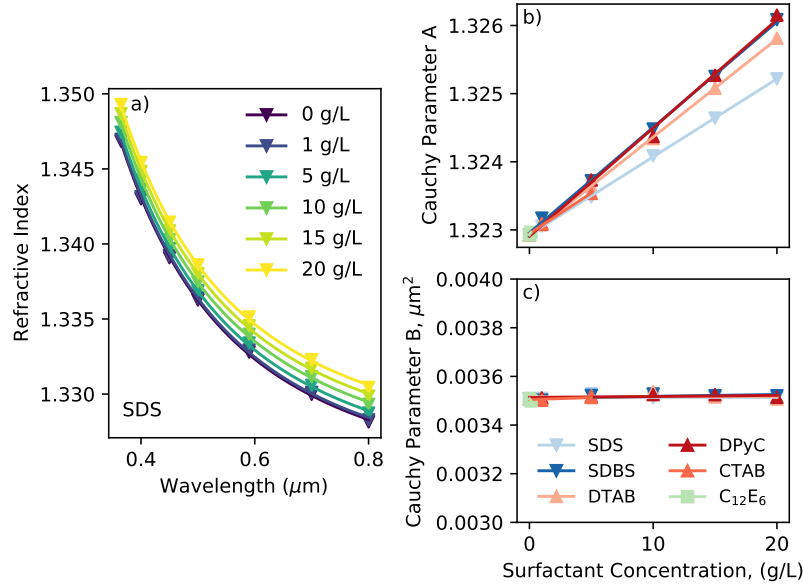


Figure 6.7: a) RI vs wavelength data for a range of aqueous SDS solutions; the fitted Cauchy model (solid lines) match the collected data (triangles) excellently; a similar agreement is found for other surfactants. From the RI curves in (a), Cauchy parameters are extracted, shown in (b) and (c).  $A$  was found to linearly vary with surfactant concentration, while  $B$  was constant for all surfactants across the concentration range studied. The investigated concentration range for CTAB and C<sub>12</sub>E<sub>6</sub> was limited by their solubility.

conducted in a single angle geometry; as such, it cannot be expected to provide detailed structural information. However, the presence of an optical ‘spacer’ in the substrate (here a thermal silica layer) results in the technique being extremely sensitive to changes in RI of interfacial layers. Like other reflectometry techniques used here, FAOR data must be analysed using a suitable optical model.

Here, FAOR was conducted in an impinging-jet flow geometry, with a He-Ne laser ( $\lambda = 632.8 \text{ nm}$ ) accessing the interface through a  $45^\circ$  glass prism; the setup is described in detail by Dijt et al. [259]. To increase sensitivity FAOR measurements were performed on silicon wafers with a thick  $820 \text{ \AA}$  silica layer formed by thermal oxidation [259]. The brushes grafted-from these wafers were measured to be between  $150$  and  $170 \text{ \AA}$  thick by ellipsometry. The FAOR setup measures a signal  $S$ , which is the ratio of parallel-polarised ( $R_P$ ) to perpendicular-polarised ( $R_S$ ) light reflected from the surface of interest. This signal can be related to the adsorbed amount of material at the interface through the sensitivity factor,  $q$ .

$$\Gamma = q \frac{\Delta S}{S_0} \quad (6.2)$$

where  $S_0$  is the baseline signal and  $\Delta S$  is the change in signal ( $S - S_0$ ). Here we substitute  $q$

for the calculable value  $q_n$ , which is the sensitivity factor at a vanishing small adsorbed mass of surfactant ( $\lim_{\Gamma \rightarrow 0} q = q_n$ ). This assumption holds as the adsorbed mass is expected to be small; simulation shows that the sensitivity factor remains within 10 % of  $q_n$  up to adsorbed masses of  $\approx 15 \text{ mg m}^{-2}$ .  $q_n$  is a function of many experimental parameters and was calculated using the *Prof. Huygens* program (DULLware Software, Wageningen University). Parameters used to calculate  $q_n$  are shown in Table 6.2.

There are two key limiting assumptions made when calculating  $q_n$ . The first is that the RI of the brush layer is assumed to be the same as the solvent at  $\Gamma = 0$ ; this affects the accuracy of the adsorbed mass calculation but will have the same effect on all surfactant identities. The second is the thickness of the adsorption layer does not change as the material is adsorbed, because  $q_n$  is dependent on the thickness of the adsorbed layer; this will result in the  $\Gamma$  being underestimated in situations where the layer swells. From modelling in *Prof. Huygens*, we estimate that a 20 % increase in layer thickness will result in the adsorbed mass being underestimated by approximately 6 %. Of course, a change in thickness will be accompanied by a change in polymer volume fraction and hence a change in the film's refractive index. These effects are not considered in the above approximation, but would also result in the adsorbed amount being underestimated. We stress that the calculation of the adsorbed amount of surfactant through the sensitivity factor method should be considered a rough approximation. Comparisons between FAOR results (e.g., different surfactant identities) are valid, as are the broad trends observed by this technique.

## 6.2.4 Ellipsometry

### For the surfactant identity study

A Woollam M-2000 spectroscopic ellipsometer was used for the ellipsometry studies in section 6.3. Dry measurements were taken between 60 and 75° inclusive at 5° intervals and fit with a single slab Cauchy model (Eq. 6.1). The Cauchy parameters for PNIPAM were taken as  $A = 1.453$ ,  $B = 0.00495 \text{ } \mu\text{m}^2$  [254]. Solvated spectroscopic ellipsometry measurements were performed at 75° with the sample contained in a Woollam 5 mL heated horizontal liquid cell atop a Woollam HLC-100 heating stage that provided temperature control. Temperature-dependent measurements were performed as a function of increasing temperature (i.e., low to high), with an equilibration time of 35 min; the data presented is at thermal equilibrium. Solution changes were made by pumping at least 50 mL of fresh solution through the cell; for solution changes where surfactant identity was changed the cell was flushed with 100 mL of MilliQ water before the injection of the new solution.

Table 6.2: Parameters used for determining sensitivity factor,  $q_n$ , for FAOR

parameter	value
angle of incidence	$71^\circ$
laser wavelength	632.8 nm
silica thickness	820 Å
polymer thickness*	600 Å
water RI	1.33 (0) <sup>†</sup>
silica RI	1.46 (0) <sup>†</sup>
silicon RI	3.85 (0.02) <sup>†</sup>
<hr/>	
$dn/dC$	
<i>SDS</i>	0.116
<i>SDBS</i>	0.159
<i>C<sub>12</sub>E<sub>6</sub></i>	0.13 <sup>‡</sup>
<i>DTAB</i>	0.146
<i>DP<sub>y</sub>C</i>	0.163
<i>CTAB</i>	0.124
<hr/>	
$q_n$	
<i>SDS</i>	49
<i>SDBS</i>	36
<i>C<sub>12</sub>E<sub>6</sub></i>	44 <sup>‡</sup>
<i>DTAB</i>	39
<i>DP<sub>y</sub>C</i>	35
<i>CTAB</i>	46

\* this is an approximation of the swollen polymer thickness based off the dry polymer thickness and the ellipsometry data of Murdoch et al. [20], which is required to calculate the sensitivity factor

<sup>†</sup> values in parentheses are the extinction coefficient (the complex component of the RI)

<sup>‡</sup> low solubility of *C<sub>12</sub>E<sub>6</sub>* reduced certainty in this value

Data analyses were carried out using the Woollam CompleteEASE ellipsometry package. A two-term Cauchy approximation was used to model the optical properties of both PNIPAM and the solution; the PNIPAM parameters were identical to those used for the dry measurement, while the relationship from Figure 6.7 was used to approximate the parameters for the solution.

Two brushes were studied with ellipsometry: one with a dry thickness of 200 Å and another with a dry thickness of 610 Å. The thinner could be satisfactorily modelled with a uniform (single-slab) effective medium approximation (EMA) model, while the thicker required a more detailed graded layer to describe the collected data. The graded layer had the functional form

$$\phi_{\text{poly}}(z) = \phi_{\text{poly}}(0) + [\phi_{\text{poly}}(1) - \phi_{\text{poly}}(0)] \times \left(\frac{\hat{z}}{E}\right)^p \quad (6.3)$$

The function is defined over  $\hat{z} = [0, 1]$ , where 0 corresponds to the base of the brush and 1 corresponds to its extent,  $E$ .  $\phi_{\text{poly}}(0)$  and  $\phi_{\text{poly}}(1)$  are the polymer volume fraction at position 0 and 1, respectively and  $p$  dictates the shape of the profile.  $\phi_{\text{poly}}(0)$ ,  $\phi_{\text{poly}}(1)$ ,  $E$  and  $p$  were allowed to vary between sensible bounds. This functional form can produce a range of profiles and was chosen as it produced significantly better fits than either a single-slab or double-slab EMA. The layer thickness was extracted from the profile by considering its first moment (Eq. 1.6).

### For the SDS-NaCl study

An Accurion nanofilm\_EP4 imaging ellipsometer was used for the ellipsometry studies in section 6.5. Dry measurement were performed in the same manner as described in section 1.5.5. Solvated spectroscopic ellipsometry measurements were performed at 65° with the sample contained in a Accurion 0.7 mL liquid cell connected to a heater/chiller unit, which provided temperature control. Measurements were performed at 12 equally spaced wavelengths from 380 to 910 nm inclusive. Temperature-dependent measurements were performed as a function of increasing temperature (i.e., low to high), and the data presented is at equilibrated temperature. Salinity-dependent measurements were likewise performed as a function of increasing concentration, with SDS concentration varied at a fixed salt concentration. Solution changes were made by pumping at least 20 mL of fresh solution through the cell.

One brush, with an interfacial volume,  $\hat{V}_I$ , of 1400 Å is studied with ellipsometry in this section. The hydrated structure of this brush was analysed with a custom model in our *refellips* package. In brief, *refellips* uses the framework of *refnx* [141] with the optical transfer matrix method of Byrnes [260] to model ellipsometric parameters  $\Psi$  and

$\Delta$ . Here, we use the model developed in chapter 4 to describe the polymer brush layer. Minimal changes were required to adapt this model for use with ellipsometry. Instead of performing a  $\phi_{\text{poly}}$  weighted sum of two scattering length density (SLD) values (for the polymer and the solvent), as in the NR model, we instead use two RI values to describe the brush layer (often termed an EMA). The thickness bounds on the proximal layer also had to be increased. Further details are included in appendix F. PNIPAM and water were modelled from refractive index data reported by Brasse et al. [261] and Hale and Query [262], respectively.

### 6.2.5 Quartz crystal microbalance with dissipation monitoring

Quartz crystal microbalance with dissipation monitoring (QCM-D) measurements were carried out as a function of concentration and temperature. In all experiments all four cells in the Qsense analyser were utilised, two cells contained blank silica-coated sensors, while the remaining cells contained silica-coated sensors decorated with 130 and 200 Å grafted-from PNIPAM brushes. The cells were all filled with identical solutions, using a pump rate of  $0.3 \text{ mL min}^{-1}$  and a minimum pumped volume of 1.5 mL. All experiments began in MilliQ water, and were not commenced until all sensor frequencies exhibited less than  $0.1 \text{ Hz min}^{-1}$  drift; this typically occurred around an hour after the cells were filled. Surfactant concentration sweeps were always conducted from low to high concentration, and sensors and tubing were washed with ethanol before surfactant identity was changed. Temperature sweeps were conducted from low to high with a minimum equilibration time of 20 min and were monitored through the inbuilt thermostat. Temperature effects on sensor frequency were accounted for via the method outlined in section 1.5.6.

### 6.2.6 Neutron reflectometry

Specular reflectometry measurements were made at angles of  $0.6^\circ$  and  $3.6^\circ$  for dry measurements and  $0.8^\circ$  and  $3.5^\circ$  for solvated measurements, yielding useful data within  $Q$ -ranges of  $0.0073$  to  $0.31 \text{ \AA}^{-1}$  and  $0.0096$  to  $0.31 \text{ \AA}^{-1}$  respectively. The two angles were reduced using the reduction protocols outlined in section 1.5.3. Solvated experiments were carried out in a standard solid-liquid cell (silicon backed) sandwiched between two heat-exchange plates, the temperature of which was controlled by a Julabo FP50-HE heater/chiller unit. The experiments were performed in  $\text{D}_2\text{O}$  to maximise contrast between the brush and the solvent, and in water contrast-matched to the SLD of PNIPAM (19.7 vol%  $\text{D}_2\text{O}$ , balance  $\text{H}_2\text{O}$  — hence refereed to as  $\text{CM}_{\text{poly}}$ ) to highlight scattering from deuterated surfactants (see appendix A for SLDs). Deuterated surfactants were used exclusively here, as they

either approximately matched the SLD of  $D_2O$  — and hence did not interfere in the determination of brush structure — or possessed high contrast in the  $CM_{poly}$  solution (see appendix A). Hydrogenous surfactant would have interfered with the determination of brush structure and not been visible in  $CM_{poly}$  solution; as such, they are not used in any of the unconfined surfactant studies. For a thorough description of the NR technique, refer to section 1.5.3.

Two PNIPAM brush coated wafers were used for the NR study in section 6.3. This was done so that measurement and sample equilibration could be conducted in parallel during the NR beamtime. One wafer was used for SDS and  $C_{12}E_5$  measurements, while the other was used for DTAB and CTAB measurements. Aside from improving this experiment’s time efficiency, this decision removed the possibility of the complexation of cationic and anionic surfactants. Both wafers were synthesised using the same methodology (see section 1.4), and both wafers had similar  $\hat{V}_I$  (112 and 116 Å, respectively). One PNIPAM brush coated wafer was used for the NR study in section 6.5. The wafer was synthesised using the methodology in section 1.4, and has a  $\hat{V}_I$  of 225 Å.

In section 6.4, we use NR coupled with the unique sample environment detailed in chapter 5 to study polymer brush systems under molecular confinement. For a detailed discussion of the sample environment, temperature control method, and data analysis procedure, see chapter 5. Two PNIPAM brush coated wafers were used for the NR confinement study, one for elevated temperature experiments, and one for elevated stress experiments, with  $\hat{V}_I$  of 165 and 150 Å respectively. In line with findings in chapter 5, we allow for at least 6 h of equilibration before each of the measurements reported in this section. All experiments are performed in the direction of increasing brush compression, that is, increasing temperature or increasing stress. Unlike in previous confinement experiments (chapter 5, the work of Abbott et al. [79]), we use the same brush-coated surface for multiple confinements; this offers a significant advance on prior confinement measurements by removing sample-to-sample variation from the analysis. We verified that the brushes remained undamaged after every confinement by rehydrating in  $D_2O$  and conducting NR measurements at 20 and 40 °C (Fig. I1); these measurements also show that SDS can be completely removed from the brush layer after confinement. In the confined experiments,  $H_2O$  is used as a solvent. For this reason, hydrogenous SDS is used when examining the polymer structure, while deuterated SDS is used when examining the distribution of surfactant within the layer.



### 6.2.7 Analysis of reflectometry data

Parameters such as the silica layer thickness and interfacial volume were characterised as outlined in chapter 4 for the wafers used in sections 6.3 and 6.5, and are documented in Figures E2, E4 and E7 in the appendix. Parameters for the wafers used in section 6.4 were determined from the dry wafer reflectometry and are documented in Figures E5 and E6 in the appendix. The distribution of brush thickness over the wafers (i.e., the smoothness) was quantified with an ellipsometry map, see Figures E8–E12 in the appendix.

The methodology outlined in chapter 4 was used to model the unconfined polymer structure in  $D_2O$ ; one of the wafers used here (for SDS and  $C_{12}E_5$  surfactant identity experiments) is the same as that used for the exemplar study in that chapter (see Fig. 4.7). When modelling brushes in surfactant solutions this method was modified by allowing the 2<sup>nd</sup> knot to exceed the volume fraction of the first. This allowed for a degree of non-monotonicity within the layer that could arise due to interactions between the polymer, surfactant and silica surface, whilst still constraining monotonicity in the tail of the brush. We allow non-monotonicity because it is possible that deuterated surfactant becomes trapped in the brush during the temperature-driven collapse, leading to non-monotonic volume fraction profiles. Unlike prior implementations of non-monotonic brush profiles [102, 263] where they are used because no satisfactory monotonic profiles can be found, here we allow non-monotonicity because we believe such structures to be possible in polymer brush-surfactant systems. The profiles presented in the results are taken from a parallel-tempered Markov chain Monte Carlo (PT-MCMC) treatment of the data run for 35 000 steps, as described in chapter 4. The presented profiles are chosen from the profile distributions produced. Generally, profiles did not exhibit multi-modality; in cases where they did, the profile that was consistent with the trend observed across concentrations and temperatures was chosen.

The  $CM_{poly}$  datasets were modelled with a modified version of the freeform profile used for the brush, detailed in appendix J1. Briefly, the knots are defined directly by volume fraction, and the extent of the spline region is governed by a thickness parameter (which can vary), not the adsorbed amount; all else is the same as described in chapter 4. The extent of the spline used to model the surfactant region is constrained at  $\pm 10\%$  of the polymer’s thickness at the corresponding condition; this constraint was made to reduce the size of the solution space. The profiles were optimised using the PT-MCMC approach described in chapter 4.

## 6.3 Results: Surfactant identity and concentration

Here, the effect of several cationic, nonionic and anionic surfactants on the thermoresponse of a PNIPAM brush are studied via ellipsometry, QCM-D, FAOR, and NR. Surfactants are chosen so that they had similar tail lengths, to keep this component of the interaction constant. The structure of the brush is measured as a function of surfactant identity and concentration by ellipsometry and NR, while QCM-D, FAOR, and contrast-matched NR provide insight into surfactant adsorption into the brush layer.

### 6.3.1 Ellipsometry

The ellipsometry measurements were carried out on two brushes, with thicknesses of 200 and 610 Å (Fig. 6.8 and 6.9), respectively. These two brushes allow us to examine the potential effects of polymer molecular weight on PNIPAM-surfactant behaviour. Different modelling techniques were required for each brush thickness; these techniques are documented in section 6.2.4. The ellipsometry experiments are summarised in Figure 6.10,

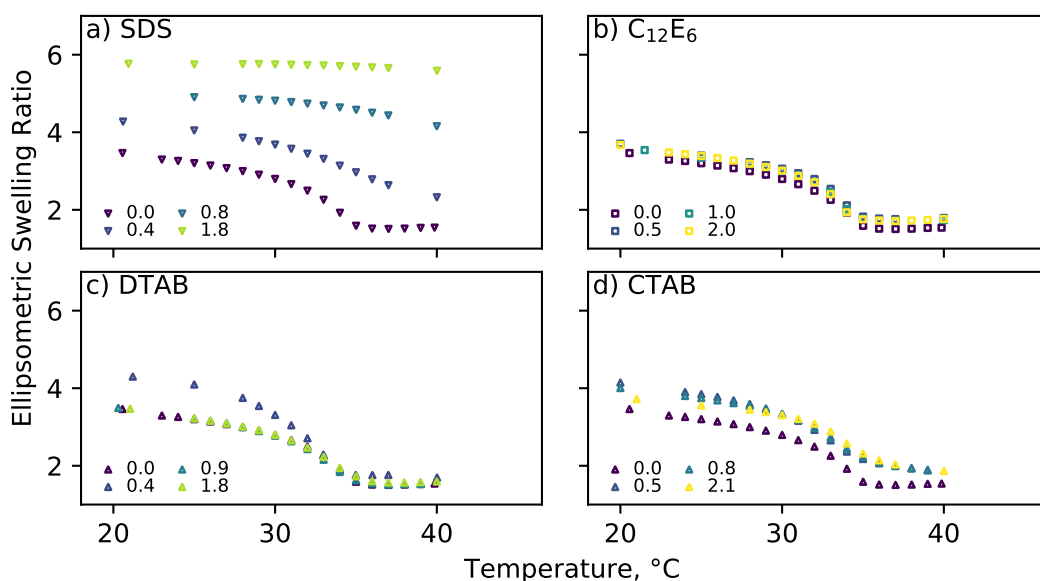


Figure 6.8: Thermoresponse of a 200 Å PNIPAM brush in different surfactant solutions as measured by ellipsometry and analysed with a single EMA slab in CompleteEASE, the swelling ratio plotted here is twice the layer thickness over  $\hat{V}_1$ . Surfactant concentrations are provided in the legends and are given as multiples of the  $\text{CMC}^\ominus$ . SDS dramatically changed the thermoresponse, shifting the CST beyond the temperature range studied at around  $1 \times \text{CMC}^\ominus$ .  $\text{C}_{12}\text{E}_6$ , DTAB and CTAB do not appreciably affect the CST;  $\text{C}_{12}\text{E}_6$  has no effect at all, while the cationic surfactants change the thickness of the layer at some conditions, but not its thermoresponse (see Fig. 6.10). At low temperatures ( $<25^\circ\text{C}$ ) CTAB may be below its Kraft point; see section 6.1.1 for implications.

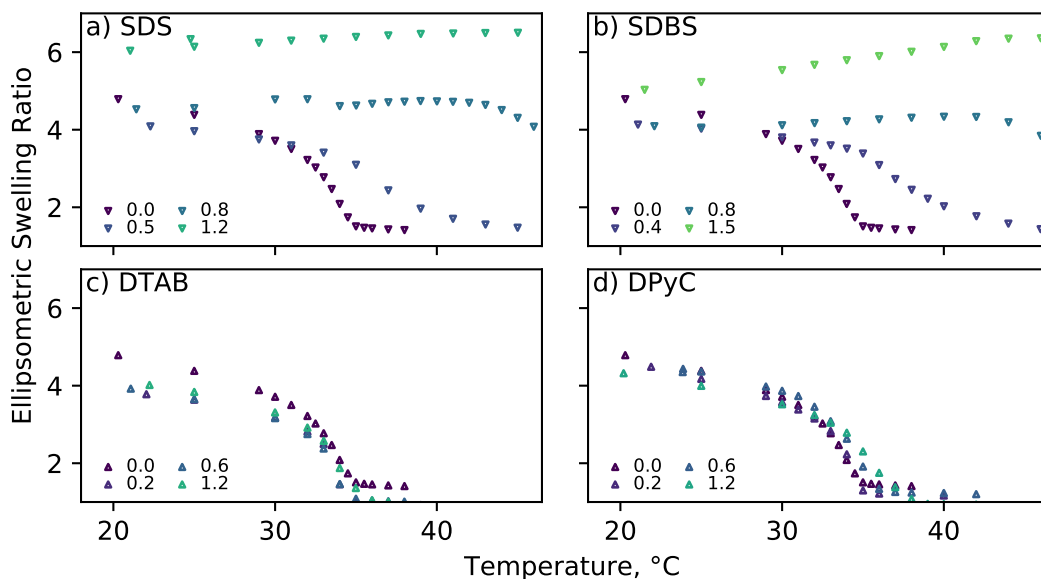


Figure 6.9: Thermoresponse of a 610 Å PNIPAM brush in different surfactant solutions as measured by ellipsometry and analysed with a graded EMA slab in CompleteEASE; the swelling ratio plotted here is twice the first moment (see Eq. 1.6) over  $\hat{V}_I$ . Surfactant concentrations are provided in the legends and are given as multiples of the  $\text{CMC}^\ominus$ . SDS and SDBS both dramatically changed the thermoresponse of the PNIPAM, shifting the CST beyond the temperature range studied at around  $1 \times \text{CMC}^\ominus$ . The cationic surfactants studied here do not appreciably affect the CST (see Fig. 6.10).

which plots the CST as a function of surfactant identity and concentration. The CST is taken as the centre of the sigmoidal fit to the data in Figures 6.8 and 6.9. Sigmoidal fits typically matched the collected data well, but are not shown in Figures 6.8 and 6.9 as they impede understanding. The thermoresponse was considered suppressed (i.e., no CST) when there was no inflexion point in the thickness vs temperature curves.

An examination of Figures 6.8, 6.9 and 6.10 reveals that anionic surfactants (at least sulphate-headed surfactants) have a drastic effect on the thermoresponse of PNIPAM, whilst nonionic and cationic surfactants do not. The anionic surfactants SDS and SDBS completely suppressed the collapse of the PNIPAM layer over the investigated temperature range at concentrations in excess of  $1 \times \text{CMC}^\ominus$ . Conversely,  $\text{C}_{12}\text{E}_6$ , DTAB, DPyC and CTAB did not appear to shift the transition temperature from its nominal aqueous value of 32 °C (Fig. 6.10). We remind the reader that  $\text{CMC}^\ominus$  refers to the of the surfactant in pure water at 25 °C. The brush thickness was not a factor in the overall behaviour of the polymer-surfactant system; both 200 and 610 Å brushes exhibited a swelling ratio of  $\approx 6$  at  $1 \times \text{CMC}^\ominus$  SDS and 25 °C, with no thermoresponse over the investigated temperature range (Fig. 6.8 and 6.9). However, the specific swelling ratios and response varied slightly between the intermediate SDS concentrations; these discrepancies are likely linked to the different modelling techniques and so are not of further interest for discussion here.

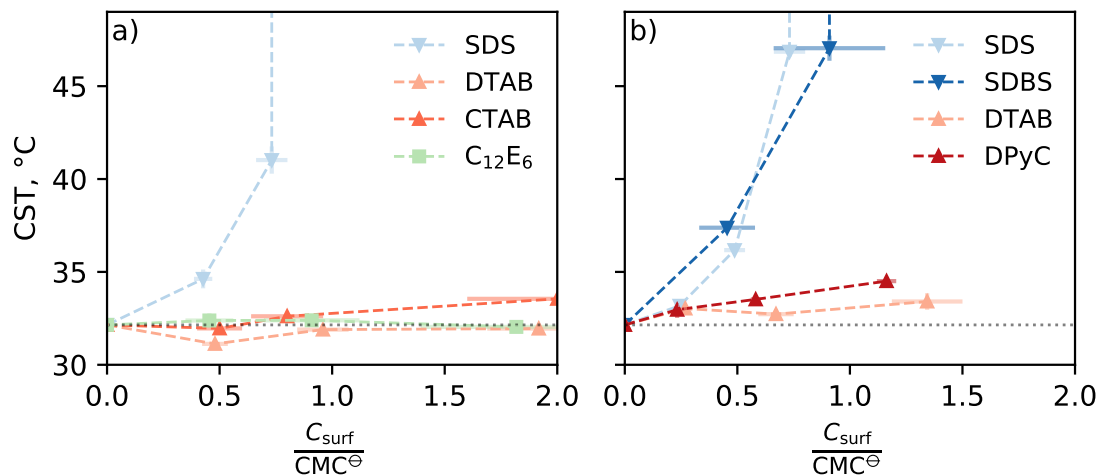


Figure 6.10: CST of PNIPAM brushes derived from fitting a sigmoid to the data in Figures (a) 6.9 and (b) 6.8. Vertical lines indicate that the brush did not exhibit a CST in the temperature range probed at surfactant concentrations above this point. The horizontal error bars represent the uncertainty in the surfactant CMC (one standard deviation, from the literature values summarised in Fig. 6.2).

Similarly, the brush thickness did not change the (negligible) effect of cationic surfactants. Patel et al. [241] show that polymer molecular weight can effect the interaction of PNIPAM with cationic and anionic surfactants for low molecular weight ( $<12$  kDa) polymers. The polymers here have molecular weights of approximately 200 to 600 kDa (Fig. 6.8 and 6.9, respectively; see Table 1.1); for polymers of this size molecular weight does not appear to have a significant effect on the interaction of PNIPAM with surfactant.

It is worth discussing the slight thickness variations in DTAB and CTAB in Figures 6.8 and 6.9. We will start with Figure 6.9c, where the brush thickness appears to decrease upon the addition of DTAB. DTAB was the last surfactant run on this wafer, and as such it is likely that some degrafting occurred, resulting in a slightly thinner brush during the DTAB experiment. The variations in Figure 6.8 are harder to explain, and are likely modelling artefacts, as  $200 \text{ \AA}$  is approaching the minimum layer thickness to which ellipsometry is sensitive. Furthermore, ellipsometry will be weakly sensitive to the presence of surfactant in the system, as surfactants have a higher RI than  $\text{H}_2\text{O}$  (Fig. 6.7), so structures formed by surfactants could be interfering in the modelling process.<sup>ii</sup> Regardless, these variations are insignificant compared to the effect of the anionic surfactants on the brush structure and CST (Fig. 6.10).

<sup>ii</sup>we later support ellipsometry results with NR, which can be made insensitive to surfactant structure through selective deuteration of components.

### 6.3.2 Quartz crystal microbalance with dissipation monitoring

QCM-D is sensitive to both the structure and adsorbed mass of layers formed on the surface of a quartz resonator (see section 1.5.6). Isothermal QCM-D results are presented in Figure 6.11, which shows the change in frequency,  $\Delta f$ , and the change in dissipation,  $\Delta D$ , as a function of surfactant concentration. The signal is plotted both as recorded (Fig. 6.11a,b) and after having the signal from a bare silica wafer in an identical solution subtracted (Fig. 6.11c,d). This baseline correction subtracts the signal corresponding to the adsorption of the surfactant onto an untreated silica surface, and accounts for any (minor) change in signal due to variation in the density, viscosity or temperature of the solution. Both unmodified and baseline-corrected signals in Figure 6.11 reveal that  $\Delta f$  and  $\Delta D$  are much greater upon the addition of SDS than CTAB or  $C_{12}E_6$ . A negative  $\Delta f$  and positive  $\Delta D$ , as seen for SDS, is indicative of a swelling brush [48]. For a swelling brush,  $\Delta f$  is caused by the adsorption of both surfactant and solvent molecules into the swelling layer. Conversely, a negative  $\Delta f$  and a  $\Delta D$  of zero, as seen for CTAB and  $C_{12}E_6$ , is indicative of adsorption within the brush layer without any change in brush swelling — one explanation for these observations is that CTAB and  $C_{12}E_6$  are adsorbing to the silica-polymer interface.

The baseline-corrected signal suggests that that CTAB and  $C_{12}E_6$  signal could be explained by adsorption at the substrate (rather than adsorption into the polymer layer), as  $\Delta f$  and  $\Delta D$  are both effectively zero in the baseline-corrected signal (Fig. 6.11c,d). Examining the differences between the overtones in Figure 6.11 also supports the substrate-adsorption model. This substrate interaction is not surprising, as both CTAB and  $C_{12}E_6$  have been shown to adsorb to silica surfaces [264, 265]. Higher harmonics do not penetrate as far into the brush layer, and as such are sensitive to different regions within the brush than lower harmonics [92]. For SDS, the change in frequency decreases at higher harmonics, which indicates that the adsorbed mass is more concentrated at the brush periphery. A greater increase in mass in the brush periphery is consistent with both the swelling of a brush with a parabolic  $\phi_{\text{poly}}$  profile and preferential adsorption of surfactant into the brush tail. Conversely, the frequency and dissipation do not change as a function of overtone number<sup>iii</sup> with the addition of CTAB and  $C_{12}E_6$ , indicating that there is no layer swelling and that the adsorbed mass is concentrated at the base of the brush (detectable by all overtones).

The behaviour of the PNIPAM-SDS system as a function of temperature was also investigated by QCM-D, with results shown in Figure 6.12. The addition of SDS results

---

<sup>iii</sup>the 3<sup>rd</sup>, 5<sup>th</sup> and 9<sup>th</sup> overtones are shown for all surfactants in Fig. 6.11, but are identical for cationic and nonionic surfactants

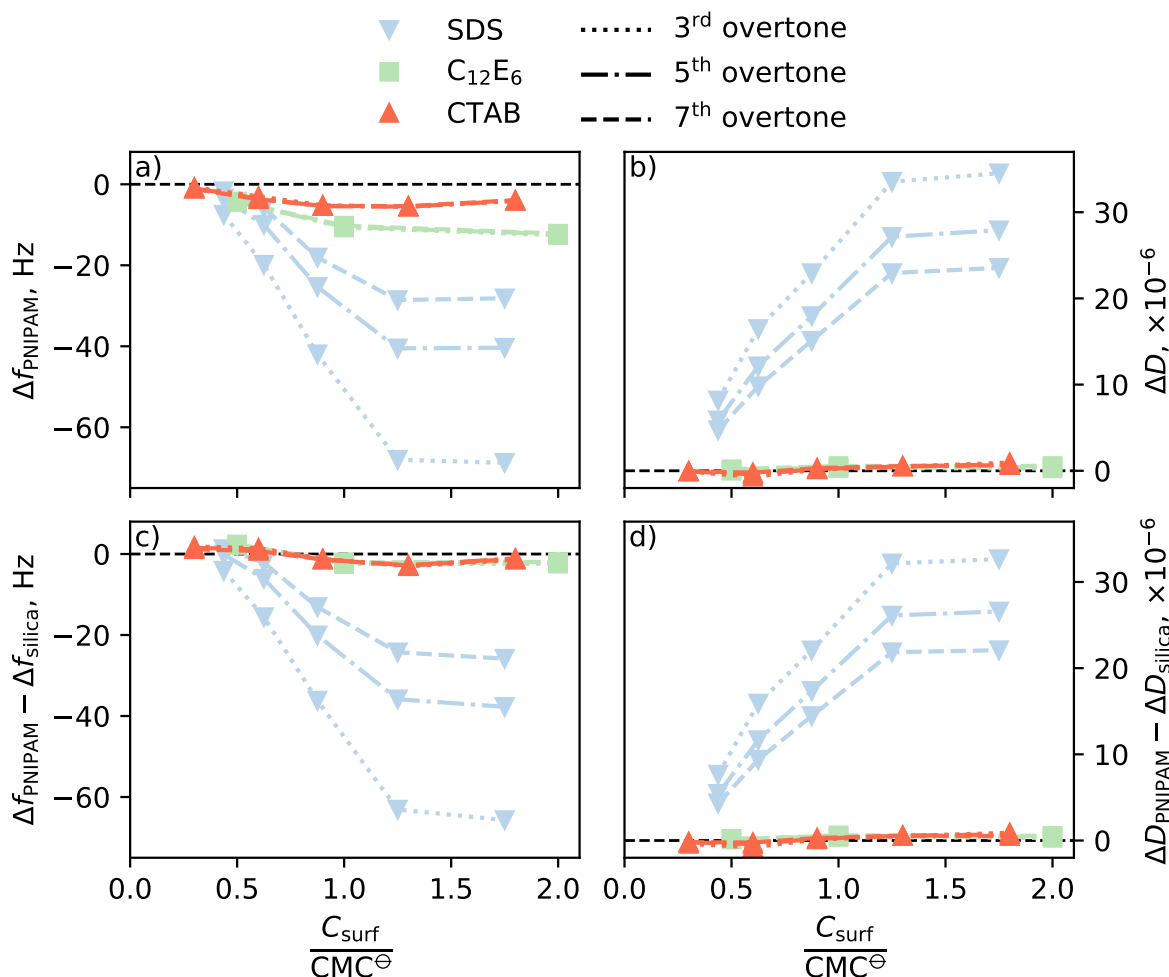


Figure 6.11: Change in (a,c) frequency and (b,d) dissipation for overtones 3, 5 and 7 for a 130 Å PNIPAM brush as a function of surfactant concentration and identity at 20 °C. Plots (c) and (d) have had the signal collected from a bare silica QCM-D wafer (in an identical solution) subtracted from that of PNIPAM-coated wafer. The addition of SDS causes significant changes in both  $\Delta f$  and  $\Delta D$ , while CTAB and  $C_{12}E_6$  induce only small changes in  $\Delta f$ . This indicates that SDS causes PNIPAM to swell, while CTAB and  $C_{12}E_6$  adsorb into the brush without promoting layer swelling. (c) and (d) indicate that most of the signal from CTAB and  $C_{12}E_6$  solutions can be accounted for by interaction with the substrate. Here CTAB is below its Kraft point, which causes its behaviour to plateau before reaching  $1 \times CMC^\Theta$ ; see section 6.1.1 for further implications. Raw data can be found in Figures H1-H3

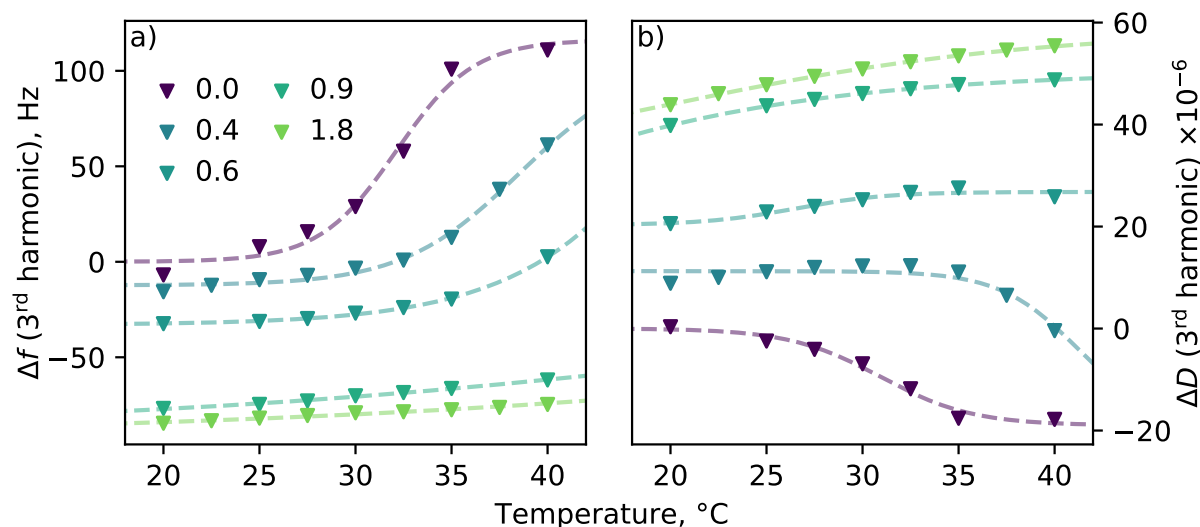


Figure 6.12: (a) Frequency and (b) dissipation showing the thermoresponse of PNIPAM in SDS solutions. As temperature is increased in pure water  $\Delta f$  increases while  $\Delta D$  decreases, corresponding to a layer that becomes less massive (the brush expels water as it collapses) and less mechanically coupled to the solvent. As SDS is added  $\Delta f$  decreases, while the  $\Delta D$  increases, indicating that the brush is adsorbing mass (water or SDS) and swelling.  $\Delta f$  and  $\Delta D$  are scaled so as to be zero in pure water at 20 °C. Raw data can be found in Figures H4-H8.

in a significant increase in  $\Delta f$  and decrease in  $\Delta D$  for the PNIPAM coated QCM-D wafer at 20 °C (as in Fig. 6.11). As temperature increases at the  $0 \times \text{CMC}^\ominus$  condition, a positive  $\Delta f$  and negative  $\Delta D$  indicate a collapsing brush. As surfactant concentration is increased this trend disappears, with  $\Delta f$  and  $\Delta D$  values becoming relatively independent of temperature. This indicates that the layer swells as surfactant is added, and no longer undergoes a thermal collapse at the temperature range investigated — the same behaviour observed via ellipsometry (Fig. 6.8, 6.9).

### 6.3.3 Fixed-angle optical reflectometry

FAOR was used to provide further insight into the adsorption of surfactants within the brush layer, as it is less sensitive to layer swelling than QCM-D. In QCM-D experiments the  $\Delta f$  is correlated to adsorbed/bound mass, but does not discriminate between solvent and surfactant molecules. Conversely, FAOR is sensitive to changes in RI at the interface so is insensitive to the presence of solvent (changing  $\phi_{\text{poly}}$  means it is still weakly sensitive to layer swelling, this will be discussed later). Figure 6.13 shows the change in adsorbed mass as a function of surfactant concentration for several different surfactants; three key conclusions can be drawn from these results. Firstly, the adsorbed mass of surfactant

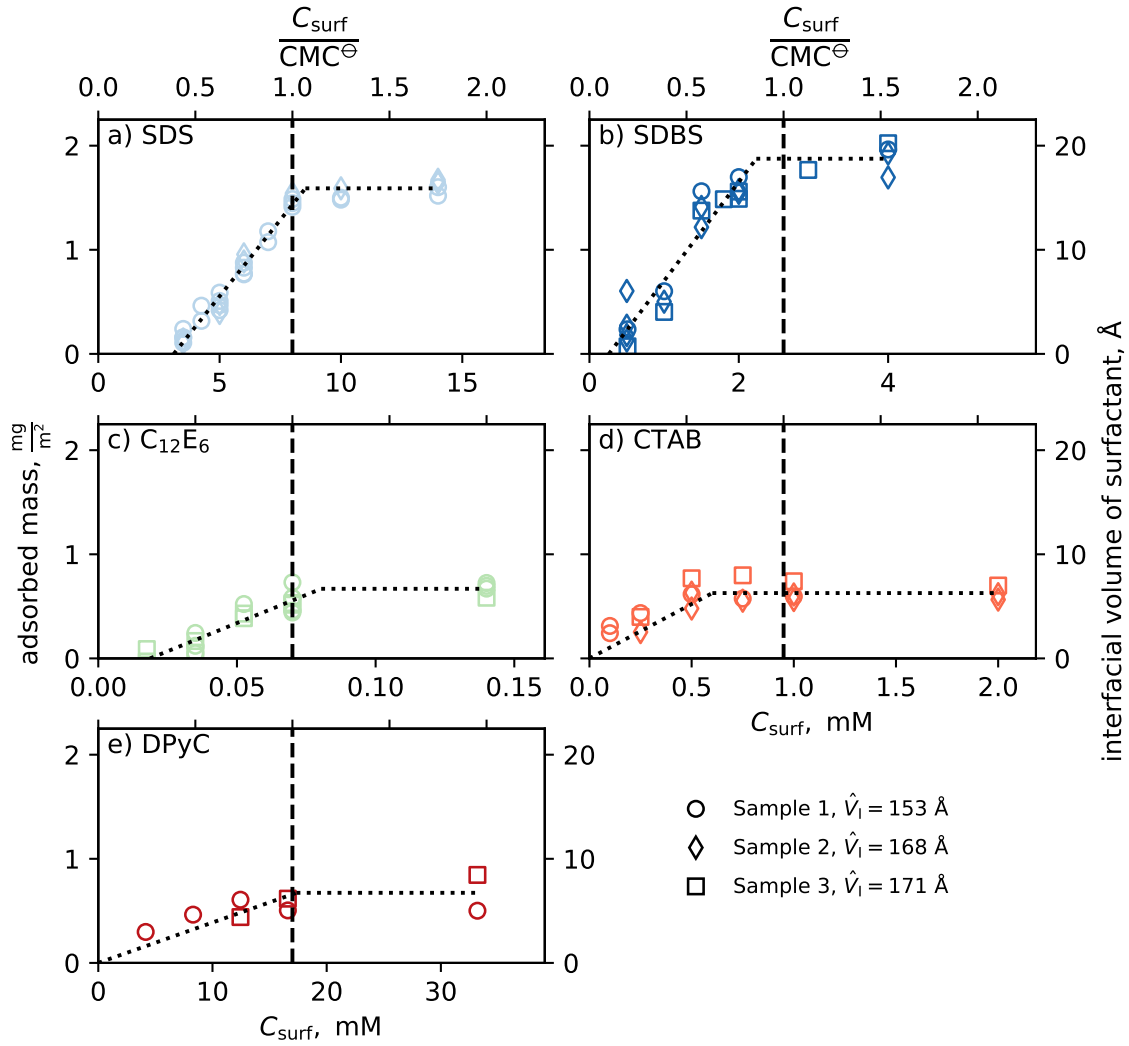


Figure 6.13: FAOR results for different surfactants. Adsorption appears to scale linearly with surfactant concentration from the CAC up to the CMC. Here CTAB is below its Kraft point, which causes its behaviour to plateau before reaching  $1 \times \text{CMC}^\ominus$ ; see section 6.1.1 for further implications. The anionic surfactants examined exhibit much higher adsorbed masses than the nonionic and cationic surfactants. Measurements were carried out on three different substrates with similar thicknesses, indicated by different marker symbols. The vertical dashed line indicates the  $1 \times \text{CMC}^\ominus$  point, the dotted lines are a guide to the eye.



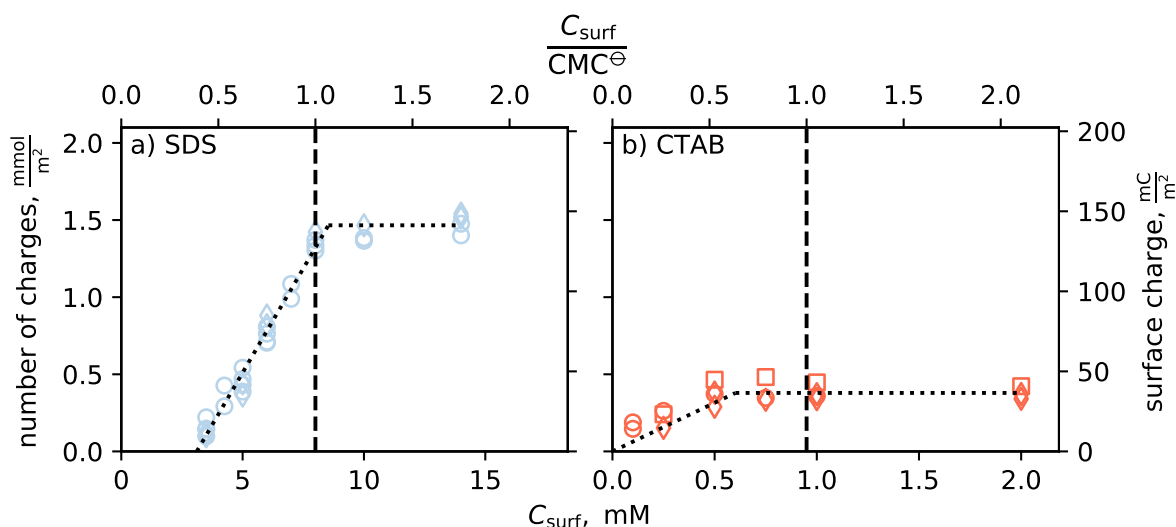


Figure 6.14: Amount of charge within the brush layer, calculated from FAOR results (Fig. 6.13), the molar mass of respective surfactants and the degree of micelle ionisation for a) SDS and b) CTAB. The concentration of charges is three times greater for SDS than for CTAB above  $1 \times \text{CMC}^\ominus$ ; shortcomings of the FAOR method mean that this value is likely underestimated. The vertical dashed line indicates the  $1 \times \text{CMC}^\ominus$  point, the dotted lines are a guide to the eye.

is roughly linear between the CAC and CMC and plateaus after the CMC is reached. Secondly, the adsorbed mass of anionic surfactants at  $1 \times \text{CMC}^\ominus$  is higher than comparable cationic or nonionic surfactants. Thirdly, the adsorbed mass of cationic and nonionic surfactants is non-zero; instead, they are approximately one-third of the value for the anionic surfactants. This third point implies that while all surfactants are concentrated within the brush layer (to some degree), only anionic surfactants have an appreciable effect on polymer structure. However, we must stress here that the swelling in PNIPAM layer during a FAOR experiment will lead to a reduction in the signal (see section 6.2.3), which will result in the calculated adsorbed amount of surfactant being underestimated; this is likely the case for the SDS system here.

Of course, if the polymer-surfactant system follows the pearl-necklace model, then the parameter of significance is the charge on the adsorbed micelles, which can be calculated from the mass of the adsorbed surfactant and the degree of micelle ionisation. Figure 6.14 approximates the adsorbed charge for SDS and CTAB based on the adsorbed mass, the surfactant molecular weight and the degree of micelle ionisation. We find that the adsorbed charge (as determined by FAOR) is substantially higher for SDS than it is for CTAB (and obviously infinitely greater than for nonionic  $\text{C}_{12}\text{E}_6$ ). The implications of this difference, and whether they can describe the difference in the behaviour of the PNIPAM-surfactant systems, will be discussed in section 6.3.5.

### 6.3.4 Neutron Reflectometry

Neutron reflectometry was used to determine the structure of PNIPAM brushes as a function of surfactant identity and concentration. SDS and  $C_{12}E_5$  experiments were carried out on the same wafer, with results shown in Figure 6.15. Measurements in CTAB solutions were carried out on a separate wafer, with results presented in Figure 6.16. For each surfactant, the system behaviour is investigated at  $0.5$  and  $2 \times CMC^\ominus$  at  $25$ ,  $32$  and  $40^\circ C$ .

We first discuss the features evident in the reflectometry data, shown in Figures 6.15b–j and 6.16b–f. In water, the reflectometry data collected from both wafers transition from featureless profiles (with a single fringe at  $Q \approx 0.08$  from the interior layer) to profiles exhibiting two distinct Kiessig fringes (Fig. 6.15b and 6.16b). This transition matches the swollen-to-collapsed transition observed by prior NR studies of brush systems [20, 73, 84, 85, 109]. Reflectometry profiles collected from PNIPAM in  $C_{12}E_5$  (Fig. 6.15h,j) and CTAB (Fig. 6.16d,f) solutions follow a similar trend to the pure  $D_2O$  profiles at both  $0.5$  and  $2 \times CMC^\ominus$ , strongly suggesting that these surfactants do not significantly change the polymer brush’s structure. While the reflectometry from the PNIPAM brush in SDS at  $25^\circ C$  is similar to that of the brush in water, the reflectometry profiles differ significantly at higher temperatures. At  $0.5 \times CMC^\ominus$  of SDS the fringe remains at  $Q = 0.08$  at  $32^\circ C$ , whereas in pure water it moves to  $Q = 0.04$ , while the fringe spacing at  $40^\circ C$  is less regular than in pure water, indicating that the brush layer is less well defined. At  $2 \times CMC^\ominus$  of SDS the reflectometry profile is independent of temperature, most closely resembling the water profile at  $25^\circ C$ . These reflectometry profiles suggests that SDS causes layer swelling at  $0.5 \times CMC^\ominus$  and completely suppresses the thermoresponse of PNIPAM at  $2 \times CMC^\ominus$ , consistent with prior ellipsometry and QCM-D experiments (Fig. 6.8, 6.9 and 6.11).

The reflectometry profiles discussed above were analysed using the freeform modelling method documented in chapter 4.<sup>iv</sup> Reassuringly, the modelled profiles support the interpretation drawn from the reflectometry data in the above paragraph. PNIPAM is more swollen at  $0.5 \times CMC^\ominus$  of SDS than at  $0 \times CMC^\ominus$ , while the thermoresponse is completely suppressed at  $2 \times CMC^\ominus$ . The thermoresponse of PNIPAM in other surfactants is mostly unchanged. The freeform modelling process does, however, produce several interesting smaller features that are worthy of discussion.

Firstly, the presence of all surfactants at  $2 \times CMC^\ominus$  and  $25^\circ C$  appear to reduce the volume fraction of the interior layer. This indicates that the surfactant is adsorbing at the silica–polymer interface, displacing physisorbed PNIPAM chain segments; this interpreta-

---

<sup>iv</sup>The data and profiles in Figure 6.15 are the same as those used in the demonstration of the method in chapter 4

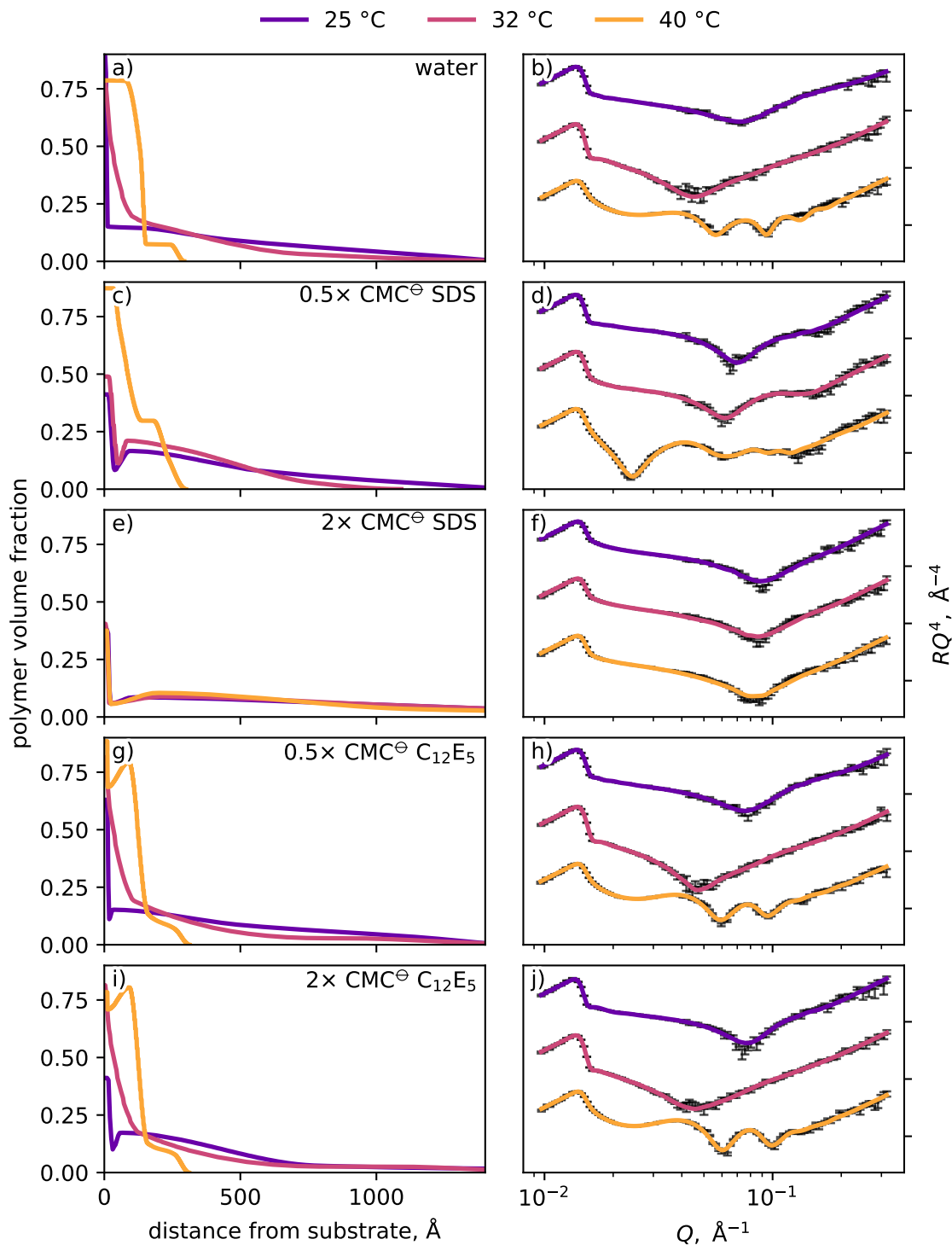


Figure 6.15: (*left panels*) Polymer volume fraction profiles with (*right panels*) corresponding modelled NR profiles and collected data. The NR profiles are vertically offset and scaled by  $Q^4$  for clarity. All measurements were carried out on the same wafer with  $\hat{V}_1 = 112 \text{ Å}$  using the fitting methodology outlined in chapter 4. The solvent environment for each set is as follows a-b)  $\text{D}_2\text{O}$ , c-d)  $0.5 \times \text{CMC}^\ominus$  d-SDS in  $\text{D}_2\text{O}$ , e-f)  $2 \times \text{CMC}^\ominus$  d-SDS in  $\text{D}_2\text{O}$ , g-h)  $0.5 \times \text{CMC}^\ominus$  d- $\text{C}_{12}\text{E}_5$  in  $\text{D}_2\text{O}$ , i-j)  $2 \times \text{CMC}^\ominus$  d- $\text{C}_{12}\text{E}_5$  in  $\text{D}_2\text{O}$ . Consistent with other techniques, NR shows that SDS has a dramatic effect on the thermoresponse and structure of PNIPAM brushes;  $\text{C}_{12}\text{E}_5$  is observed to have no appreciable effect on either.

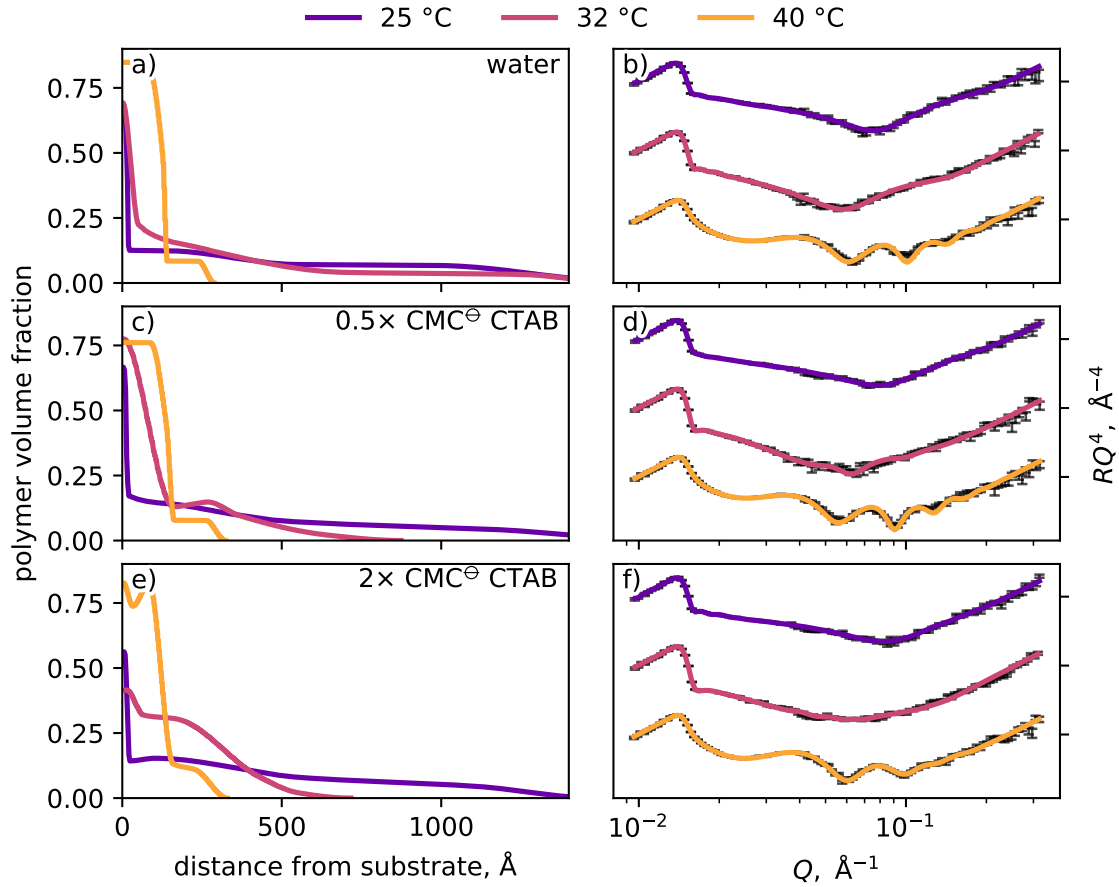


Figure 6.16: (*left panels*) Polymer volume fraction profiles with (*right panels*) corresponding modelled NR profiles and collected data. The NR profiles are vertically offset and scaled by  $Q^4$  for clarity. All measurements were carried out on the same wafer with  $\hat{V}_1 = 116 \text{ \AA}$  using the fitting methodology outlined in chapter 4. The solvent environment for each set is as follows a-b)  $\text{D}_2\text{O}$ , c-d)  $0.5 \times \text{CMC}^\Theta$  d-CTAB in  $\text{D}_2\text{O}$ , e-f)  $2 \times \text{CMC}^\Theta$  d-CTAB in  $\text{D}_2\text{O}$ . While the 20 and 40 °C structures in both d-CTAB (c-f) concentrations do not differ from those measured in  $\text{D}_2\text{O}$  (a-b), the structures at 32 °C are anomalous.

tion supports the conclusions made regarding the interior layer in chapter 2. The second interesting feature generated by the modelling process is the non-monotonic profiles produced for the collapsed brush systems (Fig. 6.15c,g,i and 6.16c,e). Here, a non-monotonic profile refers to a profile where the volume fraction of a component increases with distance from the substrate at some point in the structure. As discussed in section 6.2.7, monotonicity is strictly enforced for pure water samples as no theoretical justification for non-monotonicity in neutral polymer brush profiles exists. However, non-monotonicity is allowed when a surfactant is present. It is tempting to ascribe this non-monotonicity to the presence of surfactant, but it must be noted that the analysis of the collapsed brush in pure water would also produce non-monotonic profiles if allowed. As such, these features could be modelling artefacts or evidence of a yet-unknown brush behaviour (independent of surfactants); we encourage the reader to consider the contrast-matched experiments documented below before deciding on an interpretation.

The last feature that must be addressed are the unusual structures produced at 32 °C for both  $0.5 \times \text{CMC}^\ominus$  CTAB concentrations (Fig. 6.16c, e). While both structures fit into the general swollen-to-collapsed trend expected of PNIPAM in CTAB solutions, they both differ markedly from the profiles produced from the pure water dataset (Fig. 6.16a). At  $0.5 \times \text{CMC}^\ominus$  CTAB an abnormally large interior layer appears, whilst at  $2 \times \text{CMC}^\ominus$  CTAB the volume fraction of the interior layer lower than even the 25 °C data. These structures are likely not fitting artefacts, as similar features are not present in Figure 6.15, and the reflectometry profiles in Figures 6.16d, f are distinct to that in 6.16b. We must then concede that deuterated CTAB is affecting the SLD profile of the PNIPAM brush coated surface in a small way which we do not yet understand. It must be emphasised that, aside from the profiles referenced above, all results indicate that only anionic surfactants have an appreciable effect on the structure and thermoresponse of a PNIPAM brush.

Now, we move on to the data collected from the  $\text{CM}_{\text{poly}}$  system. Here, the primary contribution to the reflectometry profiles comes from surfactant adsorbed within the PNIPAM brush layer because the solvent has been matched to the SLD of PNIPAM (see section 6.3.4). As before, we first discuss the trend in the reflectometry profiles, shown in the insets of Figure 6.17. In each inset two profiles are shown: that from the PNIPAM brush in pure  $\text{CM}_{\text{poly}}$  (where only the silica layer contributes to the reflection pattern) and that from the PNIPAM brush in the deuterated surfactant- $\text{CM}_{\text{poly}}$  mix. Showing these two reflection profiles overlaid emphasises that the presence of deuterated surfactant significantly changes the collected reflectivity profile.

The  $0.5 \times \text{CMC}^\ominus$  SDS sample (inset of Fig. 6.17a, b) displays minimal divergence from the pure  $\text{CM}_{\text{poly}}$  sample at 25 °C, save for the development of a slight fringe at  $Q = 0.1 \text{ \AA}^{-1}$ . This fringe deepens as the sample is heated to 40 °C, which results in the reflectometry

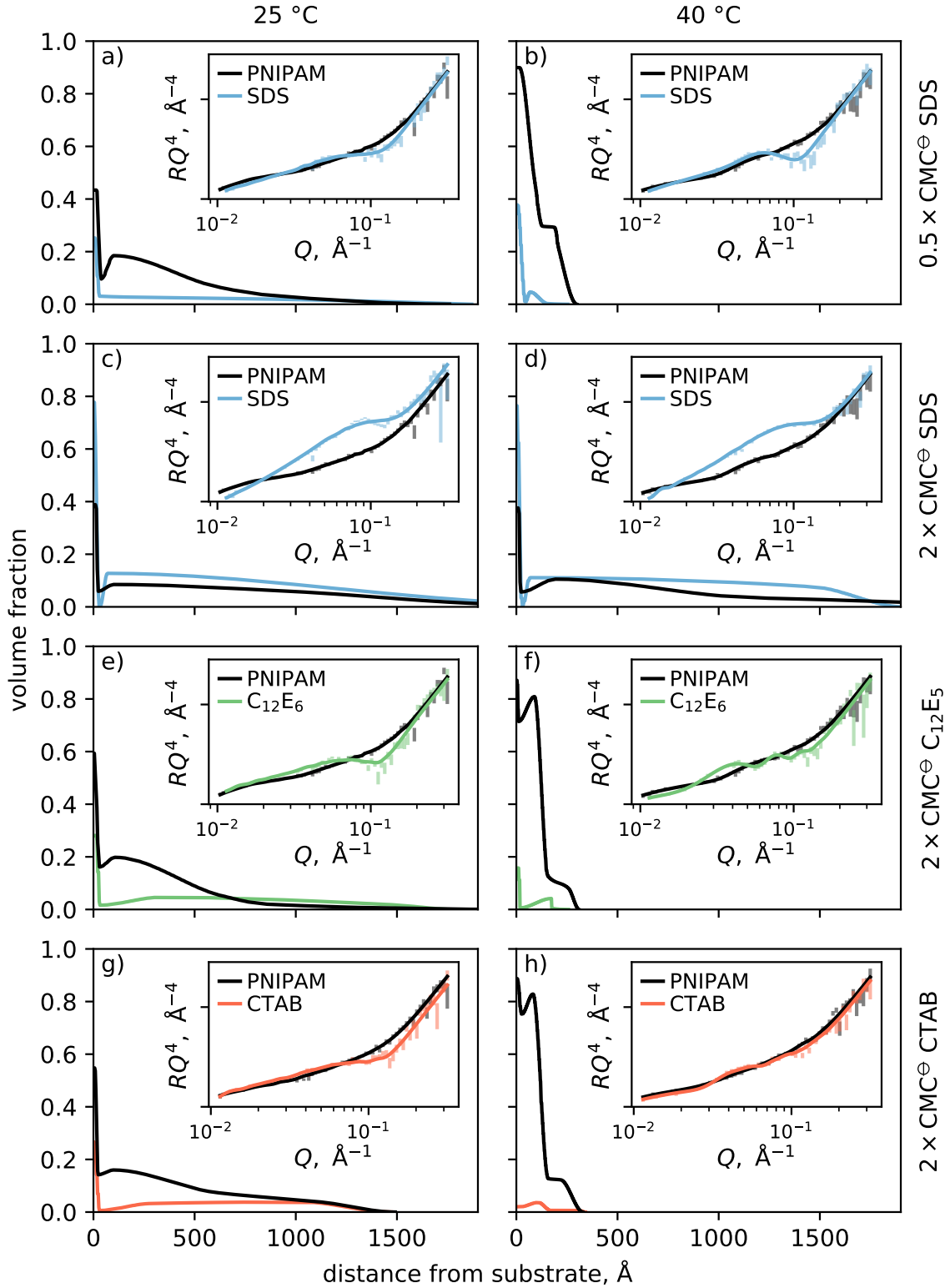


Figure 6.17: SDS, C<sub>12</sub>E<sub>5</sub> and CTAB volume fraction profiles derived from NR experiments where the solvent SLD is matched to that of PNIPAM by mixing H<sub>2</sub>O and D<sub>2</sub>O (CM<sub>poly</sub>). The modelled profiles show all surfactants appear to aggregate at the silica interface and associate with the polymer throughout the entire layer. Polymer volume fraction profiles from fitting the D<sub>2</sub>O contrast data (Fig. 6.15, 6.16) are plotted in black. Reflectometry data from the brush in the absence of surfactant in CM<sub>poly</sub> are plotted in black in the inset, to illustrate that there is a significant change in the reflectometry profile when surfactant is added. SDS associates to a much greater degree than both C<sub>12</sub>E<sub>5</sub> and CTAB.

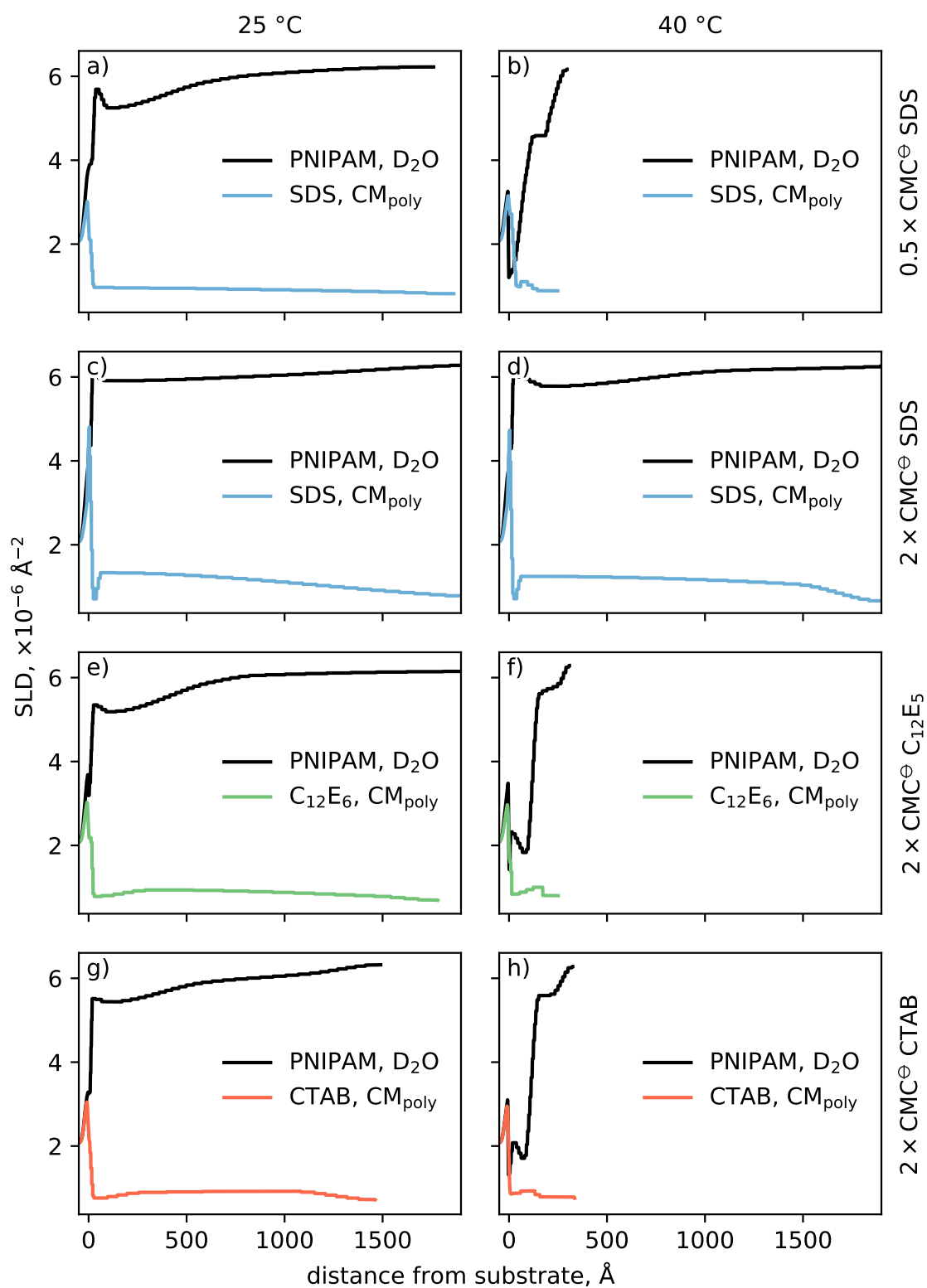


Figure 6.18: SLD profiles corresponding to volume fraction profiles in Figure 6.17.

profile diverging further from that of the pure  $\text{CM}_{\text{poly}}$  sample, indicating that surfactant is being concentrated in the collapsed brush layer. Interestingly, the fringe location does not change, only its depth, indicating that the corresponding feature changes in volume fraction, but not in thickness. The reflectivity of the  $2 \times \text{CMC}^\ominus$  SDS sample (inset of Fig. 6.17c, d) deviates significantly from the pure  $\text{CM}_{\text{poly}}$  sample at both 25 and 40 °C, which is unsurprising given how much of an effect the addition of  $2 \times \text{CMC}^\ominus$  SDS has on the behaviour of PNIPAM. Surprisingly, the reflectivity from the  $2 \times \text{CMC}^\ominus$   $\text{C}_{12}\text{E}_5$  (Fig. 6.17e–f, inset) and CTAB (Fig. 6.17g–h, inset) samples also deviates from the pure  $\text{CM}_{\text{poly}}$  sample. The 25 °C sample roughly resembles that at  $0.5 \times \text{CMC}^\ominus$  SDS and 25 °C, while the 40 °C sample features fringes that correspond to a  $\approx 200$  Å thick layer. These profiles are remarkable, as no change was observed in the corresponding polymer-contrast profiles (Fig. 6.15j compared to b), meaning that surfactant is present within the layer without changing the structure of the layer.

The  $\text{CM}_{\text{poly}}$  datasets were modelled with a modified version of the freeform profile used for the brush, detailed in appendix J1. PT-MCMC sampling, shown in Figure 6.19, reveals several ‘families’ of profiles that have similar posterior probabilities but are structurally very different. This large range of viable profiles is due to the low contrast in the system and the lack of prior information.<sup>v</sup> PT-MCMC allows us both to identify multimodality as a problem and identifies several viable families of profiles (plotted in different colours in Fig. 6.19). We then select the family that is most compatible with the results from our other experiments and take that families profile of best fit<sup>vi</sup> as the final profile (plotted in Fig. 6.17). This clearly demonstrates the usefulness of the uncertainty quantification methodology laid out in chapter 4; without using PT-MCMC sampling, the wrong profile would likely have been accepted for at least one of the datasets in Figure 6.19.

The accepted modelled profiles are presented in Figure 6.17, with corresponding SLD profiles shown in Figure 6.18. These profiles show where in the brush the surfactant is located, and allow us to calculate the volumetric binding ratio,  $\phi_{\text{poly}}/\phi_{\text{surf}}$ , in the bulk of the brush. There is very little surfactant observed in the  $0.5 \times \text{CMC}^\ominus$  SDS,  $2 \times \text{CMC}^\ominus$   $\text{C}_{12}\text{E}_5$  or  $2 \times \text{CMC}^\ominus$  CTAB sample at either 25 or 40 °C. At these conditions, modelling reveals an enriched surfactant region near the substrate, with a uniform distribution of surfactant throughout the rest of the layer. At 40 °C the surfactant seems to be expelled from the polymer layer, as the surfactant:polymer volume ratio is much higher at 25 °C than 40 °C. As might be expected, the surfactant volume fraction is highest in the case

---

<sup>v</sup>We have little information with which to constrain the model. The adsorbed amounts from FAOR are not suitable as they are for a single temperature and we are uncertain of the absolute accuracy due to the effect of brush swelling (discussed in section 6.2.3).

<sup>vi</sup>highest posterior probability



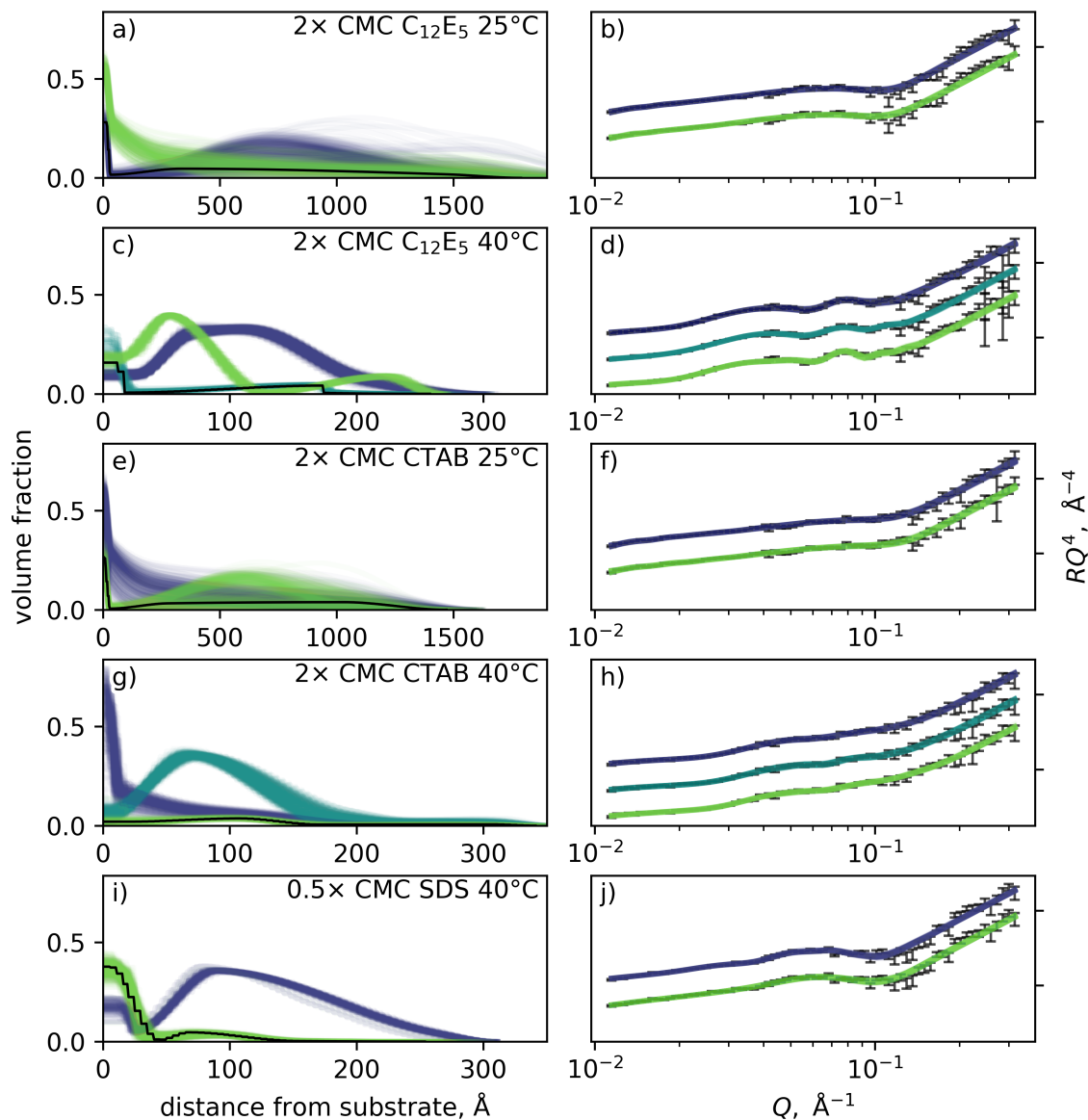


Figure 6.19: Distribution of surfactant volume fraction profiles attained by the PT-MCMC approach outlined in chapter 4 for (a)  $2 \times \text{CMC}^\ominus \text{C}_{12}\text{E}_5$  in  $\text{CM}_{\text{poly}}$  at  $25^\circ\text{C}$  (c)  $2 \times \text{CMC}^\ominus \text{C}_{12}\text{E}_5$  in  $\text{CM}_{\text{poly}}$  at  $40^\circ\text{C}$  (e)  $2 \times \text{CMC}^\ominus \text{CTAB}$  in  $\text{CM}_{\text{poly}}$  at  $25^\circ\text{C}$  (g)  $2 \times \text{CMC}^\ominus \text{CTAB}$  in  $\text{CM}_{\text{poly}}$  at  $40^\circ\text{C}$  (i)  $0.5 \times \text{CMC}^\ominus \text{SDS}$  in  $\text{CM}_{\text{poly}}$  at  $40^\circ\text{C}$ . Corresponding NR profiles are shown in the right panels, with different families plotted against the same data separately; profiles are offset for clarity and each family has a similar fit-quality. The distributions are divided into ‘families’ that possess similar structures post-PT-MCMC sampling, with each family being plotted here in different colours. The data is the same as that shown in Figure 6.17; these datasets are shown here as PT-MCMC analysis indicated they were multimodal. The profile of best fit was chosen from the family that best matched our knowledge of the system; these profiles are plotted in black.

of  $2 \times \text{CMC}^\ominus$  SDS. Once again, an enriched surfactant region is observed near the interface, while the volume fraction of surfactant is proportional to that of the polymer throughout the bulk of the brush. In the bulk of the brush the volumetric binding ratio is approximately equal to 1. There is no obvious feature observed within any of the surfactant volume fraction profiles that would explain the non-monotonicity observed in Figures 6.15 and 6.16. However, the surfactant volume fraction does seem to mimic the polymer volume fraction profile, with depletion regions appearing in the same location in both profiles. It is tempting to argue that the depletion region is due to a electrostatic interaction between the surfactant and the substrate, however, the depletion region is also present for the nonionic surfactant. We conclude that the non-monotonicity does not stem from the presence of the surfactant; it may be a fitting artefact or subtle feature of PNIPAM brushes that is not yet understood. Regardless, it does not affect the overall findings of our study.

### 6.3.5 Discussion

In this section, we have shown via ellipsometry and QCM-D that anionic surfactants swell PNIPAM brushes and suppress their thermoresponse, while cationic and nonionic surfactants do not. QCM-D and FAOR indicated that more anionic surfactant is adsorbed within the brush layer, compared to either cationic and nonionic surfactant. NR confirmed the above findings, revealing the polymer volume fraction profile as well as the volume fraction profiles of various surfactants within the brush. All techniques indicated that the adsorption of the surfactants studied is completely reversible.

Here, we will discuss the behaviour of the various PNIPAM-surfactant systems studied above, starting with the remarkable behaviour of the PNIPAM-SDS system. We then move on to discussing the differences between the anionic systems and the nonionic and cationic systems, concluding that the head-group plays a significant role in the PNIPAM-surfactant interaction. Finally, we propose a model for the system structure based on existing literature and collected evidence.

#### Behaviour of PNIPAM-SDS system

In section 6.3, we have shown that SDS has a remarkable effect on the structure and thermoresponse of planar PNIPAM brushes, as has been reported previously for free PNIPAM [239, 241, 242, 246, 247, 249, 266] and nanoparticle-grafted PNIPAM brushes [74]. As in the free-polymer literature, we find that SDS at the CMC is able to completely suppress the thermoresponse of PNIPAM over the temperature range probed. We find that the effect of SDS on PNIPAM plateaus above the surfactant CMC; this plateau is not

always observed in free-polymer literature [241], likely because of the discrepancy between the total surfactant concentration and the free-surfactant concentration due to adsorption of SDS onto PNIPAM. The NR results in Figure 6.17 show that SDS and PNIPAM have a volumetric binding ratio of approximately 1:1 in pure water above the CMC (as the densities of both compounds are close to  $1\text{ g mL}^{-1}$ , this corresponds to a 1:1 mass ratio), agreeing reasonably well with the values reported by Mylonas, Staikos, and Lianos [249] and Mears et al. [246], (0.6 and 0.5, respectively). The difference can be explained by the sensitivity of  $\text{CM}_{\text{poly}}$  NR to all polymer-proximal surfactant, rather than just bound surfactant. We conclude that the binding ratio of 8 calculated from the results of Chen et al. [252] is erroneous.

### Effect of surfactant headgroup

Ellipsometry, QCM-D and NR convincingly show that anionic surfactants affect both the structure and thermoresponse of PNIPAM in the brush geometry. In contrast, the cationic and nonionic surfactants studied do not. These results agree well with prior work (see sections 6.1.2–6.1.4), and demonstrate that the brush geometry is a good model system for studying general polymer phenomena. However, the real value of the brush geometry here is that QCM-D, FAOR and  $\text{CM}_{\text{poly}}$  NR experiments can be used to reveal polymer-surfactant interaction. By quantifying both polymer structure (the effect of the surfactant) and the presence of surfactant in the layer (the affinity of the surfactant for the polymer), we can unpick the mechanism behind the PNIPAM-SDS interaction.

The obvious question raised by the above findings is this: Why do DTAB/CTAB (cationic surfactants) have such a markedly different effect on the behaviour of PNIPAM compared to SDS (anionic surfactant)? Prior work (that typically examines only SDS) has claimed that SDS interacts with PNIPAM through the surfactant tail group binding to the hydrophobic polymer backbone [239, 246, 251, 254]. The interaction model indicates that DTAB,  $\text{C}_{12}\text{E}_6$  and SDS would have similar affinities for PNIPAM, which would result in similar adsorbed amounts. However, our QCM-D, FAOR and  $\text{CM}_{\text{poly}}$  NR experiments clearly show that SDS adsorbs in much greater amounts than the other surfactants.

Of course — when considering the effects of surfactants on polymers — it is primarily the adsorbed charge, not the adsorbed mass, that dictates polymer structure. In Figure 6.14, the adsorbed charge is shown for SDS and CTAB as a function of concentration. Clearly, SDS results in more adsorbed charge within the brush layer than CTAB, but it appears that the difference in adsorbed charge is not sufficient to account for the behaviour change completely. At  $0.5 \times \text{CMC}^\ominus$  SDS the adsorbed charge appears to be  $\approx 0.3\text{ mmol m}^{-2}$ , less than the adsorbed charge for CTAB at  $1 \times \text{CMC}^\ominus$ , which is

approximately  $\approx 0.4 \text{ mmol m}^{-2}$ . However,  $0.5 \times \text{CMC}^\oplus$  SDS has a measurable effect on the structure and thermotransition of PNIPAM (Fig. 6.8a, 6.9a and 6.15b) while  $1 \times \text{CMC}^\oplus$  of CTAB does not (Fig. 6.8d, 6.9d and 6.16e). As identified in section 6.2.3, FAOR will underestimate surfactant adsorption if there is layer swelling, which we expect a small amount of at  $0.5 \times \text{CMC}^\oplus$  SDS and  $20^\circ\text{C}$  (Fig. 6.8a and 6.9a). However, the error in the FAOR is likely to be less than 10 % for low surfactant concentrations, and NR measurements confirm that there are comparable amounts of surfactant adsorbed within the brush layer at  $0.5 \times \text{CMC}^\oplus$  SDS and  $2 \times \text{CMC}^\oplus$  CTAB. Therefore, while the dominant cause of the difference between sulphate-headed and trimethylammonium-headed surfactants interacting with PNIPAM appears to be their affinity (i.e., sulphate headed surfactants like PNIPAM more), it appears that there may be additional secondary factors. One such factor may be the partitioning of cationic and nonionic surfactants to the silica-polymer interface.

### Interaction mechanism

We conclude that the interaction between SDS and PNIPAM cannot be solely driven by hydrophobic interaction between the surfactant tail and the hydrophobic moieties on the polymer, as previous studies have suggested [248, 251, 254]. From Figures 6.10, 6.11, 6.13, and 6.17, as well as other work [239, 241, 242], we see that the surfactant head-group plays a significant role in the interaction between PNIPAM and surfactants.

This head-group dependent behaviour has been observed in MD studies of the PEO-surfactant system [256, 257, 267, 268]. We believe that the best model for PNIPAM-SDS interaction is that the polymer binds to the surface of the surfactant micelle — the same mechanism proposed for SDS-PEO systems by Shang, Wang, and Larson [257]. In this model, the hydrophobic moieties bind to the exposed regions of the micelle core, reducing the surface energy of the micelle. The binding of hydrophobic PNIPAM moieties to the micelle in this matter matches the NMR study of Chen, Spěvák, and Hanyková [254], which finds that SDS alkyl protons are near the isopropyl groups on the PNIPAM. Simultaneously, the PNIPAM amide forms ionic hydrogen bonds with the sulphate headgroups, explaining the head-group dependence observed here and elsewhere [239, 241, 242].

It appears that there is also a second mechanism through which the local concentration of the surfactants studied here is increased in the presence of PNIPAM without strongly affecting polymer structure. We draw this conclusion primarily from Figure 6.14 and the surfactant volume fractions in Figure 6.17, which show that cationic and nonionic surfactants are present in the brush layer at concentrations where SDS has some effect on the thermotransition. This fits with reports of cationic surfactants having a small effect

on the behaviour of PNIPAM [239, 241, 269–271]. Potentially this could be the second mode of surfactant interaction observed by Walter et al. [248]. The mechanism behind this behaviour could be polymer-precipitated micellisation, where the presence of polymer serves as an aggregation point, allowing the formation of micelles below the CMC. These precipitated micelles are not strongly bound to the polymer, and hence do not strongly affect the polymer behaviour. Alternatively, a small number of cationic micelles may attach to the polymer chain through hydrophobic mechanisms.

## 6.4 Results: Effect of SDS on the confined behaviour of a PNIPAM brush

From section 6.3, we know that SDS (and other anionic surfactants) interact strongly with PNIPAM, imbuing it with polyelectrolyte-like properties. This pseudo-polyelectrolyte structure may resist mechanical confinement better than PNIPAM in water, as polyelectrolytes have been shown to better resist confinement compared to neutral polymers. In the study of Abbott et al. [79], the behaviour of neutral PEO brushes are compared to charged poly(acrylic acid) (PAA) brushes. They find that PAA is more swollen under confinement than PEO, although the magnitude of this difference is not as great as expected. Furthermore, they modulate the charge on PAA by controlling the pH of the solution; the normalised separation (inferred from Fig. 7 in their work and the dry thicknesses given in the Supporting information) for the uncharged brush is 1.1, for the moderately charged brush is 1.25, and for the fully charged brush is 1.5. The preference for polyelectrolytes to swell more in water than neutral polymers can also be seen in the difference between the force-curves in the atomic force microscopy (AFM) work of Murdoch et al. [20] and Willott et al. [272]. In this brief section, we will use the methodology developed in chapter 5 to probe the behaviour of PNIPAM-SDS complexes under mechanical confinement.

### 6.4.1 Neutron Reflectometry

As in previous sections we examine the behaviour of the PNIPAM-SDS systems above and below the CMC, here using surfactant concentrations of  $0.6 \times \text{CMC}^\ominus$  and  $1.75 \times \text{CMC}^\ominus$ . We conduct two types of measurement here, one in hydrogenous SDS (referred to as simply SDS) and one in deuterated SDS (d-SDS). Hydrogenous SDS experiments are sensitive to the separation between the confining poly(ethylene terephthalate) (PET) film and the silica substrate (as in 5). In contrast, d-SDS experiments are sensitive to the structure of the d-SDS within the confined layer. The conditions of greatest interest to us are those where the PNIPAM brush in water is most confined, that is, at high temperatures and high confining stresses. At these conditions, we expect the presence of the SDS to make the most difference to the system structure. We examine the system at 1 bar, 35 °C (low pressure, high temperature) and 5 bar, 25 °C (high pressure, low temperature).

The results from the hydrogenous confinement study are presented in Figure 6.20. As in chapter 5, we use both a modelling approach and a fringe-spacing analysis (section 1.5.2) to determine the separation between the confining PET film and the silica substrate. Both modelling and fringe-spacing analyses yield similar trends and show clearly that

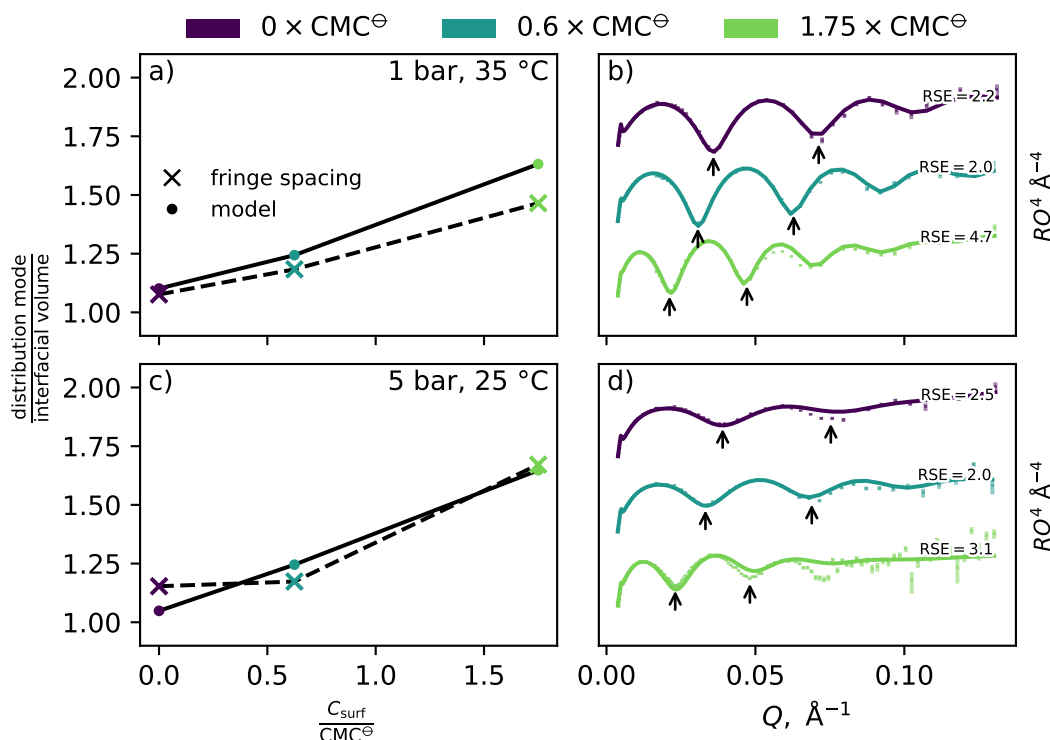


Figure 6.20: Normalised separation as a function of surfactant concentration for (a) the surface confined by 1 bar of stress at 35 °C and (b) the surface confined by 5 bar of stress at 25 °C.  $\text{H}_2\text{O}$  is the solvent in all conditions. The reflectometry profiles are vertically offset and scaled by  $Q^4$  for clarity; fringe locations are indicated by black arrows. The agreement of the modelled reflectometry profile and collected data decreases as the surfactant concentration increases, likely because of an uneven distribution of surfactant within the brush (see Fig. 6.21).

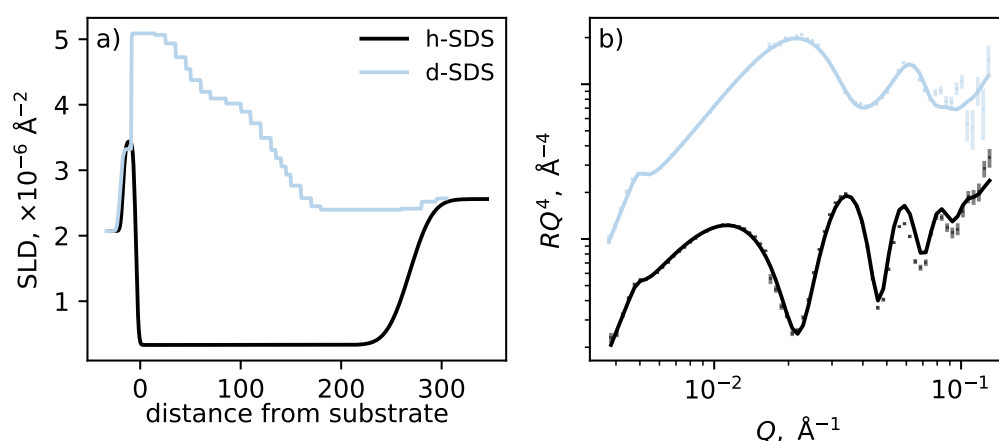


Figure 6.21: (a) Fitted SLD and (b) corresponding reflectivity profiles for the confined system at 35 °C and 1 bar with SDS and d-SDS (black and blue lines, respectively). The hydrogenous SDS data and structure is taken from modelling in Figure 6.20; the SLD profile is taken from modal distributions

the addition of SDS increases layer thickness. As expected, this increase in thickness is greater at  $1.75 \times \text{CMC}^\oplus$  than it is at  $0.6 \times \text{CMC}^\oplus$ . That SDS increases the layer thickness is evident from a casual examination of the reflectometry profiles in Figure 6.20c, d, as the spacing of the fringes clearly shrinks. At both conditions studied, PNIPAM in pure water exhibited a normalised separation of  $\approx 1.1$ , consistent with the results from chapter 5, while the  $1.75 \times \text{CMC}^\oplus$  SDS system exhibited a normalised separation of  $\approx 1.5$ .

To examine the distribution of SDS within the confined layer, we substituted deuterated SDS for d-SDS (as used elsewhere in this work). The d-SDS has a significantly higher SLD (see appendix A) than any other component in the system. Therefore, the experiment becomes sensitive to the surfactant distribution within the confined layer, rather than the silica-PET separation. We first attempted to model this system with a slab or distribution (as detailed in chapter 5) model, but these did not achieve a satisfactory agreement with the collected data. This lack of agreement was not unexpected, as there is no theoretical justification for a uniform surfactant distribution. Consequently, this interface was modelled with the same freeform model used for the  $\text{CM}_{\text{poly}}$  modelling in sections 6.3 and 6.5. The modelled region's thickness was fixed to the thickness derived from the modelling in Figure 6.20. To account for the water-backed regions observed in chapter 5, 15 % of the reflecting area was modelled as a silica-water interface. The SLD of the backing water was allowed to vary from  $-0.56$  to  $1 \times 10^{-6} \text{ \AA}^{-2}$  to account for the presence of the d-SDS within the system. The SLD profile of the confined section and corresponding reflectometry data are shown in Figure 6.21.

As the structural model used has many degrees of freedom, we will first ground our argument in the reflectometry profiles. For this purpose, the profiles have been re-plotted in Figure 6.22. The reflectometry profiles for the SDS and d-SDS samples are unequivocally distinct, with large differences in the fringe-spacing, fringe-magnitude and profile shape. This stark difference indicates that a significant amount of surfactant is trapped in the layer upon mechanical confinement, as d-SDS is clearly modifying the SLD of the layer. We note that, while a simple fringe spacing analysis would indicate that the layer is significantly thinner in d-SDS than SDS, the conservation of system volume means that this is not possible. The inversion of the fringe intensity, which is more evident when reflectometry is plotted on a  $\log(R)$  vs  $Q$  plot (Fig. 6.22), indicates that the SLD of the confined layer is higher than the SLD of the PET membrane. This high SLD requires a significant amount of d-SDS in the layer. Assuming the second component is PNIPAM, with an SLD of  $0.8 \times 10^{-6} \text{ \AA}^{-2}$ , the volume fraction of d-SDS must be greater than 0.34 for the confined layer to have an SLD greater than that of PET. Consequently, as  $\hat{V}_1$  is constant throughout the compression, and the layer must comprise of a significant fraction (on the order of 35 %) of d-SDS, the layer cannot be thinner than approximately  $\hat{V}_1/(1 - 0.35)$ ,



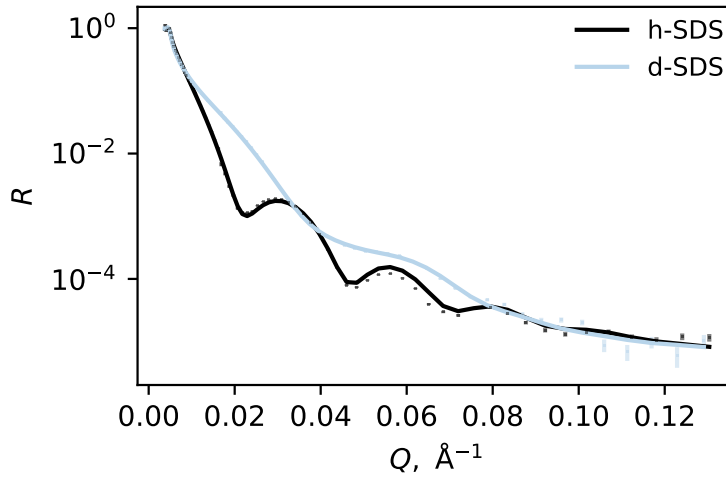


Figure 6.22: Reflectivity profiles from Figure 6.21b plotted on alternative axes. Profiles are not offset to allow for direct comparison.

here 250 Å. This thickness is equivalent to the thickness of the layer in SDS. We must therefore explain the increase in fringe spacing (corresponding to decreasing thickness) in the d-SDS system relative to the SDS system. Here, we postulate that there must be an uneven distribution of surfactants within the confined brush layer, such that the shape of the SLD profile is not uniform. This could result in the structure that dominates the reflection (that is most prominent in the SLD profile) possessing a thickness significantly less than the thickness of the silica-PET separation.

Having thoroughly discussed the differences between the reflectometry profiles from the SDS and d-SDS systems, we now turn to examine the model output in Figure 6.21a. The modelling shows that the d-SDS is enriched near the substrate, with concentration dropping in proximity to the confining surface. In isolation, the SLD profile indicates that the PNIPAM-d-SDS layer is only 180 Å thick, but as discussed in the paragraph above, this can not be the case. Figure 6.21a shows that the distribution of surfactants in the confined region is uneven; this behaviour would produce non-uniform SLD profiles in the confined region (see appendix A for SLDs) for the hydrogenous data. This explains why we cannot accurately model the collected reflectometry profiles at high surfactant concentrations (Fig. 6.20a, c).

### 6.4.2 Discussion

This increased normalised separation for SDS-containing systems indicates that SDS remains in the polymer layer upon macroscopic confinement. We observe similar swelling ratios to the PAA study of Abbott et al. [79], with our ‘maximally charged’ ( $1.75 \times \text{CMC}^\ominus$ )

pseudo-polyelectrolytes exhibiting a swelling ratio of over 1.5 (Fig.6.20). However, our results indicate that the primary mechanism through which SDS increases the layer thickness is steric in nature (rather than electrostatic or osmotic). The steric mechanism operates through excluded-volume interactions between trapped surfactant molecules and the polymer; here the layer consists of a tightly packed PNIPAM-SDS film. Conversely, a confined film where electrostatic or osmotic interaction dominated would still contain a considerable amount of water.

First, we will consider the evidence for the steric hypothesis from the hydrogenated SDS experiments. Unconfined experiments (section 6.3.4) indicate that a volumetric PNIPAM:SDS binding ratio of approximately 1:1.<sup>vii</sup> If this volumetric binding ratio were to stay constant upon compression, then the normalised solvent-free (i.e., just PNIPAM and SDS) layer thickness would be 2. We observe normalised separations of  $\approx 1.5$ ; indicating that there is less SDS in the confined system than in the unconfined system. Unless almost all of the SDS has left the layer (i.e., the binding ratio for free and confined systems is very different), and the remainder is contributing to the increase in thickness through electrostatic/osmotic effects, the normalised separations we measure supports the steric hypothesis.

The modelling of the d-SDS shows clearly that the SDS is concentrated within the confined layer. Analysis of the SLD profile in Figure 6.20 indicates that the interfacial volume of SDS is approximately 110 Å. Given that the polymer interfacial volume is 165 Å, and the layer is approximately 280 Å thick, there is clearly little room left for water. We do not believe that our determination of surfactant  $\hat{V}_I$  is particularly accurate, and as such, there is likely more water in the system than is indicated by this analysis. However, NR modelling suggests that the confined layer consists of tightly-packed PNIPAM-SDS, strongly supporting the steric hypothesis.

This tightly-packed structure is likely not at equilibrium. When the PNIPAM-SDS system undergoes a thermal collapse (as can occur at low surfactant concentrations) we observe that the SDS is mostly ejected from the brush layer (Fig. 6.15); Chen et al. [252] observe similar behaviour in free-polymer systems. Here, this surfactant is instead trapped by the macroscopic confining barrier. The structure in Figure 6.21 provides some insight as to how the SDS gets trapped. The SLD profile in Figure 6.21a shows that the surfactant is concentrated at the base of the brush. This is likely caused by a top-down collapse of the PNIPAM-SDS system in response to confinement. A top-down collapse would force SDS out of the brush periphery first — at low confining stresses SDS would escape through the solvated-brush to a region of lower confinement (Fig. 5.1b) However, as

---

<sup>vii</sup>Literature reports molar binding ratios of 0.5 and 0.6 [246, 249]

confining stress increased the SDS would be forced deeper into the brush; this surfactant could not escape due to the high  $\phi_{\text{poly}}$  throughout the layer. Interestingly, there does not appear to be an enrichment of the surfactant near the hydrophobic PET interface. One explanation for this is that PET-bound surfactant is able to escape from the system upon confinement, whilst polymer-bound surfactant becomes trapped at the base of the brush. Another explanation is that at high confining stresses, the polymer and surfactant layers are not distinct, with significant interpenetration resulting in no defined surfactant layer on the PET interface.

The application of the confinement cell introduced in chapter 5 to PNIPAM-SDS systems show that these systems resist confinement to a greater degree than pure PNIPAM systems; however, this behaviour is revealed to be due to entrapment of the surfactant within the brush. This tight-packed polymer-surfactant system forms due to a top-down collapse of the brush and resists compression due to the excluded volume effects of trapped surfactant molecules.

## 6.5 Results: Effect of ionic strength

In section 6.3, we find that anionic surfactants (specifically SDS) significantly affect the structure and thermoresponse of a PNIPAM brush. This behaviour can be explained by the pseudo-polyelectrolyte model [254], a natural extension of the pearl-necklace model, whereby the electrostatic charge associated with polymer-anchored surfactant micelles cause the neutral polymer to act as a polyelectrolyte. For an outline of the behaviour of polyelectrolytes in the brush geometry see section 6.1.7. We cannot easily categorise the PNIPAM-SDS complex as either a weak or strong pseudo-polyelectrolyte. In pure water, we expect the PNIPAM-SDS complex would have a charge every 4 to 8 repeat units in pure water. This is certainly less than a strong polyelectrolyte, such as poly(sodium styrene sulfonate) (PSS) (charged fraction of 0.8 in pure water [273]), but cannot sensibly be compared to a weak polyelectrolyte without specifying a pH and salinity. Regardless, here we are concerned with the behaviour of these PNIPAM-SDS complexes in the salted regime, in which both strong and weak polyelectrolytes should collapse.

Adding salt to the PNIPAM-SDS system allows for the pseudo-polyelectrolyte model to be tested, as polyelectrolytes collapse at high salt concentrations. Examining the behaviour of PNIPAM and SDS in electrolyte solutions may provide further clues as to the complex mechanism by which SDS interacts with, and affects the structure of, PNIPAM. Additionally, as discussed in section 6.1.6, the presence of an electrolyte modulates the CMC of an ionic surfactant through decreasing the Debye length, hence decreasing the energetic penalty for micelle formation. We show above that the behaviour of the PNIPAM-surfactant system seems to scale around the CMC of the surfactant, raising the question of whether the system behaviour will scale around a salt-modulated CMC. Other polymer systems' behaviour has been demonstrated to scale around the salt-modulated  $\text{CMC}^{\text{eff}}$  [274], however, the work of Patel et al. [241] suggests that this is not the case for PNIPAM. Studying this system in the brush geometry with the techniques that we have already demonstrated above allows us to determine the effect of surfactant and salt on the structure and mechanical properties of the PNIPAM brush, as well as the presence of surfactant within the brush layer. Here, we use NaCl as the model salt and SDS as the surfactant, chosen as both species are ubiquitous and well-characterised.

Before proceeding to experimental results, it is worth recapping the expected contributions to PNIPAM behaviour in the mixed SDS-NaCl systems. As is documented above, SDS causes PNIPAM chains to swell through the attachment of SDS micelles to the PNIPAM chain as per the pearl-necklace model; this behaviour scales around the CMC (Fig. 6.3). Salt has been shown to reduce the solubility of PNIPAM in water (with

chaotropes at low concentrations a notable exception [275, 276]), with NaCl having a moderate effect (corresponding to chloride’s position in the middle of the Hofmeister series). Salt has also been shown to affect polyelectrolytes’ solubility, significant here because of the pseudo-polyelectrolyte hypothesis. At low concentrations ( $<50$  mM) salt increases the solubility of weak polyelectrolytes (the osmotic brush regime [108, 109]) while not affecting the solubility of strong polyelectrolytes [108]. At high concentrations ( $>250$  mM) the electrolyte reduces the solubility of both strong and weak polyelectrolytes [108, 109]. Finally, the decreased Debye length also reduces the CMC of ionic surfactants like SDS, as discussed in section 6.1.6.

From this, we expect that — at a fixed SDS concentration below the CMC — the addition of salt will first lead to polymer swelling (as the effective CMC is lowered) followed by a decrease in swelling (due to screening of surfactant charges). We expect that at SDS concentrations above the CMC the addition of salt will have little effect on PNIPAM at low concentrations, and will reduce the solubility of PNIPAM-SDS complexes at higher concentrations (due to screening of surfactant charges), as they would for a real polyelectrolyte.

To maintain consistency with prior sections the concentrations of SDS are referred to as multiples of their CMC in pure water at  $25^\circ\text{C}$ ,  $\text{CMC}^\ominus$ . Of course, the system temperature (Fig. 6.2) and presence of salt (Fig. 6.5) will change the CMC of the SDS; again, this modified value is referred to as  $\text{CMC}^{\text{eff}}$ . Here we will study two concentrations of SDS,  $0.5$  and  $2 \times \text{CMC}^\ominus$ , at a range of salt concentrations between  $0$  and  $500$  mM (covering  $0.5$  to  $25 \times \text{CMC}^{\text{eff}}$ ).

### 6.5.1 Ellipsometry

The first technique we use to study the behaviour of PNIPAM-SDS-NaCl systems is ellipsometry. However, these experiments differ from those reported above in at least two ways. Firstly, the brush studied here is much thicker than those typically studied with ellipsometry, with an interfacial volume of approximately  $1400 \text{ \AA}$ . A thicker brush was chosen to increase ellipsometry’s sensitivity to the polymer volume fraction profile and to demonstrate the capabilities of our *refellips* analysis tool. Because ellipsometry is more sensitive to the brush structure, a more advanced model is required to analyse the collected data. This leads naturally to the second difference; the ellipsometry data here is modelled with the *refellips* ellipsometry analysis package, addressed in section 6.2.4 and detailed in appendix F.

Figure 6.23 shows polymer volume fraction profiles derived from ellipsometry. The profiles are produced by optimising the freeform model in chapter 4 against the ellipsometric

parameters  $\Delta$  and  $\Psi$ , shown in the inset plots. A casual examination of Figure 6.23a, which shows the thermoresponse of PNIPAM in pure water, indicates that the  $\Delta$  and  $\Psi$  profiles are sensitive to the collapse of the layer. Furthermore, we find excellent agreement between the modelled  $\Delta$  and  $\Psi$  values and the collected data.

To verify that our modelling methodology is producing sensible results, we will first discuss the behaviour of the binary systems. The addition of SDS is found to swell the brush layer (a to c), in keeping with the trends observed in this section 6.3. However, at  $2 \times \text{CMC}^\ominus$  in pure water, the layer is more temperature-sensitive than in previous ellipsometry (Fig. 6.8 and 6.9) and NR experiments (Fig. 6.15). As extracting *a priori* interfacial structure from ellipsometry data is an immature method (to our knowledge this is the first time it has been attempted), the technique's sensitivity is unknown. However, the  $\Delta$  and  $\Psi$  profiles collected at  $2 \times \text{CMC}^\ominus$  SDS are visibly different, and the trend observed in thickness does make sense (collapsing with increasing temperature). Another explanation is that the synthetic conditions that produced this thicker brush change the structure in some way (as discussed in chapter 1), which moderates the thermoresponse of the layer (through the  $\phi_{\text{poly}}$  dependent  $\chi$  of PNIPAM, discussed in section 1.2).

Similarly, the response to salt concentration is in line with literature reports of the system behaviour. Humphreys, Wanless, and Webber [276] conclude that KCl reduces the CST of PNIPAM brushes, with a 500 mM solution resulting in a CST of  $\approx 27^\circ\text{C}$ , while Zhang et al. [275] report similar findings for free PNIPAM in NaCl solutions. In Figure 6.23, the addition of salt results in the  $32^\circ\text{C}$  profile transitioning from a two-phase profile (Fig. 6.23a) to a collapsed profile (Fig. 6.23q), consistent with a CST reduction of  $\approx 5^\circ\text{C}$ . Although the ellipsometry modelling technique used here is untested, it agrees with both results from earlier in this chapter and literature reports. Consequently, we have confidence in the profiles produced by the technique for the salt-surfactant conditions.

The ellipsometry data are summarised in Figure 6.24, which plots the swelling ratio (twice the first moment divided by  $\hat{V}_1$ ) against the salt concentration. At  $0.5 \times \text{CMC}^\ominus$  (4 mM) SDS the addition of salt initially caused the PNIPAM layer to swell, with the ellipsometrically determined structures becoming practically indistinguishable from the  $2 \times \text{CMC}^\ominus$  profile at a NaCl concentration of 50 mM. This behaviour is consistent with the PNIPAM-SDS behaviour scaling around the salt-modulated CMC of SDS, as the CMC of SDS reaches 4 mM at a NaCl concentration of approximately 20 mM (Fig. 6.5). As with previous experiments, above  $1 \times \text{CMC}^{\text{eff}}$  minimal thermoresponse was observed over the investigated temperature range. As the salt concentration was further increased incremental swelling was observed; at no point did the addition of NaCl begin to collapse the brush. A similar trend was observed for the  $2 \times \text{CMC}^\ominus$  (16 mM) system. The addition of salt caused a slight increase in the layer's apparent thickness and a reduction in the

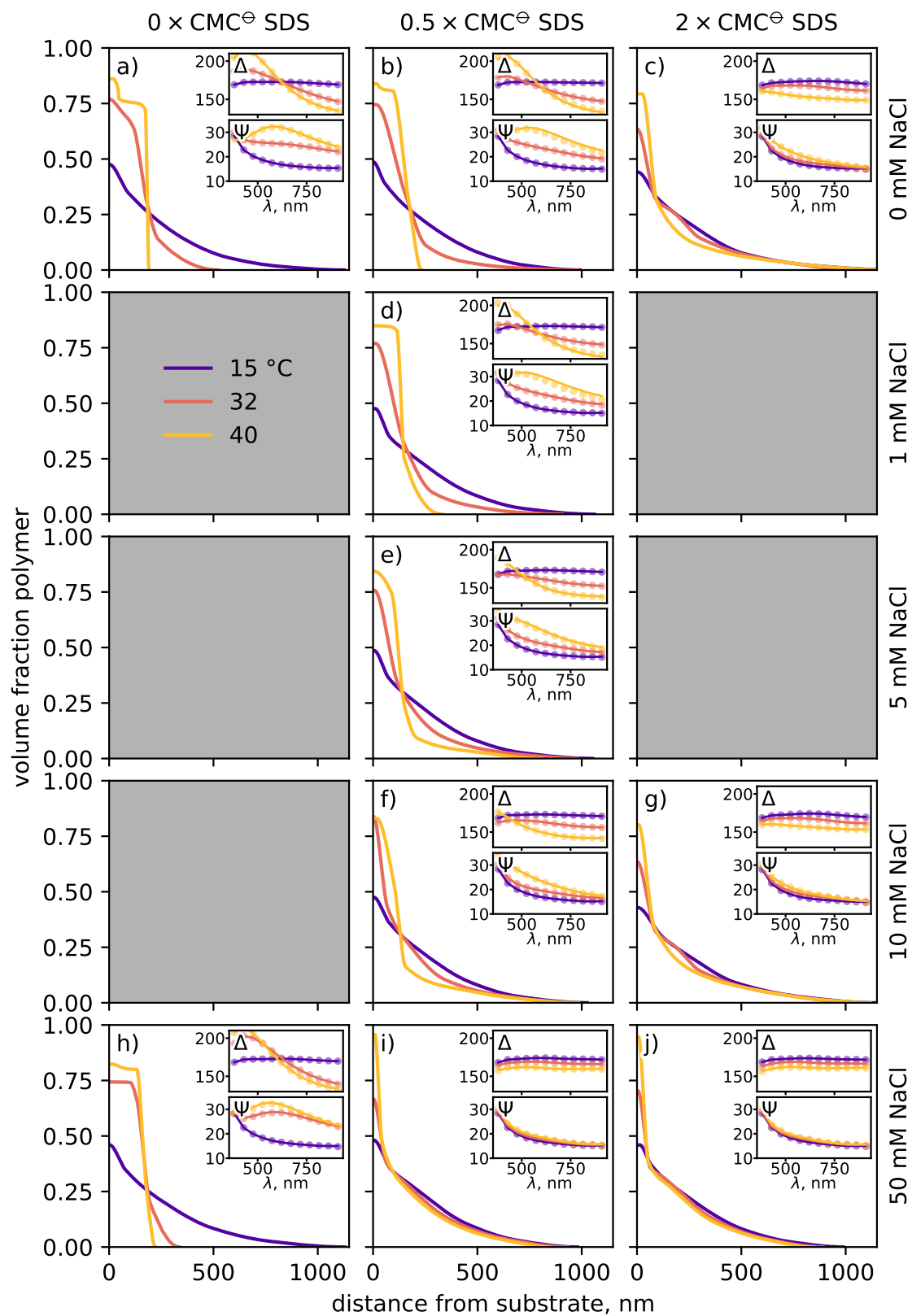


figure continues overleaf

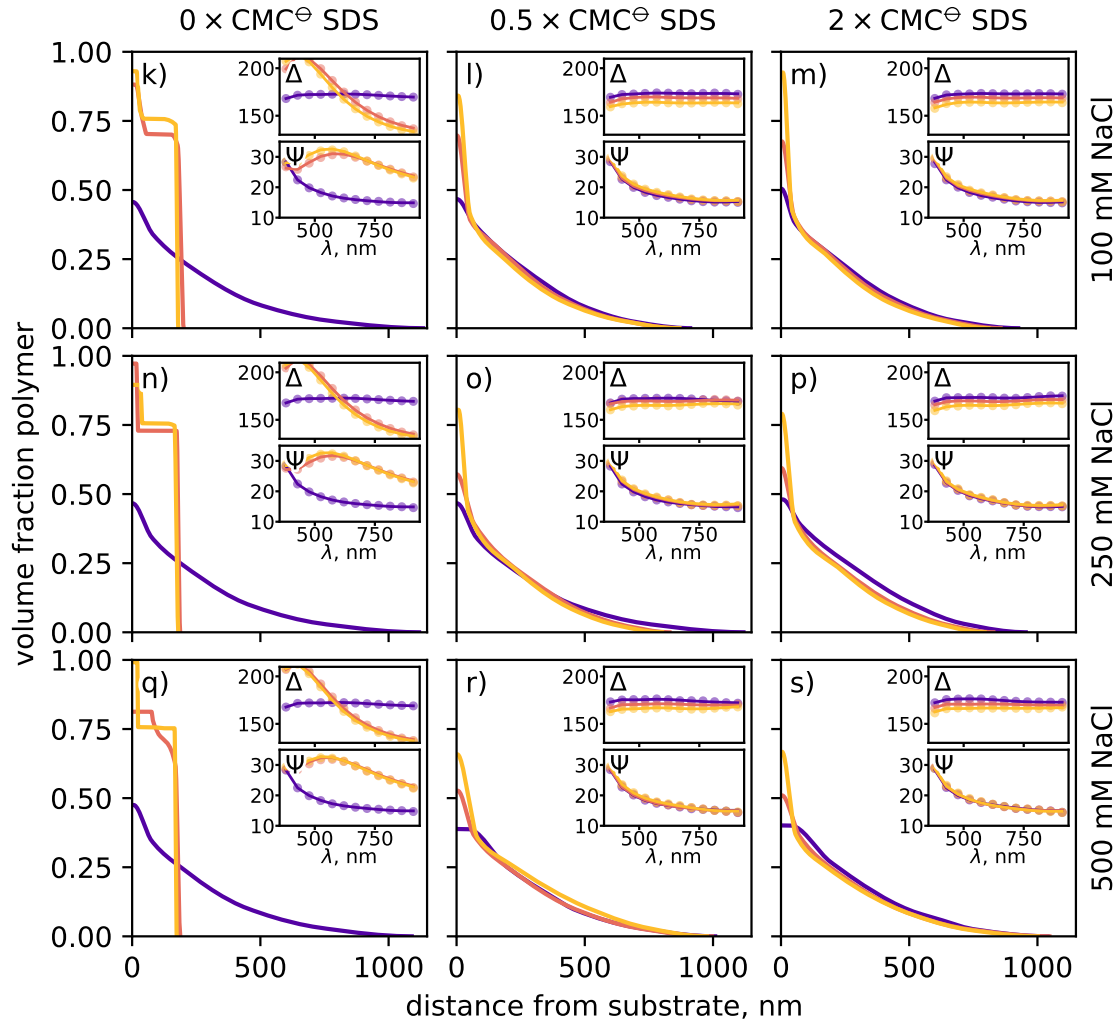


Figure 6.23: Volume fraction profiles of a PNIPAM brush ( $\hat{V}_1 = 1400 \text{ \AA}$ ) as a function of SDS concentration (left to right), NaCl concentration (top to bottom) and temperature (indicated by different coloured profiles), derived from ellipsometry. The volume fraction profiles are produced by fitting the ellipsometric parameters  $\Delta$  and  $\Psi$  (inset) with the freeform model outlined in chapter 4, adapted for use with ellipsometry (appendix F). At zero NaCl concentration the brush swells as the SDS concentration increases (a,b,c), consistent with the results in this work (Fig 6.8–6.15) as well as results from literature [74, 241, 246, 247]. At zero SDS concentration the brush collapses as the NaCl concentration increases (a-q), consistent with prior studies of PNIPAM in electrolyte environments [20, 275, 276]. However, as the salt concentration increases at SDS concentration of  $0.5 \times \text{CMC}^\ominus$  (b-r) the brush swells, consistent with a decreasing  $\text{CMC}^{\text{eff}}$ . At both SDS concentrations salt does not collapse the brush.



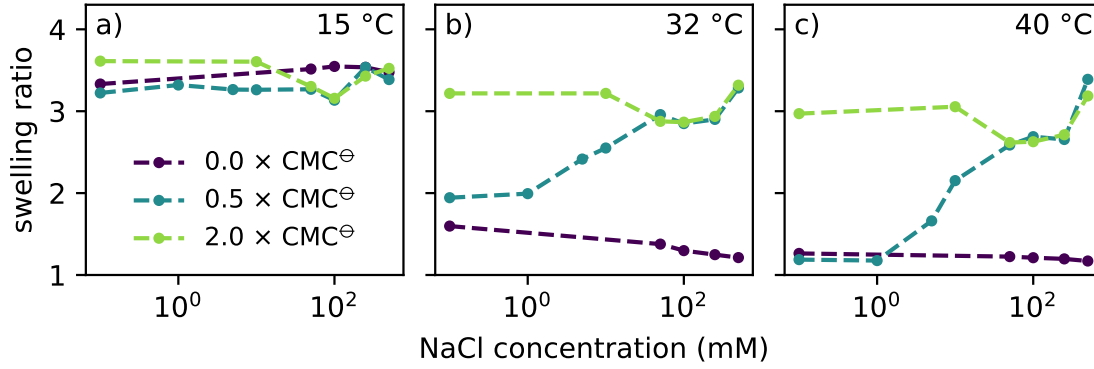


Figure 6.24: Swelling ratios, extracted from the volume fraction profiles in Figure 6.23, plotted against NaCl concentration as a function of temperature (a-c) and SDS concentration (colours). Swelling ratio is independent of NaCl and SDS concentration at 15 °C, but becomes a strong function of both as temperature is increased. Behaviour of the system relative to  $\text{CMC}^{\text{eff}}$  is explored in Figure 6.25

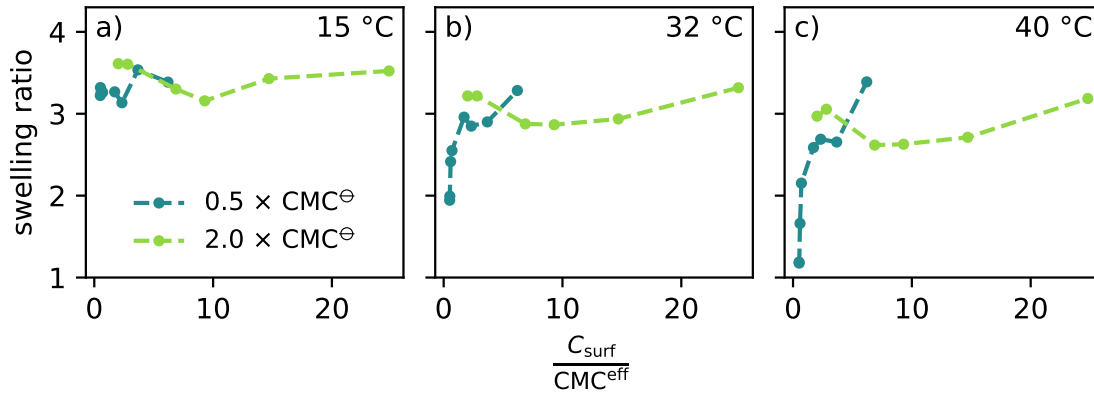


Figure 6.25: Data from Figure 6.24, with SDS concentration plotted as  $C_{\text{surf}}$  over  $\text{CMC}^{\text{eff}}$ . The swelling behaviour of the system appears to be predominately sensitive to the concentration of SDS relative to the  $\text{CMC}^{\text{eff}}$ , although the contribution of NaCl appears to increase at high concentrations (i.e., 500 mM).

thermoreponse observed at  $2 \times \text{CMC}^{\ominus}$ . As with the  $0.5 \times \text{CMC}^{\ominus}$  series, at no point did the addition of salt collapse the brush.

To further investigate the dependence of the system behaviour of  $\text{CMC}^{\text{eff}}$  we replot the data in 6.24 against  $C_{\text{surf}}/\text{CMC}^{\text{eff}}$  in Figure 6.25. We find that, below NaCl concentrations of 500 mM, the structure of the PNIPAM-SDS system can largely be explained by the concentration of SDS relative to its  $\text{CMC}^{\text{eff}}$ , with  $0.5$  and  $2 \times \text{CMC}^{\ominus}$  curves exhibiting similar trends and values at the crossover point ( $C_{\text{surf}}/\text{CMC}^{\text{eff}} = 1$ ). The behaviour of the system at 500 mM NaCl will be discussed in section 6.5.4.

Another feature of the ellipsometry data worth discussing briefly in the presence of an interior layer in some of the profiles that appears similar to that observed by reflectometry.

Firstly it must be stressed that the scale for the distance from the substrate in Fig. 6.23 is in nanometers, whereas it is in angstrom for the NR-derived volume fraction profiles included in this thesis. The difference in scale means that the interior layer in Fig. 6.23 is an order of magnitude thicker than the layers observed by NR. More work needs to be done to determine if these interior layers are required to fit the collected data. A Markov chain Monte Carlo (MCMC) approach like that used in chapter 4 could be used to determine the suitability of ellipsometry for the determination of brush volume fraction profiles; this would be an interesting avenue for future work to investigate.

## 6.5.2 Quartz crystal microbalance with dissipation monitoring

QCM-D experiments were performed at a constant temperature as a function of surfactant and salt concentration, in an experiment similar to that shown in Figure 6.11. As in the ellipsometry experiment shown in Figure 6.23 system behaviour is explored at  $0.5 \times \text{CMC}^\ominus$  and  $2 \times \text{CMC}^\ominus$  SDS concentrations at a broad range of salt concentrations. The temperature was maintained at 20 °C. Like in previous QCM-D results (Fig. 6.11c,d), the  $\Delta f$  and  $\Delta D$  values in Figure 6.26 are relative to the frequency and dissipation value of the wafer in pure water and have had the signal collected from a blank QCM-D wafer in an identical solution subtracted from them. This means that the signal is due only to the interaction of the solution components with the PNIPAM brush, not the solution density or viscosity. For more implementation details, see section 1.5.6. The same wafers were used in this study as were used in section 6.3.2 (dry thickness of 130 and 200 Å). While only the results from the 130 Å wafer are shown here, we stress that the same trends were observed across both wafers.

The behaviour of the PNIPAM-SDS and PNIPAM-NaCl systems will be discussed before the results from the mixed system are addressed. The addition of SDS at 25 °C decreases the frequency and increases the dissipation of the brush-coated wafer (as in Fig. 6.11), indicating that surfactant is being adsorbed into the brush and causing it to swell. This behaviour is dependent on the surfactant concentration, with the changes in  $\Delta f$  and  $\Delta D$  values increasing between  $0.5 \times \text{CMC}^\ominus$  and  $2 \times \text{CMC}^\ominus$  SDS concentrations. As NaCl is added to the system (purple data in Fig. 6.26) the frequency increases and dissipation decreases, indicative of a collapsing polymer brush. That the brush collapsed upon the addition of salt is consistent with the above ellipsometry experiments (Fig. 6.23) and prior experimentation [275, 276].

In the mixed system at low salt concentrations ( $<50$  mM) changes in  $\Delta f$  and  $\Delta D$  remain dependent on surfactant concentration. However, both signals become nearly identical when the  $0.5 \times \text{CMC}^\ominus$  sample reaches  $1 \times \text{CMC}^{\text{eff}}$ , mirroring the trend observed

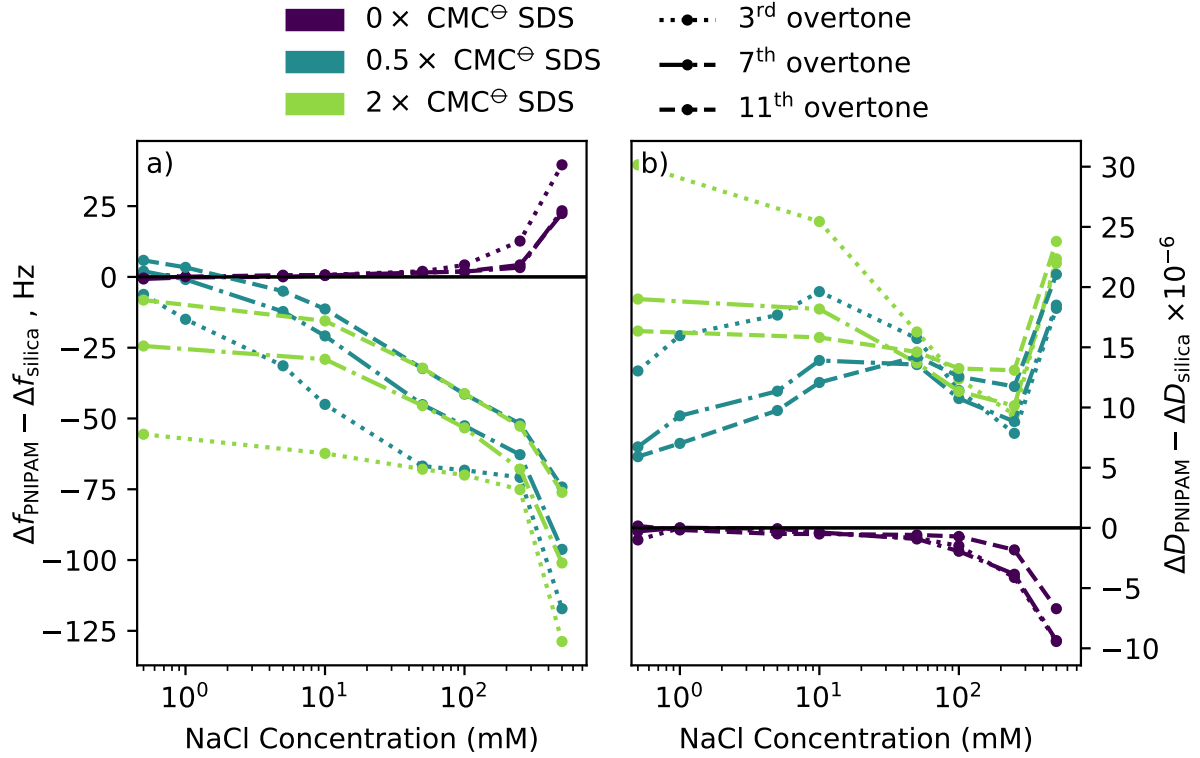


Figure 6.26: (a) Frequency and (b) dissipation for the 3<sup>rd</sup>, 7<sup>th</sup> and 11<sup>th</sup> overtones from a 130 Å PNIPAM brush at 20 °C as a function of SDS and NaCl concentration, as measured by QCM-D.

in the ellipsometry data (Fig. 6.24). Once again, the point at which the behaviour of  $0.5 \times \text{CMC}^\ominus$  and  $2 \times \text{CMC}^\ominus$  converge is at approximately 20 mM salt — corresponding to  $1 \times \text{CMC}^{\text{eff}}$  for the  $0.5 \times \text{CMC}^\ominus$  series (Fig. 6.5).

However, the dissipation and frequency trends as a function of salt concentration are rich and can provide much more insight into system behaviour than simply supporting the ellipsometry results. Starting with the trends in frequency, we observe that  $\Delta f$  does not plateau above  $\text{CMC}^{\text{eff}}$  in Figure 6.26 (more obvious in Fig. 6.27) like it does in Figure 6.11. Instead, it steadily decreases as the NaCl concentration is increased. The  $\Delta f$  trends across the overtones measured are also noteworthy. As lower overtones penetrate further into the brush layer, examining the relative overtone intensities yields insight into the mechanics of the system as a function of distance from the substrate [92]. At low NaCl concentrations higher overtone signals are less sensitive to the presence of surfactant than lower overtone signals, with the 11<sup>th</sup> overtone barely sensitive at all to surfactant concentration at 0 mM NaCl, however, as salt is added the frequency response of the overtones becomes comparable (Fig. 6.26). This indicates that the mass (which could be either adsorbed SDS, NaCl, or associated water) adsorbs more strongly into the

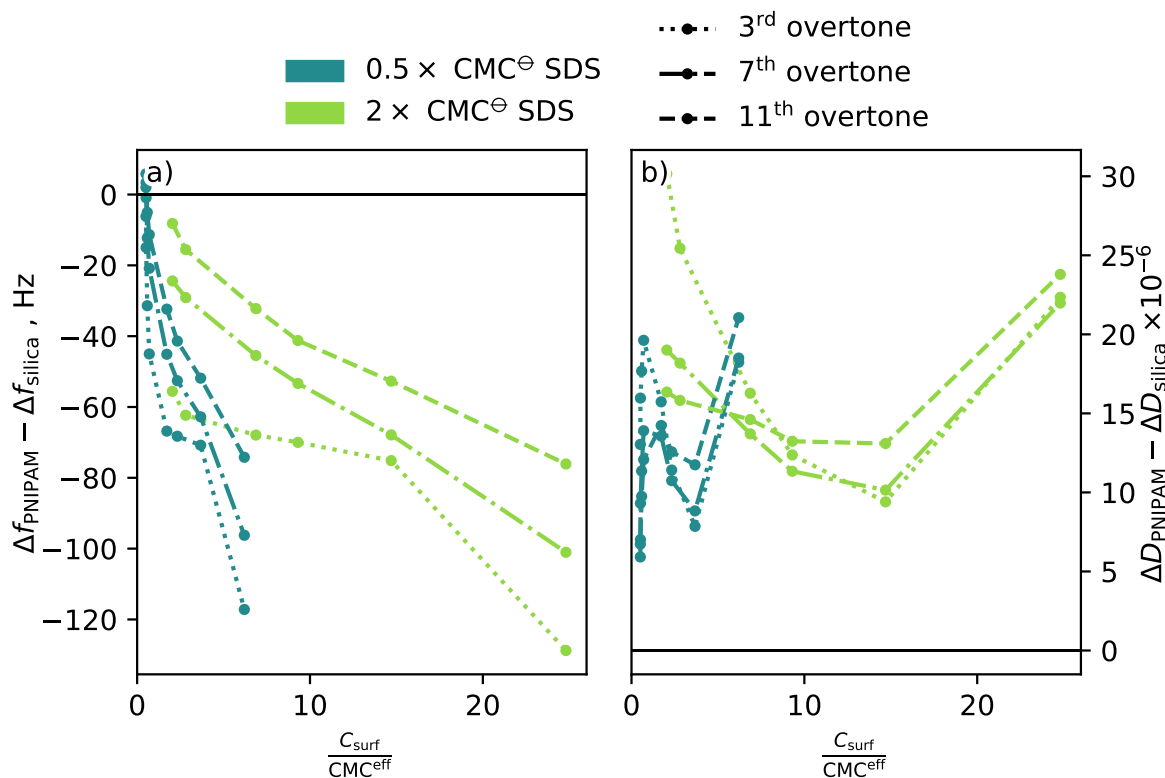


Figure 6.27: (a) Frequency and (b) dissipation data from Figure 6.26, plotted as  $C_{\text{surf}}$  over  $\text{CMC}^{\text{eff}}$ . Clearly, salt affects the system independent of modulating the CMC of the surfactant.

periphery of the brush at low salt concentrations, but becomes more evenly dispersed as the salt concentration increases further. This implies a transition from a typical parabolic or exponential brush profile to a more uniform ‘slab’ like structure.

The trend in dissipation seen in Figure 6.26b is even more complex. Like the frequency trend across overtones, there is initially a significant difference between overtones at low salt concentrations. This difference decreases as the salt concentration increases, with overtones overlying each other above 100 mM. Once again, this suggests that the brush becomes more slab-like as salt concentration is increased. However, the most notable feature is the inflection point at 250 mM in Figure 6.26b. Below this point, the system acts as expected, with the signal from the  $0.5 \times \text{CMC}^0$  condition initially rising until it reached  $1 \times \text{CMC}^{\text{eff}}$ , where it intersected with that of the  $2 \times \text{CMC}^0$  condition (which up until then had remained reasonably static). Above 50 mM NaCl, the signals started to slowly decrease, matching the trend of the pure NaCl condition. However, it is unlikely that this decrease in dissipation corresponds to a collapsing layer, as a brush collapse would be accompanied by an increase in frequency (here the opposite is observed). More likely the dissipation decrease between 10 to 250 mM corresponds to an increase in the

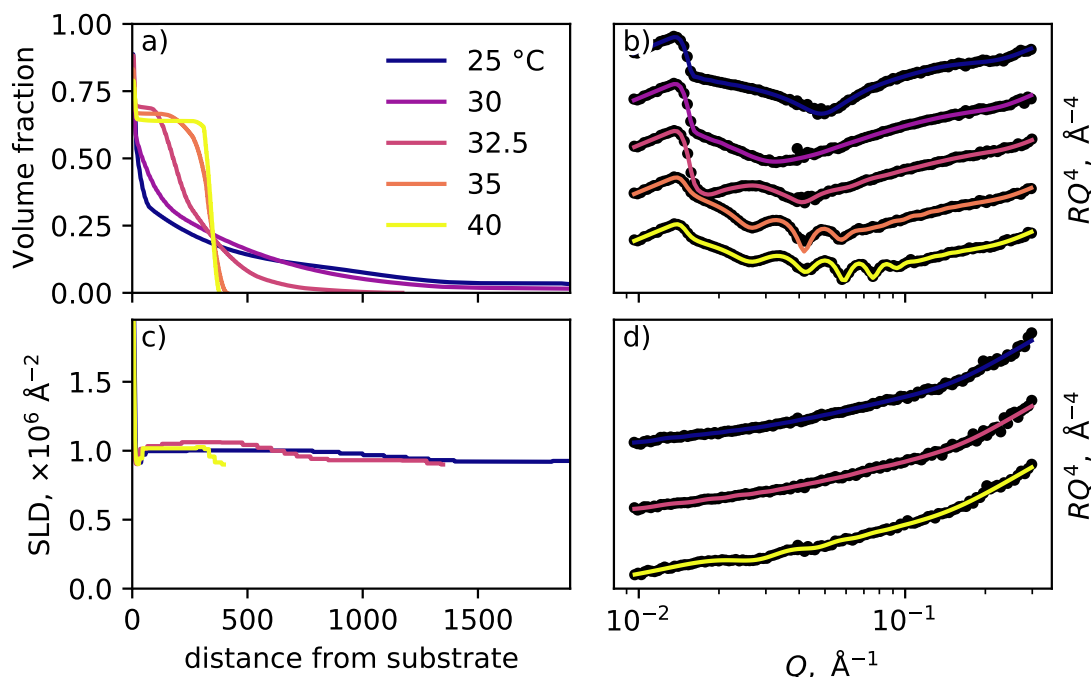


Figure 6.28: (a) Volume fraction profiles of PNIPAM in  $D_2O$  as a function of temperature with (b) accompanying reflectometry profiles, as well as (c) SLD profiles modelled to match (d) reflectometry profiles collected from PNIPAM in a  $CM_{poly}$  solution. The reflectometry profiles are vertically offset and scaled by  $Q^4$  for clarity. The PNIPAM brush undergoes a typical thermal collapse in (a), and (c) shows that the  $CM_{poly}$  solution is a near-perfect match for PNIPAM. These measurements serve as a control for the NR measurements in Figure 6.30.

stiffness of the brush. Above 250 mM NaCl the dissipation suddenly increases. Once again, we stress that this feature is present in all overtones and in both 130 and 200 Å samples, so is not due to experimental error. Furthermore, it is not the result of our data treatment (where the signal from a blank wafer is subtracted from the signal of interest), as these features are not present in the signal from the blank wafer (Fig. H9). The behaviour of the system at 500 mM will be discussed further in section 6.6.1.

### 6.5.3 Neutron reflectometry

NR experiments were performed at a fixed concentration of surfactant over a range of temperatures and salt conditions informed by prior QCM-D and ellipsometry measurements. Here, we study the  $0.5 \times CMC^{\ominus}$  SDS system at an increasing salt concentration. This is the most interesting surfactant concentration, as it allows us to explore behaviour above and below  $CMC^{\text{eff}}$ .

Control measurements in both pure  $D_2O$  and  $CM_{poly}$  were performed in the absence of salt and surfactant, with results shown in Figure 6.28. The measurements in  $D_2O$

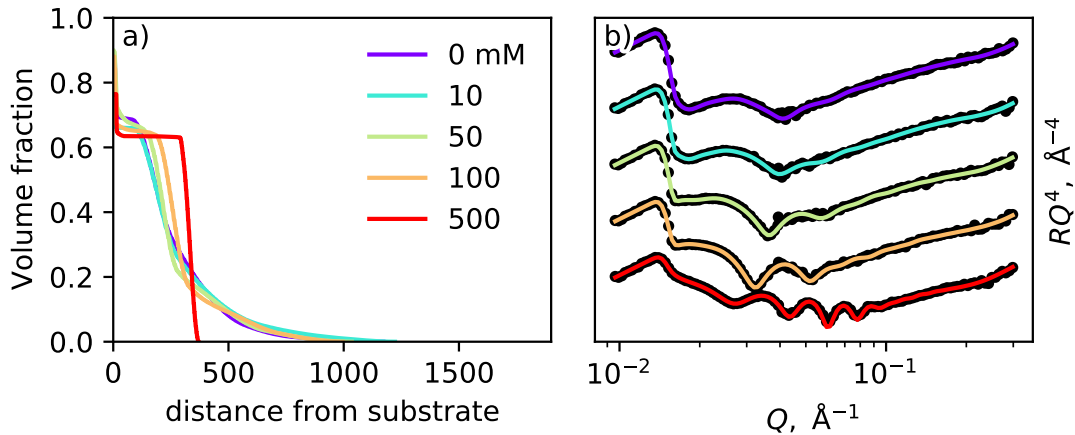


Figure 6.29: (a) Volume fractions of PNIPAM in D<sub>2</sub>O at 32.5 °C as a function of salt concentration with (b) accompanying reflectometry profiles. The reflectometry profiles are vertically offset and scaled by  $Q^4$  for clarity. Consistent with literature and prior experiments, the PNIPAM brush collapses as the NaCl concentration is increased. These measurements serve as a control for the NR measurements in Figure 6.30.

confirm that the PNIPAM brush used here responds in much the same way as those studied elsewhere in this thesis, while those in  $\text{CM}_{\text{poly}}$  show that  $\text{CM}_{\text{poly}}$  matches the SLD of PNIPAM well. Additional control measurements were carried out at a range of temperatures and NaCl concentrations to characterise the response of the brush to NaCl. The results for 0 to 500 mM NaCl at 32.5 °C are shown in Figure 6.29. As reported in the literature and observed in prior experiments, the addition of NaCl results in the brush collapsing, with structural changes most evident above 100 mM.

We now turn to examining the PNIPAM-SDS-NaCl system. As in section 6.2.7, we start by discussing trends in the reflectometry profiles, before discussing the output of the modelling. As the temperature is increased the 0 mM NaCl  $0.5 \times \text{CMC}^\ominus$  SDS system exhibits the typical swollen-to-collapsed transition seen in the control measurements (Fig. 6.28b), albeit with a higher apparent CST. This is consistent with the brush collapsing at  $0.5 \times \text{CMC}^\ominus$  SDS in section 6.3. At 10 mM NaCl the reflectometry profiles no longer develop the hallmark fringes of a collapsed brush, indicating that the layer is significantly more swollen than at 0 mM NaCl. Above 10 mM NaCl, very little change is observed in the reflectometry profile as a function of temperature, indicating that the layer no longer collapses above this salt concentration.

Moving on to the profiles collected from the  $\text{CM}_{\text{poly}}$  system, we see that the shape of all profiles differs significantly from the control measurements in Figure 6.28, indicating that there is adsorption of surfactant at all conditions. At the zero salt condition fringes develop as the temperature is increased, indicating that some surfactant remains in the layer upon brush collapse. These fringes do not appear at higher salt concentrations,

consistent with the lack of layer collapse predicted from the  $D_2O$  dataset. The shape of the reflectometry profile for 50 and 100 mM conditions is comparable at all temperatures, indicating similar levels of adsorption at these conditions; the shape of the profile at 500 mM is distinct. This fits with ellipsometry and QCM-D results, which indicated exceptional behaviour at 500 mM.

We now examine the profiles produced for the  $D_2O$  system via the freeform method outlined in chapter 4. At all temperatures studied the PNIPAM brush swells as salt is added and the  $CMC^{eff}$  of the SDS is reduced. This swelling follows the trend identified by ellipsometry in Figure 6.23 and QCM-D in Figure 6.26. The polymer profiles collected here strongly support the veracity of the novel ellipsometry modelling presented in Figure 6.23. Examining Figure 6.30a reveals that the addition of salt produces a more swollen layer even at 25 °C, reminiscent of the swelling upon the addition of SDS in Figure 6.15.

As exemplified in section 6.3.4, the unique power of NR in studying this system is its ability to examine not just the structure of the polymer but also the distribution of SDS within the brush. However, it must be stressed that in this more complex system some of the signal in the SDS contrast data will be due to the presence of sodium and chloride ions, which have an SLD greater than that of the  $CM_{poly}$ . The exact contribution of these ions is impossible to calculate, as their volume is strongly dependent on their chemical environment. Coupled with our imprecise knowledge of the SLD of d-SDS, resolving individual salt and surfactant volume fraction profiles is a daunting task. Instead, we assume that the non-polymer, non-solvent, component (which produces the reflectivity profiles in Fig. 6.30) has an SLD of  $6 \times 10^{-6} \text{ \AA}^{-2}$  and report corresponding volume fraction profiles. As such, the magnitude of these volume fraction profiles is an approximation, but their overall shape will remain unchanged. The similarity of the profiles in Figure 6.30 to those in Figure 6.17c and d indicates that most of the signal is produced by the d-SDS, not by sodium and chloride ions.

Modelling of the  $CM_{poly}$  datasets in Figure 6.30 was carried out using the same method used to analyse the  $CM_{poly}$  data in section 6.3.4. The surfactant volume fraction profiles produced for high salt concentrations are similar in shape to those observed at the  $2 \times CMC^{\circ}$  SDS condition in Figure 6.17, fitting well with the system behaviour scaling around  $CMC^{eff}$ . Interestingly, the quantity of adsorbed material increases markedly at 500 mM, matching the step-change in  $\Delta f$  and  $\Delta D$  observed via QCM-D. One inconsistency between the NR results from surfactant-identity and salt-concentration studies (Fig. 6.17 and Fig. 6.30) is the surfactant volume fraction profile at 0 mM salt at high temperatures. The adsorbed quantity of SDS is much greater in Figure 6.30; which indicate that SDS remains in the layer upon collapse. We are unable to fit this data with any profile other than those shown in Figure 6.30, and we repeated measurements at the

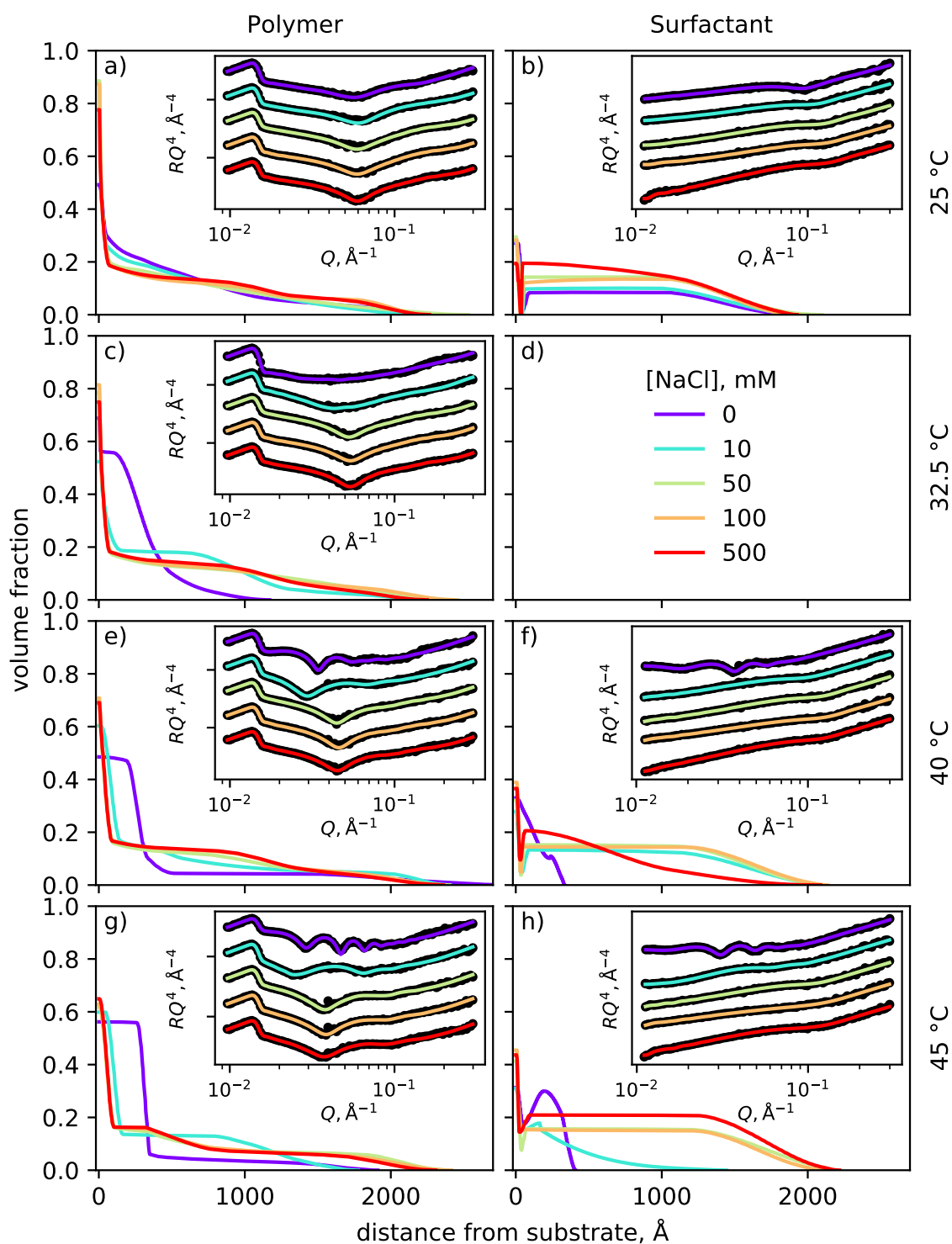


Figure 6.30: Volume fraction profiles for (*left panels*) PNIPAM and (*right panels*) SDS for the PNIPAM-SDS-NaCl system as a function of increasing temperature (top to bottom) and salt concentration (colours). The corresponding reflectometry data and modelled profiles are inset; reflectometry profiles are vertically offset and scaled by  $Q^4$  for clarity. The SDS concentration is fixed at  $0.5 \times \text{CMC}^\oplus$ . As NaCl is added to the system, the brush swells and its thermoresponse is suppressed. Added salt appears to increase the amount of SDS in the brush, although it is impossible to differentiate between surfactant in the brush layer and salt in the brush layer due to their SLDs.



0 mM NaCl condition to ensure our observation of fringes was not the result of experimental error. There are two potential explanations for this behaviour. The first is the unexpected adsorption (and slow-release kinetics) of salt within the brush (in both 0 mM NaCl measurements the prior condition was at 500 mM salt); here the adsorbed signal would be predominantly due to adsorption of salt. The second is that the difference in brush thickness between the two studies (115 Å vs 225 Å) changes the way surfactant adsorbs.

### 6.5.4 Discussion

Here, we will first discuss the effect of NaCl on the structure of the PNIPAM-SDS system in regard to relevant literature, before noting that the system structure is governed by the SDS concentration relative to  $\text{CMC}^{\text{eff}}$ . We will then speculate as to the cause of the odd behaviour observed by all techniques at 500 mM NaCl. We will then compare the behaviour of the PNIPAM-SDS system to conventional polyelectrolytes and discuss the absence of the common salting out phenomena for our system. Finally, we will summarise the behaviour of our system based on the findings in this chapter.

#### Effect of NaCl on structure of SDS-PNIPAM system

All techniques employed here clearly show that the addition of NaCl promotes the swelling of the PNIPAM-SDS system. The primary mechanism that drives this behaviour is the reduction of the  $\text{CMC}^{\text{eff}}$ , which we discuss below. Here we comment on the phenomenological aspects of our system and draw comparisons with available literature.

Our observation of NaCl swelling the PNIPAM-SDS system disagrees with the findings of Patel et al. [241]. Patel et al. study a free-PNIPAM system and report that NaCl decreases the CST of PNIPAM-SDS systems; relevant results are included here in Figure 6.6. Unsurprisingly, our results indicate that salt increases the amount of surfactant that can bind to the PNIPAM (Fig. 6.30, 6.26). Our findings here agree well with other reports of SDS behaviour [226, 233, 277], and reflects NaCl reducing the Debye length, allowing charged micelles to stack closer together. The discrepancy between our work and that of Patel et al. is probably due to the depletion of free surfactant in their free-polymer study. Our results indicate mass binding ratios as high as 2 for SDS and PNIPAM in the presence of salt, which would result in the total depletion of surfactant from solution even at the highest surfactant concentration probed in the work of Patel et al.

We note that behaviour similar to what we observe here has been reported for other polymer systems. For instance, Masuda et al. [274] study a PEO-SDS system, and found

that the addition of NaCl both reduced the SDS concentration required to swell the polymer and increased the swelling magnitude.

### Scaling of behaviour around $\text{CMC}^{\text{eff}}$

The primary mechanism by which the addition of NaCl induces layer swelling appears to be through the modulation of the  $\text{CMC}^{\text{eff}}$  of the surfactant, shown most clearly in Figures 6.25 and 6.27a. We remind the reader that  $\text{CMC}^{\text{eff}}$  is the effective value of the free-surfactant CMC at a particular condition (e.g., NaCl concentration, Fig. 6.5). In this sense, NaCl is only modulating the interaction between SDS and PNIPAM — any other change to the system that decreased the CMC and CAC of the surfactant (i.e., substituting for a more hydrophobic surfactant like SDBS, shown in Fig. 6.9) would likely have a similar effect. We conclude that at low salt concentrations ( $<200$  mM) in PNIPAM-SDS-NaCl systems, the polymer structure can be explained by the system temperature and the SDS concentration relative to  $\text{CMC}^{\text{eff}}$ .

However, there seem to be some secondary effects on brush structure at higher salt concentrations that cannot be explained by a changing  $\text{CMC}^{\text{eff}}$ . The first, and most obvious, effect is the step-change observed at 500 mM NaCl by all techniques; this will be discussed in detail below. The second effect of increasing salt concentration is the subtle increase in swelling in the interior of the brush, which is only observable with QCM-D, and to a lesser extent NR. While the  $\Delta f$  of the 3<sup>rd</sup> overtone in QCM-D experiments appeared to be predominantly dependent on the surfactant concentration relative to  $\text{CMC}^{\text{eff}}$  (ignoring the 500 mM data point), the 7<sup>th</sup> and 11<sup>th</sup> overtones did not (Fig. 6.27). Consequently, our QCM-D results in Figure 6.27 indicate that adding salt to the system at a fixed  $C_{\text{surf}}$  biases adsorption/swelling in the brush interior, rather than in its periphery. This conclusion is supported by the NR results, which show salt reducing  $\phi_{\text{poly}}$  at the base of the brush (Fig. 6.30a).

We now turn to consider the  $\Delta D$  results from the QCM-D study, which cannot be explained by the  $C_{\text{surf}}/\text{CMC}^{\text{eff}}$  at any overtone. Dissipation measures the rate at which the layer dissipates kinetic energy to its environment. It can be thought of as a measure of stiffness vs softness or elasticity vs viscosity. In Figure 6.27,  $\Delta D$  indicates that the layer gets stiffer as salt is added above  $1 \times \text{CMC}^{\text{eff}}$ . An examination of the overtones shows that this change in stiffness is more pronounced at the exterior of the brush layer. Decreasing dissipation with the addition of salt is not unexpected for polyelectrolyte brushes [83]. However, this typically corresponds to a brush collapse, which is not observed by any other technique. Several mechanisms could contribute to the observed trends in  $\Delta D$ . The first of these is that the decrease in Debye length electrostatically decouples

the (charged) polymer-surfactant complexes from micelles in solution. This explanation fits with the salt-induced reduction in  $\Delta D$  being more significant at  $2 \times \text{CMC}^\oplus$  than at  $0.5 \times \text{CMC}^\oplus$  and explains why the effect is much more pronounced at the brush periphery. The second is that the high local concentrations of surfactant and salt within the brush, brought about by increased ionic strength, results in the layer becoming more mechanically rigid. However, increased rigidity should also reduce the difference between the frequency overtones, which is not evident in Figure 6.27; as such, we prefer the decoupling argument presented above. Probing the mechanical properties of the system via AFM, or a lower-stress version of the confinement in section 6.4, could confirm this brush stiffening.

### Behaviour of the system at 500 mM NaCl

All techniques exhibit a step-change at 500 mM NaCl. Ellipsometry shows an increase in thickness at high temperatures (Fig. 6.24), QCM-D shows a sudden increase in  $\Delta D$  and a marked decrease in  $\Delta f$  (Fig. 6.26), and NR shows an increase in surfactant adsorption within the layer (Fig. 6.30). Of these trends, the abrupt change in the  $\Delta D$  is the most difficult to explain. Below 500 mM NaCl, increasing salt concentration decreases  $\Delta D$  as discussed above. However, at 500 mM there is a sudden increase in  $\Delta D$  that is present across all overtones and samples.

It has previously been reported that the micelles formed by SDS transition from spherical to worm-like at a NaCl concentration of 450 mM [215, 216, 233]. This transition in micelle morphology is likely responsible for the changes observed by ellipsometry, QCM-D and NR. Polymer-attached worm-like micelles could interact with those in solution, which would explain the increase in dissipation observed. Worm-like micelles would also allow for the binding ratio of PNIPAM to SDS to increase, further increasing the amount of surfactant in the brush layer and explaining the ellipsometry and NR results.

### Absence of salting-out phenomina

Our work here indicates that PNIPAM-SDS systems are immune to the salting-out effect common to polyelectrolytes. Here, we examined behaviour up to 500 mM of NaCl; strong polyelectrolytes have been observed to begin collapsing above  $\approx 200$  mM [278, 279]. For our system, large changes in the structure of the PNIPAM-SDS system were not expected below the CST, as PNIPAM is reasonably swollen at this condition in pure water. However, we expected to see a significant collapse above the CST in the presence of 500 mM salt for all SDS concentrations. Naïvely, an SDS decorated PNIPAM chain at 40 °C is comparable to a polyelectrolyte with a hydrophobic backbone; at high salt concentrations, we expect that the structural influence of the tethered charges will be negated by the NaCl

solution, resulting in a hydrophobic polymer. This reasoning is dubious even without the current work, due to the complex phase behaviour of PNIPAM. We discussed the thermal collapse of PNIPAM at length in section 1.2, emphasizing that the polymer undergoes a complex entropy-driven re-arrangement at its CST which cannot be reduced to a simple hydrophilic to hydrophobic transition. Even still, the absence of any salting-out effect is remarkable.

The key difference between a conventional polyelectrolyte and the PNIPAM-SDS complex is that the number of charges is fixed in the polyelectrolyte system. In contrast, the number of charges in the complexed system is hypothetically limited only by the packing of surfactant onto a strongly-stretched polymer chain. It is known that as the ionic strength of a solution increases the Debye length shrinks and charged moieties can pack more tightly [226, 233, 277]. Taken together with the decrease in  $\Delta f$  (in QCM-D experiments, Fig. 6.26) and increase in the surfactant volume fraction (in NR experiments, Fig. 6.30), this strongly suggests that the presence of salt allows for the accumulation of surfactant on the polymer chain, increasing the number of effective charges on the polymer. These charges bring in additional salt and water, resulting in a higher osmotic pressure within the brush and causing additional swelling. It is this mechanism that negates the typical ‘salting-out’ phenomena seen in these systems.

### Summary of system behaviour

In light of our findings above and relevant literature, we propose a model for the structure of the PNIPAM-SDS-NaCl system as a function of salt and surfactant concentration, which we present in Figure 6.31.

At no-salt (or very low salt,  $<1$  mM) conditions, SDS adsorbs to PNIPAM as micelles. These micelles are always smaller than equivalent free-micelles, but vary in size depending on the surfactant concentration — with aggregation numbers varying from  $\approx 8$  at the CAC (Fig. 6.31a) to  $\approx 22$  at the CMC (Fig. 6.31b) [249].<sup>viii</sup> The addition of SDS promotes layer swelling and retards the thermoresponse of PNIPAM, with the influence beginning above the surfactant CAC and stabilising after the CMC [252].<sup>ix</sup> However, SDS only associates with PNIPAM that is solvated (i.e., not collapsed) [252], causing two-phase intermediate regions (Fig. 6.15c, Fig. 6.31a).

At intermediate salt concentrations ( $<250$  mM NaCl), the system behaviour can be explained almost entirely by the concentration of the surfactant relative to the salt-modulated CMC,  $\text{CMC}^{\text{eff}}$ . At surfactant concentrations less than  $1 \times \text{CMC}^{\text{eff}}$  (Fig. 6.31c)

<sup>viii</sup>Chen et al. [252] find that the CAC is  $\approx 0.82$  mM.

<sup>ix</sup>we observe SDS influencing PNIPAM behaviour above  $\approx 3$  mM

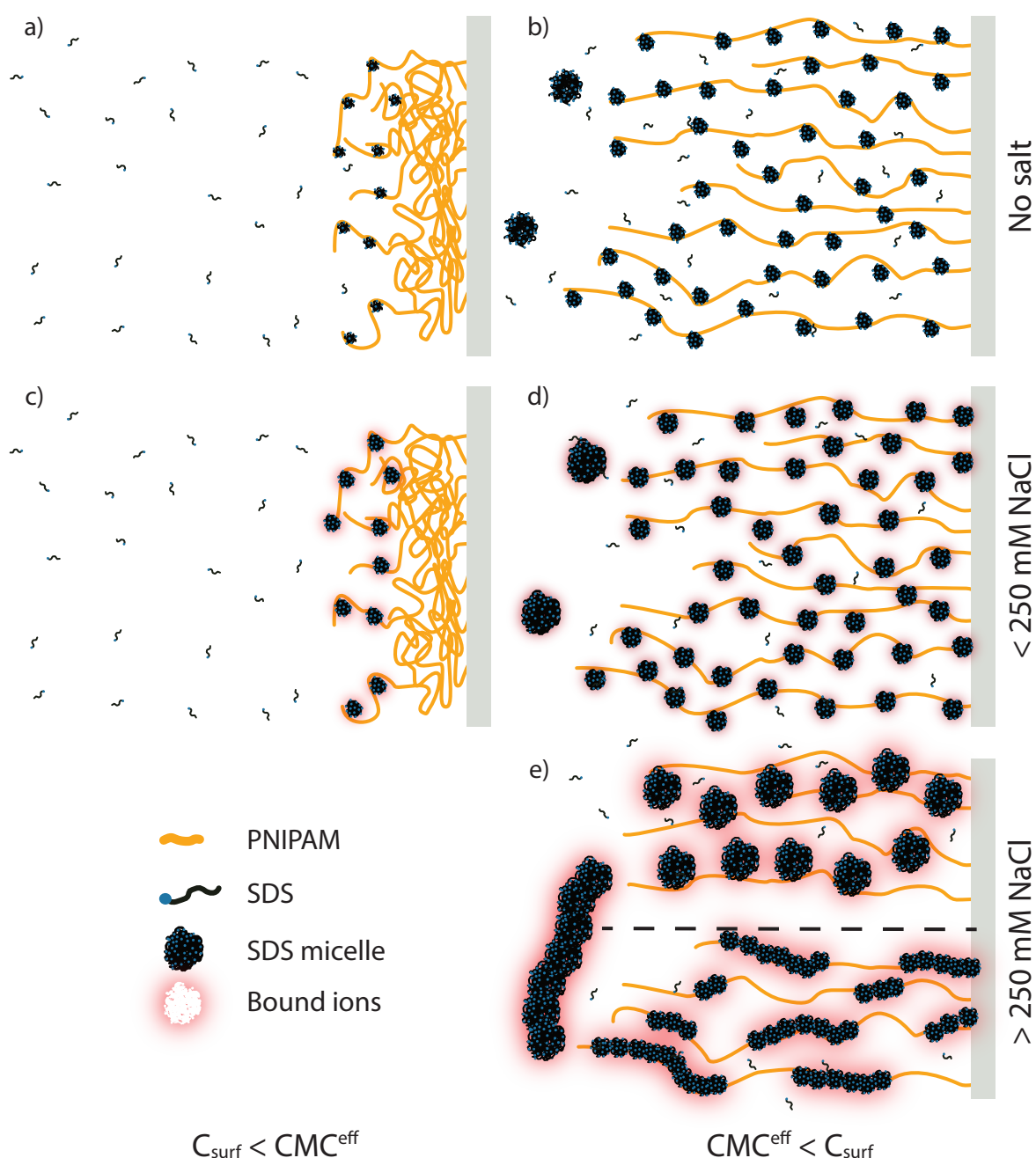


Figure 6.31: Schematic of the proposed structure for the PNIPAM-SDS-NaCl system. Here the system is shown above the (pure-water) CST of PNIPAM. (a) Below the  $\text{CMC}^{\text{eff}}$  in the no-salt condition, SDS either associates with PNIPAM, swelling it, or does not interact at all [251, 252], resulting in two-phase volume fraction profiles (Figs. 6.15, 6.30). (b) At concentrations near and above the  $\text{CMC}^{\text{eff}}$  in the no-salt condition, SDS strongly swells PNIPAM and suppresses its thermoresponse. (c, d) Moderate ionic strengths promote the growth of micelles, but the structure of the polymer still scales around the  $\text{CMC}^{\text{eff}}$ . (e) Higher ionic strengths further promote micelle growth, causing changes in brush structure and mechanical properties that cannot be explained by the concentration of the surfactant relative to  $\text{CMC}^{\text{eff}}$ . At a particular ionic strength (around 450 mM NaCl, indicated by the dashed line) we hypothesise that the geometry of the polymer bound micelles transitions from spherical to rod-like.

the micelles grow with increasing salt concentration, behaving in much the same way as the system in pure water with equivalent  $C_{\text{surf}}/\text{CMC}^{\text{eff}}$ . When the surfactant concentration is greater than  $1 \times \text{CMC}^{\text{eff}}$  (Fig. 6.31d) the amount of polymer tethered SDS begins to increase. Most likely this increase manifests as an increase in micelle size, as it does in free solution (Fig. 6.5) [226, 233], but could be due to the density of tethered micelles increasing. Either way, the increased amount of SDS inside the brush is due to the screening of the headgroup charge.

Finally, at high salt concentrations ( $\geq 450$  mM, Fig. 6.31e), the micelles transition from spherical to worm-like [215, 216, 233]. As we have not examined the behaviour of different surfactants at high salt and surfactant concentrations, we cannot comment on whether the mode of interaction changes from the polymer adsorbing to the micelle surface to being incorporated into the micelle core. However, the parsimony principle would imply that the interaction mechanism does not change, and the polymer remains adsorbed to the surface of the worm-like micelles. In our work, we only probe salt concentrations up to 500 mM; it is possible that at higher salt concentrations salting-out phenomena could be observed. At NaCl concentrations of around 1500 mM, the SDS is expected to precipitate out of solution, forming hydrated crystals [258] (i.e., the surfactant will be below the Krafft point). The exact point where precipitate begins to form will depend on the surfactant concentration and system temperature. We make no predictions as to the ternary system behaviour at these conditions.

## 6.6 Conclusion

In this chapter, we have extensively studied the structure and mechanical properties of behaviourally complex PNIPAM-surfactant systems using a number of surface-sensitive techniques. The significance of this work can be divided into two sections. The first is the knowledge gained regarding the interaction of PNIPAM with surfactants, particularly SDS. The second is that we have demonstrated and field-tested many of the NR techniques developed throughout this thesis to investigate a complex system.

### 6.6.1 Understanding PNIPAM-surfactant systems

We have confirmed the behaviour of PNIPAM-surfactant systems reported by phenomenological studies of the system [239, 241, 242], finding that only anionic surfactants (at least sulphate-headed surfactants) modify the structure and thermoresponse of PNIPAM. Techniques sensitive to the mass and distribution of the surfactant adsorbed within the brush revealed that the primary reason for the exceptional behaviour of the anionic system is that anionic surfactants have an affinity for PNIPAM, while the cationic and nonionic surfactants studied do not. However, while SDS resulted in more adsorbed charge within the brush layer than CTAB, the difference in adsorbed charge could not completely account for the behaviour change. Therefore, the change in behaviour between anionic and cationic surfactants is due not just to the affinity between polymer and surfactant, but also their interaction mechanism.  $CM_{poly}$  NR indicates that the SDS:PNIPAM mass binding ratios of approximately 1:1 in pure water above the CMC, agreeing reasonably well with the values reported by Mylonas, Staikos, and Lianos [249] and Mears et al. [246], (0.6 and 0.5, respectively). The difference can be explained by the sensitivity of  $CM_{poly}$  NR to all polymer-proximal surfactant, rather than just bound surfactant.

The marked difference between the interaction of anionic and cationic surfactants with PNIPAM implies that the interaction is mediated by the surfactant head-group, rather than by the surfactant tail as previously reported [248, 252, 254, 280]. These conflicting models have both been proposed for some time [244], here we have clarified the state of the art and conclusively shown that anionic surfactants have a greater affinity for PNIPAM than neutral or cationic surfactants. We suggest that the PNIPAM-surfactant interaction is the same as the model proposed for PEO-surfactant systems. In this model, the polymer adsorbs onto the micelle surface, with the hydrophobic polymer moieties in contact with the hydrophobic surfactant tail, and the hydrophilic polymer moieties in contact with the surfactant headgroup. This arrangement is energetically favourable due to the polymer covering the exposed portions of the micelles hydrophobic core, enabling

PNIPAM-anchored micelles to form below the solution  $\text{CMC}^{\text{eff}}$ .

We probe the confined behaviour of PNIPAM-SDS systems using the sample environment and modelling methodology established in chapter 5. We observe SDS remains in the brush layer during macroscopic confinement, resulting in a thicker confined layer. Isotopic substitution of SDS for d-SDS shows extremely high SDS concentrations within the brush, revealing that the mechanism by which SDS increases the final thickness of the collapsed brush is steric. We find that the collapsed brush in water and the collapsed brush in  $1.75 \times \text{CMC}^{\oplus}$  SDS solution have comparable water fractions. The SDS within the collapsed layer is concentrated close to the substrate. We hypothesise that this is due to a top-down collapse of the brush in response to confinement that pushes SDS from the extremities of the brush towards the substrate, where it becomes trapped.

To further probe the exceptional behaviour of PNIPAM-SDS systems, we have investigated their behaviour upon the addition of an electrolyte (NaCl). We find that below 500 mM NaCl the PNIPAM structure (i.e., the volume fraction profile) scales with the salt-modulated  $\text{CMC}^{\text{eff}}$ . However, QCM-D shows that the mechanical properties of the system do not scale around the  $\text{CMC}^{\text{eff}}$ , with the addition of NaCl below 500 mM resulting in the brush becoming stiffer. At 500 mM NaCl, a step-change is observed by all techniques; we hypothesise that this is due to the transition of the SDS micelles from a spherical to a worm-like geometry both within the brush and in free solution. Previous studies have reported that this transition occurs for SDS micelles in solution at 450 mM NaCl [215, 216, 233]. We also find that the PNIPAM-SDS appears to resist the classic salting-out phenomena associated with polyelectrolytes. We hypothesise that this is due to an increase in salt concentration, allowing more SDS to adsorb to an individual polymer chain. The addition of SDS molecules increases the number of polymer-associated counter-ions and water molecules, promoting further swelling. We note that the QCM-D experiments described in this chapter would benefit from a modelling approach that provides deeper insight into mechanical properties as a function of distance from the substrate, and allows adsorbed surfactant mass to be determined independently of brush structure.

We find that, although the structure and swelling behaviour of PNIPAM-SDS systems can be compared to that of a polyelectrolyte, they do not behave identically. Most notably, their lack of salting-out behaviour and the different mechanism through which they resist confinement (compared to Abbott et al. [79]) distinguish them from conventional polyelectrolytes.



### 6.6.2 Demonstration of improved NR analysis

In this chapter, we have applied the NR analysis techniques developed in chapters 4 and 5 to answer open questions about specific both polymer brush behaviours and polymer-surfactant phenomena more generally. The freeform model developed in chapter 4 allowed for the determination of the brush structure in systems where there was no existing theoretical description of its behaviour. In this analysis, the model parameter bounds were informed by the transient nature of the interior layer uncovered through the characterisation in chapter 2. Similarly, the SLD range and the relationship between  $\hat{V}_I$  and dry thickness for PNIPAM were drawn from findings in chapter 3.

Furthermore, the adaptation of the freeform model from chapter 4 (appendix J1) enables the determination of surfactant volume fraction profiles in the  $CM_{poly}$  experiments (Fig. 6.17, 6.30). This is particularly valuable, as the prior information regarding the distribution of surfactants within polymer brushes is minimal. The value of the PT-MCMC approach introduced in chapter 4 was also demonstrated here. When determining the distribution of adsorbed surfactant, PT-MCMC sampling revealed a multimodal solution space (Fig. 6.19), allowing us to select the profile that best agreed with prior FAOR and QCM-D studies. The final profiles were not those that were located by a differential evolution optimisation.

Lastly, the confinement apparatus and modelling methodology in chapter 5 enable the study of confined PNIPAM-SDS systems. We combine the confinement model and freeform model (appendix J1) to describe the SLD profile of d-SDS trapped within the collapsed brush, revealing mechanistic details regarding the confined system.

Hence, the work in this chapter demonstrates the need for and usefulness of improved reflectometry analysis methods in understanding the behaviour of complex brush systems.

# Chapter 7:

## Conclusions and future work

## 7.1 Conclusions

This thesis has detailed analysis techniques and experimental methods that improve our ability to resolve the structure of solvated polymer brushes and enable the study of more complex brush systems using NR. In chapters 2 and 3, we used NR to better understand the formation and unsolvated behaviour of PNIPAM brushes prepared via ATRP. In chapters 4 and 5, we developed new modelling techniques to allow the structure of the brush to be rigorously determined in both solvated and confined conditions. Finally, in chapter 6 the findings from chapters 2 and 3 and techniques from chapters 4 and 5 are brought together to study the behaviour of complex PNIPAM-surfactant systems.

In chapter 2, control over the grafting density is demonstrated before a novel *in situ* observation of the polymerisation is conducted by NR. Successful *in situ* observation of polymer growth required adjustment of instrument angle and resolution, as well as reaction conditions. While decreasing grafting density lowers the growth rate of interfacial volume during polymerisation, it does not remove the interior layer observed by previous NR experiments. As this interior layer is not observable in either dry or solvated states before the polymerisation, it must be formed from surface-adsorbed polymer chains. Understanding the origin of the interior layer contextualises and explains the volume fraction profiles reported by previous NR work [20, 22, 73, 85, 101–104].

In chapter 3, the solvation and thickness of dry PNIPAM brushes are studied as a function of temperature and relative humidity. Dry PNIPAM brushes are found to exhibit a thermoresponse, expelling water at higher temperatures, which becomes more pronounced as relative humidity is increased. A maximum change in thickness with temperature of approximately 10 % was observed between 20 and 40 °C. The careful study of the dry PNIPAM film confirms that the amide in PNIPAM deuterates in the presence of D<sub>2</sub>O [82]. The SLD for both deuterated and undeuterated PNIPAM is determined. The relationship between the hydration of the layer and the relative humidity, as well as knowledge of the PNIPAM SLD, allows for the interfacial volume to be accurately determined in later chapters.

Chapter 4 introduces the freeform brush model, which is the core contribution of this thesis to the analysis of solvated polymer brush NR data. This model allows for the efficient implementation of sensible assumptions, such as profile monotonicity and constant interfacial volume, without making unreasonable assumptions regarding the shape of the volume fraction profile. The model is paired with PT-MCMC sampling, enabling the method to evaluate the parameter posterior probability distribution; this represents the most rigorous statistical treatment of polymer brush NR data to date. The method can

identify multimodality in the modelled volume fraction profiles, ensuring that all viable profiles are made known to the user. PT-MCMC sampling from objectives with differing interfacial volume bounds reveals that knowledge of the interfacial volume is crucial to the robust determination of polymer brush structure, emphasising the importance of the characterisation in chapter 3. To demonstrate this method, it is used to analyse a PNIPAM brush undergoing its characteristic thermoresponse in water.

Chapter 5 introduces a confinement apparatus capable of subjecting thin films to uniform molecular confinement. This apparatus is used to investigate the structure of a PNIPAM brush under mechanical confinement as a function of temperature. The presence of dust between the confining membrane and the substrate means that a novel ‘distribution model’ is required to model data collected using this technique. To guide our NR experiments, we use nSCFT to simulate a thermoresponsive polymer under differing degrees of confinement and analyse AFM data from existing literature using a Derjaguin inspired modelling process. NR and nSCFT find that confining stress results in the polymer brush density profile becoming slab-like, losing its characteristic parabolic profile. Confined PNIPAM is still found to exhibit a thermoresponse, exhibiting a change in thickness of around 10% between 20 and 40 °C. Significant hysteresis in the confined swelling behaviour is observed by NR but not for AFM. We hypothesise that this is due to the time-scales associated with each experiment and the stability of the extremely collapsed PNIPAM layer, analogous to the partial vitrification phenomenon observed in free-polymer.

Chapter 6 brings together the techniques and findings from chapters 2-5, focusing them on the PNIPAM-surfactant system. The freeform model developed in chapter 4 is used to determine the PNIPAM volume fraction profile in surfactant systems, where there is no existing theoretical description of its behaviour. In this analysis, the model parameter bounds were informed by the transient nature of the interior layer uncovered through the characterisation in chapter 2. Similarly, the SLD range and the relationship between interfacial volume and dry thickness for PNIPAM were drawn from findings in chapter 3. The freeform model was also adapted to enable the determination of surfactant volume fraction profiles. This model-free approach was particularly valuable here, as the distribution of surfactants within polymer brushes has not been previously studied. The PT-MCMC approach from chapter 4 was used to great effect, revealing multimodal solution spaces for the surfactant structures, thereby allowing the surfactant volume fraction profile that best matched our complimentary experiments to be selected and honestly communicating the information contained in the neutron reflectometry data. Finally, the confinement apparatus and modelling methodology from chapter 5 were used to study confined PNIPAM-SDS systems.

The confluence of techniques in chapter 6 advances our understanding of PNIPAM surfactant systems. System behaviour was found to scale around the surfactant concentration relative to the CMC, with the effect of surfactant on PNIPAM plateauing after this point. The phenomenological reports of only anionic surfactants affecting PNIPAM conformation are confirmed by our detailed structural measurements, implying that the PNIPAM-surfactant interaction is mediated by the surfactant head-group, rather than by the surfactant tail as often reported. Current experiments are sensitive to the adsorbed mass of surfactants, conclusively showing that the remarkable effect of anionic surfactants is due to their greater affinity for PNIPAM, compared to neutral or cationic surfactants. We suggest that the polymer adsorbs onto the micelle surface, with the hydrophobic polymer moieties in contact with the hydrophobic surfactant tail and the hydrophilic polymer moieties in contact with the surfactant headgroup. When confined, the SDS was shown to remain in the brush layer, contributing to layer swelling through excluded volume effects.

At NaCl concentrations below 500 mM the polymer volume fraction profile was sensitive to the surfactant concentration relative to the salt-modulated ,  $\text{CMC}^{\text{eff}}$ . However, QCM-D and NR show that the adsorbed mass and mechanical properties of the system do not scale around the  $\text{CMC}^{\text{eff}}$ . Instead, NaCl increases the amount of surfactant within the layer, likely through promoting the formation of larger micelles, resulting in the brush becoming stiffer. All techniques showed a change in system behaviour at 500 mM NaCl; we hypothesise that this is due to the transition of the SDS micelles from a spherical to a worm-like geometry both within the brush and in free solution. Interestingly, PNIPAM-SDS mixtures resist the classic salting-out phenomena associated with polyelectrolytes, likely due to an increase in salt concentration allowing more SDS to adsorb to the polymer.

This thesis demonstrates the need for and usefulness of improved reflectometry analysis methods in understanding the behaviour of complex brush systems. These analysis methods will empower future NR experiments to better understand and harness the mechanisms behind interfacial phenomena in soft-matter systems.

## 7.2 Future work

The techniques and findings presented here highlights opportunities for future research. These are briefly outlined below.

## Observation of dynamic polymer behaviour with time-resolved neutron reflectometry

In chapter 2 we demonstrate that time-of-flight NR (performed on *PLATYPUS*) can resolve diffuse structures with time-slices as low as one minute. Time-resolved NR is a powerful technique that could be used to study other surface-initiated polymerisation methods or other kinetic processes, such as adsorption of a foulant into a brush layer. Currently, these experiments can only cover a narrow  $Q$  range, but newer instruments (such as the planned Freia reflectometer at the European Spallation Source) will be able to cover a much wider  $Q$  range while improving time resolution. If we performed the kinetic measurements described in chapter 2 on such an instrument, we would be able to describe the volume fraction profile at each step in the synthesis using the freeform model in chapter 4. This level of structural resolution could be key in observing complex dynamic phenomena such as the top-down collapse of a polymer brush.

## Behaviour of dry PNIPAM with humidity and temperature

A repeat of the NR experiment contained within chapter 3 with better control of the vapour temperature is required to verify conclusions drawn from the QCM-D study in the same chapter. This experiment would potentially be able to conclusively observe a type II phase transition in PNIPAM for the first time. Additionally, the comparison of experiments at different total pressures would be an interesting way of testing the suitability of Flory–Huggins theory for thin polymer systems in solvent vapours.

## Analysis of neutron reflectometry data collected from diffuse interfaces

The freeform model detailed in chapter 4 is flexible and can be applied to a wide range of interfaces. It has already been used to model POEGMA brushes in mixed salt solutions [73, 85] and non-monotonic copolymer brushes [102, 263]. We also used a modified version of this model to describe the surfactant volume fraction profile within a polymer brush in chapter 4.

The code required to implement this model is freely available online, as are examples of its use. We envisage uses for the model and PT-MCMC treatment of NR data for a number of soft-matter substrates, including studies of more complex brush systems and multi-layer adsorption phenomena. We anticipate that as computing power becomes more accessible, both freeform modelling and Monte Carlo techniques, which trade off user time for computation time, will become more widespread. The methodology outlined in chapter 4 can easily be deployed to compute clusters for the timely fitting of large

reflectometry datasets.

### Observation of confined polymer behaviour

The confinement cell and corresponding analysis methodology presented in chapter 5 are one of the only methods available to researchers seeking to understand the confined structure of soft, thin films. However, as it stands the method is held back by the minimum attainable confining stress of approximately 1 bar. At 1 bar, all of the layers we observe are almost completely collapsed. This is true also for the polyelectrolyte layers observed with a similar technique by Abbott et al. [79]. This minimum pressure is likely the result of the mechanical properties of the PET membrane used. A membrane with a lower elastic modulus would likely enable lower confining stresses to be probed. Furthermore, a method of performing simple confinement experiments without the requirement of a neutron beam would greatly accelerate the development of such sample environments.

The confinement study in chapter 6 raises questions regarding the difference between macroscopic and microscopic confinement, as it is likely that there is a confinement length-scale where surfactant would be able to escape the polymer layer. This is primarily related to the mass transfer of the solvent into and out of the confined surface. A better understanding of the interdependence of confinement area and time scale could be probed through the use of a patterned confining membrane (e.g., 1 mm wide, 100  $\mu\text{m}$  deep channels in a  $5 \times 5$  mm grid). A patterned membrane could reduce the effective confined area. The analysis method outline in chapter 5 would be able to account for the signal produced by such a sample.

### PNIPAM-surfactant systems

To further investigate the mechanism behind the PNIPAM-SDS interaction, the range of surfactant head-groups studied could be expanded. Of particular interest would be a series of carboxylic acids, from acetic acid to steric acid. The carboxylic acid series would allow comparison between the salting-out behaviour of formic and acetic acid [20] and the apparent swelling induced by surfactants. Observing the behaviour of a homologous series would grant insight into the mechanisms by which salts and surfactants affect brush structure.

# Appendices



## A Tabulated SLD values

The SLD values used in this thesis are collated below. Values determined from the density and molecular formula of compounds are indicative only; there were not used for detailed calculations.

Table A1: Tabulated SLDs of materials used in this thesis.

Compound	SLD, $\text{\AA}^{-2}$	Compound	SLD, $\text{\AA}^{-2}$
Si	2.07 <sup>a</sup>	PET	2.57 <sup>b</sup>
SiO <sub>2</sub>	3.47 <sup>a</sup>	SDS	0.28 <sup>b</sup>
H <sub>2</sub> O	-0.56 <sup>a</sup>	d-SDS	6.16 <sup>b</sup>
CM <sub>poly</sub>	0.809 <sup>b</sup>	CTAB	-0.45 <sup>b</sup>
D <sub>2</sub> O	6.34 <sup>a</sup>	d-CTAB	6.66 <sup>b</sup>
d-MeOD	5.80 <sup>b</sup>	C <sub>12</sub> E <sub>5</sub>	0.02 <sup>b</sup>
PNIPAM	0.72 <sup>c</sup>	d-C <sub>12</sub> E <sub>5</sub>	4.18 <sup>b</sup>
PNIPAM*	1.25 <sup>c</sup>		

<sup>a</sup>taken from literature

<sup>b</sup>calculated from density and molecular formula

<sup>c</sup>experimentally derived

\* for PNIPAM with a deuterated amide

## B Definition of $\chi^2$

$\chi^2$  is used to refer to the sum of errors squared — it should not be confused with the Flory–Huggins interaction parameter,  $\chi$ . Where  $\chi^2$  is referred to in the manuscript, it is calculated using the following formula

$$\chi^2 = \sum_{n=1}^L \left( \frac{y_n - y_{\text{model},n}}{\sigma_n} \right)^2 \quad (\text{B1})$$

where  $y_n$  is the measured data point,  $y_{\text{model},n}$  is the corresponding model value and  $\sigma_n$  is the statistical error on  $y_n$ . The reduced  $\chi^2$  is the  $\chi^2$  divided by the total number of datapoints.

## C *In situ* polymerisation method development

Due to the relative novelty of time-resolved NR in general, and observation of polymer synthesis with NR in particular, details regarding the method development and suggestions for future experiments are included below.

### C1 Neutron Reflectometry

Initially, we attempted to observe the development of the polymer layer at an angle of  $2^\circ$  in order to reach a higher  $Q$ ; however, when reduced at the desired time-resolution ( $<5$  min) the majority of the collected signal was below background. While changes in the collected reflectometry profile were observed early on in the polymerisation, there was no significant difference observed after  $\approx 10$  min. We subsequently measured the reflection at an angle of  $0.8^\circ$ , which produced the data shown in Fig. 2.9 (*in situ* sample 1). The maximum temporal resolution we could achieve at  $0.8^\circ$  was one minute.

### C2 Solution exchange

After the success of sample 1, the polymerisation recipe was revised to more closely match that used in the rest of this thesis (Table 2.1). Four different grafting densities (100, 75, 50 and 25 %) were prepared and *in situ* syntheses were carried out with identical polymerisation mixtures. These subsequent samples tended to feature more regions where no polymer had grown; presumably these spots had been the location of a bubble. These bubbles were quite large, and in the case of the 75 and 50 % experiments resulted in the corresponding data being discarded. Bubbles were not a problem for the first round of *in situ* polymerisation experiments, of which sample 1 was the culmination. One key difference between the two experiments was that sample 1 was first filled with a 2:3  $D_2O$ :d-MeOD mix before being placed on the sample stage and aligned, while samples 2 and 3 were first filled with  $D_2O$ . The wafer's surface after the bromination step is hydrophobic; if  $D_2O$  is the first liquid that is injected into the cell after assembly, the formation of static bubbles will be favoured due to the high surface tension. Conversely, if alcohol (or an alcohol mix) is injected, the lower surface tension will allow the removal of large bubbles from the cell, leading to a less patchy surface. For future experiments, we recommend that the cell first be filled with pure ethanol, to assist in displacing bubbles from the hydrophobic initiator surface, before the desired solution is injected.

Another reason for the evenness of the polymer layer may have been the difference in polymerisation solution volume exchanged with the cell. In synthesis 1, 5 mL of polymeri-

sation volume was pumped into the cell, while 3 mL was used for subsequent syntheses. The time taken to pump the solution was the same (2 min), so it is possible that a combination of the volume of the solution and the rate that it was transferred resulted in a better exchange of the polymerisation solution with the  $\text{D}_2\text{O}:\text{d-MeOD}$  that was already in the cell. For future experiments, we recommend that the polymerisation solution volume is no less than 5 mL and is pumped into the cell at a rate of no less than  $2.5 \text{ mL min}^{-1}$ .

## D Determining $T_{\text{vap}}$ in chapter 3

The NR results in chapter 3 are complicated by uncertainty in the relevant vapour temperature. During the design of the experiment it was assumed that  $T_{\text{vap}} = T_{\text{sample}}$ . This assumption was considered reasonable, as the mean-free path of a water molecule at a partial pressure of 10 mbar and 25 °C is approximately 1  $\mu\text{m}$ . However, there are numerous reasons that this assumption may not have been reasonable, most notably convective mass transfer due to the temperature gradients within the cell. The cell's external temperature was not logged, but was measured manually to ensure that it was above the saturation temperature of the  $\text{D}_2\text{O}$  vapour. The sample environment was initially at room temperature (low vapour pressure) with a final temperature of 32 °C (high vapour pressure). In Chapter 3 we use Equation 3.4 to calculate the effective  $\text{D}_2\text{O}$  saturation pressure (and hence the RH, through Eq. 3.1). This treatment produces the results in Figure 3.9, which agree well with collected QCM-D data. The temperature of the vapour according to Equation 3.4 is shown in Figure 3.8.

However, if we take  $T_{\text{vap}} = T_{\text{sample}}$  when calculating relative humidity, Figure D1 is produced. Figure D1 indicates that the thermoresponse of PNIPAM is inverted (i.e., a greater affinity for water at high temperatures), which contradicts the typical thermoresponse (i.e., a greater affinity for water at low temperatures) observed by QCM-D in Figure 3.6. To reconcile the QCM-D and NR experiments one or more of the following assumptions made for the NR experiment must **not** hold:

1. Film thickness is sensitive only to RH (i.e., independent of total pressure); or

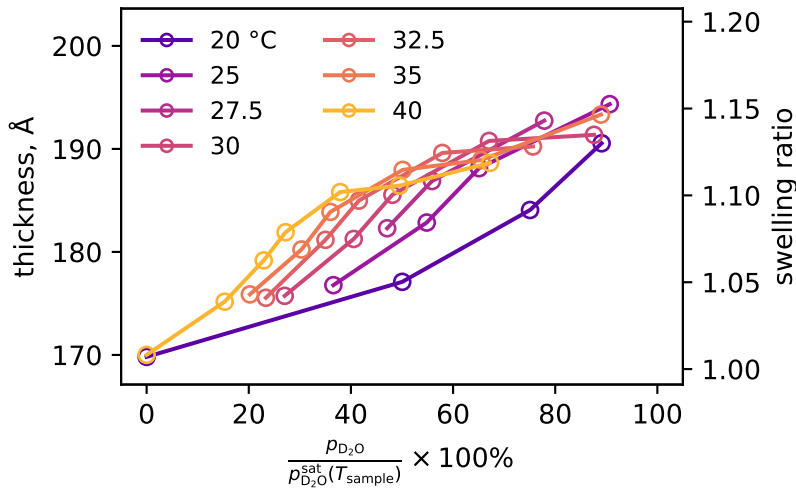


Figure D1: Thickness (*left axis*) and corresponding SR (*right axis*) as a function of RH assuming that the relative vapour temperature is the sample temperature.

2. The phase behaviour of PNIPAM at high polymer volume fractions is comparable for  $D_2O$  and  $H_2O$  systems; or
3.  $T_{\text{vap}}$  is equal to  $T_{\text{samp}}$

Assumption 1 is used in many studies of the response of thin films to humidity [75, 78, 116, 124, 126, 281] (although it must be noted that other experiments are conducted at atmospheric pressure). Furthermore, assumption 1 is based on the common thermodynamic assumption that each species in the gas phase behaves independently of all other species at low pressures.<sup>i</sup> Similarly, there is good reason to believe that assumption 2 holds. Widmann et al. [82] investigate PNIPAM microgel films in  $H_2O$  and  $D_2O$ , and while they observe differences in the swelling kinetics and ultimate hydration of the films between  $H_2O$  and  $D_2O$ , the film responds in the same manner to both solvents. Studies of PNIPAM in liquid  $D_2O$  and  $H_2O$  environments report that the films respond in much the same way, with the CST observed at the same temperature [20, 68, 276]. Given the evidence for the validity of assumptions 1 and 2, we conclude that the discrepancy between QCM-D and NR data is due to assumption 3.

As such, we produced a semi-empirical equation to define the vapour temperature as a function of both the sample and environment temperature (Eq. 3.4). The coefficients in Equation 3.4 were chosen as the surface area of the sample environment exterior was approximately three times larger than the heated sample/sample stage. This relationship yields the vapour temperature trend shown by the thin line in Figure 3.8a. Using this approximation for  $T_{\text{vap}}$  Figure 3.9 is attained, which closely resembles the trend observed by QCM-D in Figure 3.6d. It is emphasised that while the temperature given by Equation 3.4 is a good attempt at an approximation for the true vapour temperature, it was chosen as it produced similar results to the QCM-D experiment. As such, all Figure 3.9 shows is that it is possible that the QCM-D and NR experiments *could be* compatible, given the failure of assumption 3. However, without further experimentation we cannot rule out contributions from the failure of either assumptions 1 or 2. We believe that, were the NR experiment rerun with the temperature of the sample environment controlled to match that of the sample, a trend similar to that in Figure 3.9 would be produced.

---

<sup>i</sup>atmospheric pressure is considered low-pressure in this context

## E Wafer characterisation

Brushes studied with NR were extensively characterised before they were modelled to ensure that samples were of high enough quality for NR analysis, and to enable the provision of detailed prior distributions to the modelling process.

Shown overleaf are corner plots (Fig. E1, Fig. E2, E4 and E7) from the co-refining [143] of data from the PNIPAM brush in air, D<sub>2</sub>O, and a PNIPAM contrast-matched H<sub>2</sub>O:D<sub>2</sub>O mix (CM<sub>poly</sub>); the solvated measurements were conducted at 40 °C. The corner plots shown for the wafer used as the exemplar in chapter 4 are shown in more detail, to better illustrate the process by which  $\hat{V}_1$  is extracted from the characterisation (Fig. E1). Silica parameters are shown in a separate corner plot to enhance clarity (Fig. E2). In the CM dataset the main contribution to the reflectometry profile comes from the native oxide layer, so this contrast is particularly well suited to determining its structure. The D<sub>2</sub>O dataset was included to enable the porosity of the silica layer to be determined. The dry dataset provides another distinct contrast to refine the silica layer against, and allows for the dry thickness to be determined. The interfacial volume is approximated by first determining the fraction of solvent in the dry film, taking the SLD of pure PNIPAM as  $0.72 \times 10^{-6} \text{ \AA}^{-2}$ . The dry thickness is then multiplied by the polymer fraction in the dry film to yield the interfacial volume (Fig. E1). An exemplar of the silica layer structure produced by this process is shown in Fig. E3, and indicates that there is a broad transition between silicon and the native silica layer. Here, the roughness is approximately half the thickness of the oxide layer, which changes the effective SLD of the silica layer. While it would have been possible to constrain the roughness, this would have placed unjustified assumptions on the structure of the silica layer.

Characterisation of the wafers used for the confined surfactant experiment in chapter 6 was performed using the dry dataset, as measurements in CM<sub>poly</sub> were not performed on this wafer. The prior distribution for the wafers in the confined study did not need to be determined with the same precision, as the parameter of interest (separation between substrate and confined layer) produced very clear features in the reflectometry profile.

We also include ellipsometric thickness maps (Fig. E8 and E9, Fig. E10, Fig. E10, Fig. E12) to show that the surfaces studied by NR are of adequate uniformity.

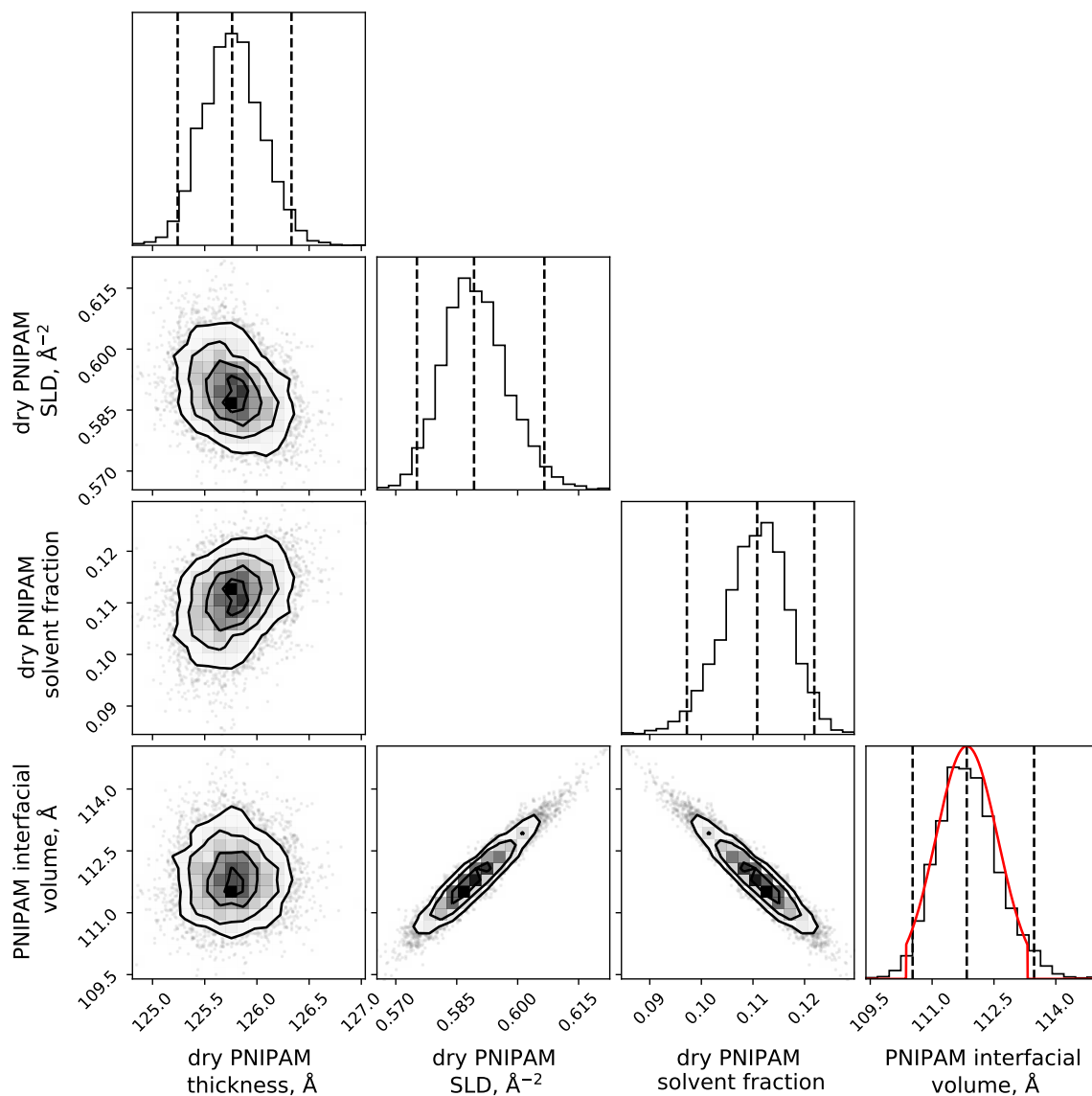


Figure E1: Corner plot of important prior parameter distributions (related to the polymer layer) for the wafer used for the exemplar dataset in chapter 4 and in the SDS and  $\text{C}_{12}\text{E}_5$  NR measurements in section 6.3. Distributions determined by PT-MCMC as per the method outline in chapter 4. The plot for the dry PNIPAM solvent fraction and dry PNIPAM SLD is not shown as the former distribution was calculated directly from the latter; as such, there is no information in the plot of their covariance. The red lines in the diagonal plots are the truncated normal distributions used to encode the prior distribution in the model.



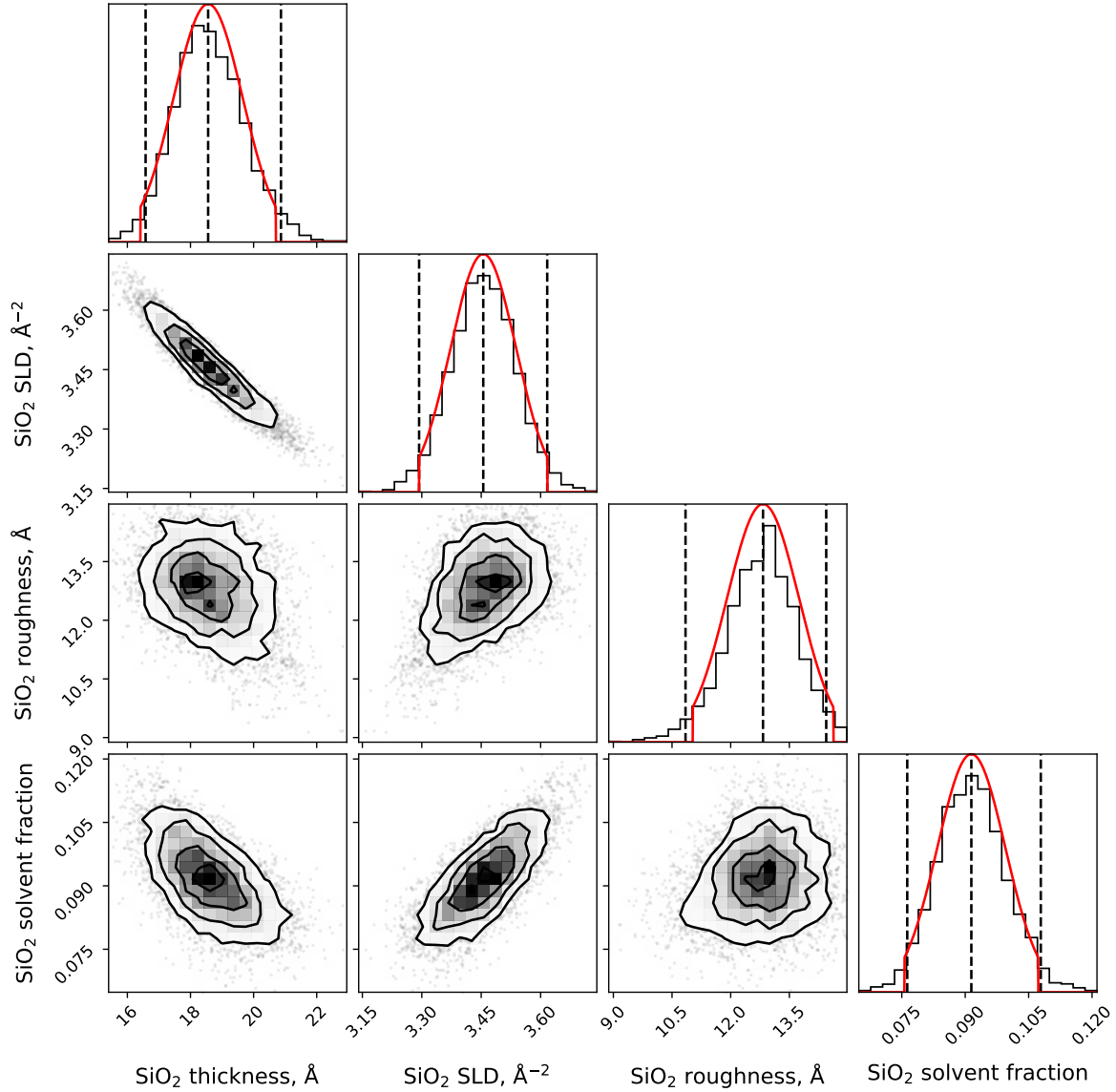


Figure E2: Corner plot of important prior parameter distributions (related to the silica layer) for the wafer used for the exemplar dataset in chapter 4 and in the SDS and C<sub>12</sub>E<sub>5</sub> NR measurements in section 6.3. Distributions determined by PT-MCMC as per the method outline in chapter 4. The red lines in the diagonal plots are the truncated normal distributions used to encode the prior distribution in the model.

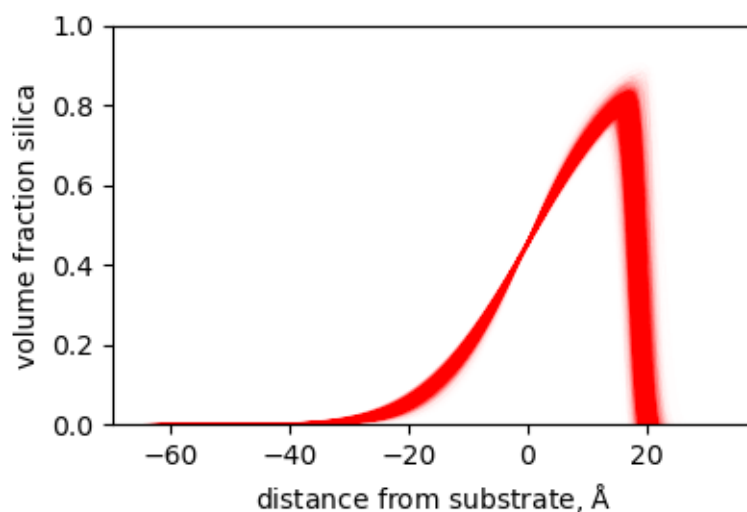


Figure E3: Volume fraction profile of the silica native-oxide layer, derived from characterisation shown in Figure E2. The thickness and SLD distributions are shown above in Figures E1 and E1. The red lines in the diagonal plots are the truncated normal distributions used to encode the prior distribution in the model.

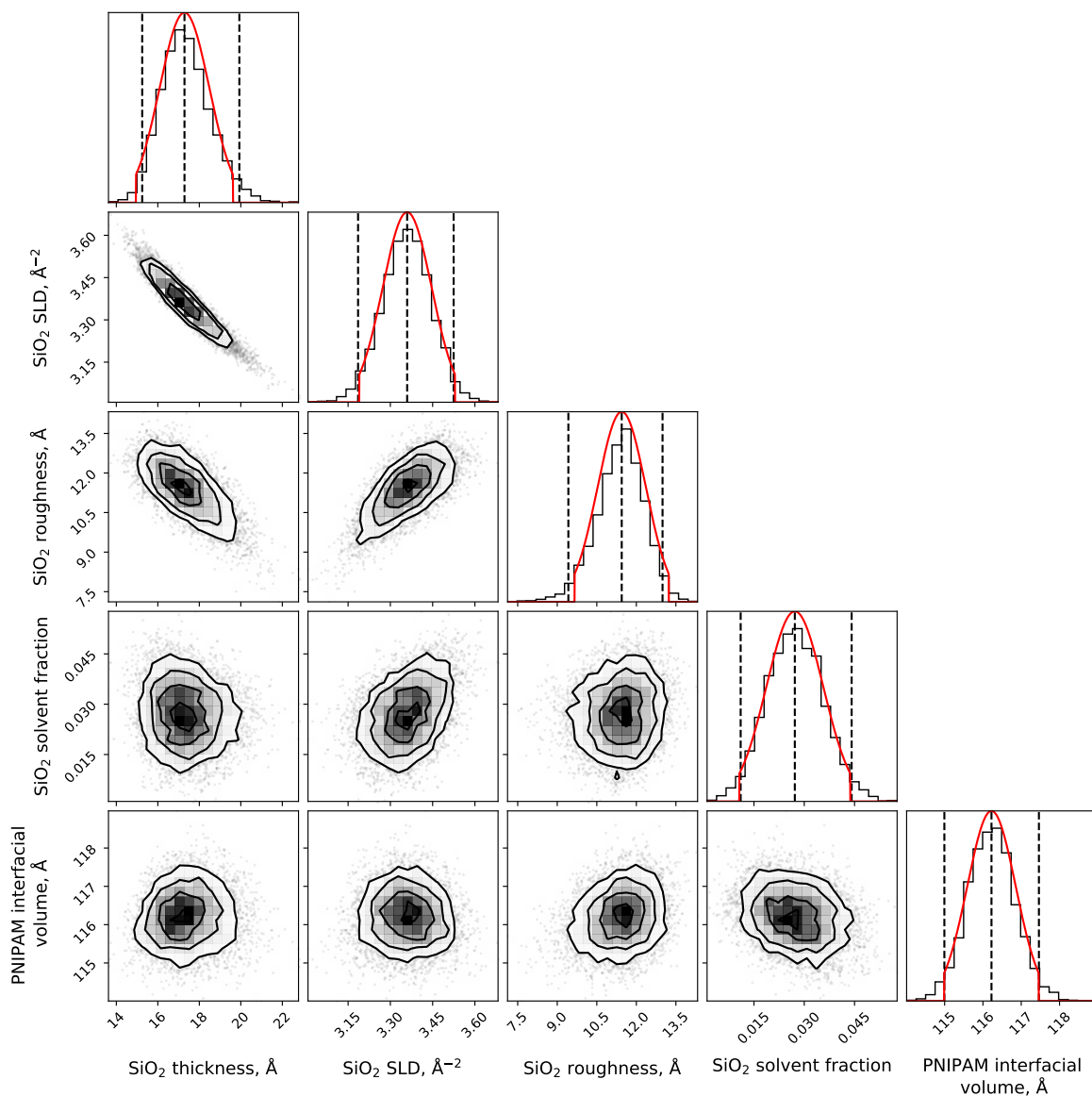


Figure E4: Corner plot of important prior parameter distributions for the wafer used for NR measurements in CTAB solutions as determined by PT-MCMC as per the method outline in chapter 4. The red lines in the diagonal plots are the truncated normal distributions used to encode the prior distribution in the model.

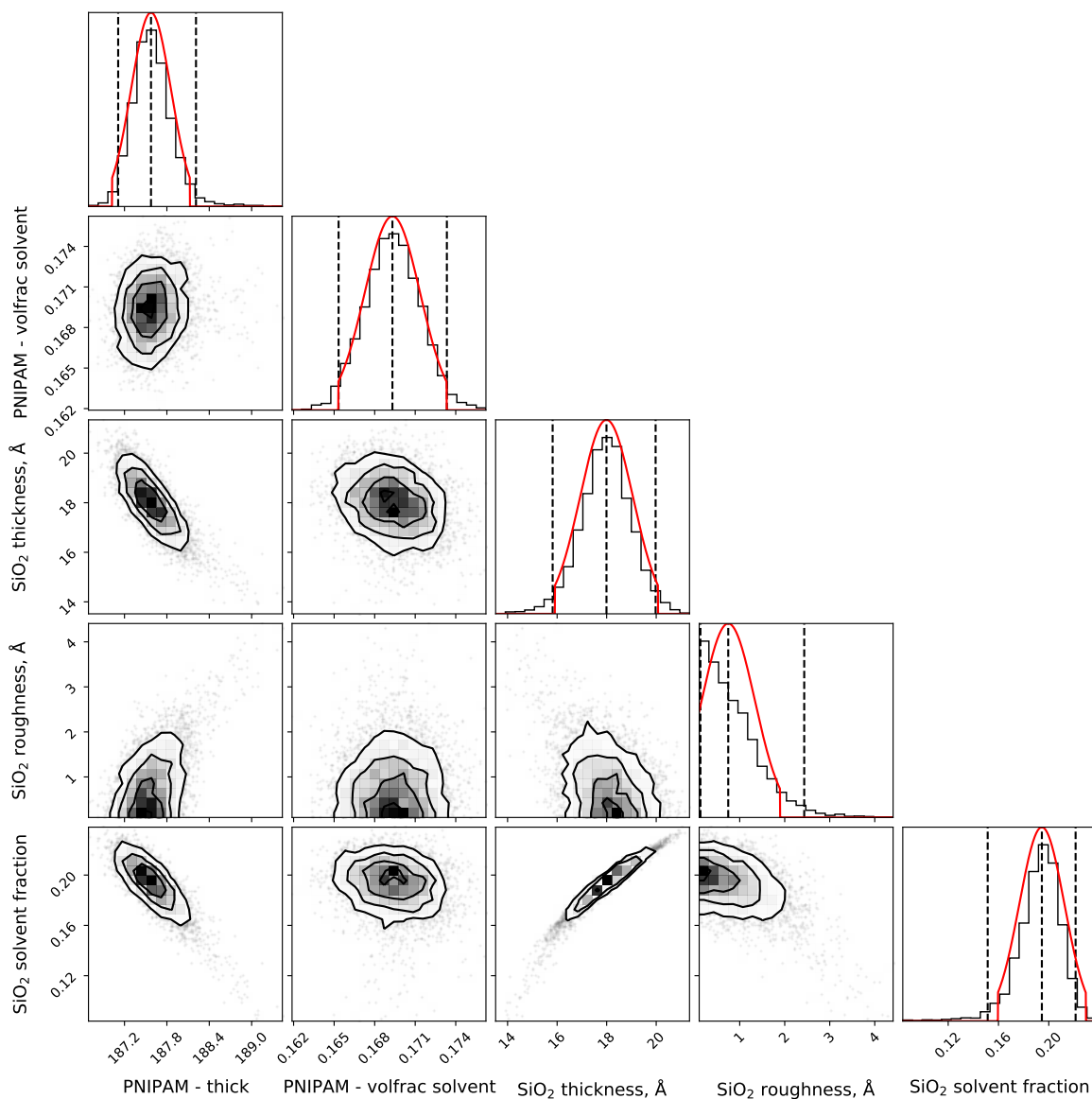


Figure E5: Corner plot of important prior parameter distributions for the wafer used for the confined 35 °C 1 bar NR measurements in SDS in section 6.4, as determined by an MCMC treatment of the dry dataset (initialised from an optima found by differential evolution). The red lines in the diagonal plots are the truncated normal distributions used to encode the prior distribution in the model.

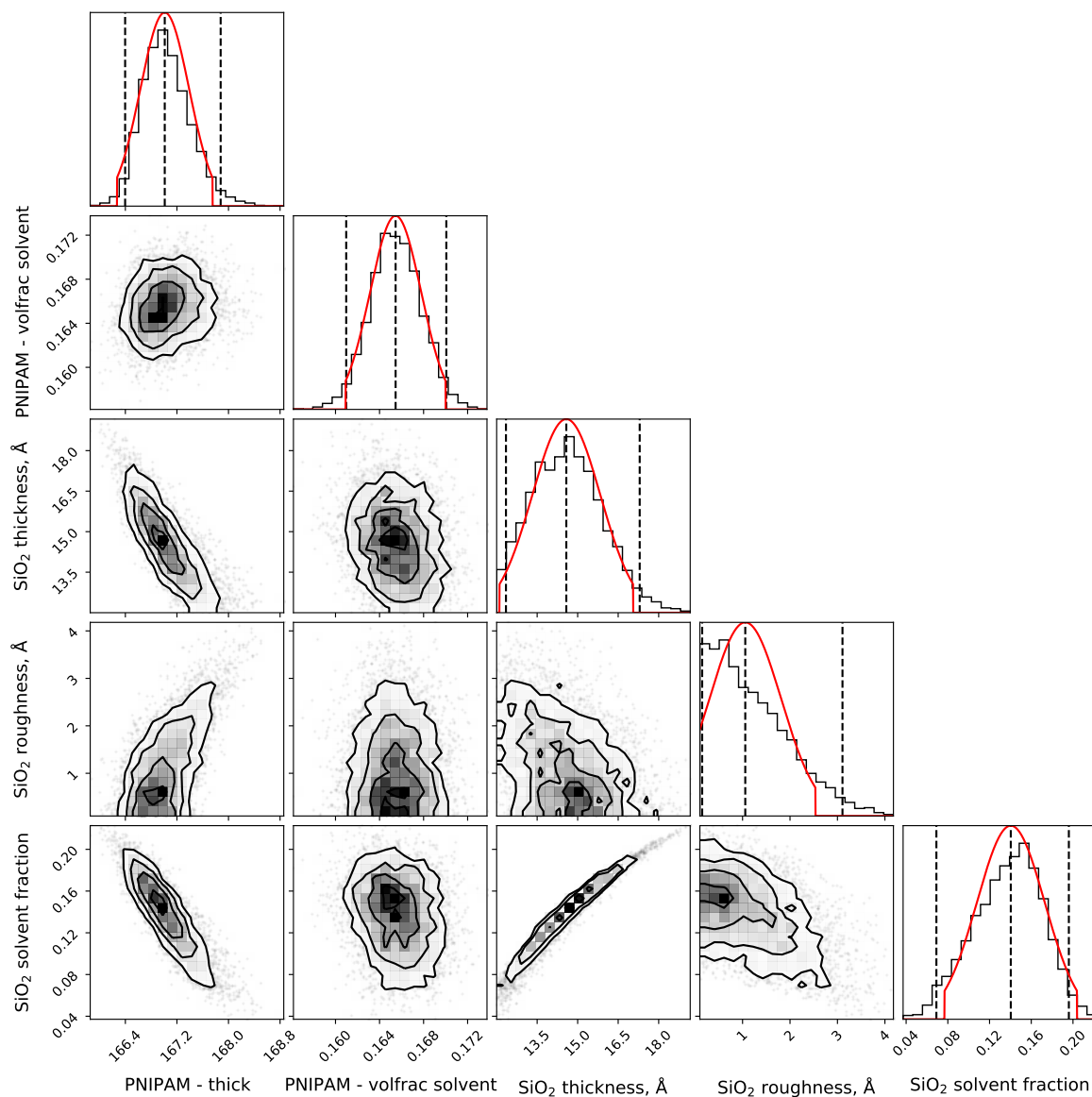


Figure E6: Corner plot of important prior parameter distributions for the wafer used for the confined 25 °C 5 bar NR measurements in SDS in section 6.4, as determined by an MCMC treatment of the dry dataset (initialised from an optima found by differential evolution). The red lines in the diagonal plots are the truncated normal distributions used to encode the prior distribution in the model.

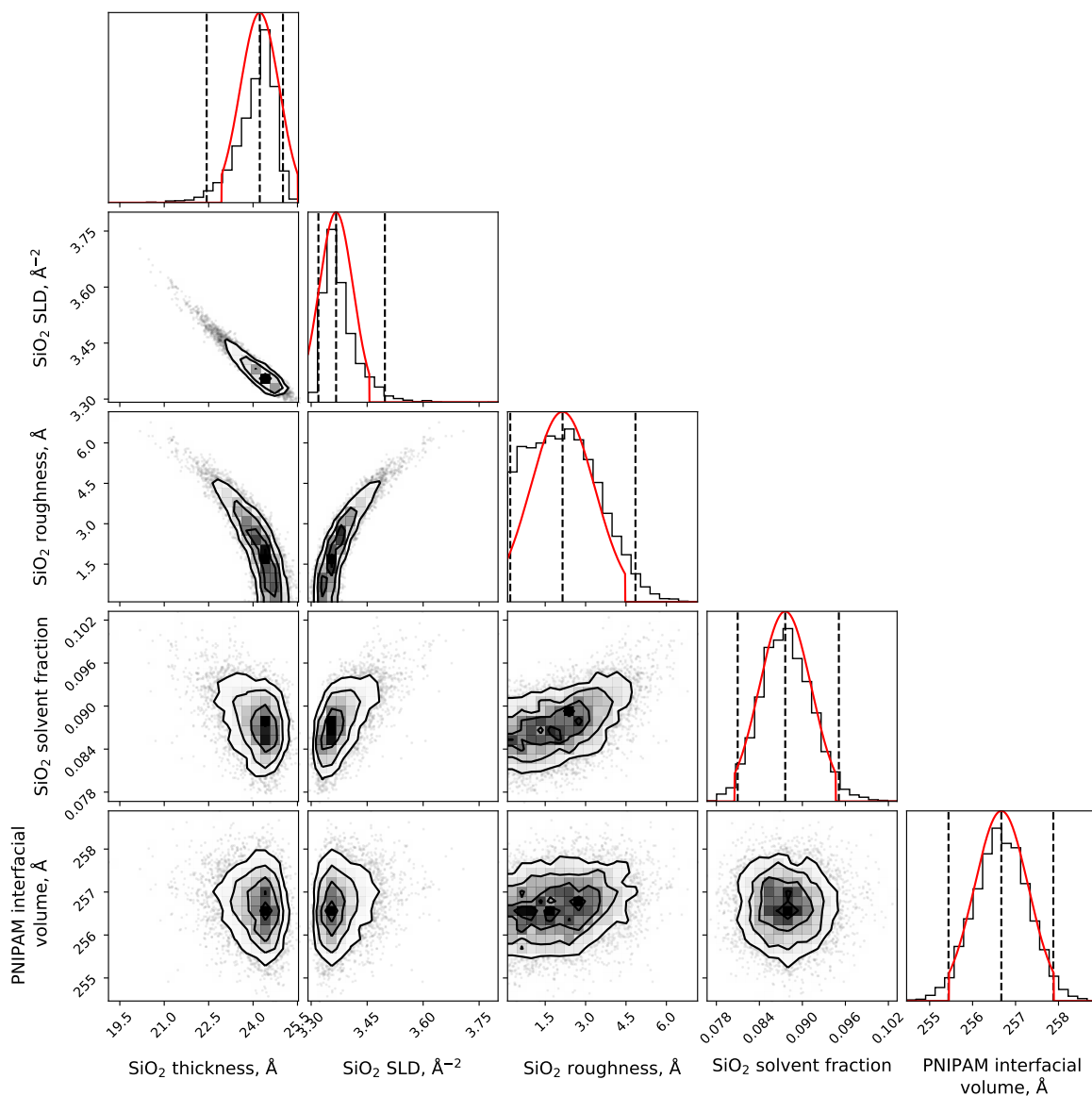


Figure E7: Corner plot of important prior parameter distributions for the wafer used for SDS-NaCl NR measurements in section 6.5. Distributions determined by PT-MCMC as per the method outline in chapter 4. The red lines in the diagonal plots are the truncated normal distributions used to encode the prior distribution in the model.

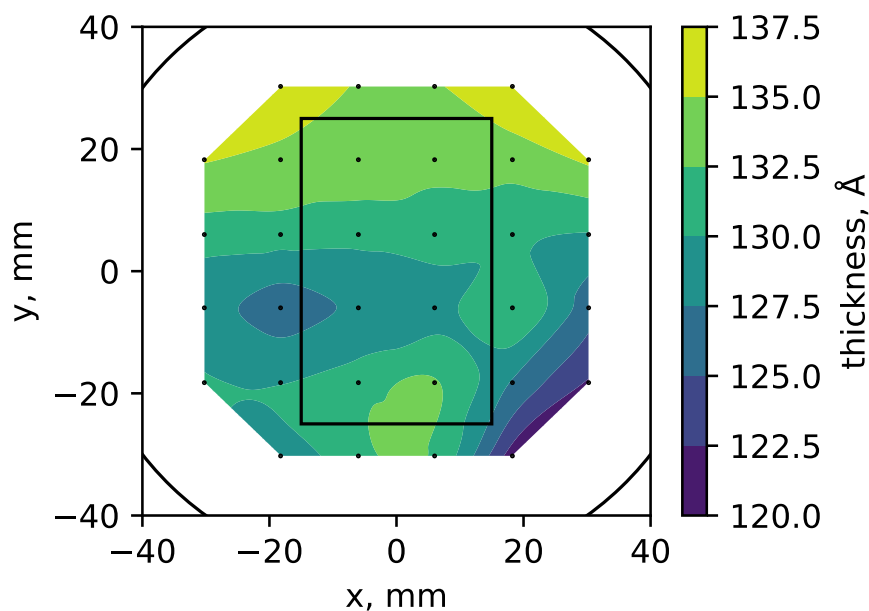


Figure E8: Ellipsometry map of the wafer used for the exemplar characterisation in chapter 4 and for measurements in SDS and  $C_{12}E_5$  in section 6.3.

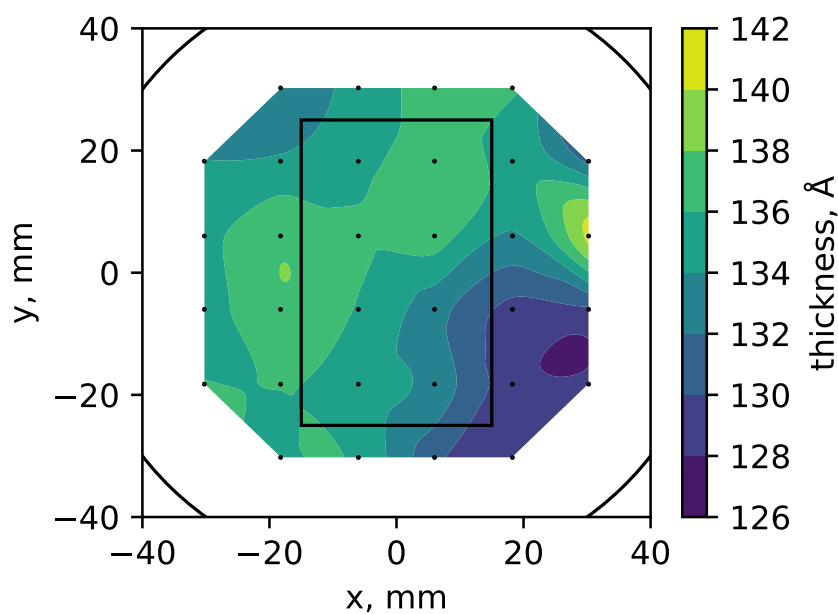


Figure E9: Ellipsometry map of the wafer used for measurements in CTAB and DTAB in section 6.3.

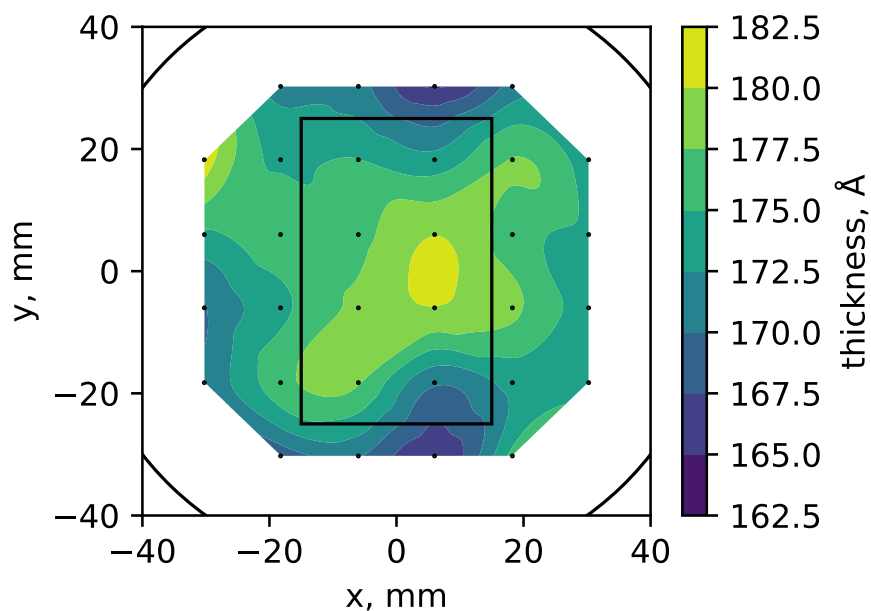


Figure E10: Ellipsometry map of the wafer used for confined PNIPAM-SDS (1 bar 35 °C) studied in section 6.4.

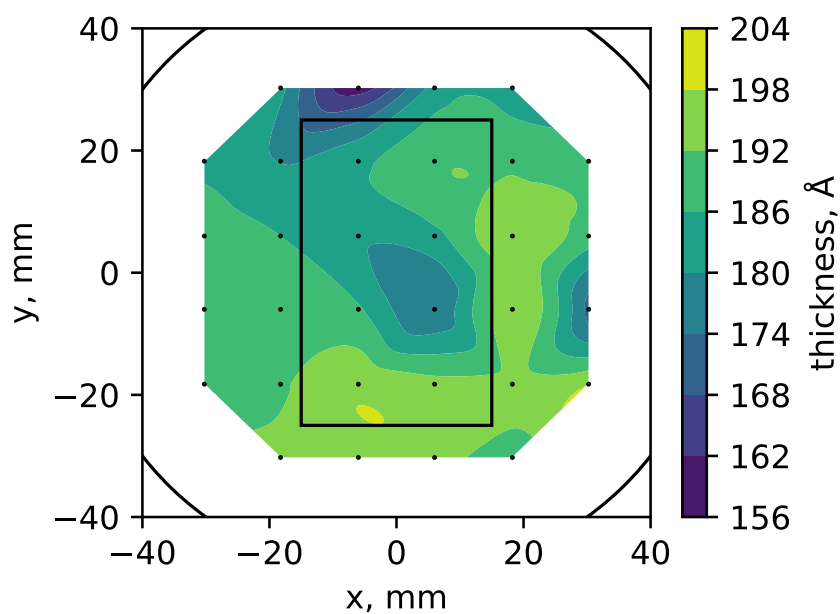


Figure E11: Ellipsometry map of the wafer used for confined PNIPAM-SDS (5 bar 25 °C) studied in section 6.4.



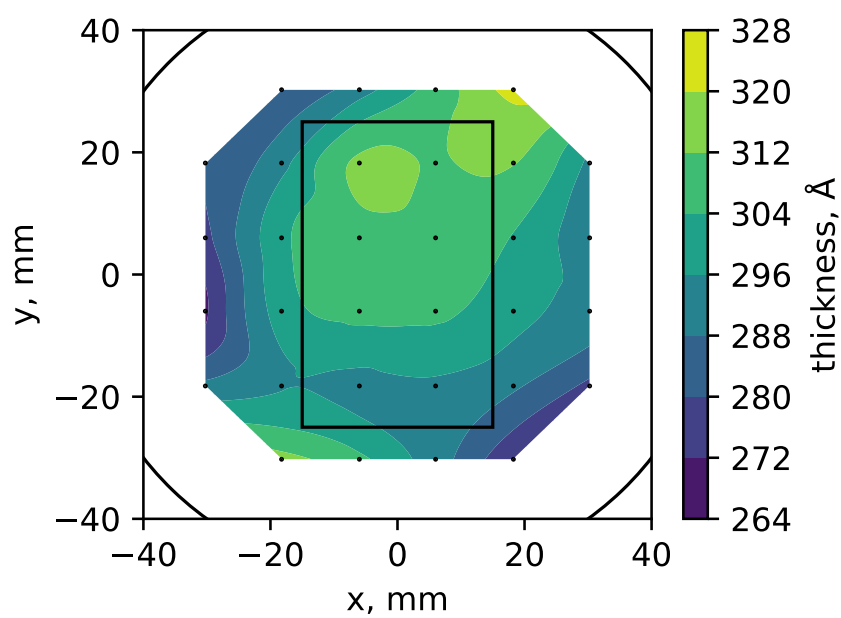


Figure E12: Ellipsometry map of the wafer used for PNIPAM-SDS-NaCl studies in section 6.5.

## F *refellips*

Currently there is no open-source package for the analysis of ellipsometry data. This lack of software prevents researchers who do not have access to an expensive Woollam ellipsometer from accessing advanced modelling techniques, and results in ellipsometry techniques being less accessible than they otherwise would be given the simplicity of the instruments involved (compared to XRR and NR). This is particularly true for solvated systems, which often require reasonably complex analysis approaches. It is for this reason that we have created *refellips*, a package that allows for the modelling of ellipsometry data within *refnx*. *refellips* is currently in development by Hayden Robertson, Isaac Gresham, and Andrew Nelson. The latest version can be found on GitHub.<sup>ii</sup>

The premise of *refellips* is to replace components of the *refnx* reflectometry calculation backend to make it capable of modelling ellipsometry data. The most significant change is the replacement of the Abeles transfer matrix with the optical transfer matrix of Byrnes [260]. Other more minor adaptations had to be made. *refnx* represents interfacial structure as a series of uniform **slabs**; layers with a thickness, roughness, volume fraction, real SLD and imaginary SLD. In *refnx* the **structure** assembles this set of slabs for substituent structural elements (i.e., the freeform model used in chapter 4), and provides it to **ReflectModel**, which calculates the corresponding reflectometry profile. We leave

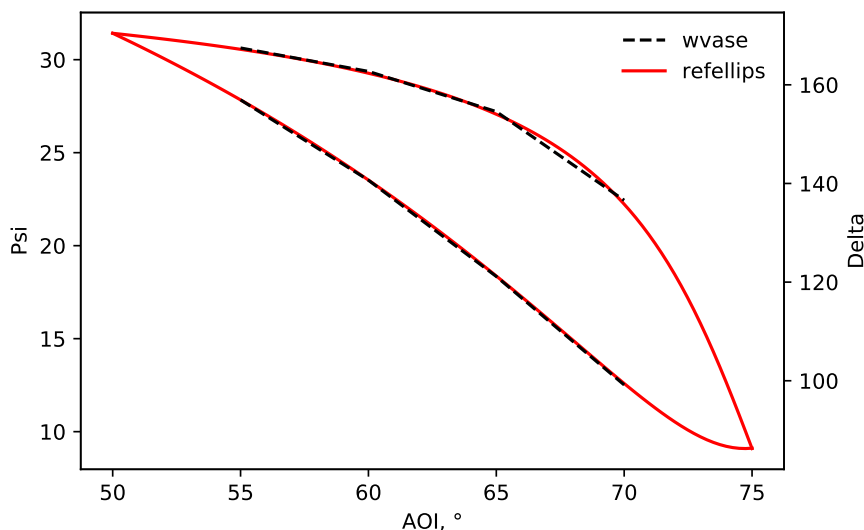


Figure F1: Comparison of simulated ellipsometry data from *refellips* and *wvase* (a conventional ellipsometry analysis package). Simulated profiles correspond to a 150 Å PNIPAM brush on a silicon substrate, with a 20 Å silica native oxide layer. Data is given as a function of angle of incidence with a fixed wavelength of 658 nm.

<sup>ii</sup><https://github.com/haydenrob/refellips>

the physical `slab` parameters untouched, replacing the real SLD with RI and imaginary SLD with the extinction coefficient; we do this by modifying the SLD component in *refnx*. Changes to `ReflectModel`, `ReflectDataset` and `Objective` were also required to enable the analysis of multi-angle, multi-wavelength ellipsometry.

The advantage of this approach is twofold. Firstly, any structural model from *refnx* is usable in *refellips* with little or no modification. Secondly, the powerful optimisation and uncertainty quantification tools available in *refnx* work by default in *refellips*. This allows advanced, well-tested analysis methods to be applied to ellipsometry data. We demonstrate this in Figure 6.23, where the freeform model we developed for analysis of polymer brush NR data is applied to ellipsometry data.

In Figure F1 we show that *refellips* and *wvase* (a conventional ellipsometry analysis package) produce identical output for a test system of a dry 150 Å PNIPAM brush on a 20 Å silica oxide layer.

Further development of this package will enable anyone to apply advanced statistical techniques (such as MCMC) and custom structures (such as *FreeformVFP*) to ellipsometry data collected from any ellipsometer. We plan to construct *refellips* such that it does not modify the underlying *refnx* install — this would enable *corefinement* of ellipsometry, XRR and NR datasets. It is anticipated that this code will be fully described in a future publication.

## G Implications of variable partial volumes (non-ideal mixing)

In typical analysis of NR data, component SLDs are assumed not to change between experimental conditions, requiring the assumption of constant molar volume, as

$$\rho = \frac{B}{V_m} \quad (\text{G1})$$

where  $B$  is the sum of the bound coherent scattering lengths of the component and  $V_m$  is the component's molecular volume.

The consequences of relaxing the assumptions behind this simplification are investigated by examining increasingly complex cases, namely:

1. constant volume, continuous solvent (typical)
2. variable volume, continuous solvent
3. variable volume, discrete solvent

### Constant volume, continuous solvent

In this simple case (Fig. G1d), the volume of the polymer repeat units does not change as a function of their environment, and the solvent is assumed to fill all ‘void’ space around the polymer — i.e. the presence of the polymer does not change the molecular volume of the local solvent. This treatment underpins the widely used space filling assumption, (Eq. 4.7) and results in  $\hat{V}_I$  remaining constant.

$$\hat{V}_I = \int \phi_{\text{poly}}(z) dz \quad (\text{G2})$$

This enables an unambiguous transformation between volume fraction profiles and scattering length density profiles. Due to its usefulness, the constant volume continuous solvent assumption is widely used.

### Variable volume, continuous solvent

Here (Fig. G1e),  $\rho_p$  is no longer assumed to be constant. A new parameter,  $\delta$ , is defined to describe the relationship between the self-solvated molecular volume at standard temperature and pressure (i.e. the molecular volume of the ‘dry layer’) to the molecular

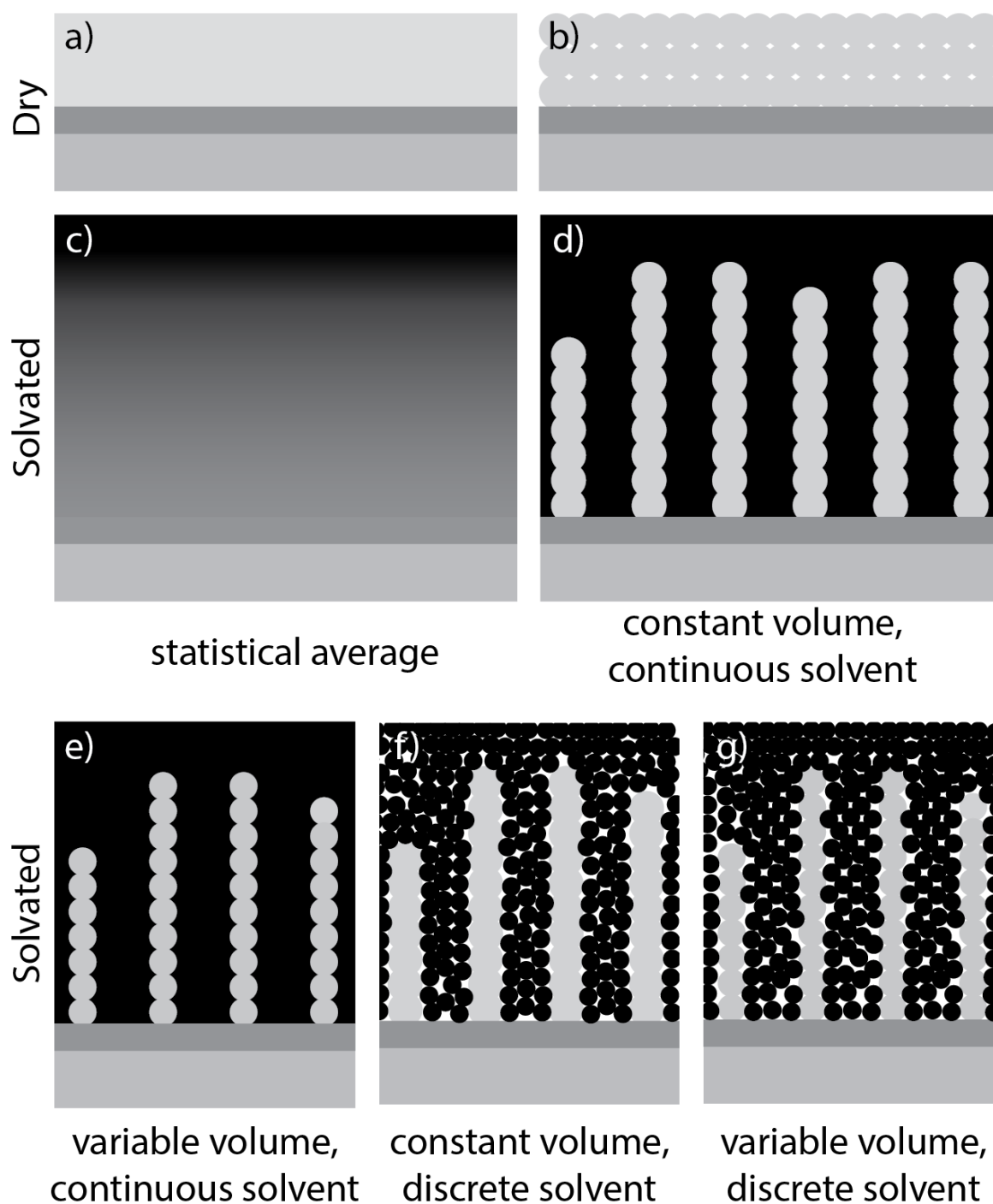


Figure G1: Schematic of the physical structure behind each of the examined treatments of the molar volume problem. (a, b) The dry system is a constant SLD layer of pure polymer containing a set number of polymer units. There are several ways of treating the solvation of this layer. The simplest (c, d) is to assume that the polymer repeat units do not change size and that the solvent is a continuous medium that fills all space around the polymer. However, the volume of the polymer units may change upon solvation (e, g) and the presence of the polymer may change the packing of individual solvent molecules (f, g).

volume at some other condition (i.e. the molecular volume in water).

$$V_{\text{m,sp}} = \delta V_{\text{m,p}} \quad (\text{G3})$$

giving

$$\rho_{\text{sp}} = \frac{\rho_{\text{p}}}{\delta} \quad (\text{G4})$$

This introduces an unknown into the equation 4.7

$$\rho(z) = \phi(z) \frac{\rho_{\text{p}}}{\delta} + [1 - \phi(z)] \rho_{\text{s}} \quad (\text{G5})$$

and obviously changes the effective interfacial volume

$$\hat{V}_{\text{I,eff}} = \delta \hat{V}_{\text{I}} \quad (\text{G6})$$

Whilst seldom explicitly acknowledged, variable volume is often accounted for by allowing the SLD of the interfacial material to vary within sensible bounds.

### Variable volume, discrete solvent

Here (Fig. G1g), the variable volume case is compounded with a non-continuous solvent, where it is possible that the presence of the polymer changes the local solvent density. This cannot be treated in the same way as a variable monomer volume as the solvent will have a different SLD within and outside of the polymer layer. This is potentially workable for well defined layers, but impossible to implement for diffuse interfaces. A better solution is to introduce a void component,  $\Omega(\phi)$ , into equation 4.7.  $\Omega(\phi)$  represents the change in density of the solvent as a function of polymer concentration; a negative  $\Omega(\phi)$  means tighter solvent packing, whilst positive values correspond to poorer packing (i.e. the formation of clathrate cages). This approach requires the definition of an additional function, further complicating the model. Combining this with the approach from case 2 yields

$$\rho(z) = \phi(z) \frac{\rho_{\text{p}}}{\delta} + [1 - \phi(z)] \frac{\rho_{\text{s}}}{\Omega(\phi(z))} \quad (\text{G7})$$

This introduces too much model freedom, as the change in polymer and solvent molecular volume upon mixing is almost impossible to quantify. As such, it is seldom acknowledged in current literature.

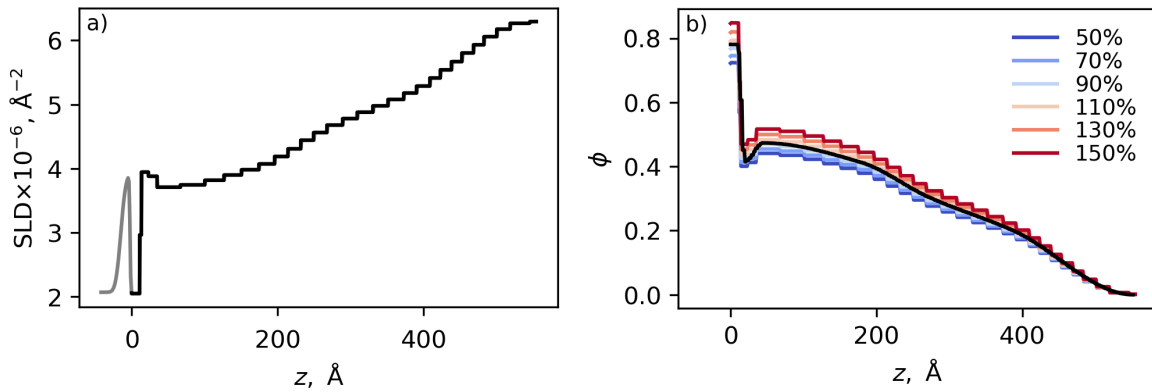


Figure G2: (a) SLD profile and (b) corresponding VF profiles based off varying polymer SLD as a fraction of the fitted SLD. The derived volume fraction profile is insensitive to changes in polymer SLD up to  $\pm 50\%$ .

### Sufficient freedom

In the absence of any concrete knowledge of  $\delta$  or  $\Omega(\phi)$ , these parameters simply contribute to model freedom.  $\delta$  essentially scales the VF and SLD profiles — it does not change their shape (Fig. G2) — whilst  $\Omega(\phi)$  adds freedom to the SLD profile. These freedoms are important in ensuring that the model can replicate the observed structure, as discussed in Section 4.1.1, but in practice introducing these parameters in a model will likely further obfuscate results.

The effect of an unknown  $\delta$  can be replicated by allowing the component SLD and  $\hat{V}_I$  to vary, whilst an unknown  $\Omega(\phi)$  does not add any more freedom than is already available in *FreeformVFP*. For the model and analysis proposed in the main text any structural contribution that could be made by  $\delta$  and  $\Omega$  can already be produced by a combination of the parameter bounds and the freeform model.

It must be acknowledged that if a rigid analytical or geometric model is being used to represent the interface then it may be required to include a sensibly defined  $\Omega(\phi)$  to ensure that the model has enough form-freedom, i.e. non-ideal polymer-solvent interaction could cause the SLD profile to differ from its theoretical shape. The uncertainty regarding the change in partial molar volume upon polymer solvation and the affect that the polymer has on the local solvent molar volume is another reason why freeform models are preferable in the modelling of these interfaces.

### Implications for model output

We can be confident that the model definition in section 4.2.1 does not preclude the structure of best fit, hence from here on it is assumed that the SLD profile produced

by the model is the SLD profile of best fit. The effect of variable monomer volume on the model output is examined by calculating VF profiles from SLD profiles with different SLD values. Even variations in the polymer SLD of  $\pm 50\%$  do not meaningfully change the polymer volume fraction profile (Fig. G2), as the difference in SLD between the polymer and the solvent is large relative to these variations. As a result, uncertainty regarding the molar volume of polymer and solvent upon their mixing does not change the methodology presented here or the physical significance of the results.



## H QCM-D time-series

Here the raw  $\Delta f$  and  $\Delta D$  signals for the various QCM-D experiments included in this thesis are presented as a function of time. These are included to give the reader an understanding of the adsorption kinetics. The data presented in the thesis is taken from the difference between the average signal over the final minute of the condition of interest and the average signal over the final minute of the subsequent control condition. We generally correct for changes in solution density and viscosity (which are always minimal) and adsorption to the substrate by subtracting the signal from a bare silicon wafer from the signal of interest. An example of this treatment is shown in Figure 6.11. The final measurements are not performed under flow; small signal deviations may be noticed approximately halfway through sample/control conditions where the pump has been turned off.

### H1 Surfactant identity

The following pages contain raw  $\Delta f$  and  $\Delta D$  signals (3<sup>rd</sup> overtone) for QCM-D experiments in the surfactant identity study.

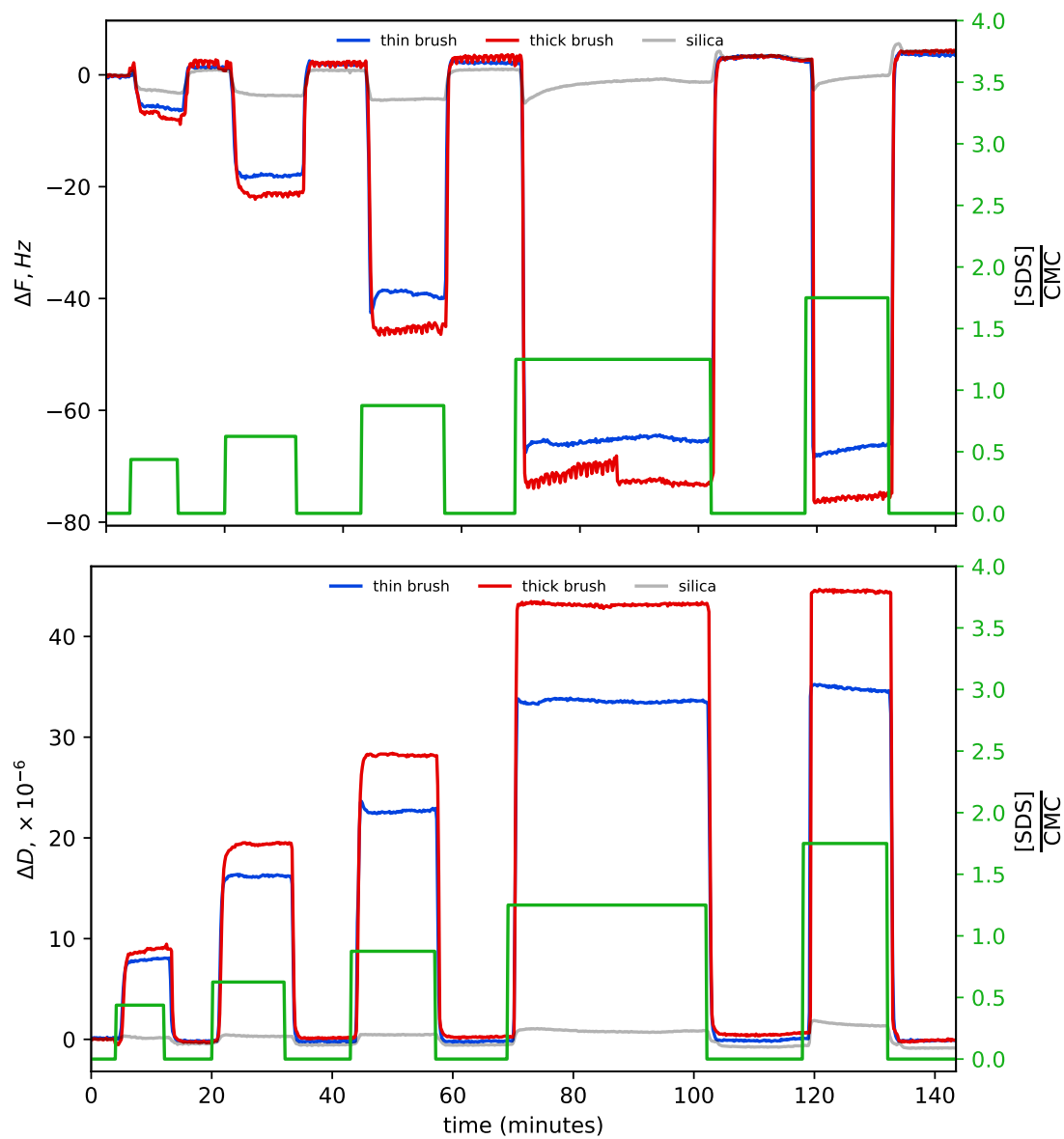


Figure H1: Raw QCM-D data for SDS datapoints in Figure 6.11, showing change in (*top*) frequency and (*bottom*) dissipation with time as SDS concentration is varied.

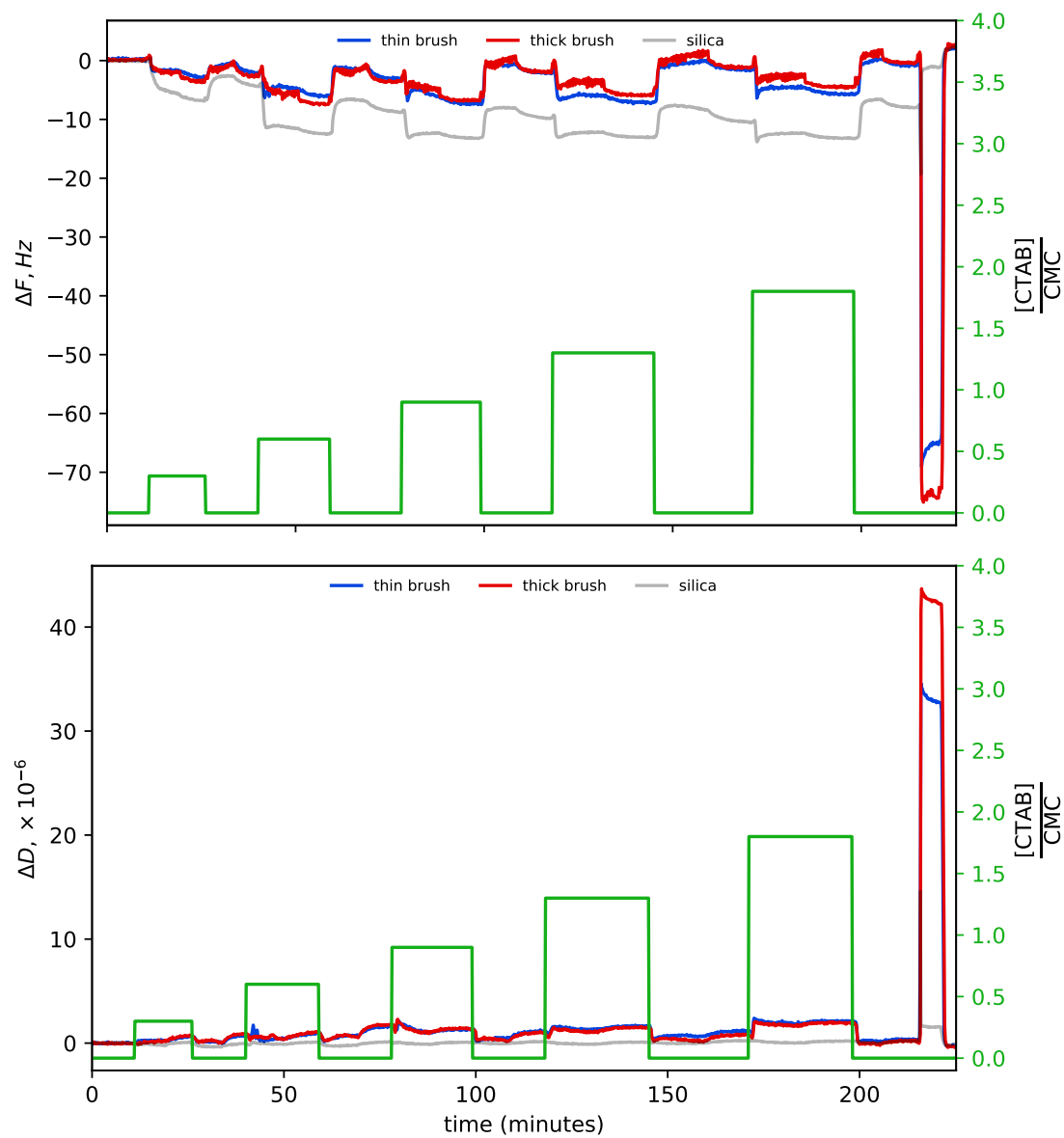


Figure H2: Raw QCM-D data for CTAB datapoints in Figure 6.11, showing change in (*top*) frequency and (*bottom*) dissipation with time as CTAB concentration is varied.

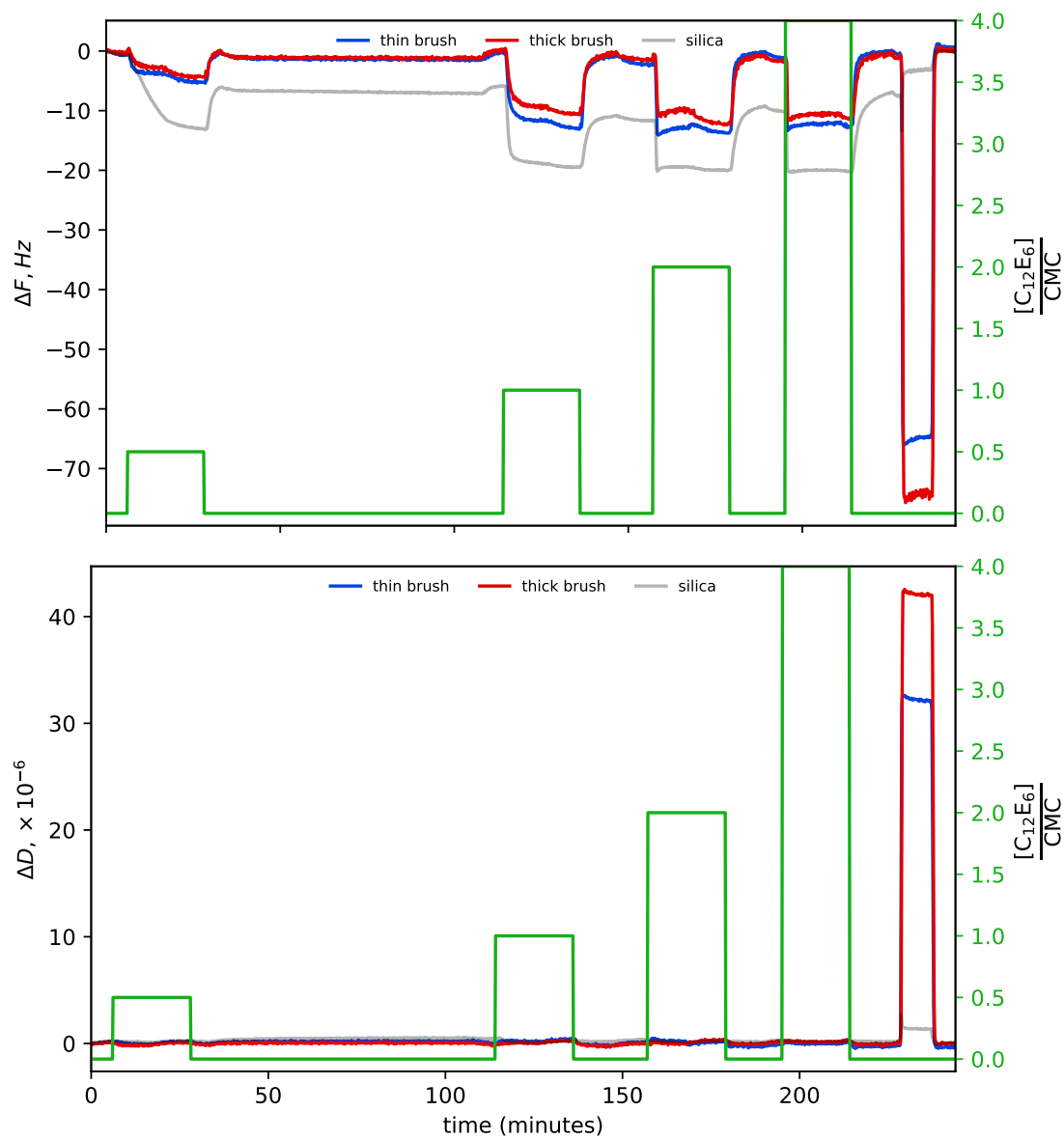


Figure H3: Raw QCM-D data for  $C_{12}E_6$  datapoints in Figure 6.11, showing change in (*top*) frequency and (*bottom*) dissipation with time as  $C_{12}E_6$  concentration is varied.

## H2 SDS temperature sweep

The following pages contain raw  $\Delta f$  and  $\Delta D$  signals for QCM-D experiments in the SDS temperature sweep study.

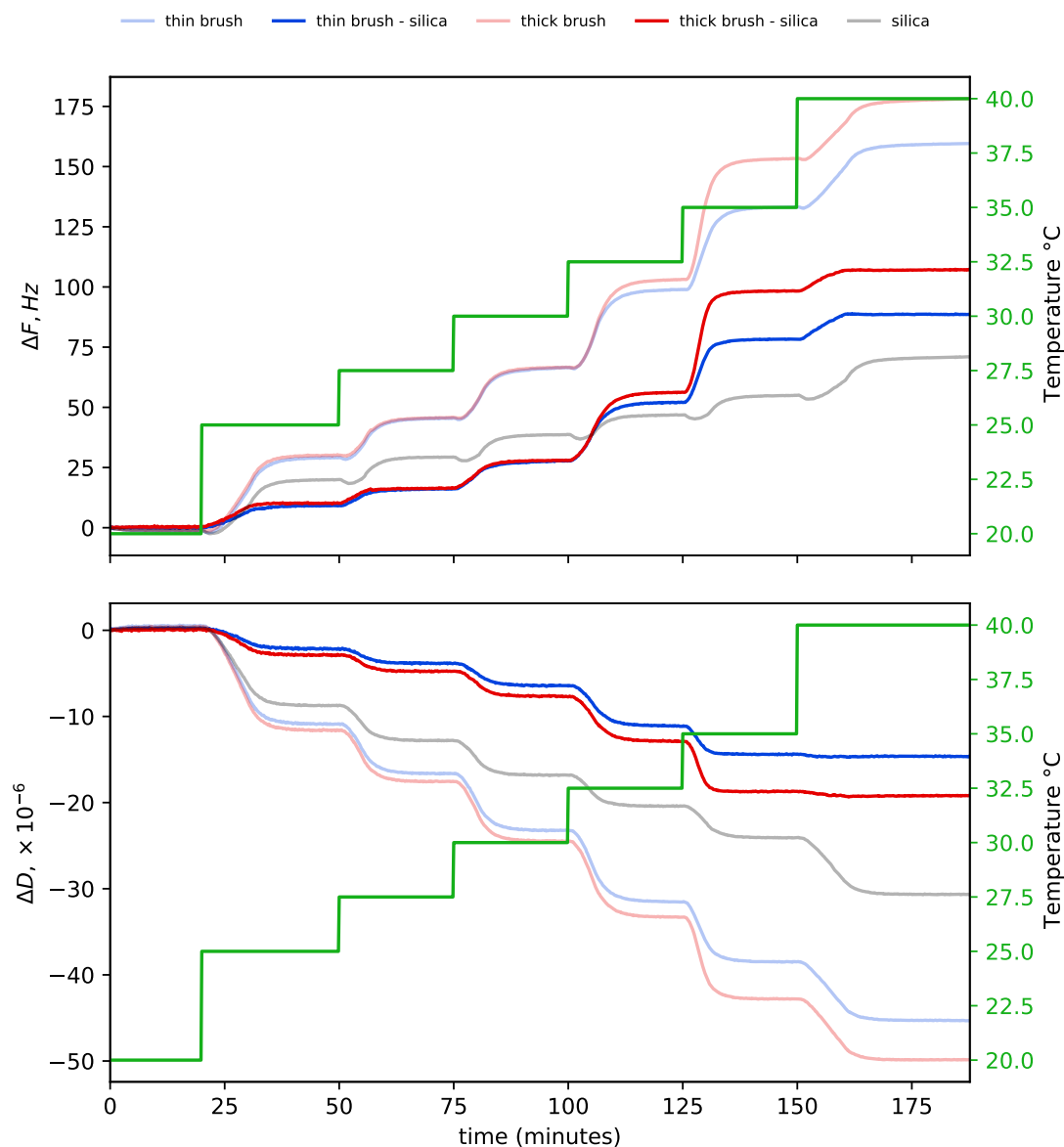


Figure H4: Raw QCM-D data from 0mM SDS datapoints in Figure 6.12, showing change in (*top*) frequency and (*bottom*) dissipation with time as temperature is varied. Lighter lines show original signal, while darker lines show the signal less that from the silica wafer, which helps to remove the effect of temperature from the raw signal. In the data presented in Figure 6.12 the temperature effect on the frequency and dissipation was removed using the signal-temperature relationship derived in Figure 1.10

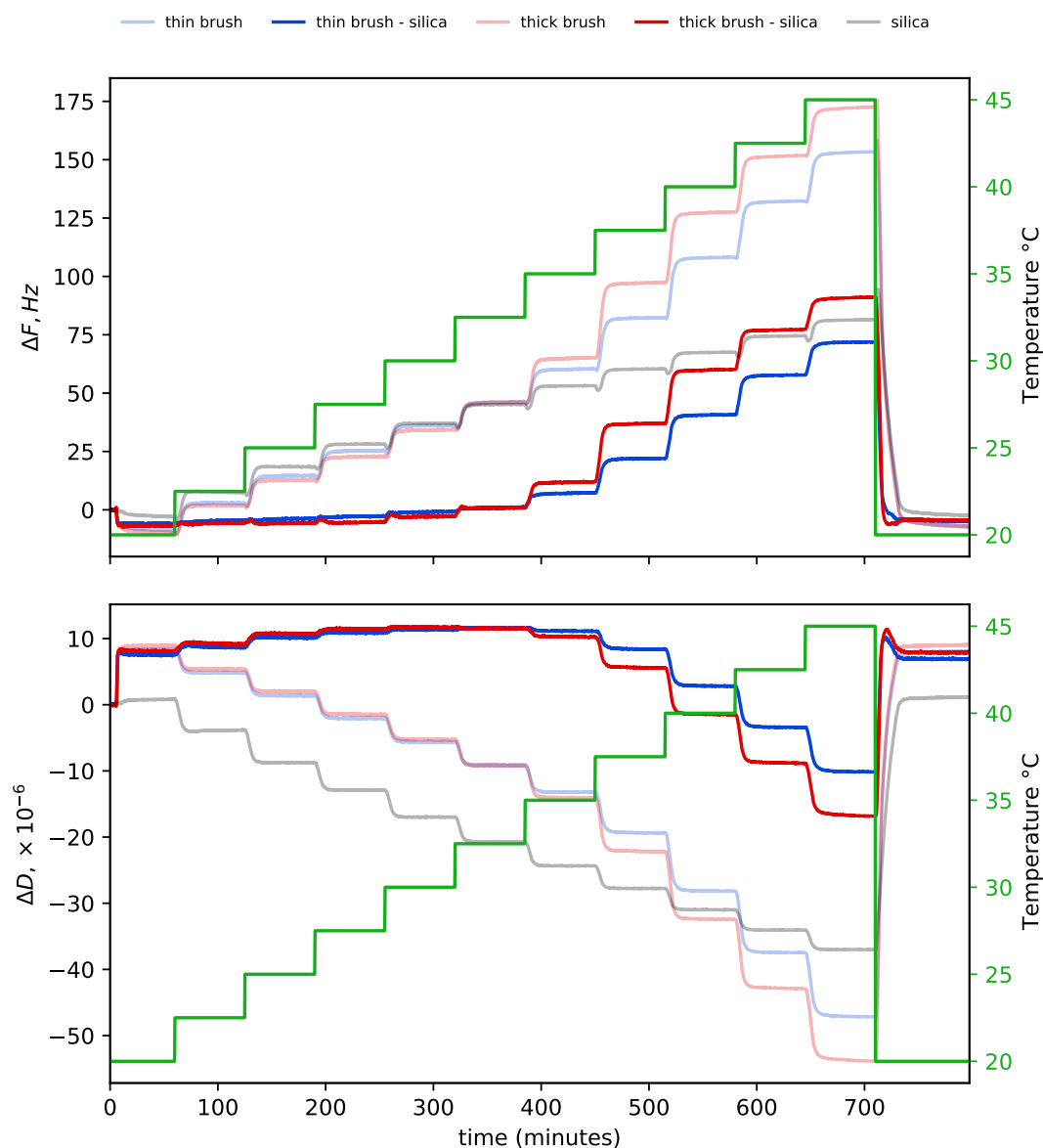


Figure H5: Raw QCM-D data from 3 mM SDS datapoints in Figure 6.12, showing change in (*top*) frequency and (*bottom*) dissipation with time as temperature is varied. Lighter lines show original signal, while darker lines show the signal less that from the silica wafer, which helps to remove the effect of temperature from the raw signal. In the data presented in Figure 6.12 the temperature effect on the frequency and dissipation was removed using the signal-temperature relationship derived in Figure 1.10

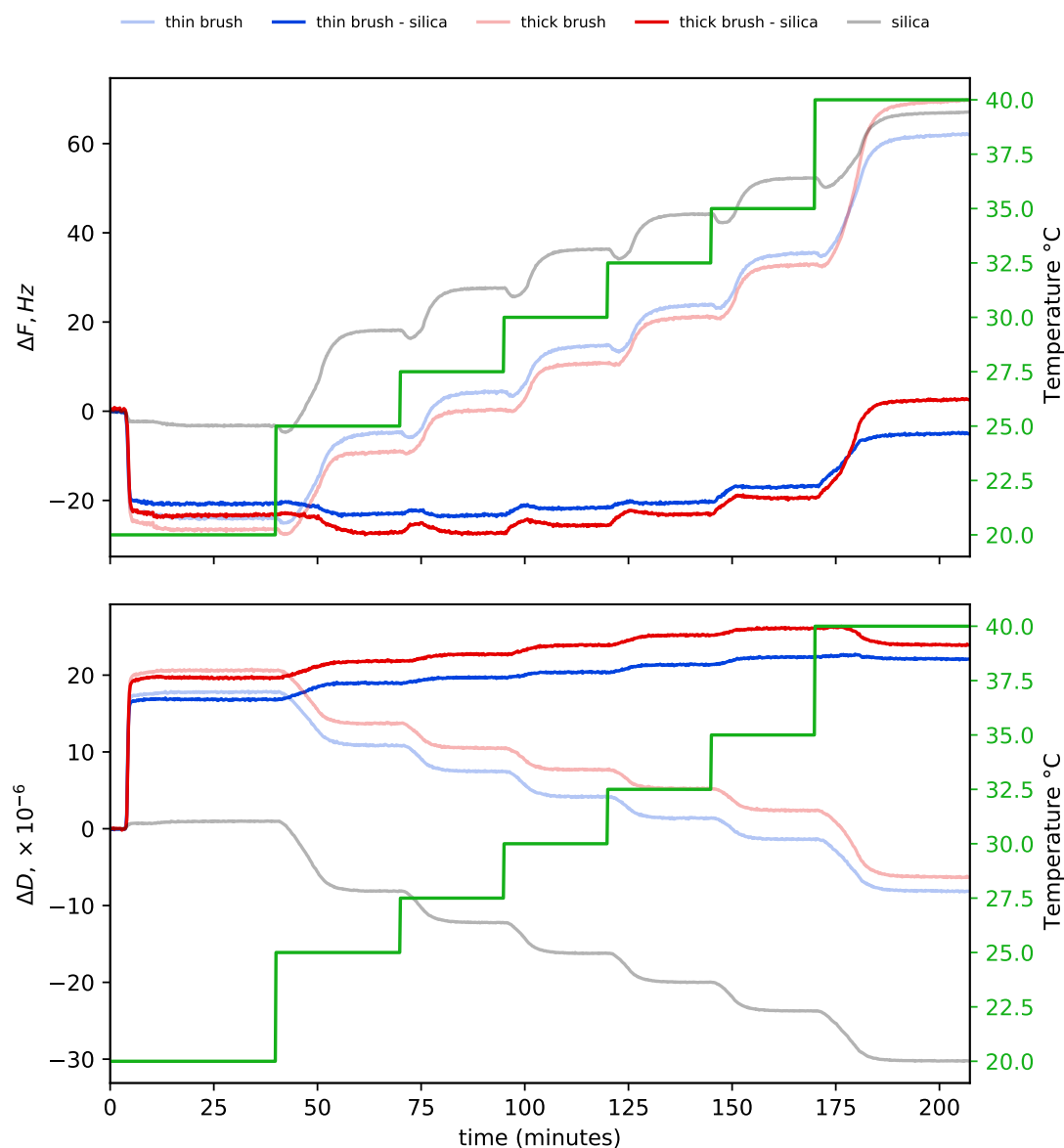


Figure H6: Raw QCM-D data from 5 mM SDS datapoints in Figure 6.12, showing change in (*top*) frequency and (*bottom*) dissipation with time as temperature is varied. Lighter lines show original signal, while darker lines show the signal less that from the silica wafer, which helps to remove the effect of temperature from the raw signal. In the data presented in Figure 6.12 the temperature effect on the frequency and dissipation was removed using the signal-temperature relationship derived in Figure 1.10

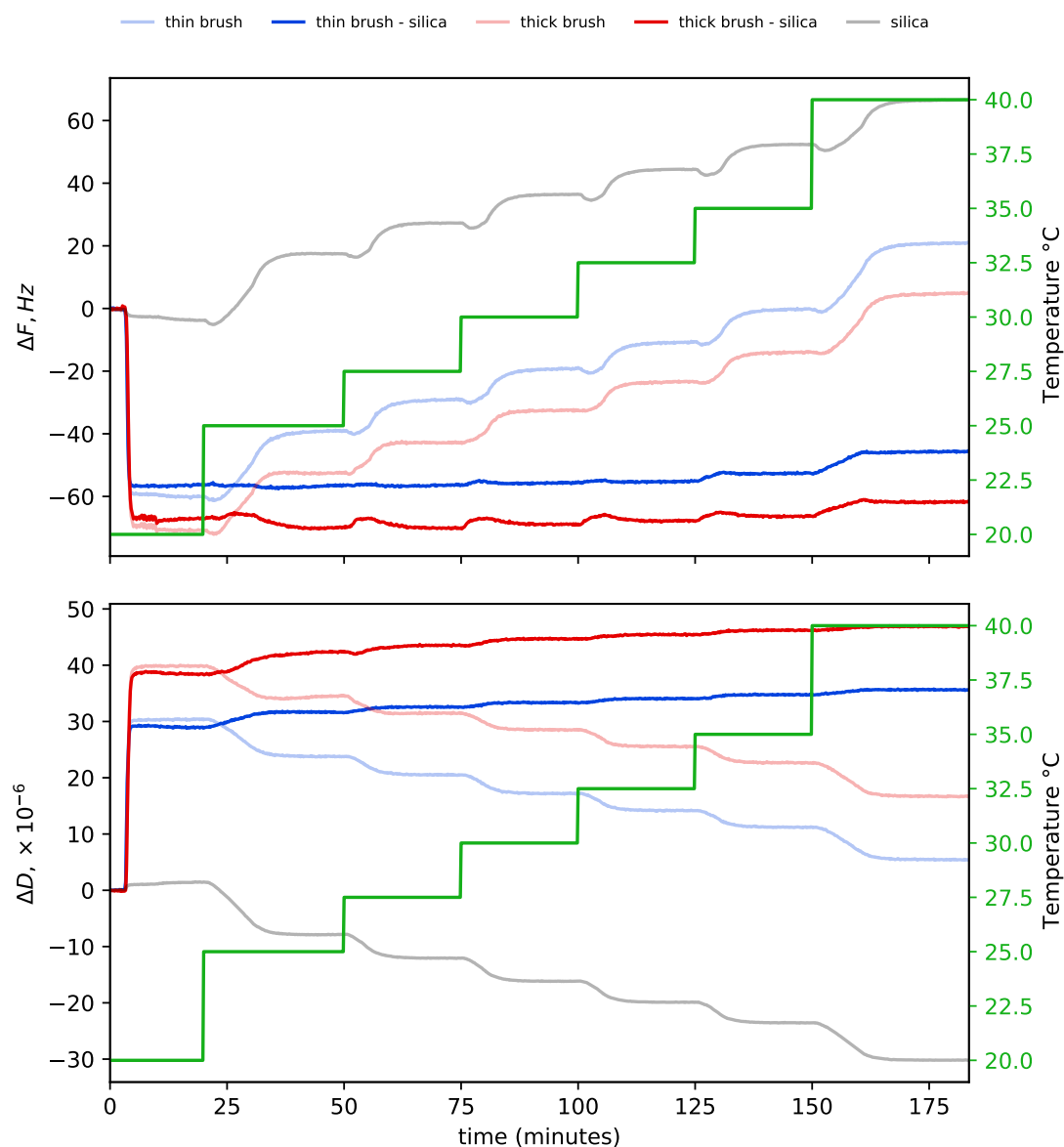


Figure H7: Raw QCM-D data from 7 mM SDS datapoints in Figure 6.12, showing change in (*top*) frequency and (*bottom*) dissipation with time as temperature is varied. Lighter lines show original signal, while darker lines show the signal less that from the silica wafer, which helps to remove the effect of temperature from the raw signal. In the data presented in Figure 6.12 the temperature effect on the frequency and dissipation was removed using the signal-temperature relationship derived in Figure 1.10



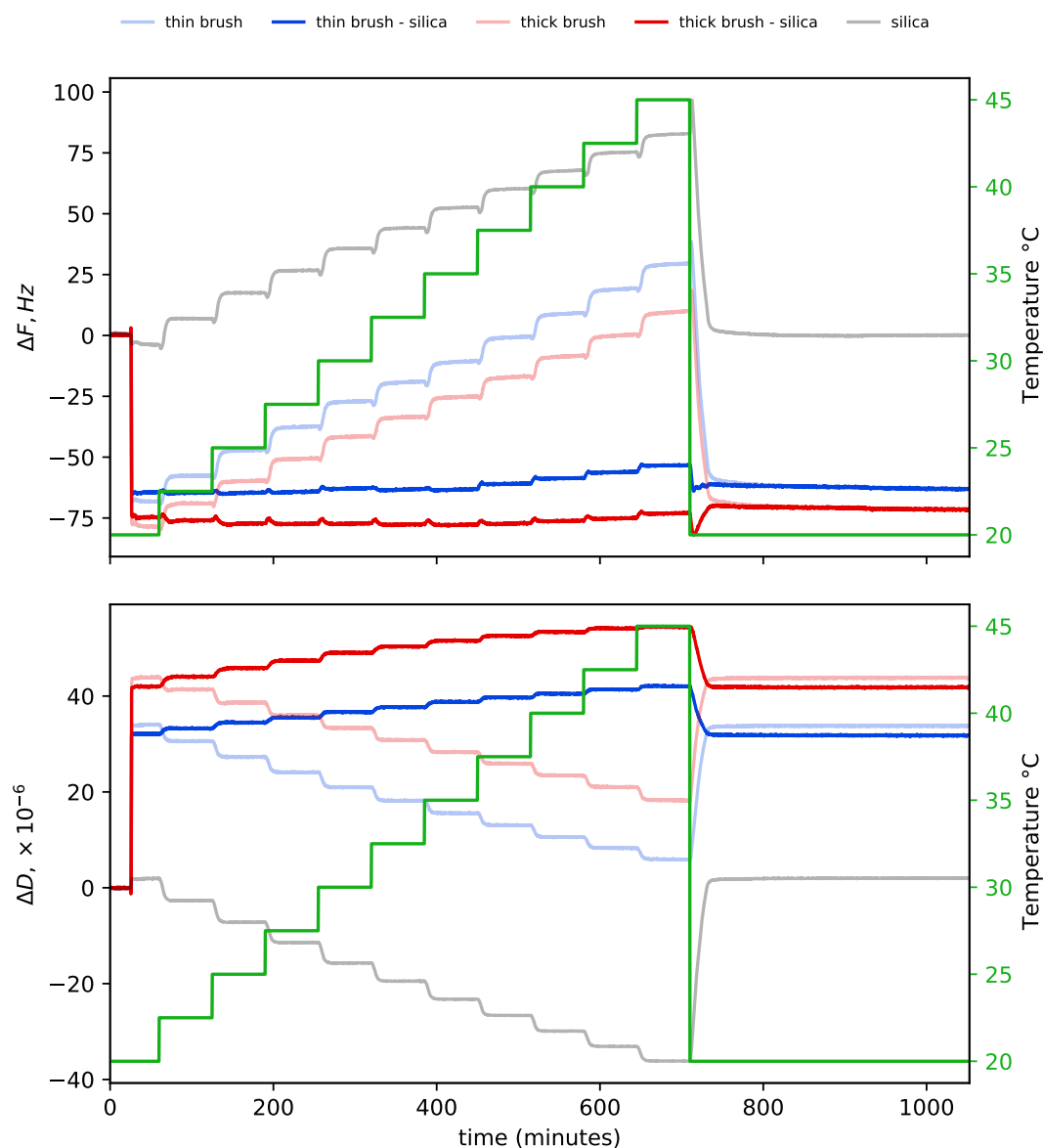


Figure H8: Raw QCM-D data from 14 mM SDS datapoints in Figure 6.12, showing change in (*top*) frequency and (*bottom*) dissipation with time as temperature is varied. Lighter lines show original signal, while darker lines show the signal less that from the silica wafer, which helps to remove the effect of temperature from the raw signal. In the data presented in Figure 6.12 the temperature effect on the frequency and dissipation was removed using the signal-temperature relationship derived in Figure 1.10

### H3 SDS-NaCl

The following pages contain raw  $\Delta f$  and  $\Delta D$  signals for QCM-D experiments in the SDS-NaCl study.

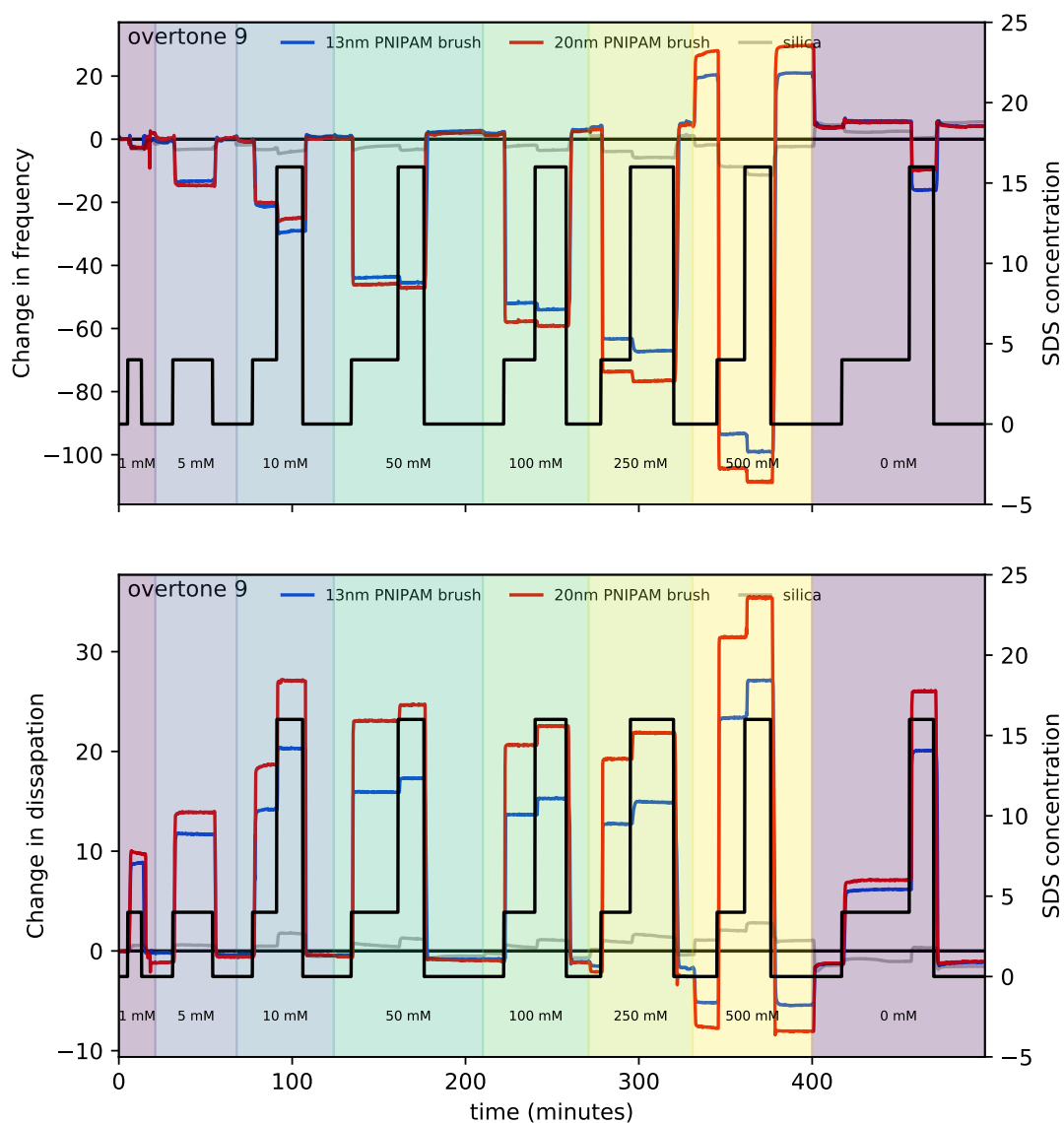


Figure H9: Raw QCM-D data from the PNIPAM-SDS-NaCl study in Figure 6.26, showing change in (*top*) frequency and (*bottom*) dissipation with time as SDS and NaCl concentration is varied. Changes in SDS concentration are shown on the right axis, while changes in NaCl concentration are indicated by the coloured regions.

## I Recovery of brush after confinement in section 6.4

After each confinement in section 6.4, the brush was rehydrated in  $D_2O$  and examined with NR at 25 and 40 °C to ensure that it still behaved as expected. The reflectometry profiles corresponding to these checks are shown in Figure I1. All checks indicate that the brush layers survived the repeated confinement steps, remaining thermoresponsive and maintaining their thickness (evident from the fringe spacing of the 40 °C dataset).

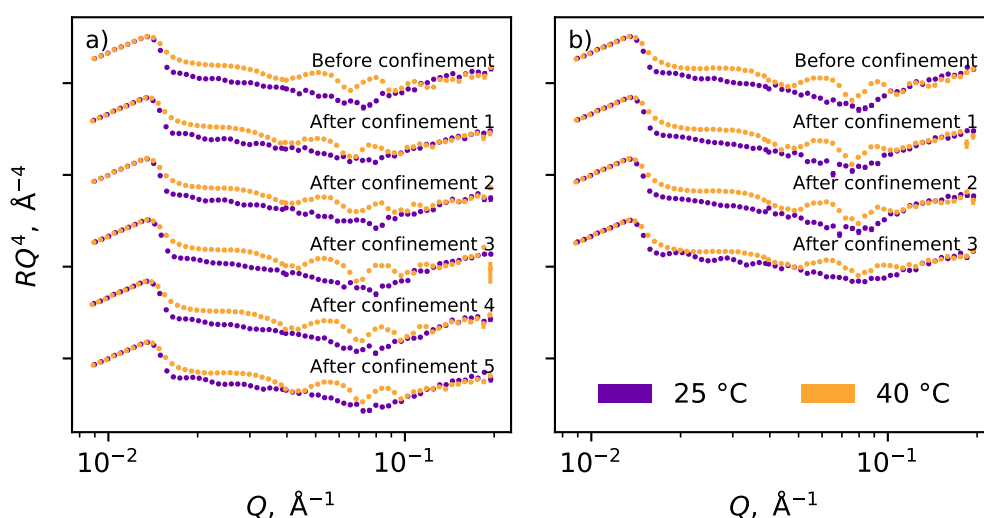


Figure I1: Reflectometry profiles from the wafers used in the confinement study in section 6.4. Profiles are acquired at 25 and 40 °C after each subsequent confinement. That the reflectometry profiles do not appear to significantly change indicates that the layer is still thermoresponsive after confinement and its thickness remains constant.

## J Python code required for replication of analysis

Here the code that was used for the various analysis in this thesis is included to enable replication of our methodologies and results. For the sake of brevity, only code that is not available elsewhere is included below. The *refnx* package is available on GitHub.<sup>iii</sup> The *refellips* package is available on GitHub.<sup>iv</sup> Additional files required to replicate the analysis in chapter 5 are available in a Zenodo repository and the supporting information for reference [282].<sup>v</sup> The files required to replicate the analysis in chapter 4 are available in a Zenodo repository.<sup>vi</sup> Additional tools and resources can be found in the *refnxttoolbox* repository on GitHub.<sup>vii</sup>

### J1 Freeform modelling where the adsorbed amount is not known from chapter 6

In chapter 4 we introduce a freeform model. One of the key features of this model is that the profile thickness (the extent,  $E$ ) is scaled based off the adsorbed amount of material at the interface. This behaviour is extremely useful when modelling polymer brushes, as  $\hat{V}_I$  is fixed and the extent of the layer is hard to estimate. However, this model is not practical for interfaces where it is easier to approximate the extent of the layer than the adsorbed amount. Furthermore, this model is constructed with the intention of constraining monotonicity, so the volume fraction of each knot is defined relative to the previous knot (Eq. 4.3). Once again, this definition is ideal for modelling layers where the  $\phi$  is generally expected to be monotonically decreasing, but not those where there is no such expectation. Consequently, *FreeformVFP* is not suitable for modelling the volume fraction profiles in the  $\text{CM}_{\text{poly}}$  NR experiments in chapter 4.

To enable the analysis of these interfaces we modify the freeform model. The first modification we make is to parameterise  $E$  directly, instead of parameterising it through  $\hat{V}_I$ . The second modification is to define the knot volume fractions directly, instead of defining them relative to the preceding knot, as in Equation 4.3. The method of defining the  $z$  position of knots is identical to that used in the freeform model (Eq. 4.5). These two modifications remove many of the assumptions from the freeform model that make it adept at modelling brushes. The constraints placed on the model are the thickness of the layer and its maximum volume fraction. The model still enforces a volume fraction of 0

<sup>iii</sup><https://github.com/refnx/refnx>

<sup>iv</sup><https://github.com/haydenrob/refellips>

<sup>v</sup><https://doi.org/10.5281/zenodo.4324394>

<sup>vi</sup><https://doi.org/10.5281/zenodo.4361678>

<sup>vii</sup><https://github.com/igresh/refnxttoolbox>

when  $z = E$ , an allows for sharp features to be produced from relatively few knots due to the variable knot spacing. We do not claim that this model is particularly efficient for modelling surfactants within a brush, but we believe that it is flexible enough to produce all physically viable structures.

The code for the modified freeform model is provided overleaf.

```

1  import numpy as np
2
3  from scipy.interpolate import PchipInterpolator as Pchip
4  from scipy.integrate import simps
5
6  from refnx.reflect import Structure, Component, SLD, Slab
7  from refnx.analysis import Parameters, Parameter, possibly_create_parameter
8
9  import warnings
10
11 EPS = np.finfo(float).eps
12
13 class FreeformVFP_ext(Component):
14     def __init__(self, extent, vf, dzf, polymer_sld, name='',
15                  left_slabs=(), right_slabs=(),
16                  interpolator=Pchip, zgrad=True,
17                  microslab_max_thickness=1):
18         """
19         Parameters
20         -----
21         extent : Parameter or float
22             The total extent of the spline region
23         vf: sequence of Parameter or float
24             Volume fraction at each of the spline knots, as a fraction of
25             the volume fraction of the rightmost left slab
26         dzf : sequence of Parameter or float
27             Separation of successive knots, will be normalised to a 0-1 scale.
28         polymer_sld : SLD or float
29             SLD of polymer
30         name : str
31             Name of component
32         gamma : Parameter
33             The dry adsorbed amount of polymer
34         left_slabs : sequence of Slab
35             Polymer Slabs to the left of the spline
36         right_slabs : sequence of Slab
37             Polymer Slabs to the right of the spline
38         interpolator : scipy interpolator
39             The interpolator for the spline
40         zgrad : bool, optional
41             Set to 'True' to force the gradient of the volume fraction to zero
42             at each end of the spline.
43         microslab_max_thickness : float
44             Thickness of microslicing of spline for reflectivity calculation.
45         """
46         super(FreeformVFP_ext, self).__init__()
47
48         assert len(vf) + 1 == len(dzf), ("Length of dzf must be one greater"
49                                         " than length of vf")
50
51         self.name = name
52
53         if isinstance(polymer_sld, SLD):
54             self.polymer_sld = polymer_sld
55         else:

```

```

56         self.polymer_sld = SLD(polymer_sld)
57
58         # left and right slabs are other areas where the same polymer can
59         # reside
60         self.left_slabs = [slab for slab in left_slabs if
61                             isinstance(slab, Slab)]
62         self.right_slabs = [slab for slab in right_slabs if
63                             isinstance(slab, Slab)]
64
65         # use the volume fraction of the last left_slab as the initial vf of
66         # the spline, if not left slabs supplied start at vf 1
67         if len(self.left_slabs):
68             self.start_vf = 1 - self.left_slabs[-1].vfsolv.value
69         else:
70             self.start_vf = 1
71
72         # in contrast use a vf = 0 for the last vf of
73         # the spline, unless right_slabs is specified
74         if len(self.right_slabs):
75             self.end_vf = 1 - self.right_slabs[0].vfsolv.value
76         else:
77             self.end_vf = 0
78
79         self.microslab_max_thickness = microslab_max_thickness
80
81         self.extent = (
82             possibly_create_parameter(extent,
83                                     name='%s - extent' % name))
84
85         # dzf are the spatial gaps between the spline knots
86         self.dzf = Parameters(name='dzf - spline')
87         for i, z in enumerate(dzf):
88             p = possibly_create_parameter(
89                 z,
90                 name='%s - spline dzf[%d]' % (name, i))
91             p.range(0, 1)
92             self.dzf.append(p)
93
94         # vf are the volume fraction values of each of the spline knots
95         self.vf = Parameters(name='vf - spline')
96         for i, v in enumerate(vf):
97             p = possibly_create_parameter(
98                 v,
99                 name='%s - spline vf[%d]' % (name, i))
100             p.range(0, 1)
101             self.vf.append(p)
102
103         self.zgrad = zgrad
104         self.interpolator = interpolator
105
106         self.__cached_interpolator = {'zeds': np.array([]),
107                                     'vf': np.array([]),
108                                     'interp': None,
109                                     'adsorbed amount': -1}
110

```

```

111     def _update_vfs(self):
112         # use the volume fraction of the last left_slab as the initial vf of
113         # the spline, if not left slabs supplied start at vf 1
114         if len(self.left_slabs):
115             self.start_vf = 1 - self.left_slabs[-1].vfsolv.value
116         else:
117             self.start_vf = 1
118
119         # in contrast use a vf = 0 for the last vf of
120         # the spline, unless right_slabs is specified
121         if len(self.right_slabs):
122             self.end_vf = 1 - self.right_slabs[0].vfsolv.value
123         else:
124             self.end_vf = 0
125
126     def _dzf_to_zeds(self):
127         zeds = np.cumsum(self.dzf)
128         # Normalise dzf to unit interval.
129         # clipped to 0 and 1 because we pad on the LHS, RHS later
130         # and we need the array to be monotonically increasing
131         zeds /= zeds[-1]
132         zeds = np.clip(zeds, 0, 1)
133         zeds = zeds[0:-1]
134         return zeds
135
136     def _extent(self):
137         # First calculate slab area:
138         slab_height = self._slab_height()
139         difference = float(self.extent) - slab_height
140
141         assert difference > 0, ("Your slab area has exceeded your adsorbed"
142                                " amount!")
143
144
145         return difference
146
147     def _slab_height(self):
148         height = 0
149
150         for slab in self.left_slabs:
151             _slabs = slab.slabs()
152             height += _slabs[0, 0]
153         for slab in self.right_slabs:
154             _slabs = slab.slabs()
155             height += _slabs[0, 0]
156         return height
157
158     def _slab_area(self):
159         area = 0
160
161         for slab in self.left_slabs:
162             _slabs = slab.slabs()
163             area += _slabs[0, 0] * (1 - _slabs[0, 4])
164         for slab in self.right_slabs:
165             _slabs = slab.slabs()

```



```

166         area += _slabs[0, 0] * (1 - _slabs[0, 4])
167     return area
168
169     def _vfp_interpolator(self):
170         """
171         The spline based volume fraction profile interpolator
172
173         Returns
174         -----
175         interpolator : scipy.interpolate.Interpolator
176         """
177         self._update_vfs()
178         zeds = self._dzf_to_zeds()
179         vf = self.vf
180
181         # do you require zero gradient at either end of the spline?
182         if self.zgrad:
183             zeds = np.concatenate([[ -1.1, 0 - EPS],
184                                     zeds,
185                                     [1 + EPS, 2.1]])
186             vf = np.concatenate([[self.start_vf, self.start_vf],
187                                 vf,
188                                 [self.end_vf, self.end_vf]])
189         else:
190             zeds = np.concatenate([[0 - EPS], zeds, [1 + EPS]])
191             vf = np.concatenate([[self.start_vf], vf, [self.end_vf]])
192
193         # cache the interpolator
194         cache_zeds = self.__cached_interpolator['zeds']
195         cache_vf = self.__cached_interpolator['vf']
196         cache_adsamt = self.__cached_interpolator['adsorbed amount']
197
198         # you don't need to recreate the interpolator
199         if (np.equal(float(self.extent), cache_adsamt) and
200             np.array_equal(zeds, cache_zeds) and
201             np.array_equal(vf, cache_vf)):
202             return self.__cached_interpolator['interp']
203         else:
204             self.__cached_interpolator['zeds'] = zeds
205             self.__cached_interpolator['vf'] = vf
206             self.__cached_interpolator['adsorbed amount'] = (
207                 float(self.extent))
208
209             interpolator = self.interpolator(zeds, vf)
210             self.__cached_interpolator['interp'] = interpolator
211         return interpolator
212
213     def __call__(self, z):
214         """
215         Calculates the volume fraction profile of the spline
216
217         Parameters
218         -----
219         z : float
220             Distance along vfp

```

```

221
222         Returns
223         -----
224         vfp : float
225             Volume fraction
226         """
227         interpolator = self._vfp_interpolator()
228         vfp = interpolator(z / float(self._extent()))
229         return vfp
230
231     def moment(self, moment=1):
232         """
233         Calculates the n'th moment of the profile
234
235         Parameters
236         -----
237         moment : int
238             order of moment to be calculated
239
240         Returns
241         -----
242         moment : float
243             n'th moment
244         """
245         zed, profile = self.profile()
246         profile *= zed**moment
247         val =.simps(profile, zed)
248         area = self.profile_area()
249         return val / area
250
251     def is_monotonic(self):
252         return np.all(self.dzf.pvals < 1)
253
254     @property
255     def parameters(self):
256         p = Parameters(name=self.name)
257         p.extend([self.extent, self.dzf, self.vf,
258                 self.polymer_sld.parameters])
259         p.extend([slab.parameters for slab in self.left_slabs])
260         p.extend([slab.parameters for slab in self.right_slabs])
261         return p
262
263     def lnprob(self):
264         return 0
265
266     def profile_area(self):
267         """
268         Calculates integrated area of volume fraction profile
269
270         Returns
271         -----
272         area: integrated area of volume fraction profile
273         """
274         interpolator = self._vfp_interpolator()
275         area = interpolator.integrate(0, 1) * float(self._extent())

```

```

276         area += self._slab_area()
277
278     return area
279
280 def slabs(self, structure=None):
281
282     cutoff = 5000
283     slab_extent = self._extent()
284
285     if slab_extent > cutoff:
286         warnings.warn('extent > %d, performing refl. calc on first %dÅ.' %
287                       (cutoff, cutoff), RuntimeWarning)
288
289         slab_extent = cutoff
290
291     num_slabs = np.ceil(float(slab_extent) / self.microslab_max_thickness)
292     slab_thick = float(slab_extent / num_slabs)
293     slabs = np.zeros((int(num_slabs), 5))
294     slabs[:, 0] = slab_thick
295
296     # give last slab a miniscule roughness so it doesn't get contracted
297     slabs[-1:, 3] = 0.5
298
299     dist = np.cumsum(slabs[:, 0]) - 0.5 * slab_thick
300     slabs[:, 1] = self.polymer_sld.real.value
301     slabs[:, 2] = self.polymer_sld.imag.value
302     slabs[:, 4] = 1 - self(dist)
303
304     return slabs
305
306 def profile(self, extra=False):
307     """
308     Calculates the volume fraction profile
309
310     Returns
311     -----
312     z, vfp : np.ndarray
313         Distance from the interface, volume fraction profile
314     """
315     s = Structure()
316     s |= SLD(0)
317
318     m = SLD(1.)
319
320     for i, slab in enumerate(self.left_slabs):
321         layer = m(slab.thick.value, slab.rough.value)
322         if not i:
323             layer.rough.value = 0
324             layer.vfsolv.value = slab.vfsolv.value
325             s |= layer
326
327     polymer_slabs = self.slabs()
328     offset = np.sum(s.slabs()[:, 0])
329
330

```

```

331     for i in range(np.size(polymer_slabs, 0)):
332         layer = m(polymer_slabs[i, 0], polymer_slabs[i, 3])
333         layer.vfsolv.value = polymer_slabs[i, -1]
334         s |= layer
335
336     for i, slab in enumerate(self.right_slabs):
337         layer = m(slab.thick.value, slab.rough.value)
338         layer.vfsolv.value = 1 - slab.vfsolv.value
339         s |= layer
340
341     s |= SLD(0, 0)
342
343     # now calculate the VFP.
344     total_thickness = np.sum(s.slabs()[ :, 0])
345     if total_thickness < 500:
346         num_zed_points = int(total_thickness)
347     else:
348         num_zed_points = 500
349     zed = np.linspace(0, total_thickness, num_zed_points)
350     # SLD profile puts a very small roughness on the interfaces with zero
351     # roughness.
352     zed[0] = 0.01
353     z, s = s.sld_profile(z=zed)
354     s[0] = s[1]
355
356     # perhaps you'd like to plot the knot locations
357     zeds = self._dzf_to_zeds()
358     zed_knots = zeds * float(self._extent()) + offset
359
360     if extra:
361         return z, s, zed_knots, self.vf
362     else:
363         return z, s

```

## K Parameter distributions for exemplar dataset in chapter 4

The parameter distributions for the polymer parameters are given as histograms in Fig. K1 through K6. We stress that it is the distribution of structures (i.e., volume fraction profiles) that we are interested in, not the distribution of parameters; this is because it is the structures that are of experimental interest and there are possibly multiple parameter configurations that correspond to a single VF profile. Consequently, these parameter distributions are included for the sake of clarity and to allow our method to be more easily followed, not because they offer extra information regarding the physical structure of the system.

It should be noted that the posterior distribution for the PNIPAM SLD varies between datasets. Ideally, this value would either be constant or monotonically increasing (as the PNIPAM amide proton is slowly exchanged for deuterium). However, this change in PNIPAM SLD has a minimal effect on the SLD profile produced, being comparable to an uncertainty in the interfacial volume of  $\pm 3.5 \text{ \AA}$ . SLD and interfacial volume are covariant in this modeling approach, as the same SLD profile can be produced with a lower interfacial volume or a higher polymer SLD. Furthermore, all posteriors have a spread of SLD values across the bounded range. As such, the differences in posterior distribution for the PNIPAM SLD are less than the range which we would expect NR to be sensitive to (for diffuse layers) and have minimal effect on the output of our methodology.

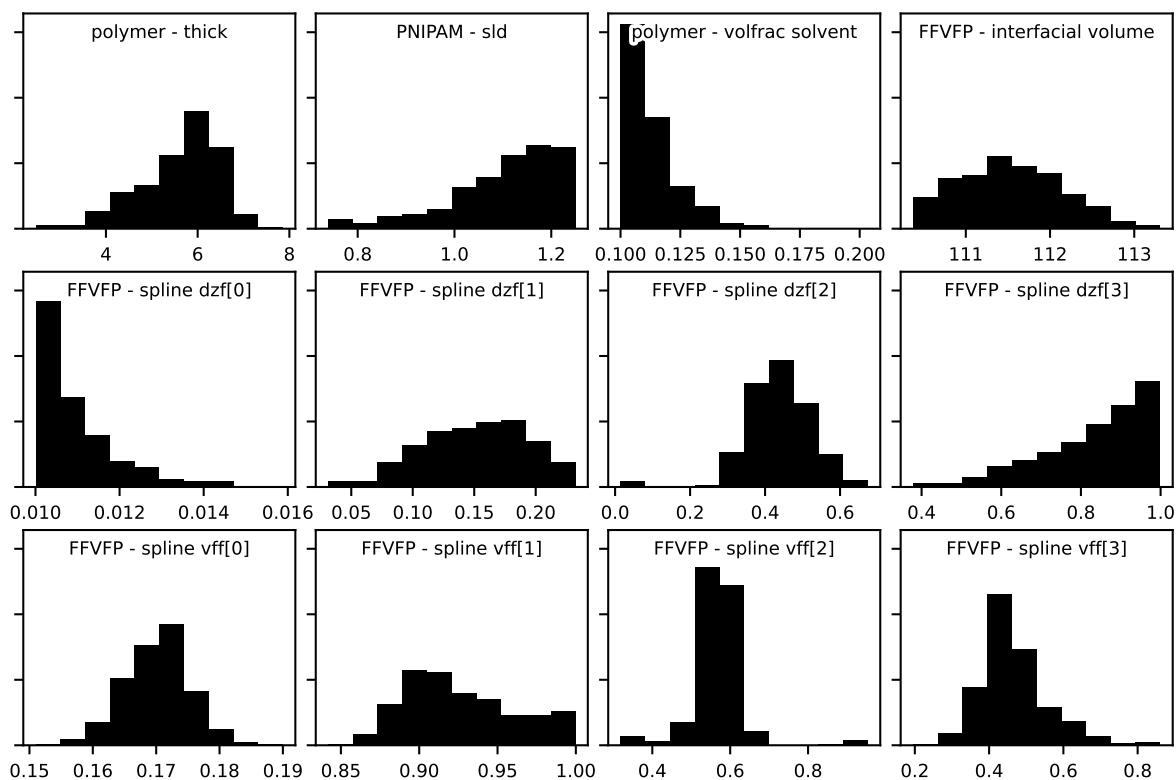


Figure K1: Parameter distributions corresponding to the 20 °C dataset in Fig. 4.7.

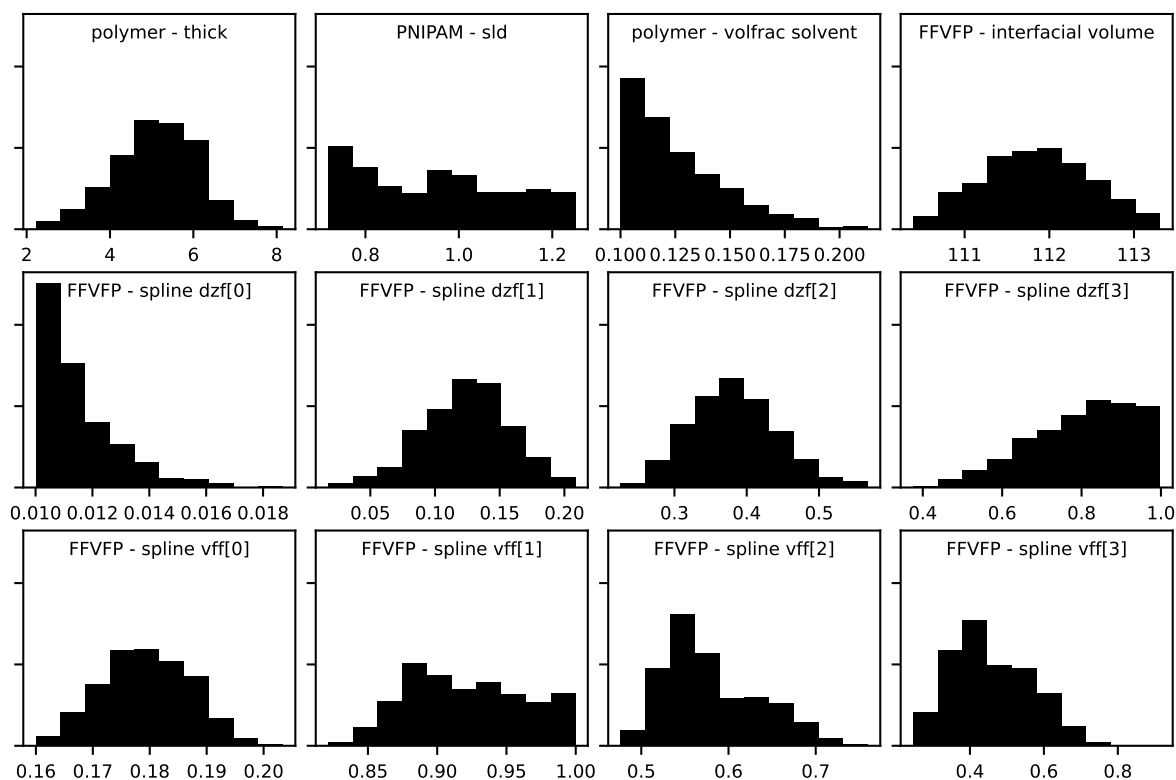


Figure K2: Parameter distributions corresponding to the 25 °C dataset in Fig. 4.7.

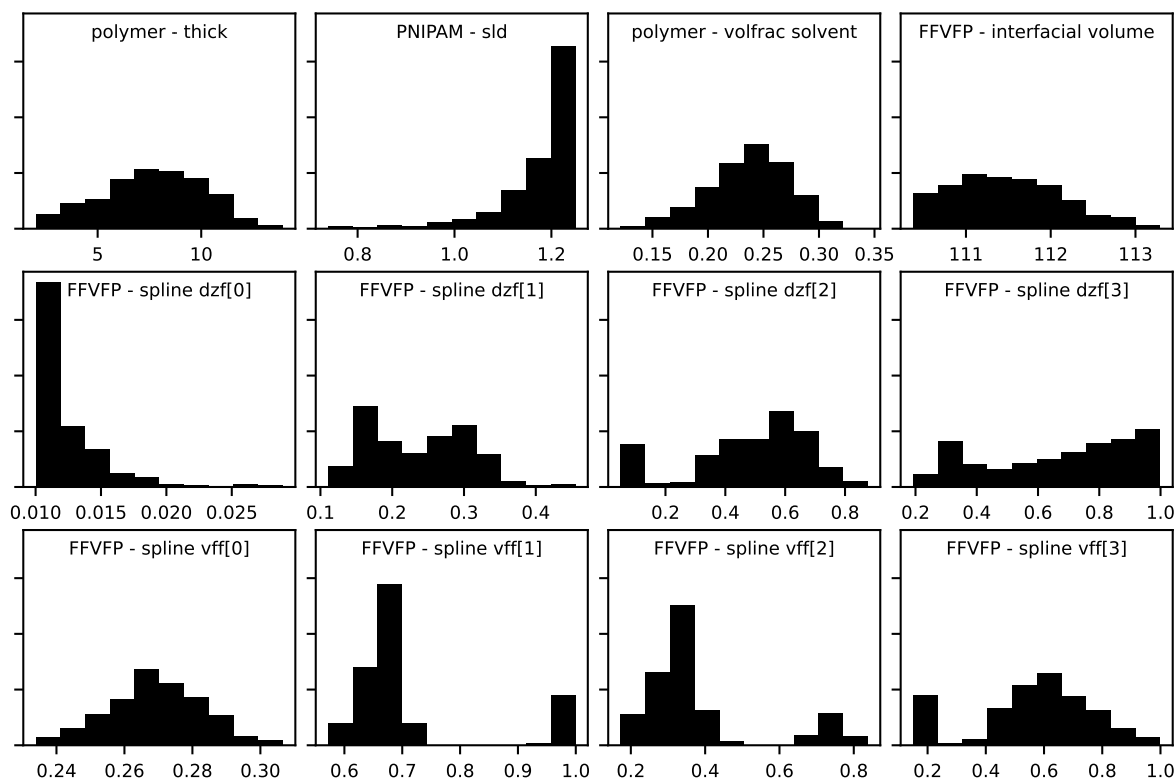


Figure K3: Parameter distributions corresponding to the 30 °C dataset in Fig. 4.7.

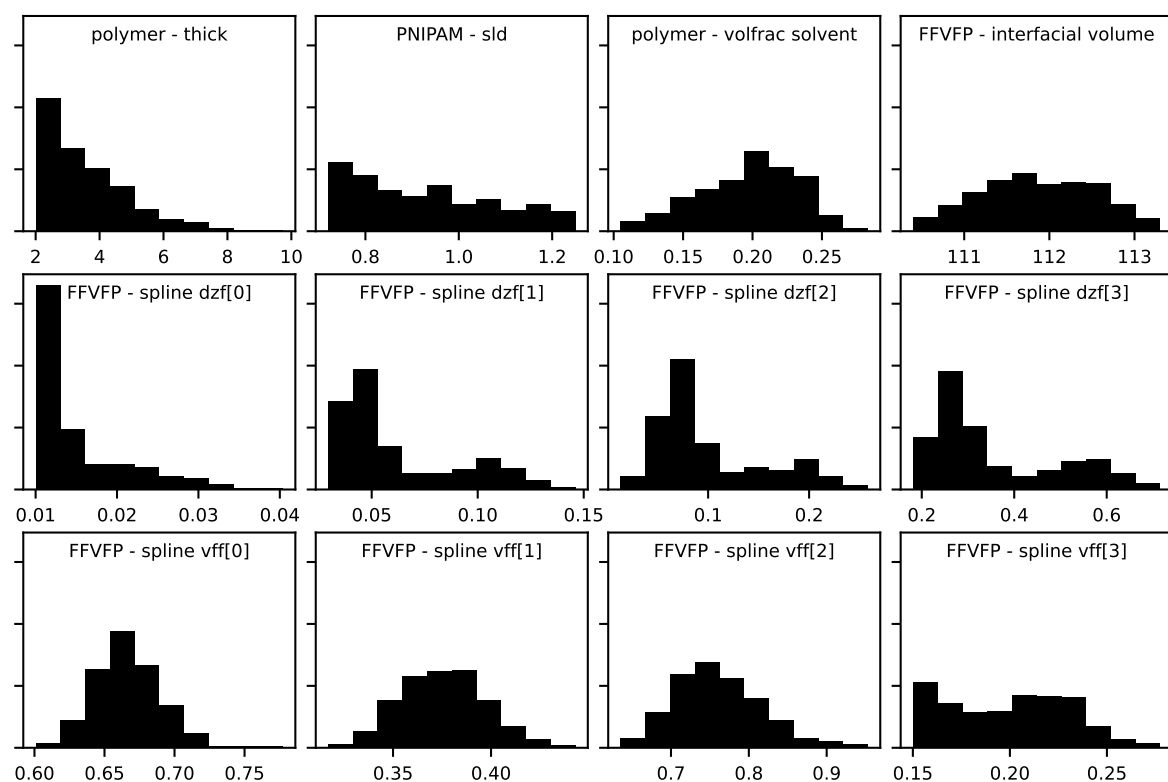


Figure K4: Parameter distributions corresponding to the 32 °C dataset in Fig. 4.7.

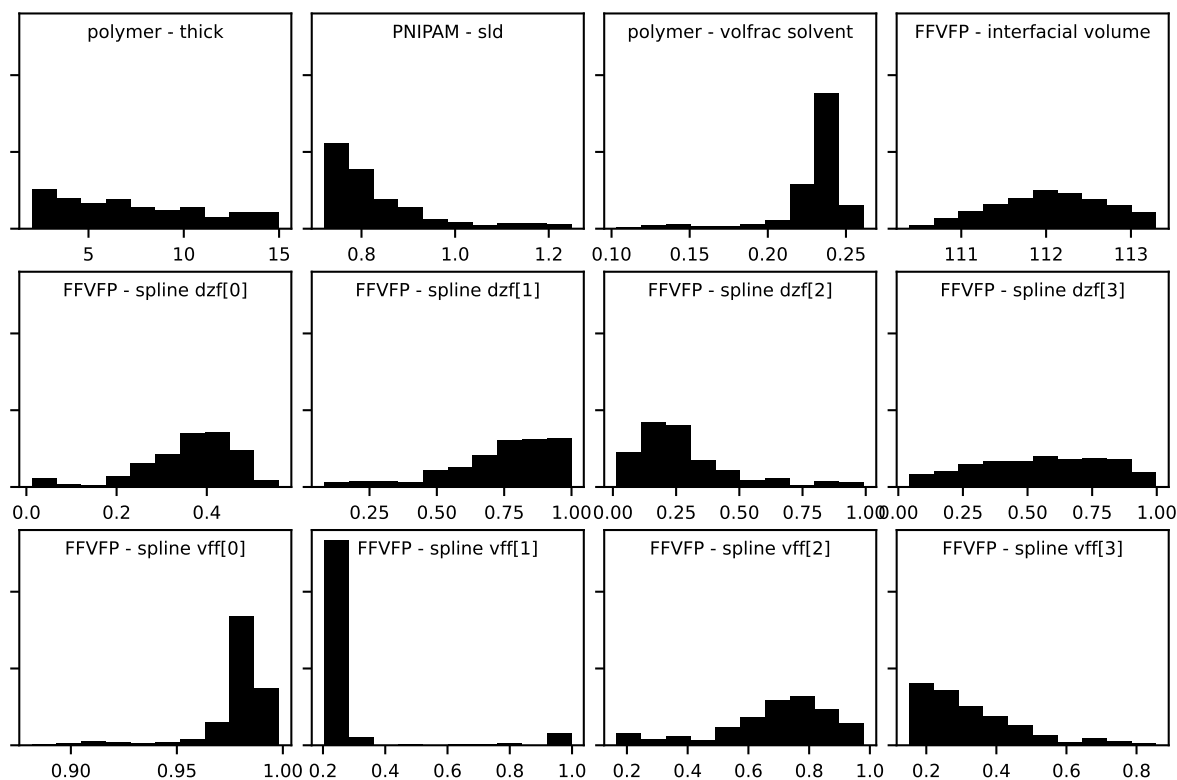


Figure K5: Parameter distributions corresponding to the 35 °C dataset in Fig. 4.7.

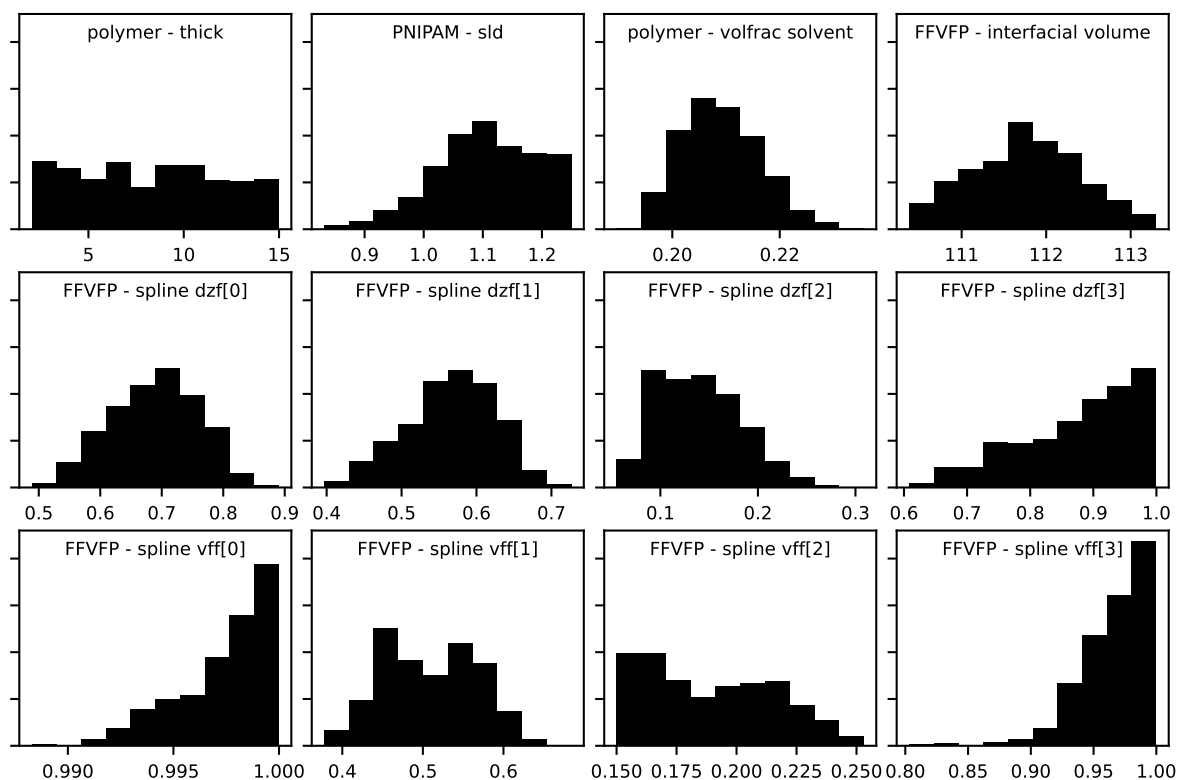


Figure K6: Parameter distributions corresponding to the 40 °C dataset in Fig. 4.7.



# Bibliography

- [1] G. W. Greene, R. Thapa, S. A. Holt, X. Wang, C. J. Garvey, and R. F. Tabor. “Structure and property changes in self-assembled lubricin layers induced by calcium ion interactions”. In: *Langmuir* 33.10 (Mar. 2017), pp. 2559–2570. DOI: 10.1021/acs.langmuir.6b03992.
- [2] W. L. Chen, R. Cordero, H. Tran, and C. K. Ober. “50th anniversary perspective: polymer brushes: novel surfaces for future materials”. In: *Macromolecules* 50.11 (2017), pp. 4089–4113. DOI: 10.1021/acs.macromol.7b00450.
- [3] R. R. Netz and M. Schick. “Polymer brushes: From self-consistent field theory to classical theory”. In: *Macromolecules* 31.15 (July 1998), pp. 5105–5122. DOI: 10.1021/ma9717505.
- [4] E. Currie, F. a. M. Leermakers, M. a. Cohen Stuart, and G. J. Fleer. “Grafted adsorbing polymers: scaling behavior and phase transitions”. In: *Macromolecules* 32.2 (1999), pp. 487–498. DOI: 10.1021/ma970525k.
- [5] W. M. de Vos and F. A. Leermakers. “Modeling the structure of a polydisperse polymer brush”. In: *Polymer* 50.1 (Jan. 2009), pp. 305–316. DOI: 10.1016/j.polymer.2008.10.025.
- [6] W. J. Brittain and S. Minko. “A structural definition of polymer brushes”. In: *Journal of Polymer Science Part A: Polymer Chemistry* 45.16 (Aug. 2007), pp. 3505–3512. DOI: 10.1002/pola.22180.
- [7] P. J. Flory. “Thermodynamics of high polymer solutions”. In: *The Journal of Chemical Physics* 9.8 (Aug. 1941), pp. 660–660. DOI: 10.1063/1.1750971.
- [8] P. J. Flory. “Thermodynamics of high polymer solutions”. In: *The Journal of Chemical Physics* 10.1 (Jan. 1942), pp. 51–61. DOI: 10.1063/1.1723621.
- [9] P. J. Flory. “The configuration of real polymer chains”. In: *The Journal of Chemical Physics* 17.3 (Oct. 1949), pp. 303–310. DOI: 10.1063/1.1748031.
- [10] M. L. Huggins. “Solutions of long chain compounds”. In: *The Journal of Chemical Physics* 9.5 (May 1941), pp. 440–440. DOI: 10.1063/1.1750930.

- [11] M. L. Huggins. “Some properties of solutions of long-chain compounds”. In: *The Journal of Physical Chemistry* 46.1 (Jan. 1942), pp. 151–158. DOI: 10.1021/j150415a018.
- [12] M. L. Huggins. “Theory of solutions of high polymers”. In: *Journal of the American Chemical Society* 64.7 (July 1942), pp. 1712–1719. DOI: 10.1021/ja01259a068.
- [13] T. Wu, K. Efimenko, and J. Genzer. “Combinatorial study of the mushroom-to-brush crossover in surface anchored polyacrylamide”. In: *Journal of the American Chemical Society* 124.32 (Aug. 2002), pp. 9394–9395. DOI: 10.1021/ja027412n.
- [14] S. Milner. “Polymer brushes”. In: *Science* 251.4996 (Feb. 1991), pp. 905–914. DOI: 10.1126/science.251.4996.905.
- [15] T. Kreer. “Polymer-brush lubrication: A review of recent theoretical advances”. In: *Soft Matter* 12.15 (2016), pp. 3479–3501. DOI: 10.1039/c5sm02919h.
- [16] A. Nomura, K. Okayasu, K. Ohno, T. Fukuda, and Y. Tsujii. “Lubrication mechanism of concentrated polymer brushes in solvents: Effect of solvent quality and thereby swelling state”. In: *Macromolecules* 44.12 (2011), pp. 5013–5019. DOI: 10.1021/ma200340d.
- [17] Y. Higaki, M. Kobayashi, D. Murakami, and A. Takahara. “Anti-fouling behavior of polymer brush immobilized surfaces”. In: *Polymer Journal* 48.4 (Apr. 2016), pp. 325–331. DOI: 10.1038/pj.2015.137.
- [18] E. Wischerhoff, K. Uhlig, A. Lankenau, H. G. Börner, A. Laschewsky, C. Duschl, and J. F. Lutz. “Controlled cell adhesion on PEG-based switchable surfaces”. In: *Angewandte Chemie - International Edition* 47.30 (2008), pp. 5666–5668. DOI: 10.1002/anie.200801202.
- [19] H. Yim, M. S. Kent, S. Mendez, S. S. Balamurugan, S. Balamurugan, G. P. Lopez, and S. Satija. “Temperature-dependent conformational change of PNIPAM grafted chains at high surface density in water”. In: *Macromolecules* 37.5 (Mar. 2004), pp. 1994–1997. DOI: 10.1021/ma0354290.
- [20] T. J. Murdoch, B. A. Humphreys, J. D. Willott, K. P. Gregory, S. W. Prescott, A. Nelson, E. J. Wanless, and G. B. Webber. “Specific anion effects on the internal structure of a poly(*N*-isopropylacrylamide) brush”. In: *Macromolecules* 49.16 (2016), pp. 6050–6060. DOI: 10.1021/acs.macromol.6b01001.

- [21] J. D. Willott, B. A. Humphreys, T. J. Murdoch, S. Edmondson, G. B. Webber, and E. J. Wanless. “Hydrophobic effects within the dynamic pH-response of polybasic tertiary amine methacrylate brushes”. In: *Physical Chemistry Chemical Physics* 17.5 (2015), pp. 3880–3890. DOI: 10.1039/c4cp05292g.
- [22] H. Jia, A. Wildes, and S. Titmuss. “Structure of pH-responsive polymer brushes grown at the gold-water interface: Dependence on grafting density and temperature”. In: *Macromolecules* 45.1 (2012), pp. 305–312. DOI: 10.1021/ma201839y.
- [23] T. J. Murdoch, B. A. Humphreys, E. C. Johnson, G. B. Webber, and E. J. Wanless. “Specific ion effects on thermoresponsive polymer brushes: Comparison to other architectures”. In: *Journal of Colloid and Interface Science* 526 (Sept. 2018), pp. 429–450. DOI: 10.1016/j.jcis.2018.04.086.
- [24] R. Kou, J. Zhang, T. Wang, and G. Liu. “Interactions between polyelectrolyte brushes and hofmeister ions: chaotropes versus kosmotropes”. In: *Langmuir* 31.38 (2015), pp. 10461–10468. DOI: 10.1021/acs.langmuir.5b02698.
- [25] D. Parasuraman and M. J. Serpe. “poly(*N*-isopropylacrylamide) microgels for organic dye removal from water”. In: *ACS Applied Materials and Interfaces* 3.7 (2011), pp. 2732–2737. DOI: 10.1021/am2005288.
- [26] M. M. Ali, S. Su, C. D. M. Filipe, R. Pelton, and Y. Li. “Enzymatic manipulations of DNA oligonucleotides on microgel: towards development of DNA–microgel bioassays”. In: *Chemical Communications* 43 (2007), p. 4459. DOI: 10.1039/b709817k.
- [27] E. S. Gil and S. M. Hudson. “Stimuli-reponsive polymers and their bioconjugates”. In: *Progress in Polymer Science (Oxford)* 29.12 (2004), pp. 1173–1222. DOI: 10.1016/j.progpolymsci.2004.08.003.
- [28] G. R. Hendrickson and L. A. Lyon. “Bioresponsive hydrogels for sensing applications”. In: *Soft Matter* 5.1 (2009), pp. 29–35. DOI: 10.1039/b811620b.
- [29] M. Das, S. Mardyani, W. C. Chan, and E. Kumacheva. “Biofunctionalized pH-responsive microgels for cancer cell targeting: rational design”. In: *Advanced Materials* 18.1 (2006), pp. 80–83. DOI: 10.1002/adma.200501043.
- [30] M. Ulbricht. “Membrane separations using molecularly imprinted polymers”. In: *Journal of Chromatography B: Analytical Technologies in the Biomedical and Life Sciences* 804.1 (2004), pp. 113–125. DOI: 10.1016/j.jchromb.2004.02.007.
- [31] S. Alexander. “Adsorption of chain molecules with a polar head a scaling description”. In: *Journal de Physique* 38.8 (1977), pp. 983–987. DOI: 10.1051/jphys:01977003808098300.

- [32] P. de Gennes. “Scaling theory of polymer adsorption”. In: *Journal de Physique* 37.12 (Dec. 1976), pp. 1445–1452. DOI: 10.1051/jphys:0197600370120144500.
- [33] S. T. Milner, T. A. Witten, and M. E. Cates. “Theory of the grafted polymer brush”. In: *Macromolecules* 21.8 (1988), pp. 2610–2619. DOI: 10.1021/ma00186a051.
- [34] S. T. Milner. “Strong-stretching and Scheutjens–Fleer descriptions of grafted polymer brushes”. In: *J. Chem. Soc., Faraday Trans.* 86.9 (1990), pp. 1349–1353. DOI: 10.1039/FT9908601349.
- [35] V. A. Baulin and A. Halperin. “Signatures of a concentration-dependent Flory  $\chi$  parameter: swelling and collapse of coils and brushes”. In: *Macromolecular Theory and Simulations* 12.8 (2003), pp. 549–559. DOI: 10.1002/mats.200350014.
- [36] F. Afroze, E. Nies, and H. Berghmans. “Phase transitions in the system poly(*N*-isopropylacrylamide)/water and swelling behaviour of the corresponding networks”. In: *Journal of Molecular Structure* 554.1 (Oct. 2000), pp. 55–68. DOI: 10.1016/S0022-2860(00)00559-7.
- [37] M. Heskins and J. E. Guillet. “Solution properties of poly(*N*-isopropylacrylamide)”. In: *Journal of Macromolecular Science: Part A - Chemistry* 2.8 (Dec. 1968), pp. 1441–1455. DOI: 10.1080/10601326808051910.
- [38] A. Halperin, M. Kröger, and F. M. Winnik. “Poly(*N*-isopropylacrylamide) phase diagrams: Fifty years of research”. In: *Angewandte Chemie - International Edition* 54.51 (Dec. 2015), pp. 15342–15367. DOI: 10.1002/anie.201506663.
- [39] K. Kubota, K. Hamano, N. Kuwahara, S. Fujishige, and I. Ando. “Characterization of poly(*N*-isopropylmethacrylamide) in water”. In: *Polymer Journal* 22.12 (Dec. 1990), pp. 1051–1057. DOI: 10.1295/polymj.22.1051.
- [40] K. Kubota, S. Fujishige, and I. Ando. “Single-chain transition of poly(*N*-isopropylacrylamide) in water”. In: *The Journal of Physical Chemistry* 94.12 (June 1990), pp. 5154–5158. DOI: 10.1021/j100375a070.
- [41] P. Kujawa, V. Aseyev, H. Tenhu, and F. M. Winnik. “Temperature-sensitive properties of poly(*N*-isopropylacrylamide) mesoglobules formed in dilute aqueous solutions heated above their demixing point”. In: *Macromolecules* 39.22 (Oct. 2006), pp. 7686–7693. DOI: 10.1021/ma061604b.

- [42] M. Andersson and S. L. Maunu. “Volume phase transition and structure of poly(*N*-isopropylacrylamide) microgels studied with  $^1\text{H}$ -NMR spectroscopy in  $\text{D}_2\text{O}$ ”. In: *Colloid and Polymer Science* 285.3 (Nov. 2006), pp. 293–303. DOI: 10.1007/s00396-006-1563-y.
- [43] Y. M. Mohan, T. Premkumar, D. K. Joseph, and K. E. Geckeler. “Stimuli-responsive poly(*N*-isopropylacrylamide-co-sodium acrylate) hydrogels: A swelling study in surfactant and polymer solutions”. In: *Reactive and Functional Polymers* 67.9 (2007), pp. 844–858. DOI: 10.1016/j.reactfunctpolym.2007.05.008.
- [44] A. Fernández-Barbero, A. Fernández-Nieves, I. Grillo, and E. López-Cabarcos. “Structural modifications in the swelling of inhomogeneous microgels by light and neutron scattering”. In: *Physical Review E* 66.5 (Nov. 2002), p. 051803. DOI: 10.1103/PhysRevE.66.051803.
- [45] N. Ishida and S. Biggs. “Effect of grafting density on phase transition behavior for poly(*N*-isopropylacrylamide) brushes in aqueous solutions studied by AFM and QCM-D”. In: *Macromolecules* 43.17 (2010), pp. 7269–7276. DOI: 10.1021/ma101113g.
- [46] G. Liu and G. Zhang. “Collapse and swelling of thermally sensitive poly(*N*-isopropylacrylamide) brushes monitored with a quartz crystal microbalance”. In: *Journal of Physical Chemistry B* 109.2 (2005), pp. 743–747. DOI: 10.1021/jp046903m.
- [47] Y. Yu, B. D. Kieviet, F. Liu, I. Siretanu, E. Kutnyánszky, G. J. Vancso, and S. De Beer. “Stretching of collapsed polymers causes an enhanced dissipative response of PNIPAM brushes near their LCST”. In: *Soft Matter* 11.43 (2015), pp. 8508–8516. DOI: 10.1039/c5sm01426c.
- [48] B. A. Humphreys, J. D. Willott, T. J. Murdoch, G. B. Webber, and E. J. Wanless. “Specific ion modulated thermoresponse of poly(*N*-isopropylacrylamide) brushes”. In: *Physical Chemistry Chemical Physics* 18.8 (2016), pp. 6037–6046. DOI: 10.1039/C5CP07468A.
- [49] H. Yim, M. S. Kent, S. Satija, S. Mendez, S. S. Balamurugan, and G. P. Lopez. “Evidence for vertical phase separation in densely grafted, high-molecular-weight poly(*N*-isopropylacrylamide) brushes in water”. In: *Physical Review E - Statistical, Nonlinear, and Soft Matter Physics* 72.5 (2005), pp. 1–7. DOI: 10.1103/PhysRevE.72.051801.

- [50] I. B. Malham and L. Bureau. “Density effects on collapse, compression, and adhesion of thermoresponsive polymer brushes”. In: *Langmuir* 26.7 (2010), pp. 4762–4768. DOI: 10.1021/la9035387.
- [51] B. A. Humphreys, E. C. Johnson, E. J. Wanless, and G. B. Webber. “Poly(*N*-isopropylacrylamide) response to salt concentration and anion identity: a brush-on-brush study”. In: *Langmuir* 35.33 (Aug. 2019), pp. 10818–10830. DOI: 10.1021/acs.langmuir.9b00695.
- [52] K. N. Plunkett, X. Zhu, J. S. Moore, and D. E. Leckband. “PNIPAM chain collapse depends on the molecular weight and grafting density”. In: *Langmuir* 22.9 (2006), pp. 4259–4266. DOI: 10.1021/la0531502.
- [53] R. Pelton. “Poly(*N*-isopropylacrylamide) (PNIPAM) is never hydrophobic”. In: *Journal of Colloid and Interface Science* 348.2 (2010), pp. 673–674. DOI: 10.1016/j.jcis.2010.05.034.
- [54] H. Feil, Y. H. Bae, J. Feijen, and S. W. Kim. “Effect of comonomer hydrophilicity and ionization on the lower critical solution temperature of *N*-isopropylacrylamide copolymers”. In: *Macromolecules* 26.10 (May 1993), pp. 2496–2500. DOI: 10.1021/ma00062a016.
- [55] K. Otake, H. Inomata, M. Konno, and S. Saito. “Thermal analysis of the volume phase transition with *N*-isopropylacrylamide gels”. In: *Macromolecules* 23.1 (Jan. 1990), pp. 283–289. DOI: 10.1021/ma00203a049.
- [56] E. C. Cho, J. Lee, and K. Cho. “Role of bound water and hydrophobic interaction in phase transition of poly(*N*-isopropylacrylamide) aqueous solution”. In: *Macromolecules* 36.26 (Dec. 2003), pp. 9929–9934. DOI: 10.1021/ma034851d.
- [57] M. Podewitz, Y. Wang, P. K. Quoika, J. R. Loeffler, M. Schauerl, and K. R. Liedl. “Coil–globule transition thermodynamics of poly(*N*-isopropylacrylamide)”. In: *The Journal of Physical Chemistry B* 123.41 (Oct. 2019), pp. 8838–8847. DOI: 10.1021/acs.jpcb.9b06125.
- [58] L. P. N. Rebelo, Z. P. Visak, H. C. de Sousa, J. Szydlowski, R. Gomes de Azevedo, A. M. Ramos, V. Najdanovic-Visak, M. Nunes da Ponte, J. Klein, M. N. Da Ponte, and J. Klein. “Double critical phenomena in (water + polyacrylamides) solutions”. In: *Macromolecules* 35.5 (Feb. 2002), pp. 1887–1895. DOI: 10.1021/ma011533a.
- [59] G. Paradossi and E. Chiessi. “Tacticity-dependent interchain interactions of poly(*N*-isopropylacrylamide) in water: toward the molecular dynamics simulation of a thermoresponsive microgel”. In: *Gels* 3.2 (Apr. 2017), p. 13. DOI: 10.3390/gels3020013.

- [60] Y. Xia, N. A. Burke, and H. D. Stöver. “End group effect on the thermal response of narrow-disperse poly(*N*-isopropylacrylamide) prepared by atom transfer radical polymerization”. In: *Macromolecules* 39.6 (2006), pp. 2275–2283. DOI: 10.1021/ma0519617.
- [61] Y. Xia, X. Yin, N. A. D. Burke, and H. D. H. Stöver. “Thermal response of narrow-disperse poly(*N*-isopropylacrylamide) prepared by atom transfer radical polymerization”. In: *Macromolecules* 38.14 (July 2005), pp. 5937–5943. DOI: 10.1021/ma050261z.
- [62] Y. Zhang, S. Furyk, L. B. Sagle, Y. Cho, D. E. Bergbreiter, and P. S. Cremer. “Effects of hofmeister anions on the LCST of PNIPAM as a function of molecular weight”. In: *The Journal of Physical Chemistry C* 111.25 (June 2007), pp. 8916–8924. DOI: 10.1021/jp0690603.
- [63] N. Brouette, C. Xue, M. Haertlein, M. Moulin, G. Fragneto, D. E. Leckband, A. Halperin, and M. Sferrazza. “Protein adsorption properties of OEG monolayers and dense PNIPAM brushes probed by neutron reflectivity”. In: *European Physical Journal: Special Topics* 213.1 (2012), pp. 343–353. DOI: 10.1140/epjst/e2012-01681-4.
- [64] Q. Chen, E. S. Kooij, X. Sui, C. J. Padberg, M. A. Hempenius, P. M. Schön, and G. J. Vancso. “Collapse from the top: brushes of poly(*N*-isopropylacrylamide) in co-nonsolvent mixtures”. In: *Soft Matter* 10.17 (2014), p. 3134. DOI: 10.1039/c4sm00195h.
- [65] X. Sui, Q. Chen, M. A. Hempenius, and G. J. Vancso. “Probing the collapse dynamics of poly(*N*-isopropylacrylamide) brushes by AFM: Effects of Co-nonsolvency and grafting densities”. In: *Small* 7.10 (2011), pp. 1440–1447. DOI: 10.1002/smll.201002229.
- [66] Y. Yu, M. Cirelli, B. D. Kieviet, E. S. Kooij, G. J. Vancso, and S. de Beer. “Tunable friction by employment of co-non-solvency of PNIPAM brushes”. In: *Polymer* 102 (Oct. 2016), pp. 372–378. DOI: 10.1016/j.polymer.2016.08.029.
- [67] G. Liu and G. Zhang. “Reentrant behavior of poly(*N*-isopropylacrylamide) brushes in water-Methanol mixtures investigated with a quartz crystal microbalance”. In: *Langmuir* 21.5 (2005), pp. 2086–2090. DOI: 10.1021/la047326w.
- [68] B. A. Humphreys, S. W. Prescott, T. J. Murdoch, A. Nelson, E. P. Gilbert, G. B. Webber, and E. J. Wanless. “Influence of molecular weight on PNIPAM brush modified colloidal silica particles”. In: *Soft Matter* 15.1 (2019), pp. 55–64. DOI: 10.1039/C8SM01824C.

- [69] E. S. Kooij, X. Sui, M. A. Hempenius, H. J. W. Zandvliet, and G. J. Vancso. “Probing the thermal collapse of poly(*N*-isopropylacrylamide) grafts by quantitative in situ ellipsometry”. In: *Journal of Physical Chemistry B* 116.30 (2012), pp. 9261–9268. DOI: 10.1021/jp304364m.
- [70] J. Li, H. Chen, G. Mu, J. Sun, Y. Sun, C. Wang, Q. Ren, and J. Ji. “Synthesis of amphiphilic block copolymers via ARGET ATRP using an inexpensive ligand of PMDETA”. In: *Reactive and Functional Polymers* 73.11 (Nov. 2013), pp. 1517–1522. DOI: 10.1016/j.reactfunctpolym.2013.07.012.
- [71] F. L. McCrackin, E. Passaglia, R. R. Stromberg, and H. L. Steinberg. “Measurement of the thickness and refractive index of very thin films and the optical properties of surfaces by ellipsometry”. In: *Journal of Research of the National Bureau of Standards Section A: Physics and Chemistry* 67A.4 (July 1963), p. 363. DOI: 10.6028/jres.067A.040.
- [72] R. R. Stromberg, E. Passaglia, and D. J. Tutas. “Thickness of adsorbed polystyrene layers by ellipsometry”. In: *Journal of Research of the National Bureau of Standards Section A: Physics and Chemistry* 67A.5 (Sept. 1963), p. 431. DOI: 10.6028/jres.067A.045.
- [73] E. C. Johnson, T. J. Murdoch, I. J. Gresham, B. A. Humphreys, S. W. Prescott, A. Nelson, G. B. Webber, and E. J. Wanless. “Temperature dependent specific ion effects in mixed salt environments on a thermoresponsive poly(oligoethylene glycol methacrylate) brush”. In: *Physical Chemistry Chemical Physics* 21.8 (2019), pp. 4650–4662. DOI: 10.1039/C8CP06644B.
- [74] P. W. Zhu. “Effects of sodium dodecyl sulfate on structures of poly(*N*-isopropylacrylamide) at the particle surface”. In: *The Journal of Physical Chemistry B* 119.1 (Jan. 2015), pp. 359–371. DOI: 10.1021/jp510350w.
- [75] M. Biesalski and J. Rühe. “Swelling of a polyelectrolyte brush in humid air”. In: *Langmuir* 16.4 (2000), pp. 1943–1950. DOI: 10.1021/la990863.
- [76] J. D. Willott, T. J. Murdoch, B. A. Humphreys, S. Edmondson, G. B. Webber, and E. J. Wanless. “Critical salt effects in the swelling behavior of a weak polybasic brush”. In: *Langmuir* 30.7 (2014), pp. 1827–1836. DOI: 10.1021/la4047275.
- [77] C. J. Galvin, M. D. Dimitriou, S. K. Satija, and J. Genzer. “Swelling of polyelectrolyte and polyzwitterion brushes by humid vapors”. In: *Journal of the American Chemical Society* 136.36 (2014), pp. 12737–12745. DOI: 10.1021/ja5065334.



- [78] C. J. Galvin and J. Genzer. “Swelling of hydrophilic polymer brushes by water and alcohol vapors”. In: *Macromolecules* 49.11 (June 2016), pp. 4316–4329. DOI: 10.1021/acs.macromol.6b00111.
- [79] S. B. Abbott, W. M. de Vos, L. L. E. Mears, B. Cattoz, M. W. A. Skoda, R. Barker, R. M. Richardson, and S. W. Prescott. “Is osmotic pressure relevant in the mechanical confinement of a polymer brush?” In: *Macromolecules* 48.7 (Apr. 2015), pp. 2224–2234. DOI: 10.1021/ma502246r.
- [80] P. Virtanen et al. “SciPy 1.0: fundamental algorithms for scientific computing in Python”. In: *Nature Methods* 17.3 (2020), pp. 261–272. DOI: 10.1038/s41592-019-0686-2.
- [81] M. James, A. Nelson, S. Holt, T. Saerbeck, W. Hamilton, and F. Klose. “The multipurpose time-of-flight neutron reflectometer “Platypus” at Australia’s OPAL reactor”. In: *Nuclear Instruments and Methods in Physics Research Section A: Accelerators, Spectrometers, Detectors and Associated Equipment* 632.1 (Mar. 2011), pp. 112–123. DOI: 10.1016/j.nima.2010.12.075.
- [82] T. Widmann, L. P. Kreuzer, N. Hohn, L. Bießmann, K. Wang, S. Rinner, J.-F. Moulin, A. J. Schmid, Y. Hannappel, O. Wrede, M. Kühnhammer, T. Hellweg, R. von Klitzing, and P. Müller-Buschbaum. “Hydration and solvent exchange induced swelling and deswelling of homogeneous poly(*N*-isopropylacrylamide) microgel thin films”. In: *Langmuir* 35.49 (Dec. 2019), pp. 16341–16352. DOI: 10.1021/acs.langmuir.9b03104.
- [83] J. D. Willott, T. J. Murdoch, B. A. Humphreys, S. Edmondson, E. J. Wanless, and G. B. Webber. “Anion-specific effects on the behavior of pH-sensitive polybasic brushes”. In: *Langmuir* 31.12 (2015), pp. 3707–3717. DOI: 10.1021/acs.langmuir.5b00116.
- [84] E. C. Johnson, J. D. Willott, W. M. de Vos, E. J. Wanless, and G. B. Webber. “Interplay of composition, pH, and temperature on the conformation of multi-stimulus-responsive copolymer brushes: comparison of experiment and theory”. In: *Langmuir* 36.21 (June 2020), pp. 5765–5777. DOI: 10.1021/acs.langmuir.0c00424.
- [85] H. Robertson, E. C. Johnson, I. J. Gresham, S. W. Prescott, A. Nelson, E. J. Wanless, and G. B. Webber. “Competitive specific ion effects in mixed salt solutions on a thermoresponsive polymer brush”. In: *Journal of Colloid and Interface Science* xxxx (2020). DOI: 10.1016/j.jcis.2020.10.092.

- [86] E. Bittrich, K. B. Rodenhausen, K.-J. Eichhorn, T. Hofmann, M. Schubert, M. Stamm, and P. Uhlmann. “Protein adsorption on and swelling of polyelectrolyte brushes: A simultaneous ellipsometry-quartz crystal microbalance study”. In: *Biointerphases* 5.4 (2010), pp. 159–167. DOI: 10.1116/1.3530841.
- [87] M. Biesalski, J. Rühe, and D. Johannsmann. “Segment density profiles of polyelectrolyte brushes determined by Fourier transform ellipsometry”. In: *The Journal of Chemical Physics* 111.15 (Oct. 1999), pp. 7029–7037. DOI: 10.1063/1.480019.
- [88] J. Campos, C. Jiménez, C. Trigo, P. Ibarra, D. Rana, R. Thiruganesh, M. Ramingam, and Z. S. Haidar. “Quartz crystal microbalance with dissipation monitoring: A powerful tool for BioNanoScience and drug discovery”. In: *Journal of Bionanoscience* 9.4 (Aug. 2015), pp. 249–260. DOI: 10.1166/jbns.2015.1310.
- [89] M. Rodahl, F. Höök, A. Krozer, P. Brzezinski, and B. Kasemo. “Quartz crystal microbalance setup for frequency and Q-factor measurements in gaseous and liquid environments”. In: *Review of Scientific Instruments* 66.7 (1995), pp. 3924–3930. DOI: 10.1063/1.1145396.
- [90] G. Sauerbrey. “Verwendung von schwingquarzen zur wägung dünner schichten und zur mikrowägung”. In: *Zeitschrift für Physik* 155.2 (Apr. 1959), pp. 206–222. DOI: 10.1007/BF01337937.
- [91] T. Nomura and M. Okuhara. “Frequency shifts of piezoelectric quartz crystals immersed in organic liquids”. In: *Analytica Chimica Acta* 142.C (Oct. 1982), pp. 281–284. DOI: 10.1016/S0003-2670(01)95290-0.
- [92] K. Ehtiati, S. Z. Moghaddam, A. E. Daugaard, and E. Thormann. “How dissociation of carboxylic acid groups in a weak polyelectrolyte brush depend on their distance from the substrate”. In: *Langmuir* 36.9 (Mar. 2020), pp. 2339–2348. DOI: 10.1021/acs.langmuir.9b03537.
- [93] S. X. Liu and J.-T. Kim. “Application of Kevin—Voigt model in quantifying whey protein adsorption on polyethersulfone using QCM-D”. In: *JALA: Journal of the Association for Laboratory Automation* 14.4 (Aug. 2009), pp. 213–220. DOI: 10.1016/j.jala.2009.01.003.
- [94] K. Sadman, C. G. Wiener, R. A. Weiss, C. C. White, K. R. Shull, and B. D. Vogt. “Quantitative rheometry of thin soft materials using the quartz crystal microbalance with dissipation”. In: *Analytical Chemistry* 90.6 (Mar. 2018), pp. 4079–4088. DOI: 10.1021/acs.analchem.7b05423.
- [95] A. Khabibullin, E. Mastan, K. Matyjaszewski, and S. Zhu. “Surface-initiated atom transfer radical polymerization”. In: 2015, pp. 29–76. DOI: 10.1007/12\_2015\_311.

- [96] K. Amoako and R. Gbyli. “Improving the hemocompatibility of biomedical polymers”. In: *Hemocompatibility of Biomaterials for Clinical Applications: Blood-Biomaterials Interactions*. Elsevier Inc., Jan. 2018, pp. 223–252. DOI: 10.1016/B978-0-08-100497-5.00016-1.
- [97] A. P. Martinez, J. M. Y. Carrillo, A. V. Dobrynin, and D. H. Adamson. “Distribution of chains in polymer brushes produced by a “grafting From” mechanism”. In: *Macromolecules* 49.2 (2016), pp. 547–553. DOI: 10.1021/acs.macromol.5b02261.
- [98] D. M. Jones, A. A. Brown, and W. T. Huck. “Surface-initiated polymerizations in aqueous media: Effect of initiator density”. In: *Langmuir* 18.4 (2002), pp. 1265–1269. DOI: 10.1021/la011365f.
- [99] E. Mastan, L. Xi, and S. Zhu. “Factors affecting grafting density in surface-initiated ATRP: A simulation study”. In: *Macromolecular Theory and Simulations* 25.3 (2016), pp. 220–228. DOI: 10.1002/mats.201500081.
- [100] J. J. Keating IV, A. Lee, and G. Belfort. “Predictive tool for design and analysis of ARGET ATRP grafting reactions”. In: *Macromolecules* 50.20 (2017), pp. 7930–7939. DOI: 10.1021/acs.macromol.7b01572.
- [101] T. J. Murdoch, B. A. Humphreys, J. D. Willott, S. W. Prescott, A. Nelson, G. B. Webber, and E. J. Wanless. “Enhanced specific ion effects in ethylene glycol-based thermoresponsive polymer brushes”. In: *Journal of Colloid and Interface Science* 490 (Mar. 2017), pp. 869–878. DOI: 10.1016/j.jcis.2016.11.044.
- [102] E. C. Johnson, I. J. Gresham, S. W. Prescott, A. Nelson, E. J. Wanless, and G. B. Webber. “The direction of influence of specific ion effects on a pH and temperature responsive copolymer brush is dependent on polymer charge”. In: *Polymer* 214.November 2020 (Feb. 2021), p. 123287. DOI: 10.1016/j.polymer.2020.123287.
- [103] D. Kesal, S. Christau, M. Trapp, P. Krause, and R. von Klitzing. “The internal structure of PMETAC brush/gold nanoparticle composites: A neutron and X-ray reflectivity study”. In: *Physical Chemistry Chemical Physics* 19.45 (2017), pp. 30636–30646. DOI: 10.1039/C7CP04404F.
- [104] I. E. Dunlop, R. K. Thomas, S. Titmus, V. Osborne, S. Edmondson, W. T. Huck, and J. Klein. “Structure and collapse of a surface-grown strong polyelectrolyte brush on sapphire”. In: *Langmuir* 28.6 (Feb. 2012), pp. 3187–3193. DOI: 10.1021/la204655h.

- [105] M. Zhu, M. Z. Lerum, and W. Chen. “How to prepare reproducible, homogeneous, and hydrolytically stable aminosilane-derived layers on silica”. In: *Langmuir* 28.1 (Jan. 2012), pp. 416–423. DOI: 10.1021/la203638g.
- [106] F. Zhang, K. Sautter, A. M. Larsen, D. A. Findley, R. C. Davis, H. Samha, and M. R. Linford. “Chemical vapor deposition of three aminosilanes on silicon dioxide: Surface characterization, stability, effects of silane concentration, and cyanine dye adsorption”. In: *Langmuir* 26.18 (2010), pp. 14648–14654. DOI: 10.1021/la102447y.
- [107] L. Giraud, R. Nadarajah, Y. Matar, G. Bazin, J. Sun, X. X. Zhu, and S. Giasson. “Amino-functionalized monolayers covalently grafted to silica-based substrates as a robust primer anchorage in aqueous media”. In: *Applied Surface Science* 370 (2016), pp. 476–485. DOI: 10.1016/j.apsusc.2016.02.141.
- [108] J. D. Willott, T. J. Murdoch, G. B. Webber, and E. J. Wanless. “Physicochemical behaviour of cationic polyelectrolyte brushes”. In: *Progress in Polymer Science* 64 (2016), pp. 52–75. DOI: 10.1016/j.progpolymsci.2016.09.010.
- [109] T. J. Murdoch, J. D. Willott, W. M. de Vos, A. Nelson, S. W. Prescott, E. J. Wanless, and G. B. Webber. “Influence of anion hydrophilicity on the conformation of a hydrophobic weak polyelectrolyte brush”. In: *Macromolecules* 49.24 (2016), pp. 9605–9617. DOI: 10.1021/acs.macromol.6b01897.
- [110] C. Huang, T. Tassone, K. Woodberry, D. Sunday, and D. L. Green. “Impact of ATRP initiator spacer length on grafting poly(methyl methacrylate) from Silica nanoparticles”. In: *Langmuir* 25.23 (2009), pp. 13351–13360. DOI: 10.1021/la901918v.
- [111] H. Elwing, S. Welin, A. Askendal, U. Nilsson, and I. Lundström. “A wettability gradient method for studies of macromolecular interactions at the liquid/solid interface”. In: *Journal of Colloid and Interface Science* 119.1 (1987), pp. 203–210.
- [112] E. M. Benetti, C. Kang, J. Mandal, M. Divandari, and N. D. Spencer. “Modulation of surface-initiated ATRP by confinement: mechanism and applications”. In: *Macromolecules* 50.15 (2017), pp. 5711–5718. DOI: 10.1021/acs.macromol.7b00919.
- [113] W. A. Braunecker, N. V. Tsarevsky, A. Gennaro, and K. Matyjaszewski. “Thermodynamic components of the atom transfer radical polymerization equilibrium: quantifying solvent effects”. In: *Macromolecules* 42.17 (Sept. 2009), pp. 6348–6360. DOI: 10.1021/ma901094s.

- [114] D. K. Schwartz. “Mechanisms and kinetics of self-assembled monolayer formation”. In: *Annual Review of Physical Chemistry* 52.1 (Oct. 2001), pp. 107–137. DOI: 10.1146/annurev.physchem.52.1.107.
- [115] Z. Bao, M. L. Bruening, and G. L. Baker. “Control of the density of polymer brushes prepared by surface-initiated atom transfer radical polymerization”. In: *Macromolecules* 39.16 (2006), pp. 5251–5258. DOI: 10.1021/ma060095a.
- [116] C. K. Pandiyarajan, O. Prucker, and J. Rühe. “Humidity driven swelling of the surface-attached poly(*N*-alkylacrylamide) hydrogels”. In: *Macromolecules* 49.21 (2016), pp. 8254–8264. DOI: 10.1021/acs.macromol.6b01379.
- [117] Y. Ko, J. R. Miles, and J. Genzer. “Determining Water Sorption and Desorption in Thin Hydrophilic Polymer Films by Thermal Treatment”. In: *ACS Applied Polymer Materials* 1.9 (Sept. 2019), pp. 2495–2502. DOI: 10.1021/acsapm.9b00607.
- [118] K. Unger, R. Resel, and A. M. Coclite. “Dynamic studies on the response to humidity of poly( 2-hydroxyethyl methacrylate) hydrogels produced by initiated chemical vapor deposition”. In: *Macromolecular Chemistry and Physics* 217.21 (2016), pp. 2372–2379. DOI: 10.1002/macp.201600271.
- [119] L. P. Kreuzer, T. Widmann, N. Aldosari, L. Bießmann, G. Mangiapia, V. Hildebrand, A. Laschewsky, C. M. Papadakis, and P. Muller-Buschbaum. “Cyclic water storage behavior of doubly thermoresponsive poly(sulfobetaine)-based diblock copolymer thin films”. In: *Macromolecules* 53.20 (2020), pp. 9108–9121. DOI: 10.1021/acs.macromol.0c01335.
- [120] L. P. Kreuzer, C. Lindenmeir, C. Geiger, T. Widmann, V. Hildebrand, A. Laschewsky, C. M. Papadakis, and P. Müller-Buschbaum. “Poly(sulfobetaine) versus poly(*N*-isopropylmethacrylamide): co-nonsolvency-type behavior of thin films in a water/methanol atmosphere”. In: *Macromolecules* (2021). DOI: 10.1021/acs.macromol.0c02281.
- [121] S. Nieuwenhuis, Q. Zhong, E. Metwalli, L. Bießmann, M. Philipp, A. Miasnikova, A. Laschewsky, C. M. Papadakis, R. Cubitt, J. Wang, and P. Müller-Buschbaum. “Hydration and dehydration kinetics: comparison between poly(*N*-isopropyl methacrylamide) and poly(methoxy diethylene glycol acrylate) films”. In: *Langmuir* 35.24 (2019), pp. 7691–7702. DOI: 10.1021/acs.langmuir.9b00535.
- [122] N. Matsunaga and A. Nagashima. “Saturation vapor pressure and critical constants of H<sub>2</sub>O, D<sub>2</sub>O, T<sub>2</sub>O, and their isotopic mixtures”. In: *International Journal of Thermophysics* 8.6 (1987), pp. 681–694. DOI: 10.1007/BF00500788.

- [123] A. Saul and W. Wagner. “International equations for the saturation properties of ordinary water substance”. In: *Journal of Physical and Chemical Reference Data* 16.4 (1987), pp. 893–901. DOI: 10.1063/1.555787.
- [124] T. Ederth and T. Ekblad. “Swelling of thin poly(ethylene glycol)-containing hydrogel films in water vapor — a neutron reflectivity study”. In: *Langmuir* 34.19 (2018), pp. 5517–5526. DOI: 10.1021/acs.langmuir.8b00177.
- [125] M. Brió Pérez, M. Cirelli, and S. de Beer. “Degrafting of polymer brushes by exposure to humid air”. In: *ACS Applied Polymer Materials* 2.8 (Aug. 2020), pp. 3039–3043. DOI: 10.1021/acsapm.0c00474.
- [126] H. Elbs and G. Krausch. “Ellipsometric determination of Flory–Huggins interaction parameters in solution”. In: *Polymer* 45.23 (2004), pp. 7935–7942. DOI: 10.1016/j.polymer.2004.09.021.
- [127] P. J. Flory. “Spatial configuration of macromolecular chains”. In: *British Polymer Journal* 8.1 (Mar. 1976), pp. 1–10. DOI: 10.1002/pi.4980080102.
- [128] P. J. Flory. *Principles of polymer chemistry*. Cornell University Press, 1953.
- [129] E. Jones, T. Oliphant, P. Peterson, and E. Al. *SciPy: Open source scientific tools for Python*. 2001. URL: <http://www.scipy.org/>.
- [130] J. E. Mark, ed. *Physical Properties of Polymers Handbook*. New York, NY: Springer New York, 2007. DOI: 10.1007/978-0-387-69002-5.
- [131] A. Halperin. “Polymer brushes that resist adsorption of model proteins: Design parameters”. In: *Langmuir* 15.7 (Mar. 1999), pp. 2525–2533. DOI: 10.1021/la981356f.
- [132] S. P. C. Alves, J. P. Pinheiro, J. P. S. Farinha, and F. A. M. Leermakers. “Particles decorated by an ionizable thermoresponsive polymer brush in water: Experiments and self-consistent field modeling”. In: *Journal of Physical Chemistry B* 118.11 (2014), pp. 3192–3206. DOI: 10.1021/jp408390t.
- [133] J. Penfold and R. K. Thomas. “The application of the specular reflection of neutrons to the study of surfaces and interfaces”. In: *Journal of Physics: Condensed Matter* 2.6 (1990), pp. 1369–1412. DOI: 10.1088/0953-8984/2/6/001.
- [134] W. M. de Vos, L. L. E. Mears, R. M. Richardson, T. Cosgrove, R. M. Dalgliesh, and S. W. Prescott. “Measuring the structure of thin soft matter films under confinement: A surface-force type apparatus for neutron reflection, based on a flexible membrane approach”. In: *Review of Scientific Instruments* 83.11 (Nov. 2012), p. 113903. DOI: 10.1063/1.4767238.

- [135] Z. Wei and S. W. Prescott. “Scattering approaches to probing surface layers under confinement”. In: *Current Opinion in Colloid and Interface Science* 20.4 (2015), pp. 253–260. DOI: 10.1016/j.cocis.2015.09.001.
- [136] M. Ballauff and O. V. Borisov. “Phase transitions in brushes of homopolymers”. In: *Polymer* 98 (Aug. 2016), pp. 402–408. DOI: 10.1016/j.polymer.2016.05.014.
- [137] S. Micciulla, Y. Gerelli, R. A. Campbell, and E. Schneck. “A versatile method for the distance-dependent structural characterization of interacting soft interfaces by neutron reflectometry”. In: *Langmuir* 34.3 (Jan. 2018), pp. 789–800. DOI: 10.1021/acs.langmuir.7b02971.
- [138] Z. Wei, S. Piantavigna, S. A. Holt, A. Nelson, P. T. Spicer, and S. W. Prescott. “Comparing surfactant structures at “soft” and “hard” hydrophobic materials: Not all interfaces are equivalent”. In: *Langmuir* 34.31 (Aug. 2018), pp. 9141–9152. DOI: 10.1021/acs.langmuir.8b01686.
- [139] J. Lu and R. Thomas. “Problems in the analysis and interpretation of neutron reflection data”. In: *Nuclear Instruments and Methods in Physics Research Section A: Accelerators, Spectrometers, Detectors and Associated Equipment* 354.1 (Jan. 1995), pp. 149–163. DOI: 10.1016/0168-9002(94)01037-4.
- [140] V. F. Sears. “Neutron scattering lengths and cross sections”. In: *Neutron News* 3.3 (Jan. 1992), pp. 26–37. DOI: 10.1080/10448639208218770.
- [141] A. R. J. Nelson and S. W. Prescott. “refnx : neutron and X-ray reflectometry analysis in Python”. In: *Journal of Applied Crystallography* 52.1 (Feb. 2019), pp. 193–200. DOI: 10.1107/S1600576718017296.
- [142] P. Kienzle, J. Krycka, N. Patel, and I. Sahin. *Refl1D*. 2011. URL: <http://reflectometry.org/danse>.
- [143] A. Nelson. “Co-refinement of multiple-contrast neutron/X-ray reflectivity data using MOTOFIT”. In: *Journal of Applied Crystallography* 39.2 (2006), pp. 273–276. DOI: 10.1107/S0021889806005073.
- [144] A. Hughes and D. Piergies. *RasCAL*. 2014. URL: <https://sourceforge.net/projects/rscl/>.
- [145] T. P. Russell. “X-ray and neutron reflectivity for the investigation of polymers.” In: *Materials Science Reports* 5.4 (Jan. 1990), pp. 171–271. DOI: 10.1016/S0920-2307(05)80002-7.

- [146] J. B. Hayter, R. R. Highfield, B. J. Pullman, R. K. Thomas, A. I. McMullen, and J. Penfold. “Critical reflection of neutrons. A new technique for investigating interfacial phenomena”. In: *Journal of the Chemical Society, Faraday Transactions 1: Physical Chemistry in Condensed Phases* 77.6 (1981), p. 1437. DOI: 10.1039/f19817701437.
- [147] M. Lovell and R. Richardson. “Analysis methods in neutron and X-ray reflectometry”. In: *Current Opinion in Colloid & Interface Science* 4.3 (June 1999), pp. 197–204. DOI: 10.1016/S1359-0294(99)00039-4.
- [148] V.-O. de Haan and G. Drikkoningen. “Genetic algorithms used in model finding and fitting for neutron reflection experiments”. In: *Physica B: Condensed Matter* 198.1-3 (Apr. 1994), pp. 24–26. DOI: 10.1016/0921-4526(94)90118-X.
- [149] E. Politsch and G. Cevc. “Unbiased analysis of neutron and X-ray reflectivity data by an evolution strategy”. In: *Journal of Applied Crystallography* 35.3 (2002), pp. 347–355. DOI: 10.1107/S0021889802004351.
- [150] D. S. Sivia, W. Hamilton, and G. S. Smith. “Analysis of neutron reflectivity data: maximum entropy, Bayesian spectral analysis and speckle holography”. In: *Physica B: Physics of Condensed Matter* 173.1-2 (1991), pp. 121–138. DOI: 10.1016/0921-4526(91)90042-D.
- [151] M. Wormington, C. Panaccione, K. M. Matney, and D. K. Bowen. “Characterization of structures from X-ray scattering data using genetic algorithms”. In: *Philosophical Transactions of the Royal Society A: Mathematical, Physical and Engineering Sciences* 357.1761 (1999), pp. 2827–2848. DOI: 10.1098/rsta.1999.0469.
- [152] D. S. Sivia and J. Webster. “The Bayesian approach to reflectivity data”. In: *Physica B: Condensed Matter* 248.1-4 (June 1998), pp. 327–337. DOI: 10.1016/S0921-4526(98)00259-2.
- [153] S. C. DeCaluwe, P. A. Kienzle, P. Bhargava, A. M. Baker, and J. A. Dura. “Phase segregation of sulfonate groups in Nafion interface lamellae, quantified via neutron reflectometry fitting techniques for multi-layered structures”. In: *Soft Matter* 10.31 (2014), pp. 5763–5776. DOI: 10.1039/C4SM00850B.
- [154] J. S. Pedersen and I. W. Hamley. “Analysis of neutron and X-ray reflectivity data. II. Constrained least-squares methods”. In: *Journal of Applied Crystallography* 27 (1994), pp. 36–49.



- [155] A. R. McCluskey, J. Grant, A. J. Smith, J. L. Rawle, D. J. Barlow, M. J. Lawrence, S. C. Parker, and K. J. Edler. “Assessing molecular simulation for the analysis of lipid monolayer reflectometry”. In: *Journal of Physics Communications* 3.7 (July 2019), p. 075001. DOI: 10.1088/2399-6528/ab12a9.
- [156] S. Shenoy, P. Shekhar, F. Heinrich, M.-C. Daou, A. Gericke, A. H. Ross, and M. Lösche. “Membrane association of the PTEN tumor suppressor: Molecular details of the protein-membrane complex from SPR binding studies and neutron reflection”. In: *PLoS ONE* 7.4 (Apr. 2012). Ed. by M. J. Buehler, e32591. DOI: 10.1371/journal.pone.0032591.
- [157] D. W. Hogg, J. Bovy, and D. Lang. *Data analysis recipes: Fitting a model to data*. Aug. 2010. URL: <http://arxiv.org/abs/1008.4686>.
- [158] O. S. Heavens. *Optical properties of thin solid films*. London: Butterworth., 1955.
- [159] M. Geoghegan, L. Ruiz-Pérez, C. C. Dang, A. J. Parnell, S. J. Martin, J. R. Howse, R. A. L. Jones, R. Golestanian, P. D. Topham, C. J. Crook, A. J. Ryan, D. S. Sivia, J. R. P. Webster, and A. Menelle. “The pH-induced swelling and collapse of a polybase brush synthesized by atom transfer radical polymerization”. In: *Soft Matter* 2.12 (2006), pp. 1076–1080. DOI: 10.1039/B611847J.
- [160] J. B. Field, C. Toprakcioglu, R. C. Ball, H. B. Stanley, L. Dai, W. Barford, J. Penfold, G. Smith, and W. Hamilton. “Determination of end-adsorbed polymer density profiles by neutron reflectometry”. In: *Macromolecules* 25.1 (Jan. 1992), pp. 434–439. DOI: 10.1021/ma00027a067.
- [161] M. Moglianetti, J. R. Webster, S. Edmondson, S. P. Armes, and S. Titmuss. “Neutron reflectivity study of the structure of pH-responsive polymer brushes grown from a macroinitiator at the sapphire-water interface”. In: *Langmuir* 26.15 (2010), pp. 12684–12689. DOI: 10.1021/la101550w.
- [162] L. Xie, Y. Wang, Y. Wang, X. Li, Q. Tian, D. Liu, G. Sun, and X. Wang. “Study of poly(acrylamidoxime) brushes conformation with uranium adsorption by neutron reflectivity”. In: *Materials Letters* 220 (June 2018), pp. 47–49. DOI: 10.1016/j.matlet.2018.02.102.
- [163] E. Currie, M. Wagemaker, M. Stuart, and A. van Well. “Structure of grafted polymers, investigated with neutron reflectometry”. In: *Physica B: Condensed Matter* 283.1-3 (June 2000), pp. 17–21. DOI: 10.1016/S0921-4526(99)01883-9.

- [164] J. B. Field, C. Toprakcioglu, L. Dai, G. Hadziioannou, G. Smith, and W. Hamilton. “Neutron reflectivity study of end-adsorbed diblock copolymers : cross-over from mushrooms to brushes”. In: *Journal de Physique II* 2.12 (Dec. 1992), pp. 2221–2235. DOI: 10.1051/jp2:1992262.
- [165] P. de Gennes. “Conformations of polymers attached to an interface”. In: *Macromolecules* 13.5 (1980), pp. 1069–1075. DOI: 10.1021/ma60077a009.
- [166] E. Politsch, G. Cevc, A. Wurlitzer, and M. Lösche. “Conformation of polymer brushes at aqueous surfaces determined with X-ray and neutron reflectometry. 1. Novel data evaluation procedure for polymers at interfaces”. In: *Macromolecules* 34.5 (Feb. 2001), pp. 1328–1333. DOI: 10.1021/ma000931v.
- [167] E. Politsch. “String fit: A new structurally oriented X-ray and neutron reflectivity evaluation technique”. In: *Journal of Applied Crystallography* 34.3 (2001), pp. 239–251. DOI: 10.1107/S0021889801001832.
- [168] W. M. de Vos, P. M. Biesheuvel, A. de Keizer, J. M. Kleijn, and M. A. Cohen Stuart. “Adsorption of anionic surfactants in a nonionic polymer brush: experiments, comparison with mean-field theory, and implications for brush-particle interaction”. In: *Langmuir* 25.16 (Aug. 2009), pp. 9252–9261. DOI: 10.1021/la900791b.
- [169] M. Reinhardt, J. Dzubiella, M. Trapp, P. Gutfreund, M. Kreuzer, A. H. Gröschel, A. H. Müller, M. Ballauff, and R. Steitz. “Fine-tuning the structure of stimuli-responsive polymer films by hydrostatic pressure and temperature”. In: *Macromolecules* 46.16 (2013), pp. 6541–6547. DOI: 10.1021/ma400962p.
- [170] S. Christau, T. Möller, F. Brose, J. Genzer, O. Soltwedel, and R. von Klitzing. “Effect of gold nanoparticle hydrophobicity on thermally induced color change of PNIPAM brush/gold nanoparticle hybrids”. In: *Polymer* 98 (Aug. 2016), pp. 454–463. DOI: 10.1016/j.polymer.2016.03.088.
- [171] X.-L. Zhou and S.-H. Chen. “Model-independent method for reconstruction of scattering-length-density profiles using neutron or x-ray reflectivity data”. In: *Physical Review E* 47.5 (May 1993), pp. 3174–3190. DOI: 10.1103/PhysRevE.47.3174.
- [172] C.-H. Chou, M. J. Regan, P. S. Pershan, and X.-L. Zhou. “Model-independent reconstruction of smooth electron density profiles from reflectivity data of liquid surfaces”. In: *Physical Review E* 55.6 (June 1997), pp. 7212–7216. DOI: 10.1103/PhysRevE.55.7212.

- [173] C.-H. Chou. “A necessary modification for groove tracking method”. In: *Physica B: Condensed Matter* 233.2-3 (May 1997), pp. 130–133. DOI: 10.1016/S0921-4526(96)01034-4.
- [174] J. S. Pedersen. “Model-independent determination of the surface scattering-length-density profile from specular reflectivity data”. In: *Journal of Applied Crystallography* 25.pt 2 (1992), pp. 129–145. DOI: 10.1107/S0021889891010907.
- [175] T. J. Murdoch, B. A. Humphreys, E. C. Johnson, S. W. Prescott, A. Nelson, E. J. Wanless, and G. B. Webber. “The role of copolymer composition on the specific ion and thermo-response of ethylene glycol-based brushes”. In: *Polymer* 138 (Feb. 2018), pp. 229–241. DOI: 10.1016/j.polymer.2018.01.053.
- [176] C. H. Chou. “Improved smoothing procedures for a smoothed groove tracking method”. In: *Physica B: Condensed Matter* 253.3-4 (1998), pp. 320–324. DOI: 10.1016/S0921-4526(98)00159-8.
- [177] C. F. Laub and T. L. Kuhl. “Fitting a free-form scattering length density profile to reflectivity data using temperature-proportional quenching”. In: *Journal of Chemical Physics* 125.24 (2006), pp. 1–8. DOI: 10.1063/1.2403126.
- [178] G. Sudre, D. Hourdet, C. Creton, F. Cousin, and Y. Tran. “pH-responsive swelling of poly(acrylic acid) brushes synthesized by the grafting onto route”. In: *Macromolecular Chemistry and Physics* 214.24 (Dec. 2013), pp. 2882–2890. DOI: 10.1002/macp.201300477.
- [179] G. Romet-Lemonne, J. Daillant, P. Guenoun, J. Yang, and J. W. Mays. “Thickness and density profiles of polyelectrolyte brushes: Dependence on grafting density and salt concentration”. In: *Physical Review Letters* 93.14 (Sept. 2004), p. 148301. DOI: 10.1103/PhysRevLett.93.148301.
- [180] M. Sambridge. “A parallel tempering algorithm for probabilistic sampling and multimodal optimization”. In: *Geophysical Journal International* 196.1 (2013), pp. 357–374. DOI: 10.1093/gji/ggt342.
- [181] A. D. Dane, A. Veldhuis, D. K. De Boer, A. J. Leenaers, and L. M. Buydens. “Application of genetic algorithms for characterization of thin layered materials by glancing incidence X-ray reflectometry”. In: *Physica B: Condensed Matter* 253.3-4 (1998), pp. 254–268. DOI: 10.1016/S0921-4526(98)00398-6.
- [182] P. R. Bevington and D. K. Robinson. *Data Reduction and Error Analysis for the Physical Sciences*. New York: McGraw-Hill, 1992.

- [183] D. W. Hogg and D. Foreman-Mackey. “Data analysis recipes: using markov chain monte carlo”. In: *The Astrophysical Journal Supplement Series* 236.1 (May 2018), p. 11. DOI: 10.3847/1538-4365/aab76e.
- [184] D. Foreman-Mackey, D. W. Hogg, D. Lang, and J. Goodman. “emcee : The MCMC Hammer”. In: *Publications of the Astronomical Society of the Pacific* 125.925 (Mar. 2013), pp. 306–312. DOI: 10.1086/670067.
- [185] S. Gupta, L. Hainsworth, J. Hogg, R. Lee, and J. Faeder. “Evaluation of Parallel Tempering to Accelerate Bayesian Parameter Estimation in Systems Biology”. In: *Proceedings - 26th Euromicro International Conference on Parallel, Distributed, and Network-Based Processing, PDP 2018* (2018), pp. 690–697. DOI: 10.1109/PDP2018.2018.00114.
- [186] W. D. Vousden, W. M. Farr, and I. Mandel. “Dynamic temperature selection for parallel tempering in Markov chain Monte Carlo simulations”. In: *Monthly Notices of the Royal Astronomical Society* 455.2 (Jan. 2016), pp. 1919–1937. DOI: 10.1093/mnras/stv2422.
- [187] D. J. Earl and M. W. Deem. “Parallel tempering: Theory, applications, and new perspectives”. In: *Physical Chemistry Chemical Physics* 7.23 (2005), p. 3910. DOI: 10.1039/b509983h.
- [188] J. Skilling. “Nested sampling for general Bayesian computation”. In: *Bayesian Analysis* 1.4 (Dec. 2006), pp. 833–859. DOI: 10.1214/06-BA127.
- [189] F. N. Fritsch and R. E. Carlson. “Monotone piecewise cubic interpolation”. In: *SIAM Journal on Numerical Analysis* 17.2 (Apr. 1980), pp. 238–246. DOI: 10.1137/0717021.
- [190] J. A. Henderson, R. W. Richards, J. Penfold, and R. K. Thomas. “Neutron reflectometry using the kinematic approximation and surface quasi-elastic light scattering from spread films of poly(methyl methacrylate)”. In: *Macromolecules* 26.1 (Jan. 1993), pp. 65–75. DOI: 10.1021/ma00053a010.
- [191] C. F. Majkrzak, N. F. Berk, and U. A. Perez-Salas. “Phase-sensitive neutron reflectometry”. In: *Langmuir* 19.19 (2003), pp. 7796–7810. DOI: 10.1021/la0341254.
- [192] B. Kirby, P. Kienzle, B. Maranville, N. Berk, J. Krycka, F. Heinrich, and C. Majkrzak. “Phase-sensitive specular neutron reflectometry for imaging the nanometer scale composition depth profile of thin-film materials”. In: *Current Opinion in Colloid & Interface Science* 17.1 (Feb. 2012), pp. 44–53. DOI: 10.1016/j.cocis.2011.11.001.

- [193] A. Karim, S. K. Satija, J. F. Douglas, J. F. Ankner, and L. J. Fetters. “Neutron reflectivity study of the density profile of a model end-grafted polymer brush: influence of solvent quality”. In: *Physical Review Letters* 73.25 (Dec. 1994), pp. 3407–3410. DOI: 10.1103/PhysRevLett.73.3407.
- [194] A. R. J. Nelson and C. D. Dewhurst. “Towards a detailed resolution smearing kernel for time-of-flight neutron reflectometers”. In: *Journal of Applied Crystallography* 46.5 (2013), pp. 1338–1346. DOI: 10.1107/S0021889813021936.
- [195] J. S. Speagle. “dynesty: a dynamic nested sampling package for estimating Bayesian posteriors and evidences”. In: *Monthly Notices of the Royal Astronomical Society* 493.3 (Apr. 2020), pp. 3132–3158. DOI: 10.1093/mnras/staa278.
- [196] R. Storn and K. Price. “Differential evolution — a simple and efficient heuristic for global optimization over continuous spaces”. In: *Journal of Global Optimization* 11.4 (Dec. 1997), pp. 341–359. DOI: 10.1023/A:1008202821328.
- [197] J. Goodman and J. Weare. “Ensemble samplers with affine invariance”. In: *Comm. App. Math. and Comp. Sci* 5.1 (Jan. 2010), pp. 65–80. DOI: 10.2140/camcos.2010.5.65.
- [198] V. A. Baulin, E. B. Zhulina, and A. Halperin. “Self-consistent field theory of brushes of neutral water-soluble polymers”. In: *The Journal of Chemical Physics* 119.ii (Nov. 2003), pp. 10977–10988. DOI: 10.1063/1.1619934.
- [199] G. D. Jay and K. A. Waller. “The biology of Lubricin: Near frictionless joint motion”. In: *Matrix Biology* 39 (Oct. 2014), pp. 17–24. DOI: 10.1016/J.MATBIO.2014.08.008.
- [200] B. Zappone, M. Ruths, G. W. Greene, G. D. Jay, and J. N. Israelachvili. “Adsorption, lubrication, and wear of lubricin on model surfaces: Polymer brush-like behavior of a glycoprotein”. In: *Biophysical Journal* 92.5 (2007), pp. 1693–1708. DOI: 10.1529/biophysj.106.088799.
- [201] M. E. Baratz, F. H. Fu, and R. Mengato. “Meniscal tears: The effect of meniscectomy and of repair on intraarticular contact areas and stress in the human knee. A preliminary report”. In: *American Journal of Sports Medicine* 14.4 (1986), pp. 270–275. DOI: 10.1177/036354658601400405.
- [202] Y. Guo, X. Zhang, and W. Chen. “Three-dimensional finite element simulation of total knee joint in gait cycle”. In: *Acta Mechanica Solida Sinica* 22.4 (2009), pp. 347–351. DOI: 10.1016/S0894-9166(09)60283-4.

- [203] C. Majkrzak, N. Berk, S. Krueger, J. Dura, M. Tarek, D. Tobias, V. Silin, C. Meuse, J. Woodward, and A. Plant. “First-principles determination of hybrid bilayer membrane structure by phase-sensitive neutron reflectometry”. In: *Biophysical Journal* 79.6 (Dec. 2000), pp. 3330–3340. DOI: 10.1016/S0006-3495(00)76564-7.
- [204] W. A. Hamilton, G. S. Smith, N. A. Alcantar, J. Majewski, R. G. Toomey, and T. L. Kuhl. “Determining the density profile of confined polymer brushes with neutron reflectivity”. In: *Journal of Polymer Science, Part B: Polymer Physics* 42.17 (2004), pp. 3290–3301. DOI: 10.1002/polb.20170.
- [205] B. Derjaguin. “Untersuchungen über die reibung und adhäsion, IV”. In: *Kolloid-Zeitschrift* 69.2 (Nov. 1934), pp. 155–164. DOI: 10.1007/BF01433225.
- [206] W. M. de Vos, F. A. M. Leermakers, A. De Keizer, J. Mieke Kleijn, and M. A. Cohen Stuart. “Interaction of particles with a polydisperse brush: A self-consistent-field analysis”. In: *Macromolecules* 42.15 (Aug. 2009), pp. 5881–5891. DOI: 10.1021/ma900819b.
- [207] J. M. H. M. Scheutjens and G. J. Fleer. “Statistical theory of the adsorption of interacting chain molecules. 1. Partition function, segment density distribution, and adsorption isotherms”. In: *The Journal of Physical Chemistry* 83.12 (June 1979), pp. 1619–1635. DOI: 10.1021/j100475a012.
- [208] A. Halperin and E. B. Zhulina. “Atomic force microscopy of polymer brushes: colloidal versus sharp tips”. In: *Langmuir* 26.11 (2010), pp. 8933–8940. DOI: 10.1021/la9047374.
- [209] K. Van Durme, H. Rahier, and B. Van Mele. “Influence of additives on the thermoresponsive behavior of polymers in aqueous solution”. In: *Macromolecules* 38.24 (Nov. 2005), pp. 10155–10163. DOI: 10.1021/ma051816t.
- [210] S. Varma, L. Bureau, and D. Débarre. “The conformation of thermoresponsive polymer brushes probed by optical reflectivity”. In: *Langmuir* 32.13 (2016), pp. 3152–3163. DOI: 10.1021/acs.langmuir.6b00138.
- [211] R. M. Espinosa-Marzal, R. M. Bielecki, and N. D. Spencer. “Understanding the role of viscous solvent confinement in the tribological behavior of polymer brushes: A bioinspired approach”. In: *Soft Matter* 9.44 (2013), pp. 10572–10585. DOI: 10.1039/c3sm51415c.

- [212] M. Ramezani, M. J. Legg, A. Haghighat, Z. Li, R. D. Vigil, and M. G. Olsen. “Experimental investigation of the effect of ethyl alcohol surfactant on oxygen mass transfer and bubble size distribution in an air-water multiphase Taylor-Couette vortex bioreactor”. In: *Chemical Engineering Journal* 319 (2017), pp. 288–296. DOI: <https://doi.org/10.1016/j.cej.2017.03.005>.
- [213] A. S. Malcolm, A. F. Dexter, and A. P. J. Middelberg. “Peptide surfactants (Peptactants) for switchable foams and emulsions”. In: *Asia-Pacific Journal of Chemical Engineering* 2.5 (Sept. 2007), pp. 362–367. DOI: [10.1002/apj.66](https://doi.org/10.1002/apj.66).
- [214] F. Tu and D. Lee. “Shape-changing and amphiphilicity-reversing janus particles with ph-responsive surfactant properties”. In: *Journal of the American Chemical Society* 136.28 (July 2014), pp. 9999–10006. DOI: [10.1021/ja503189r](https://doi.org/10.1021/ja503189r).
- [215] M. Almgren, J. C. Gimel, K. Wang, G. Karlsson, K. Edwards, W. Brown, and K. Mortensen. “SDS micelles at high ionic strength. A light scattering, neutron scattering, fluorescence quenching, and cryoTEM investigation”. In: *Journal of Colloid and Interface Science* 202.2 (1998), pp. 222–231. DOI: [10.1006/jcis.1998.5503](https://doi.org/10.1006/jcis.1998.5503).
- [216] S. Hayashi and S. Ikeda. “Micelle size and shape of sodium dodecyl sulfate in concentrated NaCl solutions”. In: *Journal of Physical Chemistry* 84.7 (1980), pp. 744–751. DOI: [10.1021/j100444a011](https://doi.org/10.1021/j100444a011).
- [217] D. Myers. *Surfactant science and technology*. Wiley, July 2020. DOI: [10.1002/9781119465829](https://doi.org/10.1002/9781119465829).
- [218] K. Minewaki, T. Kato, H. Yoshida, M. Imai, and K. Ito. “Small-angle X-ray scattering from the lamellar phase formed in a nonionic surfactant (C16E7)-water system. Analysis of peak position and line shape”. In: *Langmuir* 17.6 (Mar. 2001), pp. 1864–1871. DOI: [10.1021/la000791i](https://doi.org/10.1021/la000791i).
- [219] Y. Barenholz. *Liposome application: Problems and prospects*. Vol. 6. 1. Elsevier, Feb. 2001, pp. 66–77. DOI: [10.1016/S1359-0294\(00\)00090-X](https://doi.org/10.1016/S1359-0294(00)00090-X).
- [220] H. Wang, P. B. Zetterlund, C. Boyer, and P. T. Spicer. “Polymerization of cubosome and hexosome templates to produce complex microparticle shapes”. In: *Journal of Colloid and Interface Science* 546 (June 2019), pp. 240–250. DOI: [10.1016/j.jcis.2019.03.069](https://doi.org/10.1016/j.jcis.2019.03.069).
- [221] S. Shah, N. Jamroz, and Q. Sharif. “Micellization parameters and electrostatic interactions in micellar solution of sodium dodecyl sulfate (SDS) at different temperatures”. In: *Colloids and Surfaces A: Physicochemical and Engineering Aspects* 178.1-3 (Mar. 2001), pp. 199–206. DOI: [10.1016/S0927-7757\(00\)00697-X](https://doi.org/10.1016/S0927-7757(00)00697-X).

- [222] S. K. Hait, P. R. Majhi, A. Blume, and S. P. Moulik. “A critical assessment of micellization of sodium dodecyl benzene sulfonate (SDBS) and its interaction with poly(vinyl pyrrolidone) and hydrophobically modified polymers, JR 400 and LM 200”. In: *Journal of Physical Chemistry B* 107.15 (2003), pp. 3650–3658. DOI: 10.1021/jp027379r.
- [223] S. K. Shah, S. K. Chatterjee, and A. Bhattacharai. “The effect of methanol on the micellar properties of dodecyltrimethylammonium bromide (DTAB) in aqueous medium at different temperatures”. In: *Journal of Surfactants and Detergents* 19.1 (Jan. 2016), pp. 201–207. DOI: 10.1007/s11743-015-1755-x.
- [224] J. J. Galán, A. González-Pérez, J. L. D. Cactillo, and J. R. Rodríguez. “Thermal parameters associated to micellization of dodecylpyridinium bromide and chloride in aqueous solution”. In: *Journal of Thermal Analysis and Calorimetry* 70.1 (2002), pp. 229–234.
- [225] B. Cabane and R. Duplessix. “Organization of surfactant micelles adsorbed on a polymer molecule in water : a neutron scattering study”. In: *Journal de Physique* 43.10 (1982), pp. 1529–1542. DOI: 10.1051/jphys:0198200430100152900.
- [226] E. Dutkiewicz and A. Jakubowska. “Effect of electrolytes on the physicochemical behaviour of sodium dodecyl sulphate micelles”. In: *Colloid and Polymer Science* 280.11 (2002), pp. 1009–1014. DOI: 10.1007/s00396-002-0723-y.
- [227] J. Ž. Manojlović. “The Krafft temperature of surfactant solutions”. In: *Thermal Science* 16.SUPPL.2 (2013), pp. 631–640. DOI: 10.2298/TSCI120427197M.
- [228] C. Vautier-Giongo and B. L. Bales. “Estimate of the Ionization Degree of Ionic Micelles Based on Krafft Temperature Measurements”. In: *The Journal of Physical Chemistry B* 107.23 (June 2003), pp. 5398–5403. DOI: 10.1021/jp0270957.
- [229] B. L. Bales. “A definition of the degree of ionization of a micelle based on its aggregation number”. In: *Journal of Physical Chemistry B* 105.29 (July 2001), pp. 6798–6804. DOI: 10.1021/jp004576m.
- [230] A. Cifuentes, J. L. Bernal, and J. C. Diez-Masa. “Determination of Critical Micelle Concentration Values Using Capillary Electrophoresis Instrumentation”. In: *Analytical Chemistry* 69.20 (1997), pp. 4271–4274. DOI: 10.1021/ac970696n.
- [231] S. A. Markarian, L. R. Harutyunyan, and R. S. Harutyunyan. “The properties of mixtures of sodium dodecylsulfate and diethylsulfoxide in Water”. In: *Journal of Solution Chemistry* 34.3 (Mar. 2005), pp. 361–368. DOI: 10.1007/s10953-005-3056-x.



- [232] E. Fegyver and R. Mészáros. “The impact of nonionic surfactant additives on the nonequilibrium association between oppositely charged polyelectrolytes and ionic surfactants”. In: *Soft Matter* 10.12 (2014), p. 1953. DOI: 10.1039/c3sm52889h.
- [233] B. Naskar, A. Dey, and S. P. Moulik. “Counter-ion effect on micellization of ionic surfactants: a comprehensive understanding with two representatives, sodium dodecyl sulfate (SDS) and dodecyltrimethylammonium bromide (DTAB)”. In: *Journal of Surfactants and Detergents* 16.5 (Sept. 2013), pp. 785–794. DOI: 10.1007/s11743-013-1449-1.
- [234] J. P. Marcolongo and M. Mirenda. “Thermodynamics of sodium dodecyl sulfate (SDS) micellization: An undergraduate laboratory experiment”. In: *Journal of Chemical Education* 88.5 (May 2011), pp. 629–633. DOI: 10.1021/ed900019u.
- [235] S. Chauhan and K. Sharma. “Effect of temperature and additives on the critical micelle concentration and thermodynamics of micelle formation of sodium dodecyl benzene sulfonate and dodecyltrimethylammonium bromide in aqueous solution: A conductometric study”. In: *Journal of Chemical Thermodynamics* 71 (2014), pp. 205–211. DOI: 10.1016/j.jct.2013.12.019.
- [236] A. M. Tedeschi, L. Franco, M. Ruzzi, L. Paduano, C. Corvaja, and G. D’Errico. “Micellar aggregation of alkyltrimethylammonium bromide surfactants studied by electron paramagnetic resonance of an anionic nitroxide”. In: *Physical Chemistry Chemical Physics* 5.19 (2003), pp. 4204–4209. DOI: 10.1039/b305324p.
- [237] J. Mata, D. Varade, and P. Bahadur. “Aggregation behavior of quaternary salt based cationic surfactants”. In: *Thermochimica Acta* 428.1-2 (Apr. 2005), pp. 147–155. DOI: 10.1016/j.tca.2004.11.009.
- [238] L.-J. Chen, S.-Y. Lin, C.-C. Huang, and E.-M. Chen. “Temperature dependence of critical micelle concentration of polyoxyethylenated non-ionic surfactants”. In: *Colloids and Surfaces A: Physicochemical and Engineering Aspects* 135.1-3 (Apr. 1998), pp. 175–181. DOI: 10.1016/S0927-7757(97)00238-0.
- [239] E. Kokufuta, Y. Q. Zhang, T. Tanaka, and A. Mamada. “Effects of surfactants on the phase transition of poly(*N*-isopropylacrylamide) gel”. In: *Macromolecules* 26.5 (Sept. 1993), pp. 1053–1059. DOI: 10.1021/ma00057a027.
- [240] H. G. Schild and D. A. Tirrell. “Interaction of poly(*N*-isopropylacrylamide) with sodium *n*-alkyl sulfates in aqueous solution”. In: *Langmuir* 7.4 (Apr. 1991), pp. 665–671. DOI: 10.1021/la00052a013.

- [241] T. Patel, G. Ghosh, S.-i. i. Yusa, and P. Bahadur. “Solution behavior of poly(*N*-isopropylacrylamide) in water: Effect of additives”. In: *Journal of Dispersion Science and Technology* 32.8 (Aug. 2011), pp. 1111–1118. DOI: 10.1080/01932691.2010.497701.
- [242] M. S. Lee and J.-c. C. Kim. “Effects of surfactants on phase transition of poly(*N*-isopropylacrylamide) and poly(*N*-isopropylacrylamide-co-dimethylaminoethylmethacrylate)”. In: *Journal of Dispersion Science and Technology* 33.2 (Feb. 2012), pp. 272–277. DOI: 10.1080/01932691.2011.561181.
- [243] B. Jean and L. T. Lee. “Noninteracting versus interacting poly(*N*-isopropylacrylamide)-surfactant mixtures at the air-water interface”. In: *Journal of Physical Chemistry B* 109.11 (2005), pp. 5162–5167. DOI: 10.1021/jp0454265.
- [244] C. Wu and S. Zhou. “Effects of surfactants on the phase transition of poly(*N*-isopropylacrylamide) in water”. In: *Journal of Polymer Science Part B: Polymer Physics* 34.9 (July 1996), pp. 1597–1604. DOI: 10.1002/(SICI)1099-0488(19960715)34:9<1597::AID-POLB8>3.0.CO;2-I.
- [245] R. D. Groot. “Mesoscopic simulation of polymer-surfactant aggregation”. In: *Langmuir* 16.19 (2000), pp. 7493–7502. DOI: 10.1021/la000010d.
- [246] S. J. Mears, Y. Deng, T. Cosgrove, and R. Pelton. “Structure of sodium dodecyl sulfate bound to a poly(NIPAM) microgel particle”. In: *Langmuir* 13.7 (Apr. 1997), pp. 1901–1906. DOI: 10.1021/la960515x.
- [247] L.-T. Lee and B. Cabane. “Effects of surfactants on thermally collapsed poly(*N*-isopropylacrylamide) macromolecules”. In: *Macromolecules* 30.97 (1997), pp. 6559–6566. DOI: 10.1021/ma9704469.
- [248] R. Walter, J. Rička, C. Quellet, R. Nyffenegger, and T. Binkert. “Coil-globule transition of poly(*N*-isopropylacrylamide): A study of polymer-surfactant association”. In: *Macromolecules* 29.11 (Jan. 1996), pp. 4019–4028. DOI: 10.1021/ma951529x.
- [249] Y. Mylonas, G. Staikos, and P. Lianos. “Investigation of the poly(*N*-isopropylacrylamide)-sodium dodecyl sulfate complexation with viscosity, dialysis, and time-resolved fluorescence-quenching measurements”. In: *Langmuir* 15.21 (Oct. 1999), pp. 7172–7175. DOI: 10.1021/la990155o.
- [250] C. K. Chee, S. Rimmer, I. Soutar, and L. Swanson. “Time-resolved fluorescence anisotropy studies of the interaction of *N*-isopropyl acrylamide based polymers with sodium dodecyl sulphate”. In: *Soft Matter* 7.10 (2011), pp. 4705–4714. DOI: 10.1039/c1sm05436h.

- [251] J. Chen, X. Gong, H. Yang, Y. Yao, M. Xu, Q. Chen, and R. Cheng. “NMR study on the effects of sodium n-dodecyl sulfate on the coil-to-globule transition of poly(*N*-isopropylacrylamide) in aqueous solutions”. In: *Macromolecules* 44.15 (Aug. 2011), pp. 6227–6231. DOI: 10.1021/ma201269u.
- [252] J. Chen, H. Xue, Y. Yao, H. Yang, A. Li, M. Xu, Q. Chen, and R. Cheng. “Effect of surfactant concentration on the complex structure of poly(*N*-isopropylacrylamide)/sodium n-dodecyl sulfate in aqueous solutions”. In: *Macromolecules* 45.13 (July 2012), pp. 5524–5529. DOI: 10.1021/ma301003r.
- [253] K. Shirahama, K. Tsujii, and T. Takagi. “Free-boundary electrophoresis of sodium dodecyl sulfate–protein polypeptide complexes with special reference to SDS–polyacrylamide gel electrophoresis”. In: *The Journal of Biochemistry* 75.2 (Feb. 1974), pp. 309–319. DOI: 10.1093/oxfordjournals.jbchem.a130398.
- [254] J. Chen, J. Spěváček, and L. Hanyková. “NMR methods to study effects of additives on phase separation of thermoresponsive polymer”. In: *Macromolecular Symposia* 339.1 (2014), pp. 24–32. DOI: 10.1002/masy.201300130.
- [255] E. Ruckenstein, G. Huber, and H. Hoffmann. “Surfactant aggregation in the presence of polymers”. In: *Langmuir* 3.3 (1987), pp. 382–387. DOI: 10.1021/la00075a019.
- [256] B. Z. Shang, Z. Wang, and R. G. Larson. “Effect of headgroup size, charge, and solvent structure on polymer-micelle interactions, studied by molecular dynamics simulations”. In: *Journal of Physical Chemistry B* 113.46 (2009), pp. 15170–15180. DOI: 10.1021/jp9057737.
- [257] B. Z. Shang, Z. Wang, and R. G. Larson. “Molecular dynamics simulation of interactions between a sodium dodecyl sulfate micelle and a poly(ethylene oxide) polymer”. In: *Journal of Physical Chemistry B* 112.10 (2008), pp. 2888–2900. DOI: 10.1021/jp0773841.
- [258] H. Iyota and R. Krastev. “Miscibility of sodium chloride and sodium dodecyl sulfate in the adsorbed film and aggregate”. In: *Colloid and Polymer Science* 287.4 (2009), pp. 425–433. DOI: 10.1007/s00396-008-1981-0.
- [259] J. Dijt, M. Stuart, J. Hofman, and G. Fleer. “Kinetics of polymer adsorption in stagnation point flow”. In: *Colloids and Surfaces* 51.C (Jan. 1990), pp. 141–158. DOI: 10.1016/0166-6622(90)80138-T.
- [260] S. J. Byrnes. *Multilayer optical calculations*. Mar. 2016. URL: <http://arxiv.org/abs/1603.02720>.

- [261] Y. Brasse, M. B. Müller, M. Karg, C. Kuttner, T. A. F. König, and A. Fery. “Magnetic and electric resonances in particle-to-film-coupled functional nanostructures”. In: *ACS Applied Materials & Interfaces* 10.3 (Jan. 2018), pp. 3133–3141. DOI: 10.1021/acsami.7b16941.
- [262] G. M. Hale and M. R. Querry. “Optical constants of water in the 200 nm to 200  $\mu$ m wavelength region”. In: *Applied Optics* 12.3 (Mar. 1973), p. 555. DOI: 10.1364/AO.12.000555.
- [263] E. C. Johnson, J. D. Willott, I. J. Gresham, T. J. Murdoch, B. A. Humphreys, S. W. Prescott, A. Nelson, W. M. de Vos, G. B. Webber, and E. J. Wanless. “Enrichment of charged monomers explains non-monotonic polymer volume fraction profiles of multi-stimulus responsive copolymer brushes”. In: *Langmuir* 36.42 (2020), pp. 12460–12472. DOI: 10.1021/acs.langmuir.0c01502.
- [264] F. Tiberg. “Physical characterization of non-ionic surfactant layers adsorbed at hydrophilic and hydrophobic solid surfaces by time-resolved ellipsometry”. In: *Journal of the Chemical Society - Faraday Transactions* 92.4 (1996), pp. 531–538. DOI: 10.1039/ft9969200531.
- [265] S. B. Velegol, B. D. Fleming, S. Biggs, E. J. Wanless, and R. D. Tilton. “Counterion effects on hexadecyltrimethylammonium surfactant adsorption and self-assembly on silica”. In: *Langmuir* 16.6 (2000), pp. 2548–2556. DOI: 10.1021/la9910935.
- [266] F. Garret-Flaudy and R. Freitag. “Unusual thermoprecipitation behavior of poly(*N,N*-diethylacrylamide) from aqueous solution in the presence of anionic surfactants”. In: *Langmuir* 17.16 (2001), pp. 4711–4716. DOI: 10.1021/la0012561.
- [267] H. Wang, H. Zhang, S. Yuan, C. Liu, and Z. Xu. “Molecular dynamics study of the adsorption of anionic surfactant in a nonionic polymer brush”. In: *Journal of Molecular Modeling* 20.6 (2014). DOI: 10.1007/s00894-014-2267-8.
- [268] M. S. Sulatha and U. Natarajan. “Molecular dynamics simulations of adsorption of poly(acrylic acid) and poly(methacrylic acid) on dodecyltrimethylammonium chloride micelle in water: effect of charge density”. In: *Journal of Physical Chemistry B* 119.38 (2015), pp. 12526–12539. DOI: 10.1021/acs.jpcc.5b04680.
- [269] M. C. Costa, S. M. Silva, and F. E. Antunes. “Adjusting the low critical solution temperature of poly(*N*-isopropyl acrylamide) solutions by salts, ionic surfactants and solvents: A rheological study”. In: *Journal of Molecular Liquids* 210 (Oct. 2015), pp. 113–118. DOI: 10.1016/j.molliq.2015.02.008.

- [270] A. Borsos and T. Gil. “Interaction of cetyl-trimethylammonium bromide with swollen and collapsed poly(*N*-isopropylacrylamide ) nanogel particles”. In: (2011), pp. 3461–3467.
- [271] W. Loh, L. A. C. Teixeira, and L.-t. Lee. “Isothermal calorimetric investigation of the interaction of poly(*N*-isopropylacrylamide) and ionic surfactants”. In: *The Journal of Physical Chemistry B* 108.10 (2004), pp. 3196–3201. DOI: 10.1021/jp037190v.
- [272] J. D. Willott, T. J. Murdoch, G. B. Webber, and E. J. Wanless. “Nature of the specific anion response of a hydrophobic weak polyelectrolyte brush revealed by AFM force measurements”. In: *Macromolecules* 49.6 (2016), pp. 2327–2338. DOI: 10.1021/acs.macromol.5b02656.
- [273] M. Raposo, J. M. Lourenço, A. M. Botelho do Rego, A. M. Ferraria, and P. A. Ribeiro. “Counterions — a new approach to control the degree of ionization of polyelectrolytes in layer-by-layer films”. In: *Colloids and Surfaces A: Physicochemical and Engineering Aspects* 412 (2012), pp. 1–10. DOI: 10.1016/j.colsurfa.2012.05.005.
- [274] Y. Masuda, K. Hirabayashi, K. Sakuma, and T. Nakanishi. “Swelling of poly(ethylene oxide) gel in aqueous solutions of sodium dodecyl sulfate with added sodium chloride”. In: *Colloid and Polymer Science* 280.5 (2002), pp. 490–494. DOI: 10.1007/s00396-001-0636-1.
- [275] Y. Zhang, S. Furryk, D. E. Bergbreiter, and P. S. Cremer. “Specific ion effects on the water solubility of macromolecules: PNIPAM and the Hofmeister series”. In: *Journal of the American Chemical Society* 127.41 (2005), pp. 14505–14510. DOI: 10.1021/ja0546424.
- [276] B. A. Humphreys, E. J. Wanless, and G. B. Webber. “Effect of ionic strength and salt identity on poly(*N*-isopropylacrylamide) brush modified colloidal silica particles”. In: *Journal of Colloid and Interface Science* 516 (2018), pp. 153–161. DOI: 10.1016/j.jcis.2018.01.058.
- [277] E. J. Wanless and W. A. Ducker. “Organization of sodium dodecyl sulfate at the graphite-solution interface”. In: *Journal of Physical Chemistry* 100.8 (1996), pp. 3207–3214. DOI: 10.1021/jp952439x.
- [278] M. Biesalski, D. Johannsmann, and J. Rühe. “Electrolyte-induced collapse of a polyelectrolyte brush”. In: *Journal of Chemical Physics* 120.18 (2004), pp. 8807–8814. DOI: 10.1063/1.1690242.

- [279] Y. Mir, P. Auroy, and L. Auvray. “Density profile of polyelectrolyte brushes”. In: *Physical Review Letters* 75.15 (1995), pp. 2863–2866. DOI: 10.1103/PhysRevLett.75.2863.
- [280] N. Wada, Y. Kajima, Y. Yagi, H. Inomata, and S. Saito. “Effect of surfactant on the phase transition of *N*-alkylacrylamide gels”. In: *Langmuir* 9.1 (Jan. 1993), pp. 46–49. DOI: 10.1021/la00025a013.
- [281] Y. Higaki, Y. Inutsuka, T. Sakamaki, Y. Terayama, A. Takenaka, K. Higaki, N. L. Yamada, T. Moriwaki, Y. Ikemoto, and A. Takahara. “Effect of charged group spacer length on hydration state in zwitterionic poly(sulfobetaine) brushes”. In: *Langmuir* 33.34 (2017), pp. 8404–8412. DOI: 10.1021/acs.langmuir.7b01935.
- [282] I. J. Gresham, B. A. Humphreys, J. D. Willott, E. C. Johnson, T. J. Murdoch, G. B. Webber, E. J. Wanless, A. R. J. Nelson, and S. W. Prescott. “Geometrical confinement modulates the thermoresponse of a poly(*N*-isopropylacrylamide) brush”. In: *Macromolecules* 54.5 (Mar. 2021), pp. 2541–2550. DOI: 10.1021/acs.macromol.0c02775.

# Acronyms

**C<sub>n</sub>TAX** trimethyl ammonium surfactants. 145

**MeOH** methanol. 34, 38, 39

**XC<sub>n</sub>S** sulfate-headed surfactants. 143, 145

**ACNS** Australian Centre for Neutron Scattering. 301

**AFM** atomic force microscopy. 110–112, 122, 125, 127–129, 134–136, 138, 181, 202, 211

**ANSTO** the Australian Nuclear Science and Technology Organisation. 20, 301

**APTES** (3-Aminopropyl)triethoxysilane. 13, 14, 31, 32, 34–37, 42, 44, 45, 301

**ARGET** activators regenerated by electron transfer. i, 14, 15, 34, 39, 45, 51

**ATRP** atom transfer radical polymerisation. i, 14, 15, 29–32, 34, 36, 38, 39, 43, 45, 51, 93, 140, 210, 302, 303

**BB** benzoyl bromide. 34, 36–38, 42, 44, 46, 47, 52, 53

**BiBB**  $\alpha$ -bromoisobutyryl bromide. 13–15, 31, 34, 36–38, 42, 44, 46–49, 53, 301

**C<sub>12</sub>E<sub>5</sub>** pentaethyleneglycol monododecyl ether. 159, 160, 169, 170, 173, 175, 176, 216, 223, 224, 230, 295

**C<sub>12</sub>E<sub>6</sub>** hexaethyleneglycol monododecyl ether. 153, 154, 156, 161, 162, 164, 165, 168, 178, 243

**CAC** critical aggregation concentration. 145–147, 167, 168, 201, 203

**CMC** critical micelle concentration. 141–150, 152, 162, 163, 167, 168, 177, 178, 180, 181, 187–189, 195, 201, 203, 206, 212, 303, *Glossary*: CMC<sup>∘</sup> & CMC<sup>eff</sup>

**CST** critical solution temperature. 8–10, 12, 50, 62, 80, 111, 138, 145–149, 151, 161–163, 189, 197, 200, 202–204, 221

- CTAB** cetyl trimethylammonium bromide. 143, 153, 154, 156, 159, 161–165, 167–169, 172, 173, 175, 176, 178, 179, 206, 216, 226, 230, 242, 295
- d-MeOD** deuterated methanol. 34, 38–40, 46–49, 216, 218, 219
- d-C<sub>12</sub>E<sub>5</sub>** deuterated C<sub>12</sub>E<sub>5</sub>. 153, 170, 216
- d-CTAB** deuterated CTAB. 153, 171, 216
- d-SDS** deuterated SDS. 153, 170, 181–185, 198, 207, 208, 216
- DE** differential evolution. 85, 92, 93, 98–101, 107
- DPyC** dodecylpyridinium chloride. 153, 156, 162
- DTAB** dodecyl trimethylammonium bromide. 143, 146, 150, 153, 156, 159, 161–163, 178, 230
- EMA** effective medium approximation. 22, 157, 158, 161, 162
- FAOR** fixed-angle optical reflectometry. 153–156, 161, 166–168, 175, 177–179, 208, 300
- GPC** gel permeation chromatography. 29, 30
- HMTETA** 1,1,4,7,10,10-hexamethyltriethylenetetramine. 13–15, 38, 39
- MCMC** Markov chain Monte Carlo. 78, 85, 92, 93, 97, 98, 103, 106, 107, 193, 227, 228, 234
- MD** molecular dynamics. 7, 30, 149, 179
- NIPAM** *N*-isopropylacrylamide. 13, 15, 21, 38, 39, 46
- NMR** nuclear magnetic resonance. 147–149, 179
- NOSEY** nuclear overhauser effect spectroscopy. 147
- NR** neutron reflectometry. i, 12, 13, 20, 21, 23, 26, 28–30, 38, 39, 42, 45–47, 50–53, 56, 61, 64, 66–68, 70, 72, 74, 76, 78–81, 110–113, 115, 127, 128, 134–136, 138, 140, 142, 158, 159, 161, 163, 169–171, 173, 176–179, 185, 189, 193, 196, 198, 201–203, 206, 208, 210–213, 218, 220–224, 226–229, 233, 234, 250, 251, 302, 303



- nSCFT** numerical self-consistent field theory. 7, 8, 110, 112, 115, 125, 127, 128, 134, 138, 211
- OPAL** Open-pool Australian Lightwater Reactor. 20, 91
- PAA** poly(acrylic acid). 181, 184
- PCHIP** piecewise cubic Hermite interpolating polynomial. 86–88, 108
- PDF** probability density function. 85, 93, 116–122
- PDMAA** poly(*N*-dimethylacrylamide). 59
- PDMAEMA** poly(2-(dimethylamino)ethyl methacrylate). 59–61
- PEO** polyethylene oxide. 146, 150, 179, 181, 200, 206
- PET** poly(ethylene terephthalate). 111, 113, 114, 117–119, 133, 181, 183, 184, 186, 214, 216
- PMDEGA** poly(methoxy diethylene glycol acrylate). 58, 60, 61
- PMMA** poly(methyl methacrylate). 29, 58
- PNIPAM** poly(*N*-isopropylacrylamide). i, 2, 5, 8–12, 14, 16, 17, 20, 21, 25, 26, 31, 38, 39, 41, 45, 50, 52, 53, 56, 57, 60–70, 73–76, 78, 80, 90, 91, 93, 96, 98–100, 103, 105, 108, 110–112, 114, 116, 118, 126–129, 132, 135–138, 140, 142, 143, 145–152, 155, 157–159, 161–166, 168–170, 172, 173, 175, 177–181, 183–189, 191–194, 196–204, 206–208, 210–214, 216, 220–223, 231–234, 249, 260, 301, 304
- PNIPMAM** poly(*N*-isopropylmethacrylamide). 60, 61
- POEGMA** poly(oligoethylene glycol methacrylate). 213
- PSPE** poly(sulfobetaine). 60
- PSPP** poly(*N,N*-dimethyl-*N*-(3-methacrylamidopropyl)-ammonio propane sulfonate). 60, 61
- PSS** poly(sodium styrene sulfonate). 187
- PT-MCMC** parallel-tempered Markov chain Monte Carlo. 79, 85, 90, 92–96, 98–101, 103, 104, 107, 108, 160, 175, 176, 208, 210, 211, 213, 223, 224, 226, 229
- PTFE** polytetrafluoroethylene. 37, 40, 63

**PVP** polyvinylpyrrolidone. 58, 146

**QCM-D** quartz crystal microbalance with dissipation monitoring. 13, 23–25, 52, 56, 63–66, 68–70, 73, 74, 76, 86, 140, 158, 161, 164–166, 169, 177, 178, 193, 194, 196, 198, 201–203, 207, 208, 212, 213, 220, 221, 240–249, 298

**RH** relative humidity. 56–64, 66, 68–70, 73–76, 210, 220

**RI** refractive index. 22, 153–156, 158, 163, 166, 234

**SANS** small-angle neutron scattering. 146, 148

**SDBS** sodium dodecylbenzene sulfonate. 142, 144, 153, 156, 162, 201

**SDS** sodium dodecyl sulphate. 13, 140, 143, 145–154, 156, 157, 159–162, 164–166, 168–170, 172, 173, 175–179, 181–189, 191–194, 196–208, 211, 212, 214, 216, 223, 224, 227–232, 241, 244–249, 295

**SFA** surface force apparatus. 111, 135, 138

**SLD** scattering length density. 19–22, 26, 41, 47, 56, 67, 68, 70, 72, 73, 75, 76, 79, 80, 83, 84, 87, 89–91, 93, 94, 97, 98, 102, 114, 116, 118, 119, 131, 158, 159, 172–175, 182–185, 196–199, 208, 210, 211, 216, 222, 223, 225, 233–239, 260, 301, 302

**SMFS** single-molecule force spectroscopy. 16, 32

**SR** swelling ratio. 57, 59–62, 69–71, 73, 220, *Glossary*: swelling ratio

**TEA** triethylamine. 13, 15, 34, 37

**THF** tetrahydrofuran. 13, 15, 34, 37

**VDS** vapour delivery system. 63

**XRR** X-ray reflectometry. 22, 61, 113, 233, 234

# Symbols

$E$  the extent of  $\phi_{\text{poly}}(z)$ ; the distance from the beginning of the polymer layer (the substrate) to the end ( $\phi_{\text{poly}} = 0$ ). 157, 251, 252

$N$  Number of monomers in a polymer chain. 4, 6, 10, 12, 15, 32

$R_g$  Radius of gyration of a polymer. 3, 4, 12, 16, 17

$T$  Temperature. 10

$T_{\text{samp}}$  Temperature of the polymer layer. 65, 66, 69, 70, 220, 221

$T_{\text{vap}}$  Effective temperature of the vapour above the polymer layer. 66, 70, 220, 221

$\Delta D$  Dissipation. 23, 24, 164–166, 193, 198, 201, 202, 240, 244, 249

$\Delta f$  Frequency of QCM-D sensor. 23, 24, 65, 69, 164–166, 193, 194, 198, 201–203, 240, 244, 249

$\Delta$  The ellipsometric parameter Delta; the phase change of polarised light reflected from a surface. 22, 158, 189, 191

$\Psi$  The ellipsometric parameter Psi; the amplitude ratio of the polarised light reflected from a surface. 22, 157, 189, 191

$\Sigma$  Reduced grafting density. 3, 16

$\chi$  Flory-Huggins polymer-solvent interaction parameter. 3, 7–10, 12, 62, 74, 75, 125–128, 189, 217, 303

$\rho(z)$  volume fraction profile of polymer. 19, 118

$\phi_{\text{poly}}(z)$  volume fraction profile of polymer. 6, 18, 157, 235, 298

$\lambda$  Wavelength. 23

$\phi_{\text{poly}}$  volume fraction of polymer. 6, 8–10, 12, 18, 19, 68, 75, 76, 86, 118, 119, 157, 158, 164, 166, 175, 186, 189, 201, 235, 298, 302

- $\phi_{\text{solv}}$  volume fraction of solvent. 62, 74–76
- $\phi$  volume fraction. 19, 94, 118, 175, 251
- $\rho$  scattering length density. 19, 118, 298
- $\sigma$  Grafting density. 3, 4, 6, 15, 16, 30, 42, 43, 46, 50
- $d$  The thickness of a polymer layer. 6, 20, 42, 46
- $d_{\text{1st}}$  the first moment of the polymer volume fraction profile. 18
- $n$  Number of carbons in a surfactant tail. 143, 145
- $p_{\text{D}_2\text{O}}$  partial pressure of  $\text{D}_2\text{O}$ . 65, 66, 70, 72
- $p_{\text{D}_2\text{O}}^{\text{sat}}$  saturation pressure of  $\text{D}_2\text{O}$  at a given temperature. 58
- $p_{\text{H}_2\text{O}}$  partial pressure of  $\text{H}_2\text{O}$ . 63, 68
- $p_{\text{H}_2\text{O}}^{\text{sat}}$  saturation pressure of  $\text{H}_2\text{O}$  at a given temperature. 58
- $z$  perpendicular distance from substrate. 6, 18, 19, 98, 118, 157, 235, 251, 252, 298, 302
- $C_{\text{surf}}$  Concentration of surfactant. 192, 201, 205
- $Q$  Momentum transfer of incident neutrons or X-rays. 79, 80, 82, 89, 91, 99, 100, 104, 106
- $R$  Reflected intensity, normalised by the intensity of the incident beam. 99
- $\Gamma$  The adsorbed mass of a given component, in units of mass per area. 154, 155, 300
- $\alpha$  Degree of ionisation for a given surfactant molecule. 143, *Glossary*: degree of micelle ionisation
- $\hat{V}_{\text{I}}$  volume of the interfacial component of interest. 4, 15, 18, 20, 22, 24, 26, 43, 51, 57–60, 62, 64, 67, 68, 79–81, 84, 86–88, 93, 94, 99, 101–104, 106, 108, 119, 126, 131, 157, 159, 161, 162, 170, 171, 183, 185, 189, 191, 208, 222, 235, 237, 238, 251, 302, *Glossary*: interfacial volume
- $\text{CMC}^{\text{eff}}$  critical micelle concentration at a given solution composition and temperature. 141, 187–189, 191–196, 198, 200, 201, 203–205, 207, 212
- $\text{CMC}^{\circ}$  critical micelle concentration for a surfactant in pure  $\text{H}_2\text{O}$  at 25 °C. 141, 161, 162, 165–172, 175–179, 181, 183, 184, 188, 189, 191–199, 202, 207

$dn/dC$  change in refractive index with change in concentration. 153, 156

$q_n$   $\lim_{\Gamma \rightarrow 0} q$ . 155, 156

$q$  Sensitivity factor for FAOR, at a given  $\Gamma$  value. 154, 155, 300

# Glossary

**D<sub>2</sub>O** Deuterated water, deuterium oxide. 21, 38–40, 45–50, 57, 60, 65–68, 72, 73, 158–160, 169–171, 173, 196–198, 210, 216, 218–221, 250, 301

**PLATYPUS** The time-of-flight reflectometer at the ACNS at ANSTO. 40, 67, 91, 113, 213

**refellips** Reflectometry analysis package developed in Python by Hayden Robertson and Isaac Gresham. See Appendix F for more details. 233, 234, 251

**refnx** Reflectometry analysis package developed in Python by Andrew R.J. Nelson. See reference [141] for more details. 20, 233, 234, 251

**AdG** The model of brush structure described by Alexander [31] and de Gennes [32]. It describes the brush as an equally-stretched array of polymer chains. 6, 7

**bromination** The second step in our polymerisation methodology, in which BiBB is reacted with the deposited APTES layer, producing a surface with tethered organobromine moieties, which serve as initiators for the polymerisation process. 14, 29, 31, 32, 34–37, 42, 43, 45, 46, 52, 53, 218

**CM<sub>poly</sub>** a mix of 80.3:19.7 H<sub>2</sub>O and D<sub>2</sub>O by volume, designed to match the SLD of PNIPAM. 20, 91, 158–160, 172, 173, 175, 176, 178, 183, 196–198, 206, 208, 216, 222, 251

**co-refine** To link parameters across reflectivity models and refine them against multiple datasets simultaneously. 68, 222, 234

**Debye length** A measure of how far the electrostatic effect of a charged moiety (i.e., an ionic surfactant headgroup) persists in a solution. 187, 188, 200, 201, 203

**degree of micelle ionisation** the fraction of surfactant headgroups that are charged in a given micelle. 143, 168

**deuterate** To replace one or more hydrogen atoms with a deuterium atom; in the context of this thesis deuteration is generally performed intentionally to raise the neutron SLD of a material. 21, 34, 38, 39, 56, 73, 76, 90, 93, 95, 142, 153, 158–160, 172, 181, 210, 216, 295, 301

**dry thickness** The thickness of the polymer layer at ambient conditions, at which the layer may contain some water. The term *interfacial volume* is used to refer to the true dry thickness. 4, 25, 41, 43, 44, 46, 47, 51, 99, 113, 114, 131, 157, 193, 208, 211

**first moment** The centre of mass of the polymer volume fraction profile, given by

$$\frac{\int_0^\infty z \phi_{\text{poly}}(z) dz}{\hat{V}_1}$$

where  $z$  is distance from the substrate and  $\phi_{\text{poly}}(z)$  is the polymer volume fraction. 189, 303

**free surfactant** surfactant not bound to an interface or solvated macromolecule (e.g., a polymer chain). 143, 145, 147, 148, 152, 200

**Hofmeister series** The Hofmeister series is a system for classifying ions based on how they modify the solubility of macromolecules (generally proteins or polymers). The mechanisms behind this series are poorly understood. 146, 188

**initiation efficiency** The percentage of tethered polymerisation initiators that successfully grow into polymer chains. 30, 32, 33, 36, 42, 43, 53

**interfacial volume** The total volume of the component of interest adsorbed or tethered to the substrate per unit area. Referred to elsewhere as the adsorbed amount or true dry thickness. 4, 18, 25, 31, 44, 48, 49, 51, 56, 57, 69, 73, 75, 76, 79, 84, 88, 93, 102–104, 106, 157, 160, 185, 188, 210, 211, 237, 302, 303

**interior layer** The dense, substrate adjacent layer that is observed for brushes prepared via surface-initiated ATRP by neutron reflectometry. 26, 28, 30, 31, 40, 41, 45, 48, 50–53, 93, 96, 137, 169, 172, 192, 193, 208, 210, 211, 303

**Kiessig fringe** An interference pattern formed by the reflection of coherent radiation from a surface coated with thin film/s with thickness on the order of the radiation wavelength. Manifests in a  $R$  vs  $Q$  plot as characteristic peaks and troughs (fringes). Fringe spacing is related to the layer thickness (for the case of a single layer), see Section 1.5.2. 19, 85, 169

**Krafft point** the temperature at which the solubility of a surfactant is equal to its CMC. 143, 205

**Kuhn length** The displacement length of the polymer segment that can be considered a rigid-rod (Kuhn segment) in the theoretical treatment of polymer behaviour. 6, 9

**micelle** A spontaneously formed liquid-phase supramolecular assembly comprised of surfactant molecules, created to maximise contact between the solvent and the solvophilic component of the surfactant, and minimise contact between the solvent and the solvophobic component. 8, 141, 143, 146–151, 168, 179, 180, 187, 200, 202–207, 212, 301

**monomer shielding** A phenomena that occurs during surface-initiated ATRP whereby longer chains prevent monomer from reaching shorter chains, as in Martinez et al. [97]. 30–32, 39, 43, 44, 51, 53

**pearl-necklace model** a structural model of a polymer-surfactant system in which complete surfactant micelles adsorb to the polymer backbone at regular intervals. 148, 151, 168, 187

**prior distribution** A distribution that encodes the knowledge of a particular parameter (or set of parameters) before evidence is taken into account. 92–94, 105, 106, 222–229

**proximal layer** The substrate-adjacent slab layer used in the modelling of polymer brush NR data (as described in chapter 4) to allow for Gaussian roughness between the silica substrate and polymer brush. While the presence of an interior layer is not enforced by the inclusion of the proximal layer in the model, the proximal layer often ends up representing the interior layer. 86–88, 158

**pseudo-polyelectrolyte** a polymer-surfactant complex that can be thought of as a polyelectrolyte, that is, a polymer chain with charged moieties. 151, 181, 185, 187, 188

**solvent quality** The ability of a given solvent to solvate a particular polymer; is generally a function of solvent identity and temperature. In some cases this can be reduced to the Flory-Huggins solvent interaction parameter,  $\chi$ . 3

**swelling ratio** The thickness of a slab-like polymer layer divided by its interfacial volume. For diffuse polymer layers the twice the first moment of the volume fraction profile is used as a proxy for the layer thickness. 57, 189, 192



**tacticity** The stereochemical arrangement of the monomers in a polymer chain; for PNIPAM it refers to the orientation of the amide with respect to the backbone.

10